SUBFILTER-SCALE TURBULENCE MODELING FOR LARGE-EDDY SIMULATION OF THE ATMOSPHERIC BOUNDARY LAYER OVER COMPLEX TERRAIN

A DISSERTATION
SUBMITTED TO THE DEPARTMENT OF CIVIL AND ENVIRONMENTAL ENGINEERING
AND THE COMMITTEE ON GRADUATE STUDIES
OF STANFORD UNIVERSITY
IN PARTIAL FULFILLMENT OF THE REQUIREMENTS
FOR THE DEGREE OF
DOCTOR OF PHILOSOPHY

Fotini Katopodes Chow
July 2004

I certify that I have read this dissertation and that, in my opinion, it is fully adequate in scope and quality as a dissertation for the degree of Doctor of Philosophy.

Robert L. Street
(Principal Adviser)

I certify that I have read this dissertation and that, in my opinion, it is fully adequate in scope and quality as a dissertation for the degree of Doctor of Philosophy.

Joel H. Ferziger
(Mechanical Engineering)

I certify that I have read this dissertation and that, in my opinion, it is fully adequate in scope and quality as a dissertation for the degree of Doctor of Philosophy.

Mark Z. Jacobson

I certify that I have read this dissertation and that, in my opinion, it is fully adequate in scope and quality as a dissertation for the degree of Doctor of Philosophy.

Francis L. Ludwig

Approved for the University Committee on Graduate Studies.

Abstract

Our ability to accurately predict the evolution and dynamics of the atmospheric boundary layer over steep, mountainous terrain is limited by the sparsity of experimental observations and deficiencies in numerical models. The difficulties with the latter arise primarily from insufficient grid resolution, inadequate turbulence models, and poor representation of the rough lower boundary. In this dissertation, several new steps towards addressing these numerical difficulties are presented for large-eddy simulations (LES) of the atmospheric boundary layer over complex terrain.

First, a new series expansion model based on Taylor series is presented to reconstruct the resolved subfilter-scale (SFS) turbulent stresses. Variations of this series expansion are combined with dynamic eddy-viscosity models for the subgrid-scale stresses to create a dynamic reconstruction model (DRM). The effect of other numerical errors is also addressed in the context of explicit filtering for LES. The DRM yields significant improvements over standard eddy-viscosity closures in simulations of low Reynolds number turbulent channel flow. In particular, the SFS stress representation obtained with increasing reconstruction levels approaches the values predicted by direct numerical simulations.

The DRM is then evaluated for neutral atmospheric boundary layer flow (over flat terrain) at high Reynolds number and with bottom roughness. A near-wall stress model is used to account for the effects of subgrid roughness elements. The agreement of the mean velocity profiles with the expected logarithmic profile predicted by similarity theory shows great improvement with the DRM over traditional turbulence closure methods. The DRM is also validated for full-scale simulations of flow over Askervein Hill, Scotland. Improved comparisons to field data are obtained over other models in this complex flow with intermittent separation in the lee of the hill.

Finally, high-resolution simulations are performed for flow in the Riviera Valley

in the Swiss Alps during the Mesoscale Alpine Programme. The steps necessary to achieve accurate simulations with such steep, complex terrain are described. Excellent agreement with field observations is obtained; valley wind transitions and the diurnal temperature variations are well reproduced. The sensitivity to soil moisture, land use data, topographic shading, and turbulence models is also determined.

Acknowledgments

My first words of thanks go to my adviser, Bob Street, who provided the perfect blend of guidance and freedom to lead me through my career at Stanford. Bob's enthusiasm for my work was always inspiring, and I thoroughly enjoyed all of our many long discussions over the years. Bob's constant encouragement especially helped when computer problems and code debugging seemed endless. I honestly could not have asked for a better adviser.

I thank the other members of my committee for their contributions as well. Joel Ferziger provided the inspiration for the original Taylor series turbulence modeling work, and shared his knowledge of the literature and history of large-eddy simulation. I thank Mark Jacobson and Frank Ludwig for asking probing questions and for their meteorological advice. A special thanks goes to Frank for his careful reading of my dissertation. I thank Jeff Koseff for his technical input and his continued mentorship throughout my time at Stanford. Finally, I thank Margot Gerritsen for serving as the chair of my oral examination committee.

I was fortunate to participate in several collaborative efforts with researchers at Stanford and elsewhere throughout my doctoral studies. I am grateful to Parviz Moin for his work with me on numerical errors in large-eddy simulations (Chapter 3). I thank Lucinda Shih for providing the DNS data used in Chapters 3 and 4 and for being a constant resource especially during the beginning years of my research. The Center for Turbulence Research Summer Program of 2002 was the venue for much fruitful discussion and discovery. I thank Jessica Gullbrand for her dedicated work with me on explicit filtering for large-eddy simulations (Chapter 5). I learned a lot from our in-depth discussions on the all the nuances of numerical simulations. Thanks are extended to Hervé Jeanmart and Grégoire Winckelmans who contributed through many discussions during the CTR summer program, and to Oleg Vasilyev

for providing the channel flow codes.

My ventures into the realm of the atmospheric boundary layer were aided by several people. First of all, the assistance of Ming Xue with the ARPS code was invaluable. His patient answers to my questions are greatly appreciated, as are his scientific contributions to my work on atmospheric boundary layer simulations (particularly Chapters 6-8). Many thanks also go to Yunheng Wang and others from the ARPS support team for their help with learning, modifying, and debugging ARPS. I am thankful to Ric Cederwall, Branko Kosović, Chin-hoh Moeng, and Peter Sullivan for discussions about neutral boundary layer simulations. Evgeni Fedorovich and Bob Conzemius pushed me to consider (and simulate) convective boundary layer flows. I thank Peter Taylor, Wensong Weng, and Gordon Stubley for providing observation data for the Askervein Hill simulations (Chapter 7). Many thanks go to Augustin Colette for his dedicated work on topographic shading and inversion layer breakup which opened the doors for studying the dynamics of valley flows.

Simulations of the Riviera Valley in Switzerland brought an exciting new dimension to my numerical modeling efforts, as well as many excellent collaborations. First, I thank Andreas Weigel for his continued work with me using ARPS to simulate such a complex flow (Chapter 8). Our many discussions and joint efforts to decipher and incorporate various dataset formats were crucial to our progress. I am especially thankful for Andreas' insightful contributions to understanding the physical features of the Riviera Valley flow and for providing me with the observation datasets for comparison. Mathias Rotach was also instrumental in this effort, and I thank him for his scientific contributions as well as for being amenable to this collaboration from our first discussions several years ago. I extend many thanks to Stephan de Wekker, who pioneered the first detailed modeling efforts of the Riviera Valley, and provided many hints, especially in the initial stages of my work. Many other people helped provide access to datasets needed for the Riviera simulations. Thanks go to Massimiliano Zappa and Karsten Jasper for providing soil moisture initialization data from WaSiM. I thank André Walser, Oliver Fuhrer, and Stephane Chamberland for helping with MC2 data. Hans Volkert and Magdalena Rucker provided access to a high-resolution topography dataset for Switzerland. Koen de Ridder helped facilitate reading ECMWF data into ARPS, and C.C. Lam helped us incorporate higher resolution landuse data into ARPS.

The Environmental Fluid Mechanics Laboratory at Stanford was a wonderful environment to work in. I am grateful to the faculty who set the tone by their example, and also to all the students and other members of the lab. I especially thank the computer system administrators (Lucinda Shih, Oliver Fringer, Yu-Heng Tseng, Ying Chen, Johanna Rosman, and Miles Davis, and my co-administrators Cristina Lozej Archer and Emily Zedler), and my officemates (Nancy Monsen, Jessie Lacy, Ying Chen, and others). I also thank Gerard Ketefian, Derek Fong, Lucinda Shih, Emily Zedler, Yu-Heng Tseng, and Oliver Fringer for being excellent sources of technical advice. I thank all of the above, as well as Rachel Simons, Nicole Saenger, Anna Michalak, Jeremy Bricker, Alex Horner-Devine, Sandy Chang, Matt Reidenbach, Jan Wang, and many, many others for their friendships, discussions on research and careers, lunches, and all the other ways they made the lab a great place to be. I also thank Jill Nomura Fong for always making sure the lab runs smoothly.

I am grateful to all of my friends, family, and mentors for their constant support and encouragement. My parents have always been a source of wisdom; I will always be grateful for their unconditional love and support. My dad somehow managed to lure me into the field of environmental fluid mechanics, and I am very happy for that. I thank him also for his professional mentorship. My mom's support through email and phone calls was absolutely invaluable. I thank my sister for always being there. I also thank my in-laws for their support. I am grateful to all my friends across the country, from all stages of my life, who have always been there to listen and to encourage me.

My deepest thanks go to my husband, Eugene, for his constant love, daily encouragement, and support. He has always helped me keep my perspective on life, and pushed me to do my best and expect the best, throughout my dissertation work and beyond. I am truly blessed to have him as my partner in life.

Financial support for this work was provided by a National Defense Science and Engineering Graduate fellowship and National Science Foundation Grant ATM-0073395 (Physical Meteorology Program: W.A. Cooper, Program Director); both are gratefully acknowledged. Acknowledgment is also made to the National Center for Atmospheric Research, which is sponsored by the National Science Foundation, for the computing time used for the simulations in Chapters 6-8.

Nomenclature

Roman Symbols

a	Near-wall stress model smoothing function; radius of earth; generic variable
a_{ij}	SGS stress model
A_{ij}	SGS stress model at test level
$\overline{A}_{ij}$	SGS stress tensor
$A_{i,j}$	Generic function of position and time
A_G	Amplitude coefficient using Gaussian filter
A_T	Amplitude coefficient using tophat filter
b	Parameter in Lambert projection; generic variable
B_{ij}	RSFS stress tensor
$B_{i,j}$	Generic function of position and time
c_{ij}	Resolvable Reynolds stress
C	Correlation coefficient
C_c	Near-wall stress model proportionality factor
C_{dm}	Log-law drag coefficient
C_ϵ	Dynamic Wong-Lilly model coefficient
C_u	Non-stationarity measure in x direction
C_v	Non-stationarity measure in y direction
C_S	Smagorinsky coefficient
D	Domain depth
ds	Linear segment
dx_i	Differential position vector
$d\mathbf{x}$	Differential position vector

$d\mathbf{q}$	Differential position vector in new coordinates
$\mathbf{e}_x, \mathbf{e}_y, \mathbf{e}_z$	Base vectors in Lambert coordinates
$\mathbf{e}_r, \mathbf{e}_\lambda, \mathbf{e}_\psi$	Base vectors in spherical coordinates
$\overline{e}_{ij}$	Filtered Reynolds stress
E	Three-dimensional energy spectrum
f	Coriolis parameter; generic variable
f_n	Coriolis parameter vector
f_v	Vertical Coriolis parameter
$\mathcal{F}$	Fourier transform operator
g	Gravitational acceleration
G	Filter operator
$\sqrt{G}$	Determinant of transformation matrix
$\overline{G}$	Explicit filter
$\hat{G}$	Test filter
$\overline{\hat{G}}$	Effective test filter
G_G	Gaussian filter in Fourier space, one-dimensional
G_T	Tophat filter in Fourier space, one-dimensional
h	Terrain height; half-width of channel
h_c	Near-wall stress model layer height
h_i	Mapping factors
h_x, h_y, h_z	Mapping factors for Lambert coordinates
H_G	Gaussian filter, one-dimensional
H_T	Tophat filter, one-dimensional
H_{ij}	Tensor in dynamic Wong-Lilly computation
i	Square root of -1; index in x or x_1 direction
I	Identity matrix
j	Index in y or x_2 direction
J_1, J_2, J_3	Jacobians of transformation
k	Wavenumber; TKE; index in z or x_3 direction
k'	Modified wavenumber
k_1, k_2, k_3	Wavenumbers in (x_1, x_2, x_3) directions
K_T	Eddy diffusivity
l	Turbulent length scale

L, L_{obu}	Obukhov length
L_{ij}	Leonard term stress tensor
m_{ij}	RSFS stress model
M_{ij}	RSFS stress model at test level
M	Number of time steps
n	Parameter in Lambert projection; index
N	Number of grid cells
nx, ny, nz	Number of grid points in x, y, z directions
O	Order of magnitude
p	Fluid pressure
Pr	Turbulent Prandtl number
q	Specific humidity
q_*	Surface heat flux
q_{ij}	Tensor in dynamic model computation
q^2	Turbulent kinetic energy
Q_j	Turbulent heat flux
r	Radial spherical coordinate
r_{ij}	Tensor in dynamic model computation
R	Ratio coefficient
Re	Reynolds number
Re_τ	Turbulent Reynolds number
rgl	Solar radiation dependence
rsmin	Surface resistance
S	Horizontal wind speed
S_{RS}	Horizontal wind speed at reference site
S_{ij}	Strain rate tensor
t	Time
u	Horizontal velocity in the x or x_1 direction
$\mathbf{u}$	Velocity vector
u_*, u_τ	Shear or friction velocity
u'	Perturbation u-velocity
u_i	Unfiltered, full velocity, using Einstein notation
$\overline{u}_i$	Spatially filtered velocity

$\tilde{u}_i$	Discretized velocity
$\tilde{u}_i^c$	Discretized velocity on coarse test grid
$\overline{\tilde{u}}_i$	Spatially filtered and discretized velocity
$\tilde{u}_i^\star$	Reconstructed velocity
$\overline{\tilde{u}}^*, \overline{\tilde{v}}^*, \overline{\tilde{w}}^*$	$\overline{\tilde{u}}, \overline{\tilde{v}}, \overline{\tilde{w}}$ multiplied by ρ^*
U	Horizontal velocity magnitude
U_g	Geostrophic wind in x direction
$u'u', v'v', w'w'$	Turbulence intensities
$\overline{u'w'}\|_0, \overline{uw}_s$	Total turbulent surface momentum flux, same for vw
v	Horizontal velocity in the y or x_2 direction
V_g	Geostrophic wind in y direction
V_{min}	Minimum velocity magnitude for log-law
w	Vertical velocity in the z or x_3 direction
$\overline{\widetilde{W}}^c$	Contravariant filtered and discretized vertical velocity
$\overline{\widetilde{W}}^*$	$\overline{\widetilde{W}}^c$ multiplied by ρ^*
x_j, x_j'	Position vectors
x,y	Horizontal coordinates
x_c, y_c, z_c	Cartesian coordinates
y	Vertical coordinate (Chapters 3 and 5)
y^+	Vertical coordinate in wall units (Chapter 5)
z	Vertical coordinate
z_i	Inversion height or boundary layer depth
z_0	Roughness length
z_{flat}	Height at which σ-coordinates become flat
z_{ref}	Reference height for σ-coordinates
z_{top}	Height of domain top

Greek Symbols

α	Filter-grid ratio
α_{eff}	Effective filter-grid ratio
β	Coefficient in scale-dependent dynamic model
γ	Coefficient in two-part eddy viscosity model
δ_{ij}	Kronecker delta or identity tensor
Δ	Filter width
$\tilde{\Delta}$	Grid spacing
$\overline{\Delta}$	Explicit filter width
$\hat{\Delta}$	Test filter width
Δ_g	Grid spacing
Δ_f	Filter width
Δ_{DNS}	DNS grid spacing
Δ_{LES}	LES grid spacing
$\Delta_x, \Delta_y, \Delta_z$	Filter width in (x, y, z) directions
$\Delta x, \Delta y, \Delta z$	Grid spacing in (x, y, z) directions
$\Delta_x^+, \Delta_y^+, \Delta_z^+$	Grid spacing in (x, y, z) directions in wall units
Δz_{avg}	Average vertical grid spacing
Δz_{min}	Minimum vertical grid spacing
ΔS	Fractional speed-up ratio
Δt	Time step; large time step
$\Delta \tau$	Small time step
$\Delta \Phi$	Wind direction deviation
ϵ	Turbulent dissipation rate
ϵ_{ijk}	Permutation tensor
θ	Potential temperature
θ_*	Potential temperature surface flux
κ	Spherical wave number; molecular diffusivity
κ_m	Maximum wave number
κ_T	Turbulent scalar diffusivity
λ	Longitude
λ_0	Reference or true longitude

μ	Terrain-following vertical coordinate
ν	Kinematic viscosity
ν_e,ν_T	Eddy viscosity
ξ, η, ζ	Mapped (x, y, z) coordinates
ρ	Fluid density; auto-correlation
ρ_0	Reference density
$\breve{\hat{\rho}}$	Favre filtered and discretized density
$< \rho >$,$< \breve{\hat{\rho}} >$	Horizontally plane-averaged density
ρ^*	$\breve{\hat{\rho}}$ multiplied by $\sqrt{G}$
σ-z	Terrain-following vertical coordinate system
σ_*	Global error measure
σ_T	Turbulent Schmidt number
τ	One-dimensional stress
τ_T	One-dimensional stress model
τ_{M1}	One-dimensional stress model
τ_{GM1}	One-dimensional stress model
τ_{ij}	Subfilter-scale turbulent stress tensor
τ_{SGS}	SGS turbulent stress tensor
τ_{RSFS}	RSFS turbulent stress tensor
$\tau_{Resolved}$	Resolved stress tensor
τ_{Total}	Total stress tensor
$\tau_{i,near-wall}$	Near-wall stress
ϕ	Wind direction; generic variable
Φ	Non-dimensional velocity gradient
ψ	Co-latitude
Ω	Coriolis vector

Acronyms

ABL	Atmospheric boundary layer
ADM	Approximate deconvolution model
agl	Above ground level
ARPS	Advanced Regional Prediction System
asl	Above sea level
B	Bardina model
CBL	Convective boundary layer
CET	Central European time
DMM	Dynamic mixed model
DNS	Direct numerical simulation
DRM	Dynamic reconstruction model
DRM1 - DRM10	Different levels of DRM with ADM
DRM-ADM	DRM with ADM
DRM-ADM1 - DRM-ADM10	DRM with different levels of ADM
DRM-MC	DRM with modified Clark model
DRM-SMAG	DRM with modified Smagorinsky near wall
DSM	Dynamic Smagorinsky model
DTM	Dynamic two-parameter model
DWL	Dynamic Wong-Lilly
ECMWF	European Centre for Medium-Range Weather Forecasts
$E2, E4, E6$	Modified Taylor-series 2nd-6th order scalar model
FD	Finite difference
FGR	Filter-grid ratio
FSL	Forecast Systems Laboratory
GC	Constant geostrophic wind case
GR	Grid ratio
GS	Constant geostrophic shear case
LAI	Leaf-area index
LES	Large-eddy simulation
MC	Modified Clark model
ML	Mixed layer

MC2	Mesoscale Compressible Community model
MM5	Mesoscale Model, Fifth Generation
MPI	Message passing interface
$MT4, MT6$	Modified Taylor-series 4th-6th order model
NBL	Neutral boundary layer
NCAR	National Center for Atmospheric Research
NCDC	National Climatic Data Center
NL	Non-linear
NP	Number of processors
NS	No shear case
PBL	Planetary boundary layer
RAMS	Regional Atmospheric Modeling System
RANS	Reynolds-averaged Navier-Stokes
rms	Root-mean-square
rmse	Root-mean-square error
RSFS	Resolved subfilter-scale
S	Smagorinsky model
SBL	Stable boundary layer
SFS	Subfilter-scale
SGS	Subgrid-scale
SMAG	Smagorinsky
SSM	Scale similarity model
$T4$	Taylor-series 4th order model
TDM	Tensor-diffusivity model
TKE	Turbulent kinetic energy
USGS	United States Geological Survey
USFS	Unresolved subfilter-scale
UTC	Universal time coordinate
WaSiM-ETH	Water Flow and Balance Simulation Model, Swiss Federal Institute of Technology

Contents

List of Tables

List of Figures

Chapter 1

Introduction and overview

High-resolution large-eddy simulations (LES) of the atmospheric boundary layer have recently become possible due to increases in available computational power. These numerical simulations provide us with three-dimensional, time-dependent velocity and scalar fields that describe physical processes in the atmosphere which can often not be captured by relatively sparse field measurements. The performance of numerical simulations is limited, however, by the accuracy of the equations, parameterizations, and boundary and initial data that are used. Because atmospheric flow simulations involve complex topography and are generally under-resolved, there are many challenges in predicting the flow correctly. Areas in which significant improvements are needed include turbulence modeling and lower boundary conditions, particularly for flow over terrain. The vast majority of existing large-scale numerical simulations rely on substandard turbulence models, which can greatly compromise the accuracy of their results. In this dissertation, new subfilter-scale (SFS) turbulence closure models are developed and applied to simulations of the atmospheric boundary layer, with a focus on flow over complex terrain. This chapter presents motivation for this work, followed by an overview of the results of this research.

1.1 Motivation and background

1.1.1 The need for better understanding of the atmospheric boundary layer

The atmospheric boundary layer (ABL) is the region of the atmosphere which most directly affects human, animal, and plant life. The ABL (also known as the planetary boundary layer, or PBL) is the lowest portion of the troposphere, the region of the atmosphere closest to the earth's surface. Surface forcings affect the ABL on a time scale of about an hour or less. The ABL varies in depth, usually extending 1-3 km into the troposphere, though this often depends on the presence of terrain (Stull, 1988).

Understanding the physical processes that occur in the ABL is crucial for weather and climate predictions, which have enormous economic impact. For example, one third ($\sim$ \$3 trillion annual revenues) of the gross domestic product contributed by private industry is thought to be affected by weather and climate (Dutton, 2002). Insurance payments for property damage and losses due to severe weather events (such as tornadoes, storms, floods, extreme hot or cold temperatures) amount to billions of dollars each year (Changnon, 2003). Furthermore, agriculture and food production, as well as transportation safety, national security, and even tourism, are affected by the accuracy of weather prediction. Public confidence in the accuracy of weather predictions also affects economic and personal choices.

Accurate predictions of wind and temperature fields near the earth's surface are also required for air quality prediction and control. A temperature inversion layer (where temperature increases with height) can cap the ABL, preventing the rise of eddy motions above this level, and effectively containing the air. New air is entrained only very gradually by wind shear at the top of the inversion layer. The inversion thus limits the dispersion of pollutants and other suspended particles and is responsible for the formation of smog layers over urban regions, such as Los Angeles. Urban environments pose a particular challenge for prediction models because of the heterogeneity of urban layouts; however, prediction systems in these areas are crucial for protecting personal health and safety (e.g. for smog control, and to mitigate the impact

of accidental chemical releases). Topographic features, such as buildings and mountains, can significantly modify the character of the ABL, as discussed below. Robust numerical simulation tools are clearly necessary to accommodate the variability and complexity of atmospheric flows and provide accurate forecasts.

1.1.2 Properties of the atmospheric boundary layer

In order to numerically simulate atmospheric flows, we must be aware of the range and significance of forcings which will influence flow in the domain of interest. The scales of motion in the atmosphere range from molecular scales smaller than 2 mm, at which molecular diffusion is important, to planetary scales larger than 10 000 km which include features such as global wind systems. At intermediate levels are the microscale (2 mm to 2 km, including eddies, plumes, and cumulus clouds), the mesoscale (2 to 2000 km, including thunderstorms and local winds), and the synoptic scale (500 - 10 000 km, including high and low pressure systems and weather fronts) (Jacobson, 1998). The range of interest for the studies described here is the mesoscale. Pielke (1984) further defines the mesoscale as having a horizontal scale large enough to use the hydrostatic equations, but small enough so that Coriolis terms are not very large. The mesoscale is also classified as the meso-β scale defined by Orlanski (1975). When vertical accelerations become important, i.e., motions are no longer hydrostatic, the scale of motions is the meso-γ scale. This is also sometimes called the cumulus scale and is smaller than the mesoscale defined above. On scales larger than the mesoscale, the Coriolis effect can be as large as the pressure gradient forcing; these scales are called regional or synoptic scales, or meso-α scales. In the studies described here, we will be interested in meso-γ scale flows, as the influence of topography will make vertical accelerations important.

The scales of fluid motions in the ABL also depend on the thermal stratification in the atmosphere, which can be stable, neutral, or convective. In a stable boundary layer (SBL), stable stratification suppresses turbulence, and vertical motions are inhibited. This type of boundary layer is the hardest to simulate as mixing is inhibited and turbulent structures become finer or intermittent and hence more difficult to resolve. In a convective boundary layer (CBL) on the other hand, surface heating drives large, resolvable, convective motions which mix the boundary layer thoroughly. This

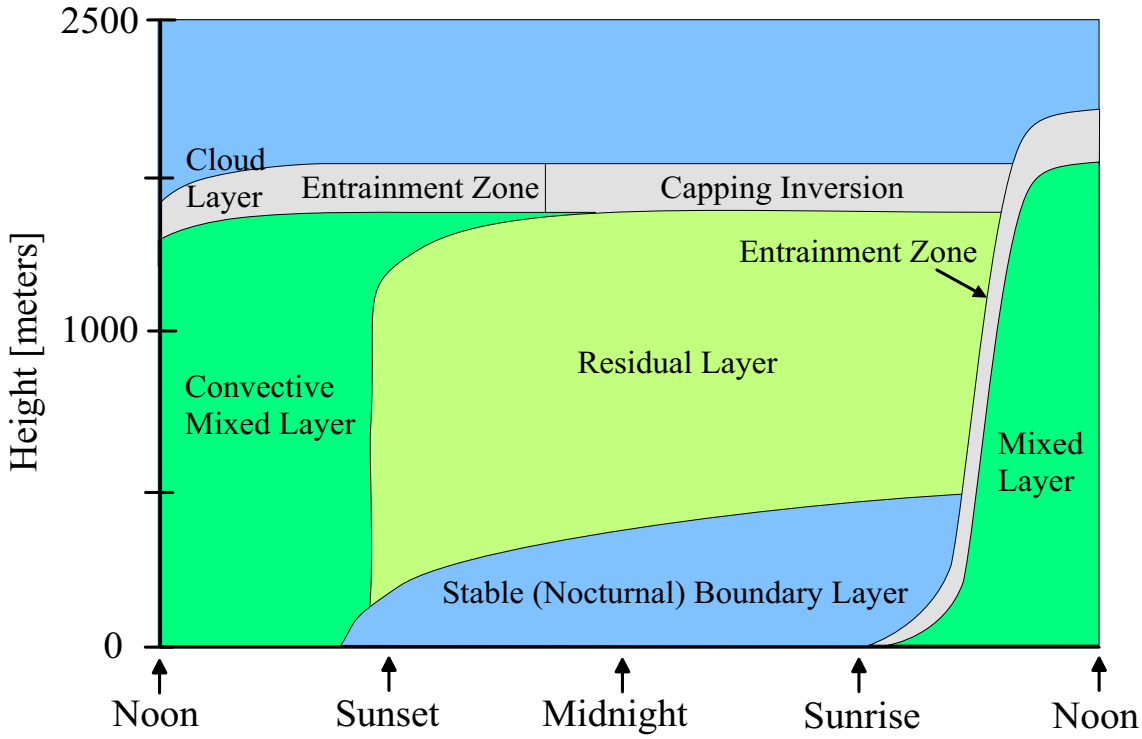

Figure 1.1: Schematic of ABL evolution throughout the day (adapted from Stull, 1988).

mixed layer (ML) grows in height during the day due to heating at the surface; in the evening, the surface cools and a stable layer is created near the surface (see Figure 1.1). A neutral boundary layer (NBL) is one in which the temperature decrease with increasing height exactly follows the adiabatic lapse rate, and is not as common in the atmosphere, though near-neutral boundary layers are often observed. (See Stull (1988) for further details on boundary layer meteorology.) In general, the ABL can be in any of these states at different heights, thus requiring that numerical models be able to accommodate any of these cases, as well as transitions between them. Much of the burden often lies with the turbulence closure scheme, which is responsible for contributing to the correct amount of mixing in the atmosphere.

1.1.3 Effects of terrain on the atmospheric boundary layer

Predictions of ABL evolution are further complicated by the presence of complex terrain, such as for flow through valleys or over hills. The evolution of the boundary layer is different in a valley because of the presence of cross-valley and along-valley winds. For example, surface heating creates anabatic (warm, up-slope) winds, while surface cooling creates katabatic (cool, down-slope) winds. Differential heating on valley slopes due to the orientation of each slope toward the sun can thus generate cross-valley circulations. Along-valley flows (mountain/valley winds) are also present due to heating/cooling effects. Flow over hills can generate lee waves, rotors, and boundary layer separation on the lee side, depending on the speed of the winds and the hill height. If the boundary layer separates behind the hill, there will be a turbulent wake region, about the same size as the hill and decaying further downwind. The height of the mixed layer (effectively the boundary layer height) can also be affected by the presence of terrain. If the inversion height, z_i is larger than the terrain or hill height, z_{hill}, slow background wind speeds can draw down the inversion due to the decrease in pressure above the hill as the wind speeds up (due to the Bernoulli principle). If winds are strong, a down-slope windstorm can occur followed by a hydraulic jump. If $z_i \gg z_{hill}$, the hill does not have much effect on the mixed layer depth. For $z_i < z_{hill}$, the air must flow around the hill as it cannot penetrate the inversion layer (Stull, 1988). The ABL is further modified by changes in terrain roughness; an internal boundary layer forms within the existing boundary layer as air flows over one roughness scale to another.

1.1.4 Needed improvements for numerical simulations

Current techniques for numerical simulations of ABL flows have many deficiencies, particularly with regard to turbulence models and lower boundary conditions. Flows in the ABL are highly turbulent, with a Reynolds number of order 10^8, placing considerable importance on the turbulence parameterizations used. In addition, the earth's surface is rough, resulting in a viscous sublayer region which is only a few millimeters thick; this is extremely small compared to a typical boundary layer depth of a few kilometers. The large range of scales of motion makes it next to impossible to resolve all of the fluid motions on a discrete grid, placing considerable importance on the

turbulence model, especially near the surface. Results are also highly dependent on the approximate boundary conditions used at the bottom surface.

The most commonly used turbulence models for LES of atmospheric flows, the Smagorinsky and the 1.5-order turbulent kinetic energy (TKE) eddy-viscosity models, have several undesirable features. Eddy-viscosity models are highly dissipative, do not allow for backscatter of energy from small scales to large scales, and do not correlate well with direct numerical simulation (DNS) data in *a priori* tests. Eddy viscosity models are also isotropic, by definition, and hence cannot account for anisotropic effects (inhomogeneities) associated with proximity to the surface (Juneja & Brasseur, 1999). The reason for the widespread use of eddy-viscosity models, despite these many known deficiencies, is their simplicity, and the belief that in the interior of the flow the simulation is relatively insensitive to the SFS turbulence model chosen (Khanna & Brasseur, 1998). This is true for the mixed layer in the atmosphere, away from boundaries, where the energy containing scales are resolved. Near boundaries, however, the horizontal scales of the velocity increase with height from the boundary, hence, the filter scale (associated with the grid spacing) is larger than the turbulent motions at the wall and the SFS model becomes critical because it must represent the energy containing scales.

Several studies have shown that errors near the surface can propagate upward and affect the solution in the entire boundary layer (see Juneja & Brasseur, 1999; Khanna & Brasseur, 1998). The eddy-viscosity models spuriously couple the anisotropy of the resolved field with that of the modeled SFS acceleration, and hence do not predict the correct energy flux between resolved and SFS scales. Juneja & Brasseur (1999) suggest that additional degrees of freedom are required in the SFS model. Indeed, numerical simulations done by Cederwall & Street (1999) using improved SFS closures (non-eddy-viscosity models) revealed turbulent motions observed in the atmosphere that had not previously been seen in simulations.

The bottom boundary condition is another important component of ABL simulations which is currently poorly represented. It is common to represent the rough boundary using similarity laws and aerodynamic drag coefficients calculated from empirical roughness heights. One of the most often applied similarity laws is Monin-Obukhov theory, which uses the Obukhov length, L, and the shear velocity, u_*, to

specify the velocity profile at the wall (Stull, 1988). The Obukhov length is proportional to the height above the surface at which buoyancy production dominates shear production of turbulence, and thus gives an indication of how convective the ABL is. Monin-Obukhov scaling results in a mixed logarithmic and linear velocity profile depending on the local stability conditions. The assumptions behind these approximate boundary conditions do not, however, allow for simulation of the general ABL, as the similarity profiles are not necessarily appropriate for complex flow over topography where separation can occur and the flow is not steady.

1.2 Overview

Improved numerical models for the atmospheric boundary layer are necessary to further our understanding of physical processes that occur in the atmosphere, particularly due to flow over complex terrain. The goal of this dissertation is to improve several aspects of numerical simulations of the ABL, with the primary focus on developing new turbulence modeling approaches for large-eddy simulations.

We begin in Chapter 2 with a discussion of the challenges and current practices in large-eddy simulations of the atmospheric boundary layer. We describe common models and recent developments for turbulence closures in LES and discuss the limitations and options for representing the drag at the lower rough boundary.

Chapter 3 describes the development of a new series-expansion model for the subfilter-scale (SFS) turbulent stresses, τ_{ij}. The expansion is based on recursive substitution of Taylor series, and provides an estimate of the unfiltered velocity in terms of the filtered velocity. The theory developed in Chapter 3 considers only the effect of a smooth spatial filter and the approximate inversion given by the series expansion approach. The series expansion model performs excellently in *a priori* test comparisons with direct numerical simulation (DNS) data. The expansion is shown to also satisfy the evolution equations for the exact τ_{ij} to any specified order of accuracy. The effect of the grid and discretization are not treated in this chapter, but cannot be ignored; particularly in simulations of the ABL, a coarse grid resolution will limit the performance of series expansion models; this is left for further investigation in Chapter 5.

In Chapter 4, we consider in detail other numerical errors (aside from the turbulence closure question) that affect the performance of LES. Using DNS data from stably-stratified shear flow to perform *a priori* tests, we examine the errors introduced by discretization errors in the advection terms of the governing equations. These discretization and aliasing errors can often be larger than the entire turbulence forcing term. In agreement with the results of Ghosal (1996), it is shown that the choice of the filter width is crucial in limiting these numerical errors. The use of larger filter widths smooths the simulated fields and makes their numerical representation more accurate. Guidelines for determining a reasonable filter width are presented, based on the chosen numerical discretization scheme.

Chapter 5 presents large-eddy simulations of low Reynolds number turbulent channel flow using a new explicit filtering and reconstruction turbulence modeling approach. In this application, the ideas presented in Chapter 3 are extended by considering the additional effects of discretization incurred in an actual simulation. The SFS motions are further divided into resolved subfilter-scale (RSFS) and subgrid-scale (SGS) motions. Using (two-dimensional) explicit filtering to limit numerical errors, and series expansions (in this case based on the approximate deconvolution approach of Stolz *et al.* (2001*a*)) for the RSFS portion, and the dynamic Smagorinsky model for the SGS portion, we obtain improved comparisons with DNS data. In particular, the SFS stress representation obtained with increasing reconstruction levels approaches the values predicted by the DNS. These simulations provide a challenging test case for the reconstruction SFS modeling ideas because of the presence of solid walls, but the size of the domain and the Reynolds number are limited to those that can be considered by a DNS. Thus, the walls are smooth and the flow is relatively well-resolved.

In the atmospheric boundary layer, the case is much more complicated, as the lower boundary is rough, and the Reynolds number is many orders of magnitude higher. Chapter 6 considers LES of the neutral atmospheric boundary layer (over flat terrain) at large scales and with bottom roughness, thus including the challenge of limited near-wall resolution. Similar explicit filtering (now in three dimensions) and reconstruction ideas presented in the previous chapter are explored, and again improved results are obtained over traditional closure models. For the RSFS component, the Taylor series expansion models or the approximate deconvolution approach

(Stolz *et al.*, 2001*a*) are used. For the SGS component, the dynamic model of Wong & Lilly (1994) is implemented. In addition, a near-wall stress model taken after Brown *et al.* (2001) is used to account for the effects of the large grid-aspect ratio and the stress induced by filtering near a wall with subgrid roughness elements. The agreement of the mean velocity profiles with the expected logarithmic profile predicted by similarity theory for neutral flows improves with the new hybrid RSFS/SGS/near-wall-stress approach compared to eddy-viscosity models such as Smagorinsky. The representation of the total SFS stresses also improves with increasing reconstruction, as compared to the SFS stress obtained from higher-resolution simulations (DNS data are not available at these Reynolds numbers).

Chapter 7 extends the results from the studies over flat terrain to flow over topography. Specifically, we consider flow over Askervein Hill, an isolated hill in western Scotland, where a field campaign was conducted under neutral stratification and steady wind conditions (Taylor & Teunissen, 1987). This flow application provides a more challenging test case for the turbulence models presented in this dissertation because of the sloping terrain and separation in the lee of the hill, but still considers somewhat ideal conditions (e.g. steady winds and uniform surface properties). To provide a realistic turbulent inflow, a separate neutral boundary layer simulation with periodic boundary conditions is performed and data are extracted from a slice in the periodic domain at every time step. This turbulent dataset is then used to specify the inflow velocity at the western entrance of the Askervein domain. Results indicate that reconstruction and dynamic eddy-viscosity models, used together with the near-wall stress model, significantly improve the predictions of flow speed-up over the hill compared to the standard TKE-1.5 closure. High resolution is needed, particularly in the vertical direction. Attempts to use increased reconstruction (greater than level 0) over Askervein requires modification of the dynamic procedure near the wall because of the sensitivity of the turbulent quantities in this region of the flow.

In Chapter 8, we present simulations of flow over steep, mountainous terrain in the Riviera Valley, in the Swiss Alps. An extensive field campaign was conducted there, providing an excellent dataset for comparison of simulation results (Rotach *et al.*, 2004). The Riviera Valley flow presents a challenge for any numerical model, because of the steepness of the terrain, the high resolution necessary to resolve the narrow valley, the heterogeneity of the surface conditions, variability in the synoptic

forcing, and sensitivity to soil properties and solar radiation models, among other issues. The steps necessary to achieve accurate simulations of such a complex flow are described. Large-scale weather features are incorporated at the largest grid level and boundary information is passed on to the next finest grid through a one-way nesting scheme. High-resolution land use and soil moisture datasets, and a topographic shading subroutine are introduced, all contributing to an improved forecast. Excellent agreement with field observations is obtained; valley wind transitions and the diurnal temperature variations are well-reproduced. The sensitivity to soil moisture, land use data, and turbulence models is also examined at the finer resolutions. These improved results will be useful for future studies of the distribution of pollution in valleys, as well as for improving local weather predictions.

Chapter 9 summarizes the contributions of this work and provides recommendations for future directions for large-eddy simulations of the atmospheric boundary layer. The appendices include some details not included in the main chapters, such as further background, results from other simulations, and derivations of equations. Appropriate references to sections in the appendices are given throughout.

1.3 Summary of contributions

In summary, the main contributions of this research are:

1. A Taylor-series reconstruction approach for the resolved subfilter-scale turbulent stresses.

2. An investigation of numerical errors in large-eddy simulation.

3. A new combined reconstruction and eddy-viscosity turbulence closure approach for explicitly filtered large-eddy simulation called the dynamic reconstruction model (DRM).

4. Improved simulations of turbulent channel flow with smooth walls using the DRM.

5. Improved simulations of the neutral atmospheric boundary layer over a flat rough lower boundary using the DRM together with an enhanced near-wall stress model for surface roughness.

6. Validation of the DRM for flow over complex terrain and improved simulation of flow over Askervein Hill, Scotland.

7. Validation of the DRM for flow over steep, mountainous terrain and accurate simulations of flow in the Riviera Valley, Switzerland.

Chapter 2

Turbulence models and boundary conditions for simulations of the atmospheric boundary layer

We begin with a description of recent developments for subfilter-scale (SFS) turbulence models for large-eddy simulation, before introducing a new model in Chapter 3. Further details on the governing equations for LES and detailed derivations for the SFS terms can also be found in Chapter 3. The second half of this chapter is devoted to a discussion of boundary conditions, particularly for atmospheric flows over rough surfaces.

2.1 SFS turbulence modeling

Large-eddy simulation employs a spatial filter to separate the small scales from the large scales. The large eddies are explicitly calculated by prognostic equations, while the effect of the smaller eddies must be modeled. The application of this filter (denoted by an overbar; e.g. a Gaussian or top-hat filter) to the incompressible Navier-Stokes and continuity equations results in

$$\frac{\partial \overline{u}_i}{\partial t} + \frac{\partial \overline{u_i u_j}}{\partial x_j} = -\frac{1}{\rho}\frac{\partial \overline{p}}{\partial x_i} + \nu \frac{\partial^2 \overline{u}_i}{\partial x_j \partial x_j} \,, \qquad \frac{\partial \overline{u}_i}{\partial x_i} = 0 \,, \tag{2.1}$$

where $\overline{u}_i$ denotes the filtered velocity field for which we seek a solution, $\overline{p}$ is the filtered pressure, and Einstein summation notation is used. The filtered product of the velocities $\overline{u_i u_j}$ appearing in the advection term creates a closure problem for the equations because the unfiltered velocity field u_i is unknown. Bringing this term to the right-hand side and rearranging, we obtain the LES equations in their traditional form:

$$\frac{\partial \overline{u}_i}{\partial t} + \frac{\partial \overline{u}_i \overline{u}_j}{\partial x_j} = -\frac{1}{\rho}\frac{\partial \overline{p}}{\partial x_i} + \nu \frac{\partial^2 \overline{u}_i}{\partial x_j \partial x_j} - \frac{\partial \tau_{ij}}{\partial x_j} \tag{2.2}$$

where $\tau_{ij} = \overline{u_i u_j} - \overline{u}_i \overline{u}_j$ is defined as the subfilter-scale (SFS) turbulent stress. This SFS term must be parameterized as a function of the filtered velocity $\overline{u}_i$ to close the equations.

The SFS motions are responsible for energy dissipation, among other processes, and it is crucial that the SFS stress representation perform well so that the resolved quantities (represented by $\overline{u}_i$) are predicted accurately. The difficulty in formulating a closure model for LES is that modeling of the unresolved motions (contained in the correlation term $\overline{u_i u_j}$) must be based only on knowledge of the resolved motions ($\overline{u}_i$). Such a requirement means that the closure model is inherently imperfect, as the exact flow is influenced by higher-order velocity moments not present in the resolved field.*

There has been much success using SFS models for LES in numerous laboratory and real-scale problems, and improvements in model performance can be expected due to increased computing speed (which allows finer grid resolution). There remains, however, a need for the development of improved SFS models. A study by Andren *et al.* (1994) of neutral boundary layer flow concluded that differences in the numerics of LES codes were not as significant as the difference in the SFS closure models used. Andren *et al.* (1994) used four LES codes with the same closure model and obtained relative convergence of the mean profiles. In general, the differences due to SFS models were found to be more significant for the neutrally stratified flow tested than for previous tests of convective flow.

The vast majority of LES studies of the ABL have used eddy-viscosity models.

*One example of this is that in channel flow simulations, the resolved velocity profile (spatially filtered) can become steady in time before the turbulent quantities do. Thus, a SFS model based on the resolved velocity (first-order moment) may have difficulty modeling the turbulent quantities accurately since higher-order moments (such as velocity correlations) are not taken into account (Ferziger, 2000).

Only very few ABL simulations have been performed using non-eddy-viscosity models (see Chapter 6 for further details), even though these models have been shown to give much-improved results and are not harder to implement.

2.1.1 Eddy viscosity models

The first SFS models mimicked the Reynolds-averaged Navier-Stokes (RANS) closure idea of an eddy-viscosity or gradient-transport model, setting $\tau_{ij} = -2\nu_T \overline{S}_{ij}$, where $\overline{S}_{ij} = \frac{1}{2}(\frac{\partial \overline{u}_i}{\partial x_j} + \frac{\partial \overline{u}_j}{\partial x_i})$. A constant eddy viscosity, ν_T, can be chosen but this gives very poor results. Smagorinsky (1963) introduced a model of the form $\nu_T = (C_S \Delta_g)^2 (\overline{S}_{ij} \overline{S}_{ij})^{1/2}$ where Δ_g is the grid spacing, and the Smagorinsky coefficient C_S must be adjusted to give the best results. In this model the length scales are based on the grid size, which determines the eddy motions resolved in the LES. The Smagorinsky model is still widely used and is the basis for the popular dynamic Smagorinsky model described later.

Closures using a prognostic equation for the turbulent kinetic energy (TKE) are also common in atmospheric boundary layer simulations. These 1.5-order TKE closures (see e.g. Deardorff, 1980; Moeng, 1984) are similar to RANS approaches such as k-ϵ or q^2-$q^2 l$ approaches (see Yamada & Mellor, 1975; Stull, 1988; Blumberg *et al.*, 1992). The eddy viscosity is represented as a function of a velocity scale and a length scale. The TKE equation (q^2 or k) is solved to obtain a representative velocity scale. In RANS closures, the length scale (l) is derived using another prognostic equation, such as for dissipation (ϵ) or $q^2 l$. The TKE and length scale equations involve numerous parameterizations for unclosed correlations and include several coefficients which are tuned to experimental data. When a TKE approach is used in LES applications, the velocity scale used in the eddy viscosity is again based on solution of the TKE equation; however, instead of solving an additional prognostic equation for the length scale, the 1.5-order TKE models use the grid spacing (Δ_g) as the basis for determining the length scale.

The continued improvement in grid resolution due to the increase in computer power has begun to diminish the distinction between RANS and LES approaches. While RANS is strictly based on time averaging, using a smaller time period for the average is akin to using a smaller filter width for the spatial average in LES. The LES

approach is, however, ultimately tied to the definition of the filter width. In numerical codes which use eddy-viscosity closures, the distinction can be made by the choice of the representative length scale. LES codes use a 1.5-order TKE method instead of k-ϵ or other higher-order models, and select the 1.5-order length scale based on the filter width.

Eddy viscosity models perform reasonably well in predicting mean flows away from boundaries, but often overpredict shear stress and do not allow the flow to re-laminarize because they require the SFS stress to be aligned with the resolved strain rate tensor. Eddy viscosity models exhibit very low correlations in *a priori* tests (see Section 3.4), meaning that there is little correlation between the modeled and actual SFS stresses. These models are also entirely dissipative; energy transfer is always from the large to the small scales. This is most often the case in real turbulent flows, but backscatter of energy from small to large scales can be significant as well (Sullivan *et al.*, 2003). Various other eddy-viscosity models have been proposed, some with nonlinear dependence on the resolved strain rate, $\overline{S}_{ij}$ (see e.g. Kosović, 1997); a few are discussed further in Chapter 6.

2.1.2 Scale-similarity models

Due to the limited success of eddy-viscosity closures, a new approach was sought. The first scale-similarity model was introduced by Bardina *et al.* (1983) and was based on the hypothesis that the largest SFS scale and the smallest resolved scale are similar. The Bardina model makes the approximation $u_i = \overline{u}_i$ (i.e., that the full velocity is equal to the filtered velocity) to close the SFS stress term, resulting in $\tau_{ij} \approx \overline{\overline{u}_i \overline{u}_j} - \overline{\overline{u}}_i \overline{\overline{u}}_j$. This model exhibits relatively high correlations with the exact SFS stress computed in *a priori* tests (see Section 3.4). It allows backscatter of energy from the small to the large scales, making it a desirable component of any SFS model. The scale-similarity model also has correct near-wall behavior (Sarghini *et al.*, 1999) and is Galilean invariant (Speziale, 1985). The model does not dissipate enough energy, however. Thus, Bardina *et al.* (1983) also introduced the mixed model, which combined the Smagorinsky and the scale-similarity model. This gave much improved correlations while allowing for adequate dissipation. Velocity estimation methods, described below, use scale-similar form as well.

The importance of the scale-similarity term may be seen in the study of four different LES codes by Andren *et al.* (1994) which confirmed that the challenge for eddy-viscosity models has long been to obtain the correct logarithmic velocity profile near the wall. Traditional simulations result in excessive shear at the wall and hence incorrectly predict the velocity profile. Using a stochastic backscatter model (i.e. the model of Mason & Thomson (1992) tested by Andren *et al.* (1994)) seemed to improve results near the wall. As scale-similar models allow for backscatter, it is expected that these will greatly improve the flow profile in the ABL, without introducing the random (and non-physically based) fluctuations of the stochastic model, as seen in Chapter 6.

2.1.3 Dynamic models

The next development in SFS modeling was the introduction of eddy viscosity models which allow the coefficient to vary in space and time dynamically, without the use of prognostic equations or predetermined coefficients. The first such model was developed by Germano *et al.* (1991) and was applied to the Smagorinsky eddy-viscosity model, which became known as the dynamic Smagorinsky model (DSM). It is based on the assumption that the same Smagorinsky coefficient can be applied at the given filter width and at the test filter level (usually twice the original filter width). Fluctuations in the dynamic Smagorinsky coefficient allow positive and negative energy transfer which simulates the forward- and backscatter of energy between large and small scales. However, large fluctuations in the coefficient are often observed, which lead to instabilities. To overcome this problem, averaging of the dynamic constant is applied over planar cross-sections which means that back-scatter or forward-scatter must occur uniformly over that entire plane. Newer formulations allow local averaging which restores some of the spatial variability to the model (Ghosal *et al.*, 1995).

Zang (1993) extended this idea of dynamic coefficients to the mixed model (Bardina *et al.*, 1983) and created the dynamic mixed model (DMM). This incorporated the scale-similarity term which is capable of accounting for backscatter on its own, thus greatly decreasing the required contribution of the eddy-viscosity component. The dynamic coefficient does not fluctuate as much as in the DSM; hence local averaging is adequate to smooth the fluctuations.

Another variation of the dynamic model is the dynamic two-parameter model

(DTM) which introduces independent coefficients in front of both the scale-similarity and eddy-viscosity parts of the mixed model (Salvetti & Banerjee, 1995). This model exhibits results comparable to the DMM model. Further variations of dynamic models have been developed, such as those of Vreman *et al.* (1996) and Cederwall & Street (1999). While dynamic models are considered the state-of-the-art, their disadvantage is that they require increased computational time as two levels of filtering must be employed, as well as averaging of the dynamic coefficient. The performance of dynamic models over a rough wall is a topic of current study (see Chapter 6 and references therein).

2.1.4 Velocity reconstruction models

The latest developments in SFS modeling have focused on estimating the unfiltered velocity directly, as opposed to modeling the SFS stress terms. Thus, rather than assuming a form such as a gradient-diffusion model for the stress tensor itself, the challenge becomes one of expressing the unfiltered velocity as a function of the filtered velocity, i.e., $u_i = f(\overline{u}_i)$. This is an inverse filter operation, or reconstruction of the unfiltered velocity from the filtered velocity. The use of the velocity approximation or reconstruction in the calculation of the SFS stress leads to models of the scale-similarity type. Indeed, the scale-similarity model of Bardina *et al.* (1983) can be classified in this category, as it estimates $u_i \approx \overline{u}_i$; this approximation can be improved, as discussed below, with higher-order models that reduce to the standard Bardina scale-similarity case at lowest order.

One of the first velocity reconstruction models was presented by Shah & Ferziger (1995). They developed the stimulated small-scale, or S^3, model in which a local approximation of total quantities in terms of filtered ones is introduced. The series expansion model in Chapter 3 is a simplified version of this method. Shah's model gave better results for turbulent channel flow LES than simulations using the DTM (Shah, 1997), demonstrating that velocity estimation models can give results comparable to dynamic models, at least in low-Reynolds number flows.

Domaradzki & Saiki (1997) and Domaradzki & Loh (1999) developed a velocity estimation model which uses an approximate deconvolution to obtain the estimated velocity in terms of the filtered velocity. The estimated velocity is determined using

a single nonlinear interaction per time step on a grid two times finer than the LES grid; this nonlinear interaction includes a tunable parameter and is introduced to mimic the behavior of the nonlinear SFS terms (where nonlinear interactions occur continuously). This procedure introduces smaller scales which "refine" the estimate of the unfiltered velocity. (The use of this nonlinear step makes this approach strictly speaking an SGS rather than an RSFS model - see Domaradzki & Adams (2002) and the discussion in Chapters 5 and 6.) Mean profiles for a channel flow show excellent agreement with DNS data for low Reynolds number cases; higher Reynolds number results show some deviation of the LES results from the DNS case.

Geurts (1997) presented an inverse filtering operation, which can be used for filters which have compact support, to approximate the unresolved velocity field, u_i. The Fourier transform of the tophat filter has infinitely many roots, so there is no exact inverse (as this would require division by zero at certain points in wave space). An approximate inverse is found by requiring that polynomials of a certain degree are recovered exactly after filtering and inversion, which gives a linear system of equations for the coefficients of the inversion operation. Using the approximate inverse, a model for the SFS stress is constructed as a generalized similarity model. Increasing the order of the polynomial expansion gives a more accurate representation for τ_{ij}.

Stolz & Adams (1999) used a similar inverse filtering idea with the iterative method of van Cittert (1931) for their approximate deconvolution method (ADM). The unfiltered velocity is approximated by a truncated series expansion of the inverse filter operator. As with Geurts (1997), the deconvolved velocities are used to compute the nonlinear terms in the momentum equations. Stolz & Adams (1999) observe correlations for this model in *a priori* tests that are greater than 0.95. They do not perform filtering in the vertical direction. Stolz *et al.* (1999*b*) introduce a relaxation term into their prognostic equation for the velocity, which acts as an SGS model to supplement the scale-similarity portion of the SFS stress (see Chapters 5 and 6). This is similar to the entropy dissipation term added by (Adams, 1999) in the application of the ADM to compressible flows with shocks. As used with a secondary filter operation, the relaxation term ensures sufficient energy dissipation (Pruett & Adams, 2000). Stolz *et al.* (1999*b*) find that the relaxation term is needed to produce good results, but disappears as the inverse filtering operation becomes more exact.

Velocity reconstruction methods have shown remarkable success since their recent

introduction. Those that perform best, however, require the use of *ad hoc* coefficients or terms. For example, the method of Domaradzki & Saiki (1997) requires an adjustable parameter for the forced nonlinear interaction terms which generate smaller scales. The method of Stolz & Adams (1999) requires a relaxation term in the dynamic equations to obtain satisfactory agreement. The need for these dissipative terms suggests the use of a two-part closure model: velocity reconstruction plus dissipation. The Taylor series expansion approach introduced in Chapter 3 considers only the velocity reconstruction contribution. The need for a dissipative term is described further in Chapters 5 and 6.

2.2 Boundary conditions

The only physical boundary condition in ABL simulations is at the bottom. Lateral and top boundary conditions are required because the computational domain is finite, so we must impose conditions on the flow at these boundaries that are as physically realistic as possible. The bottom boundary, however, also poses problems because the earth's surface is rough; the effects of trees, buildings, and other structures, cannot be resolved and are instead treated as subgrid roughness by using so-called "wall models". The term "wall model" is used loosely to describe models used to represent drag at any "wall", including the earth's surface. The remainder of this chapter describes typical implementations of boundary conditions in ABL simulations and recent efforts to improve wall models in LES. Many of the detailed descriptions apply to the Advanced Regional Prediction System (ARPS), a mesoscale meteorological LES code described and used later in Chapters 6-8.

2.2.1 Lateral and top boundary conditions

The top of the mixed layer is often used as the upper boundary in small-scale simulations of the ABL. A rigid, free-slip lid is imposed, assuming there is little flux across the inversion layer at the top. Flow over topography requires more sophisticated boundary conditions, as the reflection of topographically-generated waves is not desired at the non-physical boundaries. The top boundary is often placed much further away from the surface. Another option is to impose radiation boundary conditions;

these are artificial conditions that allow waves to pass undisturbed across the boundary and out of the domain (Klemp & Durran, 1983). The exact radiation boundary condition is expensive to implement numerically since it requires time integration and hence storage of a time sequence of data. When some terms are neglected, integration can be avoided; this approximate method gives good results except for large scale Rossby waves. A Rayleigh damping layer is another alternative for the upper boundary, introducing damping in the upper region of the domain so that waves entering this region die out and are not reflected by the rigid lid. These damping layers are effective but computationally inefficient since as much as half of the computational domain must be used (Klemp & Durran, 1983). For flow over a 2-D mountain, results are the same with radiation boundary conditions as with Rayleigh damping, but much less computation time and storage are required (Klemp & Durran, 1983). The radiation boundary condition has been applied to 3-D atmospheric flows as well (such as with ARPS), where good results and comparable savings to the 2-D case can be achieved.

At the lateral boundaries, the inflow velocities, velocity gradients, open radiation conditions, or periodicity can be prescribed. To simulate real events in the atmosphere, time-dependent boundary conditions imposed by a larger, coarser-scale model must be used in a grid nesting approach. Results from the coarse simulations are then interpolated to a finer grid and lateral boundary conditions are provided at the edges of the fine domain throughout the duration of the simulation. One-way nesting passes information from the coarse to the fine grid. Two-way nesting allows the fine grid to feed information back into the coarser grid, which can be challenging over complex terrain. Warner *et al.* (1997) provide guidelines for lateral boundary conditions for flows including complex terrain. An application of one-way nesting over complex terrain using ARPS is given in Chapter 8. Other real-time forecasting applications using grid nesting with ARPS are described in Appendix C.

2.2.2 Bottom boundary conditions

Ironically, the one physical boundary condition in the problem, i.e., the earth's surface, poses a more difficult problem than either the lateral or top boundary conditions. Because the surface beneath the atmospheric boundary layer is rough and the flow

highly turbulent, it is impractical (and currently impossible) to resolve all of the scales of fluid motion and apply a no-slip condition for the velocity at the surface because of grid resolution limitations. Traditionally, atmospheric models use similarity or log-law approximate boundary conditions to parameterize the effect of the bottom roughness on the flow. The following subsections discuss typical bottom boundary conditions for the ABL, describe the effects of the wall grid resolution and aspect ratio on the flow solution, and summarize recent attempts at creating new wall models.

Flux boundary conditions in ABL simulations

The most frequently-used bottom boundary conditions in ABL simulations are based on similarity theory, which empirically relates dimensionless groups in the boundary layer. Important parameters in the surface layer are the height of roughness elements, the mean wind velocity, and the height above the surface. The roughness elements determine the drag generated at the bottom surface. The parameter known as the aerodynamic roughness length, z_0, can be determined by wind measurements at different elevations and application of a similarity profile (for neutral cases, this reduces to a logarithmic profile). The parameter z_0 is the height at which the wind speed goes to zero and is less than the height of the physical roughness elements. From these variables, dimensionless relations can be formed, after which a functional relationship can be determined. These parameterizations are based on flat boundary layer flows, and are not generally valid over complex terrain.

Surface flux models for heat, momentum, and moisture are based on the local stability and roughness length. In ARPS, the models are based on the formulation of Businger *et al.* (1971). For the vertical momentum flux ($\overline{u'w'}$) associated with the x-direction, the formulation is

$$\overline{u'w'}|_0 = C_{dm} \max(V, V_{min}) u \tag{2.3}$$

where u is the velocity (in the x-direction) at the lowest grid level, and V is the wind magnitude at that level. V_{min} (set to 0.1 m/s) is included to prevent the shear from going to zero in cases where there is no mean wind, as it is unlikely that surface flux on the rough bottom is zero everywhere over a grid area even if the mean (resolved) wind happens to be zero. Similar parameterizations are used for the heat and moisture

fluxes. The drag coefficient C_{dm} is either prescribed or computed based on further parameterizations. The parameterization used depends on the stability of the flow; different formulations are used for stable, neutral, and unstable conditions. The ARPS code uses models by Byun (1990) for unstable and neutral cases, and by Deardorff (1972) for free convection and stable flows.

Effect of near-wall grid resolution on SFS motions

The approximate boundary conditions provided by similarity theory and drag laws perform well in some situations and give computational savings as the motions near the wall do not have to be resolved; however, the effect of the low near-wall resolution on turbulence parameterizations and hence on the entire flow field solution is unclear. Errors in the near-surface velocity fields can induce errors in the development of the boundary layer and hence in the transport of scalars.

Traditional closure models ignore the change in turbulence characteristics that occurs in the near-wall region. The Smagorinsky model has been used extensively in the ABL because LES is relatively insensitive to the SFS closure away from the surface where most of the motions are resolved. However, near-ground small-scales cannot be resolved by LES, because horizontal velocity components scale with distance above the surface and the grid is too coarse to resolve the flow. Juneja & Brasseur (1999) argue that eddy-viscosity models create errors in velocity and temperature because of an over-prediction of mean shear near the ground; these errors are then carried vertically by buoyancy driven fluxes to contaminate the entire ABL calculation. Juneja & Brasseur (1999) suggest that the over-prediction of mean shear is due to a spurious feedback loop from the coupling of the resolved field with that of the modeled SFS acceleration. The random fluctuations introduced in the stochastic SFS model of Mason & Thomson (1992) break the feedback loop and hence yield improved results over the standard eddy-viscosity models. Thus, a two-component model which also allows for energy backscatter (i.e. using velocity estimation with an eddy-viscosity model), should perform better near the wall and diminish the impact of the coarse resolution. In Chapter 6, we examine the performance of various turbulence closures with coarse resolution near the surface.

Effect of grid aspect ratio at the bottom boundary

ABL simulations often employ a terrain-following coordinate system. The σ-z coordinates used by ARPS are defined as

$$\mu = (z_{flat} - z_{ref})\frac{z - h}{z_{flat} - h} + z_{ref} \quad \text{for} \quad z_{ref} \leq z \leq z_{flat} \ , \tag{2.4}$$

where z is the physical height, z_{ref} is a reference height at the bottom of the domain, h is the height of the terrain, and D is the depth of the domain. Above z_{flat}, the physical height is used to minimize distortion of the grid, i.e.,

$$\mu = z \quad \text{for} \quad z_{flat} < z \leq D + z_{ref} \ . \tag{2.5}$$

The range of the mapped grid variable is thus from z_{ref} at the lower boundary to z_{flat}. In addition to mapping, the grid can be stretched by cubic or hyperbolic tangent functions, which can be combined piece-wise with sections of non-stretched grid (Xue *et al.*, 1995).

Terrain-following coordinates are best for terrain with slopes much less than 45°, as calculation of horizontal gradients becomes inaccurate when the physical coordinate lines are too steep Pielke (1984). The terrain slope limitation is also necessary for the hydrostatic assumption to hold in the transformed coordinates; however, this is not an issue in ARPS, as it is non-hydrostatic. When the terrain slopes are steep, large roundoff errors arise when calculation of the pressure gradient involves differences between large terms. ARPS alleviates this problem somewhat by first subtracting the horizontally averaged base-state variables, so that pressure gradient calculation errors are reduced (Xue *et al.*, 2000).

While fine grid resolution is desired for turbulence modeling, the choice of the aspect ratio of the grid near the surface can affect the accuracy of the solution and is important for parameterizing flux conditions at the surface. In traditional LES applications (e.g. low Reynolds number channel flows), the grid aspect ratio $\Delta x/\Delta z$ is usually about 3; however, much higher ratios have been used in laboratory-scale simulations with success (Cui, 1999; Zang *et al.*, 1993). In ABL applications, this aspect ratio is much larger, i.e., the horizontal resolution is much coarser because of the larger domain sizes. The grid aspect ratio affects the size of eddies which are

resolved in the flow; even if the flow is well-resolved in the vertical, the eddy size may be limited by the horizontal grid size (Kaltenbach, 1998). The study by Kravchenko *et al.* (1996) using zonal embedded grids indicates that having a small grid aspect ratio near a wall helps to produce excellent results in LES. Lund & Kaltenbach (1995) also found that refining the grid in the wall-normal direction produced little improvement in flow statistics unless the horizontal directions were refined as well. They explain that refining the grid in the vertical direction is more efficient in obtaining a rough prediction of the mean velocity profile, while correctly predicting the finer details of the profile seems to require reduction of numerical errors (e.g. by using explicit filtering, see Chapter 5).

In contrast, Wyngaard *et al.* (1998) argue that the surface-exchange coefficients commonly used to parameterize surface fluxes are a good representation only if the grid at the surface has a *large* aspect ratio. Thus, for what they call a traditional LES with small aspect ratio, the coefficients would no longer represent an averaged effect; they would have too many fluctuations, which would affect the resolvable scale motions. The exchange coefficients are well established for ensemble-averaged fluxes. For a small grid aspect ratio, however, the authors argue that it may be better to treat the coefficient as a fluctuating variable. As the grid aspect ratio increases, the fluctuating values of the exchange coefficients should approach the ensemble-averaged quantities. Wyngaard *et al.* (1998) wrote conservation equations for the coefficients to model the fluctuations, but did not see much improvement in the results, as they found that the SFS closure scheme was inadequate near the surface where there is inadequate grid resolution. The Smagorinsky model in particular performed very poorly, as shown in their *a priori* tests.

The velocity estimation model presented in Chapter 3, as well as the other reconstruction approaches used in Chapters 5-8 are anisotropic, and can accommodate non-uniform grids, which are features shown to be very important near solid boundaries. The effects of grid resolution on the simulation results are investigated in all of the flow applications in this work. The performance of the turbulence models with different grid aspect ratios is evaluated in Chapter 6. For the high grid resolution and low aspect ratio case which resolves eddy motions, it may be necessary to use fluctuating surface-flux coefficients (as done by Wyngaard *et al.*, 1998); however, a method for their estimation is left to future work.

New attempts at wall-models for LES

Several recent studies using approximate boundary conditions on smooth walls have illustrated the difficulty of the wall modeling problem and provide direction for further research with rough walls, which pose additional challenges. Baggett *et al.* (1997) estimate that to fully resolve a smooth boundary layer, the number of grid points for LES has to scale with the Reynolds number, which can become very computationally expensive. Approximate boundary conditions allow more efficient computations because they do not fully resolve the near-wall flow yet attempt to incorporate the wall effects on the outer flow. The outer flow does not scale with the Reynolds number, so considerable savings could be achieved. Unfortunately, there has been limited success with this approach, even for smooth walls. When wall-stress models are used with coarse grids, the near-wall points are poorly predicted; the flow is too fast relative to the outer flow, and hence the skin friction is overpredicted (for a given mass flow). Using a coarse grid also means that the effect of the SFS model becomes even more important, as a larger fraction of the SFS motions must be captured by the closure model. Similar issues exist for wall-models applied to rough walls.

The review article of Piomelli & Balaras (2002) summarizes the inadequacy of the current state-of-the-art models even for simplified geometries. For example, in their tests over smooth walls, Cabot & Moin (2000) found little difference in results from an instantaneous log-law model, full thin boundary layer equations near the wall, or a shifted log-law model. Cabot *et al.* (1999) conclude that the first few points near the wall may never be well-predicted using such wall models. Other studies include those of Wang & Moin (2002), who developed a dynamic wall model using the thin boundary layer equations, Kaltenbach (2003), who performed *a priori* tests to evaluate wall models for separated flows, and the suboptimal control theory approach of Nicoud *et al.* (2001), all of which had limited success.

Another wall-model option is to couple RANS and LES models, with RANS used in the coarse near-wall grid region and adjusted to match the LES result further from the wall (Baggett, 1998; Cabot, 1995; Kaltenbach, 1998). These hybrid RANS-LES studies are for smooth walls; over a rough wall, the RANS portion would again require a wall model to set the bottom boundary condition. Artificially increasing the eddy viscosity near the wall is another approach, which moves the resolved velocity

profile closer to the log profile. Recently, Ding (2002) and Zedler (2002) have added an artificial eddy viscosity based on the work of Davies (1972) for simulation of a turbulent channel flow. The increased eddy viscosity near the wall helps to adjust the mean velocity profile, which is usually too large in LES of channel flows, but this model is ad hoc and may not have general applicability.

Even for smooth walls, wall-models have had very limited success. Instantaneous log laws, which specify that the resolved velocity profile is always a log law, even in reverse-flow (separated) regions, have shown results as reasonable as any others and are the simplest to implement (Cabot & Moin, 2000). Whether the log-law assumption is physically realistic in complex-terrain flows is questionable. The fundamental flaw is the necessary assumption of a mean velocity profile, which is not applicable to general flow situations. ABL simulations have the further challenge of a coarse wall which cannot be resolved at all, hence absolutely requiring the use of wall models. Several modifications have been proposed for wall models for ABL flow. For instance, Sullivan *et al.* (1994) found that adjusting the flow at the first few grid points so that the mean shear matches the profile from similarity theory improves results. Brown *et al.* (2001) adapted a canopy model used for flow through vegetation to improve the representation of wall-induced stresses on the flow. These developments for the ABL are discussed further in Chapter 6.

Chapter 3

Subfilter-scale models for LES using Taylor series*

A new subfilter-scale (SFS) stress model for large-eddy simulation (LES) is proposed using successive inversion of a Taylor series expansion to represent the unknown full velocity in terms of the filtered velocity. The resulting expression for the SFS stress satisfies the SFS stress evolution equations to a predefined order of accuracy in the filter width (the truncation order of the series expansion). The modeled SFS stress is thus influenced by buoyancy, viscous, pressure, and Coriolis effects just as the velocity field is. The series expansion model is of scale-similarity form, and reduces to the Bardina model (Bardina *et al.*, 1983) at lowest order. Preliminary tests of the model are presented using a modified wave number analysis and *a priori* testing using a direct numerical simulation (DNS) of sheared, stably-stratified homogeneous turbulence. The model exhibits very high correlations with the exact SFS stress. This chapter does not consider the effects of discretization, which are discussed in Chapters 5 and 6.

*This chapter is a reproduction (with minor modifications) of Technical Report 2000-K1 from the Environmental Fluid Mechanics Laboratory, Stanford University, entitled "A theory for the subfilter-scale model in large-eddy simulation" by Fotini Katopodes (the principal author), Robert L. Street, and Joel H. Ferziger (Katopodes *et al.*, 2000*b*).

3.1 Introduction

Large-eddy simulation is a method in which the larger scales of a turbulent flow are simulated accurately, while the smaller, subfilter, scales are not resolved in the numerical simulation and must be modeled. (We use the term "subfilter-scale", rather than "subgrid-scale", to denote the unresolved velocity and stress fields, as the size of the filter should be greater than the size of the grid upon which spatial discretization is based (Ghosal, 1996).) The subfilter-scale model must be based on knowledge of the resolved scale behavior alone. Leonard (1974) provided early theoretical and practical bases for LES. Bardina *et al.* (1983) made a seminal contribution by introducing the scale-similarity model, which has been shown to be an essential component of a correct SFS model. While eddy-viscosity models such as that used by Smagorinsky (1963) assume a form for the SFS stress, scale-similarity models create an approximation to the full velocity field and use this to estimate the SFS stress, $\tau_{ij} = \overline{u_i u_j} - \overline{u}_i \overline{u}_j$. Thus, in the Bardina model, the full velocity is approximated by the filtered velocity, $u_i \approx \overline{u}_i$, to obtain $\tau_{ij} \approx \overline{\overline{u}_i \overline{u}_j} - \overline{\overline{u}}_i \overline{\overline{u}}_j$. This was the first SFS model that used the smallest resolved scales as its basis.

Further improvement in estimates of the SFS stress were seen with the introduction of dynamic models. Zang *et al.* (1993) introduced a two-component model based on Bardina's mixed model (Bardina *et al.*, 1983) and the dynamic model of Germano *et al.* (1991). Mixed models can represent both back-scatter of small-scale energy to the larger scales and forward-scatter or dissipation of large-scale energy by the small scales; both are essential for a reasonable representation of the subfilter-scale effects. Piomelli (1999), Sarghini *et al.* (1999), and Lesieur & Métais (1996) give comprehensive reviews of and further insights to large-eddy simulation and the variety of subfilter-scale models that have been introduced.

In the scale-similarity approach, the approximation for τ_{ij} would be more accurate if a higher order approximation to the full velocity field could be obtained. A more exact representation of SFS motions is especially desirable for applications of LES to computation of complex flows, including geophysical flows. In such cases the subfilter scales are probably not isotropic, as assumed in eddy-viscosity SFS models. Shah & Ferziger (1995) proposed a new non-eddy-viscosity model (the stimulated small scale, or S^3, model) in which a local approximation of total quantities in terms of filtered

ones is introduced; the scale-similarity model is a special case. In this chapter we propose a simplified version of the S^3 model.

Domaradzki & Saiki (1997) also developed a method which creates an estimate of the subfilter-scale velocity based on the resolved scales. This estimate is then used to calculate the SFS stress. Their model is a generalization of Bardina's scale-similarity model. The model was designed for spectral space calculations, but has been extended to physical space by Domaradzki & Loh (1999). With a similar approach, Geurts (1997) developed a generalized scale-similarity model using a polynomial to approximate the inverse filtering operation. Recently, Stolz & Adams (1999) also proposed an approximate deconvolution procedure for estimating the velocity.

Velocity estimation methods that lead to models of the scale-similarity type are only valid for flows in which the interaction between resolved and unresolved scales occurs primarily in the vicinity of the filter cutoff. As noted by Domaradzki & Saiki (1997), this seems to be the case for all low Reynolds number cases that have been investigated experimentally and numerically (see e.g. Liu *et al.*, 1994).

In the SFS model described here, the unresolved velocity is represented by successive inversion of a Taylor series expansion of the resolved velocity field. This representation is used to estimate the velocity in the same spirit as the recently introduced methods described above. The expansion is easily derived and can be shown to be a good approximation to the unresolved velocity field, at least in low Reynolds number flows. The mathematical expansion serves to close the Navier-Stokes equations by providing an expression for the subfilter stress, τ_{ij}. Furthermore, in analogy to Reynolds-averaged modeling where the Reynolds stress equations are modeled, one can derive the evolution equations for the subfilter-scale stress. These evolution equations allow systematic evaluation of the relative contributions by advection, diffusion, dissipation, pressure, rotation, and stratification in the subfilter-scale effects felt by the resolved components of the flow. The approach is similarly applied to the scalar transport equation, as done by Katopodes *et al.* (2000*a*) (see Appendix B).

In this chapter, we prove that the model for the stresses obtained by the series expansion method is an *exact* solution of the evolution equations for the subfilter-scale stresses, to a known accuracy (the series truncation order) in the filter width. We subsequently illustrate the behavior of this model applied to a test function, and give results from *a priori* tests based on DNS data for a stably-stratified shear flow.

An important feature of the series model is that it is easily applied when the filter width is not equal in all directions, which is the case for the DNS data used herein. No parameters occur in the model, and nothing is assumed about the form of the SFS motions. The model should thus be able to capture anisotropic motions better than eddy-viscosity models. Furthermore, the order of accuracy of the method is determined by the series truncation order chosen. Models of the scale-similar form are also invariant under Galilean transformations (Speziale, 1985), and exhibit correct near-wall behavior (Sarghini *et al.*, 1999). The S^3 model of Shah & Ferziger (1995), to which this model is related, has been shown to be superior to the Smagorinsky and mixed models in LES of plane channel flow and flow past a cubic obstacle (Shah, 1998). Similar behavior is expected with the series expansion model as the two models are equivalent to fourth order in the filter width (Ding, 2000). The model presented here is also easy to implement.

3.2 Derivation of SFS evolution equations and series expansion model

In the following discussion, all variables are assumed to be smooth; no discretization is applied. We begin with the Navier-Stokes equations, written with the Boussinesq approximation for buoyancy effects and the Coriolis force included,

$$\frac{\partial u_i}{\partial t} + u_j \frac{\partial u_i}{\partial x_j} = -\frac{1}{\rho_0}\frac{\partial p}{\partial x_i} + \nu \frac{\partial^2 u_i}{\partial x_j \partial x_j} - \frac{\rho}{\rho_0} g \delta_{i3} + \epsilon_{imn} f_n u_m \; . \tag{3.1}$$

Here u_i denotes the velocity, ρ the density, ρ_0 the reference density, ν the kinematic viscosity, p the pressure, and f_n the Coriolis parameter. Repeated indices indicate summation. The spatially filtered equations are

$$\frac{\partial \overline{u}_i}{\partial t} + \overline{u}_j \frac{\partial \overline{u}_i}{\partial x_j} = -\frac{1}{\rho_0}\frac{\partial \overline{p}}{\partial x_i} + \nu \frac{\partial^2 \overline{u}_i}{\partial x_j \partial x_j} - \frac{\overline{\rho}}{\rho_0} g \delta_{i3} + \epsilon_{imn} f_n \overline{u}_m - \frac{\partial \tau_{ij}}{\partial x_j} \tag{3.2}$$

where the SFS stress is defined as

$$\tau_{ij} = \overline{u_i u_j} - \overline{u}_i \overline{u}_j \; . \tag{3.3}$$

Properties of the filter (indicated by an overbar) are described later. The filtered equations are not closed due to the nonlinear term $\overline{u_i u_j}$ included in τ_{ij}. We can seek to close the problem by developing an evolution equation for τ_{ij} by the following procedure.

We first obtain an evolution equation for $u_i u_k$ by multiplying the Navier-Stokes equation for u_i by u_k, the analogous equation for u_k by u_i, and adding the two equations together. We then use integration by parts to express the viscous and pressure terms in more familiar forms. Filtering the resulting equation gives the evolution equation for $\overline{u_i u_k}$. Similarly, we can develop an evolution equation for $\overline{u}_i \overline{u}_k$. Subtracting the equation for $\overline{u}_i \overline{u}_k$ from the equation for $\overline{u_i u_k}$, we obtain an evolution equation for τ_{ij}:

$$\begin{aligned}
\frac{\partial \tau_{ik}}{\partial t} + \overline{u}_j \frac{\partial \tau_{ik}}{\partial x_j} &= -\overline{u_j \frac{\partial u_i u_k}{\partial x_j}} + \overline{u}_j \frac{\partial \overline{u_i u_k}}{\partial x_j} + \overline{u}_k \frac{\partial \tau_{ij}}{\partial x_j} + \overline{u}_i \frac{\partial \tau_{kj}}{\partial x_j} \\
&- \frac{1}{\rho_0}\left(\frac{\partial \overline{u_i p}}{\partial x_k} - \frac{\partial \overline{u}_i \overline{p}}{\partial x_k} + \frac{\partial \overline{u_k p}}{\partial x_i} - \frac{\partial \overline{u}_k \overline{p}}{\partial x_i} \right) \\
&+ \frac{1}{\rho_0}\left(\overline{p \frac{\partial u_i}{\partial x_k}} - \overline{p} \frac{\partial \overline{u}_i}{\partial x_k} + \overline{p \frac{\partial u_k}{\partial x_i}} - \overline{p} \frac{\partial \overline{u}_k}{\partial x_i} \right) \\
&+ \nu \frac{\partial^2 \tau_{ik}}{\partial x_j \partial x_j} - 2\nu \overline{\frac{\partial u_i}{\partial x_j} \frac{\partial u_k}{\partial x_j}} + 2\nu \frac{\partial \overline{u}_i}{\partial x_j} \frac{\partial \overline{u}_k}{\partial x_j} \\
&- \frac{g}{\rho_0}(\overline{\rho u_k}\delta_{i3} - \overline{\rho}\,\overline{u}_k \delta_{i3} + \overline{\rho u_i}\delta_{k3} - \overline{\rho}\,\overline{u}_i \delta_{k3}) \\
&+ f_n(\epsilon_{imn}\tau_{mk} - \epsilon_{kmn}\tau_{mi}) \; . \qquad (3.4)
\end{aligned}$$

It has been assumed that the filtering operation commutes with the spatial derivatives, which is true for a spatially homogeneous filter. Some error is introduced if this is not so (Ghosal & Moin, 1995).

Equation 3.4 describes the evolution of the SFS stress tensor τ_{ik}; it is seen that τ_{ik} is influenced by advection, diffusion, pressure, buoyancy, and Coriolis terms. The pressure terms are written in the familiar form separating the so-called "pressure-diffusion" and "pressure-strain" terms. The viscous terms include the effects of transport and dissipation (Hinze, 1975, p. 74). Several advection terms appear due to the rearrangement of the equations, one of which is the triple velocity correlation term. It is desirable that a model for the SFS stresses capture the effect of all of these terms. Note that these equations involve the full velocity and pressure fields, as no

decomposition has been made. If the Reynolds decomposition is performed, separating all terms into average and fluctuating components, and the averaging rules of the Reynolds-Averaged Navier-Stokes equations are used, Eq. 3.4 reduces to the well-known Reynolds stress evolution equation. There, the "pressure strain" and other familiar terms arise as correlations of fluctuating variables instead of the full variables.

Equation 3.4 is not closed because new correlation terms have appeared. If we are to obtain an expression for τ_{ik} to be used in the resolved flow equation (3.2), we must make approximations to relate the unclosed terms to known terms from the resolved flow. The traditional procedure has been to use scaling and physical arguments to model the unclosed terms. Here, we follow a purely mathematical approach to obtain an approximate solution to these equations. With that aim, we introduce a multi-dimensional Taylor expansion for the velocity, density, and pressure fields at any point, e.g.,

$$u_i(x'_j) \approx u_i(x_j) + (x'_m - x_m)\frac{\partial u_i(x_j)}{\partial x_m} + \frac{1}{2}(x'_m - x_m)(x'_n - x_n)\frac{\partial^2 u_i(x_j)}{\partial x_m \partial x_n} + \cdots \ , \quad (3.5)$$

using index notation for compactness. The Taylor expansion was used in this way thirty years ago by Leonard (1974).

We now apply an anisotropic Gaussian filter:

$$\overline{u}_i(x,y,z) = \int_{-\infty}^{\infty}\int_{-\infty}^{\infty}\int_{-\infty}^{\infty} G(x-x', y-y', z-z')u_i(x',y',z')\ dx'dy'dz' \quad (3.6)$$

where

$$G(x,y,z) = \frac{6^{3/2}}{\pi^{3/2}\Delta_x\Delta_y\Delta_z}\exp\left(-\frac{6x^2}{\Delta_x^2} - \frac{6y^2}{\Delta_y^2} - \frac{6z^2}{\Delta_z^2}\right) \quad (3.7)$$

and $\Delta_x, \Delta_y, \Delta_z$ are the filter sizes in each direction. Other filters could be used here, including asymmetric filters, with a change in the expansion coefficients below (but see the consequences of using spectral cutoff filters, as discussed in the following sections). The Gaussian filter eliminates all terms with odd powers of x, y, or z due to symmetry, so that

$$\begin{aligned}\overline{u}_i(x,y,z) &= u_i + \frac{\Delta_x^2}{24}\frac{\partial^2 u_i}{\partial x^2} + \frac{\Delta_y^2}{24}\frac{\partial^2 u_i}{\partial y^2} + \frac{\Delta_z^2}{24}\frac{\partial^2 u_i}{\partial z^2} \\ &+ \frac{\Delta_x^4}{1152}\frac{\partial^4 u_i}{\partial x^4} + \frac{\Delta_y^4}{1152}\frac{\partial^4 u_i}{\partial y^4} + \frac{\Delta_z^4}{1152}\frac{\partial^4 u_i}{\partial z^4}\end{aligned}$$

$$+ \quad \frac{\Delta_x^2\Delta_y^2}{1728}\frac{\partial^4 u_i}{\partial x^2\partial y^2} + \frac{\Delta_y^2\Delta_z^2}{1728}\frac{\partial^4 u_i}{\partial y^2\partial z^2} + \frac{\Delta_x^2\Delta_z^2}{1728}\frac{\partial^4 u_i}{\partial x^2\partial z^2} + O(\Delta^6)\ . \quad (3.8)$$

Asymmetric filters would give a more complex expression because all derivative terms would be retained; they are not included in this work. Rearranging and using Eq. 3.8 recursively, we obtain

$$\begin{aligned} u_i(x,y,z) \;\approx\; & \overline{u}_i(x,y,z) - \frac{\Delta_x^2}{24}\frac{\partial^2\overline{u}_i}{\partial x^2} - \frac{\Delta_y^2}{24}\frac{\partial^2\overline{u}_i}{\partial y^2} - \frac{\Delta_z^2}{24}\frac{\partial^2\overline{u}_i}{\partial z^2} \\ & + \frac{\Delta_x^4}{1152}\frac{\partial^4\overline{u}_i}{\partial x^4} + \frac{\Delta_y^4}{1152}\frac{\partial^4\overline{u}_i}{\partial y^4} + \frac{\Delta_z^4}{1152}\frac{\partial^4\overline{u}_i}{\partial z^4} \\ & + \frac{5\Delta_x^2\Delta_y^2}{1728}\frac{\partial^4\overline{u}_i}{\partial x^2\partial y^2} + \frac{5\Delta_y^2\Delta_z^2}{1728}\frac{\partial^4\overline{u}_i}{\partial y^2\partial z^2} + \frac{5\Delta_x^2\Delta_z^2}{1728}\frac{\partial^4\overline{u}_i}{\partial x^2\partial z^2} + O(\Delta^6)\,, \end{aligned} \quad (3.9)$$

which expresses the full velocity at a point (x, y, z) in terms of the filtered velocity at that point. If the filter is isotropic, Eq. 3.9 reduces to

$$\begin{aligned} u_i(x,y,z) \approx \overline{u}_i(x,y,z) - \frac{\Delta^2}{24}\nabla^2\overline{u}_i + \frac{\Delta^4}{1152}\left(\frac{\partial^4\overline{u}_i}{\partial x^4} + \frac{\partial^4\overline{u}_i}{\partial y^4} + \frac{\partial^4\overline{u}_i}{\partial z^4}\right) \\ + \frac{5\Delta^4}{1728}\left(\frac{\partial^4\overline{u}_i}{\partial x^2\partial y^2} + \frac{\partial^4\overline{u}_i}{\partial y^2\partial z^2} + \frac{\partial^4\overline{u}_i}{\partial x^2\partial z^2}\right) + O(\Delta^6)\ . \end{aligned} \quad (3.10)$$

This simplified form of the Taylor expansion will be used in the remaining derivations, as the anisotropic form is more cumbersome algebraically. Terms of $O(\Delta^4)$ and higher will also be ignored subsequently. The anisotropic results to fourth order can be recovered by replacing $\frac{\Delta^2}{24}\nabla^2$ by

$$\frac{\Delta_x^2}{24}\frac{\partial^2}{\partial x^2} + \frac{\Delta_y^2}{24}\frac{\partial^2}{\partial y^2} + \frac{\Delta_z^2}{24}\frac{\partial^2}{\partial z^2}\ . \quad (3.11)$$

3.2.1 Generation of expanded evolution equations for τ_{ij}

In Reynolds-averaged modeling, the evolution equations for τ_{ij} are often simplified by neglecting various terms. It is therefore of interest to determine the importance of these terms in the evolution of the SFS stress as given by Eq. 3.4. To obtain a closed form of the equations, we now substitute the expansion in Eq. 3.10 (and similar expansions for pressure and density) into the unclosed terms in Eq. 3.4 and simplify.

The evolution equation for τ_{ik}, accurate to $O(\Delta^4)$, is then

$$
\begin{aligned}
\frac{\partial \tau_{ik}}{\partial t} + \overline{u}_j \frac{\partial \tau_{ik}}{\partial x_j} &= -\overline{\overline{u}_j \frac{\partial \overline{u}_i \overline{u}_k}{\partial x_j}} + \frac{\Delta^2}{24}\left(\overline{\overline{u}_j \frac{\partial \overline{u}_i \nabla^2 \overline{u}_k}{\partial x_j}}\right) + \frac{\Delta^2}{24}\left(\overline{\overline{u}_j \frac{\partial \overline{u}_k \nabla^2 \overline{u}_i}{\partial x_j}}\right) \\
&+ \frac{\Delta^2}{24}\left(\overline{\nabla^2 \overline{u}_j \frac{\partial \overline{u}_i \overline{u}_k}{\partial x_j}}\right) + \overline{u}_j \frac{\partial \overline{\overline{u}_i \overline{u}_k}}{\partial x_j} - \frac{\Delta^2}{24}\overline{u}_j \left(\frac{\partial \overline{\overline{u}_i \nabla^2 \overline{u}_k}}{\partial x_j}\right) \\
&- \frac{\Delta^2}{24}\overline{u}_j \left(\frac{\partial \overline{\overline{u}_k \nabla^2 \overline{u}_i}}{\partial x_j}\right) + \overline{u}_k \frac{\partial \tau_{ij}}{\partial x_j} + \overline{u}_i \frac{\partial \tau_{kj}}{\partial x_j} \\
&- \frac{1}{\rho_0}\left[\frac{\partial \overline{\overline{u}_k \overline{p}}}{\partial x_i} - \frac{\Delta^2}{24}\left(\frac{\partial \overline{\overline{p} \nabla^2 \overline{u}_k}}{\partial x_i}\right) - \frac{\Delta^2}{24}\left(\frac{\partial \overline{\overline{u}_k \nabla^2 \overline{p}}}{\partial x_i}\right) - \frac{\partial \overline{u}_k \overline{p}}{\partial x_i}\right. \\
&+ \left.\frac{\partial \overline{\overline{u}_i \overline{p}}}{\partial x_k} - \frac{\Delta^2}{24}\left(\frac{\partial \overline{\overline{p} \nabla^2 \overline{u}_i}}{\partial x_k}\right) - \frac{\Delta^2}{24}\left(\frac{\partial \overline{\overline{u}_i \nabla^2 \overline{p}}}{\partial x_k}\right) - \frac{\partial \overline{u}_i \overline{p}}{\partial x_k}\right] \\
&+ \frac{1}{\rho_0}\left[\overline{\overline{p} \frac{\partial \overline{u}_k}{\partial x_i}} - \frac{\Delta^2}{24}\left(\overline{\overline{p} \frac{\partial \nabla^2 \overline{u}_k}{\partial x_i}}\right) - \frac{\Delta^2}{24}\left(\overline{\left(\nabla^2 \overline{p}\right) \frac{\partial \overline{u}_k}{\partial x_i}}\right) - \overline{p} \frac{\partial \overline{u}_k}{\partial x_i}\right. \\
&+ \left.\overline{\overline{p} \frac{\partial \overline{u}_i}{\partial x_k}} - \frac{\Delta^2}{24}\left(\overline{\overline{p} \frac{\partial \nabla^2 \overline{u}_i}{\partial x_k}}\right) - \frac{\Delta^2}{24}\left(\overline{\left(\nabla^2 \overline{p}\right) \frac{\partial \overline{u}_i}{\partial x_k}}\right) - \overline{p} \frac{\partial \overline{u}_i}{\partial x_k}\right] \\
&+ \nu \frac{\partial^2 \tau_{ik}}{\partial x_j \partial x_j} - 2\nu \overline{\frac{\partial \overline{u}_i}{\partial x_j} \frac{\partial \overline{u}_k}{\partial x_j}} + \nu \frac{\Delta^2}{12} \overline{\frac{\partial \overline{u}_i}{\partial x_j} \frac{\partial \nabla^2 \overline{u}_k}{\partial x_j}} \\
&+ \nu \frac{\Delta^2}{12} \overline{\frac{\partial \nabla^2 \overline{u}_i}{\partial x_j} \frac{\partial \overline{u}_k}{\partial x_j}} + 2\nu \frac{\partial \overline{u}_i}{\partial x_j} \frac{\partial \overline{u}_k}{\partial x_j} \\
&- \frac{g}{\rho_0}\left(\overline{\overline{\rho u}_k} - \frac{\Delta^2}{24}\overline{\overline{\rho} \nabla^2 \overline{u}_k} - \frac{\Delta^2}{24}\overline{\overline{u}_k \nabla^2 \overline{\rho}} - \overline{\rho}\, \overline{u}_k\right) \delta_{i3} \\
&- \frac{g}{\rho_0}\left(\overline{\overline{\rho u}_i} - \frac{\Delta^2}{24}\overline{\overline{\rho} \nabla^2 \overline{u}_i} - \frac{\Delta^2}{24}\overline{\overline{u}_i \nabla^2 \overline{\rho}} - \overline{\rho}\, \overline{u}_i\right) \delta_{k3} \\
&+ f_n(\epsilon_{imn}\tau_{mk} + \epsilon_{kmn}\tau_{mi}) \,. \qquad (3.12)
\end{aligned}
$$

Equations 3.12 are a closed set of equations for τ_{ik}; the contribution of all the filtered quantities to the evolution of τ_{ik} can be explicitly computed. Such a set of equations could be solved for the six independent components of τ_{ik}, without need for further

simplifications or assumptions. Although feasible, this would add a significant computational expense to the solution of the resolved flow equation (3.2). The solution obtained for $\overline{u}_i$ would be accurate to $O(\Delta^4)$.

3.2.2 Generation of the τ_{ij} models

In the spirit of velocity estimation models, instead of solving six more equations for τ_{ij}, we derive models for τ_{ij} by substituting the series expansion for the velocity (Eq. 3.10) directly into Eq. 3.3. When the unclosed term is expanded, and terms fourth order and higher are neglected, we obtain

$$\text{Model 1:} \quad \tau_{ik} = \overline{\overline{u}_i\overline{u}_k} - \overline{u}_i\overline{u}_k - \frac{\Delta^2}{24}\overline{\overline{u}_i\nabla^2\overline{u}_k} - \frac{\Delta^2}{24}\overline{\overline{u}_k\nabla^2\overline{u}_i} \; . \tag{3.13}$$

This form is not Galilean invariant, and should only be used if care is taken with the formulation of the advective terms (e.g. if the reconstruction is implemented directly in the advective terms). If the explicit term, $\overline{u}_i\overline{u}_j$, is also expanded, the representation becomes

$$\text{Model 2:} \quad \tau_{ik} = \overline{\overline{u}_i\overline{u}_k} - \overline{\overline{u}}_i\overline{\overline{u}}_k - \frac{\Delta^2}{24}\overline{\overline{u}_i\nabla^2\overline{u}_k} - \frac{\Delta^2}{24}\overline{\overline{u}_k\nabla^2\overline{u}_i} + \frac{\Delta^2}{24}\overline{\overline{u}}_i\nabla^2\overline{\overline{u}}_k + \frac{\Delta^2}{24}\overline{\overline{u}}_k\nabla^2\overline{\overline{u}}_i \; , \tag{3.14}$$

which is Galilean invariant. To second order in the filter width, Eq. 3.14 reduces to the Bardina scale-similarity model. This scale-similarity property of Eq. 3.14 will later be shown to have desirable effects (see *a priori* test section). The higher order terms that are not present in the Bardina model can be shown to be dissipative (Clark *et al.*, 1977). Further properties of these two models will be discussed in the sections that follow.

Although we did not directly solve the evolution equations for τ_{ik}, we can substitute Eq. 3.13 into the evolution equation (3.12) to demonstrate that it is indeed a solution, as the resulting equation is the sum of the evolution equations for the components of Eq. 3.13. It is perhaps more straightforward to construct the evolution equation for the approximate form (Eq. 3.13) and show that it is the same as Eq. 3.12. This is done by a procedure similar to the derivation of Eq. 3.4. After adding and subtracting the evolution equations for each term that makes up the approximate τ_{ik},

and simplifying using the series expansion introduced previously to effectively "unbar" certain terms (see text leading to Eq. A.2 in Appendix A), we obtain Eq. 3.12 to $O(\Delta^4)$. Thus, to fourth-order accuracy in the filter width, Δ, we have a solution for the subfilter-scale stresses, τ_{ik}. As can be shown by a similar procedure, Eq. 3.14 is a solution, to fourth order, of the analogous version of Eq. 3.12 that is obtained when the closed terms are expanded as well. Note that the evolution equation developed for the approximate τ_{ik} indicates that these subfilter-scale stresses are influenced by buoyancy and Coriolis forces, as well as by diffusion, pressure and advection terms, as are the resolved velocities. Thus the expressions in Eqs. 3.13 and 3.14 for τ_{ik} capture the effects of the relevant physical mechanisms, to fourth order in the filter width.

Two final observations are worthwhile. First, the preceding analysis can be carried out with any spatially homogeneous filter. Indeed, up to fourth order in the filter width, the analytical results for the tophat filter (see Eqs. 3.16 and 3.17 below) are identical. However, special consideration is needed if a spectral cutoff filter is used. As concluded by Domaradzki & Saiki (1997) after examining several analyses and theories, "the SGS energy transfer is dominated by energy exchanges among resolved and unresolved scales from the vicinity of the cutoff." Thus, as Leonard (1974) pointed out, "large wave-number Fourier modes need the assistance of small wave-number modes to transfer energy from large scales to small scales. In the Fourier method the sharp cutoff in wave-number space precludes such a transfer." Accordingly, the sharp-cutoff filter is ill-suited to velocity estimation methods, including the series expansion model presented here. If it were used, two different cutoff wavenumbers would be needed for terms filtered more than once to prevent the Bardina term from disappearing (Zang *et al.*, 1993).

Second, any fourth-order approximation to the full velocity in terms of the resolved field would yield a SFS stress model accurate to fourth order in the filter width. The nice feature of the series expansion model used above is that if the velocity field is sufficiently smooth, the fourth-order approximation is a simple mathematical expression that does not involve empirical modeling.

3.3 Rudimentary tests of the model

Following the example of Geurts (1997), we perform a modified wave number analysis of the models in Eqs. 3.13 and 3.14. We consider one mode of a velocity field, $u = \exp(ikx)$, and evaluate the one-dimensional SFS stress,

$$\tau = \overline{u^2} - \overline{u}^2 \ . \tag{3.15}$$

We use two different filters, defined in one-dimensional form as

$$\overline{f}(x) = \int_{-\infty}^{\infty} H(x - x') f(x') dx' \tag{3.16}$$

where

$$H_G(x) = \sqrt{\frac{6}{\pi\Delta^2}} \exp\left(-\frac{6x^2}{\Delta^2}\right) \quad ; \quad H_T(x) = \begin{cases} 1/\Delta & for \quad |x| \leq \Delta/2 \\ 0 & for \quad |x| > \Delta/2 \end{cases} \tag{3.17}$$

for the Gaussian filter and the tophat filter, respectively. The filtered velocity takes the form

$$\overline{u} = G(k\Delta) \exp(ikx) \ , \tag{3.18}$$

where

$$G_G(k\Delta) = \exp\left(-\frac{k^2\Delta^2}{24}\right) \quad ; \quad G_T(k\Delta) = \frac{\sin(k\Delta/2)}{k\Delta/2} \ , \tag{3.19}$$

for the Gaussian and tophat filters, respectively. The series expansion used to represent the unfiltered velocity becomes

$$u^\star = A(k\Delta) G(k\Delta) \exp(ikx) \ , \tag{3.20}$$

where

$$A_G(k\Delta) = \left(1 + \frac{k^2\Delta^2}{24} + \frac{k^4\Delta^4}{1152}\right) \tag{3.21}$$

for the Gaussian filter, and

$$A_T(k\Delta) = \left(1 + \frac{k^2\Delta^2}{24} + \frac{7k^4\Delta^4}{5760}\right) \tag{3.22}$$

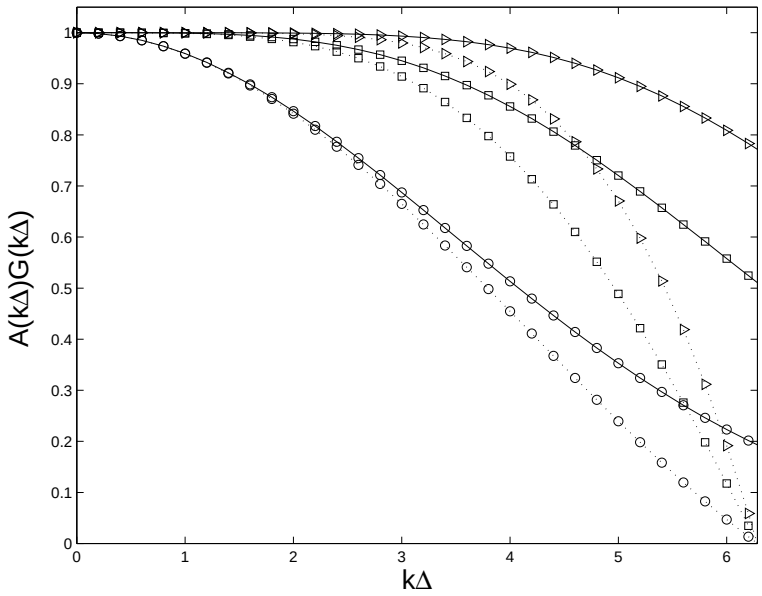

Figure 3.1: Amplitude of velocity estimates. Solid line: Gaussian filter, dotted line: tophat filter. ∘: 2nd order; □: 4th order; ▷: 6th order.

for the tophat filter. The truncation order of $A(k\Delta)$ can be specified, and is $O(\Delta^6)$ above.

In Fig. 3.1 we plot the amplitude, $A(k\Delta)G(k\Delta)$ (of Eq. 3.20) versus $k\Delta$ for the two filters with different truncation orders of the expansion in $A(k\Delta)$. This corresponds to Fig. 1 in Geurts (1997). The fourth-order accurate approximation (6th-order truncation error) gives the best results. In all cases, the amplitude deviation from 1 increases with $k\Delta$, but the agreement is good for $k\Delta < \pi$, the range of interest. The Gaussian filter gives a better approximation to the full velocity than the tophat filter, especially at higher k.

The exact form of the SFS stress for $u = \exp(ikx)$ is

$$\tau_G = \left[G_G(2k\Delta) - G_G^2(k\Delta)\right] \exp(2ikx) \;, \tag{3.23}$$

for the Gaussian filter, and

$$\tau_T = \frac{1}{2}\left[1 - G_T^2(k\Delta)\right] - \frac{1}{2}\left[G_T(2k\Delta) - G_T^2(k\Delta)\right] \exp(2ikx) \;, \tag{3.24}$$

for the tophat filter, which is the equation given by Geurts (1997). The approximate

forms are found by using the estimate of the unfiltered velocity given in Eq. 3.20 to obtain the 1-D representation of Eq. 3.13:

$$\text{Model 1:} \quad \tau_{M1} = \overline{u^{\star 2}} - \overline{u}^2 \ , \tag{3.25}$$

so that

$$\tau_{GM1} = G_G^2(k\Delta)\left[A_G^2(k\Delta)G_G(2k\Delta) - 1\right]\exp(2ikx) \ , \tag{3.26}$$

$$\tau_{TM1} = \frac{1}{2}G_T^2(k\Delta)\left[A_T^2(k\Delta) - 1 - (A_T^2(k\Delta)G_T(2k\Delta) - 1)\exp(2ikx)\right] \ . \tag{3.27}$$

Alternatively, if we also use the approximate velocity (Eq. 3.20) in the calculation of the second term in Eq. 3.15, as done in Eq. 3.14, we obtain

$$\text{Model 2:} \quad \tau_{M2} = \overline{u^{\star 2}} - \overline{u^{\star}}^2 \ , \tag{3.28}$$

and

$$\tau_{M2} = A^2(k\Delta)G^2(k\Delta)\,\tau \ , \tag{3.29}$$

for both the tophat and Gaussian filters. This approximate form is simply the application of the filter and expansion operators, $A(k\Delta)G(k\Delta)$, on τ twice.

The amplitude of the oscillating parts of τ_{GM1}, τ_{TM1}, and τ_{M2} are shown in Figs. 3.2-3.5 for different truncation orders of the models. The approximate forms are shown versus the amplitudes of the oscillating parts of the exact τ given in Eqs. 3.23 and 3.24 for each filter. Again, the agreement for $k\Delta < \pi$ is good. Of the models for τ, Model 1 seems to perform better than Model 2, and the Gaussian filter models are more effective than the tophat models in representing the subfilter stress at higher wave numbers. Figures 3.6 and 3.7 show a comparison of Model 1 and Model 2 for each filter type. It is seen that for the Gaussian filter, Model 1 is very close to the exact subfilter stress, and Model 2 is also quite good. Model 1 also performs better than Model 2 for the tophat filter.

The tophat filter version in Eq. 3.29 shown in Fig. 3.3 can be compared to Fig. 2 in Geurts (1997). The fourth-order model derived here gives results comparable to or perhaps slightly better than the case $L = 2$ in Geurts (1997). As was done by

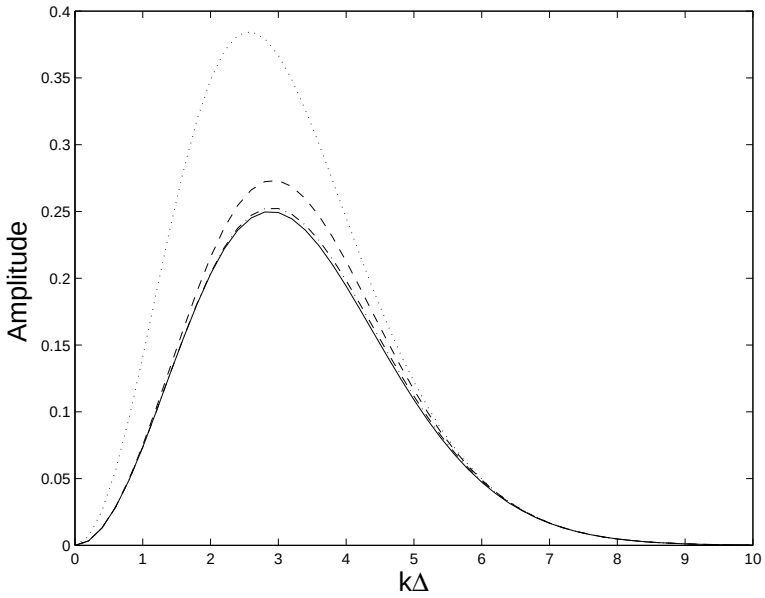

Figure 3.2: Amplitude of τ_{GM1} (Gaussian filter) and exact τ. Solid line: exact; dotted line: 2nd-order model; dashed line: 4th-order model; dash-dotted line: 6th-order model.

Geurts, this test could be extended to the general case $u = \sum_k \exp(ikx)$; this is not done here, as it provides very similar information about the velocity approximation.

3.4 *A priori* tests

A more robust preliminary test of the subfilter-scale model is provided by an *a priori* test (Clark *et al.*, 1979; Bardina *et al.*, 1983; Liu *et al.*, 1994), in which data from a direct numerical simulation (DNS) are filtered and compared to the model. *A priori* tests indicate the degree of correlation between the modeled and exact subfilter-scale terms and are useful indications of the expected performance of a SFS model in actual LES computations (*a posteriori* tests). Comparisons can be made at the tensor (τ_{ij}), vector ($\partial\tau_{ij}/\partial x_j$), and scalar ($\tau_{ij}\partial u_i/\partial x_j$) levels.

Although a high correlation (close to one) with the exact value is not a sufficient condition for a good SFS model, it is certainly a desirable feature. Of the commonly used SFS models, it is known that the Smagorinsky model does poorly in *a priori* tests, as the modeled τ_{ij} is not aligned with the actual stress tensor. The Smagorinsky model is, however, able to provide adequate dissipation and thus performs fairly well

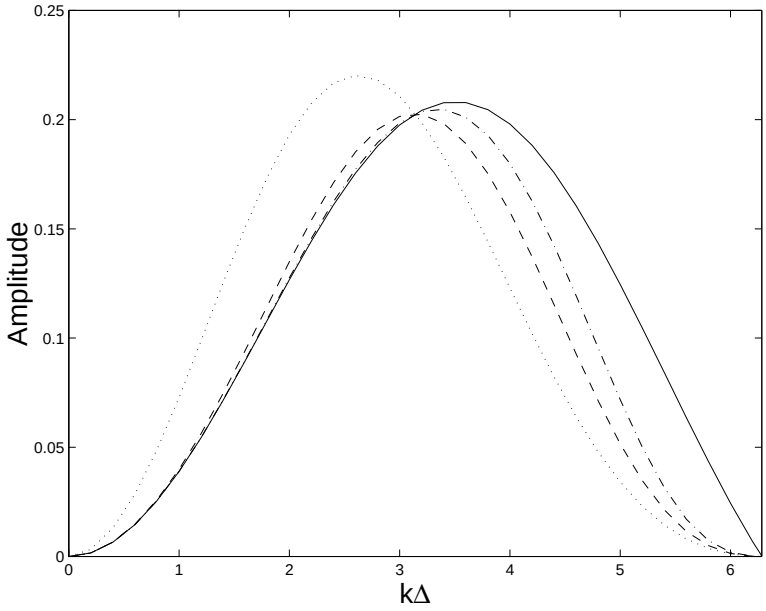

Figure 3.3: Amplitude of τ_{TM1} (tophat filter) and exact τ. Solid line: exact; dotted line: 2nd-order model; dashed line: 4th-order model; dash-dotted line: 6th-order model.

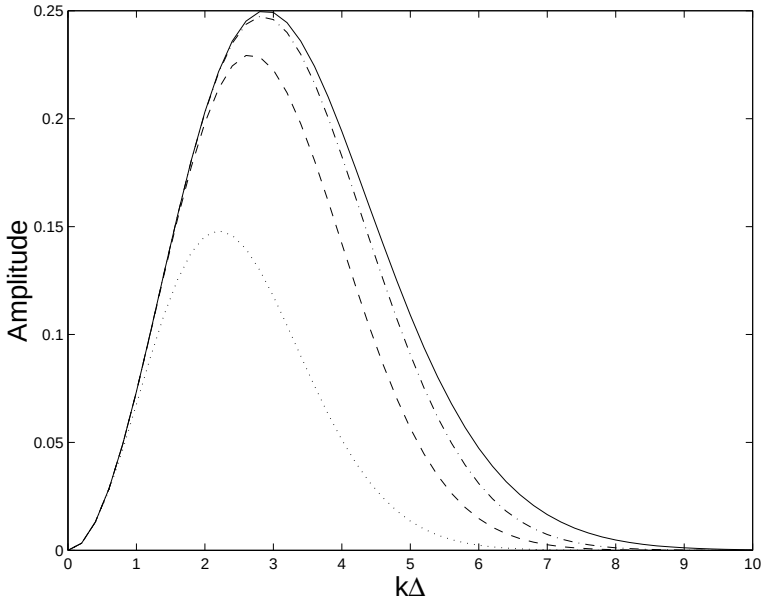

Figure 3.4: Amplitude of τ_{GM2} (Gaussian filter) and exact τ. Solid line: exact; dotted line: 2nd-order model; dashed line: 4th-order model; dash-dotted line: 6th-order model.

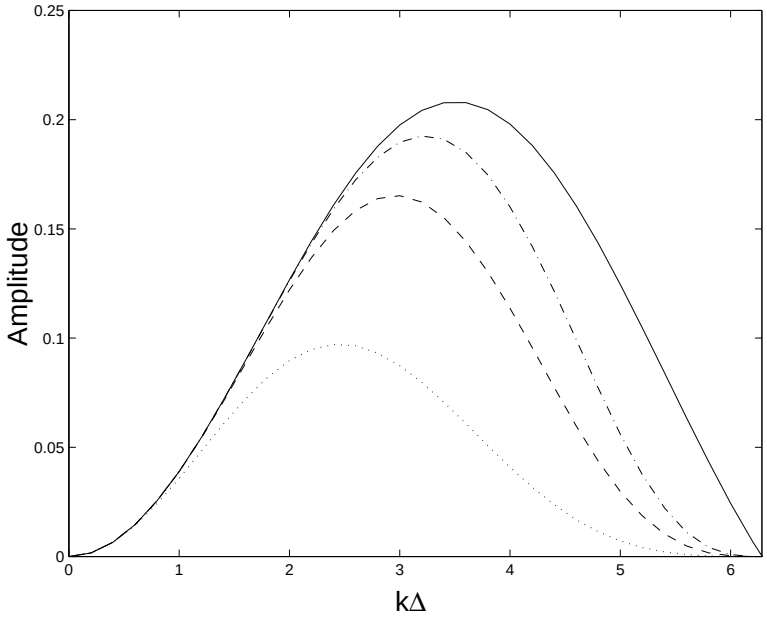

Figure 3.5: Amplitude of τ_{TM2} (tophat filter) and exact τ. Solid line: exact; dotted line: 2nd-order model; dashed line: 4th-order model; dash-dotted line: 6th-order model.

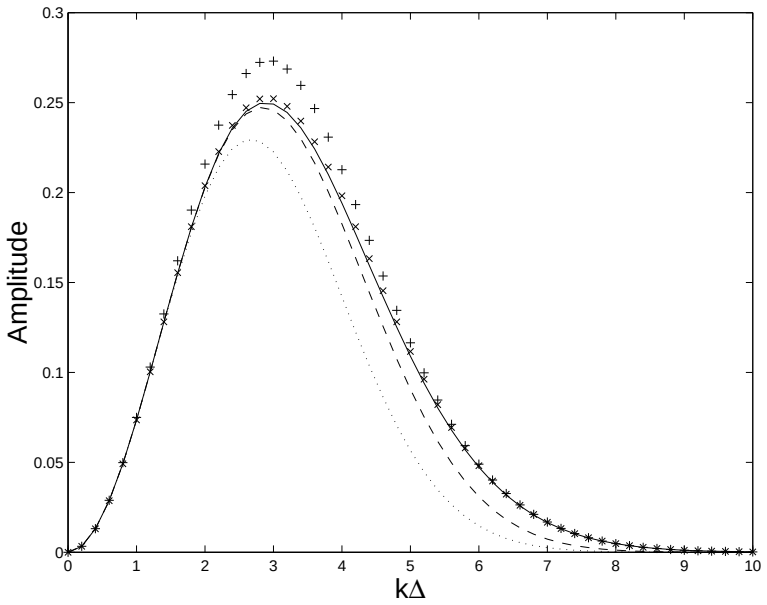

Figure 3.6: Amplitude of τ_{GM1}, τ_{GM2} (Gaussian filter) and exact τ. Solid line: exact; $+++$: 4th-order Model 1; $\times\times\times$: 6th-order Model 1; dotted line: 4th-order Model 2; dashed line: 6th-order Model 2.

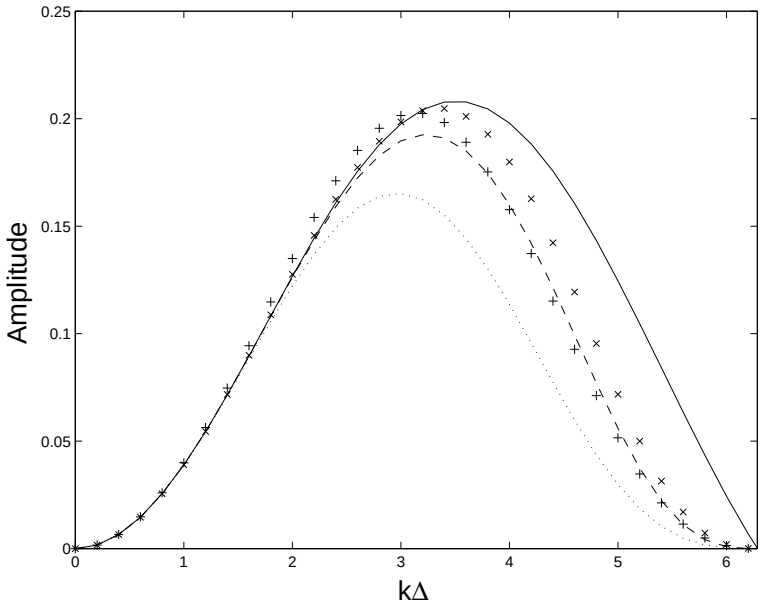

Figure 3.7: Amplitude of τ_{TM1}, τ_{TM2} (tophat filter) and exact τ. Solid line: exact; +++: 4th-order Model 1; $\times\times\times$: 6th-order Model 1; dotted line: 4th-order Model 2; dashed line: 6th-order Model 2.

in some actual LES. Scale-similarity models (*e.g.*, the Bardina model), on the other hand, display very good correlations, but do not dissipate enough energy when implemented in LES. *A posteriori* tests are necessary to obtain complete information on a model's performance and, in particular, on the actual level of energy dissipation; see results for atmospheric boundary layer flow simulations in Chapter 6. Nevertheless, ratios between modeled and exact quantities (particularly at the scalar level) from *a priori* tests provide a quick assessment as to whether the model provides adequate dissipation.

The DNS dataset used here is from the sheared and stably-stratified homogeneous turbulent flow computations performed by Shih *et al.* (2000). The Reynolds number based on the Taylor microscale is 89.44, the Richardson number is 0.16, and the nondimensional shear number is 2.0. The DNS data, u_i, are defined on a 128^3 grid with domain size $2\pi^3$ where $\Delta_{DNS} < \Delta_{LES}$. The DNS grid is anisotropic due to coordinate stretching factors used for computation of the homogeneous shear flow. Here, x_1 is the streamwise direction, x_2 is the vertical direction, and x_3 is the spanwise direction; shear is applied in the x_1, x_2-plane. The DNS data are sampled on the scale of the LES grid and filtered using a Gaussian filter of width $\Delta = 2\Delta_{LES}$ to obtain

		τ_{12}	$\frac{\partial \tau_{1j}}{\partial x_j}$	$\tau_{ij}\frac{\partial u_i}{\partial x_j}$
S	C	0.1610	0.4746	0.6962
	R	3.5042	2.8092	1.4780
B	C	0.9525	0.9194	0.9665
	R	1.3367	1.9179	1.3666
MC	C	0.9602	0.7981	0.9700
	R	1.2927	1.9024	1.3158
$T4$	C	0.9239	0.9135	0.9430
	R	1.0352	1.1037	1.0790
$MT4$	C	0.9875	0.9763	0.9917
	R	1.0702	1.2636	1.0724
$MT6$	C	0.9969	0.9937	0.9972
	R	1.0097	1.0611	1.0062

Table 3.1: Gaussian Filter: Correlations, $GR = 2$, $FGR = 2$.

the LES field, $\overline{u}_i$. This filter-grid ratio is chosen so that the discretization errors in an actual LES would be smaller than the contribution of the SFS terms (Ghosal, 1996). Since the DNS data represent the exact velocity field, the exact subfilter-scale stress can be computed at each point on the grid. The modeled SFS stress can be computed from the LES field defined on the LES grid, and compared to the exact stress at the same points on the LES grid. The correlation coefficient and the ratio of the root-mean-square (rms) values are then computed for each of the SFS stress components. The correlation coefficient measures the degree of linearity in the relationship between the modeled and exact SFS stress, while the ratio gives information about the coefficient of proportionality.

Tables 3.1-3.3 show correlation coefficients (C) and ratios (R) for selected subfilter-scale quantities: τ_{12} is the SFS shear stress in the shear flow, $\partial \tau_{1j}/\partial x_j$ is the divergence of the subfilter stress which appears in the momentum equations, and $\tau_{ij}\partial u_i/\partial x_j$ is the SFS stress dissipation. The ratio is the exact DNS rms value divided by the modeled rms value, and should be close to one. For the dissipation term, the ratio gives an indication of the magnitude of energy dissipated by the model. Results are presented for the following subfilter-scale models: Smagorinsky (S), Bardina scale-similarity (B), modified Clark (MC), 4th-order series expansion using Eq. 3.13 (T4), modified 4th-order series expansion using Eq. 3.14 (MT4), and modified 6th-order series expansion using Eq. 3.14 (MT6). The models are given in Appendix A. LES

		τ_{12}	$\frac{\partial \tau_{1j}}{\partial x_j}$	$\tau_{ij}\frac{\partial u_i}{\partial x_j}$
S	C	0.1557	0.4169	0.6029
	R	3.8231	2.9590	1.5601
B	C	0.8881	0.8748	0.9048
	R	1.6934	2.6138	1.8056
MC	C	0.9082	0.7750	0.9151
	R	1.5108	2.4327	1.6210
$T4$	C	0.8282	0.8013	0.8599
	R	1.1623	1.2721	1.2548
$MT4$	C	0.9544	0.9440	0.9591
	R	1.1800	1.5072	1.2307
$MT6$	C	0.9831	0.9764	0.9831
	R	1.0411	1.1662	1.0663

Table 3.2: Gaussian Filter: Correlations, $GR = 4$, $FGR = 2$.

to DNS grid ratios of $GR = 2, 4, 8$ are considered, where $\Delta_{LES} = GR\ \Delta_{DNS}$. In each case the filter-grid ratio is $FGR = \Delta/\Delta_{LES} = 2$.

The correlations for the Bardina scale-similarity model are quite high; however, the ratios are not very good, indicating that the model does not capture energy dissipation correctly, as noted previously. The Smagorinsky model does not perform well at all, but the ratio for the dissipation is better than that for the Bardina model for $GR = 4, 8$. The MT4 model contains the scale-similarity terms of the Bardina model, while model T4 does not. It seems that the inclusion of these terms significantly improves the correlation coefficients; however, the improvement in the ratios is more evident only in the 6th-order representation, MT6. (This is also seen in the single mode tests done in the previous section: Model 1 performs better than Model 2, which has the Bardina model form, in amplitude comparisons.) The modified Clark model, derived from the T4 model, performs comparably to the other series expansion models, often with slightly higher correlations but poorer ratios.

The correlations are highest for the MT6 model, the 6th-order expression for the series expansion model, with values over 0.99 for $GR = 2$. Ratios as good as 1.0062 are obtained for the SFS dissipation modeled with MT6 showing that the dissipation is captured to within 1% of the exact value. The correlation decreases when the LES grid becomes coarser, i.e., as GR increases and the resolved scale wavenumber cutoff becomes smaller; it is harder to represent the higher wavenumbers with a smaller

		τ_{12}	$\frac{\partial \tau_{1j}}{\partial x_j}$	$\tau_{ij}\frac{\partial u_i}{\partial x_j}$
S	C	0.0925	0.3041	0.3920
	R	4.9880	3.1754	2.0092
B	C	0.7759	0.7852	0.8181
	R	2.8324	4.1177	3.1285
MC	C	0.7960	0.7104	0.8263
	R	2.1099	3.3449	2.4171
$T4$	C	0.6691	0.6032	0.7470
	R	1.6837	1.7023	1.8542
$MT4$	C	0.8769	0.8729	0.8939
	R	1.5989	2.0326	1.7325
$MT6$	C	0.9407	0.9326	0.9422
	R	1.2301	1.4111	1.3038

Table 3.3: Gaussian Filter: Correlations, $GR = 8$, $FGR = 2$.

range of resolved scales. This is an important limitation when we apply LES to large domains and Reynolds numbers for which the LES to DNS grid ratio is necessarily high. However, even at $GR = 8$, the MT6 model captures most of the SFS stress, and has a correlation of 0.9422, significantly higher than the other models. Though the discretization error of the numerical scheme used in many actual LES is larger than 6th order, it may help to use a more accurate SFS model such as MT6. Similar results to those in Tables 3.1-3.3 are obtained when a tophat filter is used, though the numbers are not quite as good overall.

The results from this *a priori* analysis compare very favorably with *a priori* tests performed by others for their models, (see e.g. Domaradzki & Saiki, 1997; Stolz *et al.*, 1999*a*; Salvetti & Banerjee, 1995). For a compressible ramp flow, Stolz *et al.* (1999*a*) obtained correlations of approximately 0.99 (as obtained in this work) for their approximate deconvolution model with seven terms in an inverse filter expansion.

As an illustration of the ability of this velocity estimation model (Eq. 3.9) to represent the full velocity field, Fig. 3.8 shows contours of the streamwise velocity for different truncation orders in the velocity estimation. The raw DNS data, which is sampled on the LES grid defined by the parameter GR, is best represented by the highest order model, MT6; unlike the lower order models, velocity contours for this case capture the smaller features of the DNS data quite well. Chapters 5 and 6 show that the model yields similar convergence when implemented in an LES code.

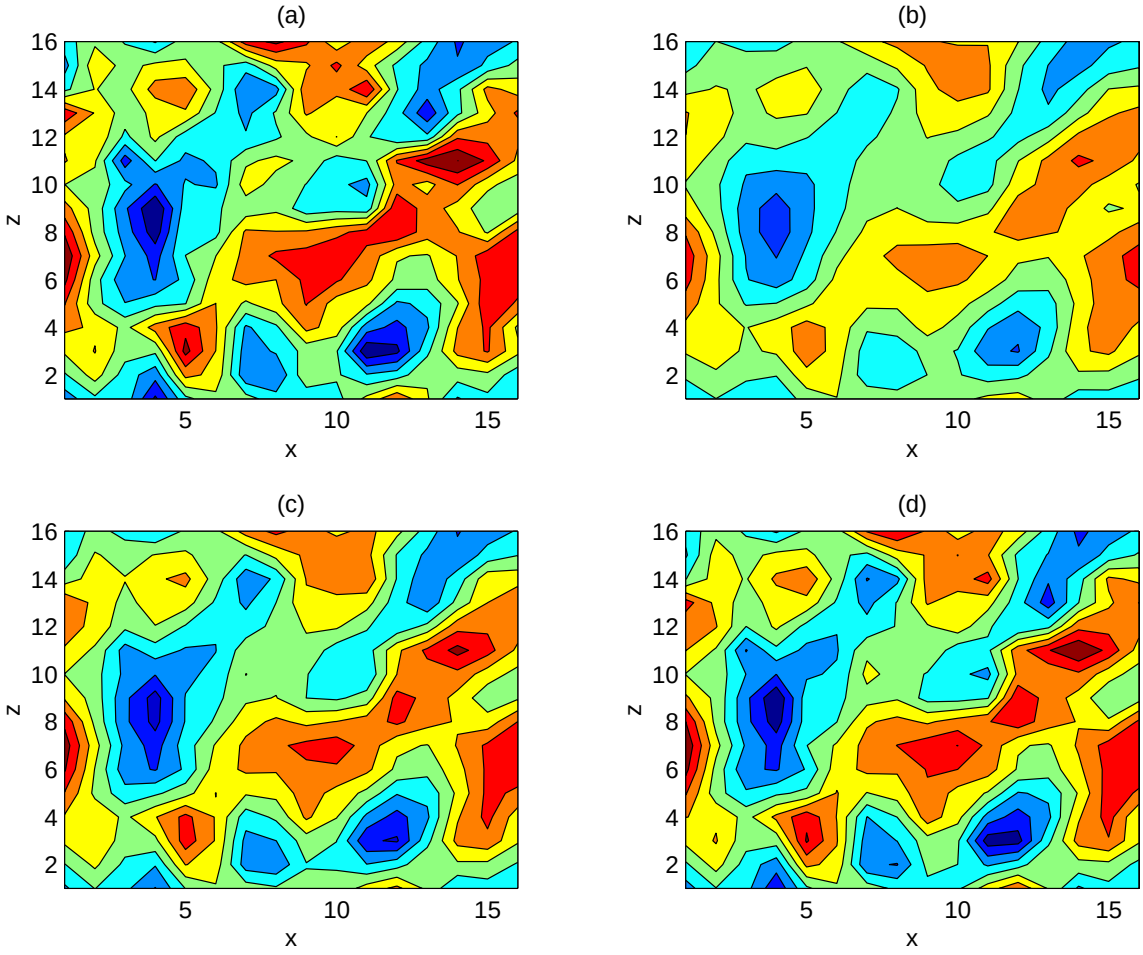

Figure 3.8: Contour plots of LES velocity estimates for u_1 on an x_1, x_3-plane, $GR = 8$. (a) Sampled DNS field; (b) 2nd-order estimate; (c) 4th-order estimate; (d) 6th-order estimate.

3.5 Taylor series convergence

An interesting aspect of the implementation of the series expansion model is the question of the validity of the Taylor series expansion on a fluctuating field. Aldama (1990) and Love (1980), for instance, claim that a Taylor series expansion for the perturbation velocity u' is not valid because this field is not smoothly varying over the filter interval Δ. Here, we have expressed the full velocity field (not just the fluctuating field) in a Taylor series expansion, to eventually express u_i as a function of the resolved velocity, $\overline{u}_i$. Vreman *et al.* (1996) also Taylor expand the full velocity field; they refute Love's claims, but also maintain that the full velocity is not smoothly varying over Δ and hence higher order terms may be larger than the terms retained. However, the Taylor series is valid for any analytic function. The series converges for any smoothly varying field, no matter how many oscillations there are over the interval Δ (an example is given below).

To illustrate the robustness of Taylor series expansions, we show below the number of terms needed to represent a cosine wave. Even at a large distance from the expansion point, the series will converge if enough terms are included. For our case, where the filter size is twice the grid size, the series must be valid in the filter integral discussed above. Thus, for a tophat filter, the Taylor series needs to be valid a maximum distance $\Delta/2$ from the point of interest. On a grid with spacing Δ_{LES}, the smallest wave that can be supported is of wavelength $2\Delta_{LES}$. With the filter twice as big as the grid, $\Delta = 2\Delta_{LES}$, the expansion needs to be valid a distance Δ_{LES} away (or half a wavelength). The plot in Fig. 3.9 shows the agreement of the Taylor series to the exact cosine function when different numbers of terms are taken. At half a wavelength away, the agreement is good for 2 or 3 terms in the series. Thus the Taylor series is a good approximation for the grid conditions chosen in this study. If the filter size were larger, however, the filtering integration would demand that the Taylor series be a good approximation at a larger distance, and then more terms in the series would be required for the solution to be as accurate (a full wavelength away, at least 7 terms are necessary!).

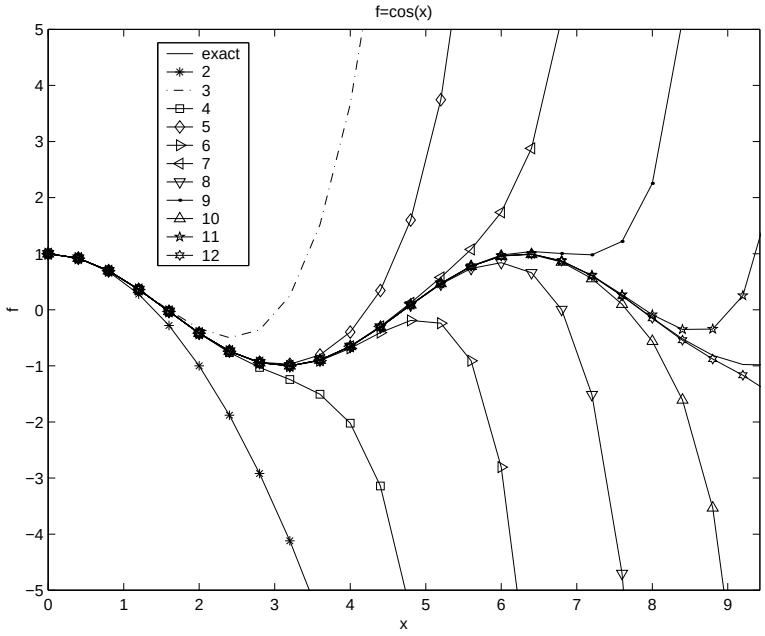

Figure 3.9: Convergence of Taylor series for function $f = \cos(x)$. Exact function and Taylor series with 2 through 12 terms are shown.

3.6 Implementation of model

One of the most attractive features of the series expansion model is its ease of implementation. The SFS stress model given by Eq. 3.13 or 3.14 can be directly computed and substituted into the resolved flow equation. Equation 3.2 must then be discretized and solved numerically, *e.g.*, by the method of Zang *et al.* (1994). The computational cost of using this SFS model will be comparable to the cost of the S^3 model (Shah & Ferziger, 1995). Results for the series model indicate that its CPU requirement is less than or equal to that for the dynamic two-parameter model (Salvetti *et al.*, 1997; Ding, 2000), depending (it appears) on whether the grid is a Cartesian grid or a mapped grid where the metrics add to the cost of computing the model terms. The greatest difficulty is implementation of the model near solid boundaries, where care must be taken in representing higher order terms, as discussed in Chapter 6.

Because the SFS stress tensor is $O(\Delta^2)$ (see Appendix A), it is important that the filter width, Δ, be larger than the grid size upon which discretization is performed. Otherwise, numerical discretization error in a second-order scheme will have an effect of the same order of magnitude as the SFS stress. The analysis of Ghosal (1996)

indicates that choosing the filter width to be at least twice the grid size is advisable.

As noted above, the tophat filter can also be used with the series expansion in three-dimensions, as was done in one dimension above. Up to fourth order, the Gaussian and tophat filters give the same expansions, which leads to identical SFS model expressions, but different numerical results because of the different behaviors of the filters. However, there is not much difference in the numerical approximation of these filters, as the Gaussian filter must be truncated, and it may be hard to distinguish between the discrete representations of these filters when implemented in a finite-difference or finite-volume simulation. In principle, any filter could be used, as long as it allows interaction of the smallest resolved and largest unresolved scales as discussed previously (requiring, therefore, two different filter cutoffs if the spectral cutoff filter is used). This means that the approach described here for subfilter-scale modeling could accommodate a commuting filter, allowing implementation of this model on non-uniform grids.

3.7 Conclusions

As LES begins to be applied to problems in which more of the energy of the flow is unresolved, the accuracy of the SFS model becomes increasingly important. The series expansion model proposed here does not assume that the SFS motions are isotropic, and the model can easily be implemented with an anisotropic filter. Indeed, *a priori* test results for an anisotropic case show very high correlations and ratios between the modeled SFS stress and the exact stress computed from DNS data, indicating that the model captures SFS motions quite accurately. Furthermore, the model satisfies the evolution equation for the SFS stress to an arbitrarily-chosen order in the filter width (4th and 6th orders are used here), making it clear that this SFS model can account for the effects of buoyancy, Coriolis, and pressure forces. There are of course small scale phenomena present in combustion or shocks that present further challenges for SFS modeling. This series model will likely have difficulty with the non-smooth velocity fields of those cases. However, this SFS model is attractive because it does not introduce any free parameters, being based on a mathematical expansion. The model can be implemented numerically with ease and can also be extended to higher accuracy as desired.

Chapter 4

Numerical errors in large-eddy simulation*

Before continuing the discussion of new subfilter-scale modeling approaches in large-eddy simulation, we consider the effect of other numerical errors in large-eddy simulations. Errors in LES arise from aliasing and discretization errors, and from errors in the subfilter-scale (SFS) turbulence model. Using a direct numerical simulation (DNS) dataset of stably-stratified shear flow to perform *a priori* tests, we compare the numerical error from several finite-difference schemes to the magnitude of the SFS force. These numerical errors can often be larger than the entire turbulence modeling term, and therefore deserve careful consideration. This is an extension of Ghosal's analysis (Ghosal, 1996) to realistic flow fields. By evaluating different grid resolutions as well as different filter-grid ratios, we provide guidelines for LES: for a second-order finite-difference scheme, a filter-grid ratio of at least four is desired; for a sixth-order Padé scheme, a filter-grid ratio of two is sufficient.

4.1 Introduction

Large-eddy simulation (LES) has become an increasingly used method for predicting turbulent flows. However, LES and direct numerical simulation (DNS) both suffer

*This chapter is a reproduction (with minor modifications) of the paper "A further study of numerical errors in large-eddy simulations" by Fotini Katopodes Chow (the principal author) and Parviz Moin, published in the Journal of Computational Physics, January 2003, Volume 184(2), pages 366-380 (Chow & Moin, 2003),

from discretization and aliasing errors that depend on the numerical schemes used. Because of computational limits, LES has an additional source of error owing to the fact that the velocity field is not fully resolved. The Navier-Stokes equations are filtered, and the effect of subfilter-scale (SFS) motions is modeled. Thus numerical errors in LES result from aliasing and discretization errors, as well as from errors in the subfilter-scale model.

Much of the current research in LES is focused on the development of improved SFS models, without reference to perhaps more significant, numerical errors that are present. However, as LES is applied to more complex problems, it will become even more important to understand errors inherent in the numerical schemes used, especially if we hope to create accurate forecast models. While a spectral, dealiased code may be able to avoid aliasing and finite-difference errors (though not SFS errors), virtually all turbulence calculations in complex domains are carried out with finite differences. When finite-differences schemes are used, truncation errors as well as the formulation used for the nonlinear terms of the Navier-Stokes equations have been shown to be important for numerical stability and accuracy (Kravchenko & Moin, 1997). Furthermore, assessment of truncation and aliasing errors is crucial for ensuring that the contribution of the SFS forcing is not dominated by numerical errors.

A systematic analysis of these numerical errors is difficult because of nonlinear interactions between them. The traditional linearized analysis of errors for partial differential equations is therefore not adequate. Ghosal (1996) was able to draw important conclusions by using statistical analysis to derive errors in LES from a random field with a von Kármán energy spectrum. He found that for an eighth-order finite-difference scheme, the LES filter size must be at least twice the grid spacing for the contribution of the SFS force to the total nonlinear force to be significant compared to the errors introduced by aliasing and truncation. For a second-order finite-difference scheme, Ghosal found that the filter must be at least four times the grid spacing. Kravchenko & Moin (1997) performed *a posteriori* tests which indicated that different (but analytically equivalent) formulations of the nonlinear terms give different results because of finite-difference and aliasing errors. Blaisdell *et al.* (1996) present results which indicate that choosing a particular form for the nonlinear terms with finite differencing may stabilize the results and reduce the need

for dealiasing. There have also recently been several studies which have developed improved higher-order finite-difference schemes with the aim of reducing numerical errors in LES (see for example Balsara & Shu (2000) and Morinishi *et al.* (1998)). Others have performed studies which have explicitly investigated numerical errors with regard to LES or specifically the computation of SFS models (see Morinishi & Vasilyev (1998), Tsubokura (2001), and Glendening & Haack (2001)).

Here we present results from error analysis performed using a direct numerical simulation dataset to generate a filtered subset representing "exact" LES data. In particular, we aim to examine the conclusions of Ghosal (1996) with a more realistic flow field. As his results from von Kármán spectra have not been verified by analysis of real data sets, we seek to re-evaluate his conclusions here, commenting on differences due to the nature of the data used. As most LES calculations of engineering interest are performed at moderate Reynolds numbers, we expect the DNS dataset to be informative. Consideration of SFS model performance in relation to numerical errors is not the focus of this chapter and will be addressed in Chapter 5.

In Section 4.2 we describe the dataset and our approach in the *a priori* testing. Following, in Section 4.3, we discuss the relative magnitudes of the SFS force and nonlinear terms in relation to filter size and resolution. Sections 4.4 and 4.5 discuss finite-difference and aliasing errors, and compare them to an ideal SFS forcing term.

4.2 Numerical tests

The DNS data used for *a priori* testing are from the stably stratified homogeneous shear flow simulations performed by Shih *et al.* (2000). (These data were also used in Chapter 3.) The Reynolds number based on the Taylor microscale is 89.44, the Richardson number is 0.16, and the nondimensional shear number is 2.0. This dataset was chosen because the flow is homogeneous (allowing use of Fourier analysis) but has the increased complexity generated by the stratification; turbulent length scales are reduced due to the stratification and therefore are more difficult to model than those from a flow with neutral stratification. We expect that the results from this dataset will be more realistic than those of a simpler homogeneous flow; however, we have also examined an isotropic turbulence case produced by the same DNS code and found similar results. The results from this analysis should therefore be appropriate

for extension to moderate Reynolds number flows.

The velocity fields used for *a priori* testing are obtained by using a sharp Fourier cutoff filter on the full 128^3 DNS data. These cutoff filtered fields are treated as "exact" data for a given grid size. Thus, u_i for a particular grid size is obtained by cutoff filtering the DNS data to remove the high wavenumbers which would not be present on a coarser grid. LES quantities such as $\overline{u}_i$ and $\overline{u_i u_j}$ are then obtained for each grid size using a Gaussian filter in spectral space. We choose not to use a spectral cutoff filter for calculation of these LES variables since our primary application area of interest is in complex geometries where finite-difference methods are used. A tophat filter could also be used to give comparable results; the discrete filter coefficients used for tophat and Gaussian filters with finite-difference methods are similar.

Figure 4.1 shows the three-dimensional energy spectra for the velocity fields used to study numerical errors. Several grid cutoff wavenumbers are considered to study the effect of different grid resolutions; the grid is reduced from 128^3 for the original DNS to 64^3, 32^3, 16^3, and 8^3 for the LES grids. Using these "exact" fields, we can compute the nonlinear and SFS terms for LES using different methods and compare results for the magnitudes of errors. Notice that the shape of these spectra are quite different than the von Kármán energy spectra used by Ghosal (1996). In particular, due to the low Reynolds number of the DNS dataset, the inertial range is very small, as seen by comparison to the $-5/3$ slope also plotted. We therefore expect that our analysis of this dataset may yield different conclusions from the high Reynolds number results of Ghosal.

The energy spectra in Fig. 4.1 and in all the following figures are computed for spherical shells and plotted versus the magnitude of the wavenumber. The spherical wavenumber is computed as $\kappa = \sqrt{k_1^2 + k_2^2 + k_3^2}$ where k_1, k_2, k_3 are the Cartesian wavenumbers. Energy from each wavenumber triplet k_1, k_2, k_3 is assigned to the corresponding wavenumber bin for κ, chosen at the nearest integer level. The spectra are often not smooth at the highest wavenumbers due to inadequate statistical sampling in the outer spherical shells. However, the 1-D spectra (not shown) for these quantities are smooth even at the tail ends. For simplicity, we will refer to the grid size and the chosen filter-grid ratio (FGR) instead of the exact cutoff wavenumber for each LES grid. In addition, most results are presented for the case when the Gaussian LES filter width is twice the grid spacing (with a 32^3 grid). We use this as our base case as

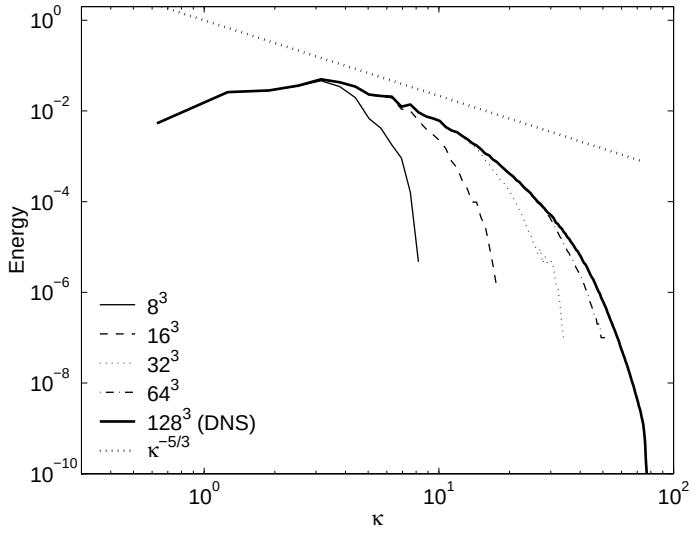

Figure 4.1: Three-dimensional energy spectra of the "exact" velocity fields used for analysis, obtained by cutoff-filtering the original DNS dataset. A $\kappa^{-5/3}$ line is also plotted for comparison.

this ratio seems to be the most commonly used in the recent literature. We consider other filter widths in our analysis and comment on their effect. All numerical tests are performed in Fourier space, as described further in the sections that follow.

4.3 Comparison of total nonlinear and subfilter-scale terms

The full nonlinear term in the Navier-Stokes equations, $\frac{\partial u_i u_j}{\partial x_j}$, creates a closure problem in LES when this term is filtered: $\overline{\frac{\partial u_i u_j}{\partial x_j}}$. The usual approach in LES is to replace this term with the closed term $\frac{\partial \overline{u}_i \overline{u}_j}{\partial x_j}$ (assuming the filter and derivatives commute) and to subtract a SFS force term, $\frac{\partial \tau_{ij}}{\partial x_j}$, from the right-hand side of the equation, where $\tau_{ij} = \overline{u_i u_j} - \overline{u}_i \overline{u}_j$. This effectively transfers the closure problem to the right-hand side of the filtered Navier-Stokes equations. Traditionally the approach has been to model τ_{ij} as a purely dissipative term, using an eddy-viscosity formulation. As described in Chapter 2, recent work has shown that this method may not be adequate, especially when the flow dynamics are sensitive to energy backscatter (counter-gradient transfer from small to large scales) in the flow.

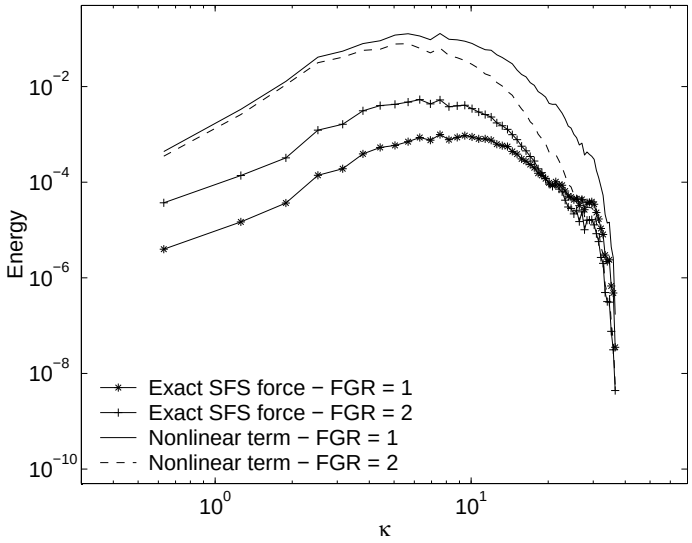

Figure 4.2: Energy spectra of the spectrally computed (filtered) nonlinear term (in the dealiased divergence form) and the SFS term for a fixed resolution (32^3 grid) and filter-grid ratios of one and two.

It is interesting to compare the relative magnitudes of the SFS term, $\frac{\partial \tau_{ij}}{\partial x_j}$, and the total nonlinear term, $\frac{\partial \overline{u}_i \overline{u}_j}{\partial x_j}$. In an ideal LES, the sum of these terms is equal to the full nonlinear term $\overline{\frac{\partial u_i u_j}{\partial x_j}}$ which can be obtained from a DNS (after filtering). In practice, the contribution to the total nonlinear term depends on the SFS model used. However, even with a perfect SFS model, the contribution of the SFS model would depend on the filter size chosen. The larger the filter size, the more energy is placed in the subfilter scales, and the larger the SFS term must be. Figure 4.2 shows the dependence of the SFS term on the filter size for a fixed grid resolution. This is similar to Fig. 2 in Ghosal's paper (Ghosal, 1996); however the spectra are quite different, as the spectrum of the nonlinear terms generated from the von Kármán spectrum increases monotonically while there is a definite downturn in the present data.

Another important trend is that as the resolution of the grids we consider increases (and hence the absolute filter width decreases for a given filter-grid ratio), the results approach that of a DNS. Thus the relative contribution of the SFS term to the total nonlinear term (at a fixed filter-grid ratio) becomes smaller as resolution is increased. This trend can be seen in Fig. 4.3 where a global measure of the nonlinear and SFS

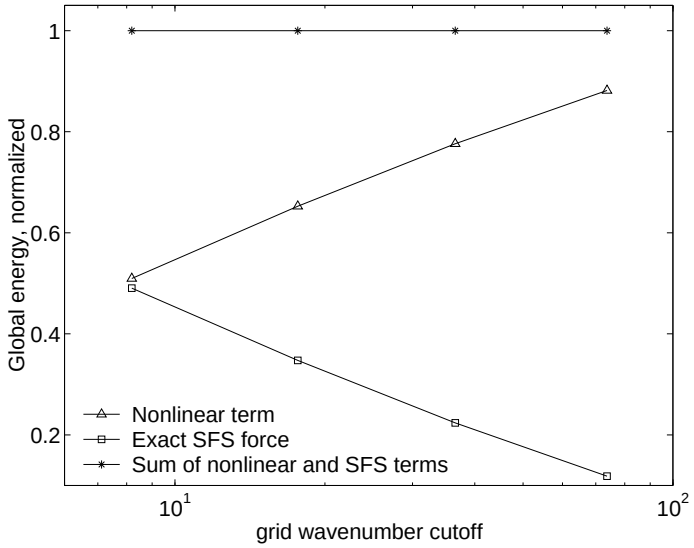

Figure 4.3: Global energies of the total nonlinear term (in the dealiased divergence form) and the SFS term for different grid resolutions, normalized by the sum of the nonlinear and SFS terms. Data points are shown at the 8^3, 16^3, 32^3, and 64^3 grid resolution locations. Filter-grid ratio = 2.

terms is plotted for different grid resolutions. The values are normalized (unlike Ghosal's Fig. 6) by the total for both the nonlinear and SFS terms, since the totals are dependent on the grid resolution. The global measure is the same as that in Ghosal's Eq. 81, which is the square root of the integral of the energy spectrum:

$$\sigma_* = \left[\int_0^{\kappa_m} E^{(*)}(\kappa) d\kappa \right]^{1/2} . \tag{4.1}$$

Here σ_* is the global measure for a particular quantity (such as the nonlinear terms, error terms etc.), $E^{(*)}$ is the three-dimensional energy spectrum for that quantity, and κ_m is the maximum wavenumber magnitude. Note that in our case the power spectrum includes the corners of the wave space, unlike Ghosal's.

Thus, the importance of accurately representing the SFS term is greatest at low resolutions where the SFS term contributes a larger percentage of the total force. However, at low resolutions, numerical error also becomes more significant because fine-scale motions are not well-represented on the grid.

4.4 Finite-differencing errors

Modified wavenumber analysis is useful for examining truncation errors of different numerical schemes. The modified wavenumber, k', for a finite-difference scheme, is derived by discrete differentiation of $u = \exp(ikx)$ (Moin, 2001). Finite-difference schemes exhibit large errors near the grid wavenumber cutoff, as evidenced by the reduced magnitude of the modified wavenumbers. Higher-order finite-difference methods perform better; however all finite-difference methods have low modified wavenumbers near the grid cutoff point. To examine the effect of truncation errors, we will insert the modified wavenumbers in place of the true wavenumber into spectral differentiation routines to compare finite-difference and spectral results, as was done by Kravchenko & Moin (1997).

Even though all spatial derivatives in the LES equations will have finite-differencing errors, we are primarily interested in the truncation error in the nonlinear term because this has the potential to be very large and overshadow the contribution of the SFS term. In Fig. 4.4 we compare the spectrum of the finite-difference error in computing the nonlinear term (computed using the divergence form defined later in Eq. 4.3) to the SFS force term, with a filter-grid ratio of unity. The finite-difference error is computed by subtracting the nonlinear term calculated with a finite-difference scheme from that of the exact (spectrally calculated) nonlinear term. We see that the trend is similar to that in Ghosal's Fig. 4: the SFS force at high wavenumbers is dominated by the error in the nonlinear terms, even when the nonlinear terms are computed with a 6th-order Padé scheme.

This situation cannot be improved by increasing the grid resolution, as also demonstrated by (Ghosal, 1996, see his Fig. 3). When the grid resolution is increased, finer-scale motions are better resolved and the role of the SFS term decreases, as seen in Fig. 4.3. The finite-difference error does not decrease, however, as the grid must now resolve a larger range of motions as these are no longer in the subfilter range. Thus the finite-difference error continues to dominate the SFS term.

Ghosal (1996) suggests that by choosing the proper filter-grid ratio in combination with a high-order finite-difference scheme it is possible to reduce the finite-difference error sufficiently. He shows that the filter-grid ratio has a pronounced effect on the magnitude of the error term. We observe the same trend when this is done for our

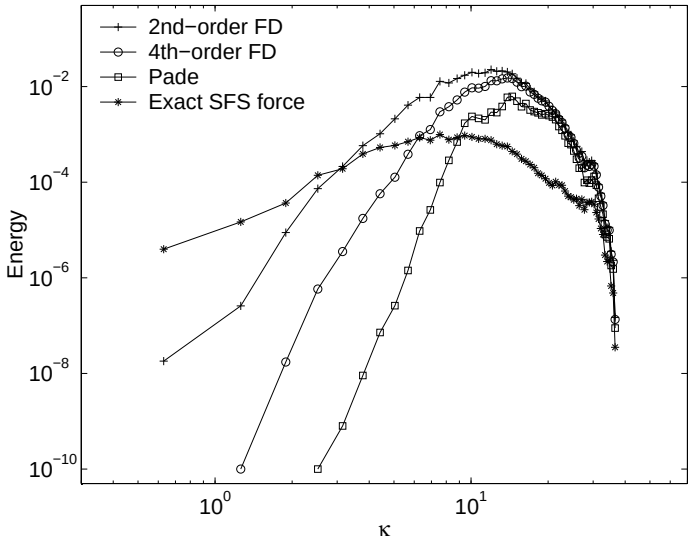

Figure 4.4: Energy spectra of the finite-differencing error in the nonlinear term in the dealiased divergence form, computed with second- and fourth-order finite-difference (FD) and sixth-order Padé schemes, compared to the SFS force term. Filter-grid ratio = 1; 32^3 grid.

DNS dataset. However, we choose to make the comparisons differently. Instead of keeping the filter cutoff fixed and changing the grid size as Ghosal does, we keep the grid size fixed and change the filter size to change the filter-grid ratio. Though the trends observed are similar, our perspective is more directly applicable to real LES computations: the grid resolution is not readily increased because of computer limitations, but the filter-grid ratio can be adjusted easily.

Figure 4.5 shows that increasing the filter-grid ratio by a factor of two improves results appreciably. The errors for the second-order and fourth-order finite-difference schemes and the Padé scheme are smaller over much of the wavenumber range, though the errors still dominate at high wavenumbers. This is consistent with Ghosal's conclusions. In particular we see similar features in our Fig. 4.5 and Ghosal's Fig. 10, for a filter-grid ratio of two. It is not until the filter-grid ratio is equal to four that the second-order finite-difference scheme becomes acceptable. Figure 4.6 shows the results for this combination, where the truncation error no longer dominates the SFS force. Ghosal's Fig. 9 also indicates that for a second-order central difference scheme, the filter-grid ratio should be at least 4, which is consistent with our results, even though his plot is for a grid 4^3 times larger.

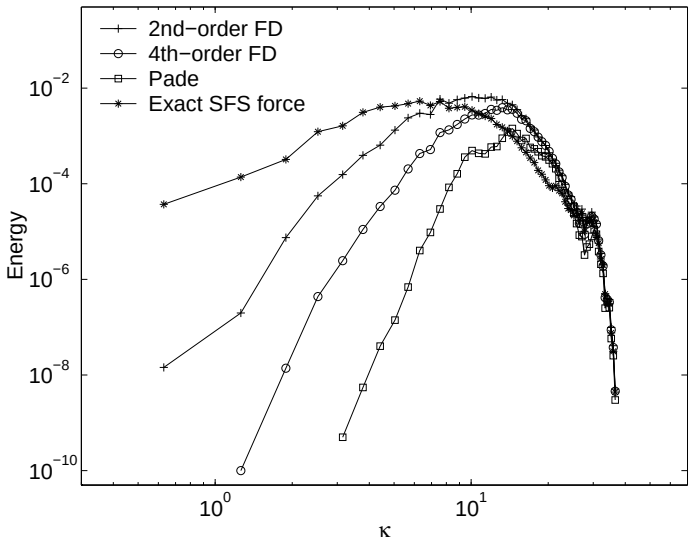

Figure 4.5: Energy spectra of the finite-differencing error in the nonlinear term in the dealiased divergence form, computed with second- and fourth-order finite-difference and sixth-order Padé schemes, compared to the SFS force term. Filter-grid ratio = 2; 32^3 grid.

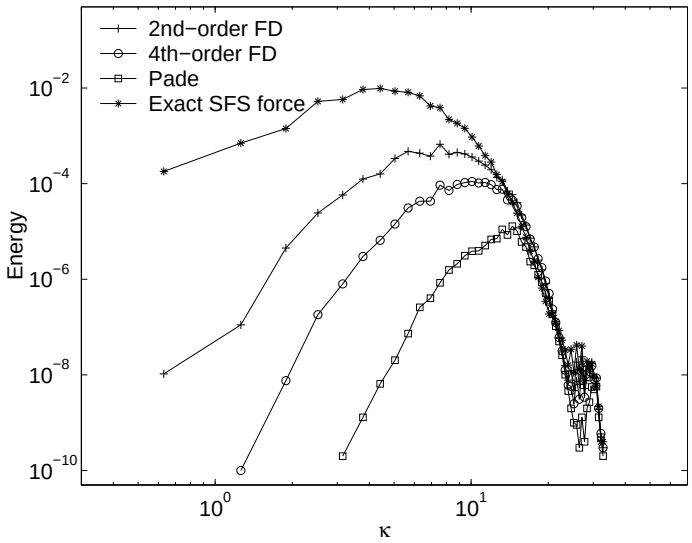

Figure 4.6: Energy spectra of the finite-differencing error in the nonlinear term in the dealiased divergence form, computed with second- and fourth-order finite-difference and sixth-order Padé schemes, compared to the SFS force term. Filter-grid ratio = 4; 32^3 grid.

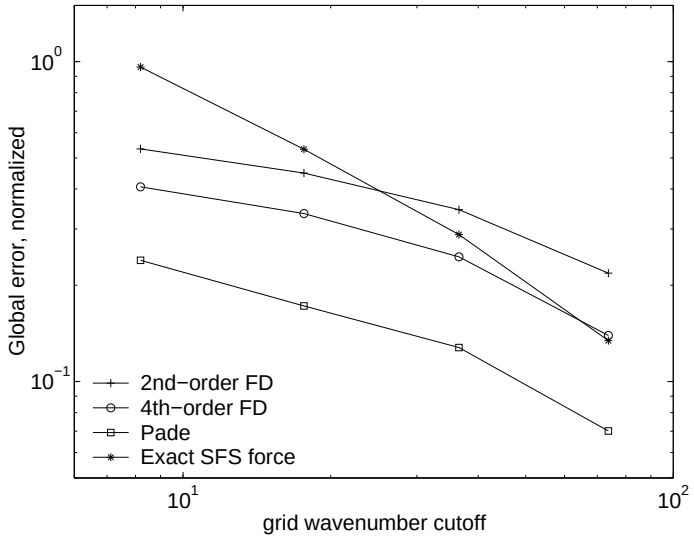

Figure 4.7: Global finite-differencing error in the nonlinear term in the dealiased divergence form, computed with second- and fourth-order finite-difference and sixth-order Padé schemes, compared to the SFS force term. Data points are normalized by the total nonlinear terms and shown at the 8^3, 16^3, 32^3, and 64^3 grid resolution locations. Filter-grid ratio = 2.

Figure 4.7 shows the global truncation error compared to the global SFS force for a filter-grid ratio of two. The terms are normalized with respect to the total nonlinear terms to adjust for the energy at different grid resolutions. For a filter-grid ratio of two, only the Padé scheme gives a total error significantly less than the SFS force for all grid resolutions. Notice that the global SFS force is larger than all the errors for grid sizes of 8^3 and 16^3, regardless of the scheme used. The explanation for this is probably that at such coarse resolution, the "exact" field we are comparing to (see Fig. 4.1) does not contain much energy or many fine scale motions, so the error from differentiation is not large since the field is smooth.

It is also important to understand exactly what the consequences are of adjusting the filter-grid ratio. When the filter size is increased on a fixed grid, a larger portion of motions must be represented by the SFS term. Figure 4.8 shows the total errors for the second-order finite-difference scheme for different grid resolution and filter-grid ratios. This verifies our conclusion from Figs. 4.4-4.6 that increasing the filter-grid ratio makes the total finite-differencing error much smaller. Figure 4.8 indicates that for all grid resolutions, error is reduced by increasing the filter-grid ratio. The

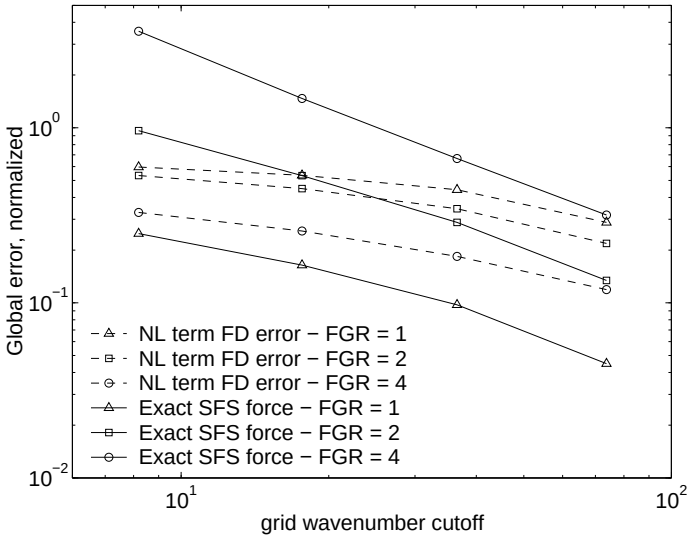

Figure 4.8: Global finite-differencing error in the nonlinear term (NL) in the dealiased divergence form with second-order finite differencing, compared to the SFS force term for different filter-grid ratios. Data points are normalized by the total nonlinear terms and shown at the 8^3, 16^3, 32^3, and 64^3 grid resolution locations.

magnitude of the SFS force increases with the filter-grid ratio, as more of the energy is placed into the subfilter scales, so that for FGR = 4 the SFS force dominates the error for all grid resolutions.

In summary, Ghosal's results lead to the conclusion that if the effect of the SFS terms is to be significant, it is necessary to compute SFS terms using a filter width that is at least twice the size of the grid spacing, and then only with an eighth-order finite-difference scheme. To achieve the same results with a second-order scheme, the filter would have to be made at least four times larger than the grid spacing. In our tests (which use realistic spectra for low Reynolds number flows), we find that the 6th-order Padé scheme performs very well for FGR = 2 or greater. If a second-order scheme is to be used, FGR = 4 will give a global finite-difference error that is smaller than the SFS term. These requirements are quite stringent. In practice, many LES codes use second-order finite-difference methods with a filter-grid ratio of unity or at best two. Some of the results of these LES codes are likely contaminated by significant numerical errors.

4.5 Aliasing errors

Aliasing errors occur when variables are multiplied in physical space; high frequency components produce higher frequency components which cannot be adequately represented on a finite grid. Thus, the frequencies beyond the grid wavenumber cutoff are incorrectly "aliased" to wavenumbers that are resolved (Moin, 2001). The contribution of aliasing errors is largest at the highest wavenumbers where any energy above the wavenumber cutoff incorrectly "folds over" into the resolved spectrum. While these aliasing errors appear to be important only at high wavenumbers, it is of interest to compare them to the SFS force term. Aliasing errors prevent a numerical method from conserving energy and hence can cause the solution to be unstable, as shown by Kravchenko & Moin (1997). Aliasing errors can be removed, but this is computationally expensive, even in spectral codes where the 3/2-rule for dealiasing is applicable and is relatively straightforward to implement. Lele (1992) suggests a filtering method for dealiasing in physical space though this method also requires extra computation. Because of this cost and the difficulty of implementation in non-spectral codes, dealiasing is not often performed in finite-difference codes, even though these are also affected by aliasing errors. Neglecting to dealias product terms may be acceptable in finite-difference codes, however, because the effect of aliasing on the total error may be somewhat reduced in finite-difference schemes, as shown below. We will compare aliasing errors in the nonlinear term to the SFS forcing, and examine the error when finite-difference schemes are used.

Figure 4.9 compares spectra of the aliasing error incurred in computing the nonlinear terms to the SFS force. The error is defined as the difference between the aliased and dealiased calculations for a particular differencing scheme. Dealiasing is performed using the 3/2-rule in the spectral space calculations. Errors are the largest for the spectral scheme. For finite-difference schemes, aliasing is reduced because the modified wavenumbers for finite-difference methods decrease near the cutoff wavenumber. Finite-differencing errors reduce the amount of aliasing error present, however they lead to a less accurate representation of the nonlinear terms at higher wavenumbers, as seen in the previous section.

These results are consistent with Ghosal's (1996), however the shape and magnitude of the spectra are quite different. Figure 4.9 shows that for FGR = 2 the errors

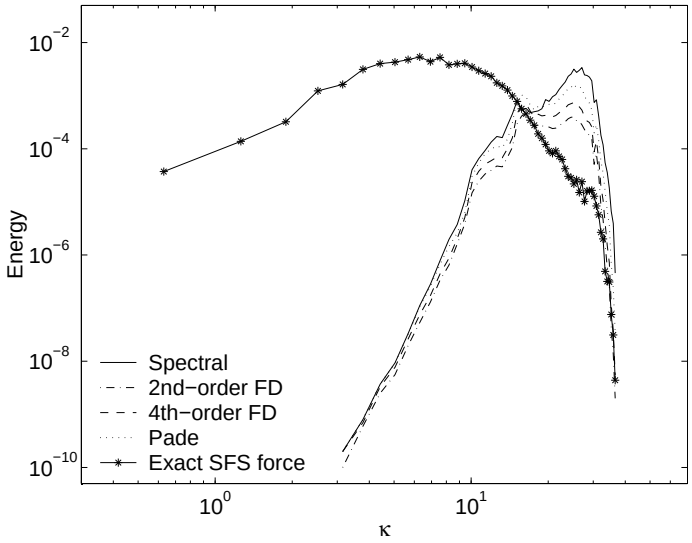

Figure 4.9: Energy spectra of the aliasing error in the nonlinear term in the divergence form, computed with spectral, second- and fourth-order finite-difference, and sixth-order Padé schemes, compared to the SFS force term. Filter-grid ratio = 2; 32^3 grid.

are larger than the SFS term only at high wavenumbers, as opposed to Ghosal's Fig. 5 where the aliasing error dominates in the entire range (for FGR = 1). In addition, in Ghosal's data the aliasing errors are more severe than the finite-difference errors. In our case, the aliasing errors are significantly smaller than the finite-difference errors for FGR = 2. By comparing Fig. 4.10 for aliasing errors to Fig. 4.7 for finite-difference errors, we see that the global SFS force dominates the global aliasing error for all grid resolutions. This difference between our results and Ghosal's may be due to the nature of the dataset used. Even though the total aliasing error is less than the SFS force, aliasing errors can have an adverse affect on the numerical solution because they are concentrated at high wavenumbers. It is also in this high wavenumber range that SFS models may act to extract information to model the subfilter scales.

Like finite-difference errors, aliasing errors can be reduced by increasing the filter-grid ratio, as product terms are more accurately represented on the grid when the original field is relatively smooth. The total aliasing errors for different grid sizes and different filter-grid ratios have been plotted in Fig. 4.11, with aliasing error computed for the spectral differencing case and the divergence form of the nonlinear force. The total aliasing error decreases with increasing filter-grid ratio, as more of the motions

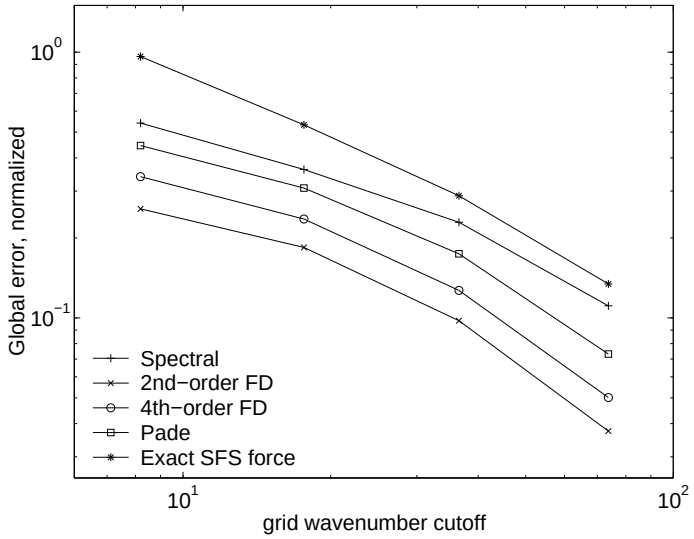

Figure 4.10: Global aliasing error in the nonlinear term in the divergence form computed with spectral, second- and fourth-order finite-difference, and sixth-order Padé schemes, compared to the SFS force term. Data points are normalized by the total nonlinear terms and shown at the 8^3, 16^3, 32^3, and 64^3 grid resolution locations. Filter-grid ratio = 2.

are smoothed out and product terms are more accurately represented on the grid. For FGR = 2 and 4, the total SFS force is larger than the aliasing errors; however for FGR = 1, the aliasing error dominates, and is comparable in magnitude to the finite-difference error in Fig. 4.8.

In addition to the effects of the finite-difference scheme and the filter-grid ratio on the aliasing error, Blaisdell *et al.* (1996) show that the form of the nonlinear terms can affect aliasing, so that proper choice of the discrete representation of these terms can reduce aliasing without any removal schemes. To further demonstrate the effect of aliasing error in the nonlinear terms, we evaluate the nonlinear terms using the rotational, divergence, convective, and skew-symmetric forms. These forms are analytically equivalent (see Kravchenko & Moin, 1997):

$$\text{Rotational:} \qquad u_j \left(\frac{\partial u_i}{\partial x_j} - \frac{\partial u_j}{\partial x_i} \right) + \frac{1}{2} \frac{\partial u_j u_j}{\partial x_i} \tag{4.2}$$

$$\text{Divergence:} \qquad \frac{\partial u_i u_j}{\partial x_j} \tag{4.3}$$

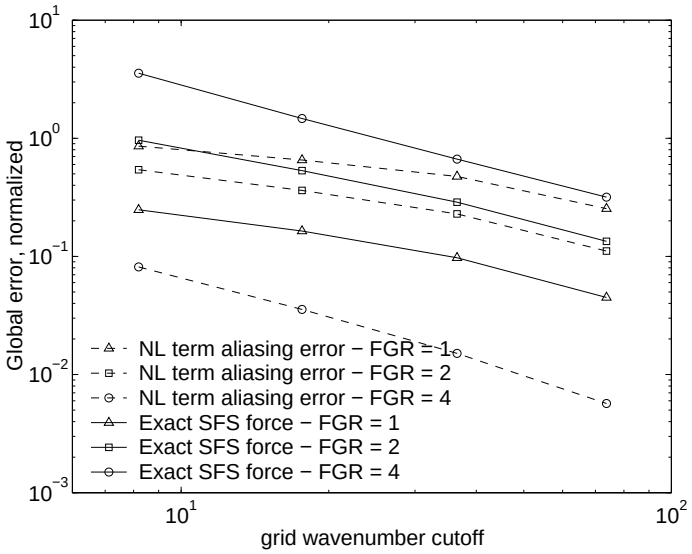

Figure 4.11: Global aliasing error in the nonlinear term (NL) in the divergence form with spectral differencing, compared to the SFS force term for different filter-grid ratios. Data points are normalized by the total nonlinear terms and shown at the 8^3, 16^3, 32^3, and 64^3 grid resolution locations.

$$\text{Convective:} \qquad u_j \frac{\partial u_i}{\partial x_j} \tag{4.4}$$

$$\text{Skew-symmetric:} \qquad \frac{1}{2}\left(\frac{\partial u_i u_j}{\partial x_j} + u_j \frac{\partial u_i}{\partial x_j}\right) . \tag{4.5}$$

In discrete form, however, these expressions may not be equivalent, as this depends on whether the product rule for differentiation holds numerically.

For dealiased spectral methods, differentiation is exact and therefore satisfies the product rule, so the four formulations perform identically. The difference in the formulations without dealiasing can be significant, as seen in Fig. 4.12 for spectral schemes, which shows spurious energy at the highest wavenumbers. For finite-difference schemes, even when all terms are dealiased the results are different because of truncation errors. When second-order finite-differences are used, the differences between these formulations are reduced (not shown) from those in Fig. 4.12, but may still be significant for numerical stability, so it is desirable to choose a formulation that gives the least error.

Figure 4.13 shows spectra of aliasing errors for the different nonlinear formulations,

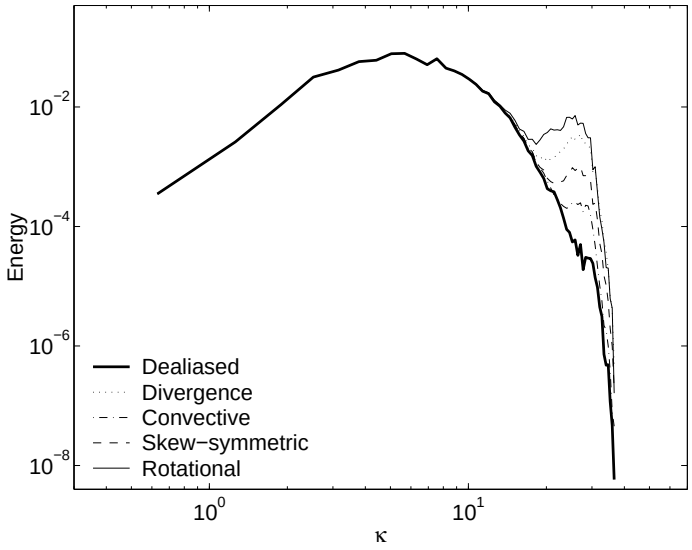

Figure 4.12: Energy spectra of the nonlinear term with divergence, convective, skew-symmetric, and rotational formulations with derivatives computed spectrally, but aliasing error not removed. The dealiased spectrum is also shown. Filter-grid ratio = 2; 32^3 grid.

compared to the SFS force. The convective formulation gives the least aliasing error, followed by the skew-symmetric and divergence forms; the rotational form gives the highest error. These results are slightly different than those of the Fourier analysis of Blaisdell *et al.* (1996) where the skew-symmetric form performs best, followed by the convective form. However, this is perhaps accounted for by the fact that their results are for compressible turbulence where the convective term consists of two parts; in incompressible flow this form reduces to one term because of the continuity condition. When directly implemented into a spectral LES code, Zang (1991) and Blaisdell *et al.* (1996) found the skew-symmetric form to be the preferred scheme because aliasing errors were minimized. Kravchenko & Moin (1997) also found that the skew-symmetric form performed best in a finite-difference code LES, while the convective form led to numerical instability which was linked to the sign of the truncation error. This poor performance of the convective form is not reflected in the spectra of errors shown here, indicating that *a posteriori* tests are needed to evaluate a particular scheme fully. We do, however, find that our error estimates are comparable to those of Zang (1991), who found that the aliasing errors from the rotational form are about

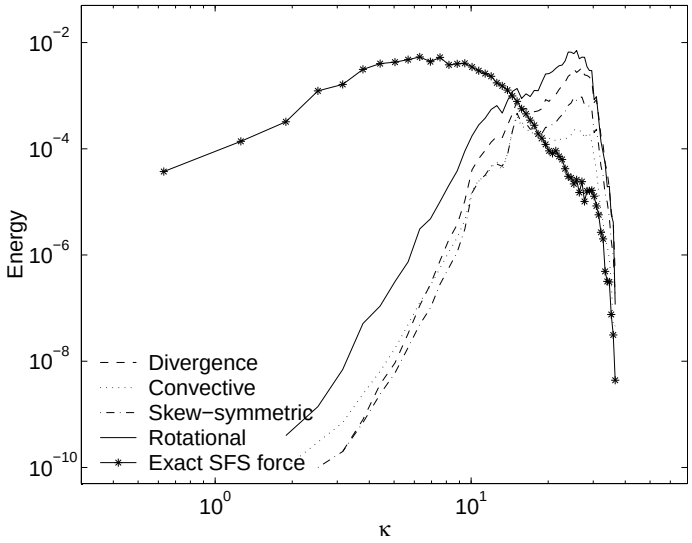

Figure 4.13: Energy spectra of the aliasing error in the nonlinear term for the spectrally computed (but not de-aliased) divergence, convective, skew-symmetric, and rotational formulations, compared to the SFS force term. Filter-grid ratio = 2; 32^3 grid.

twice as large as those for the convection, divergence and skew-symmetric forms. Figure 4.14 shows the global error for different grid sizes using different nonlinear term formulations. For FGR = 2, the global errors from the rotational form are approximately two times larger than the errors from the other formulations, and are comparable in magnitude to the total SFS terms.

Overall we observe a similar trend to Ghosal (1996) in analyzing the aliasing errors, however, the magnitude and shape of the spectra are different. In our case the aliasing error is concentrated at large wavenumbers and does not dominate the SFS terms throughout the spectrum as long as the filter-grid ratio is greater than unity. Aliasing error is greatest for the higher-order finite-difference schemes, and decreases with an increasing filter-grid ratio. For a non-dealiased finite-difference code, it may be possible to use a particular formulation of the nonlinear terms to limit aliasing errors. It can be shown that aliasing errors of the two terms in the skew-symmetric form help to cancel each other out, so this form is often well-behaved even without dealiasing (Kravchenko & Moin, 1997). Blaisdell *et al.* (1996) propose that the skew-symmetric version of the nonlinear terms eliminates most of the aliasing error, and hence provides a cheaper alternative to implementing a de-aliasing scheme.

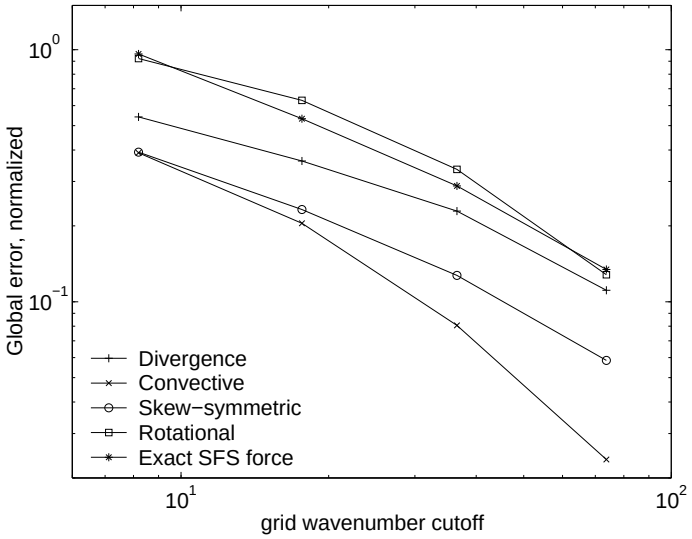

Figure 4.14: Global aliasing error in the nonlinear term with divergence, convective, skew-symmetric, and rotational formulations (computed spectrally but not dealiased), compared to the SFS force term. Data points are normalized by the total nonlinear terms and shown at the 8^3, 16^3, 32^3, and 64^3 grid resolution locations. Filter-grid ratio = 2.

4.6 Conclusions

Following the approach of Ghosal (1996), the analysis of DNS data presented here demonstrates some of the issues involved in the numerical representation of nonlinear terms and SFS terms. Results from our DNS dataset are similar to Ghosal's statistical analysis, confirming the need for careful selection of numerical parameters in LES. A few specific differences were noted.

To ensure that the SFS terms are larger than numerical errors from calculation of the nonlinear terms, the choice of the filter size is important. Our results indicate that the filter size should be at least twice as large as the grid spacing for a 6th-order Padé scheme. For a second-order finite-difference scheme, the filter size should be at least four times the grid spacing. Because of the effect of the modified wavenumber, aliasing is less important for finite-difference methods than for spectral calculations; however, the representation at higher wavenumbers is less accurate because of the larger truncation errors. More accurate finite-difference methods can be used to represent the solution at higher wavenumbers better, but dealiasing or a particular

discretization (*e.g.* the skew-symmetric form) of the nonlinear terms may then become necessary.

The results in this chapter are a confirmation of Ghosal's results for high Reynolds numbers for flows at moderate Reynolds numbers. The above guidelines for LES are of course only directly applicable to moderate Reynolds number flows such as the one considered here. However, the general recommendations that require a specific filter-grid ratio to limit numerical errors in LES appear to apply to the entire range of Reynolds numbers, from low-to-moderate Reynolds number engineering flows to high Reynolds number geophysical flows.

Chapter 5

Turbulent channel flow simulations*

This chapter applies the reconstruction modeling ideas presented in Chapter 3 to small-scale turbulent channel flow simulations. The effects of the grid and discretization errors are introduced in the SFS modeling procedure. Simulations are performed using second- and fourth-order finite-difference codes. A systematic comparison of the large-eddy simulation (LES) results for different grid resolutions, finite-difference schemes, and several turbulence closure models is performed. The use of explicit filtering to reduce numerical errors is compared to results from the traditional LES approach. Filter functions that are smooth in spectral space are used, as the findings of this investigation are intended for application of LES to complex domains. Explicit filtering introduces resolved subfilter-scale (RSFS) as well as subgrid-scale (SGS) turbulence terms. The former can theoretically be reconstructed; the latter must be modeled. For turbulence models, the dynamic Smagorinsky model, the dynamic mixed model, and the new dynamic reconstruction model are all studied. It is found that for explicit filtering, increasing the reconstruction levels for the RSFS stress improves the mean velocity as well as the turbulence intensities. When compared to LES without explicit filtering, the difference in the mean velocity profiles is

*This chapter is a reproduction (with minor modifications) of the paper "The effect of numerical errors and turbulence models in large-eddy simulation of channel flow, with and without explicit filtering" by Jessica Gullbrand and Fotini Katopodes Chow (equal contributors), published in the Journal of Fluid Mechanics, November 2003, Volume 495, pages 323-341 (Gullbrand & Chow, 2003),

not large; however, the turbulence intensities are improved for the explicit filtering case.

5.1 Introduction

The equations for large-eddy simulation (LES) are obtained by applying a low-pass filter to the Navier-Stokes equations. This filtering operator divides the flow into so-called resolved and subfilter-scale (SFS) motions. When the equations are solved on a discrete grid, a discretization operator is applied to the equations as well, which further divides the turbulent flow field; the subfilter scales are divided into resolved SFS and unresolved SFS regions. The unresolved SFS motions are commonly called subgrid-scale motions (see also the notation used by Zhou, Brasseur & Juneja, 2001). Figure 5.1 depicts these regions of the flow field which are described further later. The effect of the resolved subfilter-scale (RSFS) and subgrid-scale (SGS) motions on the resolved velocity field must be considered. The RSFS contribution can theoretically be reconstructed, but the SGS stress must be modeled. The filter shape as well as the filter width and, of course, grid resolution are free parameters in LES.

For engineering purposes, second-order numerical methods are usually used when performing LES for complex flow fields. In LES the smallest resolved scales are often used to model the contribution from the unresolved scales. Therefore, it is of great importance that these scales be resolved to high accuracy. High accuracy LES results can be achieved by high-order numerical methods (see e.g. Morinishi *et al.*, 1998) and/or by explicit filtering (Lund & Kaltenbach, 1995). The complexity in implementing high-order methods as well as the computational cost become prohibitive when studying flow fields in complex geometries. Therefore, the use of explicit filtering may provide a favorable alternative.

In traditional LES solution methods, the computational grid and discretization operators are considered "implicit" filtering of the Navier-Stokes equations. Using this approach, there is no need to define a filter function, but neither can the implicit filter be determined. The only actual filter that may be applied in the simulations is used in models for the RSFS and/or SGS contributions. One example is the need for a test filter in the dynamic Smagorinsky SGS model to determine the model coefficient.

In contrast, when explicit filtering is applied in LES, an explicitly defined filter

function is needed. In this approach, the defined filter is used when calculating the RSFS contribution. If the dynamic Smagorinsky model (DSM) is used as the SGS model, an additional filter function (with larger width than the explicit filter) must also be defined for the test filter in the dynamic procedure. Both the RSFS and the SGS contributions must be included in the simulations. The differences in the implementation of the traditional LES and the explicitly filtered LES approaches might be considered subtle; however, the effect on the LES results is considerable.

The explicit filtering approach has recently been proposed as a method to minimize the influence of discretization error in finite-difference codes (Lund & Kaltenbach, 1995). All finite-difference approximations have a truncation error that grows with increasing wavenumber. This truncation error can be reduced or eliminated when explicit filtering with a filter width larger than the computational grid cell size is applied (Lund, 1997). Several researchers have investigated explicit filtering in turbulent channel flow. Lund & Kaltenbach (1995) used sharp cutoff filters (in spectral space) in the homogeneous directions with a second-order finite difference code (the same code used in this chapter). They concluded that the explicit filtering improved the accuracy of the LES results; however, mesh refinement without explicit filtering improved the results at a greater rate. All of their simulations used the DSM with a cutoff filter, which is not applicable to general geometries. Carati, Winckelmans & Jeanmart (2001) developed a useful framework for the explicit filtering approach. They proposed governing equations for LES which carefully distinguish between the discretization and filtering procedures. These equations are also used here to separate the RSFS and SGS effects used in explicit filtering. Winckelmans *et al.* (2001) performed simulations with explicit filtering using a fourth-order finite-difference code (also used in this chapter). They applied second-order commutative filters in three dimensions, which introduce commutation errors in the wall-normal direction due to the stretched grid (Ghosal & Moin, 1995). The explicit filtering approach (with low-order RSFS reconstruction) did not perform as well as DSM without explicit filtering (with a sharp cutoff test filter), though the authors suggested that higher-order reconstruction of the RSFS terms could improve the results obtained with explicit filtering. Gullbrand (2001) performed explicit filtering (also with low-order RSFS reconstruction) in three dimensions using commutative filters with the DSM in the same fourth-order finite-difference code. Results without explicit filtering showed

better agreement with direct numerical simulation (DNS) data, also suggesting that higher-order reconstruction is needed for the RSFS terms.

In this chapter, we study the influence of numerical errors on the LES results, as well as the influence of the filtering approach and the reconstruction level on the turbulence models. The numerical error is studied by performing simulations of a turbulent channel flow using both second-order and fourth-order finite-difference codes. The advantage of studying the channel flow is that both sharp cutoff and smooth filter functions can be used. In this work, the sharp cutoff filter is used only for comparison purposes, as our aims are to investigate approaches for LES over complex domains where sharp cutoffs cannot be used. The sharp cutoff is therefore used only for traditional LES, without explicit filtering. A smooth filter is applied for LES with explicit filtering. Higher-order reconstruction models for the RSFS stress are investigated with filters applied only in the homogeneous directions, as this avoids introducing commutation errors. The effect of three-dimensional filtering must ultimately be considered, but is left to future work. For turbulence models, the DSM, the dynamic mixed model (DMM), and the new dynamic reconstruction model (DRM) are all investigated. The DSM is used as the SGS model in all the simulations presented here. The DMM is a linear combination of the scale similarity model (SSM) of Bardina *et al.* (1983), which acts as the RSFS model, and the DSM. In the DRM, the RSFS stress is modeled by using an estimate of the unfiltered velocity in the unclosed term; the SGS stress is again modeled by the DSM.

5.2 Governing equations

The governing equations for incompressible flow are the continuity equation together with the Navier-Stokes equations, used here in nondimensional form:

$$\frac{\partial u_i}{\partial x_i} = 0 \,, \qquad \frac{\partial u_i}{\partial t} + \frac{\partial u_i u_j}{\partial x_j} = -\frac{\partial p}{\partial x_i} + \frac{1}{Re_\tau}\frac{\partial^2 u_i}{\partial x_j \partial x_j} \,. \tag{5.1}$$

Here u_i denotes the velocity, p pressure and Re_τ the Reynolds number based on the friction velocity and the channel half-width. Repeated indices indicate summation.

In computational LES, the governing equations are filtered in space and solved numerically on a grid. The traditional procedure for LES has been to treat the grid

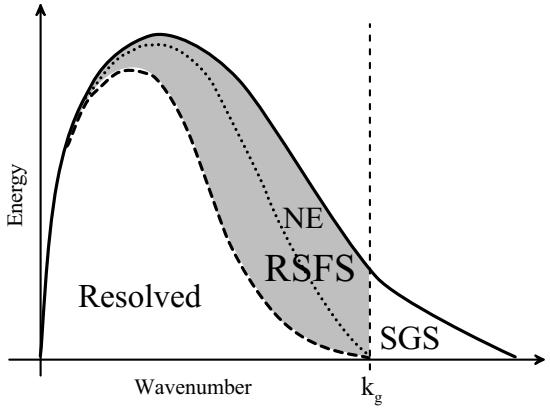

Figure 5.1: Schematic of velocity energy spectrum showing partitioning into resolved, subfilter-scale, and subgrid-scale motions. The numerical error region is also shown. The grid is indicated by the vertical dashed line, and the filter by the curved dashed line.

and the discretization operators as the filtering procedure of the governing equations. Here, we instead follow the approach of Carati *et al.* (2001) and Winckelmans *et al.* (2001) where the filtering and discretization procedures are treated separately. The discretization operator is represented by a tilde and the filtering operator by an overbar. The filter function G is applied to a flow variable f in physical space as

$$\overline{f}(x,\Delta,t) = \int_{-\infty}^{\infty} G(x,x',\Delta) f(x',t) dx' \ , \tag{5.2}$$

where Δ is the filter width. Thereby $\tilde{u}_i$ denotes a variable on the grid, and $\overline{\tilde{u}}_i$ denotes a filtered variable on the grid. Figure 5.1 shows a schematic of a typical energy spectrum from a turbulent flow. The spectrum can be separated into three parts (Carati *et al.*, 2001; Zhou *et al.*, 2001). The low-wavenumber portion is well resolved on the grid and is contained in the velocity $\overline{\tilde{u}}_i$. The shaded portion represents RSFS motions; this region contains filtered information that is still resolved on the grid. The subdomain between the dotted and solid lines is denoted the numerical error (NE) region, which is present due to the discretization errors. This region would not exist if spectral methods were used; in this particular case, the complete RSFS stress could be recovered. If numerical errors are present, the RSFS motions cannot be fully reconstructed. Finally, the high-wavenumber portion contains SGS motions

that cannot be resolved on the grid and must be modeled.

Hence, the LES momentum equations on a discrete mesh are written as

$$\frac{\partial \overline{\tilde{u}}_i}{\partial t} + \frac{\partial \widetilde{\overline{\tilde{u}}_j \overline{\tilde{u}}_i}}{\partial x_j} = \frac{\partial \overline{\tilde{p}}}{\partial x_i} + \frac{1}{Re_\tau} \frac{\partial^2 \overline{\tilde{u}}_i}{\partial x_j \partial x_j} - \frac{\partial \tilde{\tau}_{ij}}{\partial x_j} \tag{5.3}$$

where the turbulent stresses are defined as $\tau_{ij} = \overline{u_i u_j} - \overline{\tilde{u}}_i \overline{\tilde{u}}_j$. The filtered equations are not closed due to the nonlinear term $\overline{u_i u_j}$. Properties of the specific filters used are described in Section 5.4. Note that each term in the equation contains the effects of discretization, denoted by the tilde operator. In a spectral code, the effect of the discretization is simply a spectral cutoff filter, where the discretization and filtering operators clearly commute (i.e., $\tilde{\overline{u}} = \overline{\tilde{u}}$). (Note that the cutoff filter is more accurately termed a "cutoff projection", as it is not reversible. However, we use the term "cutoff filter" as is commonly done in the literature.) With finite differences, each term in the governing equations is affected differently by the discretization. The modified wavenumber effect (Moin, 2001) will damp motions near the grid cutoff, as indicated in the NE region of Fig. 5.1. Thus the discretization acts as a smooth filter that is applied to the flow fields (though the exact nature of this smooth filter is unknown). In this work, we also assume $\tilde{\overline{u}} = \overline{\tilde{u}}$ when finite differences are used. When simulations are performed using the actual LES code, numerical errors due to the space and time discretization schemes will interact, making the effects of explicit spatial filtering and the grid cutoff filter impossible to separate. Conceptually, however, Fig. 5.1 serves to separate these effects so that we can address each as is appropriate.

Following Carati *et al.* (2001), the turbulent stresses can be separated into two parts, $\tau_{ij} = B_{ij} + \overline{A}_{ij}$, where

$$B_{ij} = \overline{\tilde{u}_i \tilde{u}_j} - \overline{\tilde{u}}_i \overline{\tilde{u}}_j \ , \qquad \overline{A}_{ij} = \overline{u_i u_j} - \overline{\tilde{u}_i \tilde{u}_j} \ . \tag{5.4}$$

$\overline{A}_{ij}$, which we call the SGS stress, depends on scales beyond the resolution domain of the LES. B_{ij}, the RSFS stress, depends on the differences between the exact and filtered velocity fields within the resolution domain. As the filter width increases, the total turbulent stress term, consisting of the SGS and RSFS terms, will increase. The RSFS component can theoretically be computed, as an infinite expansion in a series model for $\tilde{u}_i$ would give the exact form (Yeo & Bedford, 1988; Katopodes, Street

& Ferziger, 2000*b*; Stolz, Adams & Kleiser, 2001*a*). Further discussion concerning partitioning of the RSFS and the SGS stresses can be found in Carati *et al.* (2001) and Winckelmans *et al.* (2001).

5.3 Resolved subfilter-scale and subgrid-scale models

When an explicit filter is applied to the Navier-Stokes equations, as in Eq. 5.3 above, information at the high wavenumbers is damped. In theory, this RSFS information can be restored exactly by using an inverse filtering operation. Several methods have been proposed to approximate this inverse filtering operation. Stolz *et al.* (2001*a*) use the van Cittert (1931) iterative method in their approximate deconvolution procedure to reconstruct the unfiltered velocity field $\tilde{u}_i$ from the filtered field $\overline{\tilde{u}}_i$. Chow & Street (2002) use Taylor series expansions to obtain the unfiltered velocity. These unfiltered fields, $\tilde{u}_i$, are then substituted into the expression for B_{ij} to obtain the RSFS reconstruction. The SSM (Bardina *et al.*, 1983) and the tensor-diffusivity model* (Leonard, 1974) can be derived from either of these reconstruction procedures by truncating the series expansions after a specified number of terms (Katopodes *et al.*, 2000*b*; Winckelmans *et al.*, 2001). By truncating these series, a model is obtained for the RSFS term B_{ij}. However, an additional stress term (A_{ij}) is still required to model the SGS stresses. Note that if the problem domain can be transformed into spectral space, the filter (if it is smooth) can be exactly inverted, and an exact reconstruction can be obtained. Explicit filtering is thus of no advantage for reducing numerical errors when smooth filters are used in spectral methods (Winckelmans & Jeanmart, 2001). If higher-order finite-difference schemes are used, explicit filtering to reduce numerical errors may also become less important.

In this study, both low-order (the SSM) and higher-order reconstructions (obtained with the van Cittert iterative method) are used to model the RSFS stresses. In order to make a fair comparison between the RSFS models, the same SGS model

*Simulations were also performed as part of this research with the second-order code using the modified Clark (tensor-diffusivity) model (see Appendices A and E, Eq. 6.10, and Winckelmans *et al.* (2001)). The results are not presented because the tensor-diffusivity model required a damping term (for stability) near the wall, and performed similarly with the approximate deconvolution procedure.

(DSM) is used in all the simulations. The combinations of RSFS and SGS models used are described below. Tests without explicit filtering are also performed for comparison purposes.

5.3.1 Dynamic Smagorinsky model

The DSM is a widely-used eddy-viscosity SGS model (Smagorinsky, 1963):

$$\tau_{ij} = -2\tilde{\nu}_e \overline{\tilde{S}}_{ij} = -2(C\tilde{\Delta})^2 |\overline{\tilde{S}}| \overline{\tilde{S}}_{ij}, \tag{5.5}$$

where ν_e is the eddy viscosity, $\tilde{\Delta}$ the effective grid cell spacing and S_{ij} the strain rate tensor. The exact definition of $\tilde{\Delta}$ is not needed as the total model parameter $C\tilde{\Delta}$ is calculated dynamically (Germano *et al.*, 1991) using the least squares approximation of Lilly (1992). The choice of the explicit filter and the test filter for the dynamic procedure greatly affects the performance of the DSM, as discussed further below. The DSM is used in our simulations with and without explicit filtering.

5.3.2 Dynamic mixed model

Low-order reconstruction of the RSFS stresses can be obtained by using the scale-similarity model proposed by Bardina *et al.* (1983). The SSM can be derived by substituting $\tilde{u}_i \approx \overline{\tilde{u}}_i$ into the definition of the RSFS stress tensor, B_{ij}. Here the RSFS stress is modeled by the scale similarity term and the DSM is used as the SGS model, in a procedure similar to that of Vreman, Geurts & Kuerten (1994):

$$\tau_{ij} = \overline{\overline{\tilde{u}}_i \overline{\tilde{u}}_j} - \overline{\tilde{u}}_i \overline{\tilde{u}}_j - 2(C\tilde{\Delta})^2 |\overline{\tilde{S}}| \overline{\tilde{S}}_{ij} \ , \tag{5.6}$$

where the contribution of the SSM is taken into account in the calculation of the dynamic coefficient. In addition, the test and explicit filters must be carefully applied in the dynamic procedure, leading to a different form of the test-filtered equations, as described by Winckelmans *et al.* (2001). The SSM term is discretized with the same method as the convective term in each code. Further description of the derivations of dynamic models is given in Appendix E.

5.3.3 Dynamic reconstruction model

Higher-order reconstruction of the RSFS stress tensor can be achieved by the iterative deconvolution method of van Cittert (1931). The unfiltered quantities can be derived by a series of successive filtering operations (G) applied to the filtered quantities with

$$\tilde{u}_i = \overline{\tilde{u}}_i + (I - G)\overline{\tilde{u}}_i + (I - G)((I - G)\overline{\tilde{u}}_i) + \cdots \tag{5.7}$$

where I is the identity matrix. The truncation order of the expansion determines the level of deconvolution, as discussed by Stolz *et al.* (2001*a*). Level-n reconstruction includes the first $n + 1$ terms of the series.

The series expansion provides an estimate for the inversion of the filter G. (Section 6.3.4 relates this expansion to the Taylor series expansion derived in Chapter 3.) If G is positive in Fourier space for all wavenumbers, the exact inverse can be obtained by simply inverting the filter kernel in wave space. If G crosses from positive to negative values in wave space at any wavenumber, exact inversion becomes impossible due to division by zero. Therefore, the series reconstruction over all wavenumbers of such a filtered field is approximate. The exact reconstruction can only be obtained as long as the filter kernel is positive in wave space. Hence, it is preferable to choose an explicit filter function that is positive for at least all the wavenumbers that are represented in the simulation (see Fig. 5.2 below for the filters used in this work).

The approximate unfiltered velocity, $\tilde{u}_i^\star$ (due to the truncated series), is substituted into the first term ($\overline{\tilde{u}_i\tilde{u}_j}$) of the RSFS stress which becomes $\overline{\tilde{u}_i^\star\tilde{u}_j^\star}$. This reconstruction was used by Stolz *et al.* (2001*a*) who called the RSFS model the approximate deconvolution model (ADM). Here the ADM is used together with the DSM:

$$\tau_{ij} = \overline{\tilde{u}_i^\star\tilde{u}_j^\star} - \overline{\tilde{u}}_i\overline{\tilde{u}}_j - 2(C\tilde{\Delta})^2|\overline{\tilde{S}}|\overline{\tilde{S}}_{ij} \ , \tag{5.8}$$

which we call the dynamic reconstruction model (DRM). The ADM portion of the DRM is discretized with the same method as the convective term. The ADM with the DSM was also independently proposed and used as a model by Winckelmans & Jeanmart (2001) for isotropic decaying turbulence. Reconstruction series of levels five and ten are used in this study and are denoted DRM5 and DRM10, respectively.

5.4 Filter functions

In finite-difference methods, the filter in the LES equations is important for limiting numerical errors. As shown by Ghosal (1996) and Chow & Moin (2003) (see Chapter 4), numerical errors from finite-difference schemes can be larger than the entire contribution from the turbulence closure term, $\partial\tau_{ij}/\partial x_j$. To avoid this problem, the explicit filter width should be at least twice as large as the cell size for a fourth-order accurate finite-difference code. For a second-order finite-difference code, these studies suggest that the filter width should be four times the cell size. In this work, the filter width in the case of the second-order code is not four times the cell size, but instead is chosen to be the same as the one used in the fourth-order code. The effect of this choice on the results warrants further study.

The correct use of the filter is especially important in the RSFS stress models, particularly in the dynamic procedure which is based on the scale-similarity assumption in the Germano identity (Germano *et al.*, 1991). To compute a quantity such as $\widehat{\overline{u}}_i$ in the dynamic procedure, the test filter ('caret' or 'hat' symbol) must be explicitly applied. To satisfy scale-similarity, it is required that the hat operator be "similar" to the overbar operator. Therefore, if the filtering operator (the overbar) is a tophat, the combined effect of the two (caret and overbar) should also be a tophat filter. Such an operator can be obtained by following the method of Carati *et al.* (2001) and Winckelmans *et al.* (2001), described below.

A discrete approximation to a tophat filter of twice the cell size can be obtained by trapezoidal rule integration. In one dimension the filter is

$$\overline{\phi}_i = 0.25\phi_{i-1} + 0.5\phi_i + 0.25\phi_{i+1} \; . \tag{5.9}$$

However, the effective filter width of this discrete filter is no longer twice the cell size, but rather $\sqrt{6}$ times the grid cell size. If Simpson's rule were used to derive a discrete version of the tophat filter, the weights would instead be $(1/6, 2/3, 1/6)$, with an effective filter width of twice the cell size. Despite the inconsistency in the effective filter width for Eq. 5.9, this filter was chosen because the function goes to zero (in spectral space) at the grid cutoff and therefore eliminates the highest wavenumber that could be sustained by the grid (see e.g. Najjar & Tafti, 1996).

To construct an appropriate test filter, it is useful to write the tophat filter in

Fourier space as $\overline{G}(k) = \sin(k\Delta)/(k\Delta)$. The combined effect of the test filter (at twice the width) and the explicit filter (the overbar) should thus also be a tophat: $\hat{\overline{G}}(k) = \sin(2k\Delta)/(2k\Delta)$. The required test filter (acting alone), would therefore be

$$\hat{G}(k) = \sin(2k\Delta)/(2\sin(k\Delta)) = \cos(k\Delta). \tag{5.10}$$

If we now transform this back into physical space, we have a discrete filter which requires only the immediate neighboring values,

$$\hat{\phi}_i = 0.5\phi_{i-1} + 0.5\phi_{i+1} \; . \tag{5.11}$$

The combined effect of the overbar and hat filters in physical space is also a tophat, but over a wider grid stencil, as expected:

$$\hat{\overline{\phi}}_i = 0.125\phi_{i-2} + 0.25\phi_{i-1} + 0.25\phi_i + 0.25\phi_{i+1} + 0.125\phi_{i+2} \; . \tag{5.12}$$

The filter functions are plotted in Fig. 5.2. Note that $\hat{\overline{G}}$ becomes negative over the upper half of the resolved wavenumber region. To guarantee similarity between $\hat{\overline{G}}$ and $\overline{G}$ this test filter should in fact be accompanied by a sharp cutoff filter at half the Nyquist frequency so that these negative values are set to zero. This sharp cutoff filter is indicated in the dynamic procedure described by Winckelmans *et al.* (2001) by $\tilde{u}^c$ where c indicates the cutoff filter at the coarser resolution of the test filter. In the implementation of the dynamic procedure used in this chapter, this coarse cutoff filter has not been explicitly applied as it is not practical for complex geometries; simulations performed with or without the coarse cutoff filter showed no discernable differences.

In this investigation, the same tophat explicit and test filters are used in both the second- and fourth-order finite-difference codes. The explicit and test filters are applied only in the homogeneous directions, as is commonly done in channel flow studies. Though this choice is not entirely self-consistent, it allows a direct comparison between the second- and fourth-order LES codes without introducing commutation errors due to filtering in the wall-normal direction over a stretched grid (Gullbrand, 2001). Note that the test filter in Eq. 5.11 is only used in the simulations with explicit filtering, as done by Winckelmans *et al.* (2001). When no explicit filter is applied,

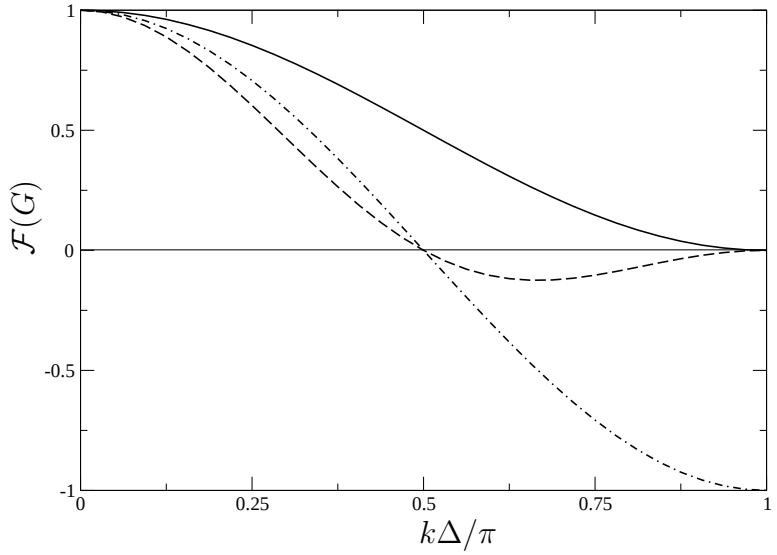

Figure 5.2: Fourier transforms of the explicit and test filters, shown in one dimension. The explicit filter (——) goes to zero at $k = \pi/\Delta x$ (the Nyquist wavenumber). The effective test filter (----) is generated by applying the test filter (—·—) to the explicit filter; the resulting filter crosses zero at $k = \pi/2\Delta x$.

the tophat in Eq. 5.9 is used as the test filter. Also note that in the finite-difference codes, for both the explicit filtering and the traditional approaches, the filters are applied only in calculations of the RSFS or SGS terms, and do not appear elsewhere in the code.

5.5 Solution algorithm

The second- and fourth-order codes represent spatial derivatives on staggered grids with second- and fourth-order central difference schemes, respectively. In the second-order code, the convective terms are discretized in divergence form, while in the fourth-order code, they are in skew-symmetric form (Morinishi *et al.*, 1998; Vasilyev, 2000). In both codes, the equations are integrated in time using the third-order Runge-Kutta scheme described by Spalart, Moser & Rogers (1991). The diffusion terms in the wall-normal direction are treated implicitly with the Crank-Nicolson scheme. The splitting method of Dukowicz & Dvinsky (1992) is used to enforce the solenoidal condition. The resulting discrete Poisson equation for the pressure is

solved in the wall-normal direction using a tri-diagonal direct matrix solver in the second-order code and a penta-diagonal matrix solver in the fourth-order code. In the homogeneous directions, the Poisson equation is solved using a discrete Fourier transform in both codes. Periodic boundary conditions are applied in the streamwise and spanwise homogeneous directions, with no-slip conditions at the channel walls. A fixed mean pressure gradient is used to drive the flow. The Reynolds number is $Re_\tau = 395$ and the computational domain is $(2\pi h, 2h, \pi h)$ in (x, y, z), where h is the channel half-width, x is the streamwise direction, y the wall-normal direction, and z the spanwise direction. The computational grid is stretched in the y-direction by a hyperbolic tangent function

$$y(j) = -\frac{\tanh(\gamma(1 - \frac{2j}{N_2}))}{\tanh(\gamma)} \quad j = 0, ..., N_2 \tag{5.13}$$

where N_2 is the number of grid points in the wall-normal (j) direction and γ is the stretching parameter, which is set to 2.75. The computational codes are compared in Gullbrand (2000).

5.6 Turbulent channel flow simulations

5.6.1 Effect of grid resolution and numerical error

As one focus of this work is to examine the effect of numerical errors in actual LES, two finite-difference codes (one second-order and one fourth-order) are used. Because of the difference in accuracy between the codes, the grid resolution needs to be chosen carefully to be able to better compare the results. Figure 5.3 shows the effect of increasing grid resolution for the second-order code, using no turbulence closure model. All results are compared to DNS data obtained using the fourth-order finite-difference code (using no turbulence model) and the same grid resolution (256,193,192) used by Moser, Kim & Mansour (1999) for their DNS calculations. (The DNS data from the fourth-order code were found to be virtually identical to the spectral code DNS data of Moser *et al.* (1999).) It is clear that the choice of resolution can significantly alter the results of the simulation. The results in Fig. 5.3 show a minimum grid resolution of (81,65,64) where the results do not seem to be largely affected by the

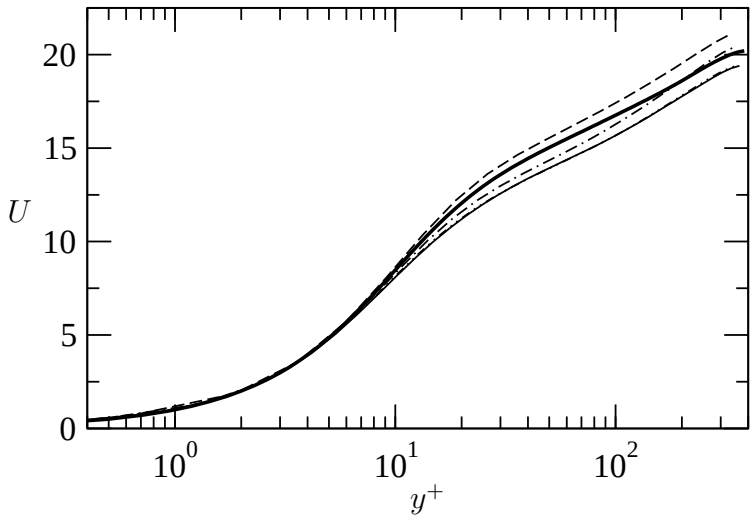

Figure 5.3: Mean velocity profiles U for different grid sizes for the second-order code using no turbulence model. ---- : 48x37x36, —·— : 64x49x48, —··— : 81x65x64, —— : 96x73x72, and —— : DNS.

numerical errors. This should be one of the necessary criteria in order to determine the required grid resolution. Of course as the grid resolution is increased the solution will eventually approach the DNS results. Due to increased accuracy (compared to the second-order code), the required minimum resolution for the fourth-order code is coarser at (64,49,48).

It is expected that for a given resolution, the performance of the fourth-order code will be better than the second-order code, due to the higher accuracy of the finite-difference schemes. Figure 5.4 shows results of simulations made with the same grid resolution (48,37,36) for both finite-difference codes and for the pseudo-spectral code of Jeanmart & Winckelmans (2002). The pseudo-spectral code uses fourth-order compact finite differences in the vertical direction and is spectral in the horizontal directions. The simulations are performed without a closure model, so that the effect of the numerical errors can be compared. As seen in Fig. 5.3, increasing resolution (and hence decreasing numerical errors) first reduces the mass flow predicted (mean velocity profile) in the simulations to a level lower than the DNS results. If the resolution is further increased, the mass flow increases and approaches the DNS results

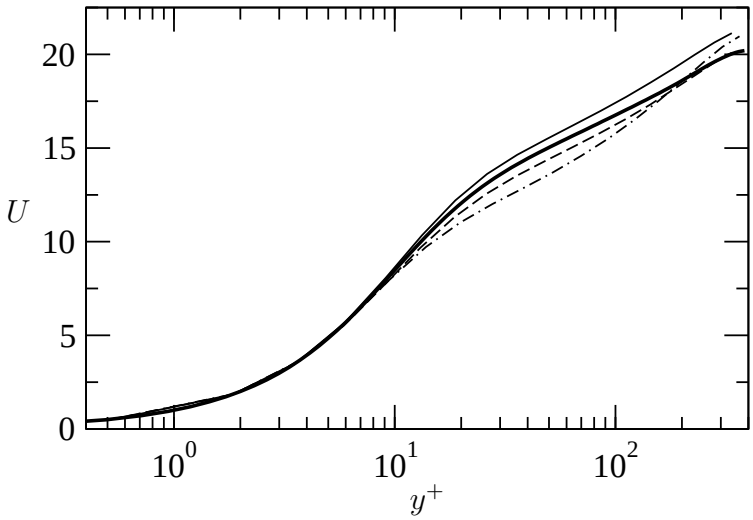

Figure 5.4: Mean velocity profiles for three different LES codes with the same grid resolution (48,37,36) using no turbulence model. —— : second-order, ---- : fourth-order, —·— : pseudo-spectral, ▬▬ : DNS.

from below. Similarly, it is expected that for a given grid resolution, the pseudo-spectral code will produce the lowest mean velocity profile of the three codes, as it has the lowest numerical errors (see Fig. 5.4). The fourth-order finite difference code also predicts a mean velocity profile that is lower than the DNS for this resolution (but higher than the pseudo-spectral code), however the second-order code does not, due to the effect of large truncation errors.

Because of the large differences in the profiles in Fig. 5.4, different grid resolutions are chosen for each finite-difference code to fairly compare results in further tests. In this way, we attempt to minimize the numerical differences at the outset of the investigation, though the interaction of these errors with different RSFS and SGS models is still an issue. To choose the appropriate resolution, simulations with the DSM using a spectral cutoff test filter with a width of twice the grid cell size were performed at different resolutions until good agreement was obtained. (Agreement at the two chosen resolutions can be seen in Figs. 5.5 and 5.6, as described later.) We use the cutoff filter case as the base case for comparison because this approach does not involve explicit filtering and thus provides an independent reference.

The grid resolutions for the remaining simulations are therefore as follows. The

fourth-order finite-difference code resolution is chosen to be (64,49,48), which is one quarter of the DNS resolution in each spatial direction. This resolution corresponds to a streamwise grid cell size of $\Delta x^+ = 39$, and a spanwise cell size of $\Delta z^+ = 26$. Nondimensional "plus" units are defined as $y^+ = yu_\tau/\nu$, where u_τ is the friction velocity and ν is the kinematic viscosity. The range of the cell size in the wall-normal direction is $0.4 \leq \Delta y^+ \leq 45$. In the simulations using the second-order code, a grid resolution of (81,65,64) is employed. This resolution corresponds to $\Delta x^+ = 31$, $\Delta z^+ = 19$ and $0.3 \leq \Delta y^+ \leq 34$. Thus the choice of grids for each code corresponds to the grid size which was shown to not largely be influenced by the numerical errors for the "no model" tests mentioned previously. The time step used is 1.5×10^{-3} and is the same in both codes. A statistically stationary solution is obtained after 30 dimensionless time units and thereafter statistics are sampled during 15 time units. The time is normalized with the friction velocity and the channel half-width.

5.6.2 SGS modeling: LES without explicit filtering

For the purpose of comparison, tests are performed using traditional SGS model formulations. These simulations do not use explicit filtering, meaning that the only filter that is actually applied is the test filter in the dynamic procedure, and this is chosen to be twice the cell size. In our test cases without explicit filtering, the reconstruction term (the RSFS stress) is not considered; only the SGS stress is modeled. By using the tophat filter (which is smooth in spectral space) as the test filter in the dynamic procedure (see below), it is assumed that the implicit filter is also a tophat; therefore the RSFS stress should in theory be considered. However, the implicit filter cannot be determined, meaning that reconstruction of the RSFS stress is questionable.

For the channel flow, the lateral periodic boundary conditions allow the use of a spectral cutoff filter for the test filter. It is well known (Piomelli *et al.*, 1988) that the Smagorinsky model performs best when used together with such a cutoff filter. The difficulty with this filter choice is that it cannot be easily applied to other geometries. The cutoff filter width in our simulations is twice the cell size, giving the filter-grid ratio $\alpha = \Delta/\Delta_g = 2$, where Δ and Δ_g are the filter width and grid cell size respectively. Because filtering is only applied in the x and z directions, the effective filter-grid ratio squared is $\alpha_{eff}^2 = 4^{2/3}$. Simulations with the DSM using a tophat

filter in physical space as the test filter are also performed. The test filter is applied as in Eq. 5.9; the filter-grid ratio in this case is $\alpha = \sqrt{6}$ and hence $\alpha_{eff}^2 = 6^{2/3}$ (see Najjar & Tafti, 1996; Lund, 1997).

Figure 5.5 shows mean velocity profiles from both the second- and fourth-order finite-difference codes, compared with DNS data. Agreement between the second- and fourth-order codes for the simulations using the cutoff filter is quite good, indicating that the chosen resolution for each code is good for comparisons. The agreement between the second- and fourth-order codes for the reduced (deviatoric) turbulence intensities for the cutoff filter case is excellent, as seen in Fig. 5.6. The turbulence intensities are adjusted by removing the trace from each tensor component, as discussed by Winckelmans, Jeanmart & Carati (2002). Results for the tophat filter are, as expected, worse than for the spectral cutoff filter. This is due to the absence of the RSFS component of the total stress, which should be present when a smooth filter is applied, as discussed further below. Though it is known to perform poorly with a smooth filter, the DSM is frequently used with the tophat filter because spectral cutoff filters cannot be applied in domains with general geometries. Note that the profiles obtained by the second-order code in Figs. 5.5 and 5.6 are slightly closer than the fourth-order code to the DNS for the tophat filter cases, which is due to the choice of higher resolution for this code than the fourth-order code. Tests performed using the same resolution (64x49x48) for both codes showed that the results from the fourth-order code are closer to the DNS data than are the results from the second-order code. This is expected based on the visible effect of numerical errors in the comparisons of the codes using no turbulence model, shown in Fig. 5.4, and as discussed previously in the choice to use different resolutions for each code.

Profiles of the SGS stress $\tilde{\tau}_{12}$ over half the channel width are shown in Figs. 5.7 and 5.8 for the fourth- and second-order codes, respectively. The contribution of the SGS stress is smaller for the second-order code because the simulations are performed using a higher resolution, meaning that more of the turbulent motions are resolved. The SGS stress is larger for the tophat filter cases for both codes because the effective filter width of the tophat is larger ($\sqrt{6}$ compared to 2), which therefore places more energy into the SGS terms. The predicted SGS stresses are compared to the SGS contribution calculated from the filtered DNS velocity data. The SGS stress tensor ($\tilde{\tau}_{ij} = \widetilde{u_i u_j} - \tilde{u}_i \tilde{u}_j$) is calculated *a posteriori* assuming the implicit filter is a sharp

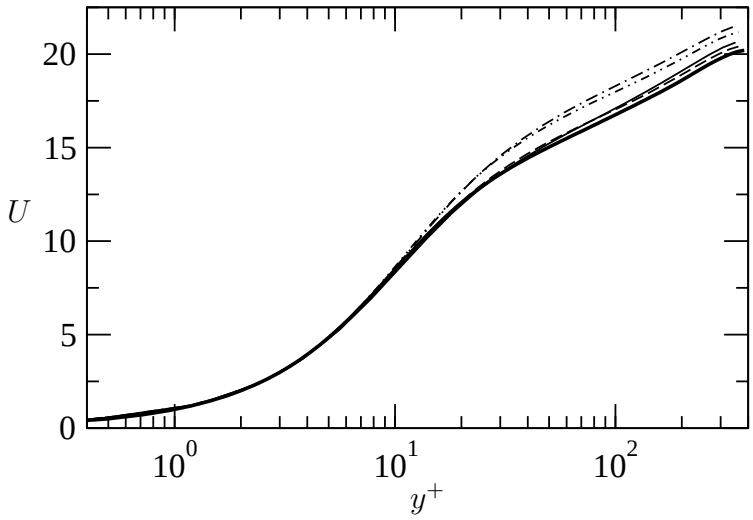

Figure 5.5: Mean velocity profiles for the second-order (81,65,64) and fourth-order (64,49,48) codes without explicit filtering. —— : fourth-order code, DSM with sharp cutoff filter, ---- : second-order code, DSM with sharp cutoff filter, —·— : fourth-order code, DSM with tophat filter, —··— : second-order code, DSM with tophat filter, and —— : DNS.

cutoff filter. The cutoff filters for filtering the DNS data are chosen separately to correspond to the two grid resolutions used: the (64,49,48) grid used for the fourth-order LES calculations, and the (81,65,64) grid used for the second-order code. No filters are applied in the vertical direction. The filtered DNS results for $\tilde{\tau}_{12}$ shown in Figs. 5.7 and 5.8 do not provide a clear indication as to the performance of the LES simulations. This poor agreement is likely due to the assumption of using a sharp cutoff filter in the DNS calculation of $\tilde{\tau}_{12}$. The actual implicit filter cannot be determined, but is likely closer to a smooth filter function since it is affected by finite difference errors (due to the modified wavenumber effect).

5.6.3 RSFS and SGS modeling: LES with explicit filtering

To attempt to minimize the influence of discretization errors in finite difference or finite volume codes, explicit filtering can be used. The difference between the implementation of this approach and that of Section 5.6.2 is in the filters used in the closure models, and thus the ability to reconstruct the RSFS terms. As this approach

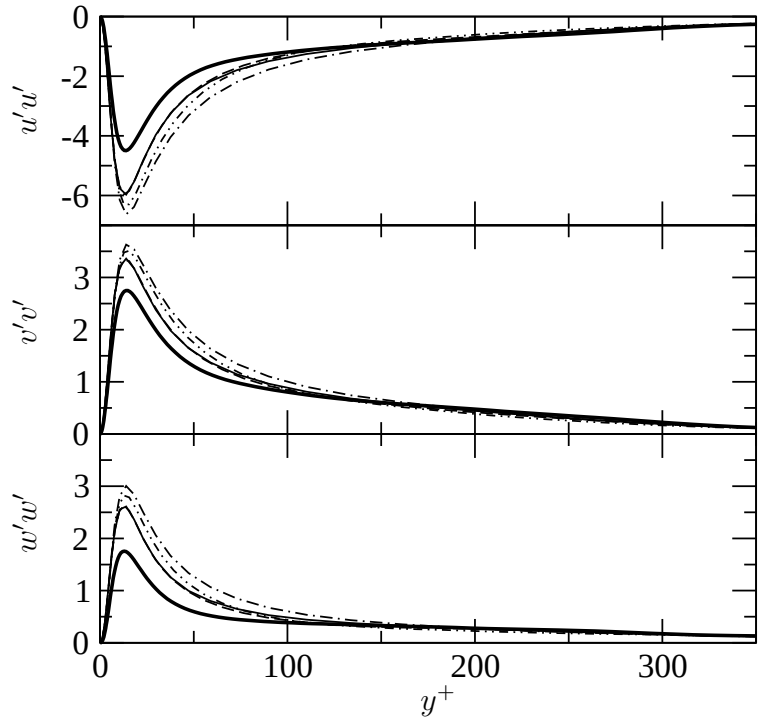

Figure 5.6: Profiles of reduced turbulence intensities in streamwise $u'u'$, wall normal $v'v'$ and spanwise $w'w'$ directions for the second-order (81,65,64) and fourth-order (64,49,48) codes without explicit filtering. The trace is removed from each tensor component. —— : fourth-order code, DSM with sharp cutoff filter, ---- : second-order code, DSM with sharp cutoff filter, —·— : fourth-order code, DSM with tophat filter, —··— : second-order code, DSM with tophat filter, and ▬▬ : DNS.

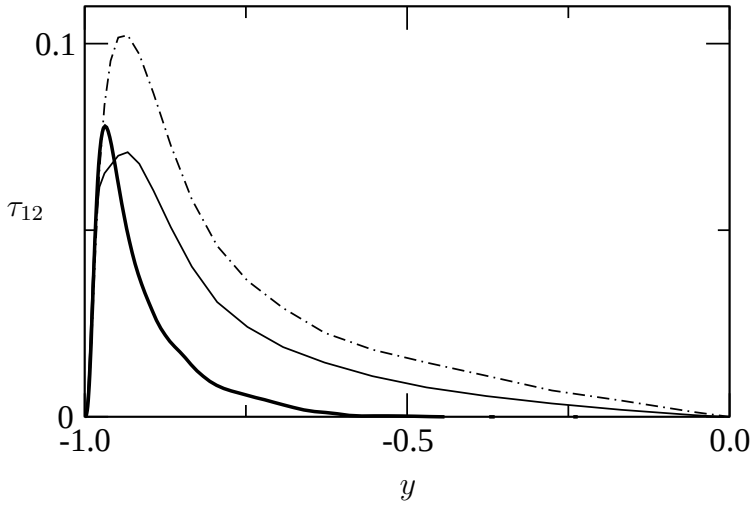

Figure 5.7: Profiles of the turbulent stress $\tilde{\tau}_{12}$ for the fourth-order (64,49,48) code without explicit filtering. —— : DSM with sharp cutoff filter, —·— : DSM with tophat filter, ——— : DNS (65,49,48).

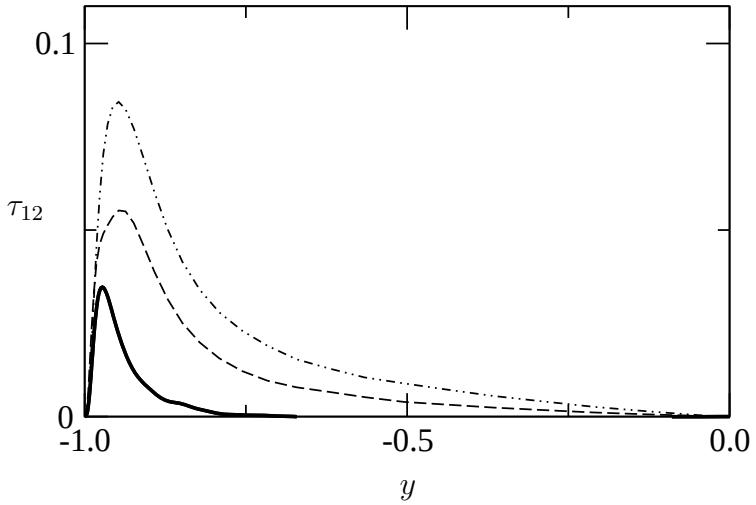

Figure 5.8: Profiles of the turbulent stress $\tilde{\tau}_{12}$ for the second-order (81,65,64) code without explicit filtering. - - - - : DSM with sharp cutoff filter, —··— : DSM with tophat filter, ——— : DNS (81,65,64).

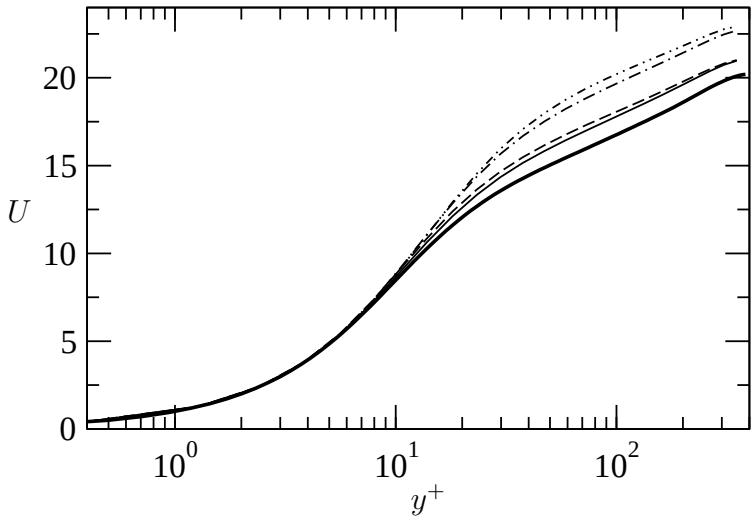

Figure 5.9: Mean velocity profiles for the fourth-order code (64,49,48) with explicit filtering (tophat) and reconstruction. —··— : DSM, —·— : DMM, ---- : DRM5, —— : DRM10, and ——— : DNS.

is geared toward finite-difference methods in complex domains, the filters used must be smooth; the spectral cutoff filter is not used here in this approach.

We performed several simulations using explicit filtering with increasing levels of reconstruction for the RSFS stresses. For the first case, the DSM is applied using an explicit filter of width twice the grid cell size and a test filter of four times the cell size. The effective filter ratio for the dynamic procedure is chosen to be two, as done by Winckelmans *et al.* (2001); the determination of the optimal ratio is left to further investigations. This first case has no reconstruction terms. Then, reconstruction to the first level is added by using the DMM, followed by the DRM5 and DRM10 with five and ten levels of reconstruction, respectively (see Sections 5.3.2 and 5.3.3). Figure 5.9 shows that the mean velocity profiles for the fourth-order code improve compared to the DNS results as the level of reconstruction increases. The improvement is very clear in the comparison of the reduced turbulence intensities in Fig. 5.10. However, the incremental improvement between DRM5 and DRM10 is not large, indicating that good reconstruction of the unfiltered velocity is most likely already obtained by DRM5. The differences between the LES results (with DRM5 and DRM10) and the DNS results are therefore most probably due to numerical errors (see the NE

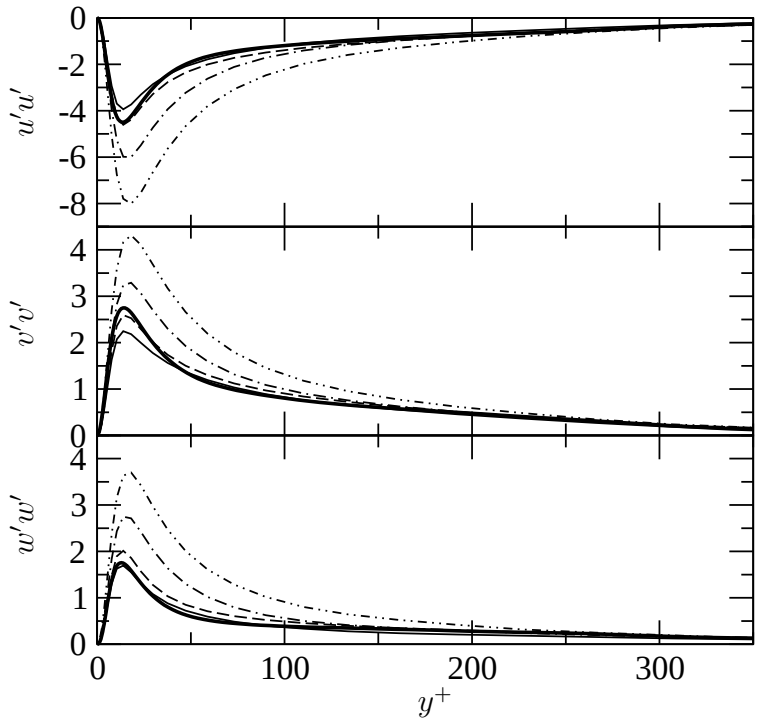

Figure 5.10: Profiles of reduced turbulence intensities in streamwise $u'u'$, wall normal $v'v'$ and spanwise $w'w'$ directions for the fourth-order (64,49,48) code with explicit filtering (tophat) and reconstruction. The trace is removed from each tensor component. —··— : DSM, —·— : DMM, ---- : DRM5, —— : DRM10, and ▬▬ : DNS.

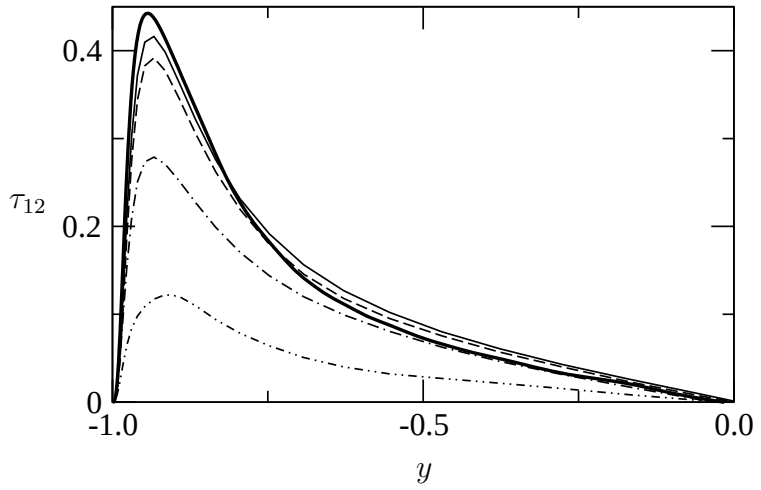

Figure 5.11: Profiles of the turbulent stress $\tilde{\tau}_{12}$ for the fourth-order (64,49,48) code with explicit filtering (tophat) and reconstruction. —··— : DSM, —·— : DMM, ---- : DRM5, —— : DRM10, and ——— : DNS.

region in Fig. 5.1) and the SGS model used. The total turbulent stress $\tilde{\tau}_{12}$ shown in Fig. 5.11 increases considerably with increasing reconstruction level (though only slightly between DRM5 and DRM10). For each case, the contribution of the DSM portion (not shown) of the model is roughly the same, with a peak of around 0.1, so the increase of the modeled stresses is almost entirely due to the RSFS model. The turbulent stresses are compared to DNS values calculated by using the definition of the turbulent stress tensor ($\tilde{\tau}_{ij} = \widetilde{\overline{u_i u_j}} - \widetilde{\overline{\tilde{u}}_i \overline{\tilde{u}}_j}$). The DNS fields are obtained using the fourth-order code as described previously in Section 5.6.2. The discrete quantities $\tilde{u}_i$ are obtained from the DNS fields *a posteriori* by using a sharp cutoff filter chosen to match the grid resolution used by the second- (81,65,64) and fourth-order (64,49,48) LES simulations. The explicit filter is then twice the corresponding LES cell spacing; for each grid size a tophat filter is constructed using the trapezoidal rule for the DNS fields to match the filter width used in each LES simulation. No filters are applied in the vertical direction. The turbulent stresses predicted by the DRM show very good agreement with the stresses calculated from the DNS data. Results for the second-order code are shown in Figs. 5.12 and 5.13. Turbulence intensities are not shown for the second-order code as the pattern of improvement is similar to that of the fourth-order code.

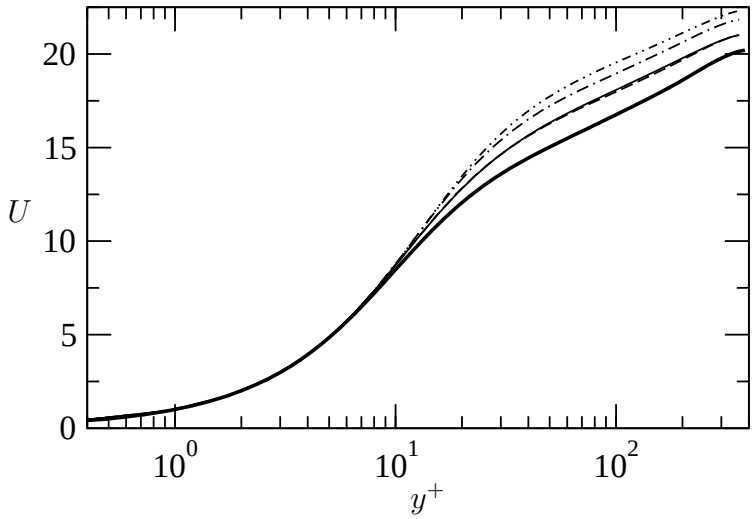

Figure 5.12: Mean velocity profiles for the second-order code (81,65,64) with explicit filtering (tophat) and reconstruction. —··— : DSM, —·— : DMM, ---- : DRM5, —— : DRM10, and ——— : DNS.

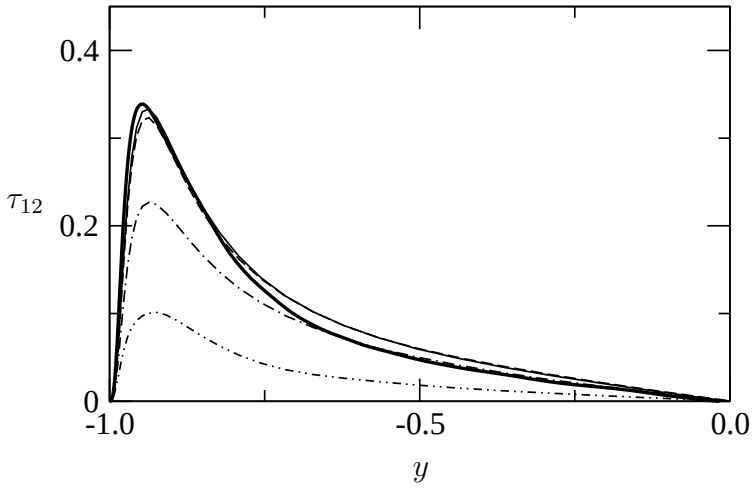

Figure 5.13: Profiles of the turbulent stress $\tilde{\tau}_{12}$ for the second-order (81,65,64) code with explicit filtering (tophat) and reconstruction. —··— : DSM, —·— : DMM, ---- : DRM5, —— : DRM10, and ——— : DNS.

5.7 Discussion and conclusions

Despite the existing theory and previous attempts at LES using explicit filtering (Carati *et al.*, 2001; Winckelmans *et al.*, 2001; Lund & Kaltenbach, 1995), the advantages of this method in practice remain unclear. Because of the extra filtering operations, the explicit filtering approach is necessarily more computationally expensive than traditional LES. However, explicit filtering offers the potential to limit the influence of numerical errors from finite-difference schemes on the flow solution.

Figure 5.14 compares results from both the second- and fourth-order codes, with and without explicit filtering. The models used are the DSM with the tophat filter (without explicit filtering, as is common in engineering applications) and the DRM10 (with explicit filtering). For both codes, there are only slight differences in the mean flow profiles for the cases with and without explicit filtering. The largest difference is seen in the reduced turbulence intensities, shown in Fig. 5.15, where the improvements due to DRM10 are quite significant. Even the magnitudes of the reduced streamwise intensities $u'u'$ for DRM10 are smaller than the DNS values, which is the opposite of what is usually observed with turbulence closures such as the DSM (Gullbrand, 2001). Better representation of turbulence intensities is, for example, very important in applications where accurate prediction of turbulent mixing is required. These results therefore demonstrate that improvements can be obtained for a given resolution and code by using explicit filtering and reconstruction.

The implications of these results on LES for engineering applications must be considered carefully. For engineering flows, traditional LES (without explicit filtering) is commonly performed with the DSM using a tophat test filter. As shown in this investigation, this method poorly predicts mean velocity profiles as well as turbulence intensities. There are several choices that must be made in determining how best to improve the performance of LES in practical applications.

Choosing the appropriate grid resolution for a simulation is necessarily the first step, as our results show great discrepancies among simulations with different grid sizes. Two main concerns must be addressed when selecting the necessary grid resolution. First, the grid should be able to resolve important physical characteristics of the flow. Second, the grid must also be fine enough to obtain a solution that is not largely affected by the numerical errors.

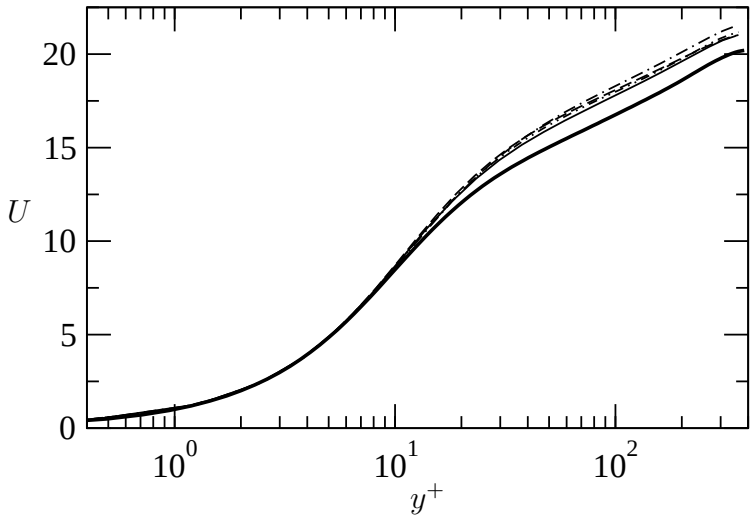

Figure 5.14: Mean velocity profiles for the second-order (81,65,64) and fourth-order (64,49,48) codes with and without explicit filtering (using tophat filters for both). —— : fourth-order code, DRM10, - - - - : second-order code, DRM10, —·— : fourth-order code, DSM no explicit filtering, —··— : second-order code, DSM no explicit filtering, and —— : DNS.

The order of accuracy of the finite-difference scheme used also greatly affects the solution. Note, for example, that the difference between the predicted mean velocity profiles for simulations using different turbulence models was larger for the fourth-order than for the second-order code. The higher sensitivity of the fourth-order code may be due to smaller numerical errors, and/or to the coarser resolution used in these simulations (compared to the resolution of the second-order code), so that the turbulence models play a larger role in the fourth-order case.

Finally, explicit filtering can be used as a means to reduce the influence of numerical errors in the high wavenumbers. Increasing the grid resolution improves the representation of the important large energy-containing scales. However, the truncation errors in the high wavenumber portion remain. It is precisely these high wavenumbers that are often used to represent SGS motions, and it is therefore imperative that they be represented as accurately as possible.

The extra computational cost due to explicit filtering to obtain increased accuracy may be worthwhile as LES continues to be applied to increasingly complex geometries and to problems where fine resolutions are not practical. The improvements

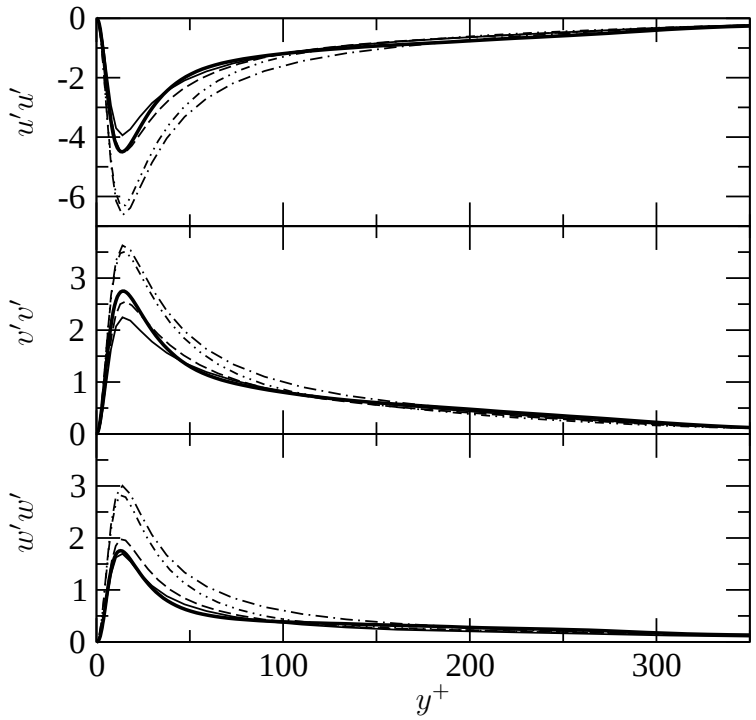

Figure 5.15: Profiles of reduced turbulence intensities in streamwise $u'u'$, wall normal $v'v'$ and spanwise $w'w'$ directions for the second-order (81,65,64) and fourth-order (64,49,48) codes with and without explicit filtering (using tophat filters for both). The trace is removed from each tensor component. ——: fourth-order code, DRM10, - - - -: second-order code, DRM10, —·—: fourth-order code, DSM no explicit filtering, —··—: second-order code, DSM no explicit filtering, and ——: DNS.

caused by use of the DRM10 (and the DRM5) model may be even more significant at coarser resolutions. Tests with DRM10 with the second-order code at a resolution of (48,37,36) show improvements over the DSM with the tophat filter (without explicit filtering) even with such an under-resolved simulation (not shown). The turbulence intensities predicted by DRM10 are much better than those from the DSM, even though the improvement in the mean velocity profile is small.

As this investigation has shown, the explicit filtering approach has the potential to improve simulation results. RSFS models with different levels of reconstruction were considered. The LES results with explicit filtering improve as the level of reconstruction is increased. No significant improvements were observed between DRM5 and DRM10, indicating that the reconstruction is most likely adequate at level five (which is also less expensive computationally); discretization errors and poor performance of the SGS model prevent the results from further approaching the filtered DNS data. The ability of the SGS (or RSFS) model to account for such numerical errors due to the discretization and finite-difference schemes is of course desirable. There is, therefore, a great need to develop SGS models that work well in the context of explicit filtering, where the accuracy of the smallest scales is increased. In addition, the effect of filtering in all three directions (and the resulting commutation errors) needs to be investigated.

Chapter 6

Neutral atmospheric boundary layer flow simulations*

Standard turbulence closures for large-eddy simulations of atmospheric flow use eddy-viscosity models and hence ignore the contribution of the resolved subfilter-scale stresses. These eddy-viscosity closures cannot produce the expected logarithmic region near the surface in neutral boundary layer flows. Here, explicit filtering and reconstruction are used to improve the representation of the resolved subfilter-scale (RSFS) stresses, and a dynamic eddy-viscosity model is used for the subgrid-scale (SGS) stresses. Combining reconstruction and eddy-viscosity models yields a generalized (and higher-order) version of the well-known mixed model of Bardina et al.; the explicit filtering and reconstruction procedures clearly delineate the contribution of the RSFS and SGS motions. A near-wall stress model is implemented to supplement the turbulence models and to account for the stress induced by filtering near a solid boundary as well as the effect of the large grid aspect ratio. Results for neutral boundary layer flow over a rough wall using the combined dynamic reconstruction model and a near-wall stress model show excellent agreement with similarity theory logarithmic velocity profiles, a significant improvement over standard eddy-viscosity closures. Stress profiles also exhibit the expected pattern with increased reconstruction level.

*This chapter is an expanded version of the paper, "Explicit filtering and reconstruction turbulence modeling for large-eddy simulation of neutral boundary layer flow" by Fotini Katopodes Chow (the principal author), Robert L. Street, Ming Xue, and Joel H. Ferziger, submitted to the Journal of the Atmospheric Sciences (Chow *et al.*, 2004*a*).

6.1 Introduction

In large-eddy simulation (LES) the fluid field is filtered to separate large eddies from smaller motions; the larger scales are simulated accurately, while the effect of the smaller, subfilter scales on the large scales is modeled. The presence of the numerical grid divides the subfilter-scale (SFS) motions into resolved and unresolved portions. The resolved subfilter-scale (RSFS) motions can be reconstructed using a scale-similarity approach, while the unresolved subfilter-scale (USFS) motions (or subgrid-scale (SGS)) must be modeled (Gullbrand & Chow, 2003). Both the RSFS and SGS models must rely on knowledge of the resolved scale behavior alone.

The partitioning of SFS motions into RSFS and SGS portions facilitates an understanding of the roles of various turbulence model components. Reconstruction modeling of the RSFS stresses requires the definition and application of an explicit filter in the LES computation. In contrast, traditional LES treats the discretization on the grid as an implicit filter operation, but the nature of the filter is both unknown, and different, for each term in the equations, making reconstruction difficult. Explicit filtering and reconstruction are especially useful for reducing numerical errors in the context of finite-volume or finite-difference codes; spectral methods do not require explicit filtering and reconstruction (Winckelmans *et al.*, 2001) but are not easily applied to flows over complex geometries.

When modeling atmospheric boundary layer flows, the limited grid resolution throughout the domain places extra importance on the turbulence closure scheme. Standard turbulence closures for these flows use eddy-viscosity models and ignore the contribution of the resolved subfilter-scale stresses. Furthermore, at large scales, the subfilter scales are probably not isotropic, as assumed in eddy-viscosity SFS models. A well-known problem in such simulations of the atmospheric boundary layer is the lack of agreement with logarithmic theory in the near-wall region, particularly for neutrally- or stably-stratified flows where the contribution of the SFS model dominates that of the resolved terms (see the discussions in Sullivan *et al.* (1994) and Kosović (1997)). Many schemes make special provisions for the near-wall region (see e.g. Sullivan *et al.*, 1994; Andren *et al.*, 1994).

In this chapter, we examine several different SFS model approaches for explicitly filtered LES (Lund & Kaltenbach, 1995; Gullbrand & Chow, 2003) of high Reynolds

number flow over a rough wall. The goal is to learn what logical steps and procedures are required for subfilter-scale modeling to bring the simulated flow fields into agreement with theoretical expectations in the near-wall region. We examine a specific test case: the neutral, rotation-influenced, large-scale boundary-layer flow considered by Andren *et al.* (1994). A state-of-the-art atmospheric mesoscale and small-scale simulation model is used, namely, the Advanced Regional Prediction System (ARPS) (Xue *et al.*, 1995, 2000, 2001). ARPS is a finite-difference LES-capable code designed for flow over irregular terrain, so spectral methods and sharp Fourier cutoffs in filters are not viable options. The enhancements to the code are those associated with the new subfilter-scale models (see also Chow & Street (2002)).

Gullbrand & Chow (2003) (Chapter 5) presented small-scale (low Reynolds number) turbulent channel flow simulations that showed that explicit filtering and reconstruction methods (using the dynamic reconstruction model, DRM) have the potential to reduce numerical errors in finite-volume and finite-difference formulations of LES models. Combining reconstruction and eddy-viscosity models yields a generalized (and higher-order) version of the well-known mixed model of Bardina *et al.* (1983); the explicit filtering and reconstruction procedures delineate clearly the contribution of the RSFS and SGS motions.

In this work, we use a similar approach for simulations of the large-scale (high Reynolds number) neutral boundary layer where the bottom boundary is rough and the top boundary is free slip. This seemingly small distinction between a smooth surface and a rough one has very large consequences. A rough bottom boundary requires approximate boundary conditions (e.g. specifying a log law). We also introduce three-dimensional filters so that our approach is general enough for flow over complex terrain where horizontal planar averages are not applicable. To the authors' knowledge, explicit filtering and reconstruction have not previously been applied to large-scale flows over rough surfaces.

The RSFS closure models implemented here include the Taylor series expansion subfilter-scale turbulence model of Katopodes *et al.* (2000*a*,*b*) (Chapter 3) and the approximate deconvolution approach of Stolz & Adams (1999). We use both of these series expansion models with the dynamic eddy-viscosity model of Wong & Lilly (1994) to represent SGS motions; these are the components of our dynamic reconstruction model (DRM). These dynamic series models require augmentation near the

lower boundary, so the near-wall shear stress term of Brown *et al.* (2001) is included to account for the stress induced by filtering near a solid boundary and for the effect of the large grid aspect ratio typically found near the boundary (Dubrulle *et al.*, 2002; Nakayama & Sakio, 2002).

The following sections summarize the framework for construction of a hybrid, or mixed, LES SFS closure model using separate RSFS and SGS components. The goal is to create a robust class of SFS models for use over rough boundaries. We then describe the implementation of the chosen models and results from simulations of the neutral boundary layer. The results using the combined DRM and near-wall stress models show excellent agreement with similarity theory logarithmic velocity profiles, which is a significant improvement over standard eddy-viscosity closures.

6.2 Decomposition of subfilter-scale stresses

To facilitate our understanding of the requirements in SFS modeling and especially to improve turbulence models in the near-wall region, it is useful to consider velocity partitioning schemes such as those of Carati *et al.* (2001), Zhou *et al.* (2001), and Hughes *et al.* (2001*a*,*b*). Figure 6.1 shows a schematic of a typical energy spectrum from a turbulent flow (this is the same as Fig. 5.1 in Chapter 5; it is repeated here for clarity of presentation). The application of a filter (which is smooth in wave space) and a discretization operator (needed to solve the LES equations on a discrete grid) separates the spectrum into three parts. The low wavenumbers are filtered and well resolved on the grid. They are contained in the velocity $\overline{\widetilde{u}}$, where the tilde operator represents the effect of discretization and the overbar an explicit smooth filter. The middle portion (shaded) represents subfilter-scale motions that are between the filter and grid cutoffs and hence resolvable on the grid. These resolved subfilter-scale motions can theoretically be reconstructed by an inverse filter operation. However, reconstruction is limited by numerical errors (NE) that increase near the grid cutoff due to the modified wavenumber effect (Moin, 2001). The portion to the right of the vertical dashed line contains subgrid-scale motions that cannot be resolved on the grid and must be modeled.

ARPS employs the spatially filtered compressible nonhydrostatic Navier-Stokes equations. For the results in this chapter, ARPS was operated in a quasi-incompressible

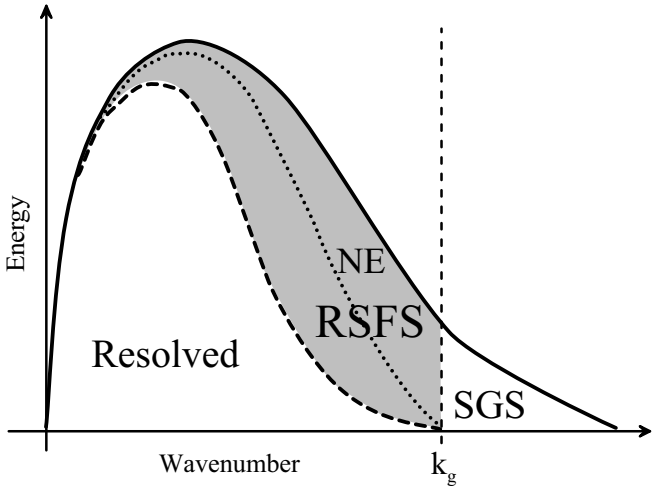

Figure 6.1: Schematic of velocity energy spectrum showing partitioning into resolved, subfilter-scale, and subgrid-scale motions. The numerical error region is also shown above the dotted line. The grid is indicated by the vertical dashed line at wavenumber k_g (corresponding to the minimum resolvable wavelength), and the explicit filter by the curved dashed line. Same as Fig. 5.1.

mode (Xu *et al.*, 1996). Further details are given in Section 6.5.1. Using the notation defined above, the LES governing equations are (given here again for the reader's convenience)

$$\frac{\partial \overline{\tilde{u}}_i}{\partial t} + \overline{\tilde{u}}_j \frac{\partial \overline{\tilde{u}}_i}{\partial x_j} = -\frac{1}{\rho}\frac{\partial \overline{\tilde{p}}}{\partial x_i} - g\delta_{i3} + \epsilon_{imn} f_n \overline{\tilde{u}}_m - \frac{\partial \tilde{\tau}_{ij}}{\partial x_j} \tag{6.1}$$

$$\frac{\partial \overline{\tilde{u}}_i}{\partial x_j} = 0 \tag{6.2}$$

where viscous terms have been neglected. Here $\overline{\tilde{u}}_i$ are the velocity components, $\overline{\tilde{p}}$ the pressure, ρ the density, and f the Coriolis parameter. While the discretization effects are different for every term in the equation (due to the various finite-difference schemes used), the same explicit filter is applied to all variables. Further details on the equations used by ARPS are given in Appendices C and D and in Xue *et al.* (2000). It is assumed that the filtering operation commutes with the spatial derivatives, which is true for a spatially homogeneous filter. Some error is introduced if this is not so (Ghosal & Moin, 1995).

We define the total SFS stress as

$$\tau_{ij} = \overline{u_i u_j} - \overline{\tilde{u}}_i \overline{\tilde{u}}_j \ . \tag{6.3}$$

Note that when the SFS stress appears in the filtered and discretized Navier-Stokes equations, it appears as $\frac{\partial \tilde{\tau}_{ij}}{\partial x_j}$, where the tilde indicates the added effect of the discretization (which is essentially a de-aliasing step as well (Chow & Moin, 2003)). The full turbulent stress can be decomposed into resolved and unresolved portions:

$$\tau_{SFS} = \tau_{ij} = \overline{u_i u_j} - \overline{\tilde{u}}_i \overline{\tilde{u}}_j = \underbrace{(\overline{u_i u_j} - \overline{\tilde{u}_i \tilde{u}_j})}_{\tau_{SGS}} + \underbrace{(\overline{\tilde{u}_i \tilde{u}_j} - \overline{\tilde{u}}_i \overline{\tilde{u}}_j)}_{\tau_{RSFS}} \ . \tag{6.4}$$

The first pair of terms on the right-hand side are the subgrid-scale stresses, τ_{SGS}. They depend on scales beyond the resolution domain of the LES, and contain the unclosed nonlinear term $\overline{u_i u_j}$ which must be modeled. The last pair of terms are the filtered-scale stresses, τ_{RSFS}, which depend on the differences between the exact and filtered velocity fields within the resolution domain. This resolved subfilter-scale component, τ_{RSFS}, can theoretically be reconstructed because it is a function of $\tilde{u}_i$ which can be obtained by deconvolution. Note that in a continuous domain, an infinite expansion in a series model for τ_{RSFS} would give an exact solution (Katopodes *et al.*, 2000*b*). Likewise, τ_{SGS} would be zero in a continuous domain, since there would be no contribution from subgrid-scale effects. In a discrete domain, the contribution of τ_{SFS}, and thus τ_{SGS}, increases with decreasing grid resolution.

Currently available SGS models do not represent the true SGS motions well. It is hoped that by reconstructing the RSFS, the overall representation of the SFS stress will be improved, as the SGS contribution will decrease overall. However, near a rough wall, eddy sizes decrease much faster than any grid stretching, and the bulk of the stress contribution comes from SGS terms (Sullivan *et al.*, 2003). In general, the total stress is given by

$$\tau_{total} = \tau_{Resolved} + \tau_{RSFS} + \tau_{SGS} \ . \tag{6.5}$$

Because eddies scale roughly as distance from the boundary and the filter and grid cutoffs are fixed, as we approach the wall ($z \to 0$), it must be that $\tau_{Resolved} \to 0$ and

$\tau_{RSFS} \to 0$ because there are no eddies in their respective spectral areas and all of the eddies are subgrid, so $\tau_{total} \to \tau_{SGS}$ as $z \to 0$. (Here and in subsequent chapters, z is the vertical coordinate.) The stress on the wall is given by a wall model such as the log law. Thus τ_{SGS} supports the total stress at the wall, suggesting the use of a specific near-wall stress model which represents the stress induced by the rough boundary. τ_{SGS} may be small away from the wall, depending on the grid discretization and the turbulent processes occurring in the flow. There could perhaps be a unified approach to τ_{SGS} over the whole domain, but we consider separate near-wall stress and general SGS models in this work.

6.3 Reconstruction models: series expansion approach

Using this framework for the turbulence closure, the RSFS and SGS components can be modeled separately. We first focus on the RSFS components, which can be reconstructed in terms of the resolved velocity. Several methods have been proposed to represent such subfilter-scale motions. Bardina *et al.* (1983) made a seminal contribution by introducing the scale-similarity model. Scale-similarity models create an approximation to the full velocity field to estimate the RSFS stress. In Bardina's model, the discrete full velocity is approximated by the filtered velocity, $\tilde{u}_i \approx \overline{\tilde{u}}_i$, to obtain $\tau_{RSFS} \approx \overline{\overline{\tilde{u}}_i \overline{\tilde{u}}_j} - \overline{\tilde{u}}_i \overline{\tilde{u}}_j$.

Later models have included those of Yeo & Bedford (1988), Shah & Ferziger (1995), Geurts (1997), Stolz & Adams (1999), Zhou *et al.* (2001), and Dubrulle *et al.* (2002) (see the review of Domaradzki & Adams (2002)). Here, we focus on approaches using Taylor series expansions (Katopodes *et al.*, 2000*b*) and the van Cittert iterative method used in the approximate deconvolution model of Stolz *et al.* (2001*a*).

6.3.1 Recursive Taylor series expansions

For the stress term τ_{RSFS}, which can be expressed in terms of the resolved velocity, we have first implemented the series model of Katopodes *et al.* (2000*a*,*b*) (see Chapter 3). This model uses successive inversion of a Taylor series expansion to express the unfiltered (but resolved) velocity in terms of the filtered velocity. Using an isotropic

Gaussian filter, the expansion reduces to

$$\begin{aligned}\tilde{u}_i(x,y,z) &= \overline{\tilde{u}}_i(x,y,z) - \frac{\Delta_f^2}{24}\nabla^2\overline{\tilde{u}}_i + \frac{\Delta_f^4}{1152}\left(\frac{\partial^4\overline{\tilde{u}}_i}{\partial x^4} + \frac{\partial^4\overline{\tilde{u}}_i}{\partial y^4} + \frac{\partial^4\overline{\tilde{u}}_i}{\partial z^4}\right) \\ &+ \frac{5\Delta_f^4}{1728}\left(\frac{\partial^4\overline{\tilde{u}}_i}{\partial x^2\partial y^2} + \frac{\partial^4\overline{\tilde{u}}_i}{\partial y^2\partial z^2} + \frac{\partial^4\overline{\tilde{u}}_i}{\partial x^2\partial z^2}\right) + O(\Delta_f^6)\ , \qquad (6.6)\end{aligned}$$

to fourth order in the explicit filter width, Δ_f. The expansion can be extended to an arbitrary order of accuracy by including more terms in the series, though these become cumbersome to compute. The approach can similarly be applied to the scalar transport equation (see Appendix B or Katopodes *et al.* (2000*a*)).

6.3.2 Approximate deconvolution method

Higher-order reconstruction of the RSFS stress tensor can also be achieved by the iterative deconvolution method of van Cittert (1931). This reconstruction is used by Stolz & Adams (1999) and Stolz *et al.* (2001*a*) who call the RSFS model the approximate deconvolution model (ADM). The unfiltered quantities can be derived by a series of successive filtering operations (G) applied to the filtered quantities with

$$\tilde{u}_i = \overline{\tilde{u}}_i + (I-G)*\overline{\tilde{u}}_i + (I-G)*((I-G)*\overline{\tilde{u}}_i) + \cdots \qquad (6.7)$$

where I is the identity operator, and G is the explicit filter. This expansion can also be extended to an arbitrary order of accuracy by including more terms in the series, though it is not immediately obvious what the order of magnitude of the next set of terms is. Level-n reconstruction includes the first $n+1$ terms of the series. Computation of higher-order terms is straight-forward, as it simply requires repeated application of the same filter operator.

6.3.3 Generation of the τ_{RSFS} models

We derive models for τ_{ij} by substituting a series expansion for the reconstructed velocity ($\tilde{u}_i^\star$) directly into Eq. 6.4 to obtain

$$\tau_{RSFS} = \overline{\tilde{u}_i^\star\tilde{u}_j^\star} - \overline{\tilde{u}_i^\star}\,\overline{\tilde{u}_j^\star}\ . \qquad (6.8)$$

The series expansions for $\tilde{u}_i$ could also be substituted directly into the filtered advection terms of the filtered Navier-Stokes equations, without moving the filtered terms to the right-hand side. This was done by Gullbrand & Chow (2003) (Chapter 5) and Stolz *et al.* (2001*a*), while the SGS contribution was added to the right-hand side as usual. In our implementation, we have both the series expansions and the SGS models on the right-hand side for ease of implementation in ARPS.

For the ADM approach, nothing further is required. In the Taylor series approach, we expand Eq. 6.8 to derive RSFS models of arbitrary order of accuracy in the (isotropic) filter width, Δ_f, giving (to fourth order):

$$\begin{aligned} \tau_{RSFS} &= \overline{\bar{\tilde{u}}_i \bar{\tilde{u}}_j} - \bar{\tilde{u}}_i \bar{\tilde{u}}_j - \frac{\Delta_f^2}{24} \overline{\bar{\tilde{u}}_i \nabla^2 \bar{\tilde{u}}_j} - \frac{\Delta_f^2}{24} \overline{\bar{\tilde{u}}_j \nabla^2 \bar{\tilde{u}}_i} \\ &+ \frac{\Delta_f^2}{24} \bar{\tilde{u}}_i \nabla^2 \bar{\tilde{u}}_j + \frac{\Delta_f^2}{24} \bar{\tilde{u}}_j \nabla^2 \bar{\tilde{u}}_i \, . \end{aligned} \tag{6.9}$$

The first two terms are analogous to the Leonard terms in the SFS stress; the higher-order derivative terms can be shown to be dissipative (Clark *et al.*, 1977). To second order in the filter width, Eq. 6.9 reduces to the Bardina scale-similarity model, as does the ADM at lowest order. An anisotropic tophat filter is used in the simulations, though an isotropic filter Δ_f is shown here for simplicity. Other spatially compact filters give similar results to the Gaussian filter used above, with a change in the expansion coefficients.

The series model in Eq. 6.9 can also be written as

$$\tau_{RSFS} = \frac{\Delta_f^2}{12} \overline{\frac{\partial \bar{\tilde{u}}_i}{\partial x_m} \frac{\partial \bar{\tilde{u}}_j}{\partial x_m}} \, , \tag{6.10}$$

which is equivalent to Eq. 6.9 to fourth order in the filter width (see Katopodes *et al.* (2000*b*)). Equation 6.9 is similar to the model proposed by Clark *et al.* (1977) (also known as the tensor-diffusivity model) but with an extra filter. This modified Clark model is considerably simpler than Eq. 6.9 to implement numerically, so we later adopt this as one of our models for τ_{RSFS}. (The original forms in Eq. 6.9 were also implemented to fourth order, but proved to be too cumbersome numerically to be useful.)

Vreman *et al.* (1996) found that a mixed model with the original Clark model

performed well for a small-scale temporal mixing layer. Winckelmans *et al.* (2001) performed a channel flow simulation using the standard Clark model (or tensor diffusivity model) together with the dynamic Smagorinsky model and found that the Clark portion needed to be damped near the wall. Iliescu & Fischer (2003) successfully used the filtered Clark model (to represent the entire turbulence term) in a channel flow. All of these studies considered small-scale flow cases where viscous motions could be resolved near the wall, which is not possible in the atmospheric boundary layer. In the rough-wall flow considered here, the viscous sublayer is not resolved and the SFS stresses do not go to zero at the wall. The behavior of the modified (filtered) Clark model near the wall is therefore acceptable. The ADM has been used in several flow simulations; it has performed well in simulations of small-scale incompressible channel flows (Stolz *et al.*, 2001*a*), and compressible flows, e.g. shock-turbulent-boundary-layer interaction (Stolz *et al.*, 2001*b*).

6.3.4 Equivalence of Taylor series and approximate deconvolution approaches

The Taylor series reconstruction method can easily be related to the van Cittert iterative method used in the approximate deconvolution method. For example, Appendix B of Stolz *et al.* (2001*a*) shows how the tensor-diffusivity model can be derived from the ADM. Using finite-difference representations, it is also easy to show the equivalence of these two reconstruction approaches. We consider the Taylor series approach to fourth-order in the filter width, in one dimension, and substitute second-order finite-difference forms:

$$\tilde{u} = \overline{\overline{u}} - \frac{\Delta_f^2}{24}\frac{\partial \overline{\overline{u}}}{\partial x} + O(\Delta_f^4) \tag{6.11}$$

$$\tilde{u}_i^\star \approx \overline{\overline{u}}_i - \frac{\Delta_f^2}{24}\frac{\overline{\overline{u}}_{i+1} - 2\overline{\overline{u}}_i + \overline{\overline{u}}_{i-1}}{\Delta x^2} \tag{6.12}$$

$$\approx \frac{4}{3}\overline{\overline{u}}_i - \frac{1}{6}\overline{\overline{u}}_{i+1} - \frac{1}{6}\overline{\overline{u}}_{i-1} \tag{6.13}$$

where we have taken $\Delta_f = 2\Delta x$, and the subscripts indicate discrete values (in this section only).

Now we consider the ADM with $n = 1$ using a $2\Delta x$ tophat filter approximated using the trapezoidal rule:

$$\tilde{u} = \overline{\tilde{u}} + (I - G) * \overline{\tilde{u}} + \cdots \tag{6.14}$$

$$\tilde{u}^\star \approx 2\overline{\tilde{u}} - \overline{\overline{\tilde{u}}} \tag{6.15}$$

$$\approx 2\overline{\tilde{u}}_i - (\frac{1}{4}\overline{\tilde{u}}_{i-1} + \frac{1}{2}\overline{\tilde{u}}_i + \frac{1}{4}\overline{\tilde{u}}_{i+1}) \tag{6.16}$$

$$\approx \frac{3}{2}\overline{\tilde{u}}_i - \frac{1}{4}\overline{\tilde{u}}_{i+1} + \frac{1}{4}\overline{\tilde{u}}_{i-1} \tag{6.17}$$

Alternatively, the Simpson's rule approximation to the tophat filter gives

$$\tilde{u}^\star \approx \frac{4}{3}\overline{\tilde{u}}_i - \frac{1}{6}\overline{\tilde{u}}_{i+1} + \frac{1}{6}\overline{\tilde{u}}_{i-1} \tag{6.18}$$

which is identical to Eq. 6.13.

A difference in implementation arises when the reconstructed velocities are substituted back into the RSFS stress expressions. In the Taylor series approach, terms of fourth-order or higher are explicitly disregarded, e.g. in the computation of the product terms. That is, we are careful to maintain the order of the final expression even after it has been substituted into τ_{ij}. Discretization is applied only after the final form has been obtained. When the ADM reconstruction terms are used, the discretely reconstructed velocities as in Eq. 6.18 are substituted directly into the RSFS expression. Therefore, higher-order terms are implicitly contained in the RSFS expressions.

Even though we use the trapezoidal representation in our implementation because of the better properties of the discrete filter (Gullbrand & Chow, 2003), we observe that the difference in the ADM ($n = 1$) vs Taylor series (fourth-order) approaches are in the fourth-order truncation terms. The Taylor series expansions more easily preserve the desired order of the reconstruction, but the ADM approach is much simpler to implement numerically.

6.3.5 Properties of the reconstructed τ_{RSFS}

A few final observations about both reconstruction methods, Eqs. 6.6 and 6.7, are worthwhile. First, neither model has parameters other than the filter width and the number of terms retained in the series, and no assumptions are made about the form of the RSFS motions. The models should thus be able to capture anisotropic motions better than eddy-viscosity models. Scale-similar models are also invariant under Galilean transformations (Speziale, 1985), and they exhibit correct near-wall behavior (Sarghini *et al.*, 1999). Their scale-similarity properties have desirable effects in *a priori* tests (Katopodes *et al.*, 2000*b*; Stolz *et al.*, 1999*a*). Furthermore, the evolution equation developed by Katopodes *et al.* (2000*b*) (see Eq. 3.12) for the approximate τ_{ij} indicates that these subfilter-scale stresses are influenced by buoyancy, Coriolis, diffusion, pressure, and advection terms, just as the resolved velocities are. Thus, the expressions in Eqs. 6.9 and 6.10 for τ_{ij} capture the effects of all relevant physical mechanisms, to fourth order in the filter width.

Second, series expansion models can can use any smooth filter, keeping in mind certain guidelines. The filter function G is applied to a flow variable f in physical space as

$$\overline{f}(x, \Delta_f, t) = \int_{-\infty}^{\infty} G(x, x', \Delta_f) f(x', t) dx' \,, \tag{6.19}$$

which is a Fredholm equation of the first kind (see Chapter 18 of Press *et al.* (1992)). A unique solution can exist, but the problem is often ill conditioned, so that any error made in computing the coefficients of the series solution causes a growing error as the number of terms is increased. If G is positive in Fourier space for all wavenumbers, the exact inverse can be obtained by simply inverting the filter kernel in wave space. If G crosses from positive to negative values in wave space at any wavenumber, division by zero makes exact inversion impossible. Carati *et al.* (2001) examined the convergence of the Taylor-series based expansion of Yeo & Bedford (1988) and Leonard (1997); they demonstrated (without a concrete mathematical proof) an increase in correlation with increasing reconstruction of the stress tensor compared to direct numerical simulation (DNS) values, therefore providing an informal proof of convergence. The contour plots in Fig. 3.8 also showed that including more terms in the series expansion improves the appearance of the velocity field (within the limitations of the

discrete grid). As described by Domaradzki & Adams (2002), difficulties with the exact inversion procedure are avoided by simply attempting to obtain an *approximate* deconvolution and not an exact one. The series reconstructions given by Eqs. 6.6 and 6.7 over all wavenumbers of such a filtered field are approximate. The exact reconstruction can only be obtained as long as the filter kernel is positive in wave space and numerical errors are kept to a minimum. Hence, it is preferable to choose an explicit filter function that is positive for at least those wavenumbers represented in the simulation, e.g. the tophat filter. It is also important that the filter width be at least twice the size of the grid spacing, otherwise discretization errors will be as large as the effect of the SFS model (Ghosal, 1996; Chow & Moin, 2003) (see Chapter 4).

The subfilter-scale modeling approach described here could accommodate a commuting filter such as those developed by Vasilyev *et al.* (1998), which would allow implementation of this model with higher-accuracy numerical schemes and would avoid commutation errors (for non-uniform grids). The more a smooth filter approaches a sharp cutoff filter, the less are the benefits for reducing numerical errors, and the less wave space is available for reconstruction; however, the use of higher-order filters is compatible with the use of higher-order schemes which have fewer numerical errors. The sharp-cutoff filter is ill-suited to velocity estimation methods, including the series expansion model presented here. This is clearest if we imagine using a cutoff filter in the van Cittert method; if $\overline{\widetilde{u}} = \overline{\overline{\widetilde{u}}}$ (where the overbar temporarily is used to denote the cutoff filter), the expansion in Eq. 6.7 would yield $\tilde{u}_i^\star = \overline{\widetilde{u}}$, and the RSFS stress would be zero.

Finally, we note that the series expansions for the RSFS terms in the filtered Navier-Stokes equations introduce higher-order derivatives, thereby requiring higher-order boundary conditions for the momentum equations. This problem is usually circumvented by applying no-slip boundary conditions repeatedly. No slip essentially applies inverse mirror conditions at solid boundaries; $\partial u/\partial x$ can be extended to the ghost cell beyond the physical boundary, then $\partial^2 u/\partial x^2$ can be computed at the wall and extended by symmetry conditions, etc. In our large-scale simulations, the bottom boundary is rough, which overwhelms any attempt to apply truly no-slip conditions at the wall; the wall stress is prescribed and higher-order derivatives do not need to be calculated on the wall. The filtering procedure near the wall is described in further

detail later. An alternative solution is to reduce the order of the series expansion near the wall, but the RSFS portion tends towards zero at the wall regardless (see Section 6.2).

In summary, the series expansion representations of the RSFS stresses are theoretically excellent. They perform well in *a priori* tests and can be used up to any order of accuracy desired. However, interaction with numerical errors in *a posteriori* tests is not easy to predict. Corresponding results are examined in the later sections. In the next section, we describe approaches to modeling SGS motions, which become increasingly important at coarse grid resolutions such as those present in atmospheric boundary layer flow simulations.

6.4 SGS and wall models

The problem of representing the RSFS stresses has essentially been solved. Aside from the issues that arise because of numerical discretization errors in the numerical model and in the reconstruction procedure itself, the above reconstruction methods are exact to within the truncation error. Unfortunately, the turbulence closure problem remains in the SGS terms. Equation 6.4 still has the unclosed term $\overline{u_i u_j}$ in the SGS portion of the total SFS stress. The interaction of the SGS and RSFS motions is also hard to predict and may create errors that limit the reconstruction as well.

Carati *et al.* (2001) suggest that there is a separation of scales of sorts between the resolved component and the subgrid component of the velocity field (see Fig. 6.1) that perhaps makes an eddy-viscosity model the best choice for the SGS motions. However, they find very poor correlations between eddy-viscosity model quantities and those calculated from DNS data. For lack of a better framework, a simple eddy-viscosity form is also assumed in this work for modeling the unclosed term:

$$\tau_{SGS} = -2\nu_T \overline{\tilde{S}}_{ij} \ , \tag{6.20}$$

where ν_T is the eddy viscosity, and $\overline{\tilde{S}}_{ij} = (1/2)(\partial\overline{\tilde{u}}_i/\partial x_j + \partial\overline{\tilde{u}}_j/\partial x_i)$ is the resolved strain rate tensor. The closure problem shifts to determining the best representation for ν_T. Despite the known shortcomings of this class of models, they are convenient

to use when energy transfer to the subgrid scales is desired. The variations of eddy-viscosity models are too numerous to describe them all. We focus on those models we have chosen for our study. These particular SGS models have been used before to represent the complete SFS stress, but none have been previously used with explicit filtering and reconstruction in large-scale flows.

6.4.1 Smagorinsky-based eddy-viscosity models

One of the most commonly used eddy-viscosity models is the Smagorinsky model (Smagorinsky, 1963), which assumes

$$\nu_T = (C_S \Delta_g)^2 (2 \overline{\tilde{S}}_{ij} \overline{\tilde{S}}_{ij})^{1/2} \,, \tag{6.21}$$

where C_S is the Smagorinsky coefficient, and Δ_g is the grid spacing. The modified Smagorinsky model (which accounts for stratification) is often used in atmospheric applications; the scheme is often referred to as Smagorinsky-Lilly scheme (Lilly (1962), see also Xue *et al.* (2000) for implementation within ARPS):

$$\nu_T = (C_S \Delta_g)^2 \left(\overline{\tilde{S}}^2 - \frac{1}{\mathrm{Pr}} \frac{g}{\overline{\tilde{\theta}}} \frac{\partial \overline{\tilde{\theta}}}{\partial z} \right)^{1/2} \tag{6.22}$$

where Pr is the turbulent Prandtl number, g is gravitational acceleration, and $\overline{\tilde{\theta}}$ the potential temperature. If the argument of the square root becomes negative, ν_T is set to zero.

The Smagorinsky model has several drawbacks, especially near the surface, where it overpredicts the stresses. All eddy-viscosity models fail to allow for backscatter of energy from small to large scales. Atmospheric measurements show that backscatter is present near the surface and should be included in LES turbulence closure schemes (see Porté-Agel *et al.*, 2001; Sullivan *et al.*, 2003). Correlations from *a priori* tests show that the eddy-viscosity stress tensors are not aligned with calculations from DNS data (Katopodes *et al.*, 2000*b*). Furthermore, Mason & Thomson (1992) showed that the failure of the Smagorinsky model near the surface could not be cured by increasing grid resolution. There will always be a region near the rough bottom boundary where the flow is under-resolved. Therefore, several modifications and alternatives to

improve performance near the surface have been proposed.

Sullivan *et al.* (1994) use a two-part Smagorinsky eddy-viscosity model consisting of the mean and fluctuating strain rate in an attempt to correct the near-wall behavior of the original model. Neutral and slightly buoyant flows simulated with this two-part model show significant improvements over the standard Smagorinsky model; however the model requires specification of a parameter γ to adjust the traditional Smagorinsky coefficient and control the contribution of the fluctuating term as a function of distance from the wall. The model does not allow for energy backscatter near the surface and it uses a planar average (possible only in idealized test cases) to separate the fluctuating and mean quantities.

Andren (1995) performed weakly-stratified boundary layer simulations using the SGS model of Sullivan *et al.* (1994). Neutral boundary layer tests using this SGS model showed improvements similar to those obtained from the stochastic backscatter model of Mason & Thomson (1992), but without the increased computational cost. Ding *et al.* (2001) modified the model of Sullivan *et al.* (1994) by assuming that the total stress is linear. This artificial linear "forcing" was applied for the bottom 20% of the boundary layer and produced stress profiles that look overly constrained. None of the above implementations modified the heat flux parameterization though the same principles should apply there.

6.4.2 Other non-dynamic eddy-viscosity models

Kosović (1997) developed a nonlinear SGS model which improved predictions of the nondimensional shear in a neutrally-stratified boundary layer flow. The model is based on constitutive theory and requires three (dependent) parameters; it assumes locally isotropic equilibrium turbulence and a -5/3 scaling law for the energy spectrum. Filtering was applied only in homogeneous directions using a cutoff filter with spectral methods, so his proposed nonlinear model is truly an SGS model with no reconstruction necessary (if we neglect the effect of finite-differences errors in the vertical). Given the improvements that were obtained, it would be interesting to explore the use of this nonlinear SGS model in a finite-difference code using explicit filtering together with a reconstruction model to account for the RSFS stress; this is left to future work.

Other recent SGS models include the multi-scale approach of Hughes *et al.* (2001*a*), where a small-scale eddy viscosity gives good results in small-scale flows. Vreman (2003) showed that the small-scale eddy-viscosity model of Hughes *et al.* (2001*a*) can be reformulated in terms of a hyper-viscosity model, which can be used with a scale-similarity model. Finally, Domaradzki & Loh (1999) presented a velocity estimation method not for the RSFS stress, but for the SGS stress; the method uses a deconvolution step followed by a nonlinear step to produce higher-wavenumber motions using a twice finer mesh. None of these methods has been used in rough-walled flows.

6.4.3 Dynamic Smagorinsky model

The standard Smagorinsky model requires the use of a pre-determined coefficient, C_S. An alternative to the above approaches is the dynamic Smagorinsky model (DSM), where the Smagorinsky coefficient C_S is determined automatically by applying the same models at the test filter level (Germano *et al.*, 1991). The DSM is widely-used as the eddy-viscosity SGS model in small-scale turbulence studies (see e.g. Germano *et al.*, 1991; Meneveau & Katz, 2000). The DSM has been used with explicit filtering in small-scale flows by Winckelmans *et al.* (2001) and Gullbrand & Chow (2003); this requires special attention to the application of the test filters.

Applications of dynamic models to high Reynolds number flows have been few. Balaras *et al.* (1995) used the dynamic Smagorinsky model in simulations of high Reynolds number channel flow with rough walls (though still at laboratory scales). Three-dimensional test filtering was used except at the wall cells, where the test filter was applied only in the homogeneous (wall-parallel) directions. The final dynamic coefficient was averaged over the entire horizontal plane at each vertical level. The authors mention that the dynamic procedure was sensitive to the interpolation procedures applied in the staggered grid system. Esau (2004) simulated the large-scale neutral atmospheric boundary layer using the DSM and the dynamic mixed model (DMM) of Zang *et al.* (1993) with some improvement over the standard Smagorinsky model. A finite-difference code was used, but filtering was applied only in the horizontal directions. Sensitivity to numerical errors in the dynamic procedure was also observed.

A problem with the formulation of the standard dynamic eddy-viscosity model (Germano *et al.*, 1991) is that it assumes that the coefficient is scale invariant. However, when the flow is under-resolved, especially near the wall, this is no longer true. Porté-Agel *et al.* (2000) developed a scale-dependent dynamic Smagorinsky model to account for the near-wall region, where motions are under-resolved. When applied to a neutral atmospheric boundary layer, they achieved improved logarithmic velocity profiles, but at the cost of an extra filtering step in the dynamic procedure and an empirical function for the scale dependence. Test filtering was only performed in the horizontal (homogeneous) directions, thereby eliminating the need to specify unknown boundary conditions at the wall. They used spectral methods in the horizontal directions and spectral cutoff filters, which are inapplicable to flows over complex geometries. The scale-dependent model also requires a scaling function β and application of a second test filter in the dynamic procedure. This model was not considered in the current work because of these limitations.

6.4.4 Dynamic Wong-Lilly model

Due to sensitivities of the DSM to the bottom boundary condition (see Section 6.5.2), as well as for ease of implementation, we instead use the dynamic model of Wong & Lilly (1994), who simulated the convective boundary layer. Wong & Lilly (1994) present a simplified base model which require no calculations of $\overline{\tilde{S}}_{ij}$ during the dynamic procedure. Instead, the base model is derived from Kolmogorov scaling, which expresses the eddy viscosity as

$$\nu_T = C^{2/3}\Delta^{4/3}\epsilon^{1/3} \,, \quad \text{or} \quad \nu_T = C_\epsilon \Delta^{4/3} \,, \tag{6.23}$$

where $C_\epsilon = C^{2/3}\epsilon^{1/3}$ is the coefficient of interest; hence the traditional requirement that the dissipation rate ϵ be equal to the SGS energy production rate (including the buoyancy term) is avoided. This base model reduces computational cost because the derivatives in Eq. 6.21 (at grid and test levels) are no longer required. In the dynamic Wong-Lilly (DWL) formulation, the coefficient is determined using the least-squares

method of Lilly (1992):

$$2C_\epsilon \Delta^{4/3} \approx \frac{\left\langle L_{ij} \hat{\overline{S}}_{ij} \right\rangle}{(1-(\hat{\Delta}/\Delta)^{4/3}) \left\langle \hat{\overline{S}}_{ij} \hat{\overline{S}}_{ij} \right\rangle} \ . \tag{6.24}$$

Here, the brackets <> denote local averaging, $\hat{}$ denotes the test filter, and

$$L_{ij} = \widehat{\widetilde{\overline{u}}_i \widetilde{\overline{u}}_j}^{\,c} - \widehat{\widetilde{\overline{u}}_i^{\,c}} \widehat{\widetilde{\overline{u}}_j^{\,c}} \tag{6.25}$$

$$\widehat{\widetilde{\overline{S}}_{ij}^{\,c}} = \frac{1}{2} \left(\frac{\partial \widehat{\widetilde{\overline{u}}_i^{\,c}}}{\partial x_j} + \frac{\partial \widehat{\widetilde{\overline{u}}_j^{\,c}}}{\partial x_i} \right) \ . \tag{6.26}$$

We use the notation of Carati *et al.* (2001) to define the test filtered terms; the $\tilde{}^c$ operator denotes the effect of the discretization operator at the coarser test-level grid.

6.4.5 Combined RSFS and SGS models

We use the modified Clark or the ADM (for the RSFS) and the DWL (for the SGS) to obtain the total SFS stress:

$$\tau_{ij} = \overline{\widetilde{u}_i^\star \widetilde{u}_j^\star} - \overline{\widetilde{u}_i^\star}\,\overline{\widetilde{u}_j^\star} - 2C_\epsilon \Delta^{4/3} \overline{\tilde{S}}_{ij} \ , \tag{6.27}$$

which we call the dynamic reconstruction model (DRM) (similar to Gullbrand & Chow (2003)). The dynamic modified Clark plus DWL is denoted DRM-MC. We also use ADM reconstruction series from levels zero through ten, denoted DRM-ADM0 through DRM-ADM10. Note that DRM-ADM0 is similar to the DMM with explicit filtering as implemented by Vreman *et al.* (1994), but with the DWL substituted for the DSM. The standard Smagorinsky model without an RSFS component is our reference case.

The eddy-viscosity coefficient in this combined RSFS/SGS approach is determined dynamically from

$$2C_\epsilon \Delta^{4/3} \approx \frac{\left\langle (L_{ij} - H_{ij}) \hat{\overline{S}}_{ij} \right\rangle}{(1-(\hat{\Delta}/\Delta)^{4/3}) \left\langle \hat{\overline{S}}_{ij} \hat{\overline{S}}_{ij} \right\rangle} \tag{6.28}$$

where we define (shown here for level zero reconstruction only)

$$H_{ij} = \left(\widehat{\overline{\widehat{\widetilde{u}_i^c}\,\widehat{\widetilde{u}_j^c}}^c} - \widehat{\widetilde{\widehat{\widetilde{u}_i^c}\,\widehat{\widetilde{u}_i^c}}}^c \right) - \left(\widehat{\overline{\widetilde{\widetilde{u}_i}\,\widetilde{\widetilde{u}_j}}^c} - \widehat{\widetilde{\widetilde{u}_i}\,\widetilde{\widetilde{u}_j}}^c \right) , \tag{6.29}$$

and ask for the reader's indulgence for the use of such compact notation. This derivation is similar to that of Zang *et al.* (1993) and Vreman *et al.* (1994), who take into account the contribution of the scale-similarity portion (in H_{ij}) while computing the dynamic coefficient. The grid cutoff (tilde, tilde-c) operators are not explicitly applied because no robust means exist for applying a cutoff filter in a finite-difference simulation like ours. The notation serves as a reminder of the effect of the discretization operators. The finite-difference schemes on the coarser grid level partially fulfill the purpose of the discretization operator by limiting aliasing effects (due to the modified wavenumbers which decay to zero near the grid cutoff). Thus, our combined RSFS and SGS models constitute a mixed model that represents both back-scatter of small-scale energy to the larger scales and forward-scatter (dissipation) of large-scale energy by the small scales. Both processes are required for reasonable representation of subfilter-scale effects.

Finally, we note that the dynamic reconstruction approach could be used with other SGS models, e.g., 1.5-order TKE-based (Deardorff, 1980; Moeng, 1984) closures commonly used in cloud-scale simulations with parameterizations of stability effects. The values of the TKE equation coefficients are often debated (see e.g. Takemi & Rotunno, 2003; Deardorff, 1971), so a dynamic procedure like that of Wong & Lilly (1994) is more desirable. Stolz *et al.* (2001*a*) use the ADM reconstruction with a relaxation term to drain energy at the smallest scales and also include a dynamic procedure for determining the coefficient. For this work, we chose familiar eddy-viscosity formulations for their known performance in large-scale flow simulations.

6.4.6 Enhanced near-wall stress model

Because there are limitations to the resolution with which large-scale atmospheric flows can be simulated, special treatment is required for the turbulence model near the lower rough boundary. We have found that any combination of RSFS and eddy-viscosity models requires augmentation near the lower boundary, where eddy size

decreases much more rapidly than the grid spacing. The vertical grid spacing is invariably smaller than the horizontal one. While eddies may be well-resolved in the vertical, they are not so in the horizontal, thus introducing errors. Because $2\Delta x$ is the minimum eddy size that can be resolved in the horizontal (arguably $4\Delta x$ is the smallest *well*-resolved eddy), over a *vertical* distance of $2\Delta x$, eddies of this size are still under-resolved. This lack of resolution implies that an additional stress term may be needed near the wall to represent these motions.

Furthermore, the physical existence of subgrid roughness may alter the distribution of stresses near the surface. Nakayama & Sakio (2002) examined the effects of subgrid roughness with DNS of flow over a wavy bottom boundary consisting of small and large wavelengths. Filtering the DNS flow field and the wavy DNS boundary produced a snapshot of an ideal LES solution over the large wavelength boundary with subgrid roughness. The filtered velocities at the surface in the LES domain were then apparently only influenced by the larger wavelength topography, but the subfilter-scale roughness elements (the smaller wavelengths in the original DNS boundary) had generated extra stress near the new, smoother boundary. The surface stress, originally distributed over the DNS boundary, became distributed over a finite vertical layer above the smoother LES boundary. Dubrulle *et al.* (2002) (see their Eq. 16) also found that filtering near a solid boundary generates extra stress terms. These studies point to the need for a near-wall stress model that distributes stresses generated at the rough wall over a region near the wall. Similar ideas have been proposed by Shaw & Schumann (1992) and Patton *et al.* (2001) for flow through and over vegetation canopies. These canopy models serve to distribute surface fluxes over the plant canopy height to account for the increased drag from the vegetation. Brown *et al.* (2001) extended the idea of plant canopy models to flow over rough surfaces.

We have implemented the model of Brown *et al.* (2001), which can be expressed as a forcing term in the horizontal momentum equations, $-C_c a(z)|\overline{u}|\overline{u}_i$, where $i = 1, 2$. Here C_c is a scaling factor and the function $a(z)$ allows for a smooth decay of the forcing function as the cutoff height, h_c, is approached. $a(z)$ is set equal to $\cos^2(\pi z/2h_c)$ for $z < h_c$ and is zero otherwise. When implemented numerically, the enhanced stress is included in the turbulence closure stress term, and therefore is

integrated numerically using the trapezoidal rule:

$$\tau_{i,near-wall} = -\int C_c a(z)|\overline{u}|\overline{u}_i dz \ , \tag{6.30}$$

where the integration constants are chosen so that $\tau_{i,near-wall} = 0$ at the top of the enhanced stress layer. This stress is then directly added to the τ_{i3} terms from the other model components.

6.5 Large-eddy simulations of neutral boundary layer flow

To test the performance of the closure models, we use the ARPS code to simulate a rotation-influenced neutral boundary layer flow case similar to that of Andren *et al.* (1994). For the laminar case, or with a constant eddy viscosity, this flow has the Ekman spiral as an analytical solution (see Stull, 1988, pp. 210-212). The fully turbulent solution has been examined by several researchers, e.g., Coleman (1999) (DNS), Sullivan *et al.* (1994), Andren *et al.* (1994), Kosović (1997), Ding *et al.* (2001), Porté-Agel *et al.* (2000) (no Coriolis forcing), Redelsperger *et al.* (2001), Carlotti (2002), and Esau (2004). Using scale analysis, Blackadar & Tennekes (1968) showed that the near-wall region of the turbulent Ekman layer should follow a logarithmic law. Typical eddy-viscosity models do not give a good logarithmic region near the wall, usually overpredicting the shear in the model with the velocity too low at the wall, and too high further away from it (Andren *et al.*, 1994).

The following sections compare the new turbulence model approach (RSFS plus SGS) with results from the standard Smagorinsky model available in ARPS. The TKE-1.5 closure in ARPS gives results similar to the Smagorinsky model, so they are not shown. The simulation setup and the effects of dynamic reconstruction on the flow solution are described below.

6.5.1 Model details and flow setup

ARPS was developed at the Center for Analysis and Prediction of Storms at the University of Oklahoma. Intended mainly for mesoscale and small-scale atmospheric

simulations, ARPS is formulated as an LES code that solves the three-dimensional, compressible, non-hydrostatic, filtered Navier-Stokes equations. ARPS details can be found in Xue *et al.* (1995, 2000, 2001), in Section 2.2, and in Appendices C and D. As noted in Section 6.2, the equations have been slightly modified to make them closer to the incompressible case studied by Andren *et al.* (1994), as detailed in Xu *et al.* (1996). After this work was completed, we performed tests with the original compressible ARPS code, but the results were essentially the same as those for the quasi-incompressible case described here. The derivations given earlier for τ_{ij} were used in the compressible version of the code after multiplying by the plane-averaged density (the base state density in ARPS), giving the stress as $\tau_{ij} = <\rho>(\overline{u_i u_j} - \overline{\widetilde{u}}_i \overline{\widetilde{u}}_j)$ (see Appendix D).

The flow is driven by a constant pressure gradient corresponding to a geostrophic wind of $(U_g, V_g) = (10, 0)$ m/s. The ARPS code is run for thirty non-dimensional time periods tf, where f is the Coriolis parameter, set equal to 1×10^{-4} s^{-1}; ($30\, tf =$ 300 000 s). This configuration results in an Ekman-like spiral for the mean velocities. The initial conditions are the analytical Ekman spiral solution with small perturbations that trigger instabilities so that the flow becomes fully turbulent (see Figure 6.6 later).

The grid size for the control case is $43 \times 43 \times 43$ with grid spacings of 32 m $\times$ 32 m in the horizontal. In ARPS this corresponds to a domain size of $\Delta x(nx-3) = 1280$ m in each horizontal direction. In the vertical, a stretched grid is used, with $\Delta z_{min} = 10$ m spacing near the bottom and up to 65 m near the top of the domain. The average spacing is 37.5 m and the domain height is 1500 m. Fourth-order spatial differencing was used for the advection terms. Temporal discretization uses a mode-splitting technique to accommodate high-frequency acoustic waves; the large time steps (0.5 s) use the leapfrog method, while first-order forward-backward explicit time stepping is used for the small time steps (0.05 s) (except for terms responsible for vertical acoustic propagation, which are treated implicitly). Higher and lower grid resolutions as well as different grid aspect ratios were also studied. Run parameters are given in Table 6.1 for all the tests and the base case.

The top and bottom boundaries are treated as rigid free-slip (also called semi-slip at the lower boundary). Surface fluxes are parameterized to account for the influence of the rough bottom surface. ARPS parameterizes momentum fluxes at the surface

Run name	Grid size	Δx	Δz_{min}	Large Δt	Small Δt	C_c	h_c
Smagorinsky*	(43,43,43)	32 m	10 m	0.5 s	0.05 s	–	–
DWL	(43,43,43)	32 m	10 m	0.5 s	0.05 s	0.5	$4\Delta x$
DRM-MC	(43,43,43)	32 m	10 m	0.5 s	0.05 s	0.65	$4\Delta x$
DRM-ADM0	(43,43,43)	32 m	10 m	0.5 s	0.05 s	0.5	$4\Delta x$
DRM-ADM1	(43,43,43)	32 m	10 m	0.5 s	0.05 s	0.5	$4\Delta x$
DRM-ADM2	(43,43,43)	32 m	10 m	0.5 s	0.05 s	0.5	$4\Delta x$
DRM-ADM5	(43,43,43)	32 m	10 m	0.5 s	0.05 s	0.5	$4\Delta x$
DRM-ADM10	(43,43,43)	32 m	10 m	0.5 s	0.05 s	0.5	$4\Delta x$
Smagorinsky	(43,43,43)	64 m	10 m	1.0 s	0.1 s	–	–
Smagorinsky	(43,43,43)	128 m	10 m	2.0 s	0.2 s	–	–
Smagorinsky	(43,43,83)	32 m	5 m	0.5 s	0.05 s	–	–
Smagorinsky	(83,83,83)	16 m	5 m	0.25 s	0.025 s	–	–
Smagorinsky	(83,83,83)	32 m	10 m	0.5 s	0.05 s	–	–
DRM-ADM0	(43,43,23)	32 m	20 m	0.5 s	0.05 s	0.4	$4\Delta x$
DRM-ADM0	(43,43,23)	64 m	20 m	1.0 s	0.1 s	0.6	$4\Delta x$
DRM-ADM0	(43,43,23)	128 m	20 m	2.0 s	0.2 s	0.8	$4\Delta x$
DRM-ADM0	(43,43,43)	16 m	16 m	0.25 s	0.025 s	0.4	$4\Delta x$
DRM-ADM0	(43,43,43)	64 m	10 m	1.0 s	0.1 s	0.75	$4\Delta x$
DRM-ADM0	(43,43,43)	96 m	10 m	1.0 s	0.1 s	0.83	$2\Delta x$
DRM-ADM0	(43,43,43)	128 m	10 m	2.0 s	0.2 s	0.85	$2\Delta x$
DRM-ADM0	(43,43,83)	32 m	5 m	0.5 s	0.05 s	0.7	$2\Delta x$
DRM-ADM0	(43,43,83)	64 m	5 m	0.5 s	0.05 s	0.85	$2\Delta x$
DRM-ADM0	(83,83,83)	16 m	5 m	0.25 s	0.025 s	0.5	$4\Delta x$
DRM-ADM0	(83,83,83)	32 m	10 m	0.5 s	0.05 s	0.5	$4\Delta x$

Table 6.1: List of simulations and parameters. Standard grid sizes are followed by those with various grid aspect ratios. * denotes the base case.

with an instantaneous logarithmic drag law (used here with constant drag coefficients) at each grid point. The bottom roughness is set to 0.1 m and the drag coefficient is derived by applying the logarithmic velocity condition to the first grid cell above the wall (at height $\Delta z_{min}/2$). At the lateral boundaries, periodic conditions are used for this idealized flat-terrain study.

6.5.2 Implementation of RSFS, SGS, and wall models

The Smagorinsky closure provides the base standard against which we compare our new turbulence modeling approaches. The Smagorinsky coefficient is chosen as $C_S = 0.18$ (see e.g. Sullivan *et al.*, 1994).

The anisotropic explicit filter for the reconstruction models was applied at twice the grid spacing, $2\Delta_g$, which is compatible with the fourth-order advection schemes used by ARPS (Ghosal, 1996; Chow & Moin, 2003). This filter appears in the calculation of the RSFS terms and in the dynamic procedure. For ease of implementation, we apply the van Cittert series expansion reconstruction in computational space which has a uniform grid (though still allowing for anisotropy); therefore the filters are applied in computational space (Jordan, 1999; Stolz *et al.*, 2001*a*). The Taylor series reconstruction is formulated in physical space, so the metric terms are included in the computation of the derivative terms, but the filters are also applied in computational space.

The greatest difficulty in implementation of the RSFS models is near solid boundaries, where care must be taken in representing higher-order terms in the Taylor series approach. Likewise, for the van Cittert iterative approach for reconstruction, numerous applications of the filter can become tricky near the wall. For rough walls, the simple no-slip condition must be modified to account for roughness effects; the boundary condition at the wall may be inadequate for accurately generating ghost points for computing derivatives and filters at the wall. We nevertheless use the ghost cells to enforce the boundary conditions. Note that "free slip" and "no slip" refer to the mathematical velocity boundary conditions; in both cases the flow is over a physically rough surface where the bottom stress is parameterized with a log law. The values at the wall can be sensitive to these bottom boundary conditions due to the repeated filtering that occurs there. However, when RSFS models are used together with SGS models at the wall, the RSFS contribution decays to zero (see Section 6.2) regardless of the specified boundary conditions.

On the other hand, our tests of the dynamic Smagorinsky SGS model in ARPS showed very strong sensitivity to the bottom boundary conditions. For flow over a rough wall, the surface stress is prescribed; in ARPS this stress is input as the value of τ_{13} at the wall. However, the dynamic Smagorinsky model requires calculations of $\overline{\tilde{S}}_{13}$ and $\widehat{\overline{\widetilde{S}_{13}}^{c}}$ at the wall. ARPS uses free-slip (zero-gradient) boundary conditions for $\overline{\tilde{u}}$ and $\overline{\tilde{v}}$ at the wall, so the calculated $\overline{\tilde{S}}_{13}$ is near zero, causing $\overline{\tilde{S}}_{13}$ and the dynamically calculated coefficient to have kinks near the wall. We tested a simple correction that extrapolates from above to better estimate $\overline{\tilde{S}}_{13}$ at the wall. This removed the kink in the C_S profiles, but still did not provide enough stress at the wall, and caused a

kink in the total stress and Φ profiles (see definition in Eq. 6.37). Planar averaging or test filtering in the dynamic procedure had little effect on the final planar-averaged profiles and did not correct the kinks. Porté-Agel *et al.* (2000) tested the standard dynamic Smagorinsky model and obtained values of the dynamic coefficient that were also too small near the wall.

The dynamic Wong-Lilly (DWL) model was not as sensitive to the chosen boundary conditions for $\overline{\widetilde{S}}_{13}$ (because ν_T does not depend on it explicitly), and did not produce a kink in the C_S or eddy-viscosity profiles. The stress provided by the DWL model is still too small at the wall, but with a smaller kink. In addition to giving more reasonable profiles near the wall, the DWL is easier to implement and more computationally efficient than the DSM. Wong & Lilly (1994) used a horizontal plane average, which is not applicable to flow over terrain; we therefore use a local filter created by applying the test filter twice. The dynamic eddy viscosity is also clipped at -1.5×10^{-5} to prevent the eddy viscosity from becoming too negative locally and causing instabilities (see Zang *et al.*, 1993; Wong & Lilly, 1994).

The effect of different smoothing functions on the final value of the eddy viscosity was investigated by comparing the percentage of points that were clipped. Figures 6.2 and 6.3 show the effect of increased smoothing on the clipping applied with the DWL and DRM-ADM0 models. Increasing the width of the smoothing function from one application of the test filter, to averaging over the entire plane, reduces the need for clipping. The clipping percentage is considerable very near the surface, then diminishes above, but grows large near the top boundary. The large values near the wall likely arise from difficulties in calculating derivatives and filters there. Near the top boundary, the clipping percentage appears to grow unreasonably large. Even with planar averaging, which should smooth all of the fluctuations in the components of C_ϵ, there is clipping in the DRM-ADM0 simulations.

Figure 6.4a shows an instantaneous profile of the numerator and denominator used to calculate ν_T with DRM-ADM0. The large negative values of ν_T near the top of the domain are likely caused by numerical errors, as the quantities are quite small, but their ratio large. Likewise, the fairly large positive regions in the middle of the flow are also a result of the division of two small numbers. There are, however, significant eddies even in the middle of the flow domain, so the large local values of ν_T may be justified (see Fig. 6.5). In any case, in an average sense, the values of ν_T

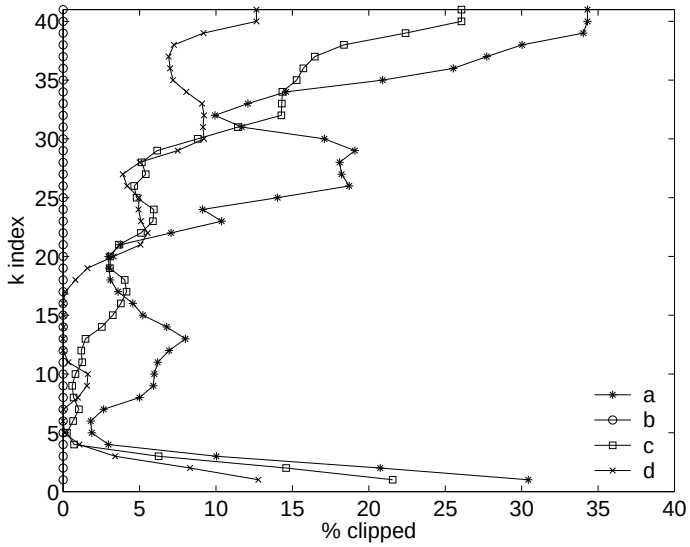

Figure 6.2: Percent clipping over each horizontal plane for the dynamic Wong-Lilly model (DWL) with different smoothing options: (a) local test filter, (b) planar average, (c) two test filters, (d) three test filters. Averaged from two instantaneous snapshots.

are insignificant when multiplied by the very small velocity gradients away from the wall; the resulting stress profile is shown in Fig. 6.4(b). We have used two test filters to somewhat minimize the amount of clipping; results for all four choices shown in Figs. 6.2 and 6.3 give quite similar results in the averaged mean velocity profiles.

The only input parameter required for the DWL is the ratio of the test and explicit filters, $\hat{\Delta}/\Delta_f$, which we choose to be two. The resulting test filter is thus $4\Delta x$, which differs from the usual test filter used without explicit filtering. When no reconstruction is used, the test filter is often chosen as twice the grid spacing (see e.g. Zang *et al.*, 1993). This is a distinguishing, though subtle, feature of explicit filtering and was used by Gullbrand & Chow (2003) as well as Winckelmans *et al.* (2001). Furthermore, the resulting test plus explicit filter must be similar in shape to the original explicit filter. The discrete tophat explicit filter is applied with

$$\overline{f}_i = 0.25 f_{i-1} + 0.5 f_i + 0.25 f_{i+1} \ , \tag{6.31}$$

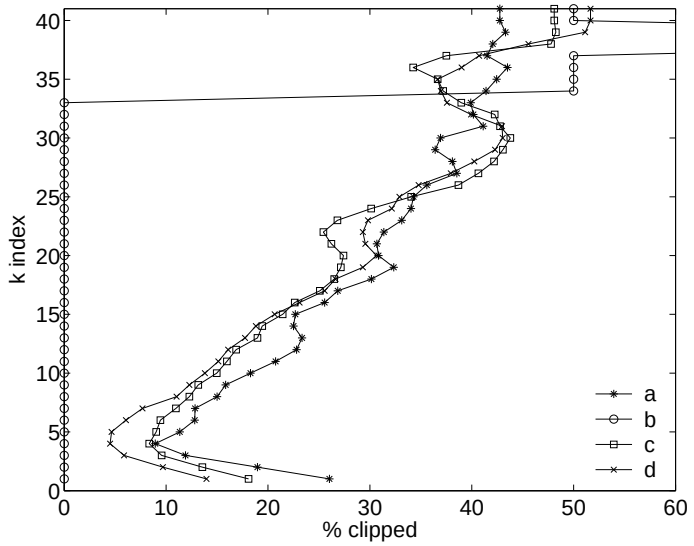

Figure 6.3: Percent clipping over each horizontal plane for DRM-ADM0 with different smoothing options: (a) local test filter, (b) planar average, (c) two test filters, (d) three test filters. Averaged from two instantaneous snapshots, therefore the planar averaged results show a few points with 50% clipping.

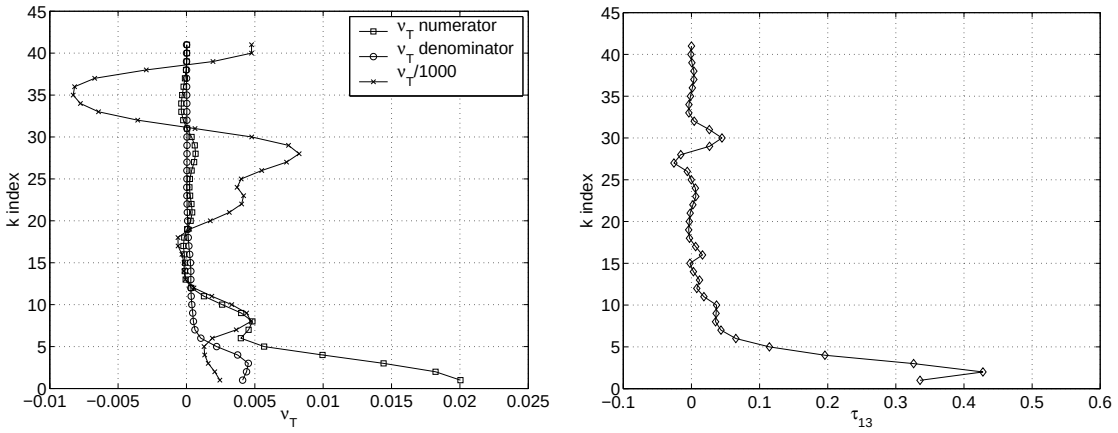

(a) (b)

Figure 6.4: (a) Instantaneous profiles of the numerator and denominator of the eddy viscosity ν_T, and the final ν_T before clipping, for DRM-ADM0 with one local test filter applied, and (b) the corresponding instantaneous τ_{13} profile.

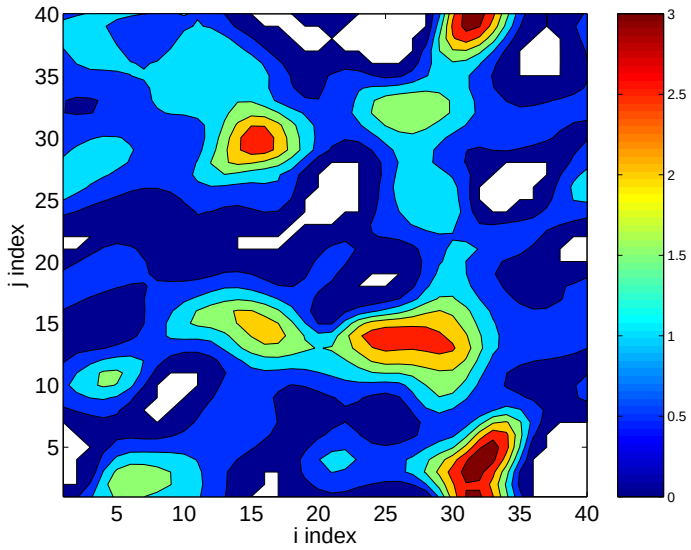

Figure 6.5: Instantaneous contours of the eddy viscosity ν_T (m^2/s^2) after clipping, for DRM-ADM0 with one local test filter, at k = 5. Clipping is indicated by the enclosed white regions with a value of -1.5×10^{-5}.

where i temporarily denotes the grid index; therefore the test filter is

$$\hat{f}_i = 0.5 f_{i-1} + 0.5 f_{i+1} \tag{6.32}$$

to give a combined test plus explicit filter of

$$\overline{\hat{f}}_i = 0.125 f_{i-2} + 0.25 f_{i-1} + 0.25 f_i + 0.25 f_{i+1} + 0.125 f_{i+2} \ , \tag{6.33}$$

which is simply a tophat filter of twice the width of the explicit filter (see Eqs. 5.11 and 5.12, and Gullbrand & Chow, 2003).

Following Brown *et al.* (2001), Cederwall (2001) and Chow & Street (2002), we implement a near-wall stress model, based on the model given previously in Eq. 6.30. Brown *et al.* (2001) choose a constant C_c so that the velocity at the top of the canopy matches experimental measurements. Cederwall (2001) selected C_c such that the near-wall stress model augmented the total stress at the first grid point above the wall to make it equal to the total local bottom shear stress. We allow C_c to be locally proportional to the bottom shear stress in each horizontal direction. The proportionality factor is chosen so that the near-wall stress model provides the necessary

augmentation that yields logarithmic mean velocity profiles near the wall. The variation of the C_c and h_c (the layer height) with grid spacing and aspect ratio is described later. The near-wall stress model is part of the SGS model component, but is treated separately from the eddy-viscosity contribution.

Finally, current turbulence models often do not provide enough dissipation at the highest frequencies, so computational mixing terms may be added for stability if desired. We follow the recommendations in ARPS and use a small fourth-order term, which can be considered to be a type of hyper-viscosity. ARPS also includes a divergence damping term to control acoustic noise. The impact of these damping terms has been assessed and found to be minimal (see also Section 6.5.3).

6.5.3 Simulation results

Time evolution

Figures 6.6a and 6.6b show the evolution of the non-stationarity measures C_u and C_v defined by (following Andren *et al.* (1994))

$$C_u = -\frac{f}{\overline{uw}_s}\int_0^{z_{top}}(<\overline{\tilde{v}}> - V_g)dz \tag{6.34}$$

$$C_v = \frac{f}{\overline{vw}_s}\int_0^{z_{top}}(<\overline{\tilde{u}}> - U_g)dz \tag{6.35}$$

$$\tag{6.36}$$

where z_{top} is the stress-free top of the simulation domain, and the $\overline{uw}_s$ and $\overline{vw}_s$ denote the total surface stresses in the uw and vw planes, respectively. The brackets $<>$ denote horizontal planar averaging, as well as time averaging, using data taken at each time step. At steady-state, both C_u and C_v should be unity, but even after 100 000 s, oscillations are apparent in Figs. 6.6a and b. Note that the spin-up time is much shorter for the DRM-ADM0 run. Andren *et al.* (1994) state that the oscillations affect primarily the first-order statistics of the flow, but some of our comparisons are quite sensitive, so we seek a solution as close to a statistically steady state as possible. Unless otherwise indicated, we average from 200 000 s to 300 000 s, where oscillations in the C_v curve especially have decayed significantly. Our simulation and averaging

times are about three times as long as those of Andren *et al.* (1994).

First-order quantities

Figure 6.7a shows semi-log plots of mean wind speed from four different turbulence model configurations: no model, static Smagorinsky, dynamic Wong-Lilly, and DRM-ADM0. The wind speed ($U = \sqrt{\overline{\tilde{u}}^2 + \overline{\tilde{v}}^2}$) is normalized by the (time averaged) friction velocity defined by $u_* = (\overline{uw}_s^2 + \overline{vw}_s^2)^{1/4}$ (found to be approximately 0.44). The theoretical log-law profile is also shown. The 'no model' and Smagorinsky results deviate considerably, but the DWL and DRM results provide good agreement. The 'no model' simulation incorporates the rough wall boundary condition, therefore the surface stress contributes at the first point above the wall and slows the wind speed.

A more sensitive measure of a model's performance is the non-dimensional velocity gradient, Φ, defined as

$$\Phi = \frac{\kappa z}{u_*} \sqrt{\left(\frac{\partial < \overline{\tilde{u}} >}{\partial z} \right)^2 + \left(\frac{\partial < \overline{\tilde{v}} >}{\partial z} \right)^2} \,. \tag{6.37}$$

Here κ is the von Kármán constant, chosen to be 0.4. In a logarithmic region, $\Phi = 1$, which we expect for approximately the first 150-250 m above the wall, or 10-15% of the boundary layer depth (Sullivan *et al.*, 1994). Profiles of Φ, shown in Fig. 6.7b have been smoothed to remove $2\Delta z$ waves present in the derivatives (but not in the original velocity fields). We see that the overshoot in Φ reaches 1.6 for the traditional Smagorinsky model, indicating the model provides excessive shear near the surface. Similar overshoots were observed in other studies (Andren *et al.*, 1994; Sullivan *et al.*, 1994; Kosović, 1997). It appears that the Smagorinsky model behaves as a large viscosity model that mimics the molecular viscosity dissipation near a smooth wall. However, in large-scale flows, the linear region is confined to a few millimeters above the surface, and the log region should cover the entire 10% near the wall in our simulation results. Our efforts at improving near-surface Φ profiles are aimed at replacing this gradient-diffusion behavior near the wall. Surprisingly, the results using no model appear fairly logarithmic after the first point above the wall, but the velocity magnitude is significantly over-predicted.

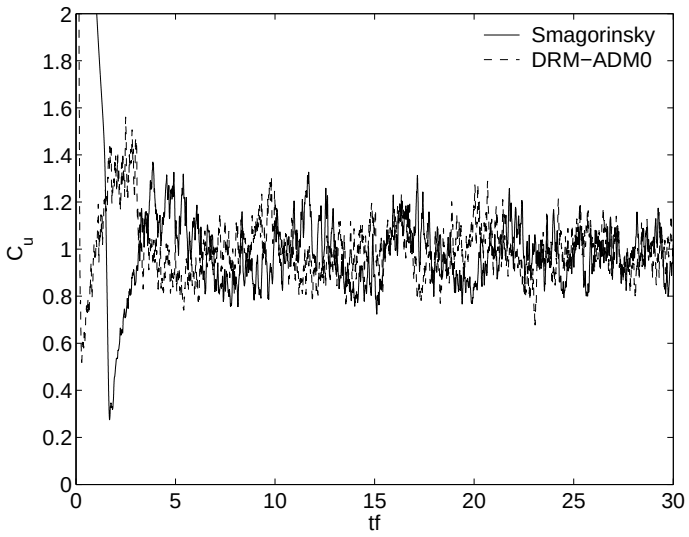

(a)

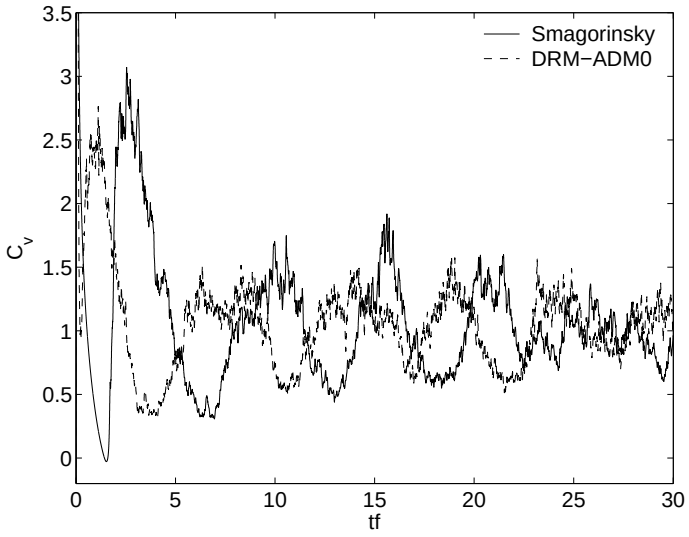

(b)

Figure 6.6: Comparison of non-stationarity parameters (a) C_u and (b) C_v for the Smagorinsky model and the DRM-ADM0 hybrid model.

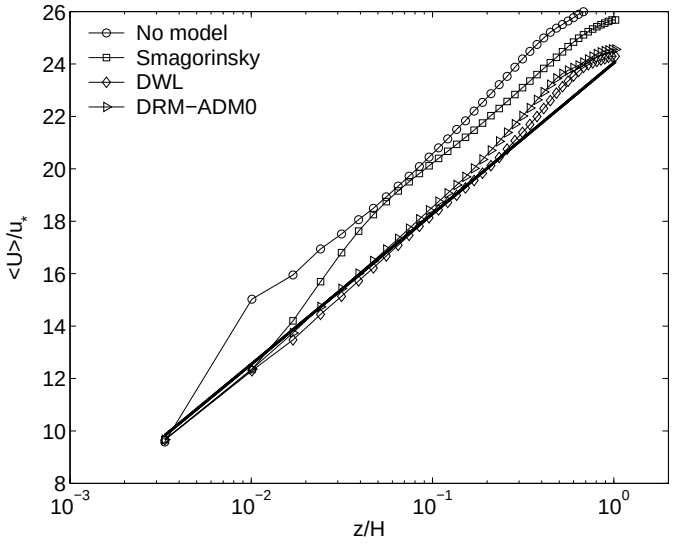

(a)

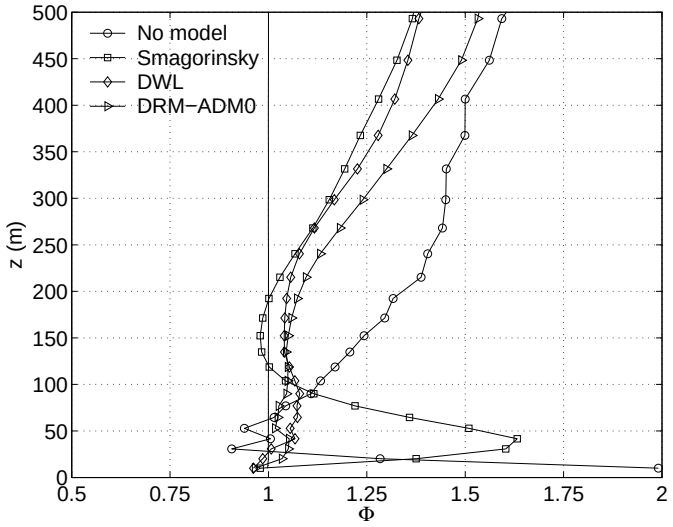

(b)

Figure 6.7: Comparison of (a) mean wind speed and (b) non-dimensional mean shear Φ profiles for no model, the Smagorinsky model, the dynamic Wong-Lilly model, and for the DRM-ADM0 hybrid model (level-0 reconstruction, DWL, and near-wall stress). Theoretical log profile also shown in (a).

When reconstruction and dynamic eddy-viscosity models are used with the near-wall stress term (DRM-ADM0), values of Φ within 0.1 of the ideal value (unity) are obtained. This represents a significant improvement over the standard Smagorinsky simulations. It is better than several previous attempts to improve Φ profiles, where agreement within about 0.2 was achieved by Sullivan *et al.* (1994), the backscatter results of Mason and Brown in Andren *et al.* (1994), and those of Porté-Agel *et al.* (2000), and Ding *et al.* (2001), using various SGS methods. Our results are comparable to those of Kosović (1997), where Φ profiles were also within 0.1 of unity. The simulations of Esau (2004) using a dynamic mixed model did not produce satisfactory results near the wall (see Esau, 2004, Figs. 11a and 15d); while the DMM provides some reconstruction, it was not used with a formal explicit filter, making the level of reconstruction ambiguous. Sensitivity to the numerical formulation with the Smagorinsky model as the base model for the dynamic procedure (as opposed to DWL) and the absence of a near-wall stress model may also have limited the improvement obtained by the DMM.

Our hybrid model has the advantage of having no adjustable parameters aside from the enhanced near-wall stress. Furthermore, the reconstruction component is of scale-similar form, and thus allows backscatter, i.e., energy flux from the small to the large scales. This is believed to be especially important in the atmospheric boundary layer when the large scales are not fully resolved and it aids in achieving a logarithmic mean velocity profile. The influence of the enhanced near-wall stress is of course strongest near the wall, where it straightens the Φ profiles. However, the impact of the near-wall stress model does not overwhelm the near-wall results to the point where the turbulence model becomes irrelevant. Tests with the near-wall stress added to the standard Smagorinsky model (without reconstruction) did not produce encouraging results. Interestingly, the DWL model without reconstruction also performs quite well; the effects of adding reconstruction will become clearer when second-order statistics are evaluated later.

Figure 6.8 compares results from using the modified Clark model for the RSFS motions and the dynamic eddy-viscosity model for the SGS stresses (DRM-MC). Note that for this reconstruction model only, the dynamic procedure does not include the contribution of the RSFS model when calculating the SGS coefficient. This avoids the calculation of H_{ij} which requires that the RSFS component be calculated on the test

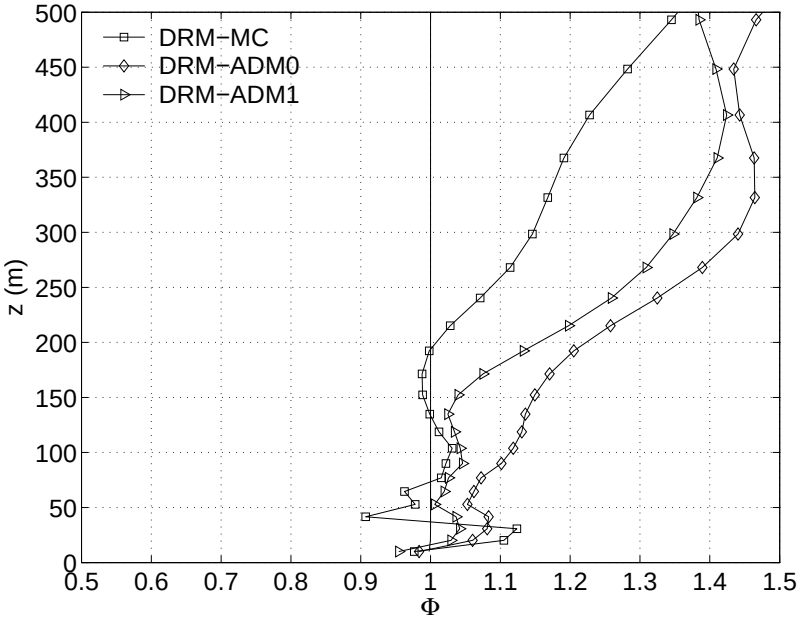

Figure 6.8: Comparison of non-dimensional mean shear Φ profiles for the dynamic modified Clark model (DRM-MC), compared to DRM-ADM0 and DRM-ADM1.

filter level; for the modified Clark model this would require computing the derivatives on the coarser grid, thus complicating the calculations. Attempts at using derivatives on the fine grid for H_{ij} did not produce good results. The DRM-ADM models were also tested without using H_{ij}. The eddy-viscosity profiles were quite similar near the wall and differences above that were largely due to numerical errors. Since the magnitude of the shear rate is small far from the wall, the contribution of the eddy-viscosity terms is negligible away from the wall regardless of H_{ij}. The comparisons of Φ in Fig. 6.8 indicate that the modified Clark simulations fall in the same category as the DRM-ADM0 and DRM-ADM1 results, as expected. (The stresses also lie between the DRM-ADM0 and DRM-ADM1 profiles but are not shown.) The DRM-MC results display slightly more oscillation near the wall than the DRM-ADM results. The oscillations are not visible when using the modified Clark model together with static Smagorinsky (instead of DWL) which is more dissipative.

Figure 6.9 shows the effect of increasing the level of reconstruction in the DRM-ADM models. It is difficult to identify the best model in the mean velocity profile plots (see Fig. 6.7). The Φ profiles indicate that while all the results remain within

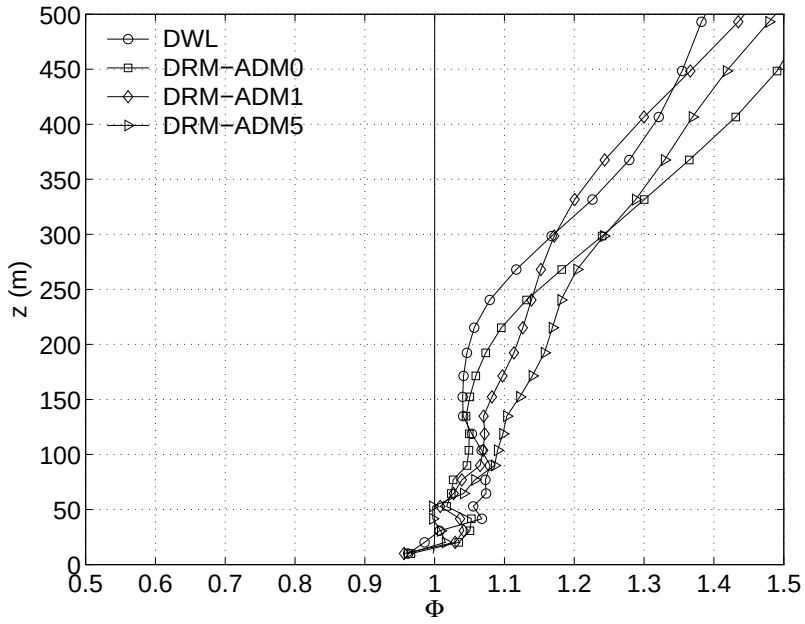

Figure 6.9: Comparison of non-dimensional mean shear Φ profiles for increasing reconstruction levels; dynamic Wong-Lilly, no reconstruction; DRM-ADM0; DRM-ADM1; DRM-ADM2.

0.1 of the ideal value, increasing reconstruction moves the profiles slightly closer to unity near the wall. Because the curves are so close together, there is some sensitivity to the time averaging period; Fig. 6.6 shows the deviations from stationarity differed in time with each different turbulence model. We found that taking a long averaging period (100 000 s) after C_u and C_v have decayed significantly gave the most reasonable results. However, it is not clear that Φ should be the sole parameter used for comparisons as it is quite sensitive to small wiggles which are not readily apparent from the mean velocity profiles in Fig. 6.7a. Second-order statistics will be examined in the following section.

To test the influence of the RSFS reconstruction further, we performed simplified boundary layer simulations with no Coriolis force (Chow & Street, 2004*b*). Without the influence of rotation, the boundary layer flow should equilibrate to a unique value of u_* that corresponds to the specified constant pressure gradient (here approximately 0.45). The flow is almost entirely confined to the x-direction, with instantaneous v velocities quite small, and linear total uw stress profiles. To obtain good statistics, the simulations were run to 400 000 s and results were averaged over the last 100 000 s.

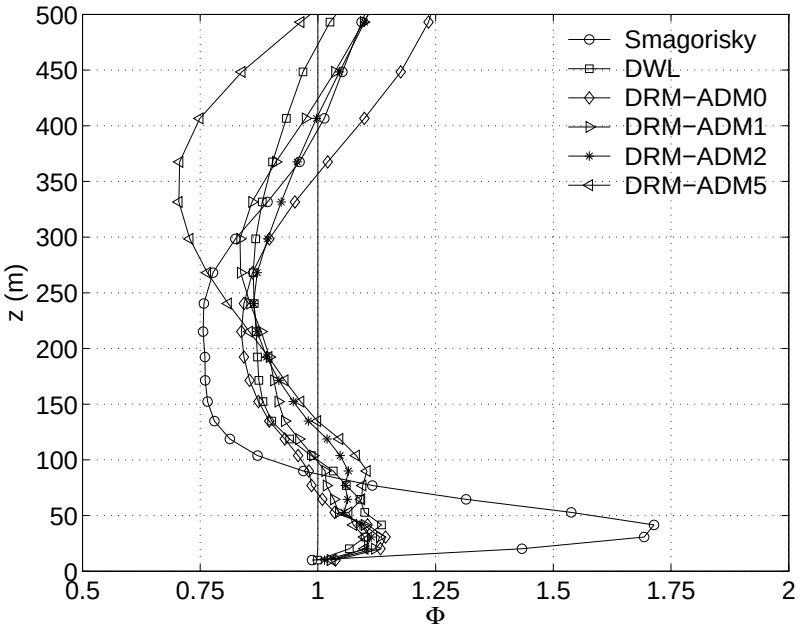

Figure 6.10: Comparison of non-dimensional mean shear Φ profiles for simulations without Coriolis forcing. Smagorinsky, DWL, DRM-ADM0, DRM-ADM1, DRM-ADM2, and DRM-ADM5 are shown.

In Fig. 6.10 we see that increasing reconstruction again improves the agreement of Φ with the logarithmic value of unity, especially close to the wall. Results from the Smagorinsky model and DWL are also shown for comparison.

Second-order quantities

While the Φ profiles presented above give a first-order comparison of methods, they do not provide a clear distinction between the models. Inertial oscillations make detailed comparison of second-order statistics also difficult, but some insight can be gained from the patterns observed.

Figure 6.11 compares the uw stress distribution for the Smagorinsky, DWL, and DRM-ADM0 cases from Fig. 6.7. The resolved uw stress is defined as $< (\widetilde{\overline{u}} - < \widetilde{\overline{u}} >)(\widetilde{\overline{w}} - < \widetilde{\overline{w}} >) >$, where $<>$ denotes planar averaging. The Smagorinsky and DWL simulations show similar contributions of the SFS stress, which is largest near the wall. When reconstruction is added, the total SFS stress increases compared to the eddy-viscosity simulations, while the resolved stress decreases accordingly. The magnitude

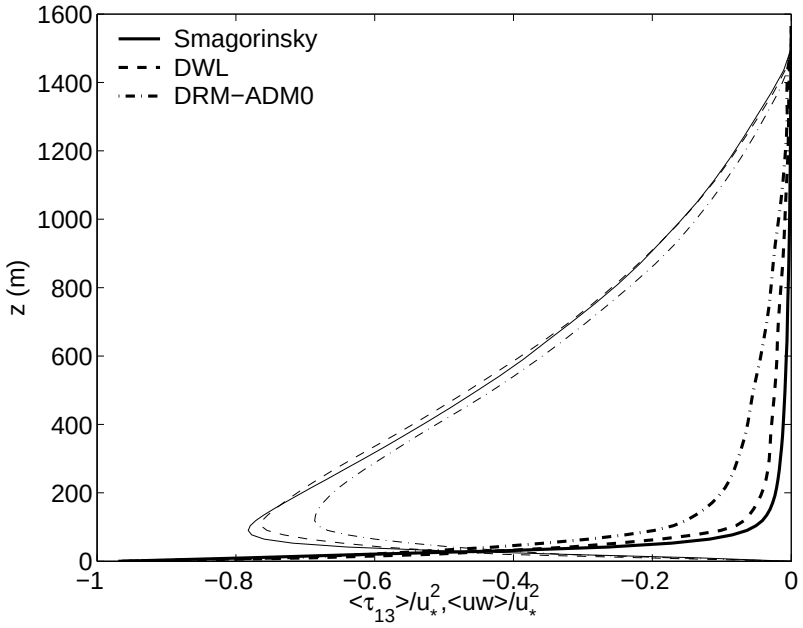

Figure 6.11: Comparison of uw resolved (thin lines) and SFS (bold lines) stress profiles for Smagorinsky, DWL, and DRM-ADM0.

of the total stress (resolved and SFS) differs slightly for the different simulations.

The contributions from each SFS stress component for DRM-ADM0 are seen in the uw stress profiles in Fig. 6.12. The stress profiles are also shown on a log plot to magnify the region near the wall.* The total uw stress (resolved plus SFS) is not linear because there is a component in the vw direction due to Coriolis forcing. The influence of the near-wall stress model decreases with height, becoming zero at $h_c = 4\Delta x = 128$ m. This is equivalent to the minimum well-resolved horizontal eddy size beneath the filter. We obtain good results with a near-wall stress model proportionality factor $C_c = 0.5$, so that the near-wall stress model contributes an amount equal to half the wall stress at the first grid point above the wall. The modified Clark or ADM reconstruction terms (RSFS stress components) decay to zero naturally at the wall in the presence of the other two model components (eddy viscosity and near-wall stress)

*The resolved stress at Δz above the wall is adjusted to account for post-processing interpolation errors. Linear interpolation is normally used to get u to compute the uw resolved stress at the τ_{13} location Δz above the wall (due to the grid staggering). Thus u is significantly underestimated because of the steep gradients in the velocity profile at the wall. Here we linearly interpolate to adjust the total stress values at $z = \Delta z$ and then compute the corresponding resolved stress at this single point only.

(see Section 6.2).

The effects of increasing reconstruction on the uw stresses are shown in Fig. 6.13. The RSFS component of the SFS stress increases with reconstruction level (levels 0, 1 and 5), while the SGS component decreases slightly. Thus, the total SFS contribution increases with increasing reconstruction (primarily due to the contribution of the reconstruction terms), and the resolved contribution decreases accordingly (as seen in Fig. 6.11). This trend was also observed in the small-scale channel flow simulations in Chapter 5 (see Figs. 5.7 and 5.8). The slightly decreasing contribution of the eddy-viscosity term is also apparent in Fig. 6.14 which shows profiles of ν_T for the same simulations as in Fig. 6.9. Near the wall, the eddy viscosity is relatively constant. This is the region where wall effects in the numerical procedure are strongest and the eddy viscosity needs the augmentation provided by the near-wall stress model.

For these high Reynolds number simulations, we have no DNS result to provide exact values of the τ_{13} SFS stresses. However, the turbulent stresses can be compared to finer grid resolution simulations treated as estimates of an exact solution. These estimates can then be used to calculate SFS stress values on the coarser grid by using the definition of the turbulent stress tensor in Eq. 6.3. The finer grid data come from ARPS simulations of twice the resolution in each direction (83,83,83). The horizontal spacing is 16 m and the minimum vertical resolution is 5 m near the wall, and stretched above that to an average of 18.75 m over a domain of the same size as the base case (43,43,43) grid. The discrete quantities $\tilde{u}_i$ can be obtained from the instantaneous high-resolution fields *a posteriori* by using a sharp cutoff filter that matches the coarse grid resolution (43,43,43) simulations. However, we do not apply the cutoff filter for simplicity (and the inability to apply it in the vertical direction); tests on the small-scale channel flow code showed that the cutoff filter applied in the horizontal directions did not change the magnitude or shape of the resulting stress profiles significantly. We have also reconstructed the velocity fields to obtain $\tilde{u}_i^\star$, which estimates the instantaneous velocity fields from a twice finer grid (163,163,163), though the reconstruction is especially limited near the wall. The high-resolution simulations also require a turbulence model; DRM-ADM0 is used instead of a standard eddy-viscosity closure, because it yields good mean velocity quantities (logarithmic near the wall). Thus we calculate $\tilde{\tau}_{ij} = \widetilde{\tilde{u}_i^\star \tilde{u}_j^\star} - \widetilde{\tilde{u}_i^\star}\,\widetilde{\tilde{u}_j^\star}$. The explicit filter is applied at twice the (43,43,43) cell spacing (i.e. 4 times the high-resolution spacing);

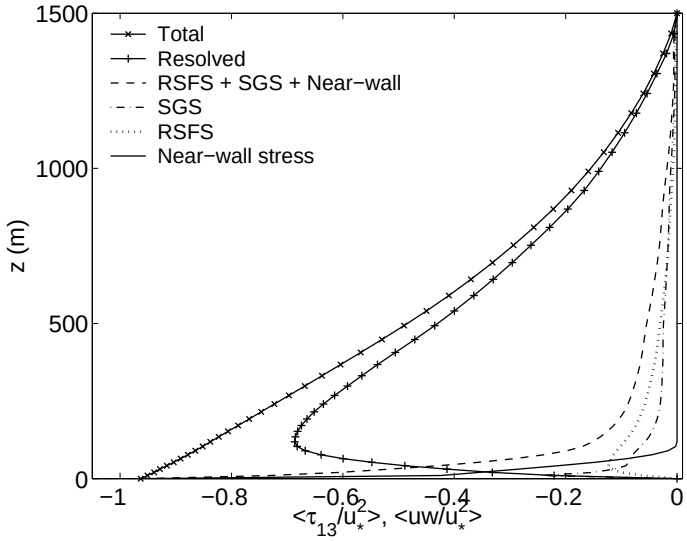

(a)

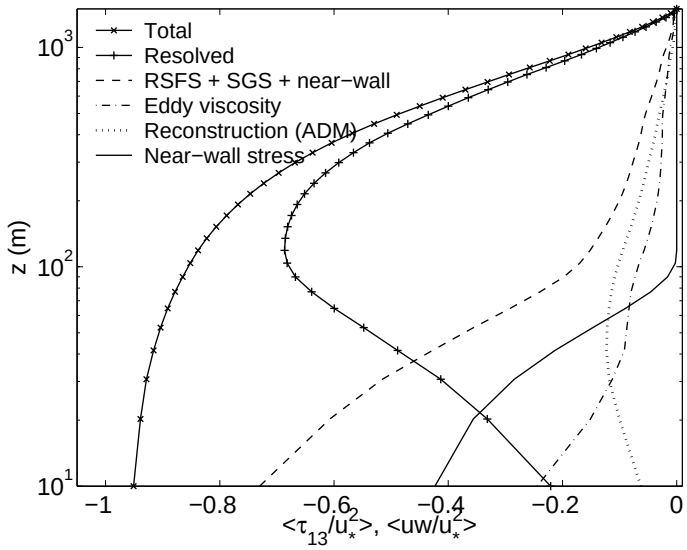

(b)

Figure 6.12: (a) Normalized vertical profiles of the uw total stress for the DRM-ADM0 model (zero-level reconstruction, dynamic Wong-Lilly model, and near-wall canopy stress), with each model component shown separately in addition to the resolved stress. (b) Same as (a) but with a logarithmic vertical axis to magnify the region near the wall.

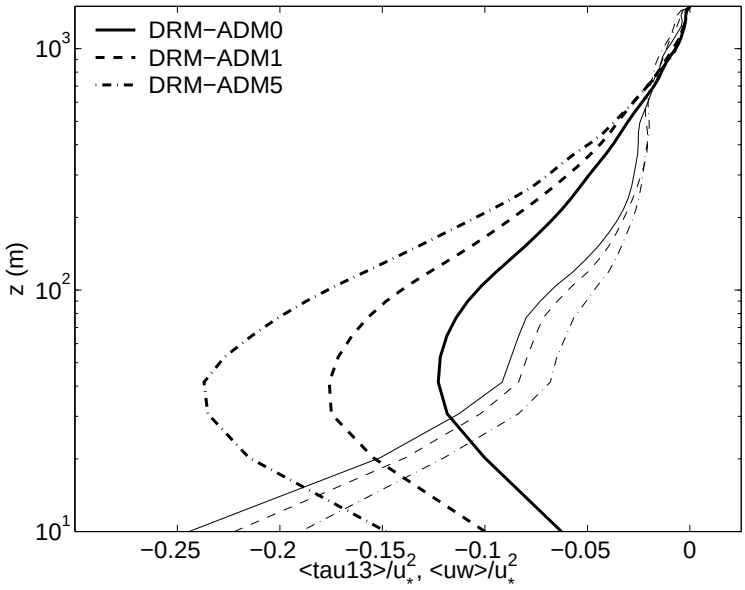

Figure 6.13: Comparison of uw SGS (thin lines) and RSFS (bold lines) stress profiles for the dynamic Wong-Lilly SGS model with increasing RSFS reconstruction levels: level-0 reconstruction; level-1 reconstruction; level-5 reconstruction.

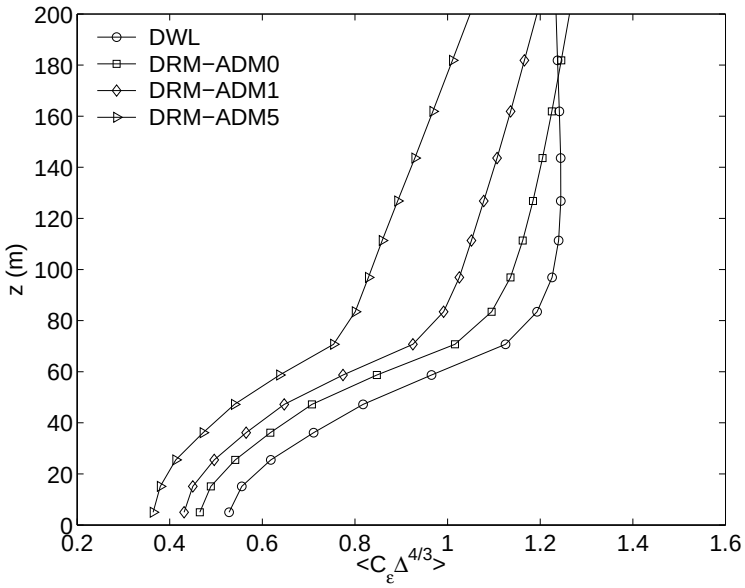

Figure 6.14: Comparison of eddy-viscosity profiles for the dynamic Wong-Lilly SGS model with increasing RSFS reconstruction levels, shown for the bottom 200 m of the domain; no reconstruction; level-0 reconstruction; level-1 reconstruction; level-5 reconstruction.

a tophat filter is constructed using the trapezoidal rule for the fine grid fields to match the filter width used in the coarse simulations. The same filters are applied in the vertical direction. While this procedure provides only an estimate of the true SFS stresses, at the very least the comparison shows how well we match highly-resolved results (that are much more expensive to compute due to the 16-fold increase in computation time when the reduced time step is taken into account).

The turbulent stresses predicted by the coarse resolution simulations using dynamic reconstruction agree well with the SFS stresses calculated from the finer resolution data. Results from DRM-ADM0 up to DRM-ADM10 are shown in Fig. 6.15 (without the near-wall stress contribution). The first point above the wall for the fine grid stress is not shown because it cannot be calculated accurately; the boundary conditions affect the application of multiple filters. In fact, the values of the extracted stress within $4\Delta x$ of the wall are approximate because of the limited resolution available. Stresses predicted by the DWL model (as well as Smagorinsky, which is not shown) are much too small. Increasing reconstruction on the coarse grid improves agreement with the high-resolution results. This suggests that the reconstruction procedure contributes appropriately to the SFS stress, unlike the models without reconstruction, which cannot capture the RSFS motions. Because the reconstruction of the RSFS and the eddy-viscosity representation of the SGS stresses are imperfect, the near-wall stress model is needed to contribute the necessary stress near the wall.

The optimal level of reconstruction is difficult to determine. Clearly, the increase in the RSFS stresses is not linearly proportional to the reconstruction level. The series expansion models should converge to a fixed contribution. Figure 6.15 shows that the increase between levels 0 and 1 is much larger than the difference between levels 5 and 10. In the small-scale simulations of Gullbrand & Chow (2003), the improvement between levels 5 and 10 was also not very large. The higher reconstruction levels appear to converge, but the results may not be exact due to SGS effects. It is also possible that numerical errors interact with the reconstruction procedure to limit our ability to capture all of the RSFS motions. Given the computation costs of reconstruction (see Section 6.5.3 below), it appears that level-2 reconstruction is a good compromise. The increased cost from level 5 to 10 does not seem warranted by the small difference in the results.

While the comparisons of mean velocity and Φ profiles did not clearly distinguish

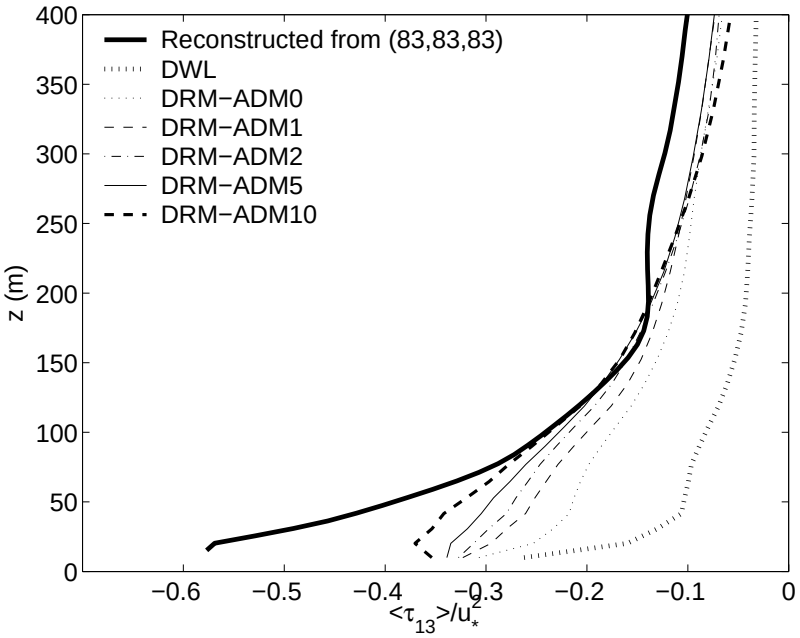

Figure 6.15: Turbulent stresses computed *a posteriori* from velocity fields reconstructed from a fine resolution simulation (reconstructed from (83,83,83)), and the sum of RSFS and SGS stresses computed by coarse grid simulations (43,43,43): DWL, DRM-ADM0, DRM-ADM1, DRM-ADM2, DRM-ADM5, and DRM-ADM10. The near-wall stress contribution is not included. Averaged over 100 000 to 120 000 s.

among the simulations, these comparisons of second-order quantities show that reconstruction is important. The DWL results (without reconstruction) also produce good mean velocity profiles (Fig. 6.7), but cannot achieve correct stress profiles. The stress profiles are especially important in predicting turbulent transport and mixing of scalars, and it is only with the dynamic reconstruction closure models that we are able to obtain accurate representations of these stresses.

Effects of grid resolution and aspect ratio

A robust turbulence model should handle a variety of different grid configurations. Figure 6.16 shows the effect of doubling the grid resolution on the Φ profiles for the Smagorinsky and DRM-ADM0 simulations. The high-resolution grid uses twice as many points in each direction over the same domain size to give horizontal resolution of 16 m and Δz_{min} of 5 m at the wall (see Table 6.1). The near-wall stress model parameters were not changed. The overshoot in the Smagorinsky simulations does not decrease; it simply moves closer to the wall. The DRM-ADM0 show equally good results at both resolutions, giving in this case a somewhat grid-independent result for Φ.

The comparisons in Fig. 6.16 use a constant aspect ratio of $\Delta x/\Delta z = 16/5$ near the bottom wall. Larger aspect ratios are common in LES applications where vertical grid refinement is important for capturing the vertical structure of the atmosphere (e.g. stratification). Aspect ratios of 100 : 1 or larger are often used in mesoscale simulations, sometimes with boundary layer parameterizations. Such large aspect ratios distort the minimum resolvable eddies near the wall and place a large unbalanced dependence on the SFS model which must compensate for this. An aspect ratio of unity would be ideal (Kravchenko *et al.*, 1996), but such computations are prohibitively expensive. To better determine the contribution required of the near-wall stress model, we have examined aspect ratios ranging from 1.0 to 12.8. Larger ratios are not feasible on our small domain, and lead to instabilities.

Figures 6.17a and b show the effects of a sample of four different grid spacings or aspect ratios on results using the Smagorinsky and DRM-ADM0 models. The near-wall stress contributions in the DRM-ADM0 simulations have been adjusted to give Φ profiles that are close to unity (see Table 6.1). The required contribution of the near-wall stress model changes, as expected, because this model was in part developed

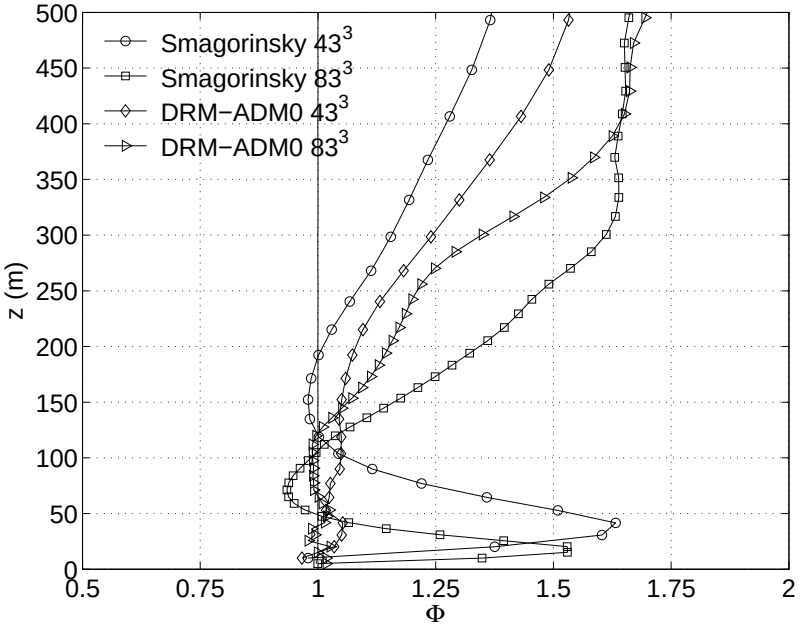

Figure 6.16: Comparison of non-dimensional mean shear Φ profiles for the Smagorinsky model and DRM-ADM0 for 43^3 and 83^3 grid sizes. Averaged from 75 000 to 100 000 s.

to accommodate different grid aspect ratios near the wall. While the ad hoc nature of the near-wall stress model is undesirable if the required contribution depends on the grid, it may be possible to compose a practical guideline for determining the best coefficients.

The two independent near-wall stress layer parameters are the layer height (h_c) and the proportionality factor (C_c). We empirically determined the parameters needed for good results over a range of grid sizes and aspect ratios. "Good results" mean the ability to achieve Φ profiles within 0.2 of unity near the wall. Tests indicate that the aspect ratio is less of a controlling factor for the first parameter, the layer height, than is the horizontal grid spacing. We argued earlier that the under-resolved region at the wall extends between $2\Delta x$ (minimum resolved eddy size) and $4\Delta x$ (minimum well-resolved eddy size) from the wall. Most of the simulations (of various grid sizes) gave good results using a near-wall stress layer height equal to $4\Delta x$; some give better results using 2 or $3\Delta x$. While the near-wall stress layer thickness appears well-determined by this simple rule, there is likely a limiting factor because the enhanced stress-layer

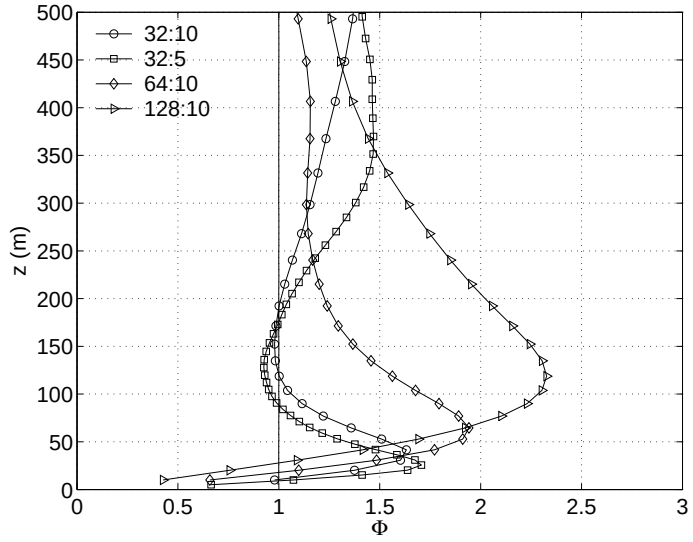

(a)

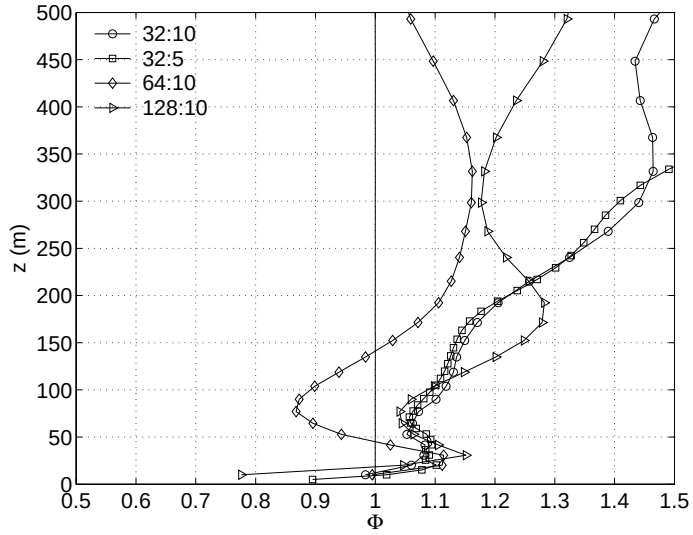

(b)

Figure 6.17: Comparison of non-dimensional mean shear Φ profiles for (a) Smagorinsky and (b) DRM-ADM0 for different grid aspect ratios: $\Delta x : \Delta z_{min} = 32{:}10$ (base case), 32:5, 64:10, 128:10. Note that the axes are scaled differently. Averaged from 75 000 to 100 000 s.

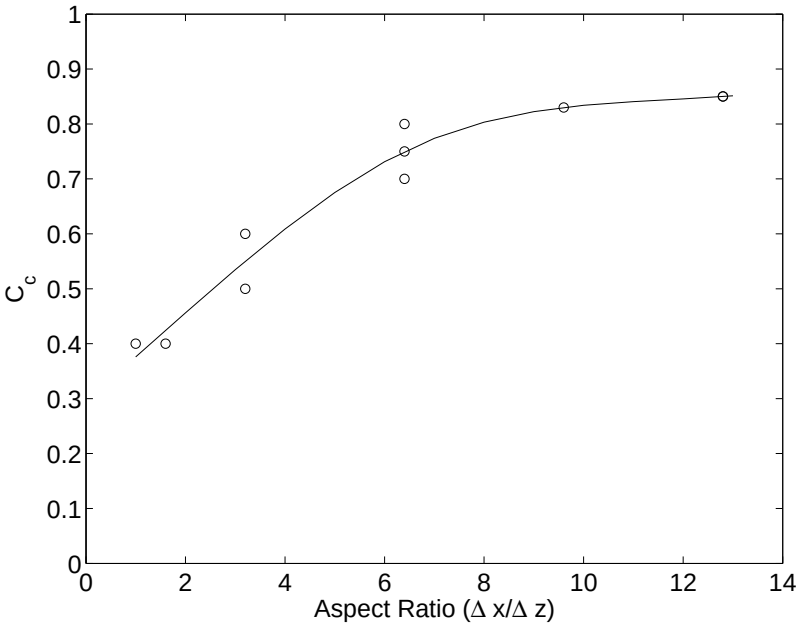

Figure 6.18: Variation of near-wall stress model proportionality constant with grid aspect ratio. A curve indicating the trend of the data is also shown.

should not grow to extend beyond the boundary layer depth.

Figure 6.18 shows the variation of C_c with the aspect ratio $\Delta x/\Delta z$. The Δz dependence of C_c is not strong, but a slightly better collapse of the data is obtained using the aspect ratio as opposed to Δx. The value of C_c cannot exceed unity, where the near-wall stress model would provide a stress at the first point above the wall exactly equal to the local wall stress. The required contribution of the near-wall stress model increases with aspect ratio (and also with Δx), confirming our hypothesis that an enhanced stress layer is necessary to compensate for the under-resolved region near the wall. The need for the near-wall stress layer does not disappear when the aspect ratio is near unity at the wall, but its influence is reduced. Numerous tests indicate that small deviations from the values in Fig. 6.18 also give acceptable results. Therefore, Fig. 6.18 provides reasonable guidelines.

Velocity contours and auto-correlation

We briefly examine the difference in flow structures generated by the different turbulence models. Figure 6.19 shows contours of the streamwise velocity correlation

function for the reference case using Smagorinsky. The auto-correlation is calculated for each horizontal plane by

$$\rho(d1, d2) = \frac{< ab > - < a >< b >}{((< a^2 > - < a >^2)(< b^2 > - < b >^2))^{1/2}} \tag{6.38}$$

where a is the streamwise velocity and b is the velocity field shifted by $d1$ and $d2$ in the x and y directions, respectively. The result is averaged over 21 snapshots separated by 2500 s intervals. Contours are shown at levels $k = 1, 10, 30$; corresponding sample instantaneous contours of the streamwise velocity are also shown. Figure 6.20 shows the corresponding results for DRM-ADM5.

As observed by Kosović (1997), the Smagorinsky model shows elongated structures in the velocity near the surface (Fig. 6.19b), whereas the DRM-ADM5 contours (Fig. 6.20b) do not. The resulting region of high correlation for the Smagorinsky (Fig. 6.19a) is significantly larger than for the DRM-ADM5 results (Fig. 6.20a). Farther from the wall (k = 10 and 30), the differences in the correlations (and in the velocity contours) are not as large. Kosović (1997) also observed this pattern (though the values shown in his Figs. 13 and 14 are much smaller away from the wall). Ideally, the autocorrelation should be zero at the edges of the domain if the length scales of interest are fully resolved. While the results in Figs. 6.19 and 6.20 show that this is not always the case for our small domain, the correlations do decay sufficiently for our purposes.

Normalized energy spectra

Finally, we examine the distribution of energy over different wavenumbers. Figure 6.21 shows one-dimensional energy spectra of the streamwise velocity $\widetilde{\overline{u}}$ at different heights above the bottom boundary. Spectra are shown for (83,83,83) simulations spanning a domain twice as large in each direction to provide a greater range of scales; grid spacing is the same as the base case (43,43,43). We use the scaling procedure of Perry *et al.* (1986) and Porté-Agel *et al.* (2000) to collapse the data. Comparing to Fig. 14 in Porté-Agel *et al.* (2000), it is clear that our spectra drop off much more quickly with increasing wavenumber, indicating that most of the energy is in the larger scales. This fall off is not seen in Porté-Agel *et al.* (2000) because they used spectral methods with dealiasing. We do, however, observe regions with k^{-1} and

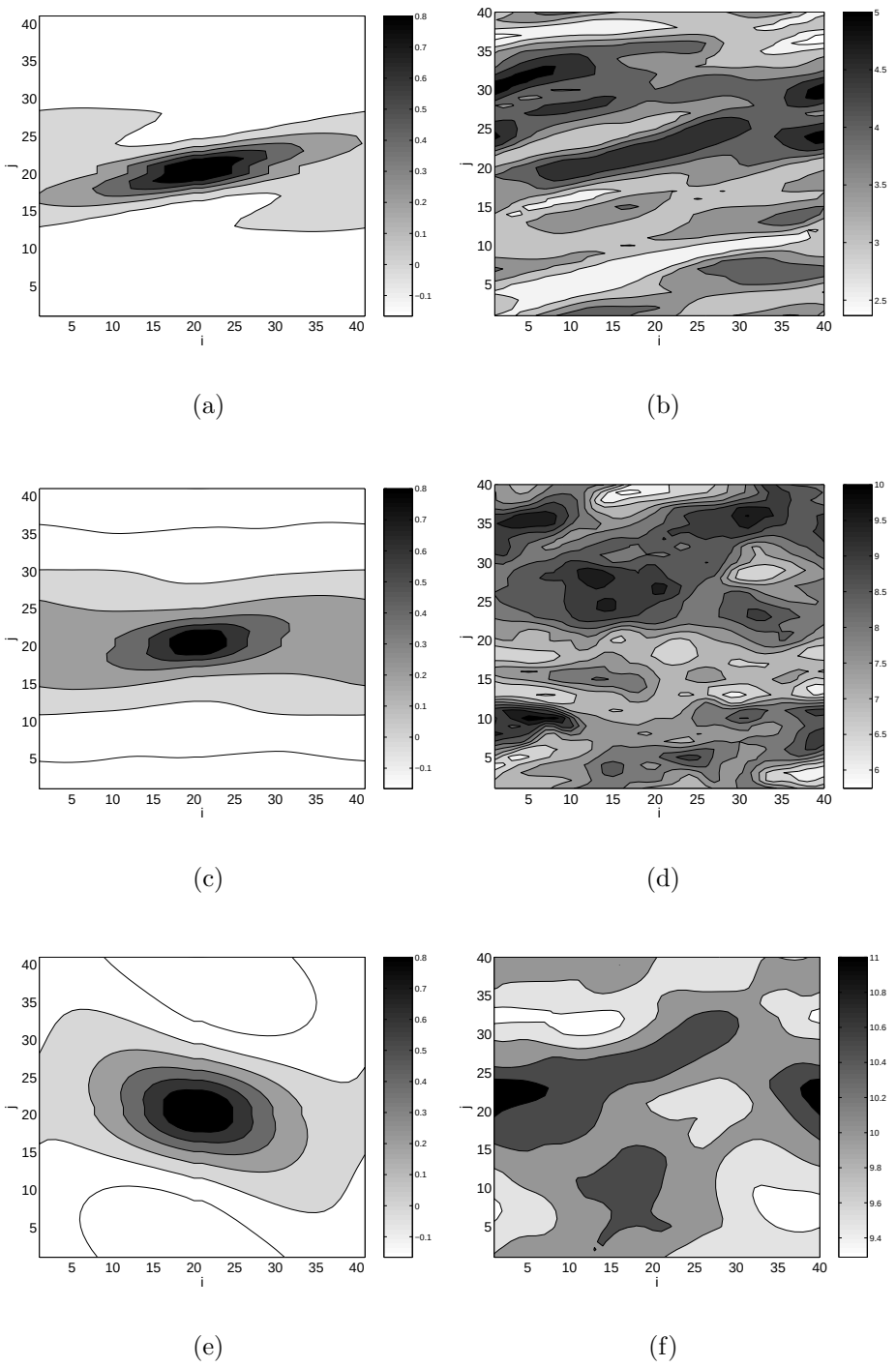

Figure 6.19: Time averaged contours of the streamwise velocity correlation (left) and instantaneous contours of the streamwise velocity (right), for Smagorinsky. (a,b) k = 1, (c,d) k = 10, (e,f) k = 30.

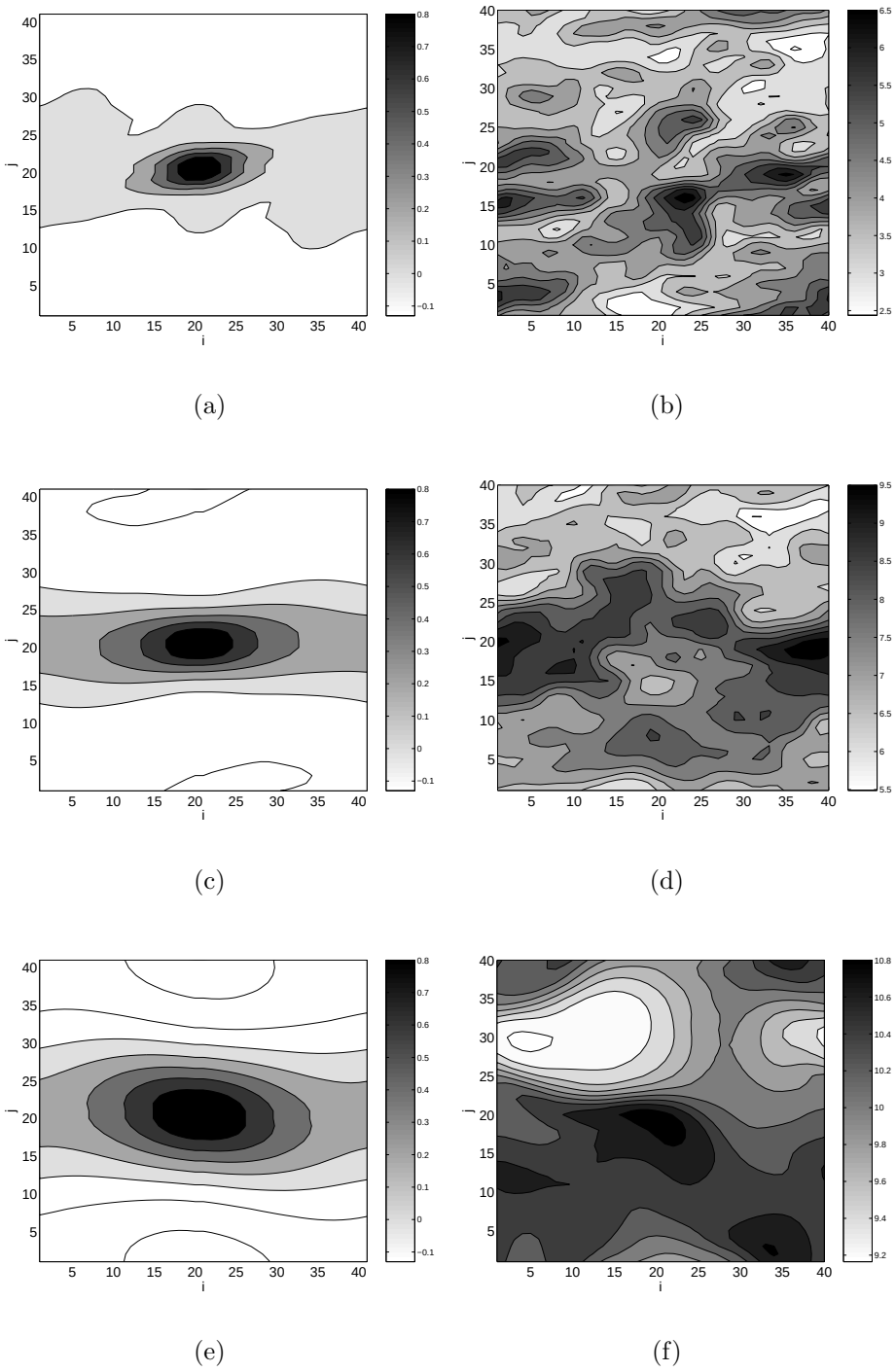

Figure 6.20: Time averaged contours of the streamwise velocity correlation (left) and instantaneous contours of the streamwise velocity (right), for DRM-ADM5. (a,b) k = 1, (c,d) k = 10, (e,f) k = 30.

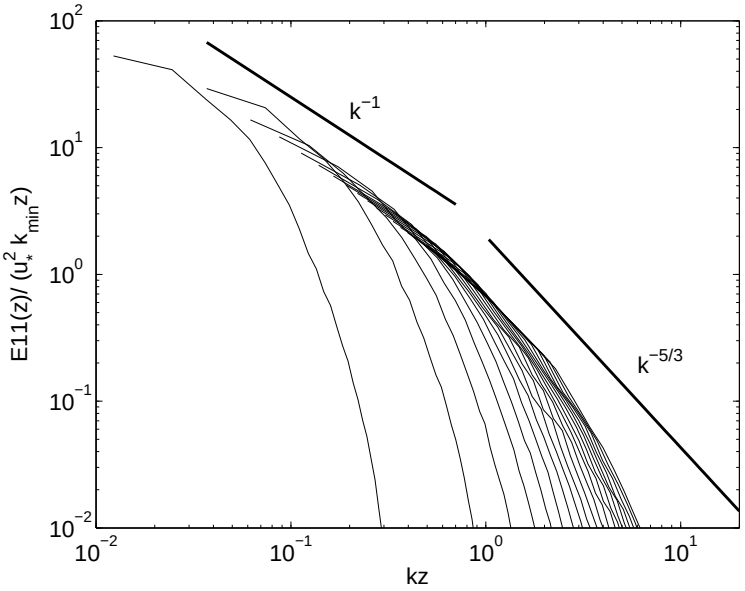

Figure 6.21: Streamwise normalized one-dimensional energy spectrum for DRM-ADM0 on a larger (83,83,83) domain. Each curve is a different height above the wall, starting at the left at the first grid point above the wall, and going up to 20 levels above the wall (from $z = 5$ to 231 m). Time averaged from 100 000 to 120 000 s.

$k^{-5/3}$ slopes (albeit over short intervals). The change of slope occurs, as expected, around $kz = 1$.

The effect of reconstruction on the energy spectra is not clear. There is little change in the spectra using DWL alone compared to DRM-ADM0 (not shown). It is interesting to compare the spectra obtained with the static Smagorinsky model with those from DRM-ADM0. Figure 6.22 shows that the Smagorinsky model is much more dissipative at high frequencies than the DRM-ADM0 results. Further from the wall (level 15) the shapes of the spectra become more similar; in this particular instance the Smagorinsky run has more energy. Each set of spectra are normalized according to the appropriate u_* for the simulation.

We also examined the effect of computational mixing. Figure 6.23 shows spectra for DRM-ADM0 with and without computational mixing for the base (43,43,43) grid size. As expected, the fourth-order computational mixing reduces the energy in the higher wavenumbers. This is more apparent near the wall, though the effect is small because the mixing coefficient is small (5×10^{-4}). Note that the simulations (even

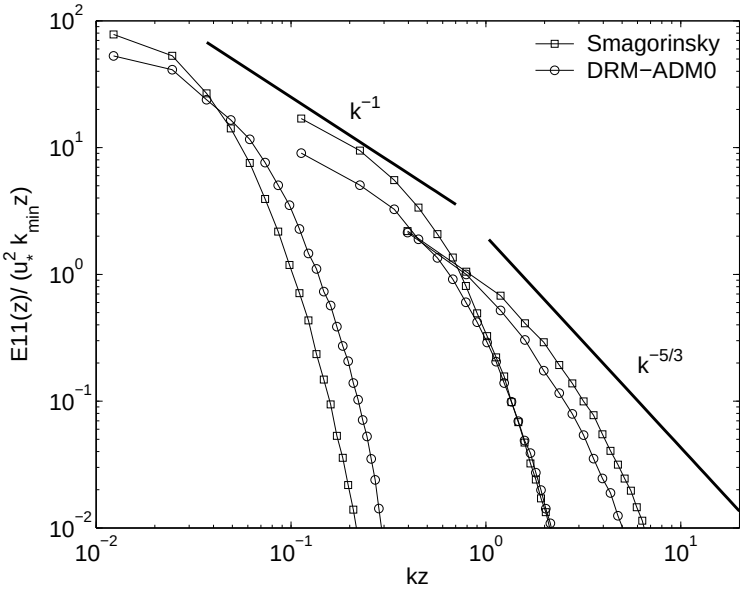

Figure 6.22: Streamwise normalized one-dimensional energy spectrum for Smagorinsky and DRM-ADM0 cases on a larger (83,83,83) domain. The first pair of curves on the left is at grid level 1 ($z = 5$ m), the second pair at level 5 ($z = 45.9$ m), and the third pair at level 15 ($z = 161.5$ m) above the wall. All spectra were time averaged from 100 000 to 120 000 s.

without computational mixing) do not have a very large $k^{-5/3}$ region because of the smaller domain size (43,43,43) shown here (compared to Fig. 6.22). Takemi & Rotunno (2003) explored the effects of computational mixing by adjusting the coefficients of the SGS models to compensate for removing any explicit computational mixing. Such an approach eliminates the need for another computational parameter, but for the present simulations we conclude that the effect of the computational mixing is small. We have included it as it is a standard component of the ARPS modeling system.

Computational cost

While the reconstruction models as well as the dynamic eddy-viscosity model are straightforward to implement, the resulting increase in computational cost is not negligible. We performed simple comparisons to determine the computational cost of the new methods, though no effort was made to optimize the changes in the turbulence modeling sections of the ARPS code. The base case simulations were performed using

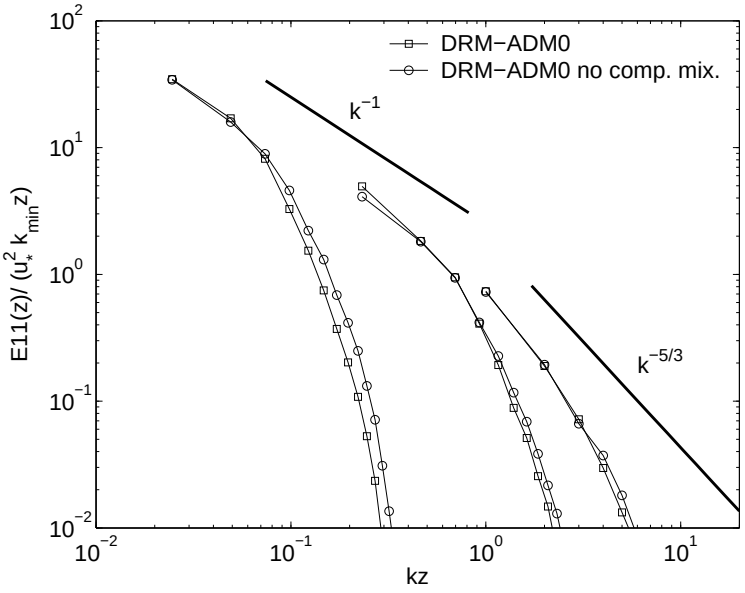

Figure 6.23: Streamwise normalized one-dimensional energy spectrum for DRM-ADM0 (43,43,43) with and without computational mixing. The first pair of curves from the left is at grid level 1 ($z = 5$ m), the second pair at level 5 ($z = 47.2$ m), and the third pair at level 15 ($z = 203.7$ m) above the wall. Time averaged from 100 000 to 120 000 s.

8 processors in distributed memory mode (via MPI) on the IBM SP machine "bluesky" at NCAR. The computation time tests were performed for 20 000 s.

Table 6.2 shows the increased computational cost of various turbulence closures compared to the standard Smagorinsky model. From tests of the DWL model with and without the near-wall stress model, we estimate that the near-wall stress model adds approximately 5% to the computation time. The reconstruction procedure also adds significantly to the computation time. The increased cost of the turbulence model alone is also shown. The cost for the DRM-MC results is lower than that for all the DRM-ADM models, but note that these did not include calculations of H_{ij} (see Section 6.5.3). Indeed, it is the numerous filter operations that lead to increased computational cost.

While the increase in cost is considerable, it must be compared with other means of obtaining equally accurate results. If, for example, the resolution were doubled in each direction, the increase in computational cost would be approximately 16 times, assuming the timestep were reduced by a factor of two. Even with this increase in

Model	Turbulence model cost factor	Total cost factor
Smag	1.00	1.00
DWL (no near-wall)	2.33	1.17
DWL	2.67	1.22
DRM-MC	3.87	1.34
DRM-ADM0	4.59	1.52
DRM-ADM1	4.75	1.51
DRM-ADM2	5.10	1.57
DRM-ADM5	5.92	1.67
DRM-ADM10	7.29	1.85

Table 6.2: Computational cost of different turbulence models compared to Smagorinsky.

resolution, Fig. 6.16 showed that the Smagorinsky model continues to overpredict the values of Φ near the wall. Given this alternative, the increases in computational time of the DRM-ADM approach seem quite reasonable for the significant improvement in the results obtained. A compromise solution might be to use DRM-ADM0 up to DRM-ADM2, with an increase in total computational cost of less than 50% over standard closure models. Finally, the increased cost of 50% seems reasonable when compared to the factor of two increase in cost over static Smagorinsky observed by Esau (2004) using the DMM, and the 50% increase for using DMM over DSM observed by Cui (1999), both in incompressible codes; the increased cost of the turbulence model portion was not reported. Further optimization (in the filtering subroutines especially) can make the code more efficient.

6.6 Conclusions

The near-wall region in atmospheric boundary layer flow simulations is plagued by poor resolution and empirically-based wall models for the bottom stress, in addition to SGS and RSFS turbulence modeling errors. This chapter presented an approach to turbulence modeling over rough boundaries which incorporates the ideas of explicit filtering, velocity reconstruction, and near-wall stress modeling. As a test case, we performed simulations of the rotation-influenced neutral boundary layer flow over flat terrain, similar to the case of Andren *et al.* (1994).

Traditional turbulence closure models fail to produce the expected logarithmic

region near the wall. We therefore began with the context provided by Carati *et al.* (2001) which led to insights about useful turbulence model decompositions. With explicit filtering, the total SFS stresses are separated into RSFS and SGS components; the RSFS portion can be reconstructed, while the SGS portion must be modeled. Even traditional closure models without explicit filtering require reconstruction when finite-difference or finite-volume schemes are used. In these cases, lack of an explicitly defined filter makes it difficult to determine a method for reconstruction. Explicit filtering is also important for reducing numerical errors from finite-difference schemes. Near the wall, the SGS contribution is enhanced by a near-wall stress model to account for the effects of poor resolution, high grid-aspect ratios, and filter-induced stresses at solid boundaries (Nakayama & Sakio, 2002; Dubrulle *et al.*, 2002). This framework aids understanding of the required contributions to subfilter-scale stresses, and the simulation results show excellent agreement with similarity theory in the logarithmic region.

Two specific alternatives were presented for velocity reconstruction: the Taylor series expansion method of Katopodes *et al.* (2000*a*) and Chow & Street (2002), and the approximate deconvolution method of Stolz & Adams (1999). The methods are equivalent within the order of accuracy of the expansions. Truncation error from Taylor series approach is kept to the desired order of the filter width by explicitly neglecting higher-order terms in the reconstruction of τ_{ij}. The ADM procedure includes higher-order quantities in τ_{ij}, so the truncation error is less well defined. However, ADM provides a simple iterative method for calculation of higher-order series expansions for reconstruction, so it is a convenient alternative to calculating the derivatives for the Taylor series. Both methods reduce to the scale-similarity model of Bardina *et al.* (1983) at lowest order and both provide backscatter of energy from small to large scales. Both models also satisfy the full τ_{ij} evolution equations to a pre-defined order of accuracy (though this is clearer when higher-order terms are neglected as done when using the Taylor series approach). While the Taylor series or ADM approaches provide good estimates for the RSFS component of the SFS stresses, the SGS component must be modeled. We implemented the dynamic eddy-viscosity procedure of Wong & Lilly (1994) which requires only the test filter width as a free parameter. The dynamic Wong-Lilly model has been used to provide necessary dissipation, without incurring the expected drawbacks of an eddy-viscosity model, because it is used

in conjunction with a scale-similarity model. The near-wall stress is enhanced using the canopy stress model of Brown *et al.* (2001).

The combinations of the Taylor series or ADM reconstruction, the DWL, and the near-wall stress model significantly improved first- and second-order statistics. The modified Clark model arises from the fourth-order accurate Taylor series expansions, and provided comparable results (DRM-MC) to the DRM-ADM0 or DRM-ADM1 results using the ADM approach. Higher-order reconstructions were performed only with the ADM, because of the ease of implementation with that model. Mean velocity profiles and nondimensional shear profiles (Φ) showed excellent agreement with similarity theory in the logarithmic region. The influence of increased reconstruction was not clear from the first-order quantities even when averaged over a time long period.

Second-order statistics, particularly the uw stress decomposition, revealed that increasing reconstruction increases the RSFS contribution as well as the total SFS stress, while correspondingly reducing the resolved uw stress. This increase in the SFS stress clearly distinguishes the DRM-ADM and DRM-MC models from the DWL and Smagorinsky models without reconstruction. Using finer resolution data to reconstruct a high-resolution field for comparison, we showed that the increased SFS stresses (from simulations at the base case low resolution) approach the required SFS stress predicted by the finer resolution data. The DWL and Smagorinsky results strongly underpredict stresses. These observations are in agreement with those of Gullbrand & Chow (2003) who showed that the stresses from small-scale channel flows using the DRM approached the predicted stresses from DNS data. Accurate prediction of stresses is especially important for atmospheric flows, where turbulent transport and mixing of scalars such as temperature, moisture, aerosols, and pollutants are of interest.

These results for high Reynolds number atmospheric flow simulations over rough boundaries are very encouraging. Several different grid resolutions and grid aspect ratios have been tested, and reasonable results have been obtained by accounting for the required variation in the near-wall stress model as a function of horizontal grid spacing and grid aspect ratio. We found that the near-wall stress model is insufficient for correcting large-eddy simulations near the lower boundary, and that it must be used in conjunction with a sophisticated explicit filtering and reconstruction

approach. The improvements obtained from the near-wall stress model point to the need for more sophisticated SGS closures that account for the effects of a rough boundary at the lower wall.

In summary, the steps required to achieve improved neutral boundary layer simulations are as follows. First, an explicit filter width must be chosen which is compatible with the discretization scheme used (Chow & Moin, 2003; Ghosal, 1996). We chose the explicit filter to be twice the grid size. The explicit filter is the basis for the reconstruction procedure, which is easiest to implement using the ADM approach. Level-0 reconstruction (DRM-ADM0) significantly improves the mean quantities, and higher-order reconstruction further improves the representation of the SFS stresses especially. The reconstruction approach is used with a dynamic eddy-viscosity procedure which requires a test filter, typically taken to be twice the explicit filter. In our case, the test filter width was four times the grid spacing. The test filter is used to calculate RSFS and SGS contributions at the test level; they are then compared to their values at the explicit filter level to determine the appropriate eddy-viscosity coefficient. Finally, the SGS contribution is not sufficient near the wall, so a separate near-wall stress model is added to enhance the stress. The thickness of this near-wall stress layer is typically chosen to be between 2 Δx and $4\Delta x$. The proportionality factor which determines the contribution of the enhanced near-wall stresses varies between 0.4 and 0.9. Thus, the combined RSFS, SGS and near-wall stress approach requires two parameters for the enhanced near-wall stress, plus *a priori* selection of the explicit and test filter widths.

As LES is applied to problems where more of the energy of the flow is unresolved, the accuracy of the SFS model becomes increasingly important. Although there is increased computational cost, the explicit filtering and RSFS approach is warranted by the resulting improvements in the results. To our knowledge, we have demonstrated for the first time that scale-similarity or reconstruction models used with explicit filtering can dramatically improve results for high Reynolds number, rough, atmospheric boundary layer flows. This approach should also be tested for other flow conditions. Preliminary tests on moderately convective boundary layer (see Appendix F) and moderately stable boundary layer simulations show improved agreement with similarity parameters.

Chapter 7

Simulations of flow over an isolated hill*

The evaluation of turbulence closure models for large-eddy simulation has primarily been performed over flat terrain, where comparisons to theory and observations are simplified. In Chapter 6, we developed improved closure models using explicit filtering and reconstruction for neutral boundary layer flow over flat but rough terrain. Now, we extend the results to flow over full-scale topography. We consider Askervein Hill, an isolated hill in western Scotland, where a field campaign was conducted in 1983 under neutral stratification and steady wind conditions. This widely-studied flow provides a more challenging test case for the new turbulence models because of the sloping terrain and separation in the lee of the hill. Results indicate that reconstruction and dynamic eddy-viscosity models, used together with the near-wall stress model, improve predictions of flow speed-up and turbulent kinetic energy over the hill. High resolution is needed, particularly in the vertical direction. We believe this is the first time that reconstruction (scale-similarity) or dynamic turbulence models have been applied to full-scale simulations of the atmospheric boundary layer over terrain. Simulations with the lowest level of reconstruction are straightforward. Increased levels of reconstruction present difficulties, however, and require modification of the closure model near the ground, pointing to the need for further study on the

*This chapter is an extended version of the paper "Evaluation of turbulence models for large-eddy simulations of flow over Askervein hill" by Fotini Katopodes Chow and Robert L. Street, which is to be published in the proceedings of the 16th Symposium on Boundary Layers and Turbulence, American Meteorological Society, August 2004 (Chow & Street, 2004*a*).

behavior of closure models in this flow region.

7.1 Introduction and background

After successfully demonstrating the performance of explicit filtering and reconstruction turbulence modeling for neutral boundary layer flows, we turn to a more challenging test case that includes the effects of terrain. Several studies have been performed over simple hills to evaluate the performance of different turbulence models; however, most are done at laboratory scales because of the availability of experimental data for comparison (Brown *et al.*, 2001; Allen & Brown, 2002; Besio *et al.*, 2003). Such simulations are convenient because they have clearly defined boundary conditions and are generally well-resolved numerically because of the low Reynolds number conditions.

As our interest is in improving the performance of mesoscale atmospheric flow simulations, we have instead chosen to simulate flow over Askervein Hill, a relatively isolated hill located along the west coast of South Uist island, Scotland (see Fig. 7.1). The Askervein Hill project collected velocity and turbulence data that provide a unique dataset for comparison to numerical simulations (Taylor & Teunissen, 1987). Similar observational datasets are also available from field campaigns performed at Black Mountain (Bradley, 1980), Cinder Cone Butte (Lavery *et al.*, 1982; Strimaitis *et al.*, 1982), Blashaval Hill (Mason & King, 1985), and Kettles Hill (Salmon *et al.*, 1988), among others. We selected Askervein Hill because turbulence measurements are available for comparison and because this flow has been extensively modeled by other researchers (Raithby *et al.*, 1987; Kim & Patel, 2000; Castro *et al.*, 2003). The goal of this chapter is to evaluate the new turbulence closure methods presented in Chapter 6 using ARPS for flow over terrain.

We follow the examples given by Raithby *et al.* (1987) and Castro *et al.* (2003), and compare our simulation results to field measurements TU-03a, TU-03b, MF-03d and TK03 of Taylor & Teunissen (1985), collected between 1200 and 1700 (British summer time = UTC + 1 hour) on October 3, 1983. These observation periods had Richardson numbers between -0.0038 and -0.011 (very slightly unstable), therefore the atmosphere can be considered approximately neutrally stratified. The moderate to strong winds (e.g. 10 m/s wind speed at the reference site (see RS in Fig. 7.2) at 10 m above ground level for TU-03a and 8.9 m/s for TU-03b) were from the southwest

Figure 7.1: Askervein Hill as seen from the reference site (RS, see Fig. 7.2). Courtesy of Peter Taylor.

(210° clockwise from North) during this time period. A long rain shower occurred earlier in the morning, and low clouds were present at approximately 300 m above ground level (agl) (at less than 300 m agl over the hills). This perhaps indicates the presence of a stable layer at about 300 m. The observed mean flow data were averaged in time over 10 minutes and turbulence data were calculated over 30 minutes (Taylor & Teunissen, 1987).

7.2 Model setup

Topographic data for Askervein were provided by Walmsley & Taylor (1996) at approximately 25 m horizontal resolution. Elevation contours are shown in Fig. 7.2. The grid (centered near Askervein Hill, 57° 11' N, -7° 22' W) was rotated 60 degrees clockwise to align the y-axis with the incoming 210°N winds. Elevations were interpolated to 35 m horizontal resolution using 163 $\times$ 163 grid points to cover a 5600 m square domain. In the vertical, 59 points are used; the minimum grid spacing is 5 m at the ground surface and is stretched using a tanh function to yield an averaging spacing of 12.5 m over the 700 m vertical extent of the domain. Simulations were also

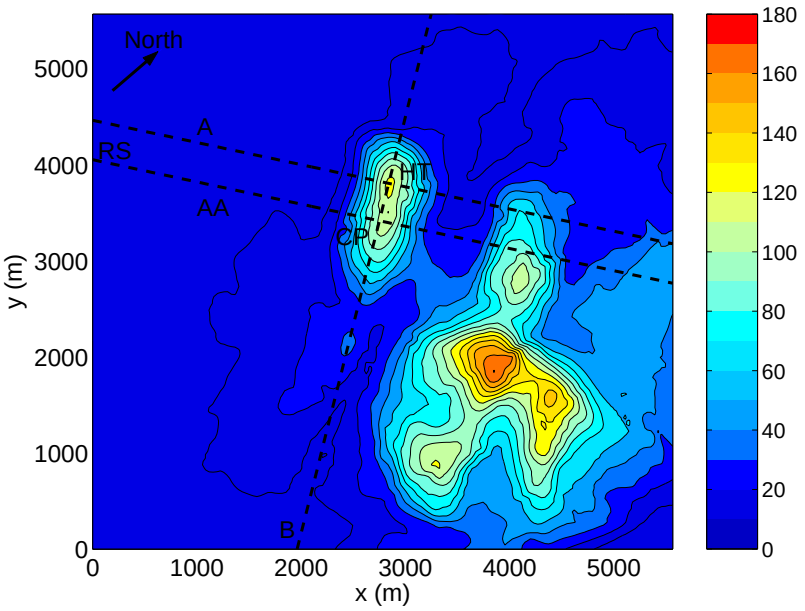

Figure 7.2: Elevation contours (m) of topography for simulations, rotated 60 degrees clockwise from north. Contour interval is 12 m.

performed with a 1000 m domain height, but with very little difference in the results, so they are not shown.

We use a roughness value of $z_0 = 0.03$ m and apply a log-law bottom boundary condition as done by Raithby *et al.* (1987) and Castro *et al.* (2003). The flow is allowed to spin up for 2700 s, after which 900 s of data are collected for averaging at 30 s intervals. For the turbulence statistics, 1800 s of data are collected.

Reference simulations were performed using the standard 1.5-order TKE closure (Deardorff, 1980; Moeng, 1984) in ARPS. These are compared to results from the dynamic Wong-Lilly (DWL) and the dynamic reconstruction (DRM) models (see Chapter 6 for details). As discussed below, reconstruction of levels greater than zero (i.e. more than the Bardina term) leads to terrain-induced instabilities. Modifications are proposed to allow for higher levels of reconstruction.

To provide a realistic turbulent inflow, a separate neutral boundary layer simulation with periodic boundary conditions and flat terrain is performed and data are extracted from a slice in the domain at every time step. This "turbulence database" is based on the simulations performed in Chapter 6 using the level-0 dynamic reconstruction closure model (DRM-ADM0), which provides a good representation of

the logarithmic velocity profile expected in a neutral boundary layer. The grid size for this periodic case is (83,163,83) with 35 m horizontal and 5 m minimum vertical resolution, covering a 2800 × 5600 × 1000 m domain. The 1000 m domain height also accommodated the grids of different vertical extent which were tested for the Askervein grid. The reference elevation for ARPS is set to 10 m above sea level (asl) so that the pressure matches that at the inflow to the Askervein domain. This turbulent dataset is then used to specify the inflow velocity at every time step on the western side of the Askervein domain. The flow throughout the domain is thus fully turbulent (see e.g. Fig. 7.12 later); in contrast, if the flow is driven by constant inflow boundary conditions, it is not able to become fully turbulent over the short length of the domain.

The north and south boundaries are set to be solid free-slip walls. At the east boundary, zero-gradient conditions are applied. The initial conditions are set to a constant logarithmic profile and neutral stratification. Severe oscillations were initially observed when the turbulent inflow data were imposed, because disturbances at the boundary propagated quickly through the pressure field into the initially uniform flow fields. This was corrected by using the pressure detrending option in ARPS, which sets the domain-wide mean perturbation Exner function to zero to control pressure drift (usually due to boundary condition effects). The effects of the detrending on the flow solution are small; the magnitude of the pressure appears only in the relatively small pressure perturbation contribution to the buoyancy term (Klemp & Wilhelmson, 1978; Xue *et al.*, 1995).

7.3 Comparison with observations

7.3.1 Mean winds

Observations along lines A and AA (43°, NE-SW) and along line B (133°, SE-NW) in Fig. 7.2 are compared with the corresponding time-averaged quantities from the three-dimensional simulated velocity fields. The interpolation schemes in the ARPS post-processing plotting software were used to extract the simulation outputs. Figure 7.3 shows the wind profile at the reference site (RS), located approximately 2.8 km southsouthwest of the hill top. In our simulations, RS is at the left edge of the domain

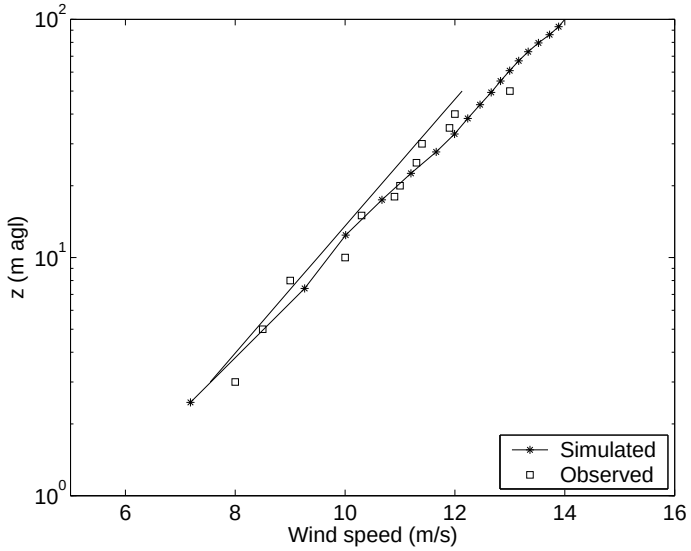

Figure 7.3: Comparisons of observed wind speed profile at reference site (RS) to simulated values from the turbulent inflow database. A logarithmic profile with $u_* = 0.654$, $z_0 = 0.03$ (as suggested by Raithby *et al.*, 1987) is also shown.

where it is intersected by line A (instead of by line AA). The observed winds agree well with the logarithmic profile from the turbulent inflow database, which is the same for each simulation.

Figure 7.4 shows the observed and simulated wind speed-up ratio at 10 m above the ground along line A. Observation data are not available more than 400 m (line A) or 600 m (line AA) beyond the hill top. The fractional wind speed-up ratio provides the most straight-forward comparison of the various model results and is defined as

$$\Delta S = \frac{S(z) - S_{RS}(z)}{S_{RS}(z)} \tag{7.1}$$

where S is the horizontal wind speed and S_{RS} is at the reference site. The speed-up is a useful nondimensional measure often used in wind engineering for siting of wind turbines. All the models underpredict the speed-up at the hill top, with the TKE-1.5 results slightly better than the rest. The underprediction at the hill top is likely caused by the fact that the peak elevation is slightly underestimated on our grid (at 122 m, because of the grid spacing) compared to the actual elevation (126 m). The greatest difference among the models is, however, in the lee of the hill,

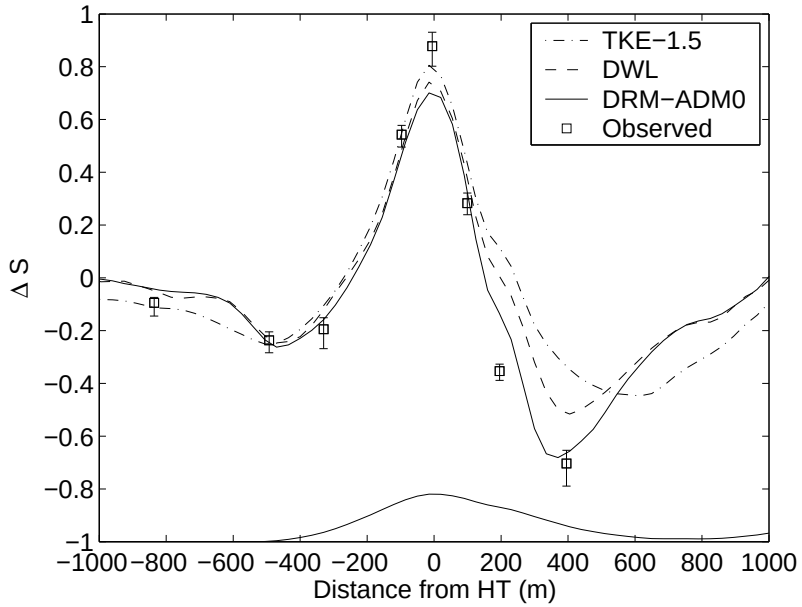

Figure 7.4: Comparisons of observed velocity speed-up along line A to simulated values using TKE-1.5, DWL and DRM-ADM0 closures. The profile of the hill is shown at the bottom of the figure.

where intermittent separation was observed in the field (Raithby *et al.*, 1987). The TKE-1.5 model fails to produce the observed flow deceleration, whereas the DWL and particularly the DRM-ADM0 results are much better. Similar speed-up results are found along line AA (Fig. 7.5).

The effect of decreased vertical resolution can be seen in Fig. 7.6, which compares the results using 10 m and 25 m, for Δz_{min} and Δz_{avg}, respectively, with using 5 m and 12.5 m (our standard case). The vertical extent of the domain is the same in both cases. The finer resolution allows slightly increased speed-up at the top of the hill. Vertical speed-up profiles are particularly improved by increased resolution, as seen later in Fig. 7.11. In the lee of the hill, the TKE-1.5 results change little with increased resolution, but they are improved for the DWL.

Fig. 7.7 compares TKE-1.5 and DWL results using a constant inflow velocity profile (chosen to match data at RS) with small perturbations with the results using turbulent inflow conditions. The speed-up ratio upstream of the hill is strongly underpredicted in the cases with constant inflow. The decrease in the speed-up in the lee of the hill appears to be better predicted using the constant inflow conditions,

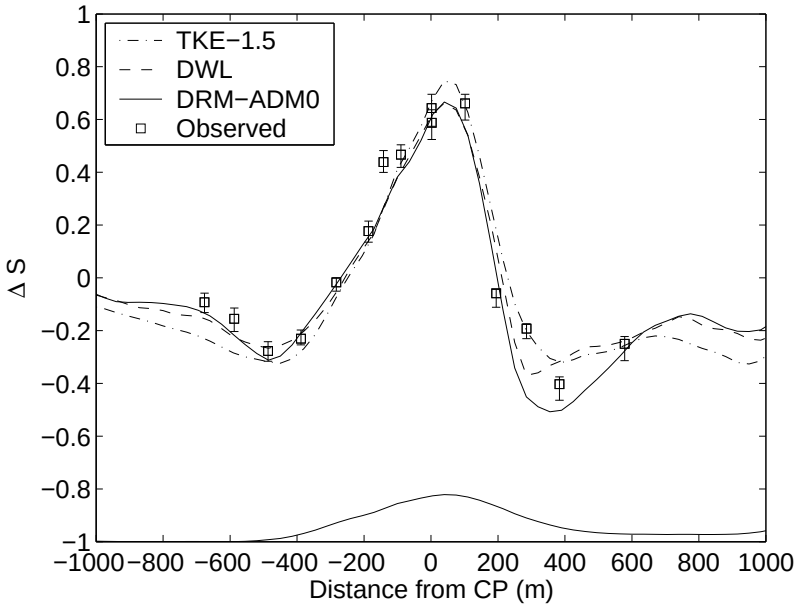

Figure 7.5: Comparisons of observed velocity speed-up along line AA to simulated values using TKE-1.5, DWL and DRM-ADM0 closures. The profile of the hill is shown at the bottom of the figure.

particularly for the TKE-1.5 model. Instantaneous velocity contours, however, reveal a completely steady flow for the TKE-1.5 simulation, with only very small perturbations visible (not shown); the flow does not appear fully developed with either turbulence model. Simulations showed that particularly at lower vertical resolution, using a constant inflow did not give satisfactory results.

The wind direction deviation from 210°, $\Delta\Phi$, is shown in Fig. 7.8. None of the models completely agrees with the observed wind directions, but the DWL and DRM-ADM0 results again show improvement in the lee of the hill.

Fig. 7.9 shows the wind speed-up along line B; here the TKE-1.5 model slightly overpredicts the wind speed-up even at the peak of the hill, whereas values were underpredicted in Fig. 7.4. This may be because of truncation errors in the interpolation procedures used to extract simulation data along lines A and B. Again the general agreement is quite good.

Vertical profiles of the wind speed-up ratio are shown at the hill top (HT) in Figure 7.10. The speed-up ratio at the hill top is underestimated (as seen in Fig. 7.4), probably again due in part to the lower hill height in the simulations. The

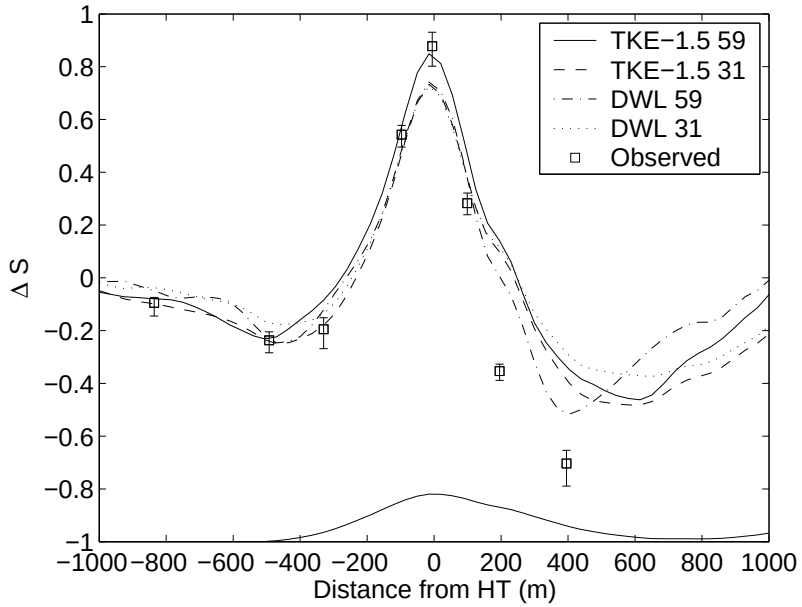

Figure 7.6: Comparisons of observed velocity speed-up along line A to simulated values using TKE-1.5 and DWL closures with coarse (nz = 31) and fine (nz = 59) vertical resolution. The profile of the hill is shown at the bottom of the figure.

general trend of the speed-up profile is well reproduced by all the turbulence models, with the shape slightly better represented by the dynamic models. The results from the coarse resolution grid, shown in Fig. 7.11, are clearly unsatisfactory near the ground.

Figures 7.12 and 7.13 show instantaneous vertical cross-sections from DRM-ADM0 simulations of the flow over Askervein to illustrate the intermittent separation observed. In Fig. 7.12 a "gust" event is visible as the winds sweep down the lee side of the hill. This contrasts with Fig. 7.13, where a separated flow region is observed in the lee of the hill. Intermittent separation is a challenge for numerical simulations which are particularly sensitive to the formulations chosen for the wall model and boundary conditions. The recirculation is responsible for the strong deceleration observed in the wind speed-up curves (Fig. 7.4). Clearly, accurate prediction of the intermittent separation is related to the ability to predict the wind speed-up. The TKE-1.5 results did not exhibit these recirculation patterns (not shown), so the speed-up ratio is over-predicted on the lee side of the hill (see Fig. 7.4).

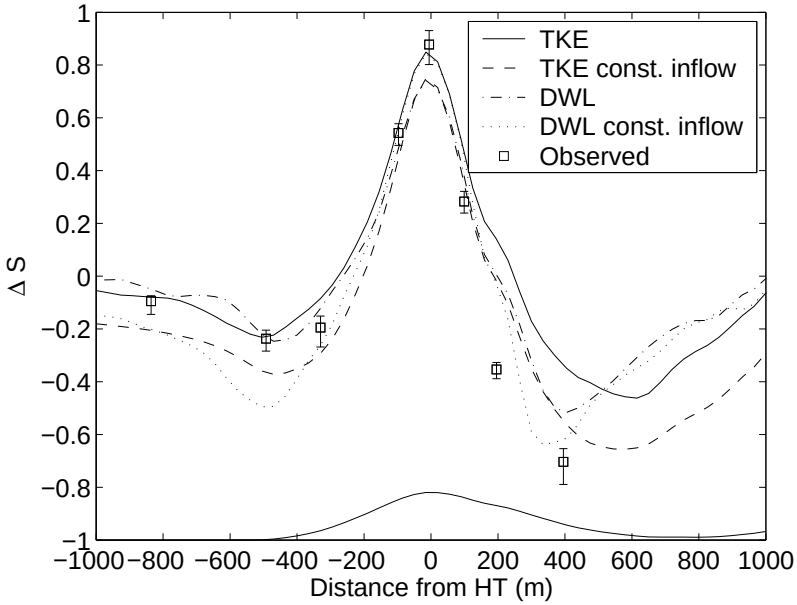

Figure 7.7: Comparisons of observed velocity speed-up along line A to simulated values using TKE-1.5 and DWL closures with turbulent or constant inflow conditions. The profile of the hill is shown at the bottom of the figure.

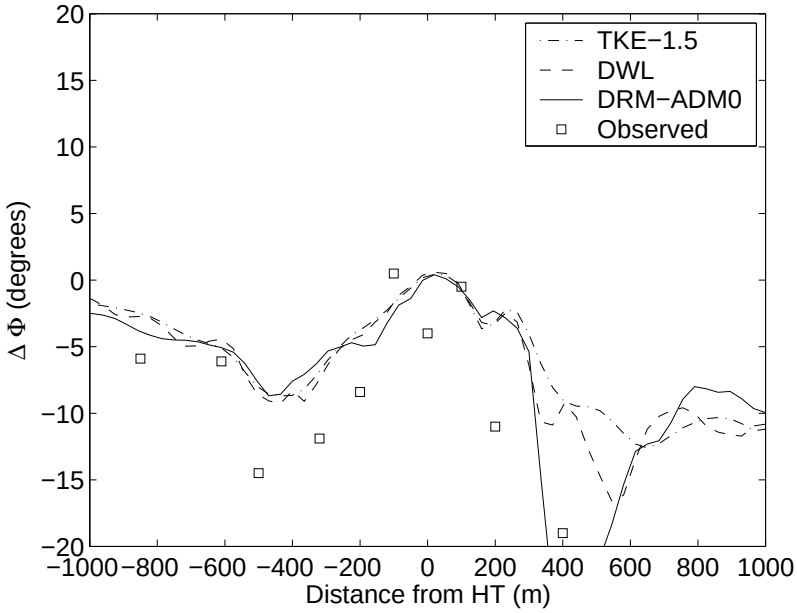

Figure 7.8: Comparisons of observed wind direction deviation from 210° $\Delta\Phi$ along line A to simulated values using TKE-1.5, DWL and DRM-ADM0 closures.

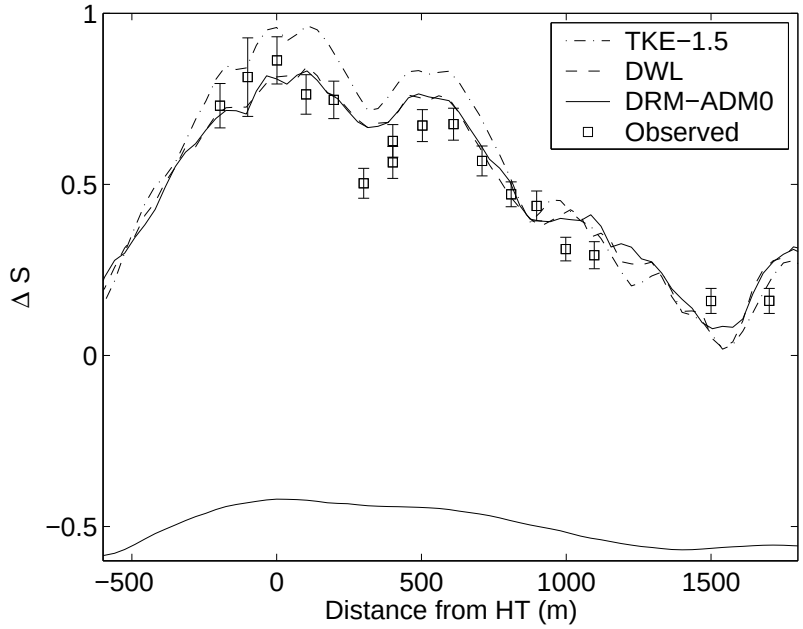

Figure 7.9: Comparisons of observed velocity speed-up along line B to simulated values using TKE-1.5, DWL and DRM-ADM0 closures. The profile of the hill is shown at the bottom of the figure.

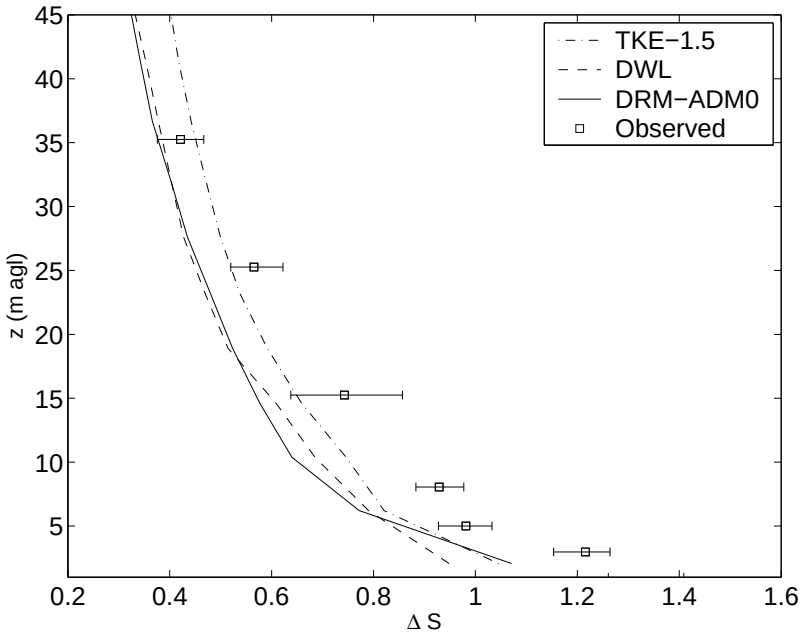

Figure 7.10: Comparisons of observed velocity speed-up profile at hill top to simulated values using TKE-1.5, DWL and DRM-ADM0 closures.

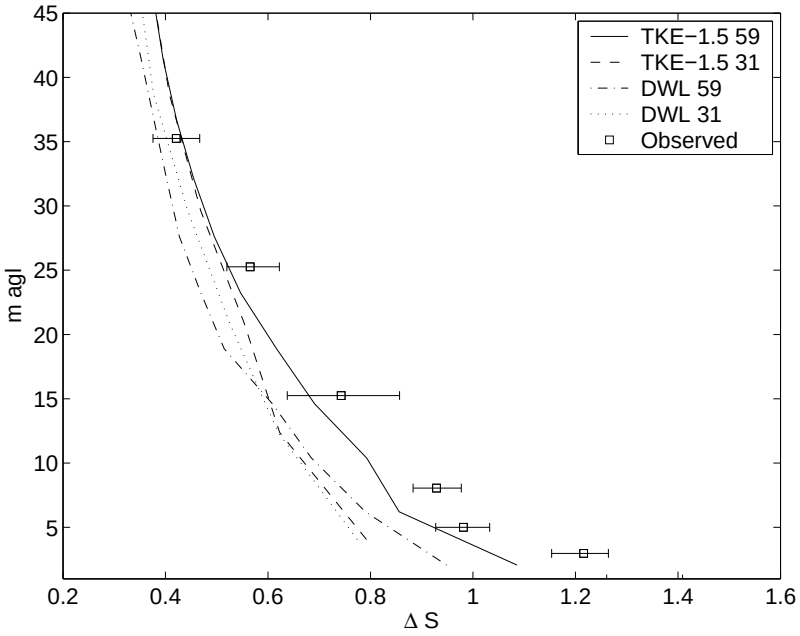

Figure 7.11: Comparisons of observed velocity speed-up profile at hill top to simulated values using TKE-1.5 and DWL closures with coarse (nz = 31) and fine (nz = 59) vertical resolution.

7.3.2 Turbulence

Comparing turbulent quantities from LES and from observations in the field can be complicated because of the different space and time averaging techniques used. The representation in LES is by definition filtered in space, at least over the dimensions of the grid cell. The measurements in the field are obtained at one specific location and averaged over time. The only option is to attempt to relate the two quantities as best as possible. One approach is to compute the total turbulent kinetic energy (TKE) from the LES following the derivation in Appendix D of Zang (1993). The total TKE is composed of resolved, subfilter scale, and Leonard term contributions calculated at a given point and averaged over time. Following Zang (1993), we define the spatially filtered Reynolds stress

$$\overline{e}_{ij} \approx \overline{c}_{ij} + < \tau_{ij} > - < L_{ij} > \tag{7.2}$$

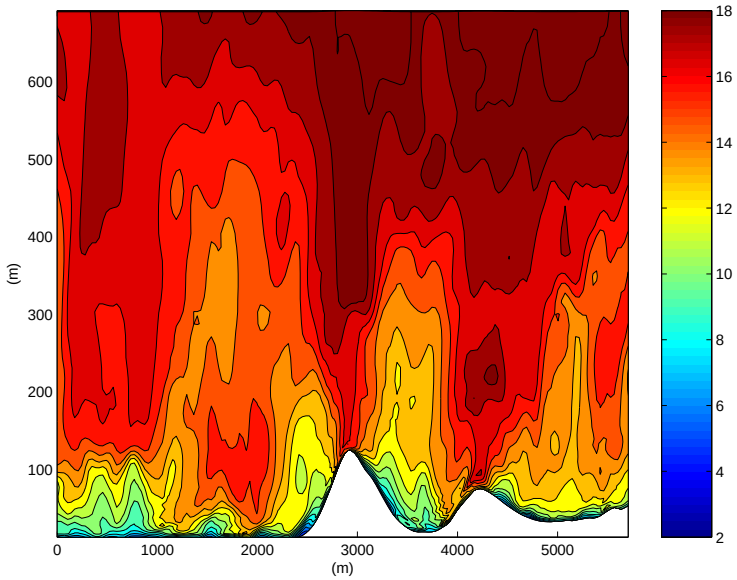

(a)

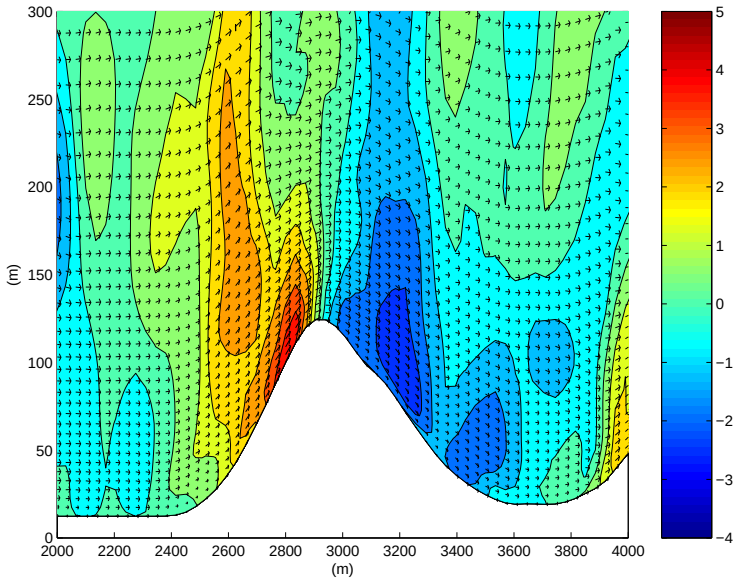

(b)

Figure 7.12: Vertical cross-section along line A of (a) u-velocity and (b) wind vectors and w-velocity (only a subregion is shown) during a "gust" event, using DRM-ADM0.

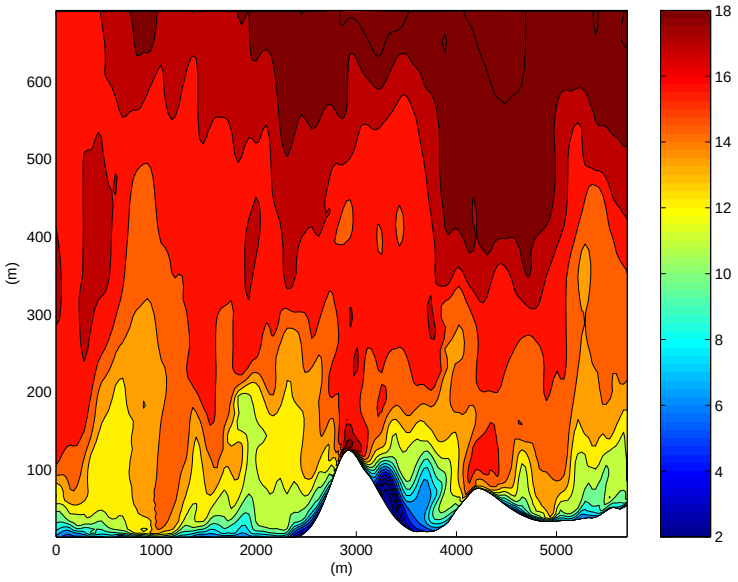

(a)

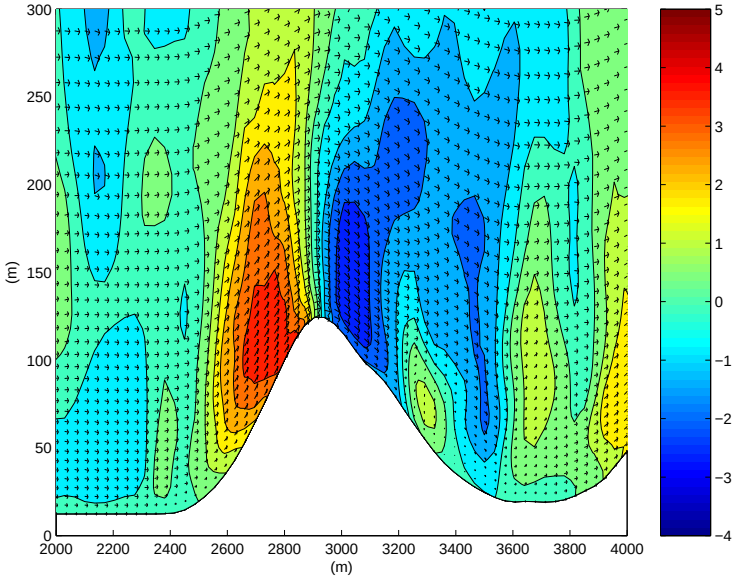

(b)

Figure 7.13: Vertical cross-section along line A of (a) u-velocity and (b) wind vectors and w-velocity (only a subregion is shown) during a "recirculation" event, using DRM-ADM0.

where the brackets <> denote time averaging and

$$c_{ij} =< (\overline{u}_i - < \overline{u}_i >)(\overline{u}_j - < \overline{u}_j >) >=< \overline{u}_i\overline{u}_j > - < \overline{u}_i >< \overline{u}_j > \tag{7.3}$$

is the resolved stress,

$$\tau_{ij} = \overline{u_i u_j} - \overline{u}_i\overline{u}_j \tag{7.4}$$

is the subfilter-scale stress (computed with a turbulence closure scheme), and

$$L_{ij} = \overline{\overline{u}_i\overline{u}_j} - \overline{u}_i\overline{u}_j \tag{7.5}$$

is the Leonard term. Note that c_{ij} must be spatially filtered and L_{ij} must be temporally averaged when using Equation 7.2. If planar averaging were possible (i.e. for a domain with periodic boundary conditions), the Leonard term would disappear, leaving the standard definition of the Reynolds stress (composed of resolved and subgrid terms).

This approach was successful for Zang (1993), but attempts to include L_{ij} here resulted in large oscillations, likely caused by the coarse grid resolution and resulting numerical errors in the calculation. Therefore, we define

$$\overline{e}_{ij} \approx \overline{c}_{ij} + < \tau_{ij} > \tag{7.6}$$

to calculate the normal stresses and shear stresses, which consists of the more familiar resolved plus subfilter contributions. (The c_{ij} term is filtered here but this does not change the results much). Time averages are performed over 30 minutes using LES data at 30 second intervals.

Figure 7.14 compares computed and observed TKE along line A. The prediction from the DRM-ADM0 is clearly superior to the others. Note, however, that the calculation of normal stresses is often difficult because the subgrid model contribution can be difficult to isolate. For example, when using the Smagorinsky model, the normal stresses are quite small because they are absorbed into the pressure term and cannot be recovered (in an incompressible code, the subgrid TKE computed by the Smagorinsky model is identically zero). Figures 7.15 and 7.16 compare simulated uw and vw stresses with observations. The stresses have been rotated to be aligned

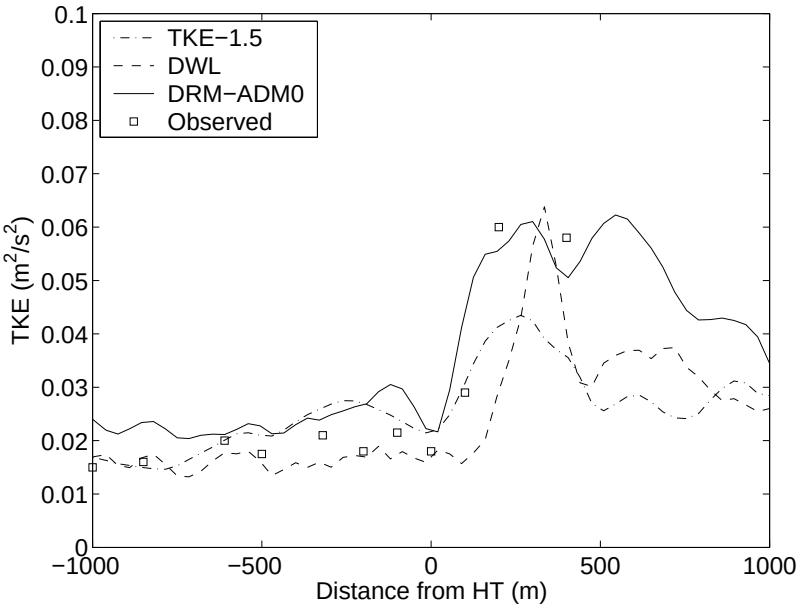

Figure 7.14: Comparisons of observed TKE along line A to simulated values using TKE-1.5, DWL and DRM-ADM0 closures.

with line A. The vw stress comparisons are quite good, but significant differences are observed in the uw plots. The contribution of the subfilter-scale stresses is larger when explicit filtering and reconstruction is used; this is consistent with the results from flow over flat terrain in Chapter 6 (see Fig. 6.13), where the SFS stresses increased with increasing reconstruction, and the resolved stresses decreased accordingly.

7.4 Performance of the dynamic reconstruction models

The above results for wind speed-up and turbulent quantities indicate quite good overall agreement between the observations and the simulations using DWL and especially DRM-ADM0. Attempts to directly increase the level of reconstruction were, however, unsuccessful. Using DRM-ADM1 resulted in instabilities that could only be controlled by increasing the fourth-order computational mixing. This had a strong impact on the velocity profiles near the wall, where gradients are largest; velocities slowed down significantly and wind speed-up predictions deteriorated.

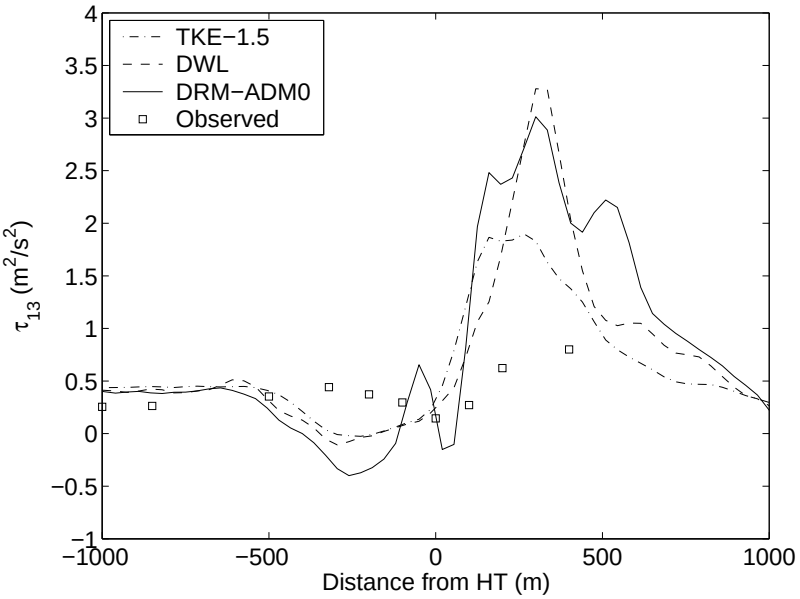

Figure 7.15: Comparisons of observed *uw* stress (rotated coordinates) along line A to simulated values using TKE-1.5, DWL and DRM-ADM0 closures.

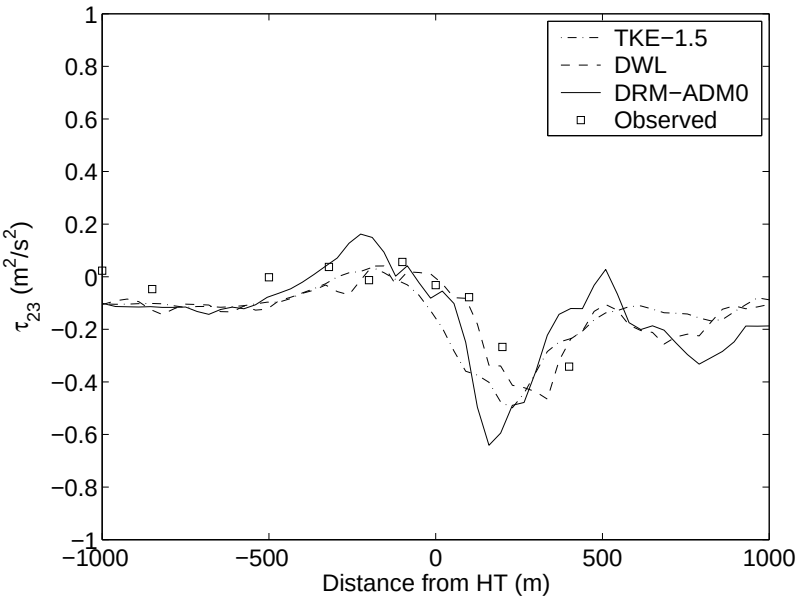

Figure 7.16: Comparisons of observed *vw* stress (rotated coordinates) along line A to simulated values using TKE-1.5, DWL and DRM-ADM0 closures.

The performance of the dynamic reconstruction model is very sensitive to the calculation of the dynamic coefficient in the Wong-Lilly model. An indication that the dynamic model struggles with flow over terrain can be seen in Fig. 7.17, showing contours of the dynamic eddy viscosity. Very near the wall (k = 1), the dynamic coefficient often becomes locally negative, so there is a considerable amount of clipping applied to reset large negative eddy viscosity to -1.5×10^{-5} for stability reasons (see Chapter 6). Further from the wall (k = 10), the percentage of clipping required is much smaller. Tests of the DWL alone over very complex terrain (see Chapter 8 on simulations in the Riviera valley) showed very large amounts of clipping and ultimately resulted in instabilities.

Iizuka & Kondo (2003) also had difficulty with the dynamic Smagorinsky model in simulations over a 2D laboratory-scale hill, where the model failed to reproduce the expected recirculation patterns. The authors cited the dynamic model underestimation of the eddy viscosity very near the wall as a key reason for the poor performance of the model over terrain. Given that our full-scale hill terrain is neither smooth, nor two-dimensional, it is not surprising that we experience further difficulties with the dynamic model.

Figure 7.18 shows sample vertical profiles of the instantaneous and time-averaged eddy viscosity at three locations along line A. The first 5-6 points above the wall exhibit the same pattern observed by Iizuka & Kondo (2003); the eddy viscosity is underpredicted because of difficulties in the dynamic procedure previously cited in the neutral boundary layer simulations in Chapter 6.

Iizuka & Kondo (2003) proposed a hybrid dynamic-static Smagorinsky model, which uses eddy viscosities from the standard static model at points near the wall where the eddy viscosity is underpredicted. This hybrid approach augmented the eddy viscosity near the wall and allowed the expected recirculation patterns to form in the lee of their hill. Figure 7.19 shows the wind speed-up ratio along line A for a similar hybrid approach, where we use static Smagorinsky at the lowest six levels (chosen based on the curves in Figs. 7.18), and the dynamic Wong-Lilly eddy viscosity elsewhere (DWL-SMAG or DRM-SMAG). The predicted speed-up is not as good as previous results from the DRM-ADM0 simulations, but the prediction of flow deceleration in the lee of the hill improves with increasing reconstruction (from DWL-SMAG to DRM-SMAG-ADM1).

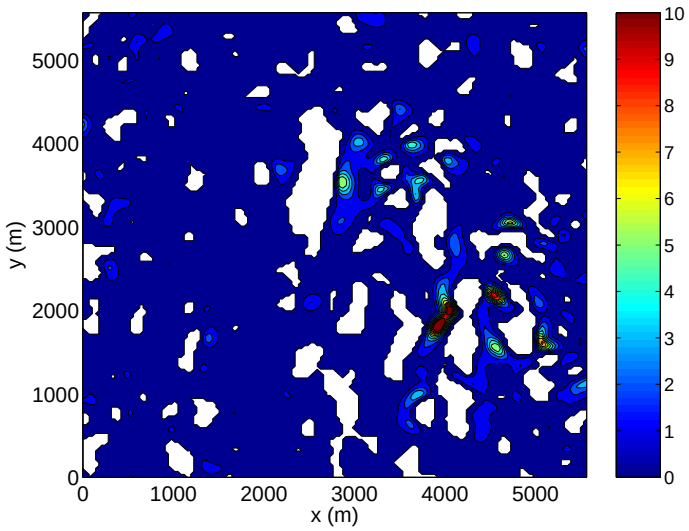

(a)

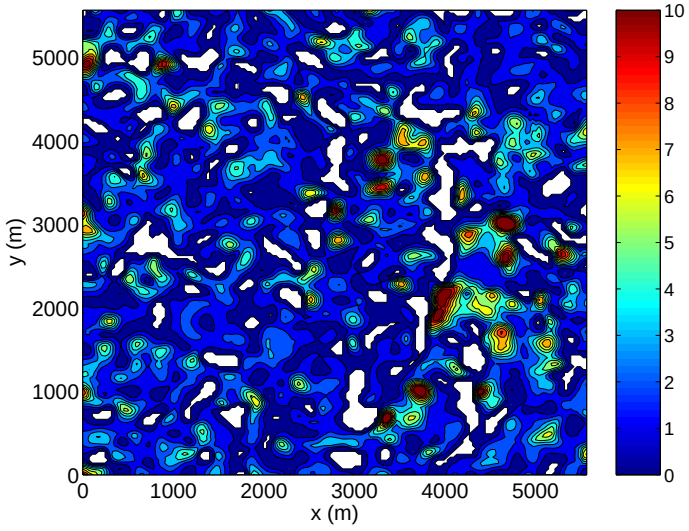

(b)

Figure 7.17: Instantaneous contours of eddy viscosity ν_T (m^2/s) after clipping is applied for DRM-ADM0 with two local test filters, at (a) k = 1 and (b) k = 10. Clipping is indicated by the enclosed white regions with a value of -1.5×10^{-5}.

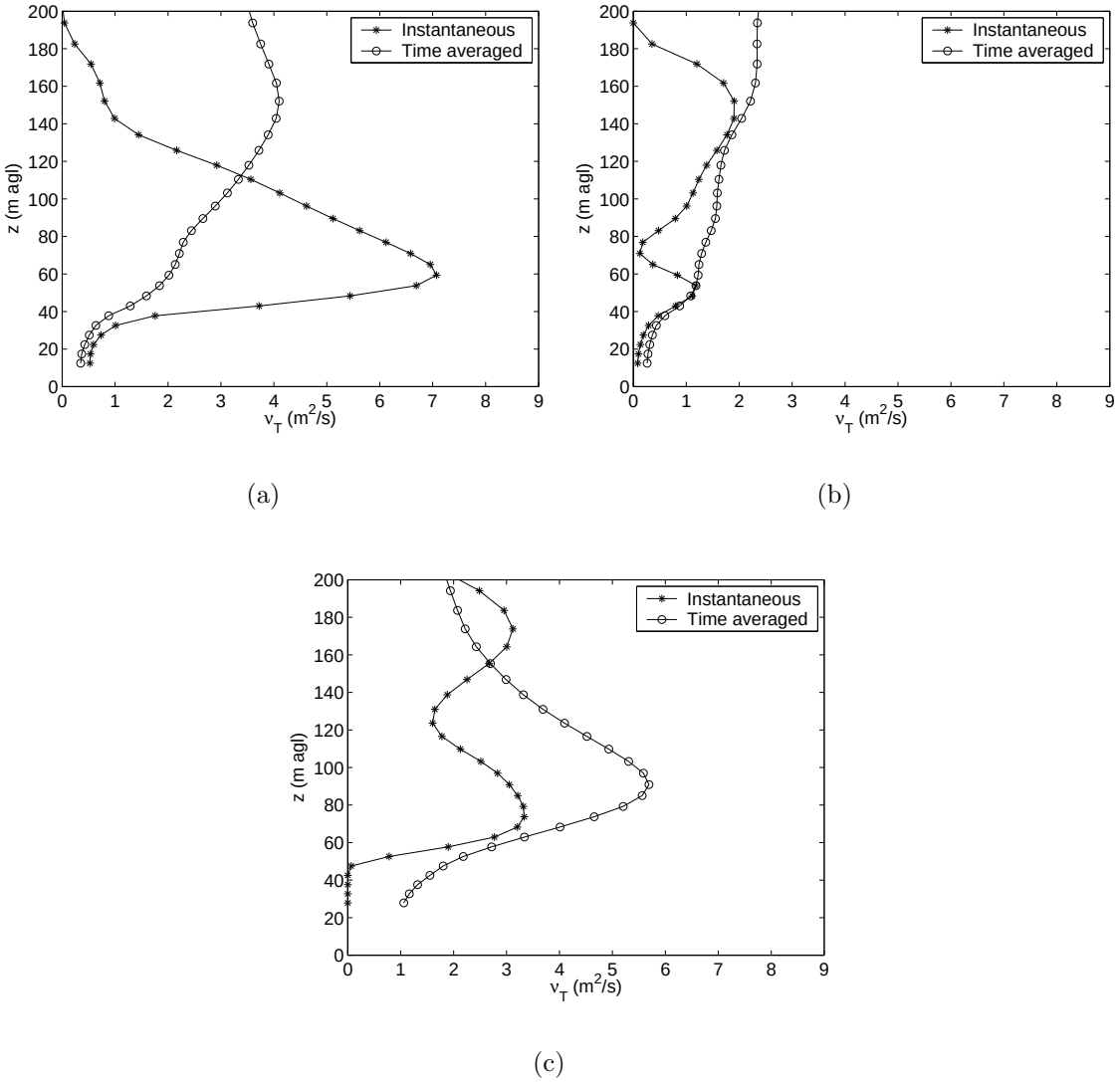

Figure 7.18: Profiles of the dynamic eddy viscosity from DRM-ADM0 results at (a) reference site, (b) on the up-slope of the hill, (c) in the lee of the hill.

All the simulations using DRM include the near-wall stress model introduced in Chapter 6, using a proportionality factor $C_c = 0.5$ and a layer height $h_c = 4\Delta x$. This near-wall stress is intended to provide much of the "missing" stress near the wall, but it appears to be too little, as the hybrid approach is needed to stabilize the simulations when higher reconstruction is used. Figure 7.20 compares the speed-up ratio along line A for different near-wall stress coefficients. Increasing the proportionality factor means increasing the near-wall stress contribution (see Chapter 6). The greatest difference among the speed-up curves is again in the lee of the hill, where increasing C_c prevents the wind from speeding up as quickly in the lee of the hill. The results with $C_c = 0.8$ look similar to those from DWL-SMAG, but the effect of the near-wall stress contribution is not enough to stabilize the simulations with higher levels of reconstruction. Tests with DRM-ADM1 and $C_c = 0.8$ and even up to 0.95 failed.

The effect of the near-wall stress and near-wall Smagorinsky contributions can be seen in Fig. 7.21 which shows wind speed profiles upstream of the hill. Increasing C_c adds near-wall stress and smooths the near-wall velocity profiles, as does the use of the Smagorinsky model near the wall. Figure 7.22 shows that at the hill top, increasing near-wall stress or using near-wall Smagorinsky improves the speed-up ratio at the first point above the wall. The results with $C_c = 0.2$ show a strange speed-up profile here, likely because the near-wall stress contribution is not adequate.

7.5 Conclusions

Large-eddy simulations of flow over Askervein Hill, an isolated hill in Scotland, were compared to the field observations of Taylor & Teunissen (1987). This flow is a challenging test for the reconstruction turbulence models which gave improved results for neutral boundary layer flow over flat terrain. This is the first time, to our knowledge, that reconstruction (scale-similarity) or dynamic turbulence models have been applied to full-scale simulations of the atmospheric boundary layer over terrain. Simulations with the lowest level of reconstruction are straightforward and showed improvement for wind speedup-ratios over the hill, when compared to results from the standard TKE-1.5 model. Predictions of turbulent kinetic energy were also improved. Results were not as clear for the uw and vw stress components. Increased

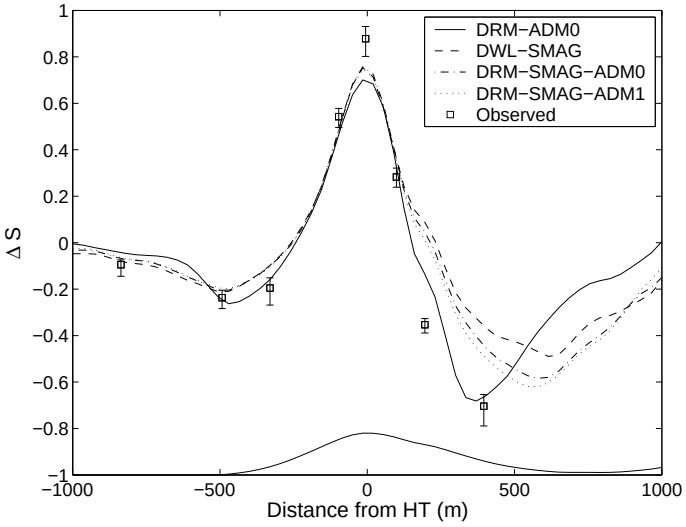

Figure 7.19: Comparisons of observed and simulated velocity speed-up along line A using DRM-ADM0, DWL-SMAG, DRM-SMAG-ADM0, and DRM-SMAG-ADM1 closures.

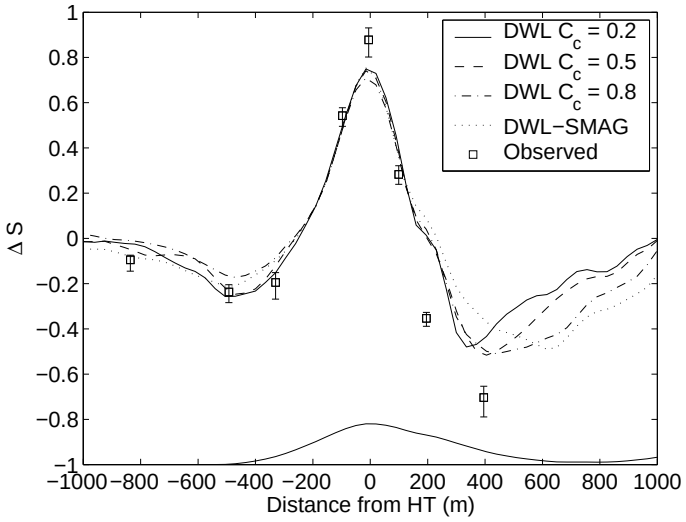

Figure 7.20: Comparisons of observed and simulated velocity speed-up along line A using DWL with increasing near-wall stress coefficients, $C_c = 0.2$, 0.5 (standard case), and 0.8, compared to results from DWL-SMAG using Smagorinsky near the wall and $C_c = 0.5$.

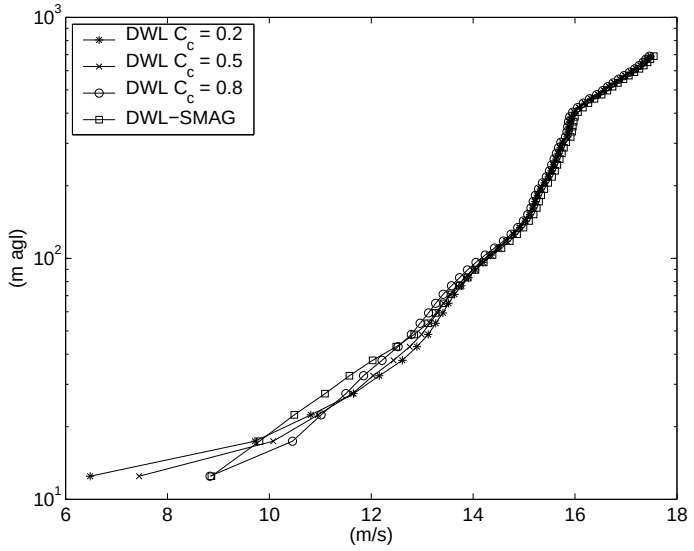

Figure 7.21: Comparisons of wind speed profile upstream of the hill using DWL with increasing near-wall stress coefficients, $C_c = 0.2$, 0.5 (standard case), and 0.8, compared to results from DWL-SMAG using Smagorinsky near the wall and $C_c = 0.5$.

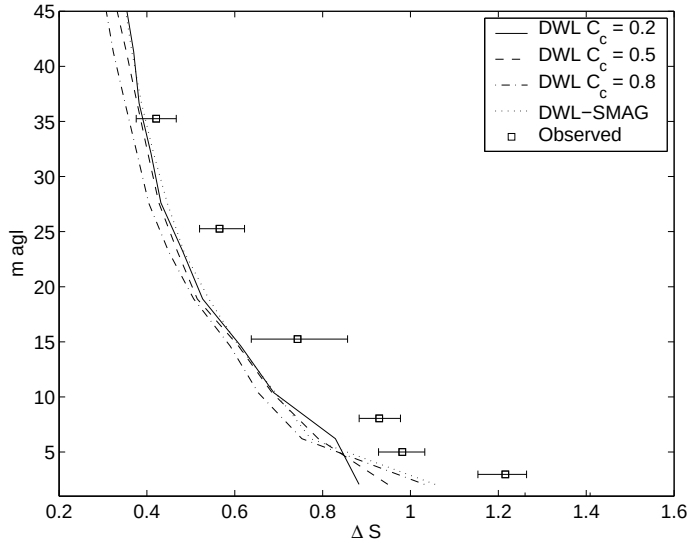

Figure 7.22: Comparisons of velocity speed-up ratio vertical profile at HT using DWL with increasing near-wall stress coefficients, $C_c = 0.2$, 0.5 (standard case), and 0.8, compared to results from DWL-SMAG using Smagorinsky near the wall and $C_c = 0.5$.

levels of reconstruction (beyond level 0) present difficulties and required modification of the closure model near the ground. This was in part because the dynamic procedure underpredicts the stress near the wall over rough surfaces. While all of the simulations using reconstruction also included a near-wall stress component, this was not sufficient to prevent instabilities. We adopted the hybrid approach of Iizuka & Kondo (2003), using the static Smagorinsky model in the lowest levels near the wall and the dynamic approach above. The specification of this static Smagorinsky layer was based on profiles of the dynamic eddy viscosity, however, the appropriate transition level from static to dynamic requires further study. The results, though promising, show that problems with the behavior of closure models in this sensitive near-wall region of the flow have not been completely solved.

Chapter 8

Large-eddy simulations of flow in a steep Alpine valley*

This chapter investigates the steps necessary to achieve accurate simulations of the flow and temperature fields in the Riviera Valley, a steep Alpine valley in southern Switzerland. We address several challenges for numerical simulations in such complex terrain. High-resolution land use and soil moisture datasets, modifications to account for topographic shading, and careful selection of grid nesting parameters are necessary to achieve good agreement with observation data. Even with strong local forcing, the onset and magnitude of the up-valley winds are highly sensitive to surface processes in areas which are well outside the high-resolution domain. Dynamic reconstruction turbulence models are also evaluated in this flow (with the near-wall stress model and modifications for steep terrain in Chapters 6 and 7). The influence of the turbulence model in the Riviera is limited to a shallow layer near the surface. The sensitivity to changes in the turbulence model is much smaller than the impact of changes to the soil moisture initialization. Further research is required to quantitatively evaluate the performance of the new turbulence models in this complex flow.

*This chapter is an expanded version of the paper entitled "High-resolution large-eddy simulations of the Riviera Valley: methodology and sensitivity studies" by Fotini Katopodes Chow (the principal author), Andreas P. Weigel, Robert L. Street, Mathias W. Rotach, and Ming Xue, published in the proceedings of the 11th Conference on Mountain Meteorology, American Meteorological Society, June 2004 (Chow *et al.*, 2004*b*). A companion paper entitled "High-resolution large-eddy simulations of the Riviera Valley: assessment of the flow structure and the heat and moisture budgets" by Andreas P. Weigel (the principal author), Fotini Katopodes Chow, Mathias W. Rotach, Robert L. Street, and Ming Xue, will not be presented here (Weigel *et al.*, 2004*b*).

8.1 Introduction and background

Increases in available computational power now allow high-resolution simulations of flow over complex terrain. Such simulations are needed for local weather prediction and air pollution modeling. Knowledge of drag effects and turbulence due to complex terrain is also necessary for global climate models. The appropriate numerical and physical parameters required by high-resolution simulations are, however, not generally known. The influence of parameterizations such as those used for turbulence, soil moisture, solar radiation, surface roughness, the configuration of initial conditions, lateral boundary conditions, and the choice of numerical grids is highly situation dependent. Simulations are generally performed using "the best available" information and datasets.

The situation is further complicated in highly complex terrain such as the European Alps, because the available parameterizations in numerical simulations are largely based on theory and observations over flat terrain. For example, steep mountain slopes affect incoming radiation by casting shadows on the neighboring terrain, and valleys act to increase local incoming longwave radiation during the night. Neither effect is included in traditional numerical codes because these effects are overshadowed by other, larger errors at the usual low spatial resolutions. However, steep slopes in the Alps require fine grids to resolve the appropriate terrain features. Increasing the grid resolution is generally straightforward, but the radiation scheme is now no longer sufficient to model the physical processes that occur in a steep valley. In addition, accompanying high-resolution surface datasets are scarce, and grid nesting causes difficulty where domain edges cut through mountains. Finally, the influence of turbulence parameterizations can become significant over complex terrain, particularly near the rough bottom boundary.

This chapter investigates the steps necessary to achieve accurate simulations of the flow and temperature fields in the Riviera Valley, located in the Alps in southern Switzerland. Our simulation tool is the Advanced Regional Prediction System (ARPS), a non-hydrostatic, compressible large-eddy simulation code written for mesoscale and small-scale atmospheric flows (Xue *et al.*, 2000, 2001). We show that a straightforward grid nesting approach is not able to accurately reproduce the observed valley winds and circulations from the MAP-Riviera project field campaign of

1999. Rather, careful initialization using high resolution land use and soil moisture data, as well as improved turbulence models, among other considerations, are necessary to achieve satisfactory results. The sensitivity of the simulations to changes in these numerical settings is explored by comparing the results to observation data from soundings and surface station measurements obtained in the Riviera Valley. It is found that the onset and magnitude of up-valley winds are highly sensitive to moisture and radiation processes in areas well outside the high-resolution domain. These processes are inadequately resolved on the coarser grid of the previous nesting level, and directly influence the flow structure in the high-resolution domain via its lateral boundary conditions.

Ultimately, the goal is to simulate accurately the physical processes in this complex valley region and to improve understanding of valley flow physics. The simulations are not intended to be used as forecasts, per se, because field observations have been incorporated at the coarsest resolutions. This allows more accurate representation of the actual flow physics. This work focuses on the numerical aspects of the large-eddy simulation needed to accurately represent the Riviera Valley flow. The physical and meteorological features of our simulated valley flows are described in Weigel *et al.* (2004*b*) where comparisons are also made to aircraft flight data in exploring the onset of up-slope and down-slope winds, along-valley wind transitions, secondary cross-valley circulations, and heat budget analyses. Figures showing the three-dimensional structure of the valley atmosphere and its evolution during the day are, however, included here for completeness.

8.1.1 Previous numerical work

Obtaining accurate simulations of flow in highly complex terrain has been the object of much research. At relatively coarse resolution, a large domain can be studied, but steep mountains and valleys cannot be resolved. Benoit *et al.* (2002), for example, performed 14 km and 3 km resolution real-time simulations of the entire European Alps during the MAP special observing period. Lu & Turco (1995) and Jacobson (2001) simulated flow over complex terrain in California at approximately 5 km resolution. At finer resolution, the topography is better resolved and the slopes become steeper, creating new difficulties. The simulations of Gronas & Sandvik (1999) of a

narrow valley in Norway and of Revell *et al.* (1996) of the New Zealand Alps region, for example, failed to reproduce the winds observed in the field. These simulations suffered from poor resolution and turbulence closures and did not incorporate synoptic data or land surface data.

More recently, Zhong & Fast (2003) compared simulations of the Salt Lake Valley region from three mesoscale models initialized with synoptic data. All three models (RAMS, MM5, and Meso ETA) were able to capture the general features of the valley flows as seen from observations, however, the details of the local circulations and vertical structure of the flow were not sufficiently well reproduced. These simulations were performed at relatively fine spatial resolution for mesoscale models; RAMS and MM5 were nested down to horizontal grid resolutions of 0.56 km; Meso ETA used a single grid with 0.85 km grid spacing. The results showed that relatively large forecast errors existed despite the increased resolution. The authors suggested that improvement in the parameterizations of the surface energy budget, vertical mixing, and radiation may improve the simulations' representation of the thermodynamic structure and circulations within the Salt Lake Valley.

Many studies point to increased grid resolution as a means to achieve better agreement with observations (see e.g. Revell *et al.* (1996); Gronas & Sandvik (1999); Grell *et al.* (2000)). Hanna & Yang (2001) suggest that errors in wind speed and direction in their simulations with four different mesoscale codes are due to errors in the representation of turbulent motions, as well as to subgrid features in the topography and land use. They then suggest that it is unlikely that model errors can be reduced any further. On the contrary, their observations provide motivation for increasing grid resolution and improving subgrid parameterization models.

Previous simulations in the Riviera Valley region have been few. Grell *et al.* (2000) simulated a southern part of the Swiss Alps which included the Riviera Valley, using MM5 and RADM2 (for chemistry) with a horizontal resolution of 1 km to examine the advection of pollutants into Alpine valleys. Their focus, however, did not lie on the Riviera, but on the neighboring Mesolcina Valley. Detailed comparisons to observation data were not presented, but again the authors state that higher spatial and temporal resolution is needed to represent the atmospheric chemistry processes accurately.

Further increasing the grid resolution, however, is not always the solution. Zängl

et al. (2004) and Gohm *et al.* (2004) simulated foehn winds in the Wipp and Rhine Valleys, respectively, using MM5. Despite using resolutions as fine as 267 m in the horizontal, Gohm *et al.* (2004) found discrepancies between the simulations and the observations; e.g., the model predicted a shallow foehn wind occurrence that was not observed. The authors pointed to the need for high-resolution representation of the surrounding topography. Zängl *et al.* (2004) found that the effect of the horizontal computational mixing was larger than the effect of increased resolution. Their model performed better with an improved computational mixing scheme at coarse resolution (3 km) than at fine resolution (1 km) with the traditional mixing scheme. Nevertheless, the predictions of the onset of foehn winds in the Rhine Valley were still delayed by two hours from the observed time.

Simulations of the Riviera Valley, for the same time period as that studied here, were performed by De Wekker *et al.* (2004) using the RAMS model (in RANS mode). Two-way grid nesting with grid spacings down to 333 m gave relatively good agreement with the observed potential temperature fields, but the numerical model did not to capture the wind structure of the valley very well. Consistent up-slope and up-valley winds were not apparent. Our simulation setup had many similarities to that of De Wekker *et al.* (2004), as discussed below.

8.1.2 Objectives for the present numerical simulations

The goal of this chapter is to evaluate the performance of large-eddy simulation using very fine resolution (down to 150 m horizontal spacing) for representing the three-dimensional flow structure over highly complex terrain. All of the studies mentioned above used RANS formulations, not LES closures for their simulations. LES separates resolved and turbulent motions using a length scale (the width of the explicit spatial filter). The differences between LES and RANS become small when similar space and time resolutions are used. However, we prefer the LES formulation for studies of turbulent flows because it is clear which physical features (length scales) are resolvable and which must be modeled.

Simulations of the Riviera Valley are complicated by the complex terrain, the low resolution of regional datasets available for initialization, numerical discretization and lateral boundary condition errors, and other issues. Several steps have been taken to

address these numerical challenges. The numerical setup and grid nesting approach are described in detail below. In particular, we investigate the effects of soil moisture, land use data, grid resolution, topographic shading, and turbulence closure models.

8.2 MAP-Riviera project flow conditions

The Riviera Valley is a medium-sized valley located between the towns of Biasca and Bellinzona in the province of Ticino in southern Switzerland (see Fig. 8.1). The valley is about 15 km long and about 1.5 km wide at the valley floor. Valley side walls have slopes of 30-35° and the surrounding peaks reach altitudes of up to 2700 m asl. The valley was the focus of an extensive field campaign, the MAP-Riviera Project (Rotach *et al.*, 2004), which was part of the larger Mesoscale Alpine Programme (MAP) conducted in the autumn of 1999 (Bougeault *et al.*, 2001). The campaign's objective was to investigate flow structure and turbulence characteristics in a typical, medium-sized Alpine valley. The field data include measurements from surface stations, radiosondes, meteorological towers, and aircraft flights, among others. The relatively large number of field measurements from the MAP-Riviera project is useful for detailed comparison to numerical simulations because of their good spatial and temporal resolution relative to measurements available from operational surface stations over longer time periods.

The Riviera Valley is located on a highly-trafficked route that connects to the Gotthard tunnel to the northwest through the Leventina Valley (see Figs. 8.2 and 8.3). Local populations have enacted legislation and are debating further measures to regulate truck traffic in an attempt to mitigate air and noise pollution. Several studies of air and noise pollution found that the heavy truck traffic and the narrow valleys combine to create a situation with worse air pollution than in the city of Zurich at peak periods (see e.g. BUWAL, 2002). Of interest, therefore, in the valley flow evolution are the transitions of slope and along-valley winds and the vertical structure of the atmosphere, which determine mixing and transport of near-surface pollutants.

Weigel & Rotach (2004) analyzed field data collected during the "convective" days of the MAP-Riviera campaign. These convective days are dominated by thermal forcing which drives the valley and slope winds and are the focus of the simulations

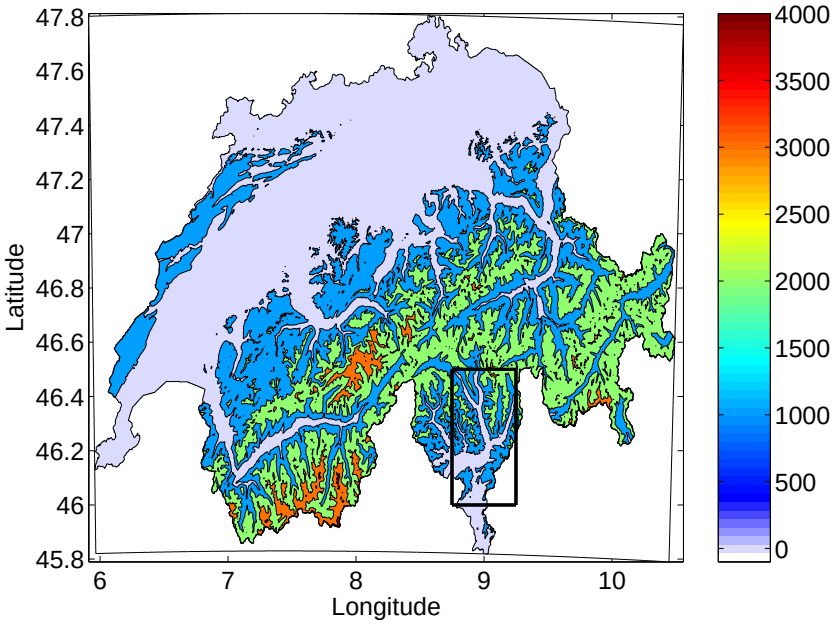

(a)

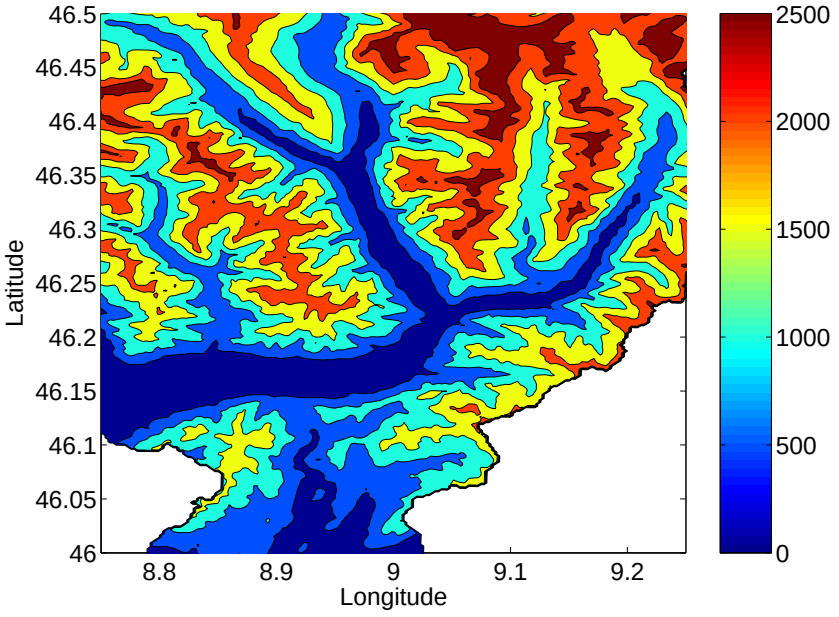

(b)

Figure 8.1: (a) Map of Switzerland, showing contours of elevation (m). Box outlines the Riviera region, shown in detail in (b). Note that axes are stretched.

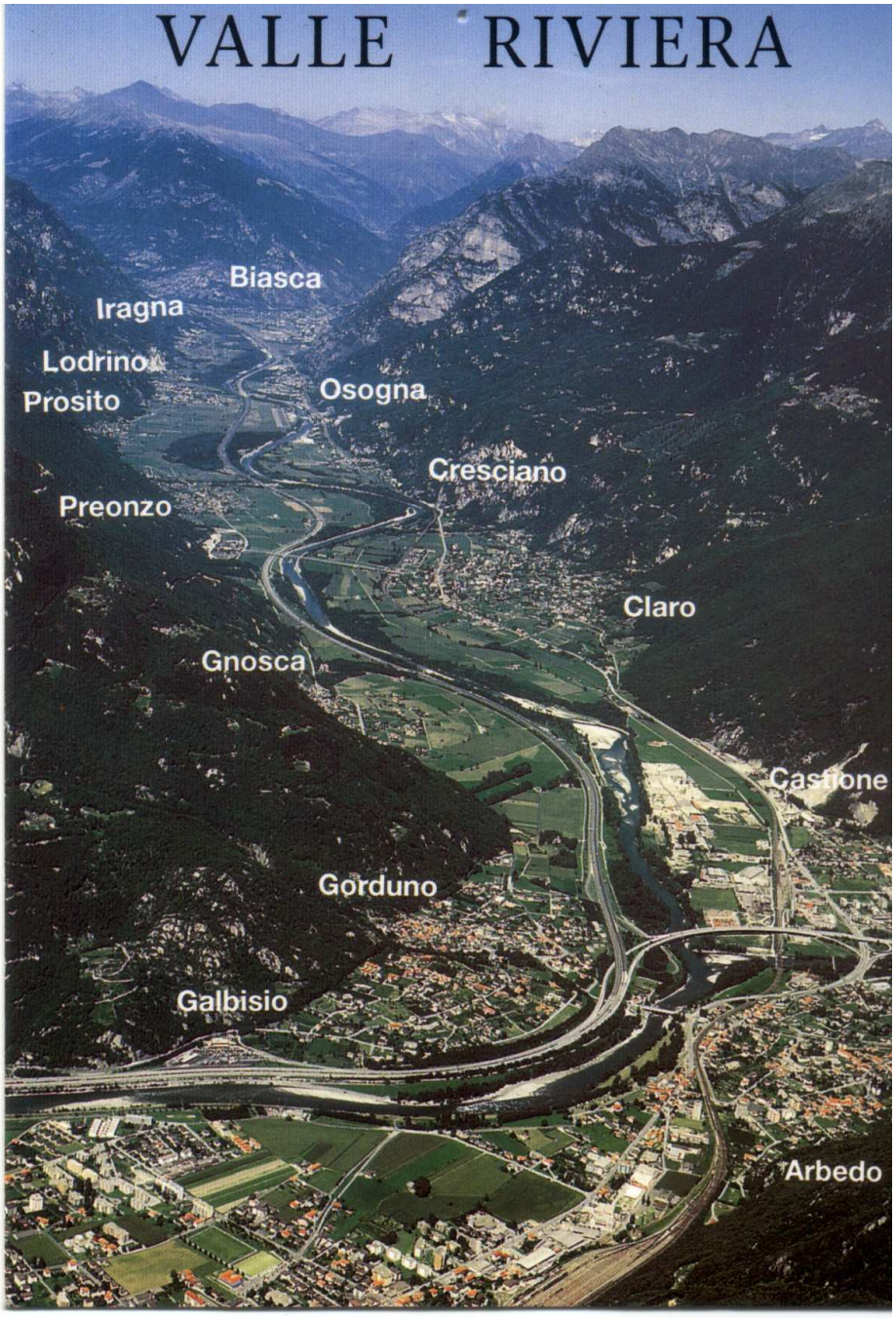

Figure 8.2: Aerial view of the Riviera Valley from a postcard (No. 207, Edizioni Alfa S.A., 6616 Losone), looking north from Bellinzona. The Gotthard tunnel is to the northwest of Biasca.

in this chapter. On days with such strong thermal forcing, it is hoped that flow in the valley will not be determined by synoptic conditions, i.e., that the slope and valley wind system will develop within the valley and will be sensitive to the local surface conditions that determine heating and cooling. Even on such convective days, however, synoptic conditions can influence the transition of the valley wind system. Weigel & Rotach (2004) determined that the prevailing synoptic wind direction affects the strength of the up-valley winds that occur in the afternoon. Barr & Orgill (1989) also noted that the details of valley drainage winds were affected by the external meteorology in virtually every case they observed, to a lesser or greater extent that depended on the penetration of the synoptic winds above the valley mountain ridges into the core of the valley flow.

Numerical simulations of convective days in the Riviera Valley cannot, therefore, ignore the external meteorology, but must include it as the background in which the valley winds occur. A numerical model should be able to use synoptic information to accurately determine the evolution of the boundary layer dynamics within the valley itself. We have simulated the convective days of August 21, 22 and 25, 1999. We focus on August 25, 1999 in this chapter because wind data were missing from radiosondes on August 21 and 22. Weather maps and a satellite image shown in Fig. 2.3 of De Wekker (2002) indicate a northwesterly synoptic flow and cloudless skies on August 25. After determining the best simulation setup for August 25, where quantitative comparisons could be made for both wind and temperature fields, simulations of August 21 and 22 were performed. A companion paper synthesizes the results from August 21 and 22 to provide a broader context for an accurate numerical depiction of the valley wind system in the Riviera (Weigel *et al.*, 2004*b*). The simulations show that not only are the valley dynamics on convective days determined by surface conditions, but also by the prevailing winds and regional atmospheric structure outside of the local Riviera Valley domain.

8.3 Numerical simulation setup

This section describes the procedures used to achieve accurate simulation of atmospheric flow in the Riviera Valley. The steps taken include the use of high-order

Run name	Configuration
REF	Reference simulation set, simple grid nesting with no additional data.
MOISLU	Additional data incorporated. 1 km grid level uses elevation-dependent soil moisture, and 350 m grid uses WaSiM soil moisture and 100 m land use data.
MOIS	Same as MOISLU but with interpolated low-resolution landuse data for all grids.
MOISLU-NS	Same as MOISLU but with no topographic shading for all grids.
MOISLU-NOTURB	Same as MOISLU but with no turbulence model at the 350 m grid.
MOISLU-DRM	Same as MOISLU but with DRM turbulence model variations at the 350 m grid.
MOISLU2	Same as MOISLU but 1 km grid uses extrapolated WaSiM soil moisture data. 350 m grid uses WaSiM soil moisture and 100 m land use data.

Table 8.1: Riviera Valley simulation configurations.

numerical methods, carefully selected grid nesting parameters, high-resolution surface data, modifications to the radiation model, and improved turbulence closure methods. The standard "acceptable" procedure, using grid nesting, standard initial conditions, and standard surface datasets, provides a reference for comparison with the enhanced simulation approach and for sensitivity studies showing the effect of each new component. Table 8.1 lists the various simulation configurations.

8.3.1 Large-eddy simulation code

ARPS was developed at the Center for Analysis and Prediction of Storms at the University of Oklahama, and is formulated as an LES code that solves the three-dimensional, compressible, non-hydrostatic, filtered Navier-Stokes equations. ARPS is described in detail by Xue *et al.* (1995, 2000, 2001) (see also Appendices C and D); so we only mention the relevant settings for this application.

Fourth-order spatial differencing is used for the advection terms. Temporal discretization is performed using a mode-splitting technique to accommodate high-frequency acoustic waves. The large time steps (Δt) use the leapfrog method; first-order forward-backward explicit time stepping is used for the small time steps ($\Delta \tau$),

Grid size (nx, ny, nz)	Δx, Δy	Δz_{min}	Δz_{avg}	Domain height	Δt/ $\Delta \tau$
$103 \times 103 \times 53$	9 km	50 m	500 m	25 km	10 s /10 s
$103 \times 103 \times 53$	3 km	50 m	500 m	25 km	2 s / 4 s
$99 \times 99 \times 63$	1 km	50 m	400 m	24 km	1 s / 1 s
$83 \times 83 \times 63$	350 m	30 m	350 m	21 km	1 s / 0.2 s
$83 \times 99 \times 83$	150 m	20 m	200 m	16 km	0.5 s / 0.05 s

Table 8.2: Nested grid configurations.

except for terms responsible for vertical acoustic propagation, which are treated semi-implicitly. Simulations were performed on parallel processors (using MPI) on IBM SP machines at NCAR's Scientific Computing Division. Appendix G gives details on computational cost.

8.3.2 Grid nesting and topography

Five one-way nested grids were used to simulate flow in the Riviera Valley at horizontal resolutions of 9 km, 3 km, 1 km, 350 m, and 150 m. The Riviera Valley first becomes reasonably well resolved at 350 m resolution (see the wavelet analysis of De Wekker, 2002). Details of the simulation domains are listed in Table 8.2. Figure 8.3 shows the topography for the 1 km, 350 m, and 150 m subdomains.

Warner *et al.* (1997) provide guidelines for setting up nested simulations to minimize contamination by lateral boundary condition choices. Perhaps the most important is that the flow region of interest should be as far as possible from the domain boundaries, i.e., in the center of the domain. All grids were centered on the Riviera Valley at 46.2881 N, 9.002 E, except for the 150 m resolution grid centered on 46.2547 N, 9.0117 E. A Lambert conformal map projection was used with the "true" latitude and longitude chosen very close to the center of the domain to minimize distortion at the center of the grid, particularly for the smaller domains.

Topography for the 9 km through 1 km grids was obtained using the USGS 30 arc second topography datasets available through ARPS. The 350 m and 150 m resolution terrain data were extracted from a 100 m dataset available for all of Switzerland (Volkert, 1990). For each nested subdomain the terrain is smoothed near the domain boundaries to match the elevations from the surrounding coarser grid.

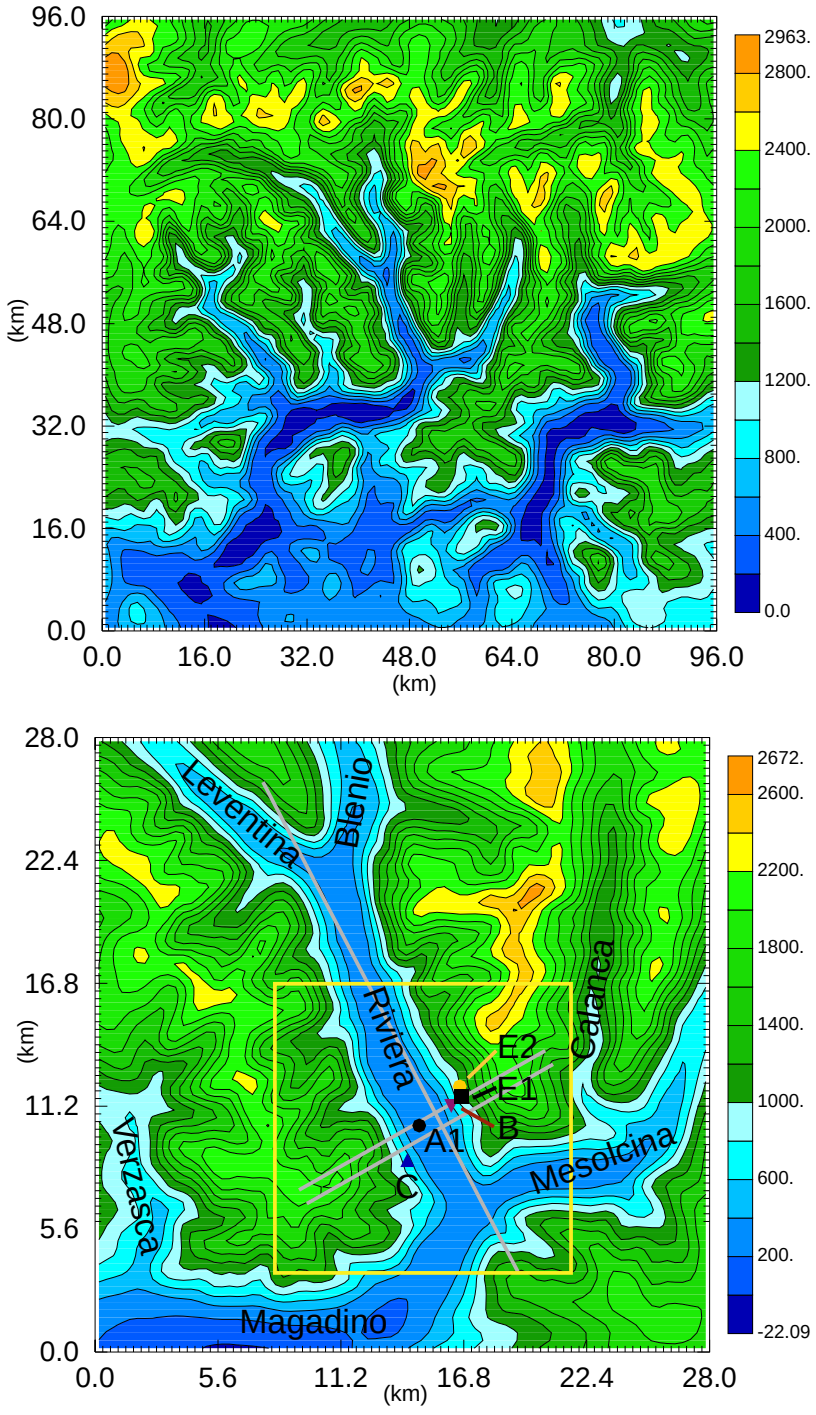

Figure 8.3: Riviera Valley elevation (m) contours for (top) 1 km grid and (bottom) 350 m grid with the 150 m grid shown within. Locations of surface stations (defined in Table 8.6) and vertical cross-sections are also shown.

8.3.3 Vertical resolution and grid aspect ratio

ARPS uses a terrain following σ-coordinate system (see Section 2.2.2). The minimum vertical grid spacings at the surface are listed in Table 8.2. The grid is stretched using a tanh function to yield an average spacing of Δz_{avg} and a domain height of $\Delta z_{avg}(nz-3)$. High vertical resolution is needed to resolve the vertical structure of the atmosphere, but if the grid aspect ratio ($\Delta x/\Delta z$) becomes too large, numerical errors become large, particularly in the horizontal gradient terms (Mahrer, 1984). Poulos (1999) and De Wekker (2002) also found that the grid aspect ratio had to be small, especially for steep terrain. Increasing the vertical resolution too much, for example, leads to instabilities. Finally, LES also requires a small aspect ratio so as to avoid distortion of resolved eddies (Kravchenko *et al.*, 1996).

Because of the large domain sizes considered here, we must compromise on one or more of the above guidelines. Indeed, at 9 km resolution the aspect ratio is 180 at the surface. We presume, however, that the general scales of the resolved flow and topography are large enough at those resolutions, that together with the parameterizations in the TKE-1.5 turbulence closure (see Section 8.3.7), they will be reasonably represented. Tests with larger values of Δz_{min} for the large grids degraded the representation of the vertical structure. The best possible aspect ratios have therefore been adopted. Particularly for the fine resolution grids, we avoid increasing the aspect ratio more than is necessary; the grid at 350 m resolution has a much reduced aspect ratio of 7.

8.3.4 Initialization and lateral boundary conditions

To obtain realistic initial and boundary conditions, data from the European Centre for Medium-Range Weather Forecasts (ECMWF) were used to force ARPS simulations at the coarsest resolution (9 km).* (Starting with a 27 km resolution grid and then nesting to the 9 km grid did not improve results.) ECMWF analyses are given at six-hour intervals with 0.5 degree (approximately 60 km) horizontal resolution and 50 vertical levels. Details of the ECMWF forecast model and analysis data are available at `http://www.ecmwf.int`. ARPS pre-processing software was used to

*Attempts were also made to use MC2 data to initialize simulations (on October 1, 1999), but this was not pursued further.

generate initial conditions at 1800 UTC on August 24, 1999. Lateral boundary forcing used the ECMWF data at six-hour intervals, linearly interpolated to intermediate times. Relaxation towards the lateral boundary values was applied to a 5-10 grid-cell zone around the edge of the domain. Simulations continued for 30 hours beginning at 1800 UTC August 24. Output stored at hourly intervals was used to generate initial and boundary condition files for subsequent nested grid simulations. The effects of changing the update intervals for the lateral boundaries are left for future research (see e.g. the work of Nutter *et al.*, 2002).

The ECMWF initialization data compare fairly well with nearby soundings, e.g. in Milan, Italy and Payerne, Switzerland, outside of the Alps, but because of poor vertical resolution cannot capture the pronounced inversion observed in the radiosonde data on August 25, 1999 (see Fig. 8.11 later). The inversion was likely created by strong regional subsidence and persisted throughout the August 25 simulation period, therefore separating the dynamics of the lower 2 km within the valley from the regional flow above. Tests were performed using the ARPS data assimilation system (ADAS) to refine the vertical structure of ECMWF data based on European radiosonde observations. The data assimilation improved the results with regard to surface potential temperature, but had some detrimental effects on the predicted velocities for August 25. The results presented here therefore do not use ADAS. Results for August 21 and 22, 1999, however, benefited greatly from the ADAS initialization; this is likely due to the more complex nature of the synoptic conditions on those days which included some cloud cover (Weigel & Rotach, 2004).

The use of ADAS is described further here for the reader's information, as it was used in the simulations of August 21 and 22 presented in the companion paper (Weigel *et al.*, 2004*b*). We used ADAS to incorporate more observational data into the simulation at the coarsest resolution (9 km). Radiosonde data throughout Europe were obtained at six-hourly intervals from the Radiosonde Data Archive (`http://raob.fsl.noaa.gov/`) maintained by the Forecast Systems Laboratory (FSL) and the National Climatic Data Center (NCDC). About 60 soundings are available in our 9 km domain at 0000 and 1200 UTC and about half as many at 0600 and 1800 UTC. Data assimilation was performed using the background field provided by the ECMWF data. The vertical range over which the background fields were forced to match the observation data was adjusted using the `zrang` parameter in ADAS. The

range was chosen to be 400, 300, 200, 100 for each of the four passes, respectively. This is a restrictive fine fit, but was found to be necessary to capture the vertical features in the potential temperature sounding data. The modified background fields (ECMWF data adjusted to sounding data) were then used as the initial and lateral boundary conditions to drive the 9 km resolution simulations. The simulation was relaxed toward the observations for all time at this resolution, to ensure that the strong inversion was not mixed out over time. The 9 km grid thus provided more vertical structure for the boundaries of the finer grids where no data assimilation was used. The vertical structure of the potential temperature, in particular, is significantly improved. The simulation results, however, were poor with regard to the velocity fields for August 25 so ADAS was not used on this date.

8.3.5 Surface characteristics

The characteristics of the land surface determine sensible and latent heat flux exchange with the atmosphere. The ARPS land-surface soil-vegetation model solves surface energy and moisture budget equations, described in detail in Xue *et al.* (1995, 2001). ARPS normally uses 13 soil types (including water and ice), and 14 vegetation classes (following the United States Department of Agriculture classifications). Land use, vegetation, and soil type data for the 1 km and coarser grids are obtained from USGS 30 second global data. The ARPS surface data pre-processor was modified to include this finer resolution data; the standard version only included data at 10 min (approximately 20 km) resolution.

For the higher resolution grids (350 m and finer), we have modified the ARPS surface data classes to incorporate even finer resolution surface data. Land use and soil type data are available for all of Switzerland at 100 m resolution from the Landnutzungskarte des Bundesamts für Statistik and the Digitale Bodeneignungskarte der Schweiz (GEOSTAT). The dataset includes 69 land use categories, which have been mapped to a new set of 30 vegetation and 14 soil types (see Tables 8.3 and 8.4), as done by De Wekker (2002) for RAMS. Different values, however, have been assigned in ARPS for the roughness length, leaf area index and vegetation fraction. A new soil type was added to represent bare rock, which makes up a significant portion of the mountain tops. The new vegetation and soil types provide much more detailed

local land coverage compared to the 30-second data (see Fig. 8.4).

For the soil temperature and moisture budgets, two soil layers of depths 0.01 m and 1.0 m for the surface and deep soil are used. Soil temperature for all grids was initialized as a constant offset from the near-surface air temperature: 0.6 K for the top layer and -2.1 K for the deep soil. The selected offset was based on observations in the Riviera Valley. Soil moisture data for the 9 km resolution grid was initialized from ECWMF data, which in the Alps range from 0 (rocky and glacial areas) to 0.37 m^3m^{-3}. The deep soil is slightly wetter than the top layer. The area near the Riviera Valley has values of about 0.35 m^3m^{-3} (surface) and 0.366 m^3m^{-3} (deep), except for the rocky outcroppings. The soil moisture values at 9 km resolution are then interpolated to the 3 km resolution grid. For the REF simulations (see Table 8.1), these ECMWF data are further interpolated to the 1 km and 350 m resolution grids.

For the MOISLU and other simulations, high-resolution soil moisture initialization data were obtained to represent the spatial variability in the Riviera Valley better. For this purpose, we followed De Wekker *et al.* (2004) and used the Water Flow and Balance Simulation Model (WaSiM-ETH) (Jasper, 2001; Schulla *et al.*, 2004; Jasper *et al.*, 2004) to obtain soil moisture information. This hydrologic model is driven by meteorological data such as air temperature and precipitation and provided 100 m resolution data for the catchment region of the Riviera. The WaSiM simulation was performed from January 1, 1999 until August 24, 1999 at 1800 UTC at which time the output was used to initialize the soil moisture in ARPS. Figure 8.5 shows the distribution of soil moisture for the two layers used at the 350 m grid level at 1800 UTC. The soil is wetter on the valley floor, significantly drier on the steep surrounding slopes, and zero on the rocky peaks of the mountains and in urban areas (e.g. in Bellinzona and Biasca). In the upper soil level, the WaSiM data have moisture values which are comparable to the ECMWF data ($\sim$ 0.32 m^3m^{-3}). At the deep soil level (where there are no plant roots to hold water) the WaSiM moisture on the steep slopes is very low (0.08-0.12 m^3m^{-3}), but on the valley floor it is still relatively high ($\sim$ 0.25 m^3m^{-3}).

The availability of WaSiM data is certainly helpful, as soil moisture observations are hard to find. A few measurements were taken in the Riviera Valley during the field campaign (Zappa & Gurtz, 2003), and these compare quite well with the WaSiM

Class	Description	LAI	Veg. Frac.	z0 (m)	rsmin (s/m)	rgl (W/m^2)	Swiss class
1	Evergreen needleleaf tree	6 (d)	0.8 (b)	1 (b)	175 (d)	30 (c)	12,13 (> 1000 m asl)
2	Deciduous needleleaf tree	5 (d)	0.8 (b)	1 (b)	175 (d)	30 (c)	—
3	Deciduous broadleaf tree	5 (d)	0.8 (b)	0.8 (b)	200 (d)	30 (c)	12,13 (< 1000m asl)
4	Evergreen broadleaf tree	5 (d)	0.9 (b)	2 (b)	120 (d)	30 (c)	—
5	Short grass	2 (b)	0.8 (b)	0.02 (b)	40 (a)	100 (c)	83-89
6	Tall grass	3 (x)	0.8 (b)	0.1 (b)	83 (d)	100 (c)	—
7	Desert	0 (b)	0.01 (x)	0.05 (b)	999 (a)	100 (c)	—
8	Semi-desert	1.5 (x)	0.1 (b)	0.1 (b)	300 (a)	100 (c)	—
9	Ice	0 (b)	0.1 (a)	0.005 (a)	999 (a)	100 (c)	—
10	Tundra	1 (d)	0.2 (d)	0.04 (b)	500 (a)	100 (c)	—
11	Evergreen shrub	3 (d)	0.8 (b)	0.1 (b)	200 (d)	30 (c)	—
12	Deciduous shrub	3 (d)	0.8 (b)	0.1 (b)	200 (d)	30 (c)	—
13	Mixed woodland	5 (d)	0.8 (b)	0.8 (b)	200 (d)	30 (c)	—
14	Water	0 (b)	0 (a)	0.001 (a)	0 (E-30) (a)	100 (c)	91,92
15	Crop/mixed farming	3 (d)	0.85 (b)	0.06 (b)	70 (d)	100 (c)	71,72,75-78
16	Irrigated crop	3 (d)	0.8 (b)	0.06 (b)	60 (d)	100 (c)	—
17	Bog or marsh	4.5 (x)	0.8 (b)	0.03 (b)	5 (a)	100 (c)	69,95,96
18	Evergreen needleleaf forest	6 (d)	0.8 (b)	0.98 (b)	175 (d)	30 (c)	10,11,14 (> 1000m asl)
19	Evergreen broadleaf forest	5 (d)	0.9 (b)	2.2 (b)	120 (d)	30 (c)	—
20	Deciduous needleleaf forest	5 (d)	0.8 (b)	0.92 (b)	175 (d)	30 (c)	—
21	Deciduous broadleaf forest	5 (d)	0.8 (b)	0.91 (b)	200 (d)	30 (c)	10,11,14 (< 1000m asl)
22	Mixed cover	5 (d)	0.8 (b)	0.87 (b)	175 (e)	30 (c)	—
23	Woodland	5.7 (e)	0.8 (b)	0.83 (b)	174 (e)	30 (c)	15,19
24	Wooded grassland	5 (e)	0.8 (b)	0.51 (b)	169 (e)	30 (c)	17,18
25	Closed shrubland	5 (e)	0.6 (b)	0.14 (b)	175 (e)	30 (c)	16
26	Open shrubland	3 (x)	0.2 (b)	0.08 (b)	179 (e)	100 (c)	—
27	Grassland	2.6 (e)	0.8 (x)	0.04 (b)	83 (d)	100 (c)	73,81,82,97
28	Cropland	3 (x)	0.8 (b)	0.11 (b)	65 (x)	100 (c)	—
29	Bare ground	0.1 (x)	0.07 (b)	0.05 (b)	999 (x)	100 (c)	99
30	Urban and built up	2 (d)	0.4 (d)	0.8 (b)	150 (d)	100 (c)	20-68,70

Table 8.3: Land use conversion from 69 Swiss categories to 30 new ARPS categories. Courtesy of Andreas Weigel. LAI (leaf area index), vegetation fraction, z0 (roughness length), "rsmin" (surface resistance), and "rgl" (solar radiation dependence) are used by ARPS to characterize each surface type. Swiss land use classes are defined in Table A2.3 of De Wekker (2002). (a) ARPS values; (b) LEAF-2 values as used in RAMS by De Wekker (2002); (c) Noilhan & Planton (1989); (d) Xiu & Pleim (2001); (e) LDAS-data (http://ldas.gsfc.nasa.gov/LDAS8th/MAPPED.VEG/web.veg.table.html); (x) Estimate based on comparison of various sources.

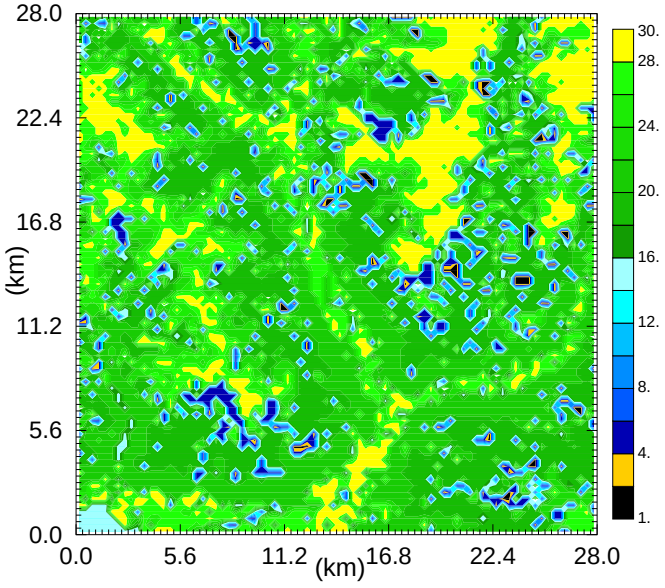

(a)

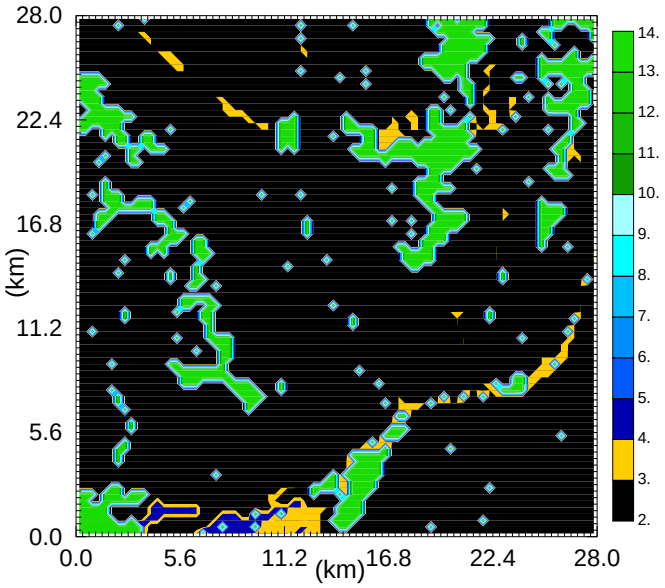

(b)

Figure 8.4: Contours of (a) vegetation type and (b) soil type at 350 m resolution using the 100 m land use dataset. Definitions of the vegetation and soil types are given in Table 8.4.

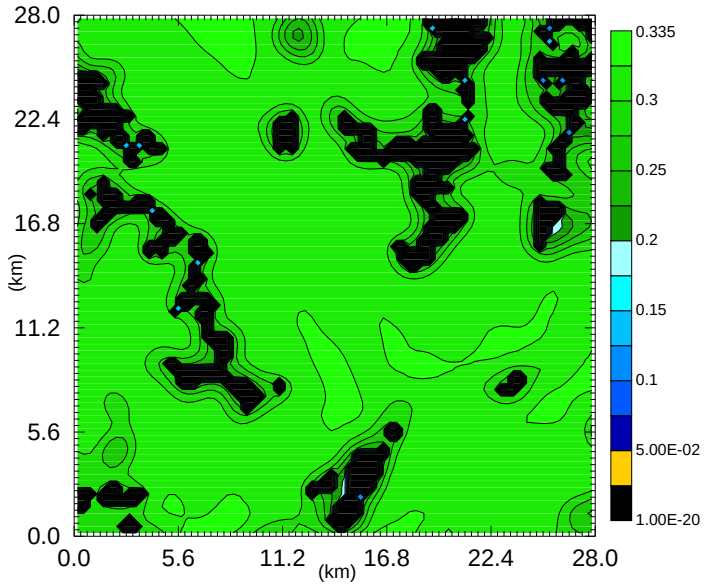

(a)

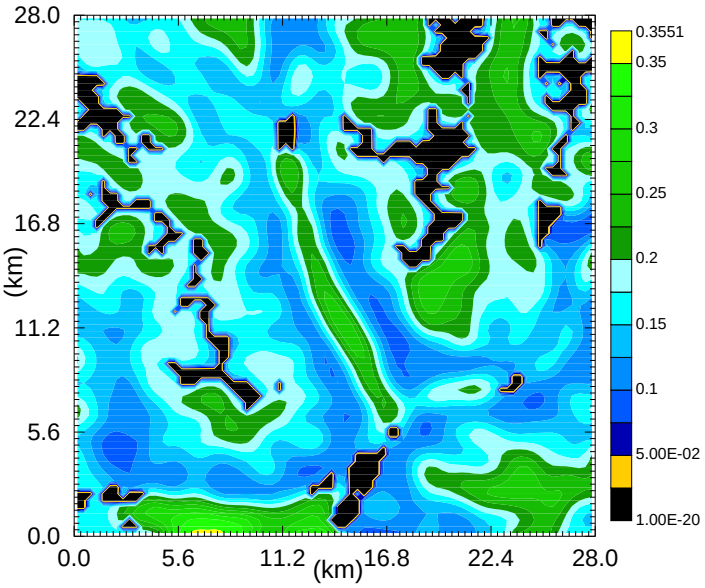

(b)

Figure 8.5: Contours of soil moisture (m^3/m^3) at (a) upper and (b) lower levels at 350 m resolution using WaSiM values.

Class	Description
01	Sand
02	Loamy sand
03	Sandy loam
04	Silt loam
05	Loam
06	Sandy clay loam
07	Silty clay loam
08	Clay loam
09	Sandy clay
10	Silty clay
11	Clay
12	Ice
13	Water
14	Rock

Table 8.4: Soil types used in the high-resolution Riviera simulations. Class 14 was added to accommodate the peaks of the Alpine mountains and is not included in the standard soil classes in ARPS.

values. For example, at 1200 UTC, measurements at site A1 (see Fig. 8.3) showed the soil moisture to be 0.318 m^3m^{-3} at the surface and 0.293 m^3m^{-3} at 25 cm depth. In contrast, site B showed 0.306 m^3m^{-3} at the surface, and 0.212 m^3m^{-3} at 25 cm depth. This near-constant moisture with depth on the valley floor and significant decrease on the slope also appears in the WaSiM data.

Given ECMWF data for the 9 km resolution grid, and WaSiM data for the 350 m and 150 m resolution grids, the question remains as to what the best values are at the intermediate resolutions of 3 km and 1 km. De Wekker *et al.* (2004) set the soil moisture to be constant on their coarser grids and found that the specific value did not significantly affect the results. Our sensitivity studies in Section 8.6, however, do show that soil moisture is a parameter to which these simulations are very sensitive, particularly at the 1 km grid level. We therefore incorporated a semi-empirical three-level soil moisture initialization for the 1 km grid, used in the MOISLU simulations. At altitudes above 2200 m where the soil type rock dominates, the soil moisture was set to 0. Between 2200m and 500m it was set to 0.18 m^3m^{-3}, and below 500m to 0.28 m^3m^{-3}. The same values were used at the surface and deep soil levels. These were selected as intermediate values between the WaSiM deep and surface layer values, and can be seen as a compromise between the WaSiM and ECMWF data. In addition to using interpolated ECMWF and three-level soil moisture initializations, we investigated the use of extrapolated WaSiM data outside

	Surface (0.01 m)	Deep (1.0 m)	
		Valley floor	Slopes
ECMWF	0.35	0.37	0.37
WaSiM	0.32	0.25	0.08-0.12
3-level	same as deep	0.28	0.18

Table 8.5: Typical soil moisture values (m^3m^{-3}) for each dataset in the surface and deep layers. All have close to zero soil moisture at the rocky outcroppings. The 3-level data are constant in each elevation range.

the Riviera catchment area. The three choices for soil moisture initialization for the 1 km grid are summarized in Table 8.5 and are discussed further in Section 8.6.1.

8.3.6 Radiation model

In steep valleys, "topographic shading" from shadows cast by neighboring topography can be important. ARPS normally only includes the effect of surface inclination when calculating incoming solar radiation. We denote this "self-shading". For example, during sunrise, the west-facing slope in the Riviera Valley is correctly characterized as in the shade, because the surface is inclined away from the sun. The valley floor, however, would not be shown as shaded in the simulation because of its horizontal slope. Self-shading accounts for much of the required modification to the incoming radiation in complex terrain; however, the valley floor is in reality also shaded from solar heating by the adjacent mountains during sunrise.

Colette *et al.* (2003) performed idealized simulations of steep valleys and found that the inclusion of topographic shading could delay inversion layer breakup during the morning by approximately half an hour. The field study of Matzinger *et al.* (2003) emphasized the importance of the topographic shade in the Riviera Valley, where local sunrise is delayed with significant effects on the net radiation balance. To improve the treatment of radiation in our simulations of a real mountain valley, we have therefore included the topographic shading method of Colette *et al.* (2003). Its effect is evaluated in Section 8.6.4. This subroutine is included in the latest version of ARPS. The complete treatment of short- and long-wave radiation is described in Xue *et al.* (1995, 2000).

8.3.7 Turbulence, computational mixing, and wall models

The standard closure models in ARPS include 1.5-order TKE (Deardorff, 1980; Moeng, 1984) and static Smagorinsky-Lilly models (Smagorinsky, 1963; Lilly, 1962). The TKE-1.5 model solves an extra equation for the turbulent kinetic energy to determine the velocity scale for use in an LES-type eddy-viscosity formulation. The model can be used for LES as long as the chosen length scale is proportional to the filter width, as it is in ARPS (Deardorff, 1980; Moeng, 1984). The TKE approach is especially useful when a large fraction of the velocity scales is contained in the subfilter scales, as for coarse resolution grids (Pope, 2000, Chapter 13). At very coarse resolution, options are available for boundary layer parameterizations in the TKE-1.5 scheme, but then ARPS would no longer be operating in LES mode, so these options are not used here.

We have used the TKE-1.5 closure in most of the simulations, but the new subfilter-scale (SFS) turbulence closure methods of Chapters 6 and 7 have also been applied at the finer resolution grids (where the grid aspect ratio is more suitable for LES). The new approach uses reconstruction modeling for the resolved subfilter scales (RSFS) and a dynamic eddy-viscosity model for the subgrid scales (SGS), and is called the dynamic reconstruction model (DRM). Simulations of neutral boundary layer flow using DRM over flat terrain were able to accurately represent the expected logarithmic layer near the wall, unlike standard eddy-viscosity models (Chapter 6). Applications to flow over Askervein Hill were also successful (Chapter 7). In the DRM approach for the Riviera Valley (MOISLU-DRM), the Smagorinsky model replaces the dynamic contribution in the lowest six levels near the wall to prevent instabilities, as described in Chapter 7. This is denoted DRM-SMAG. The DRM approach also includes an enhanced near-wall stress model to account for the stress induced by the poor grid-aspect ratio, filtering near the surface, and subgrid roughness. The near-wall stress model is applied over a height of $2\Delta x$ and with a proportionality factor of 0.5. The vertical extent may be too large (given $\Delta x = 350$ m); the near-wall static Smagorinsky modification is used over about 400 m. Further investigation is needed to determine the appropriate settings for flow over such complex terrain. The DRM was also applied to the transport equation for potential temperature (see Appendix B) but not for moisture variables.

Finally, fourth-order computational mixing is used to damp high-frequency motions that can build up due to nonlinear interactions; this can be considered a type of hyper-viscosity. ARPS also includes a divergence damping term to control acoustic noise. The impact of both of these damping terms has been investigated and the coefficients set to give the minimum amount of mixing required for stability. For example, increasing the fourth-order mixing coefficient by a factor of ten results in very small differences; the potential temperature profiles are slightly smoothed near the wall only during the night when the stratification is stable. Decreasing the coefficient by a factor of ten makes the simulation unstable.

8.4 Results and comparison to field data

Detailed results comparing the REF and MOISLU simulations and observation data for August 25, 1999 are given in this section. All results are from the 350 m resolution grid unless otherwise noted.

8.4.1 Mean wind patterns

Typical thermally-driven valley wind patterns include the onset of up-slope winds on the valley walls in the morning, and up-valley winds developing during the day. In the evening, the winds transition to down-slope and down-valley winds. Slope winds are generated by differential heating of air near the surface along the slopes and air in the middle of the valley. A pressure gradient results, which during the day drives the lighter, warmer air up the slope, and at night drives the heavier, cooler air down the slope. The mechanism for along-valley winds is not as simply explained, but can in part be described by the "topographic amplification factor" or the effect of valley geometry on the energy budget (Steinacker, 1984; McKee & O'Neal, 1989) and subsidence heating of the valley core (Rampanelli *et al.*, 2004). A comprehensive discussion of valley wind mechanisms is given by Whiteman (2000).

The winds in the Riviera exhibit some aspects of the typical valley patterns. Figure 8.6 shows the evolution of surface wind speed and direction on August 25, 1999 at Bosco di Sotto (site A1, see Table 8.6 and Fig. 8.3) near the center of the simulation domains. Surface station and radiosondes observations were collected at this location

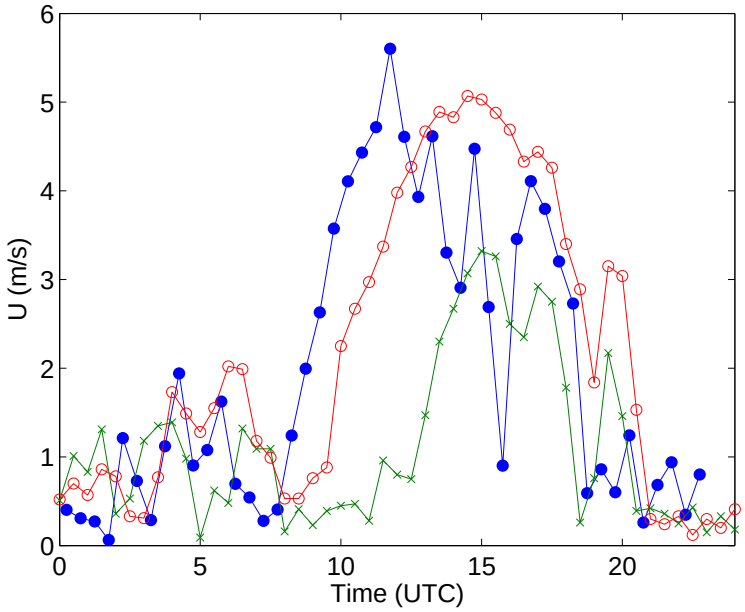

(a)

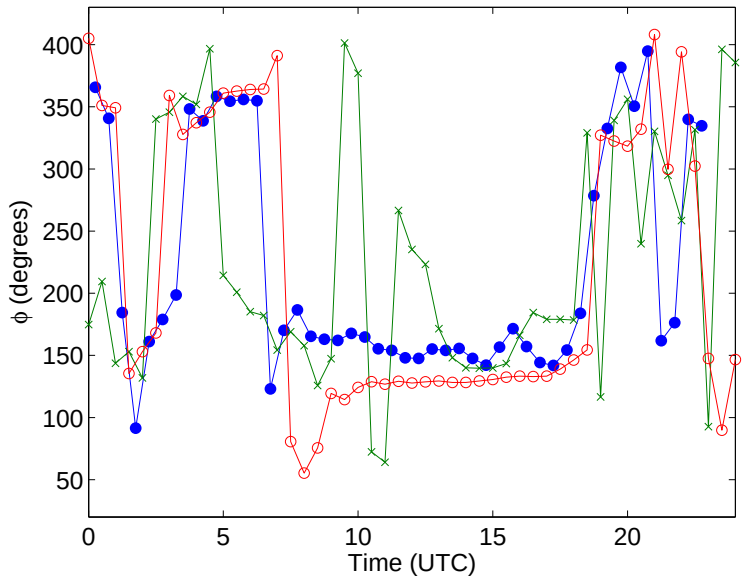

(b)

Figure 8.6: Surface data time series comparisons at Bosco di Sotto (site A1, valley floor) for (a) wind speed and (b) wind direction. —●— Observations at 28 m agl; —○— MOISLU; —×— REF

Site	Name	Location	Elev. asl	Meas. hgt. agl
A1	Bosco di Sotto	Valley floor (46.265 N, 9.012 E)	250 m	15.9, 28 m
B	Rored	Eastern slope (46.263 N, 9.031 E)	760 m	22, 28 m
C	Pian Perdascio	Western slope (46.238 N, 9.005 E)	340 m	5 m
E1	Roasco	Eastern slope (46.267 N, 9.037 E)	1060 m	2,12.7 m
E2	Monte Nuovo	Eastern slope (46.271 N, 9.036 E)	1030 m	16.8,22.7 m

Table 8.6: Surface station locations, shown in Fig. 8.3.

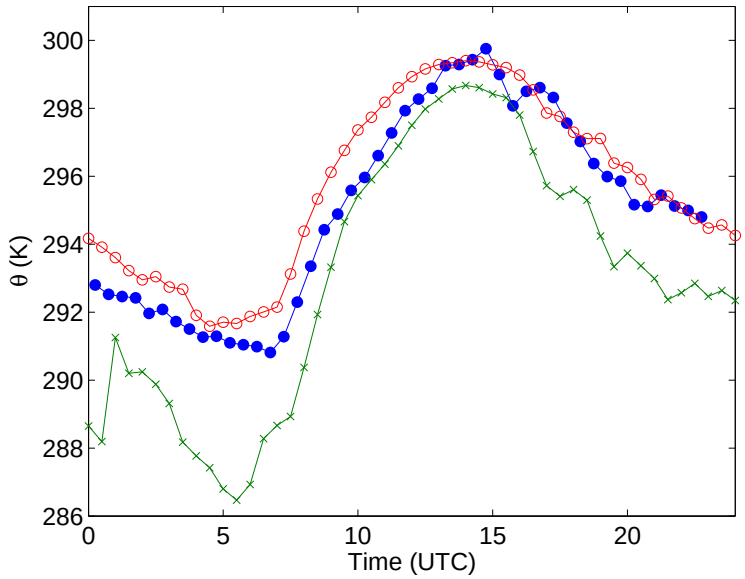

Figure 8.7: Surface potential temperature time series at Bosco di Sotto (site A1). —●— Observations at 28 m agl; —○— MOISLU; —×— REF

during the field campaign. The observations are compared to the REF and MOISLU results. During the first 6-7 hours on August 25, 1999, the dominant winds were down-valley (about 330°). Between 0600 and 0800 UTC (CET local daylight savings time = UTC + 2 hours), winds shift to up-valley (about 150°). Local sunrise is at approximately 0700 UTC at the valley floor, but is earlier on the east-facing slopes and in the Magadino Valley (see Fig. 8.3). Sunset is at approximately 1600 UTC, and the winds shift to down-valley starting at about 1800 UTC. The surface winds are generally weak at night and become stronger with the onset of the up-valley flow during the day.

The MOISLU predictions of the wind speed in Fig. 8.6 show that the onset of the up-valley winds is about 1 to 2 hours later than observed at 28 m agl at Bosco di

Sotto. This is significantly better than the REF simulations, where the delay in up-valley winds is 3-4 hours. The wind direction fluctuates a lot when the wind speed is weak, making comparisons with LES results difficult. Nevertheless, the surface wind direction and speed are quite well reproduced by the MOISLU results. The ARPS data are from the lowest model level, which for the horizontal winds and temperature is at $\Delta z_{min}/2$ (see Table 8.2). Comparison is usually made to the closest observation level, but there often appear to be surface layer effects, due to the plant canopy, that are not captured in the model. Thus, comparisons to the higher measurement level are often better. The results of De Wekker *et al.* (2004) showed a 2-hour delay in the onset of the up-valley winds and did not to capture the evening transition to down-valley winds. The most likely reason for the delayed transitions in the ARPS simulations is poor representation of surface soil conditions. Soil moisture and temperature control the heating and cooling of the surface, thus controlling the strength of along-valley and slope winds. Sensitivity tests in Section 8.6.1 confirm that changes in the soil moisture can significantly change the onset of valley wind transitions. Sensitivity to the soil temperature initialization was not as large, and was not investigated further. Figure 8.7 shows the evolution of the surface potential temperature at the same measurement location. Again we see significant improvement in the results from the MOISLU simulations compared to the REF results, particularly during the morning and evening hours.

The surface station observations at the valley floor provide a simple reference for evaluating the simulation results. However, Grell *et al.* (2000) advise that simulation results should be compared to several sites because the complex topography can lead to different wind transitions at different locations. Figures 8.8 and 8.9 show observed and simulated winds at surface stations at Pian Perdascio (site C, east-facing slope) and Monte Nuovo (site E2, west-facing slope) (see Fig. 8.3). These sites show quite good agreement for the MOISLU simulations compared to the REF results, particularly for the wind speed. Comparisons along the slopes are often difficult because of the effect of the plant canopy, and can be very sensitive to the exact location chosen; moving 100 m to the right or left can change the elevation by almost 100 m.

A more quantitative comparison can be obtained by examining the magnitude of

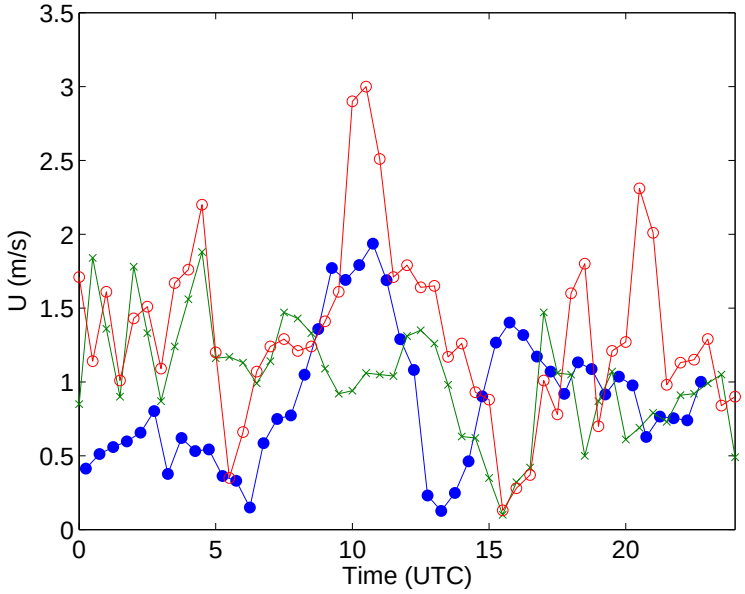

(a)

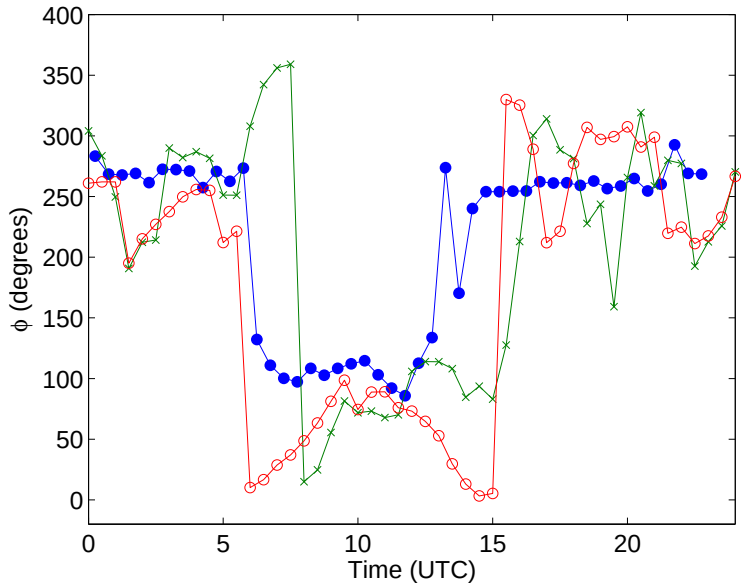

(b)

Figure 8.8: Surface data time series comparisons at Pian Perdascio (site C, on western slope) for (a) wind speed and (b) wind direction. —●— Observations at 5 m agl; —○— MOISLU; —×— REF

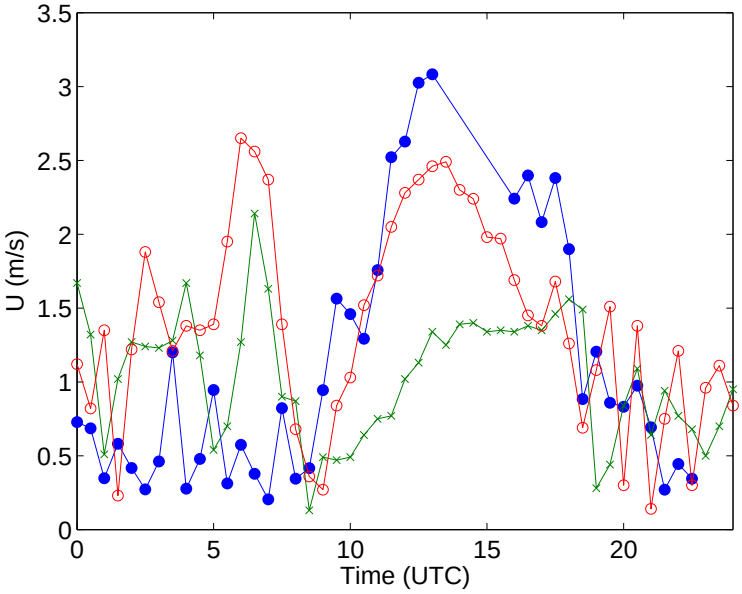

(a)

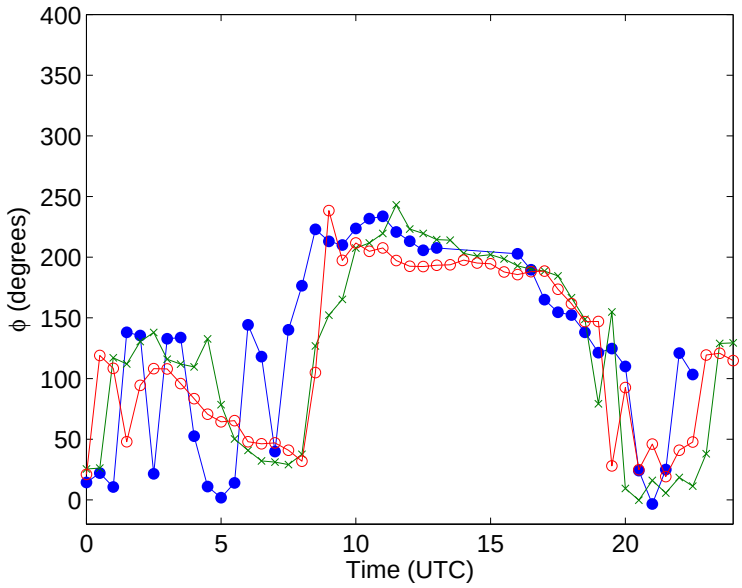

(b)

Figure 8.9: Surface data time series comparisons at Monte Nuovo (site E2, on eastern slope) for (a) wind speed and (b) wind direction. —●— Observations at 22.7 m agl; —○— MOISLU; —×— REF

differences between the observed and simulated results. Table 8.7 shows the root-mean-square errors (rmse) and mean errors (bias) for wind speed and direction and potential temperature at surface station A1, as well as a composite of the errors at three sites on the eastern slope (sites B, E1 and E2). The bias provides an indication of the average direction of deviation of the modeled from the observed data, whereas the rmse provides an estimate of the magnitude of the error. They are defined:

$$\text{bias} = \frac{1}{M}\sum_{j=1}^{M}\frac{1}{N}\sum_{i=1}^{N}(A_{i,j} - B_{i,j}) \tag{8.1}$$

$$\text{rmse} = \sqrt{\frac{1}{M}\sum_{j=1}^{M}\frac{1}{N}\sum_{i=1}^{N}(A_{i,j} - B_{i,j})^2} \tag{8.2}$$

where M is the number of time steps, N is the number of grid points, and $A_{i,j}$ and $B_{i,j}$ are the datasets being compared. Overall, the errors between simulated (MOISLU) and observed fields in the Riviera Valley are quite small (e.g. less than 1 K for potential temperature), especially when compared to the results of other typical simulations. Zängl *et al.* (2004) found surface potential temperature rmse values ranging from 2.3 to 4.4 K and bias values from -0.2 to -4.0 K for 1 km resolution simulations in the Rhine Valley. Their rmse and bias values were for a nine-hour period, whereas ours are for 24 hours and for 350 m resolution. The MOISLU results significantly reduce all the errors except the wind direction bias, where the REF results exhibited more fluctuations and hence a lower overall bias.

8.4.2 Boundary layer evolution

The vertical structure of the atmosphere, as measured by radiosondes, reflects important features of the flow not captured by surface station observations. Figures 8.10a and 8.10b compare the REF and MOISLU simulated potential temperature, wind speed, wind direction, and specific humidity, with radiosonde data obtained at Bosco di Sotto (site A1). The lowest 6 km above the ground are shown. The temperature structure of the atmosphere early in the morning (0739 UTC) is characterized by a stable layer below 1.5 km asl, a very stable layer between 1.5 and 2.2 km asl, and a mixed or slightly stable layer above, extending to about 4.5 km asl. The strong

	Site A1		Sites B, E1, E2	
	REF	MOISLU	REF	MOISLU
θ rmse (K)	3.20	0.69	1.12	0.85
θ bias (K)	-3.04	-0.41	-0.53	0.04
U rmse (m/s)	1.47	1.28	1.13	1.20
U bias (m/s)	-0.53	0.57	-0.35	0.11
ϕ rmse (deg)	86.42	63.21	71.13	67.28
ϕ bias (deg)	-1.50	-11.05	-1.97	-9.01

Table 8.7: Root-mean-square errors and mean errors (bias) for potential temperature (θ), wind speed (U), and wind direction (ϕ), for simulations compared to observations at Bosco di Sotto (site A1), using average of 15.9 and 28 m values, and at three sites on the eastern slope (sites B, E1 and E2), using data from a variety of measurement heights.

capping inversion at about 2 km asl is also present in the synoptic flow and is likely due to large-scale subsidence; for example, soundings in Milan, well outside of the Alps, also exhibit this inversion. Typical valley inversion layer breakup theory predicts that the mixed layer will continue to grow while there is surface heating, as on such a "convective" day Whiteman (2000), and will eventually extend over the entire valley depth. The radiosonde observations, however, show only growth to a 500-800 m mixed layer thickness near the ground at 1208 and 1508 UTC. The rest of the valley atmosphere remains stable. That the evolution of the vertical structure is atypical can be seen further by the sounding at 1508 UTC, where the surface temperature has increased by another degree, but the mixed layer depth has decreased. This indicates the presence of other processes acting to inhibit mixed layer growth, as also discussed by Weigel & Rotach (2004).

Figure 8.11 shows the observed potential temperature soundings together, making it clear how the atmosphere warms overall, but remains stable throughout the day above 700 m asl. The profiles exhibit a pattern similar to "Pattern 2" inversion layer destruction described by Whiteman (1982), but they do not fit the description completely. Pattern 2 includes convective layer growth at the surface, with subsidence warming from above which compensates for the air removed by up-slope winds. In the Riviera Valley, however, the potential temperature profiles change slope near the top of the inversion instead of simply sinking downward. (See page 110 of (De Wekker, 2002) for a sketch of the potential temperature evolution.) Growth from the

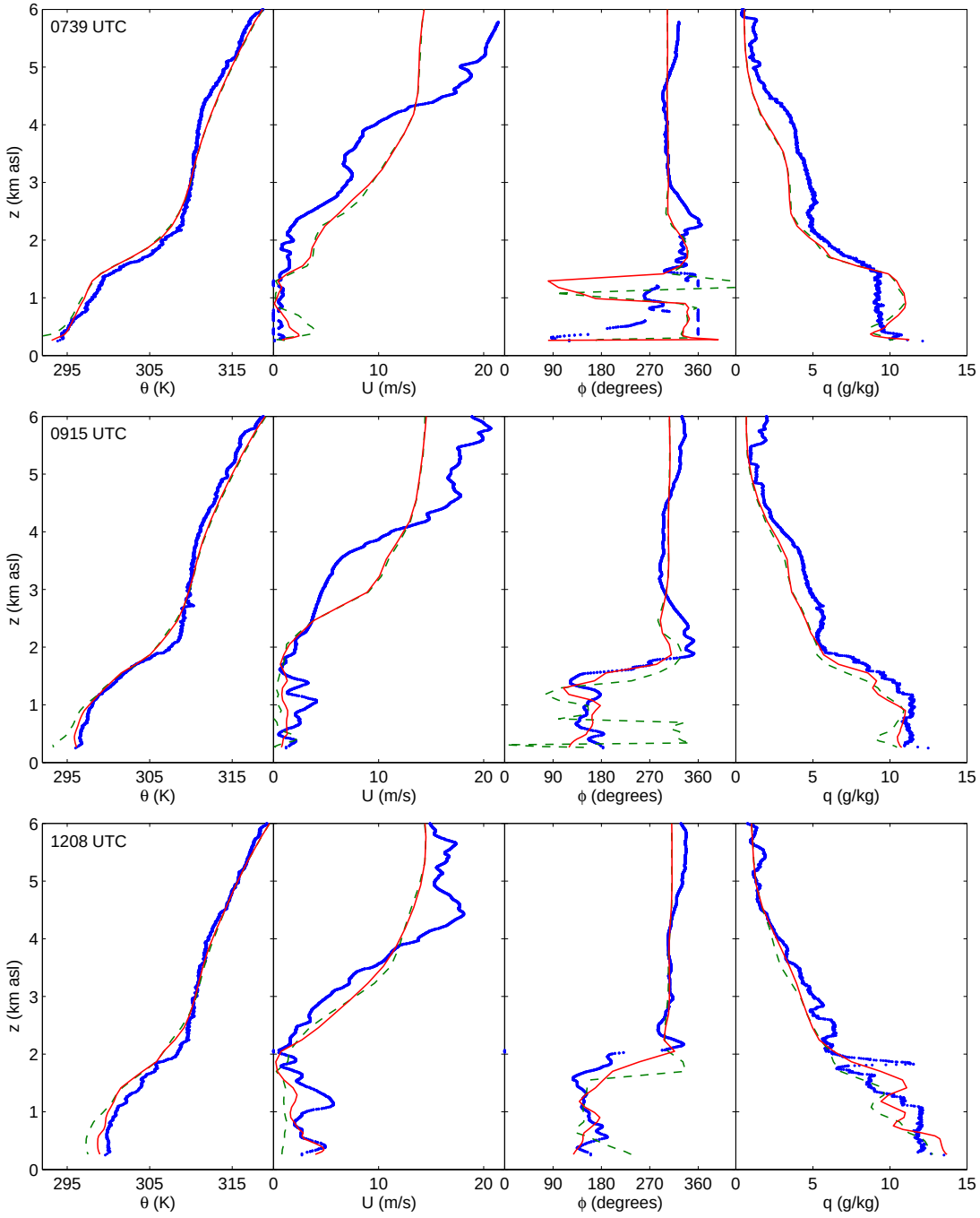

Figure 8.10a: 0739, 0915, and 1208 UTC radiosonde observations compared to simulations at Bosco di Sotto (site A1) of potential temperature, wind speed, wind direction, and specific humidity on 25 August, 1999. ····· Observations; —— MOISLU; - - - - REF

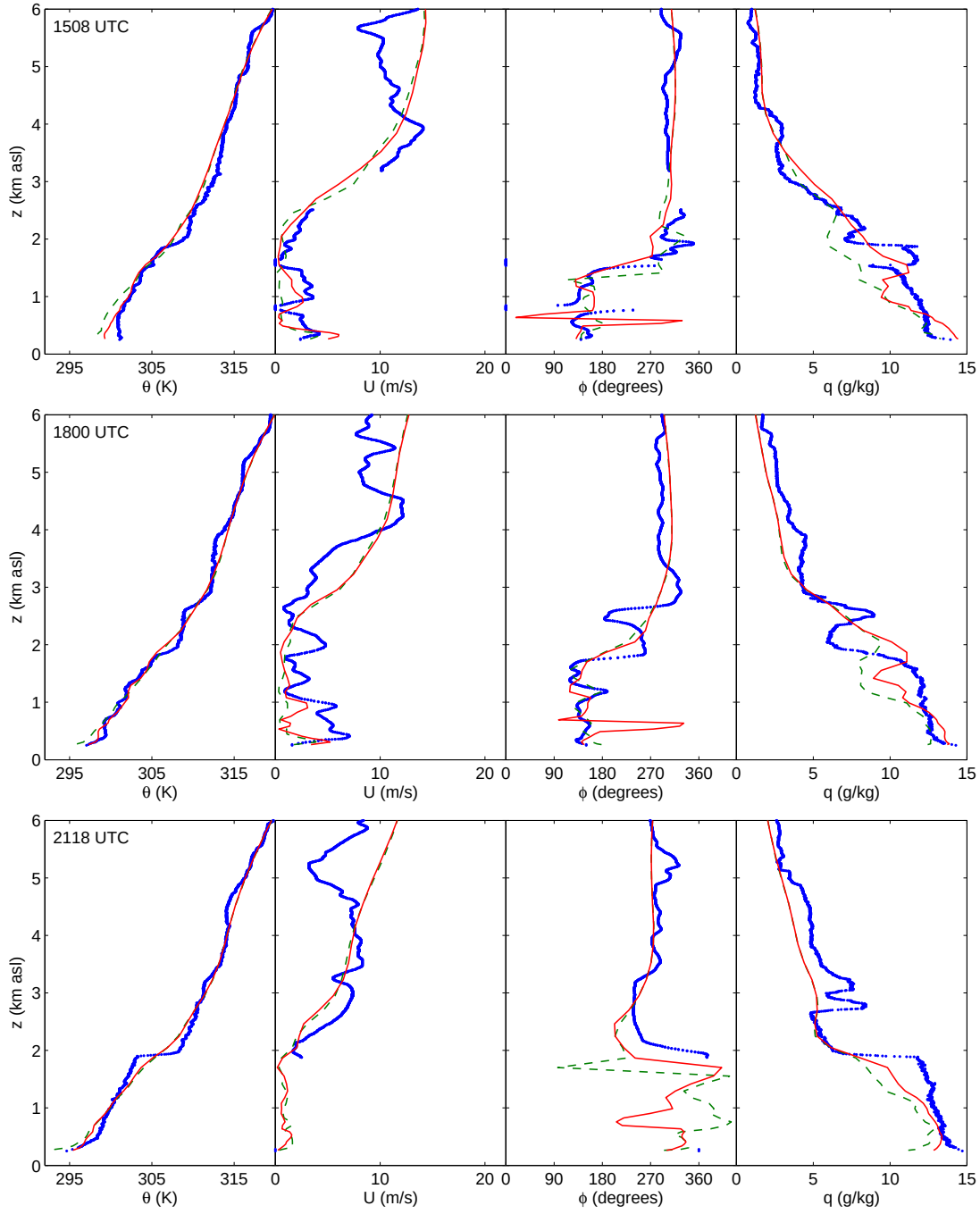

Figure 8.10b: 1508, 1800, and 2118 UTC.

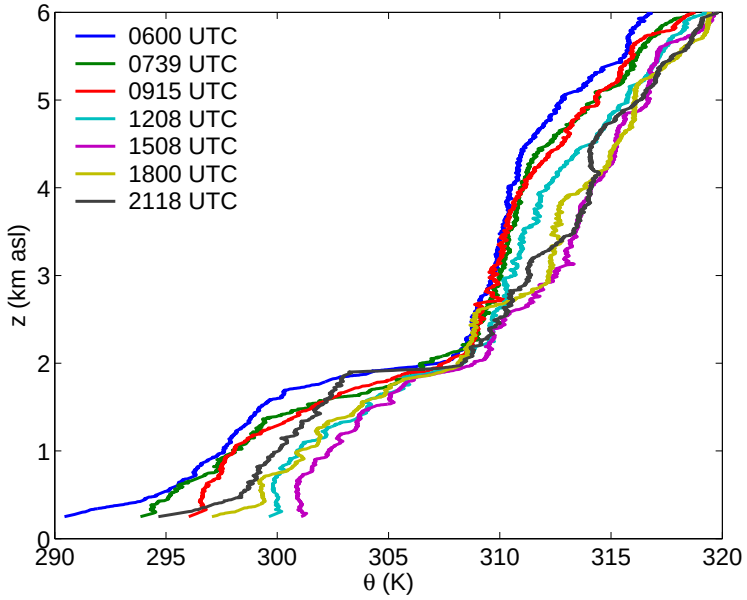

Figure 8.11: Potential temperature radiosonde observations at Bosco di Sotto.

surface is also inhibited, as previously discussed. Thus, in the Riviera the destruction of the stable layer is not complete. One reason for the persistence of the stable layer throughout the day may be the presence of a strong secondary circulation and warming due to subsidence in the valley; this is particularly evident on August 21 and 22, and is discussed further in Weigel & Rotach (2004) and in the companion paper to this chapter (Weigel *et al.*, 2004*b*).

The observed wind profiles corroborate the measurements at the surface stations which show the increased strength of the winds during the up-valley wind period in the afternoon. Above the capping inversion, the wind speeds increase significantly and are consistently in the down-valley or north-northwest direction. These strong winds move the sounding balloon away from its starting (x, y) location. The balloon rises at about 1 m/s and thus provide a time evolving profile, capturing fluctuations in the atmosphere as it rises; observation errors in soundings also increase with height. The simulation data profiles represent the hour or half hour closest to the balloon ascent time, interpolated horizontally to the balloon launch location.

The agreement of the MOISLU results with the observed profiles in Figs. 8.10a and 8.10b is excellent, much better than the REF results which do poorly near the ground. In particular, the REF simulations do not reproduce the mixed layer near the

ground that was observed at 0915 UTC. The wind direction predicted by REF also fails to exhibit the observed up-valley flow at 0915 and even does not do well at 1208 UTC near the surface. Both simulations fail to match the observed surface warming during the afternoon, particularly at 1508 UTC. The wind speed profiles are especially difficult to compare because observed winds depend on fluctuations of the balloon's position as it rises. We cannot expect the LES results to provide exactly the same instantaneous profiles, but rather to represent the "mean" or resolved-scale structure (Germano, 1996). Another significant discrepancy between the observations and the simulation results is found at 2118 UTC, when the inversion at 2 km asl sharpens; the simulations do not have enough resolution to resolve this feature in the temperature or humidity profiles. Wind data at 2118 UTC are missing near the surface, but the simulations indicate that the winds have reversed to down-valley, in agreement with the surface station time series observations. The results of De Wekker *et al.* (2004) showed good surface temperature agreement at 0915, 1208 and 1508 UTC, but further above the ground the modeled profiles were too smooth and did not compare as well with observations as our MOISLU results. Specific humidity is also better reproduced in our simulations. It is difficult to compare wind predictions as De Wekker *et al.* (2004) only presented vector profiles.

Table 8.8 shows the rmse and bias for the MOISLU simulations for each profile, including data up to about 6 km asl; the errors are quite small (e.g. ~ 2 m/s for wind speed) and confirm the good agreement between simulations and observations seen visually. Gohm *et al.* (2004), for example, found wind speed rmse errors from vertical profiles of about 5 m/s and mean errors of $\pm$ 1.5 m/s for simulations in the Alps at 800 m resolution. Table 8.9 compares the overall rmse and bias for all sounding times for the MOISLU and REF simulations.

8.5 Flow structure and transitions

Given the excellent agreement of the MOISLU simulations with the surface station and sounding observations at Bosco di Sotto, we proceed to investigate the three-dimensional structure of the valley atmosphere.

	0001	0600	0739	0915	1208	1508	1800	2118	All
θ rmse (K)	1.17	1.26	0.82	0.66	1.06	0.99	0.56	0.75	0.94
θ bias (K)	0.21	0.48	-0.38	-0.34	-0.80	-0.77	0.00	-0.15	-0.22
U rmse (m/s)	1.94	NA	2.35	1.99	1.75	1.81	2.77	2.29	2.04
U bias (m/s)	-0.05	NA	0.93	-0.38	-0.41	-0.09	-0.90	0.20	-0.12
ϕ rmse (deg)	38.00	NA	65.88	31.74	24.26	61.29	54.09	23.96	45.73
ϕ bias (deg)	-16.33	NA	-7.10	-11.30	-4.27	-8.71	16.13	-10.36	-5.99
q rmse (g/kg)	1.02	1.16	1.15	0.93	1.24	1.21	1.33	1.26	1.17
q bias (g/kg)	0.28	-0.35	-0.15	-0.79	0.04	0.08	-0.06	-0.95	-0.24

Table 8.8: Root-mean-square errors and mean errors (bias) for potential temperature (θ), wind speed (U), wind direction (ϕ), and specific humidity (q), for each radiosonde launch for MOISLU. Wind observation data were not available (NA) for 0600 UTC. ARPS data were taken from output at nearest half hour.

	REF	MOISLU
θ rmse (K)	1.43	0.94
θ bias (K)	-0.73	-0.22
U rmse (m/s)	2.29	2.04
U bias (m/s)	-0.35	-0.12
ϕ rmse (deg)	55.47	45.73
ϕ bias (deg)	3.96	-5.99
q rmse (g/kg)	1.45	1.17
q bias (g/kg)	-0.75	-0.24

Table 8.9: Root-mean-square errors and mean errors (bias) for potential temperature (θ), wind speed (U), wind direction (ϕ), and specific humidity (q), for all radiosonde launches for MOISLU and REF simulations.

8.5.1 Along-valley wind and potential temperature structure

Figures 8.12a-8.12d show the valley winds in a planar cross-section at 500 m asl. The data are from the 150 m grid which covered only the southern half of the valley. At 0600 UTC and 0800 UTC, valley winds are primarily down-valley. Vertical velocities are near zero throughout most of the domain, but a narrow up-slope flow region is clearly evident along the east-facing slopes at 0800 UTC. By 1100 UTC, the flow has shifted to up-valley and is strongest on the east side of the valley. This is due to the curvature of the flow entering from the Magadino Valley to the south. Up-slope winds are evident along both walls of the valley at this time. The up-valley jet generates waves further north, as seen from the sign changes in vertical velocity. This structure is also visible in the along-valley vertical cross section shown later in Fig. 8.13b. As

the up-valley flow strengthens, these waves disappear (by 1300 UTC). One vertical velocity feature persists from 1100 to 1600 UTC: at the valley entrance, air sinks on the western side of the valley and rises on the eastern side; this is likely orographically induced as the air is forced over the slopes as it curves into the Riviera. Further up the valley, where the up-valley jet is on the east side, there is a region of strong circulation with sinking air on the east side of the valley evident from 1100 to 1600 UTC. Even further north, there is evidence of a classical valley circulation (1300 UTC), with air rising along both slopes, and sinking in the middle of the valley. By late afternoon (1600 UTC), the up-slope winds persist only on the sunlit west-facing slopes. The transition to down-valley flow occurs gradually. Large horizontal eddies develop at 1900 UTC, where flow on the east side of the valley is up-valley, and flow on the opposite side is down-valley. By 2100 UTC the down-valley flow is accompanied by shallow down-slope winds on both sides of the valley.

Figures 8.13a-8.13d show potential temperature contours on a vertical plane along the valley axis, at the middle of the valley, for the same times as Figs. 8.12a-8.12d. The slice through the valley axis is not exactly centered along the valley floor because the valley is not perfectly straight (see Fig. 8.3). Wind vectors, projected on the plane, are included to show the general valley flow at each time. The north end of the valley is to the left, so that down-valley winds go from left to right. Early in the morning (0600 and 0800 UTC), the stratification is quite uniform along the length of the valley. By 0800 UTC, the northern end of the valley has warmed slightly. At 1100 and 1300 UTC, we see what appears to be a mass of potentially cooler air propagating up the valley axis. High above the valley floor, the synoptic winds persist in the down-valley direction. The internal wave structures discussed earlier (Fig. 8.12b) are visible. While the cooler air is advected up the valley, the valley atmosphere also warms considerably through the afternoon (1600 UTC) due to other processes (see below). At a given elevation (within the valley atmosphere), the potential temperature is warmer to the north. Between 1900 and 2100 UTC, the valley winds shift to down-valley, the valley cools, and the stratification again becomes more uniform along the valley axis. Detailed analysis of the valley heat budget derived from the ARPS results is given by Weigel *et al.* (2004*b*); the budgets extracted from observation data are given by Weigel & Rotach (2004). Both analyses delineate the delicate balance that exists between the cooling effects of up-valley advection and the

heating due to subsidence, i.e. vertical advection. These processes combine to give a net heating effect during the day, as seen in Figs. 8.13a-8.13d.

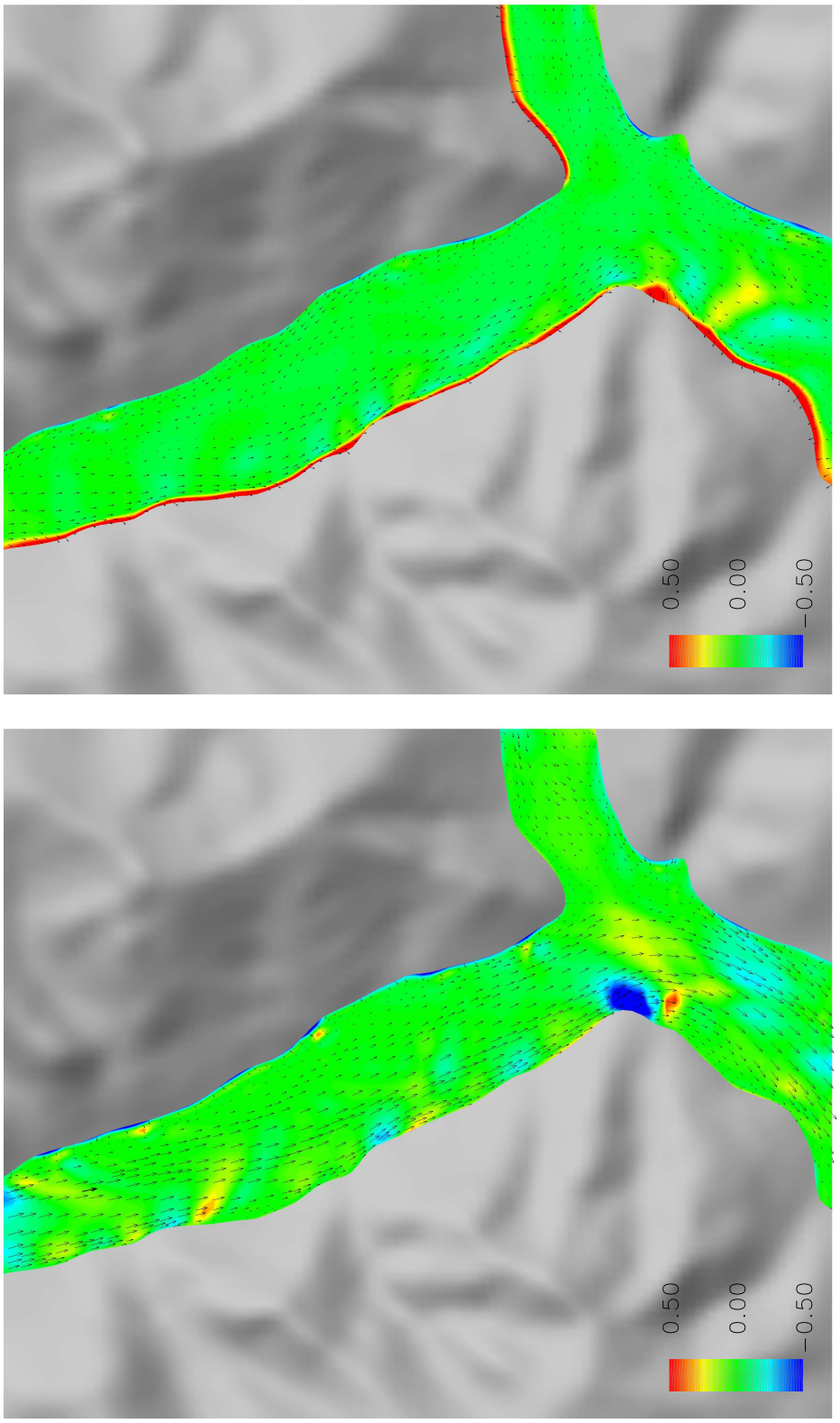

Figure 8.12a: 0600 UTC and 0800 UTC. Along-valley winds (vectors) and vertical winds (m/s, shaded: blue (down), red (up)) from the 150 m grid, at 500 m asl. Vectors are not uniformly spaced due to interpolation, and not all vectors shown.

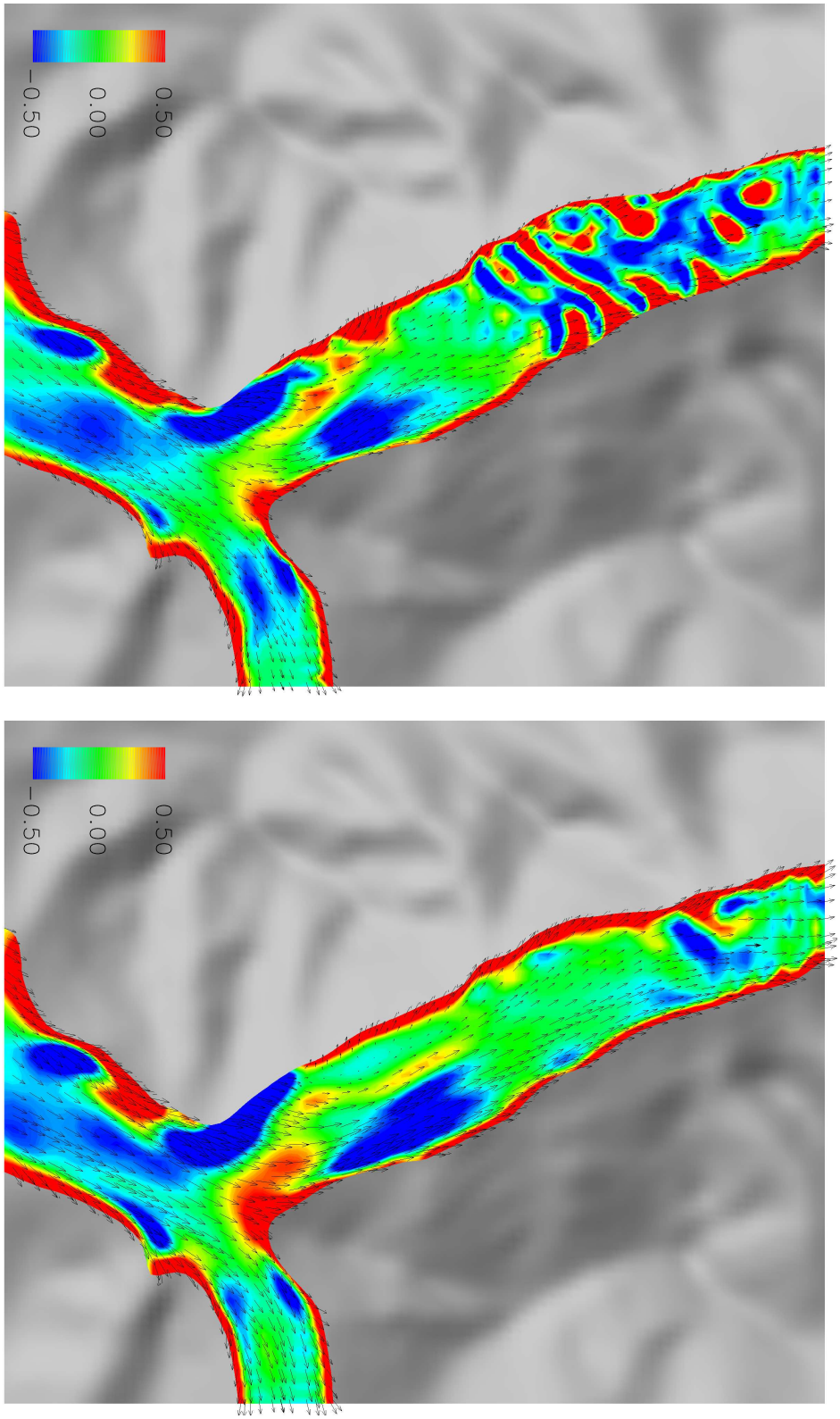

Figure 8.12b: 1100 UTC and 1300 UTC

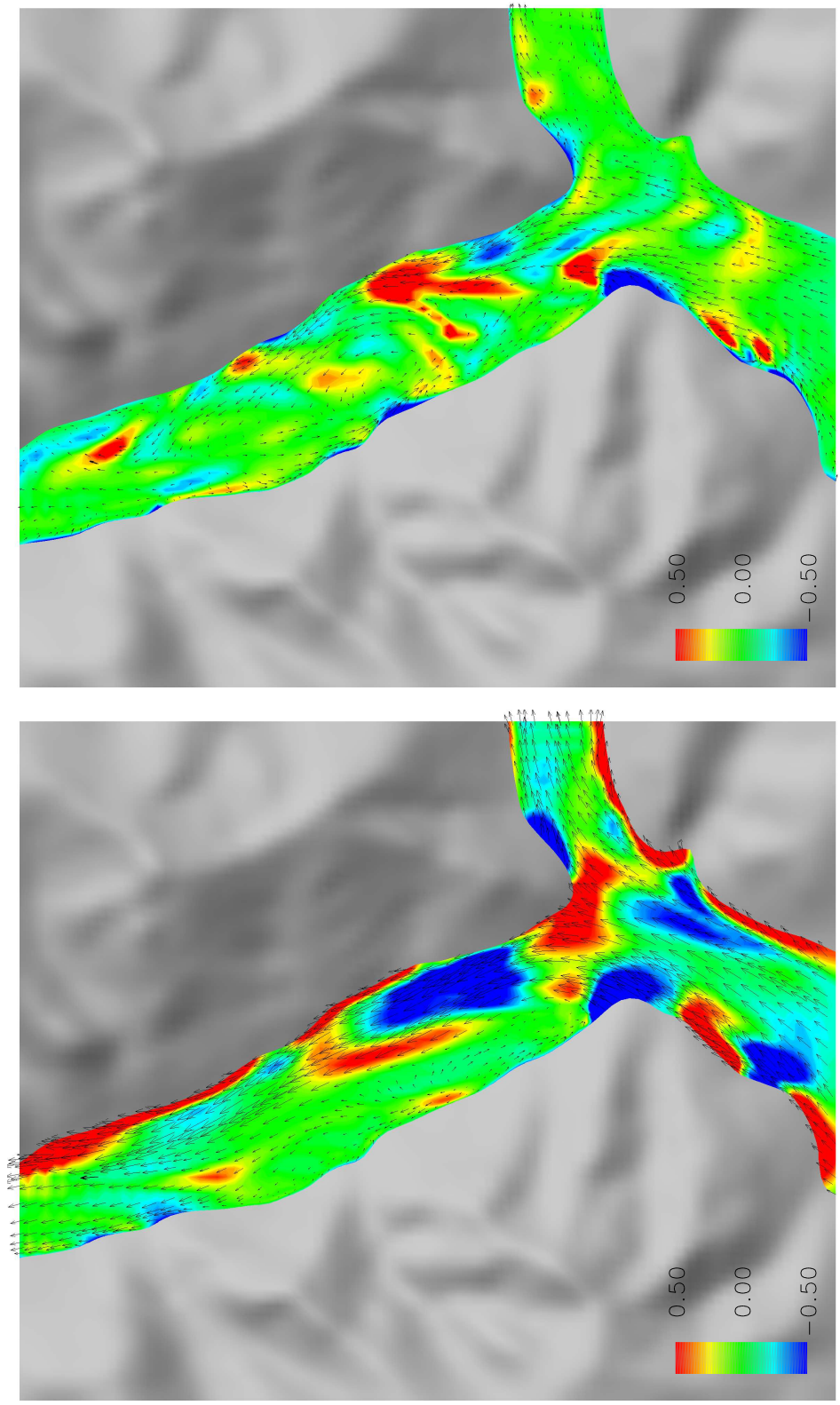

Figure 8.12c: 1600 UTC and 1900 UTC

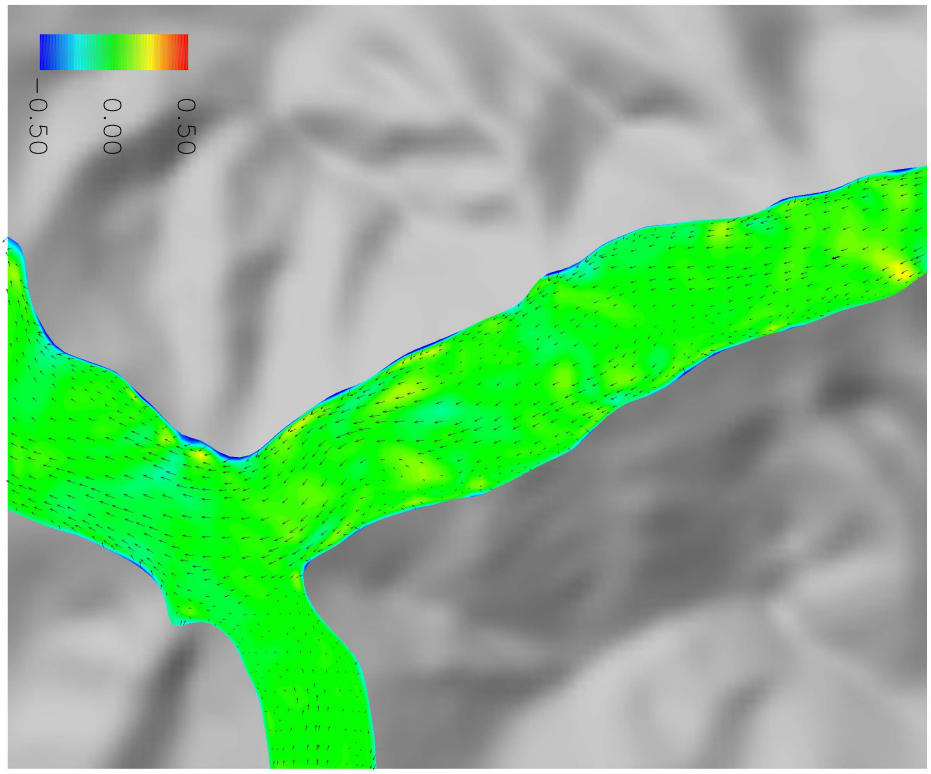

Figure 8.12d: 2100 UTC

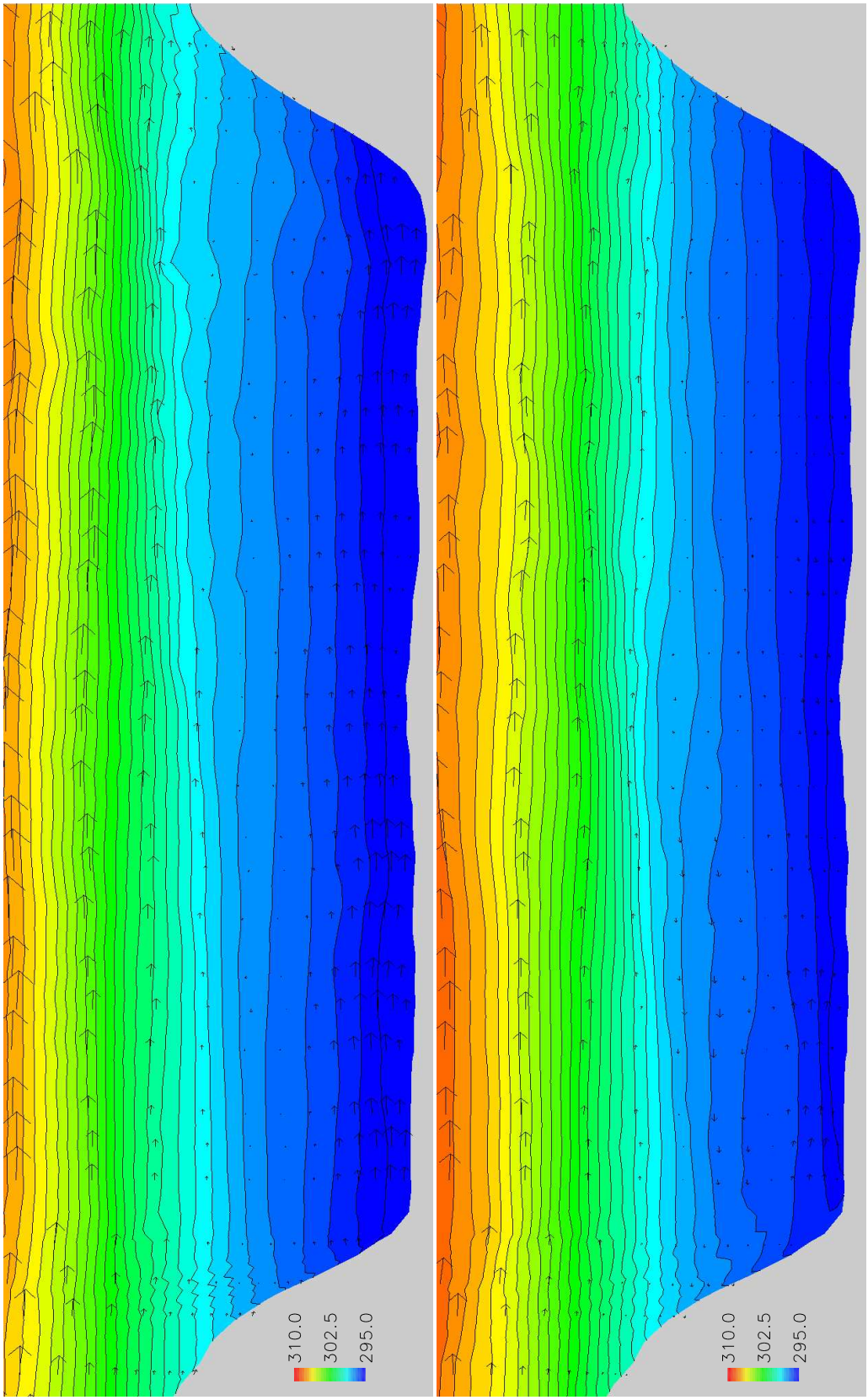

Figure 8.13a: 0600 UTC and 0800 UTC. Valley winds (vectors) and potential temperature (K, shaded) in a vertical plane (left side is north, right side is south) along the valley axis. Plot axes are stretched so the valley is not to scale. Vectors not uniformly spaced, and not all vectors shown.

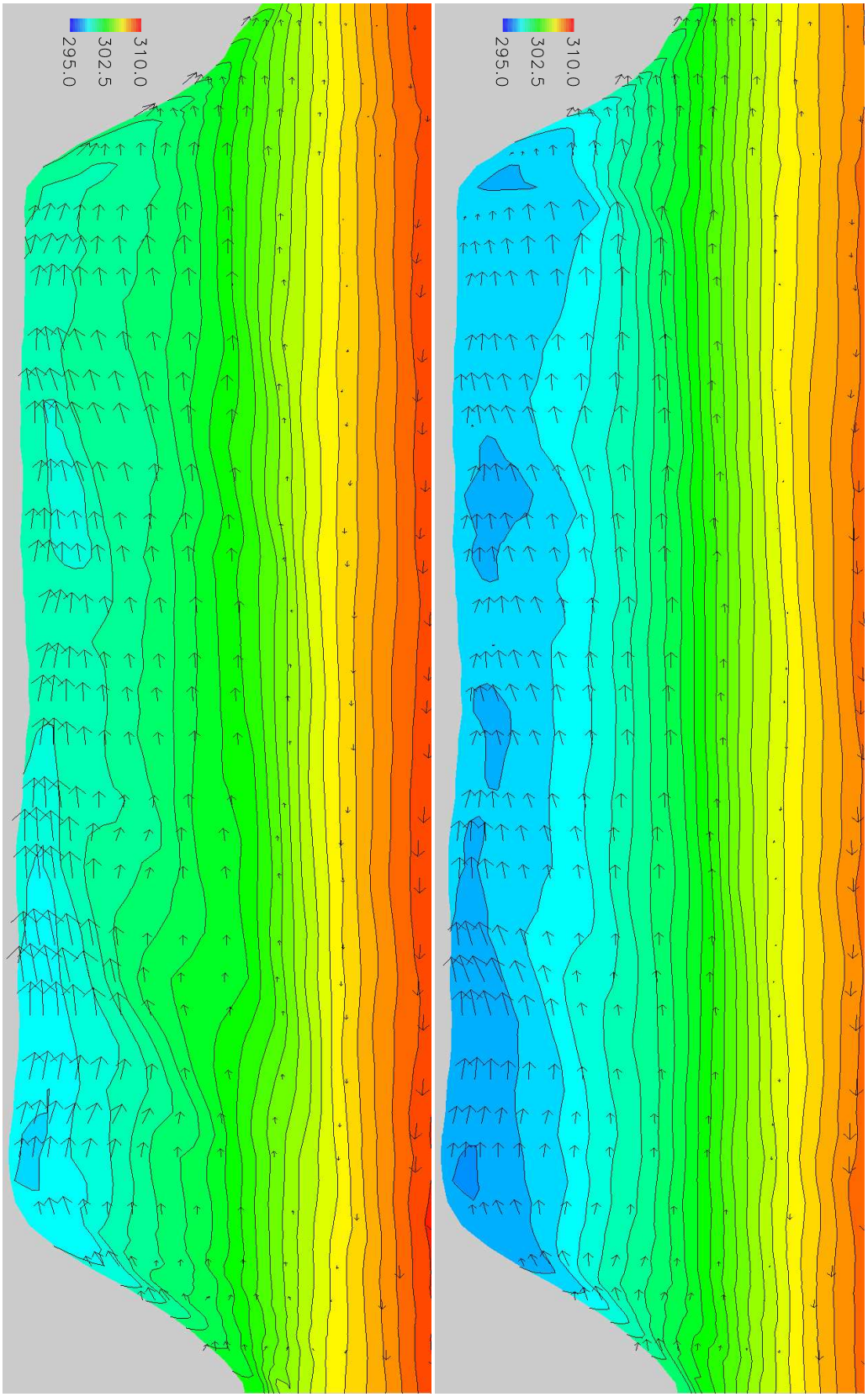

Figure 8.13b: 1100 UTC and 1300 UTC

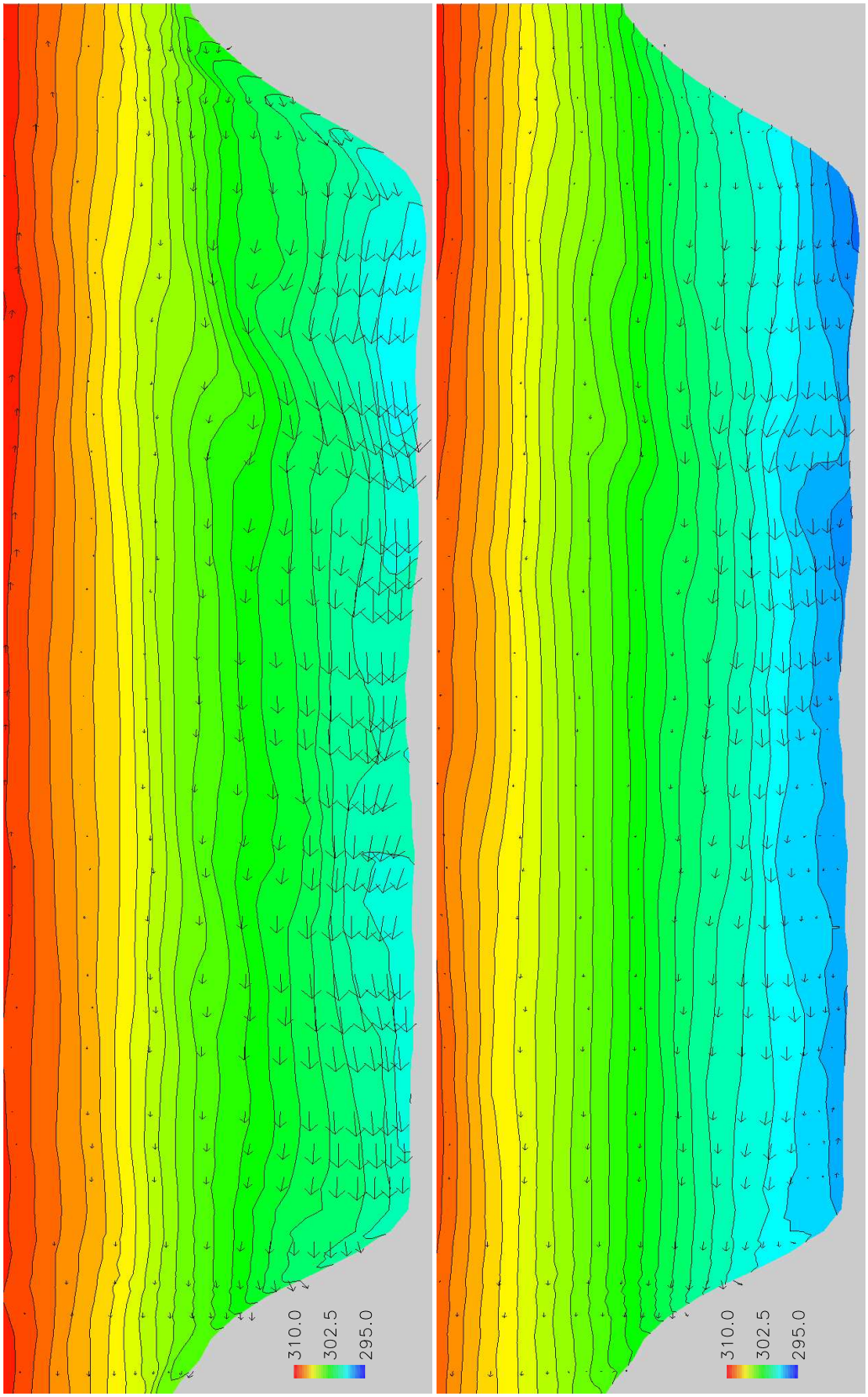

Figure 8.13c: 1600 UTC and 1900 UTC

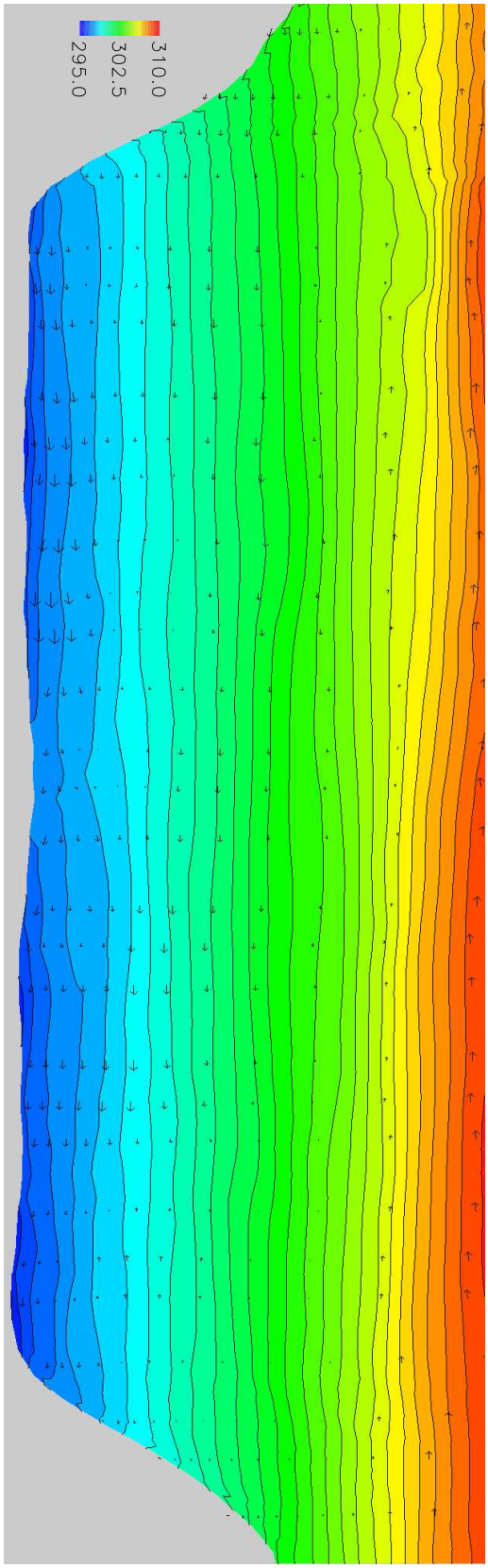

Figure 8.13d: 2100 UTC

8.5.2 Cross-valley wind structure

Figures 8.14a-8.14g show vertical cross sections perpendicular to the valley axis (at 29.5°). This cross section is placed slightly south of site A1 (see Fig. 8.3) and the available flight data to capture the secondary circulation better. Comparisons to flight data at the cross-section through A1 are given later in Fig. 8.15. Contours of along-valley winds (rotated 29.5° to be aligned with the valley) are shown together with vectors of the cross-valley winds (perpendicular to the valley axis). At 0800 UTC, down-valley winds dominate the core valley flow. Upslope winds can be seen only on the sunlit east-facing slope, as in Fig. 8.12a. By 1100 UTC, both valley walls are well-lit, producing significant up-slope winds on both sides. The core valley wind has also shifted to up-valley, and a strong cross-valley circulation is observed. The winds on the east slope are down-slope above the surface, a consequence of the clockwise secondary circulation. This circulation is generated by a pressure gradient formed when the up-valley core flow is shifted to the right as it enters from the Magadino Valley (see Fig. 8.12b). The secondary circulation is also evident in the observation data near the southern valley entrance (Weigel & Rotach, 2004). Further up the valley, the circulation diminishes (see Fig. 8.12b-8.12c), indicating that it is not due to a lid-driven cavity effect (induced by shear at the mountain tops), but rather by the incoming up-valley jet. The west-facing slope continues to receive direct sunlight, so up-slope winds persist as late as 1600 UTC, while weak down-slope winds begin along the east-facing slope. After 1600 UTC, the up-valley jet, and hence the secondary circulations weaken. Later in the evening at 2100 UTC, both sides have weak down-slope winds and the valley flow has shifted to the down-valley direction as well.

The simulations also agree quite well with aircraft observation data. Figure 8.15 compares the aircraft data and the simulation results (from a cross section passing through site A1) at approximately 1300 UTC. Both show the presence of a shifted up-valley jet of similar structure and magnitude.

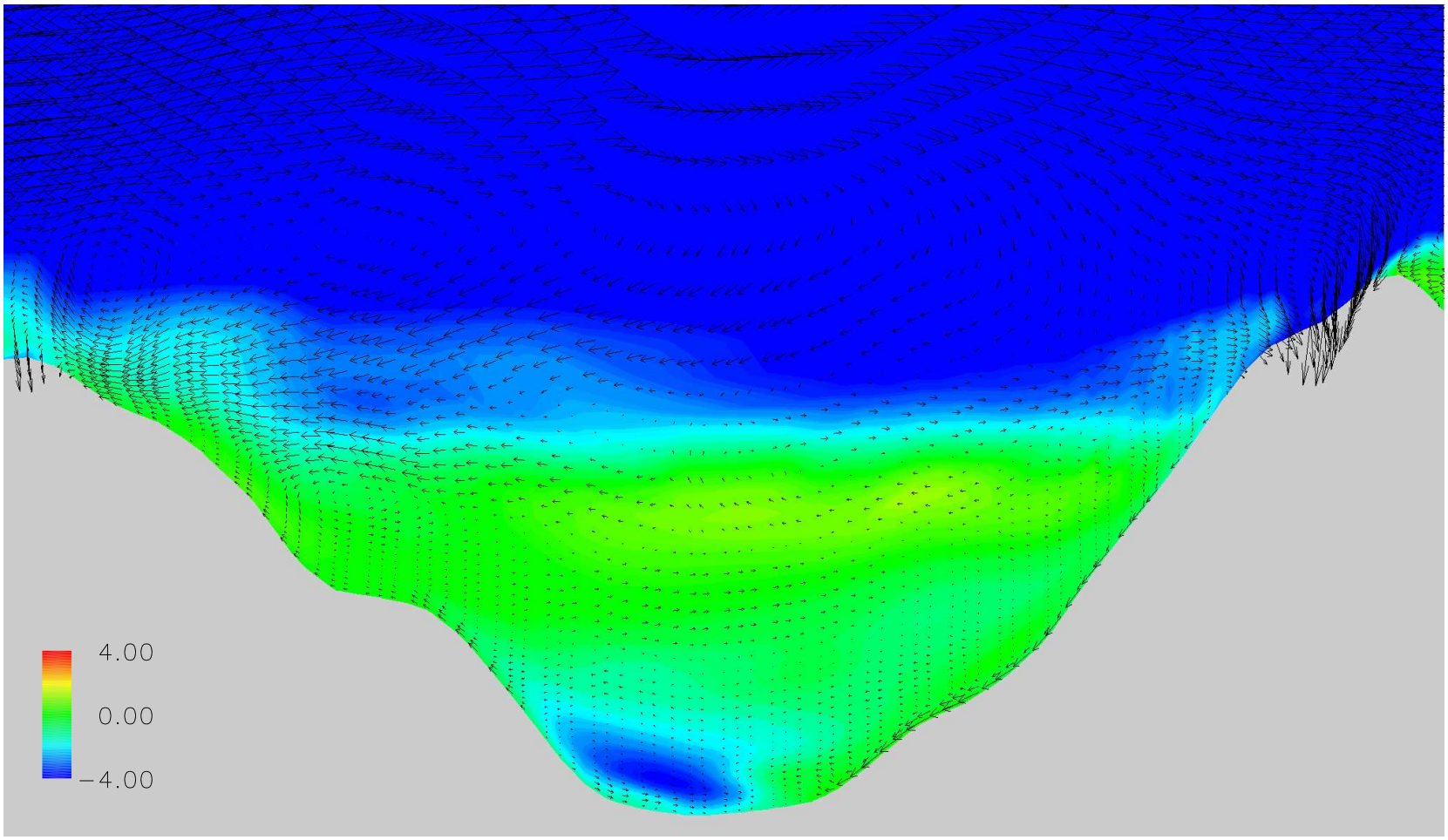

Figure 8.14a: 0600 UTC. Vertical cross-section of cross-valley winds (vectors) and along-valley winds (shaded: blue (down-valley), red (up-valley)) from the 150 m grid. Vectors are not uniformly spaced, and not all vectors shown. Plot axes are stretched so the valley is not to scale.

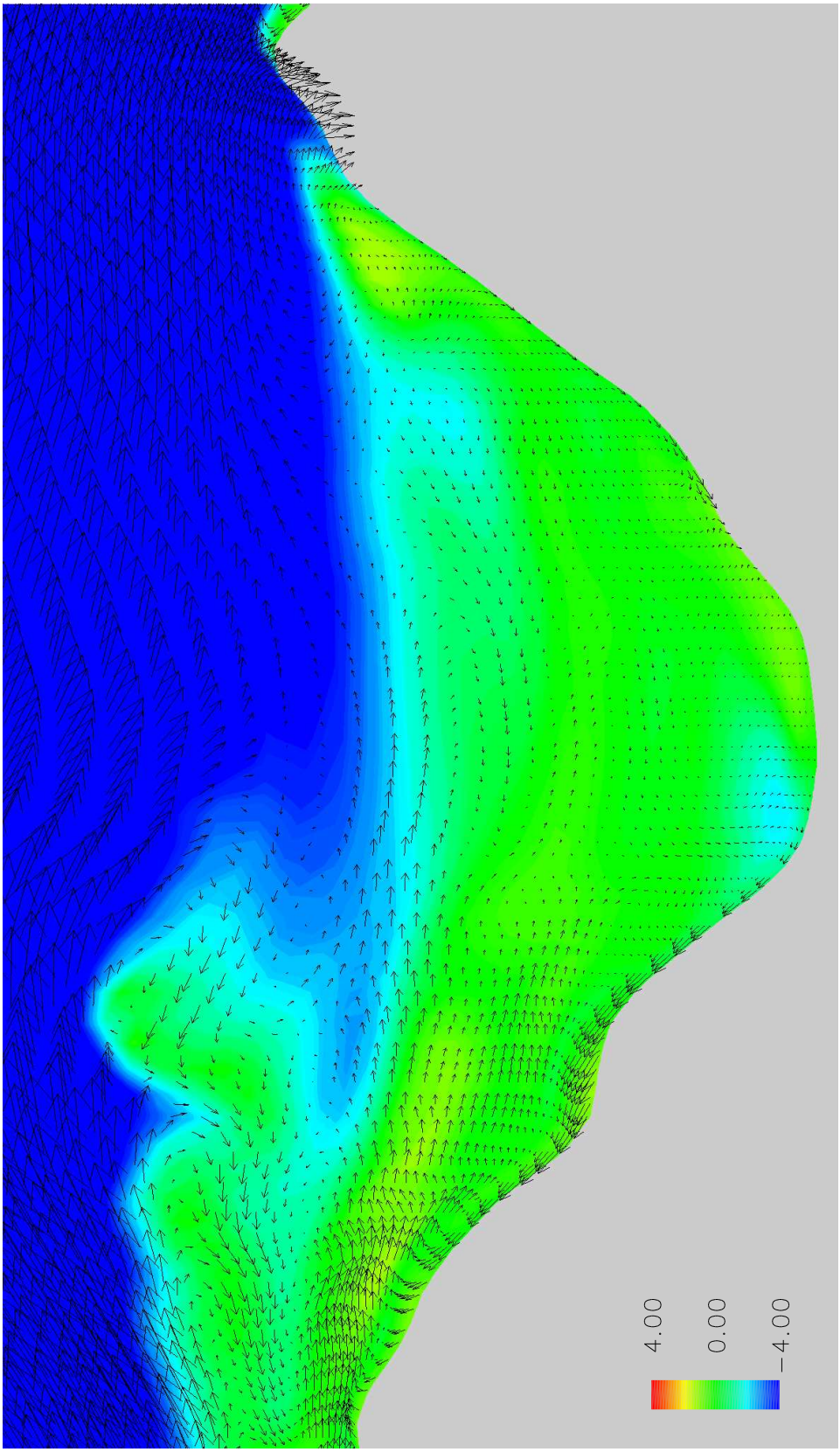

Figure 8.14b: 0800 UTC

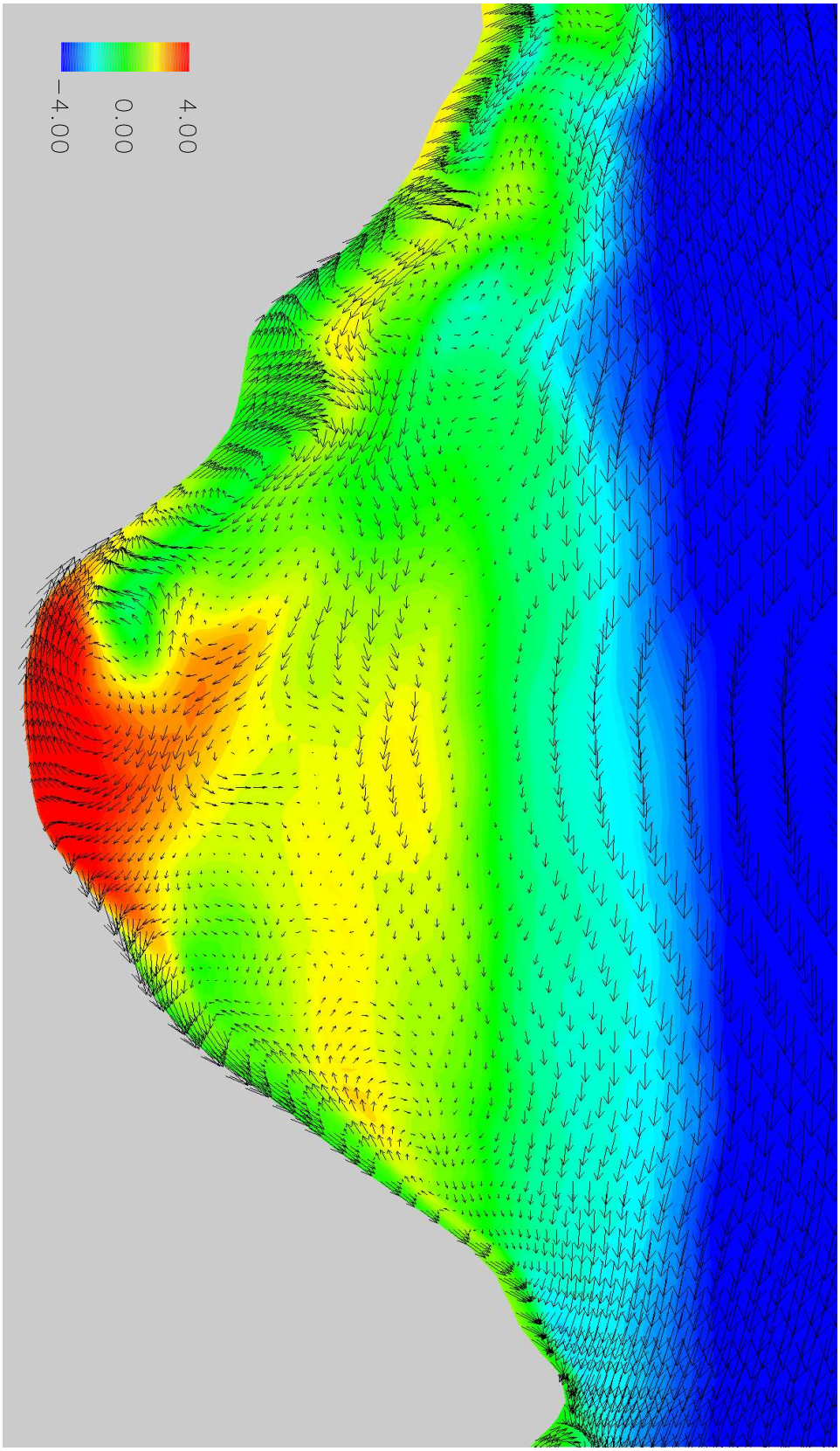

Figure 8.14c: 1100 UTC

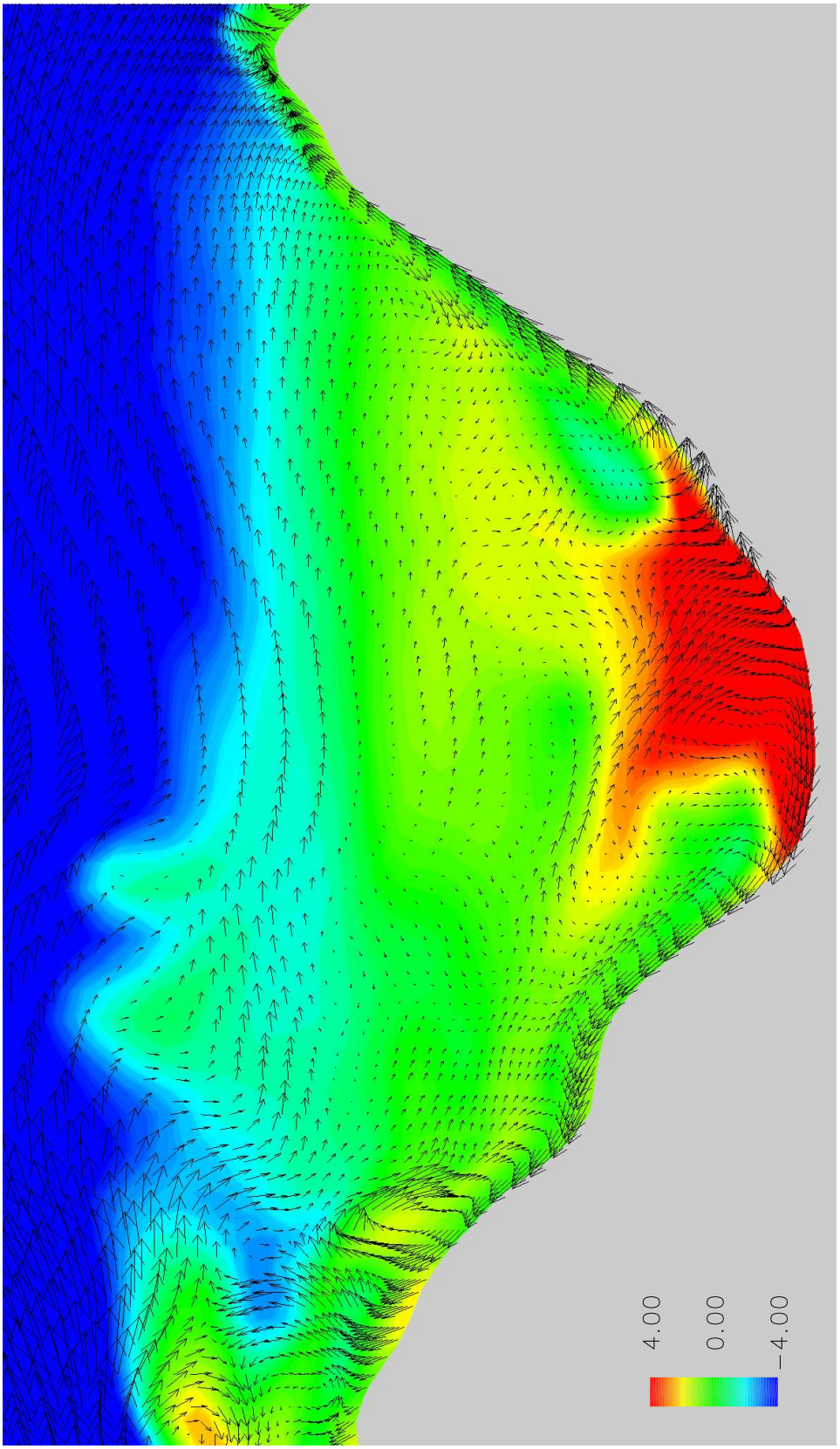

Figure 8.14d: 1300 UTC

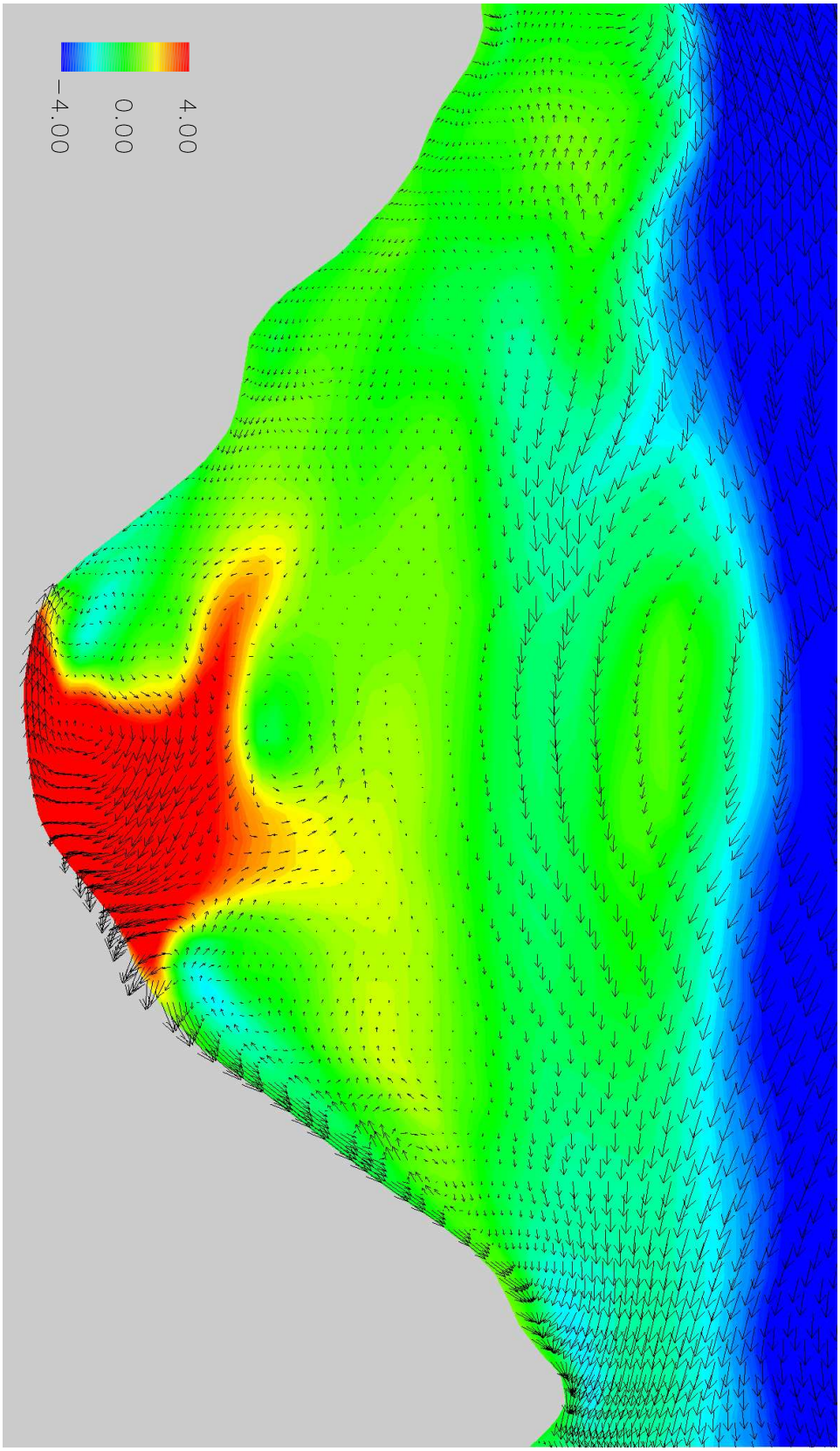

Figure 8.14e: 1600 UTC

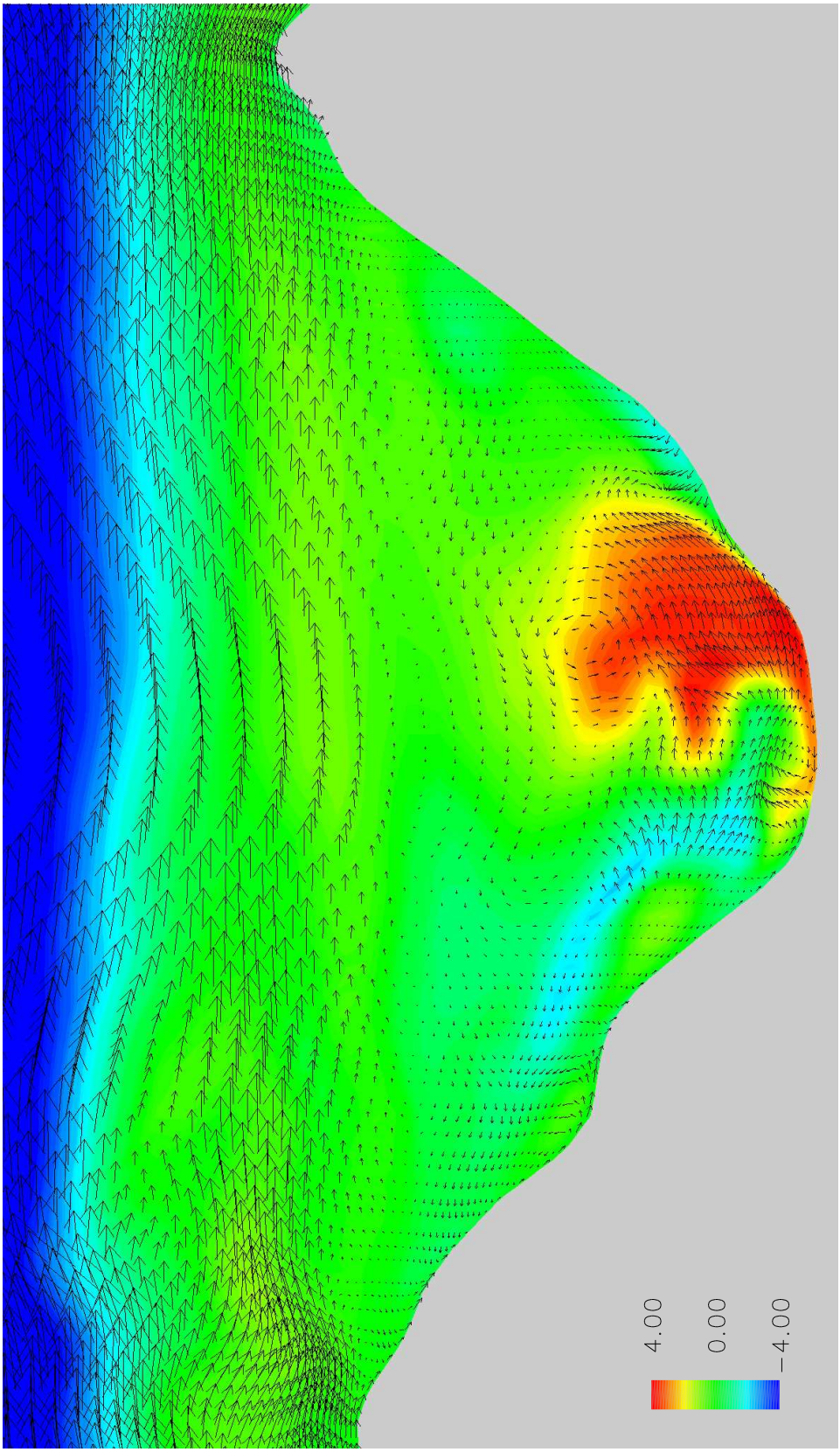

Figure 8.14f: 1900 UTC

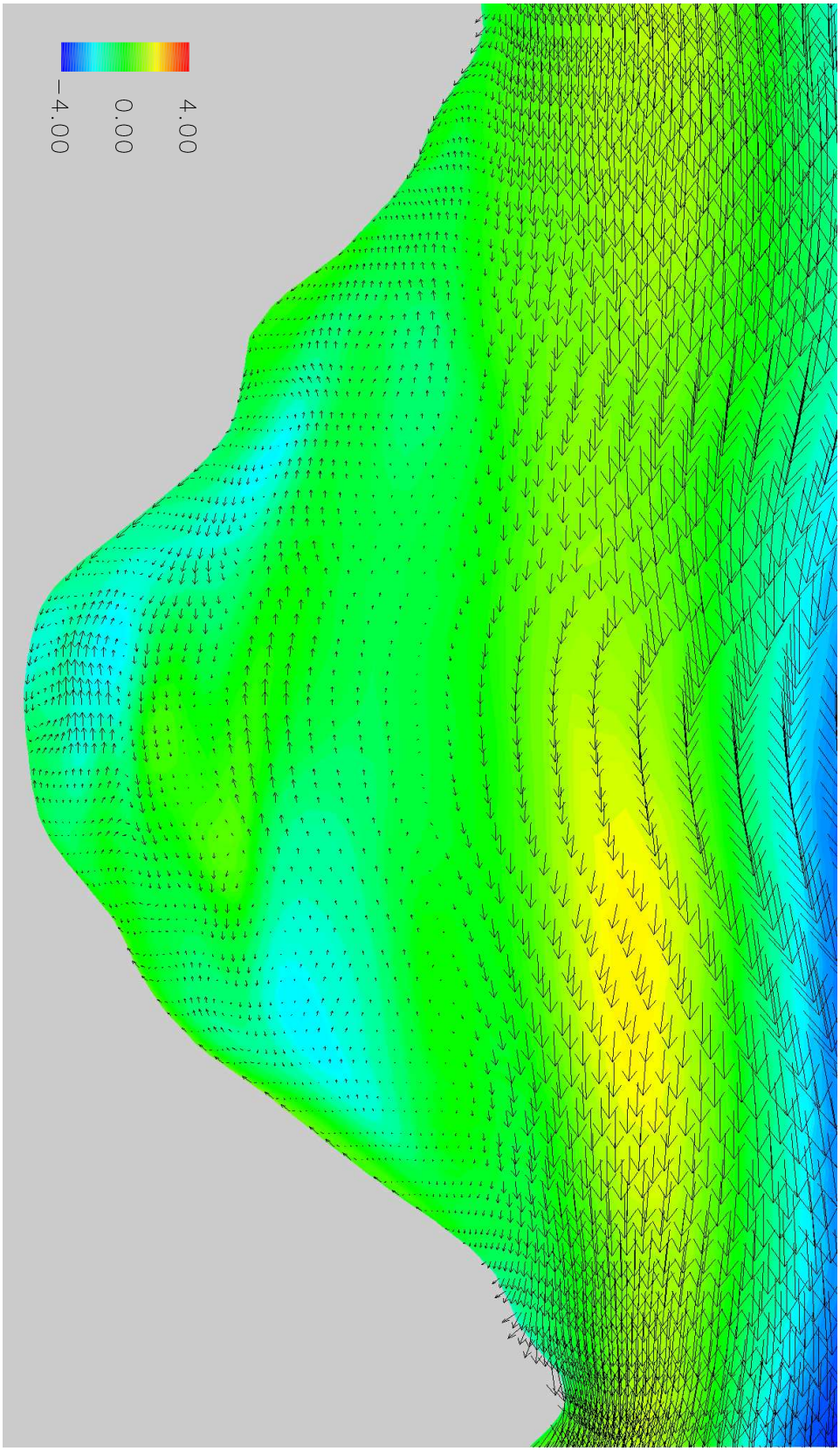

Figure 8.14g: 2100 UTC

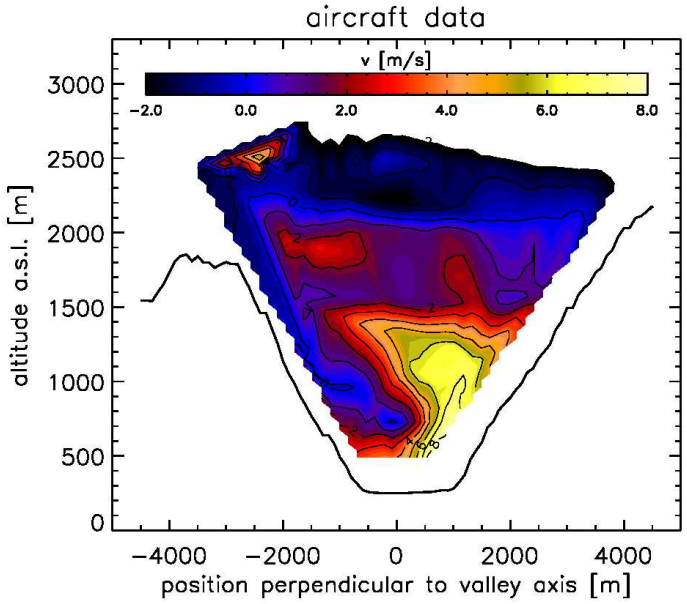

(a)

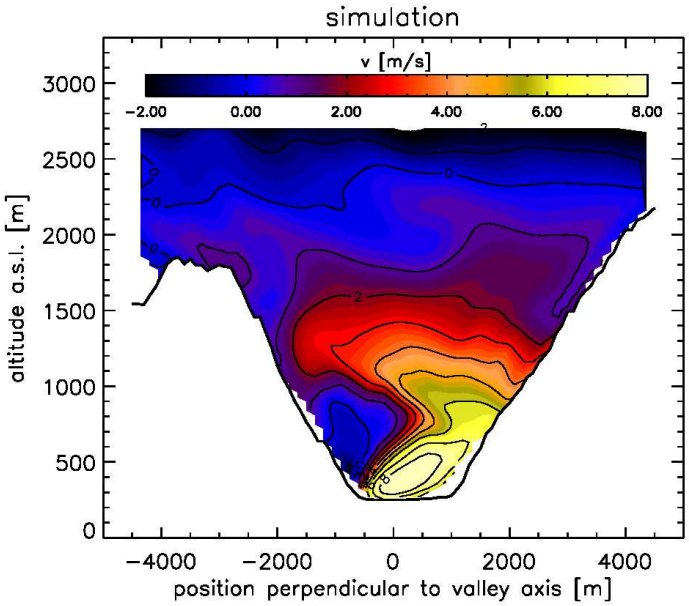

(b)

Figure 8.15: Along-valley winds (shaded: blue (down-valley), red (up-valley)) from (a) aircraft measurements and (b) simulations. Courtesy of Andreas Weigel.

8.5.3 Transition of valley winds during sunrise

Figures 8.16a-8.16d show the MOISLU simulated surface winds at four times during the three hours following sunrise. The grey shading indicates the intensity of incoming solar radiation at the surface. Black indicates that the area is receiving no sunlight, and white indicates bright sunshine. At 0630 UTC, the east side of the valley and the valley floor are in darkness. There are weak surface winds along the valley floor, and weak down-slope winds on shaded slopes. By 0730 UTC, up-slope winds have begun on the east-facing slope, and they continue to strengthen. By 0830 UTC, winds on the east slope have also begun to shift to up-slope, and the transition to up-valley flow has been completed over the entire valley axis. Approximately three hours after sunrise (0930 UTC), we see significant up-slope winds on both slopes, and a strong up-valley component along the whole valley floor as well. The transition in wind direction clearly occurs first along the slopes and then along the valley floor as the core of the valley wind shifts to up-valley. Note that the same wind sequence occurs in the Calanca Valley (roughly parallel to the Riviera Valley on the east).

Figures 8.17a-8.17d show the transition of valley winds during sunrise at a higher level, 1000 m asl. Also shown are contours of the potential temperature at this elevation. Over the two-hour period from 0700 to 0900 UTC, the valley winds shift from down-valley to up-valley. At this elevation the up-valley winds are stronger on the west side of the valley, perhaps because there is less curvature at the south end of the valley at this elevation than at 500 m, where Fig. 8.12b showed the jet is shifted to the right. It is interesting to observe that the northern reaches of the Riviera Valley (the Leventina and Blenio Valleys) are warmer than the main Riviera Valley, as also seen in Fig. 8.13b. This may be due to the narrower valley cross-section further north. The Verzasca Valley (parallel and to the west) is also warmer, particularly along its slopes. The temperature gradient along the valley axis, and the air at the same elevation is driven from cooler to warmer regions. This is consistent with the topographic amplification concept of Steinacker (1984).

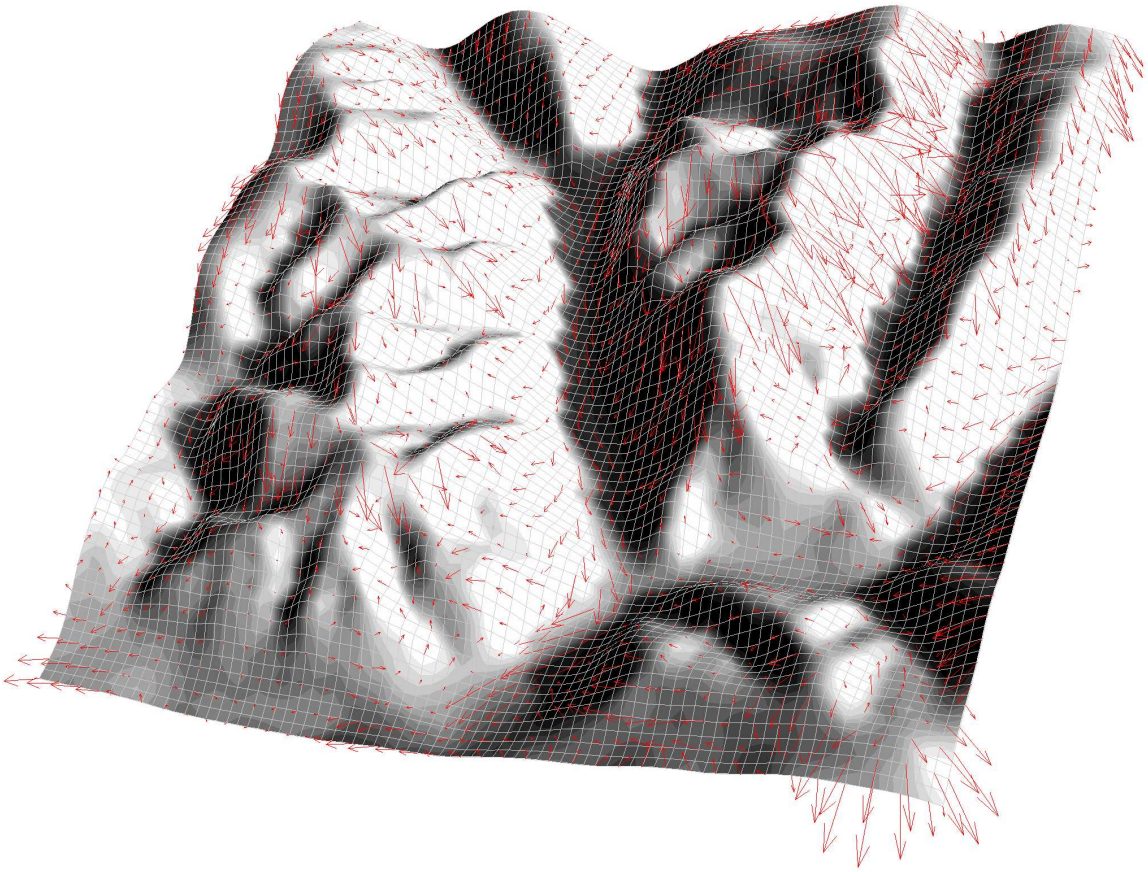

Figure 8.16a: Surface winds (vectors) and incoming solar radiation (shaded: black (no sunlight, 0 W/m^2), white (bright sun, $>$ 400 W/m^2)). 0630 UTC.

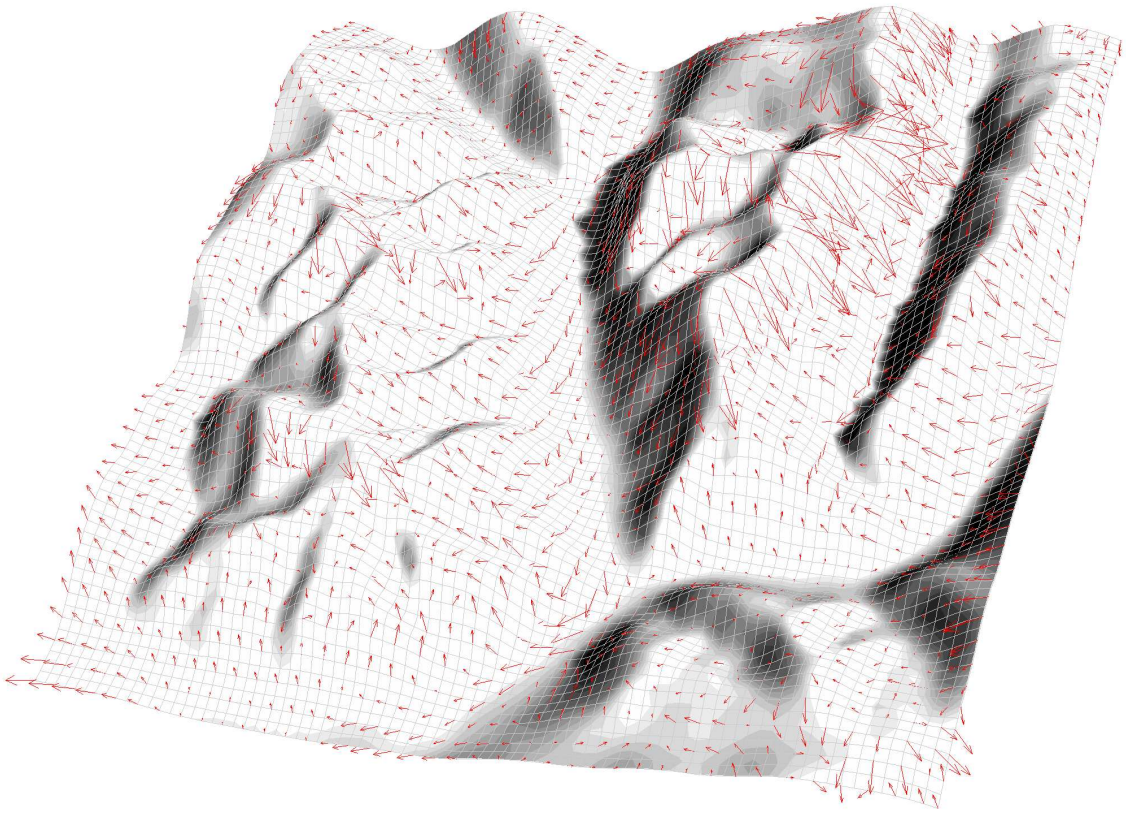

Figure 8.16b: 0730 UTC

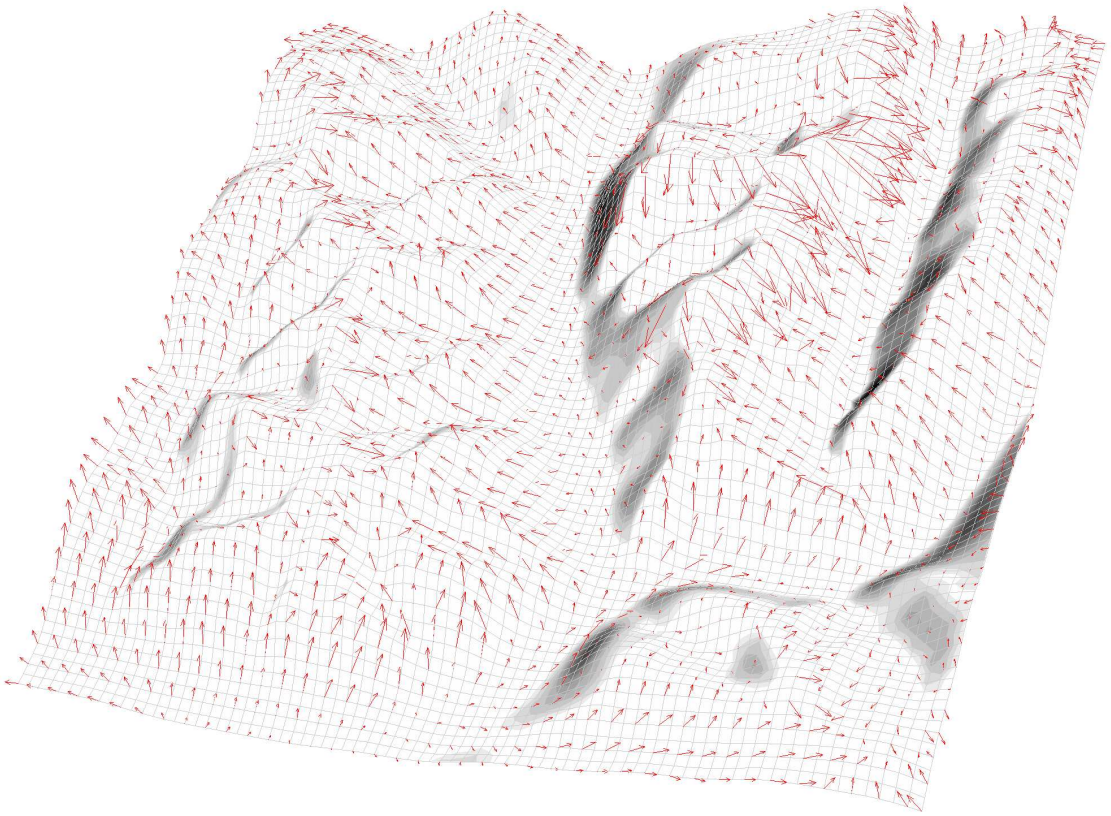

Figure 8.16c: 0830 UTC

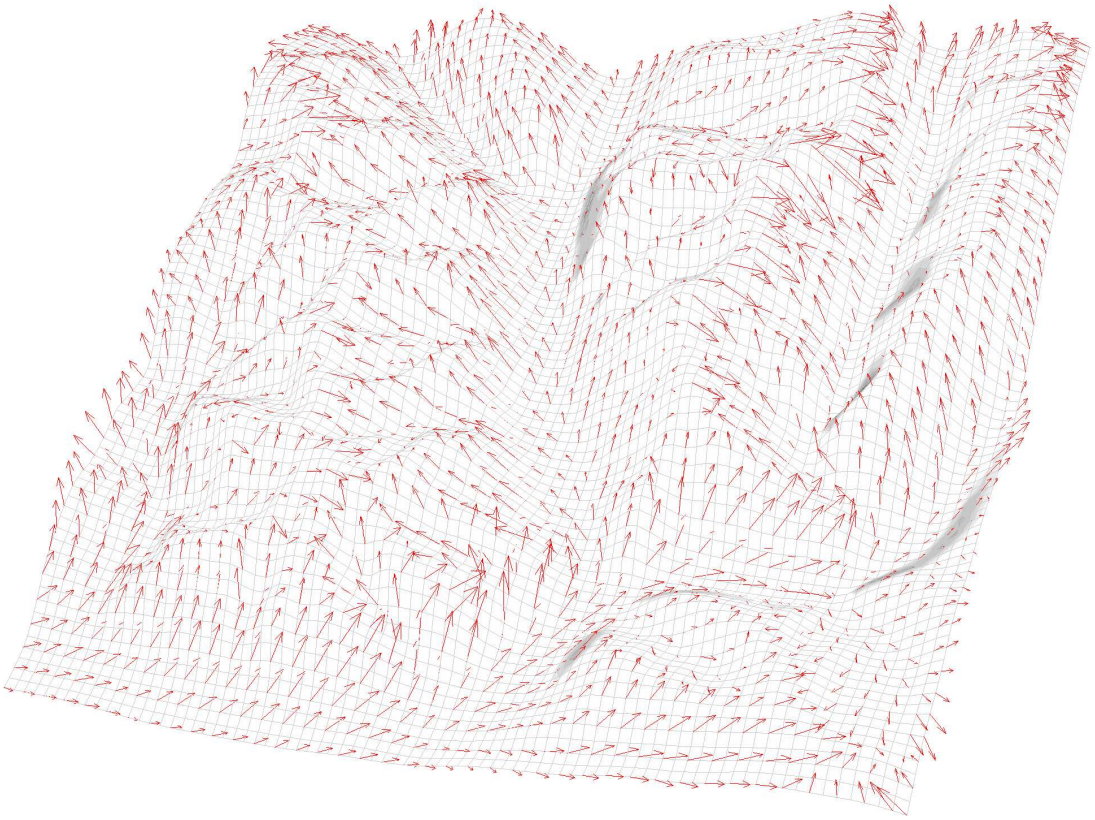

Figure 8.16d: 0930 UTC

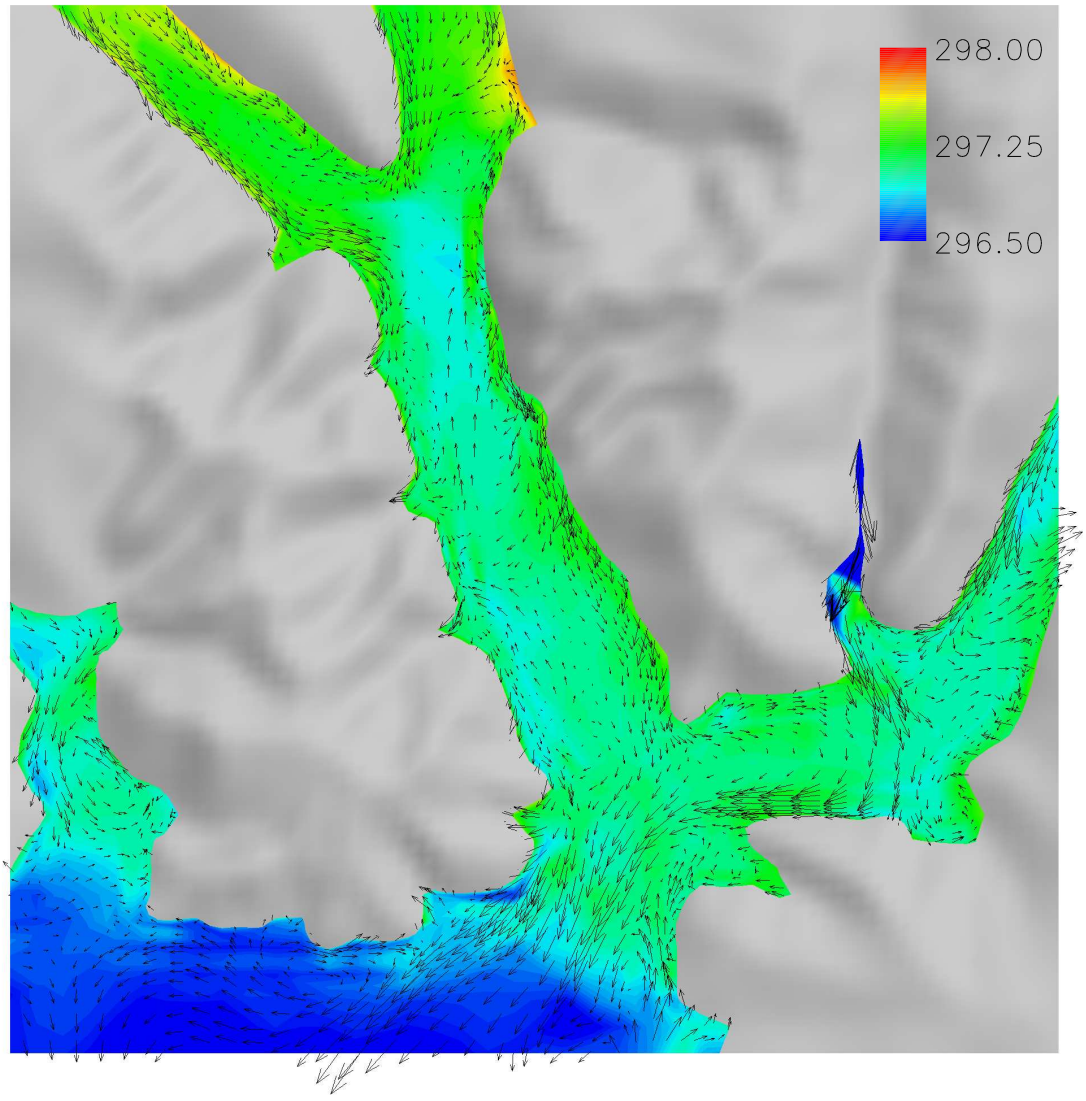

Figure 8.17a: 0700 UTC. Valley winds (vectors) and potential temperature (shaded, K) at 1000 m asl. Vectors are not uniformly spaced due to interpolation, and not all vectors are shown.

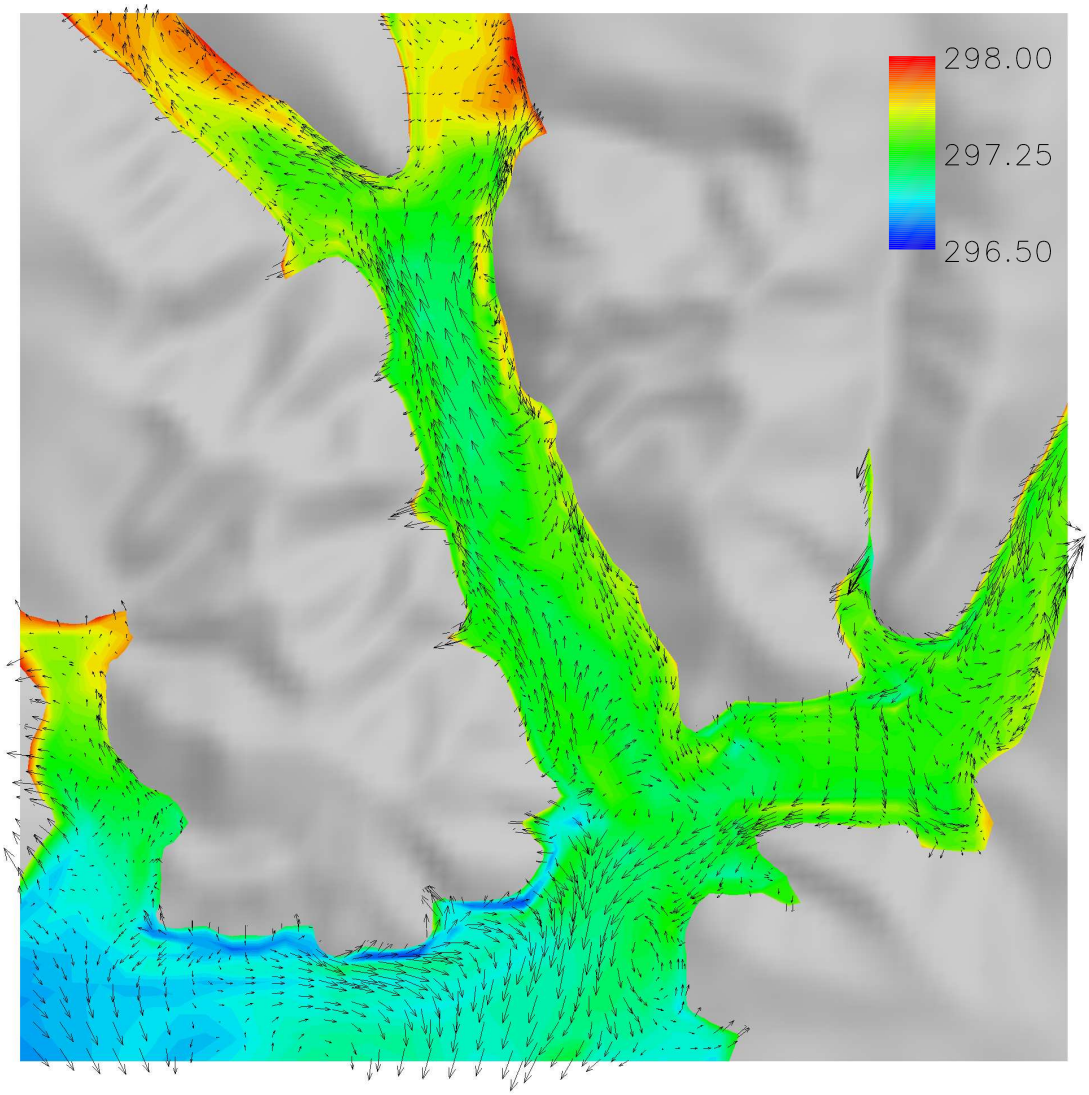

Figure 8.17b: 0800 UTC

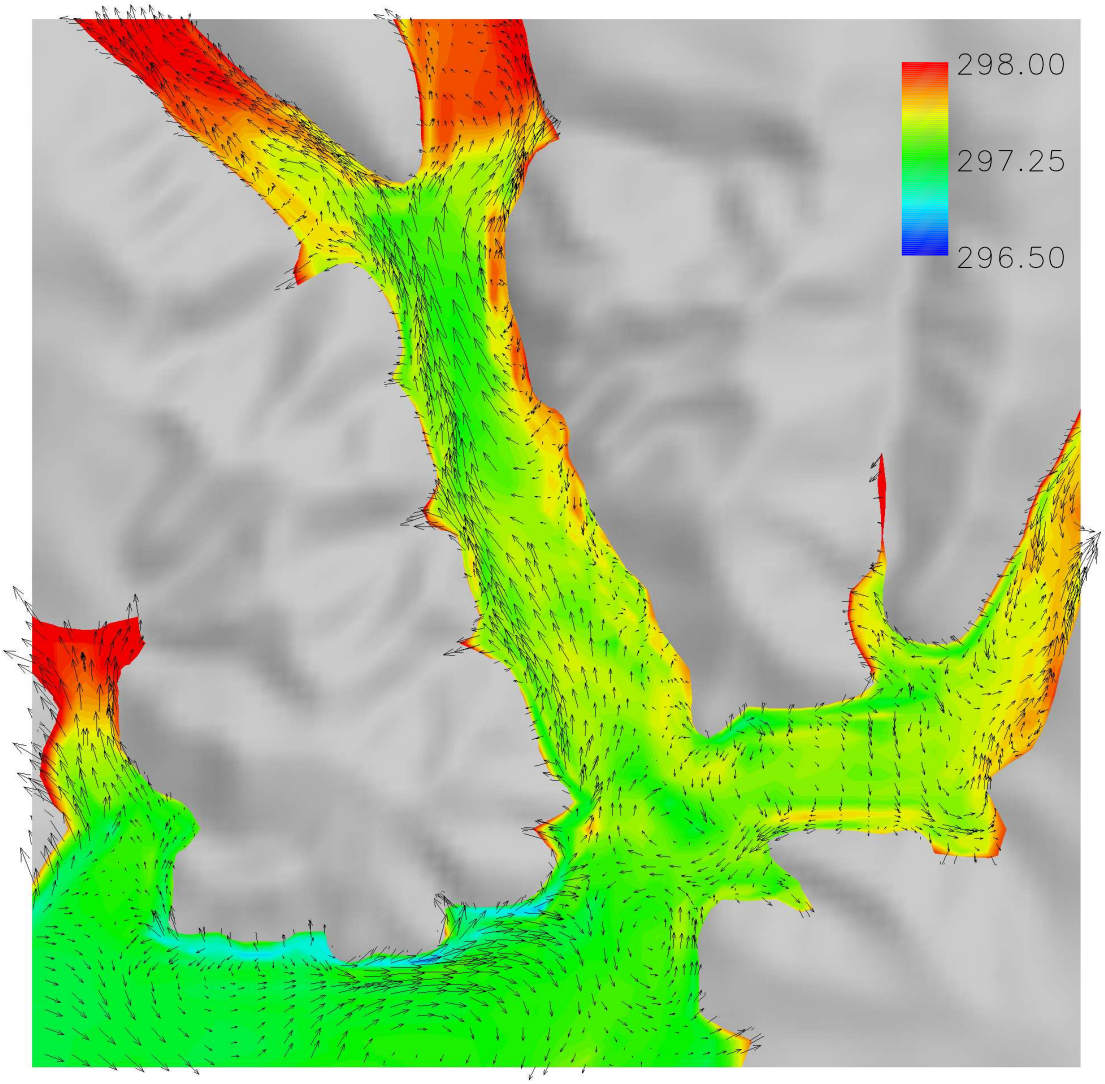

Figure 8.17c: 0830 UTC

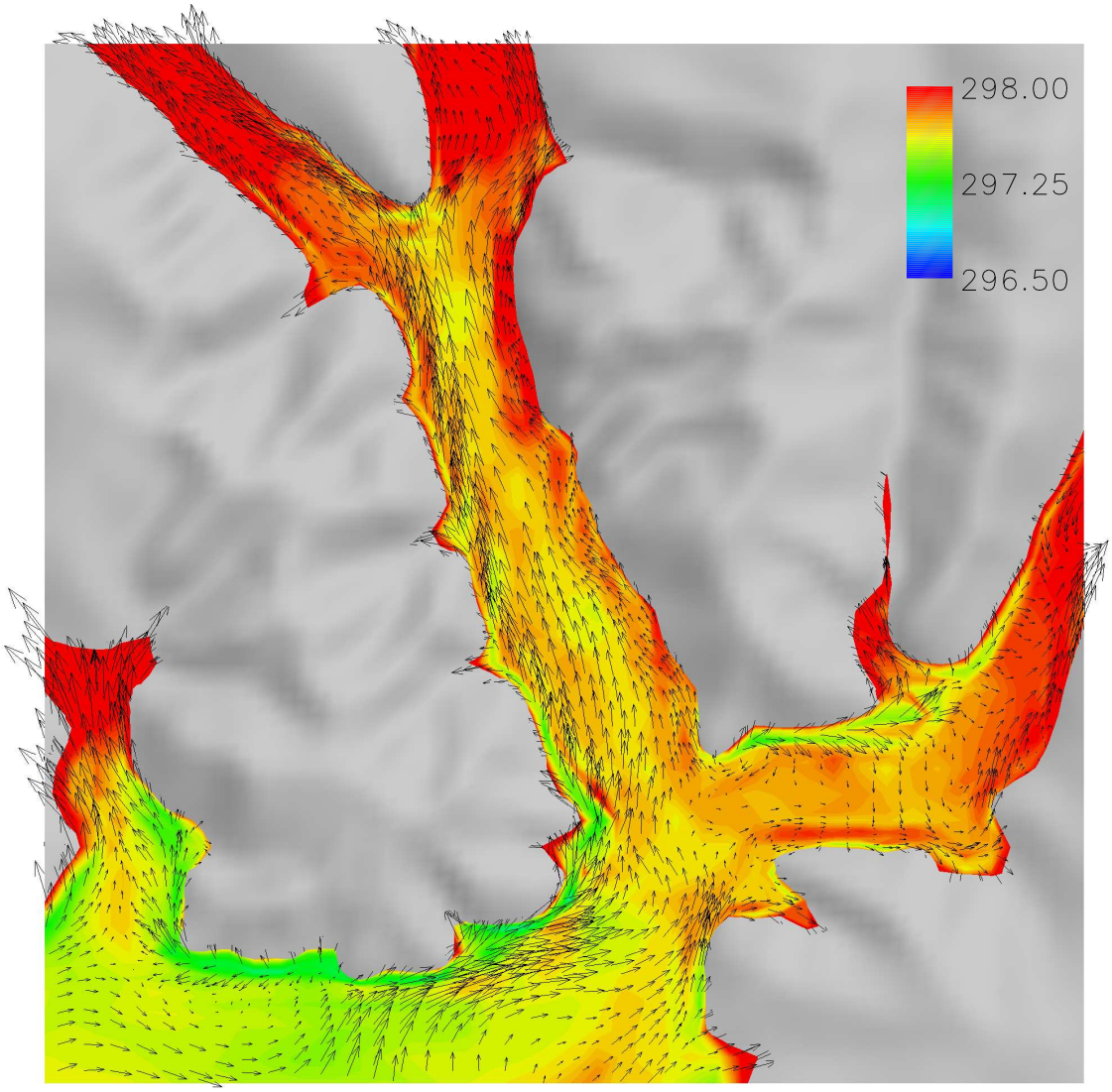

Figure 8.17d: 0900 UTC

8.5.4 Turbulence structure

Before looking at the vertical structure of the turbulent contributions to the momentum equation, we can compare the surface heat fluxes produced by ARPS with the observations. Figure 8.18 shows the time series evolution of the sensible heat flux at surface stations A1 (valley floor) and B (eastern slope). The heat flux is the kinematic heat flux defined as $\overline{w\theta}$. Surface fluxes in ARPS are calculated from similarity theory and provide a boundary condition for the heat flux equation. The model results compare quite well to the observations, especially given the high spatial variability observed in the valley. The time series obtained at the five points nearest the surface station are shown. With 350 m grid spacing and steep slopes, large elevation differences can accompany a change in horizontal position. Station B on the east slope exhibits more cooling at night than station A1 (0000 to 0700 UTC). Significant heating occurs during the day at both sites, with ARPS giving higher values at the valley floor than observed during the latter half of the afternoon. The peak heat flux is delayed on the east slope relative to the valley floor because the slope does not receive direct sunlight until later in the morning, and is heated until later in the afternoon. The peak magnitude is much larger at site B because of the surface inclination and exposure of the site in the afternoon. Similar time series are obtained for the momentum fluxes ($\overline{uw}$ and $\overline{vw}$, not shown).

Surface heating generates convective eddies, so the turbulence contribution is greatest in the afternoon. Figures 8.19-8.20 show vertical cross sections of the resolved and SFS stress contributions for uw and vw averaged over 1300 to 1500 UTC. The velocities have again been rotated to be aligned with the valley axes. The vertical slice is perpendicular to the valley axes at site A1 (see Fig. 8.3). The resolved stress is computed from $< uw >_{res} = < \overline{\tilde{u}\tilde{w}} > - < \overline{\tilde{u}} >< \overline{\tilde{w}} >$ with the time average denoted by $<>$. The plotted SFS stress is simply $< \tau_{13} >$, and likewise for the vw stresses. The contribution of the SFS stresses is significant only very near the surface, below about 500 m. There, the SFS stresses are several times larger than the resolved stresses, as also seen in the profiles in Fig. 8.21. Profiles taken during the early morning hours showed significantly smaller stresses, as expected.

The SFS stress contributions are not large outside the near-surface layer, perhaps explaining why using different turbulence models does not have very large effects (see

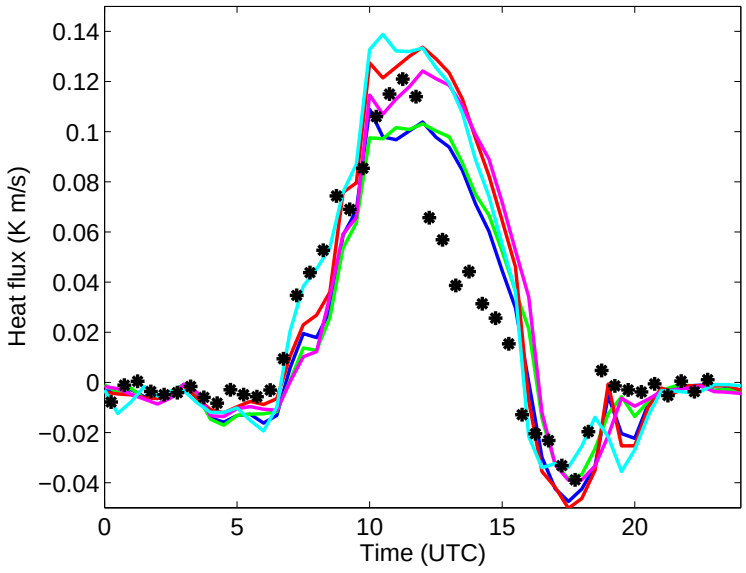

(a)

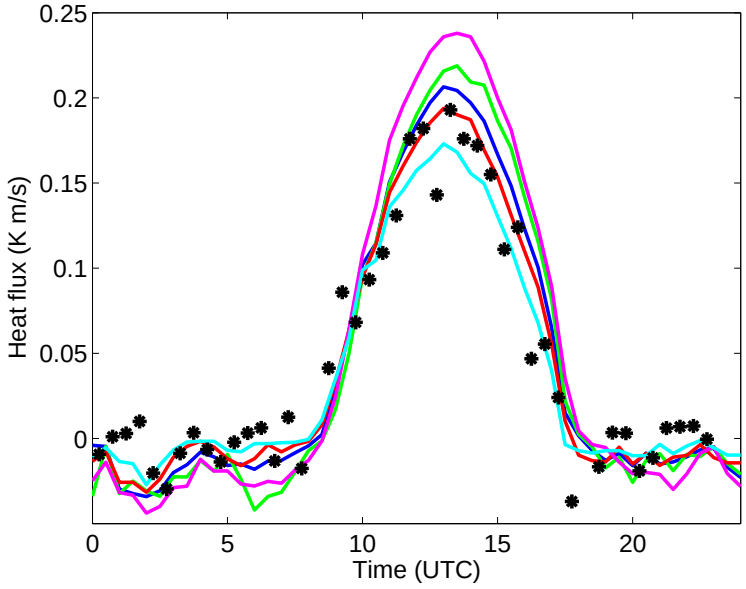

(b)

Figure 8.18: Time series of surface sensible heat flux at (a) site A1 (valley floor) and (b) site B (eastern slope). $*$ Observations; Solid lines: MOISLU results from five nearest points to observation site, with blue being the closest. Note the different vertical axes.

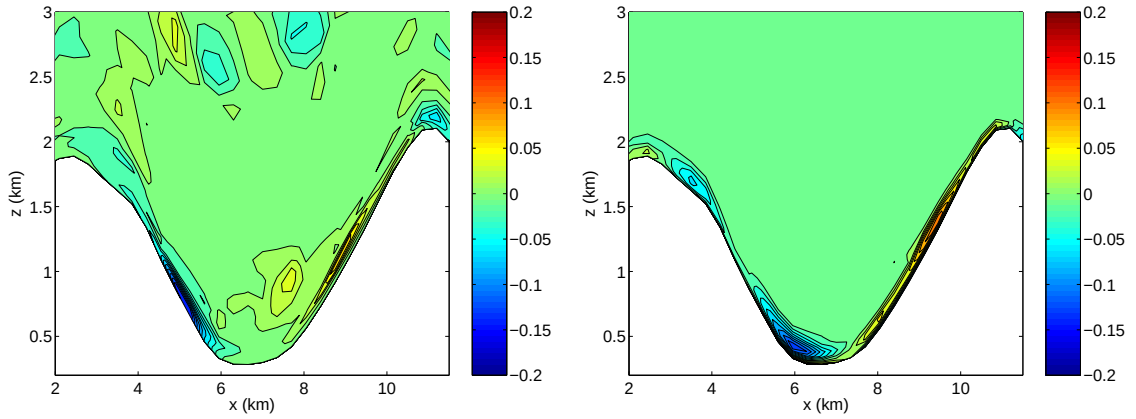

(a) (b)

Figure 8.19: Vertical cross-sections of (a) resolved uw and (b) SFS τ_{13} stress (m^2/s^2) perpendicular to valley axis at site A1. Time averaged between 1300 and 1500 UTC at 300 s intervals.

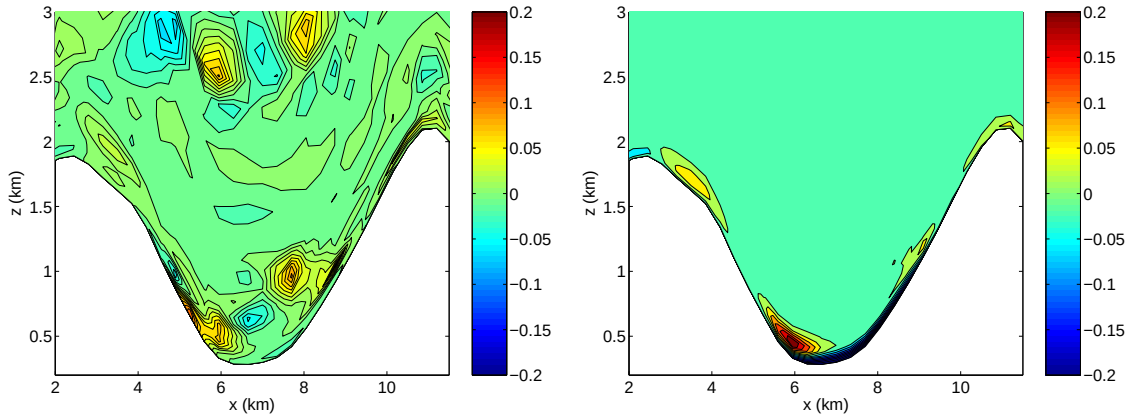

(a) (b)

Figure 8.20: Vertical cross-sections of (a) resolved vw and (b) SFS τ_{23} stress (m^2/s^2) perpendicular to valley axis at site A1. Time averaged between 1300 and 1500 UTC at 300 s intervals.

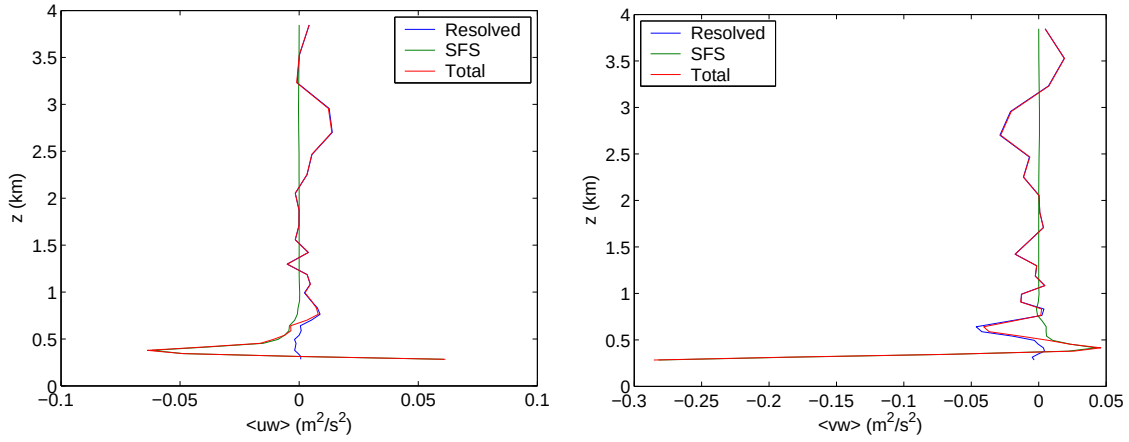

(a) (b)

Figure 8.21: Vertical profile of resolved, subfilter-scale, and total stress for (a) uw and (b) vw at the valley floor. Time averaged between 1300 and 1500 UTC at 300 s intervals.

Section 8.6.5). The atmosphere in the Riviera is stably stratified throughout the day except very near the surface (see Fig. 8.11), and the TKE-1.5 closure will not produce SFS turbulence when the flow is stable (as measured by the Richardson number) or when there is only weak shear in the flow. Likewise, the Smagorinsky model used by ARPS has a stability criterion that limits the contribution of SFS stresses under stable stratification.

8.6 Sensitivity tests

The comparisons in Section 8.4 contrasted the improved results from MOISLU with those from the standard "acceptable" procedure using the standard initial conditions and surface datasets (REF). We now examine the separate effects of individual pieces of the MOISLU simulation approach.

8.6.1 Soil moisture

The improved results from the use of high-resolution WaSiM soil moisture data have already been shown in Figs. 8.6-8.10b which compare the REF and MOISLU simulations. The REF simulations used ECMWF soil moisture data; the result is that the up-valley wind transition occurs too late (by 3-4 hours) throughout the entire nesting set. The MOISLU surface layer soil moisture values are slightly lower (0.33 m^3m^{-3}) than those from ECMWF (0.35 m^3m^{-3}). The deep soil values are comparable (0.35 m^3m^{-3}) at the valley floor, but the WaSiM data give much lower deep soil values on the slopes. Banta & Gannon (1995) found that increased soil moisture decreases the strength of katabatic winds; this is due to slower cooling caused by the increased thermal conductivity of moist soil and increased downward longwave radiation (because the air near the surface has higher humidity). Ookouchi *et al.* (1984) showed that increased soil moisture decreases up-slope winds because the wetter soil does not heat as quickly and hence produces smaller horizontal pressure gradients. Accordingly, with wetter soil (REF), the transition to up-valley winds begins later, while the drier soil (MOISLU) better reproduces the transition. This simple explanation is complicated, however, by the complexity in the topography of the Riviera Valley and its tributaries (the Magadino, Mesolcina, Leventina and Blenio Valleys), where the effect of soil moisture will be different in each valley. For example, strong down-valley winds from the Mesolcina Valley could block the entrance of up-valley winds from the Magadino Valley into the Riviera Valley.

That the soil moisture effect is not straightforward is demonstrated by an attempt to use the WaSiM data at coarse resolutions as well. The WaSiM data cover only the Ticino and Verzasca river catchment areas, i.e., only the immediate vicinity of the Riviera. We have, however, applied the WaSiM data over the 1 km grid (MOISLU2 simulations) where data are available. Over the rest of the domain, we use elevation-dependent values at three levels determined from averages of the WaSiM data (similar to the MOISLU setup, see Table 8.5). Thus, we extrapolate the values from the center of the domain, where the WaSiM data are available, to the rest of the Alps region covered by the 1 km grid. The wind speed and direction from MOISLU and MOISLU2 in Fig. 8.22 differ significantly, although there is not as much difference in the temperatures in Fig. 8.23. The greater delay in the onset of the valley winds is

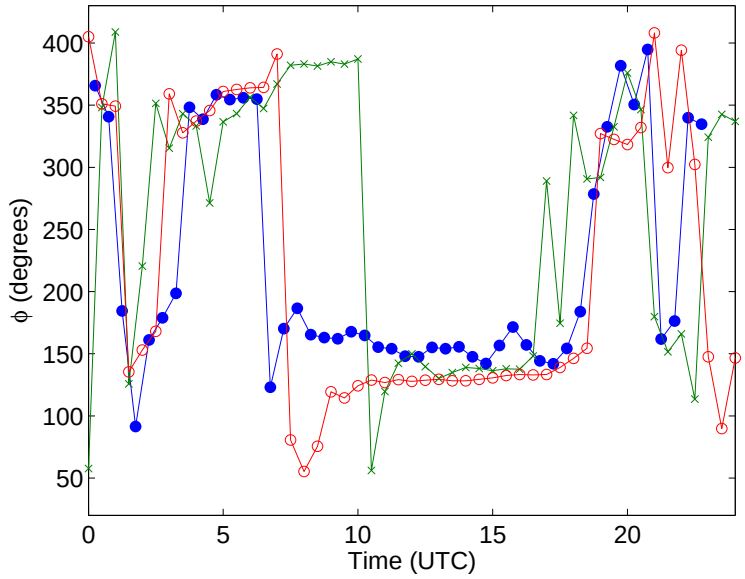

(a)

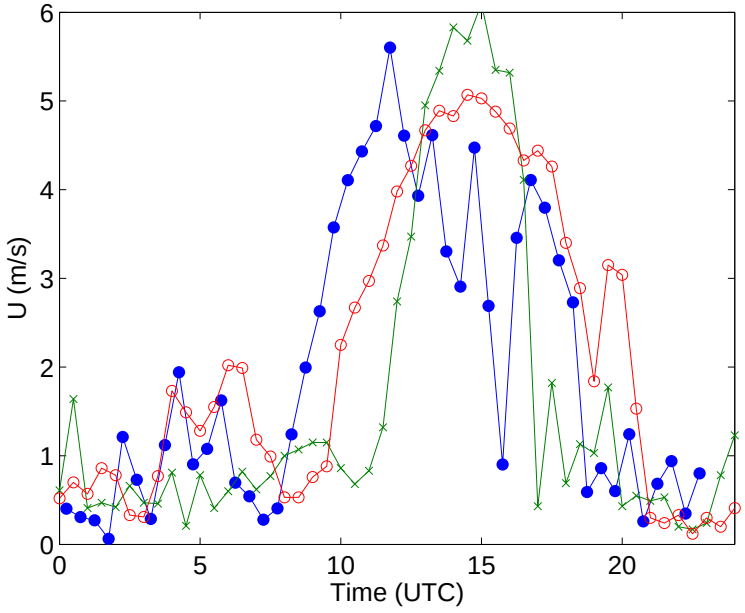

(b)

Figure 8.22: Surface wind direction and speed at Bosco di Sotto (site A1). —●— Observations; —○— MOISLU; —×— MOISLU2

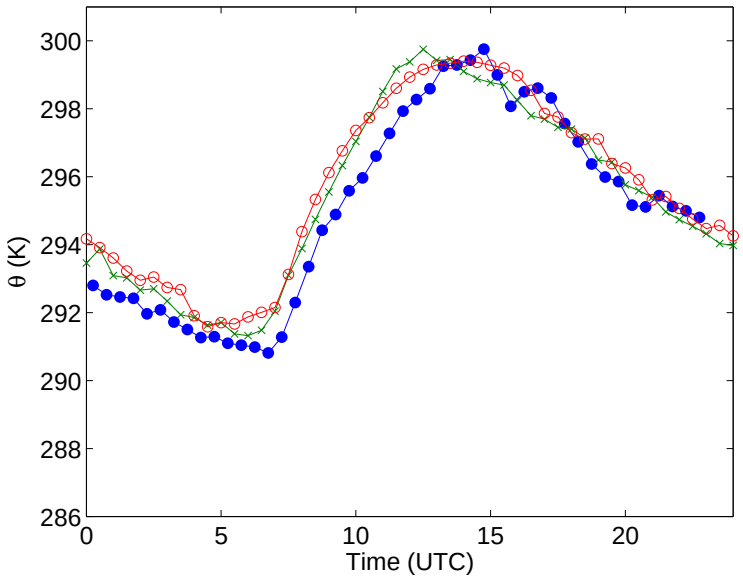

Figure 8.23: Surface potential temperature at Bosco di Sotto (site A1). —●— Observations; —○— MOISLU; —×— MOISLU2

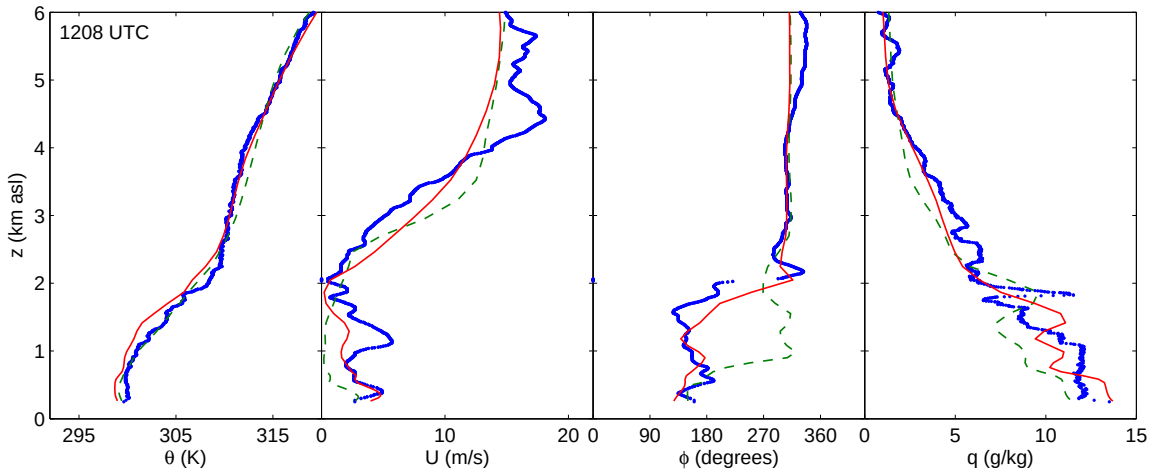

Figure 8.24: Soundings at 1208 UTC. ····· Observations; —— MOISLU; - - - - MOISLU2

particularly visible in the wind speed time series for the MOISLU2 simulations and in the soundings in Fig. 8.24. The wind speed time series also show that the up-valley winds die out too soon in the evening.

The results from the MOISLU, MOISLU2 and REF comparisons indicate that the soil moisture outside the fine-grid (350 m) domain is crucial for accurately predicting the wind transitions. The simulations deteriorate in quality when we assume the large scale soil moisture distribution (ECMWF) also holds on the 1 km domain (REF). Likewise, assuming that the local soil moisture distribution (WaSiM) in the Riviera Valley also holds over the larger 1 km domain (MOISLU2), also yields poorer results than the three-level soil moisture used for the MOISLU simulations. This points to the need for high-resolution soil moisture measurements over a broader region (such as all of the Alps) to provide accurate input to large-eddy simulations.

8.6.2 Land use data

We have introduced 100 m resolution land use data for the 350 m grid level, as described previously in Section 8.3.5. To measure the impact of the increased number of vegetation and soil classes, we performed simulations with interpolated low-resolution land use data and original vegetation and soil types (results are denoted MOIS) instead of the 100 m data. The MOIS wind direction in Fig. 8.25 shows erratic behavior during the down- to up-valley transition, and the wind speed indicates that up-valley winds are delayed an additional half hour relative to the MOISLU results. Figure 8.26 shows differences in the potential temperatures as well; during the morning hours, the MOIS simulations predict cooler values than observed. Differences in vertical sounding profiles are quite small except near the surface (not shown). Nevertheless, the overall results indicate that the high-resolution land use representation brings improvements.

8.6.3 Grid resolution

High grid resolution is particularly important over complex terrain like the Riviera Valley, where the terrain features that channel the flow must be well resolved. The width of the Riviera Valley floor is approximately 2 km. Given that the minimum well-resolved eddy for LES is $4\Delta x$, a horizontal resolution of 500 m would barely

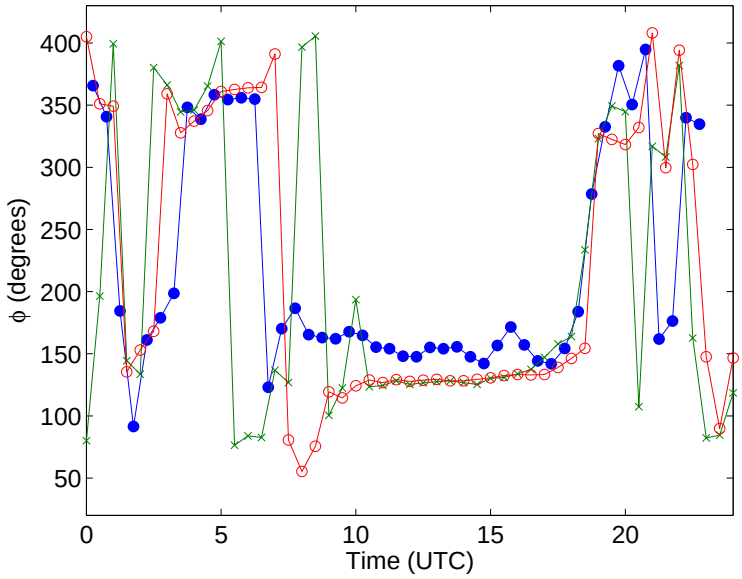

(a)

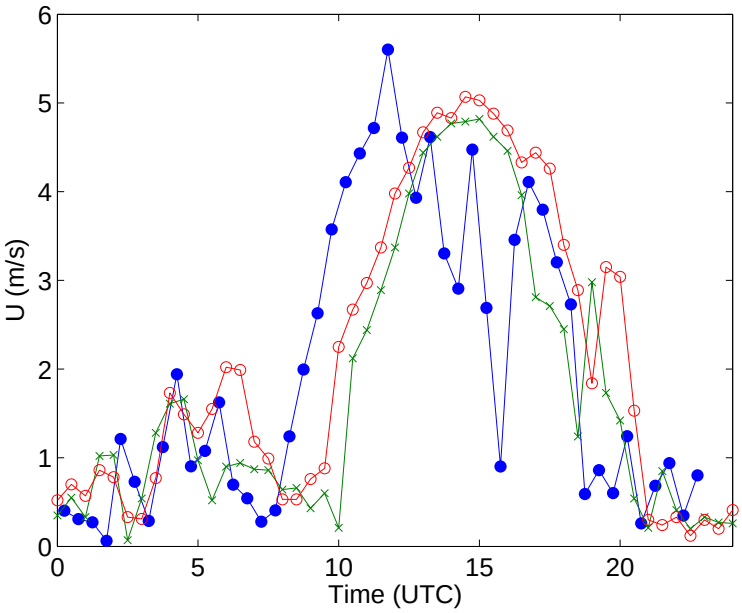

(b)

Figure 8.25: Surface wind direction and speed at Bosco di Sotto (site A1). —●— Observations; —○— MOISLU; —×— MOIS

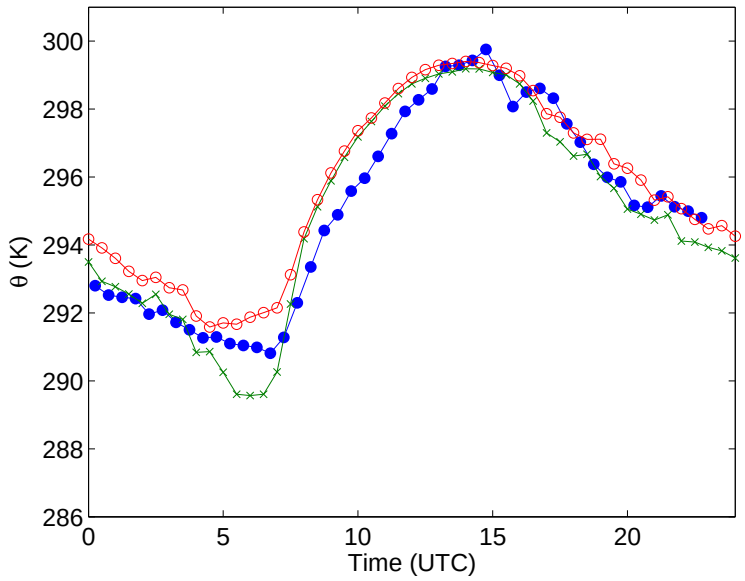

Figure 8.26: Surface potential temperature at Bosco di Sotto (site A1). —●— Observations; —○— MOISLU; —×— MOIS

resolve the valley floor. Coarse resolutions also do not represent the terrain elevation accurately. For example, the elevation of Bosco di Sotto (site A1) is 1123 m, 794 m, 334 m, and 263 m asl on the 9 km, 3 km, 1 km, and 350 m resolution grids, respectively. This is an enormous height difference that greatly affects the LES representation of near-surface flow.

Figures 8.27-8.29 show comparisons of the results from 1 km, 350 m, and 150 m horizontal resolutions, using the MOISLU simulation set of nested grids. The 1 km grid in this instance includes the 3-level elevation dependent soil moisture. The 350 m and 150 m grids use WaSiM data, as noted previously. The general trends in the wind and temperature data are very well captured even at 1 km resolution. The wind shifts in Fig. 8.27 are particularly well-represented at 1 km, and the finer nested grids follow. Potential temperature (Fig. 8.28) for the 1 km grid is too high at the surface; this is likely caused by elevation differences at Bosco di Sotto (334 m asl on the 1 km grid vs. 263 m asl for the 350 m grid). The 150 m grid shows slightly high temperatures during the first six hours of the day. This may be due to the fact that data are plotted at the first grid cell center, which is at 10 m for the 150 m grid and at 15 m for the 350 m grid. The finer horizontal resolution simulations also have

finer vertical resolution (see Section 8.3.2) and resolve stratified layers better. Indeed, Fig. 8.29 shows that the largest differences in potential temperature (at 1800 UTC) between the different resolutions occur near the surface. Even though the 350 m and 150 m resolution results do not match the data perfectly, they seem to capture the near surface inversion that was likely the result of down-slope winds.

The differences between the 350 m and 150 m results in Figs. 8.27-8.29 are not large. This is likely due to the lateral boundary forcing and the limited domain sizes. The 150 m grid is strongly forced by the 350 m resolution results. The increased resolution is, however, clearly necessary for an accurate representation of this complex flow. The general results (e.g. wind transitions) are determined at the 1 km level, so it is important to have good soil moisture values at this resolution (see Section 8.6.1 and Weigel *et al.* (2004*a*)). Finer resolution allows a larger range of flow structures to be resolved, thereby better representing near-surface features (e.g. stratification), and placing less energy in the SFS turbulence models. At the same time, the unsatisfactory REF results (using interpolated coarse grid surface data) show that high resolution surface data is necessary in addition to fine grid resolution.

8.6.4 Topographic shading

Figure 8.30 shows the surface radiation balance through the day from the 350 m resolution ARPS results corresponding to measurements at surface station A1. The model slightly overpredicts incoming shortwave radiation. The peak of the curve is highly sensitive to location and local surface inclination and could be adjusted to match the observations better by improving the spatial interpolation from the simulation results. The dip at 1300 UTC was due to a brief period of clouds. The net radiation is generally underpredicted day and night, which implies that the longwave radiation balance is at fault: either the incoming radiation is too low or the outgoing radiation is too large. Zhong & Fast (2003) found that night-time net radiation was also too low in their simulations of Salt Lake Valley, and suggested that the incoming longwave radiation was underestimated because the surface temperatures were lower than observed (giving smaller outgoing longwave radiation). Our results show good temperature comparisons in the Riviera Valley, so it is difficult to conclude which component is responsible. The outgoing longwave radiation is often thought to be

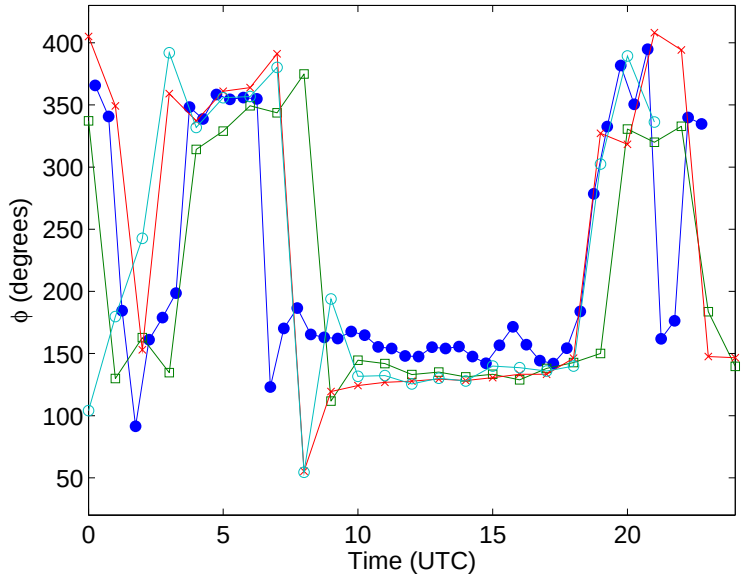

(a)

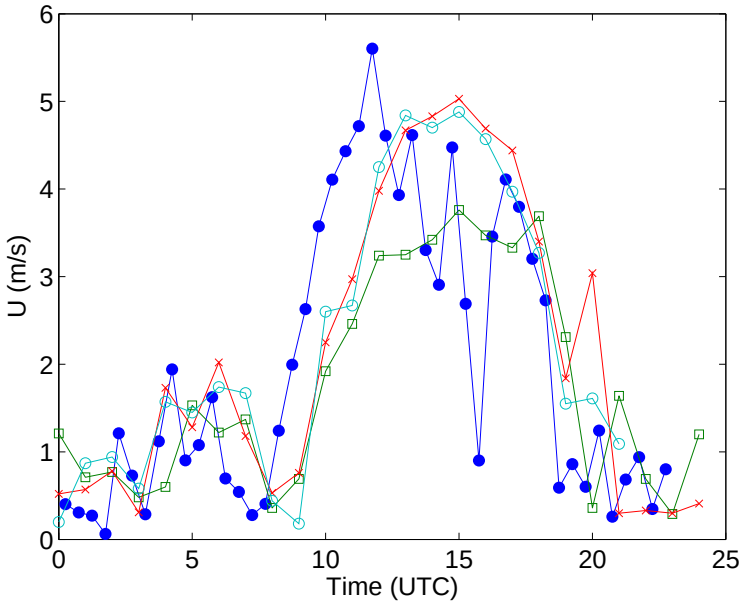

(b)

Figure 8.27: Surface wind direction and speed at Bosco di Sotto (site A1). —●— Observations; —□— 1 km; —×— 350 m; —○— 150 m

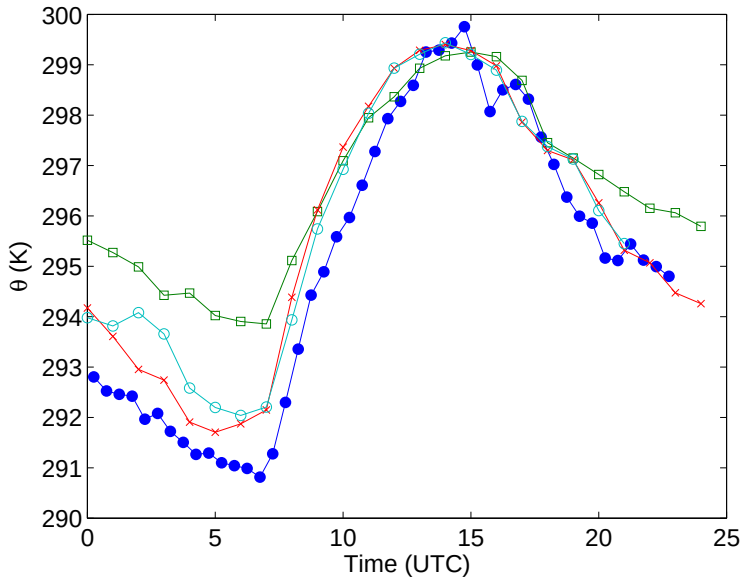

Figure 8.28: Surface potential temperature at Bosco di Sotto (site A1). —●— Observations; —□— 1 km; —×— 350 m; —○— 150 m

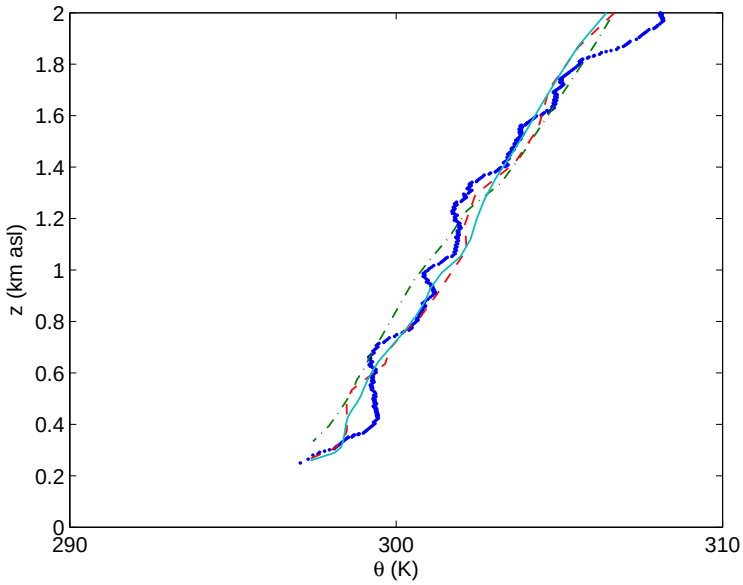

Figure 8.29: Close-up of potential temperature soundings at 1800 UTC. ····· Observations; —·— 1 km; - - - - 350 m; —— 150 m. The data at 1 km do not extend below 334 m.

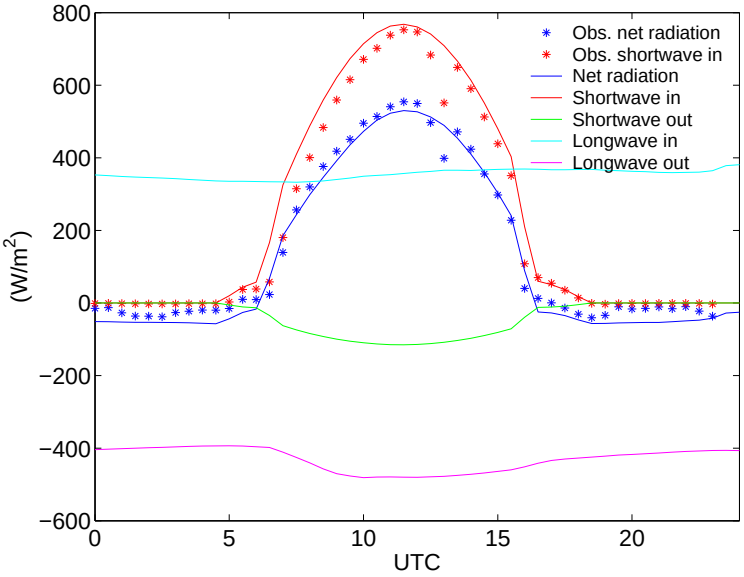

Figure 8.30: Radiation budget components compared to observations.

underestimated in valleys because the radiation models are one-dimensional (in the vertical); the models do not account for the incoming longwave emissions from the valley walls at night and therefore allow too much cooling.

Zhong & Fast (2003) also suggest that the absence of topographic shading in their simulations caused discrepancies. Figure 8.31 shows the incoming shortwave radiation with and without topographic shading. The incoming shortwave radiation is significantly reduced around sunrise and sunset when topographic shading is included, and therefore compares better with the measurements. The topographic shading model does not affect the longwave radiation balance at night.

Figure 8.32 shows the spatial variation of differences in incoming shortwave radiation at 0600 UTC when topographic shading is included. The east-facing slopes are shaded while the sun is low on the horizon, resulting in nearly 300 W/m^2 less insolation. The differences are largest at sunrise and sunset, as seen in Fig. 8.31.

A series of simulations was performed without topographic shading for the entire set of simulations (MOISLU-NS). The differences were insignificant at the coarser resolutions, because terrain slopes are smaller. On the 350 m grid, surface temperatures are slightly warmer without shading ($\sim$ 0.5-1.0 K) during sunrise and sunset, as expected. The influence of topographic shading in the radiosonde comparisons

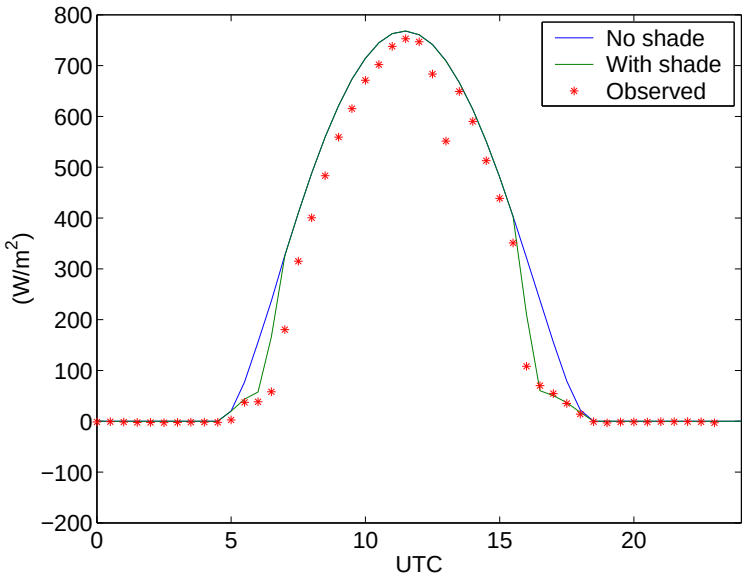

Figure 8.31: Incoming solar radiation, with and without topographic shading.

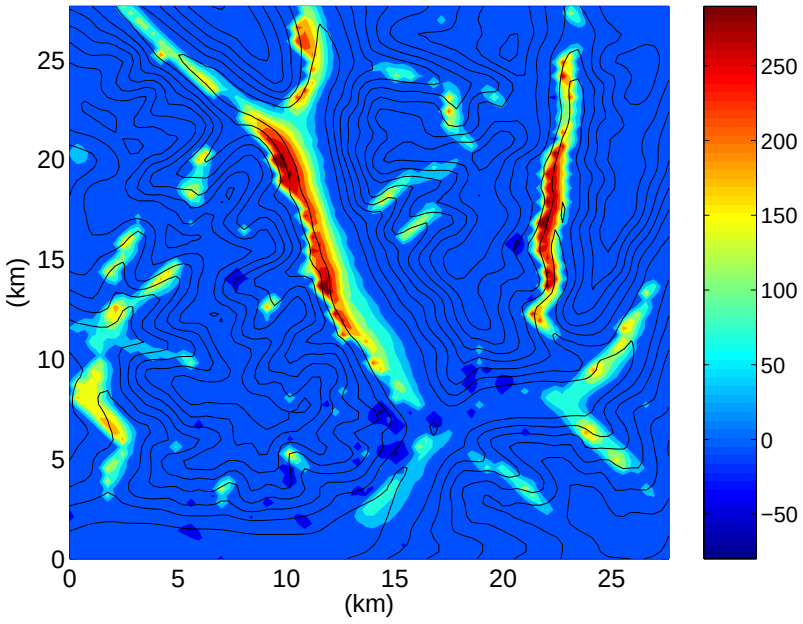

Figure 8.32: Difference in shortwave incoming radiation (filled contours, W/m^2) with and without shading (unshaded minus shaded) for the 350 m grid at 0600 UTC. Elevation contours (lines) shown at 250 m intervals.

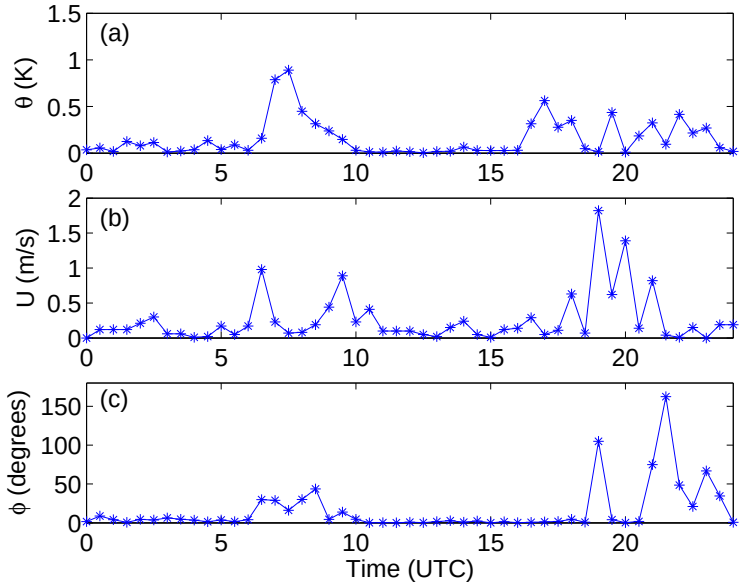

Figure 8.33: Absolute difference for surface station time series at site A1 for MOISLU and MOISLU-NS simulations, for (a) potential temperature, (b) wind speed, and (c) wind direction.

is quite small. Figure 8.33 shows a time series of the absolute value of differences at surface station A1 (Bosco di Sotto) for the MOISLU and MOISLU-NS results. Figure 8.34 shows the overall root-mean-square differences for the two simulations for sounding profiles at site A1 as a function of time. The effect of the topographic shading is concentrated near the surface, so the rms differences are not as large when averaged over the lowest 6 km. Nevertheless, it is clear that the largest changes from topographic shading occur during sunrise and sunset.

Figure 8.35 shows the difference in surface winds between the MOISLU and MOISLU-NS simulations at 0700 UTC. The MOISLU-NS simulations show increased up-slope winds along the east-facing slope of the Riviera as expected; however, differences are only on the order of 0.1 m/s, occasionally up to 0.5 m/s. The differences on the west-facing slope do not form a consistent pattern. Larger differences from topographic shading were observed in the idealized simulations of Colette *et al.* (2003), where along-valley winds were absent. Another reason why the impact of topographic shading is weaker here may be that the valley winds originate in the Magadino and

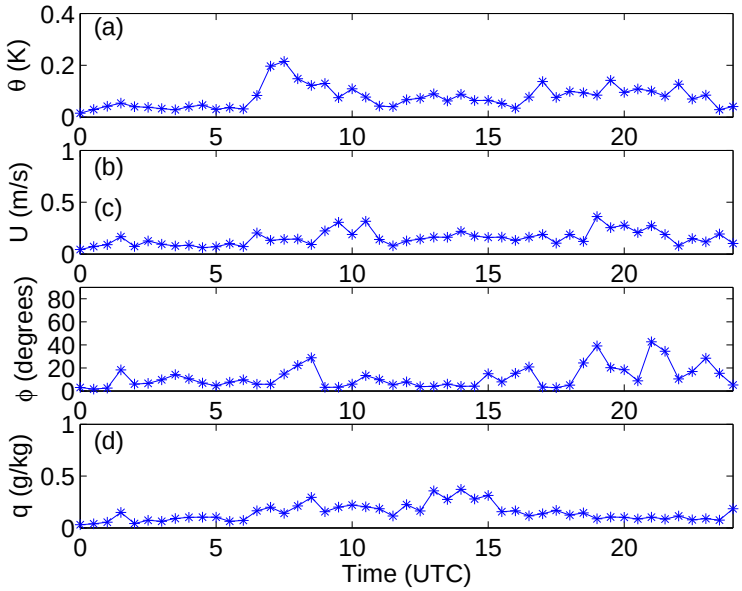

Figure 8.34: Root-mean-square difference for sounding profiles at site A1 for MOISLU and MOISLU-NS simulations as a function of time, for (a) potential temperature, (b) wind speed, and (c) wind direction.

Leventina Valleys (to the south and north of the Riviera, respectively). These valleys are oriented more nearly east-west and are thus less affected by shading in the morning. While the differences between the MOISLU and MOISLU-NS simulations are small, the improvement in the radiation curves in Fig. 8.31 is significant. The computational cost of the subroutine is negligible (Colette *et al.*, 2003), so we include the topographic shading in our simulations.

8.6.5 Turbulence closure

Figures 8.36-8.38 compare results from the MOISLU simulations with and without a turbulence closure model. The "no model" simulations (MOISLU-NOTURB) do not perform as well. The surface wind and potential temperature predictions in Figs. 8.36-8.37 have some significant differences; for example the surface winds show more oscillations, as expected for a simulation with less dissipation. The potential temperature profiles at 1208 UTC in Fig. 8.38, however, are not very different except very near the surface where the MOISLU runs produce slightly more mixing. The small difference is at first surprising; although 350 m is considered high resolution for

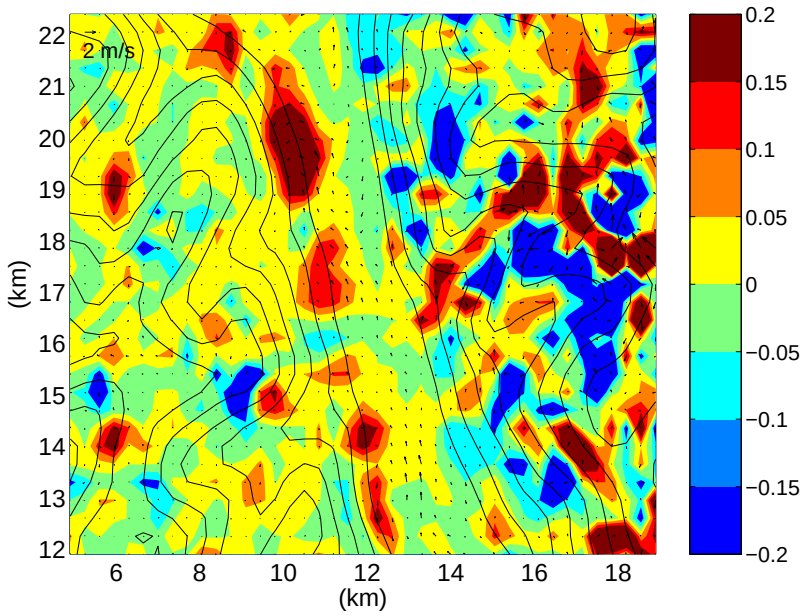

Figure 8.35: Difference in vertical velocity (shaded, m/s) and horizontal velocity (vectors, m/s) with (MOISLU) and without (MOISLU-NS) shading for the 350 m grid at 0700 UTC in the central region of the valley (unshaded minus shaded). Colorbar is truncated at ± 0.2. Vector scale is shown in upper left corner. Topography contours (lines) are shown at 250 m intervals.

the atmosphere, it still leaves much of the flow unresolved. All of the simulations still include the fourth-order computational mixing, which acts like a hyper-viscosity term and appears to dominate the effects of the turbulence model at 350 m resolution. The numerical errors from finite-difference schemes also contribute to the dissipation of energy from large to small scales.

Given similar coefficients for the computational mixing, we expect that at finer resolution the relative importance of the turbulence term will increase. This follows from the relative scaling of the mixing terms: the computational mixing is fourth-order in the grid spacing, while the turbulence terms are second-order in the filter width (see Chapter 3). Our current 150 m resolution simulations, however, are strongly forced by the 350 m results, which limits the development of finer scales. The 150 m results are not significantly different from the 350 m grid (see e.g. Fig. 8.27).

The SFS stress contribution is limited to the lowest 500 m, as shown in Figs. 8.19-8.21, so the effect on the flow is also limited. Figures 8.39-8.40 compare the results

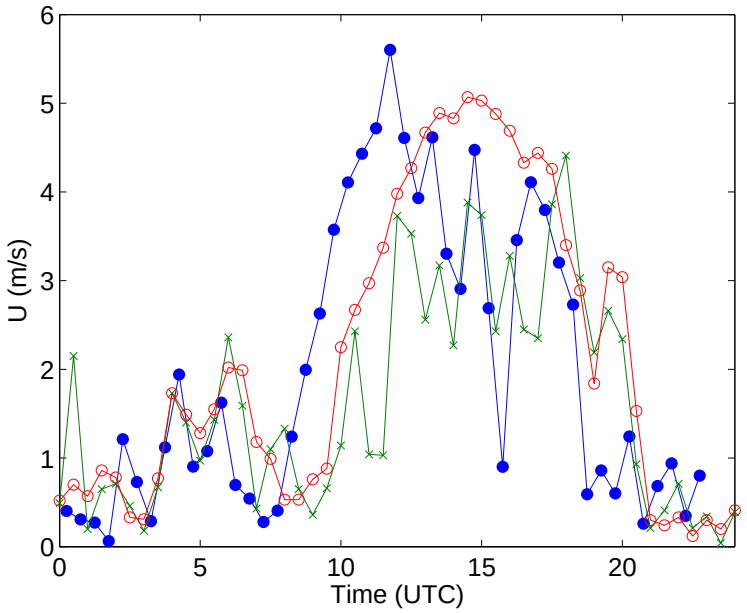

(a)

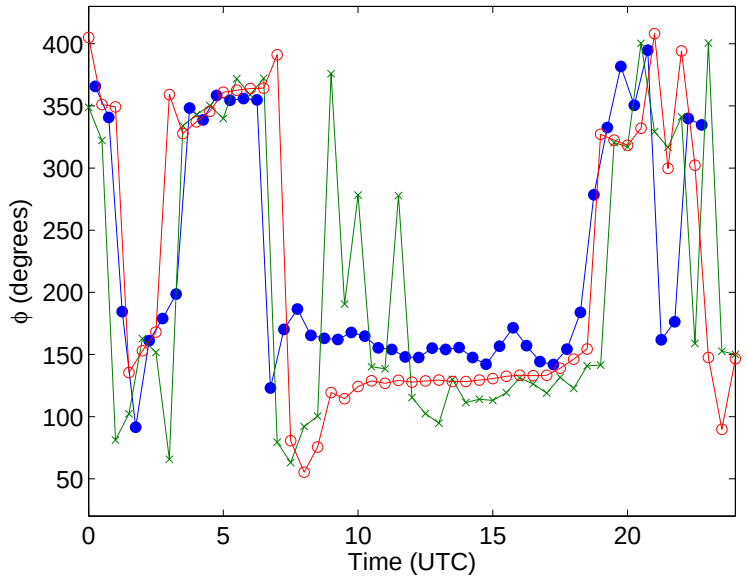

(b)

Figure 8.36: Surface wind time series comparisons at Bosco di Sotto (site A1) for (a) wind speed and (b) wind direction. —●— Observations; —○— MOISLU; —×— MOISLU-NOTURB

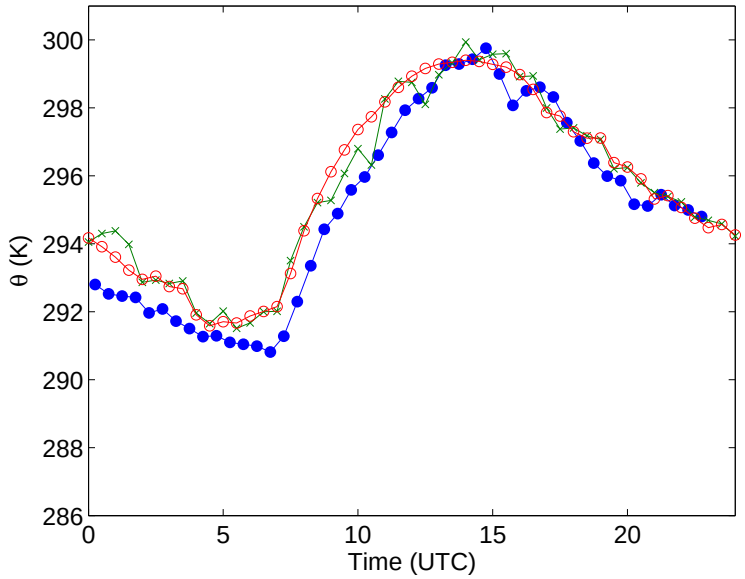

Figure 8.37: Surface potential temperature time series. —●— Observations; —○— MOISLU; —×— MOISLU-NOTURB

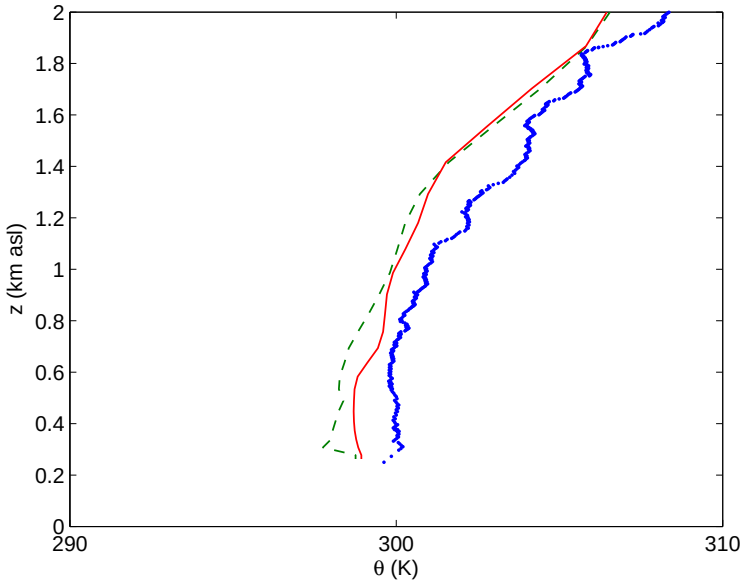

Figure 8.38: Potential temperature soundings at 1208 UTC. ····· Observations; —— MOISLU; - - - - MOISLU-NOTURB

using the DRM models with the base case TKE-1.5 closure (used in the MOISLU simulations). Specifically, we use the dynamic Wong-Lilly closure (DWL-SMAG, with the near-wall static Smagorinsky modification and the near-wall stress model) and the model with the lowest level of reconstruction (DRM-ADM0-SMAG) (see Chapters 6 and 7). The differences in the TKE-1.5 and DRM simulations are not large. Figure 8.41 shows one of the largest differences observed in the vertical potential temperature profiles during the day.

Figures 8.42-8.44 show vertical cross-sections and profiles of time-averaged resolved and SFS stresses in the uw and vw planes from DRM-ADM0-SMAG results. Compared to Figs. 8.19-8.21, the DRM-ADM0-SMAG results give a significantly larger contribution from the SFS terms. This is consistent with the findings in Chapters 6 and 7 where the SFS stresses using DRM were larger (than those from an eddy-viscosity model) due to the RSFS contribution. The distribution of stress is also different throughout the valley.

Figures 8.45 and 8.46 show diurnal variations of the absolute and root-mean-square differences for surface station and sounding profiles at A1 (Bosco di Sotto) between the TKE-1.5 and DRM-ADM0-SMAG results, as done in Figs. 8.33 and 8.34. The differences at site A1 are largest at night and during along-valley flow transitions, but the timing is different for different parameters. The largest wind speed difference, for example, occurs in the late afternoon to evening, while the largest specific humidity difference occurs earlier.

The relative insensitivity of the simulation results to the turbulence model (compared to soil moisture, for example) may reflect the influence of the lateral boundary forcing. The lateral boundary conditions are time dependent, but are only updated hourly. Intermediate values are linearly interpolated. The simulations of flow over Askervein Hill (Chapter 7) showed that realistic turbulent inflow conditions were necessary for satisfactory results. The lateral forcing in the Riviera is not fully turbulent, so the turbulence must develop while the flow progresses through the domain and is influenced by the complex topography. Small-scale motions are present in the simulations (see the contour plots and cross-sections in Section 8.5), but the afternoon winds are quite strong, yielding a relatively short effective residence time of air parcels in the valley when compared to the 30-hour simulation time. Thus, small differences that

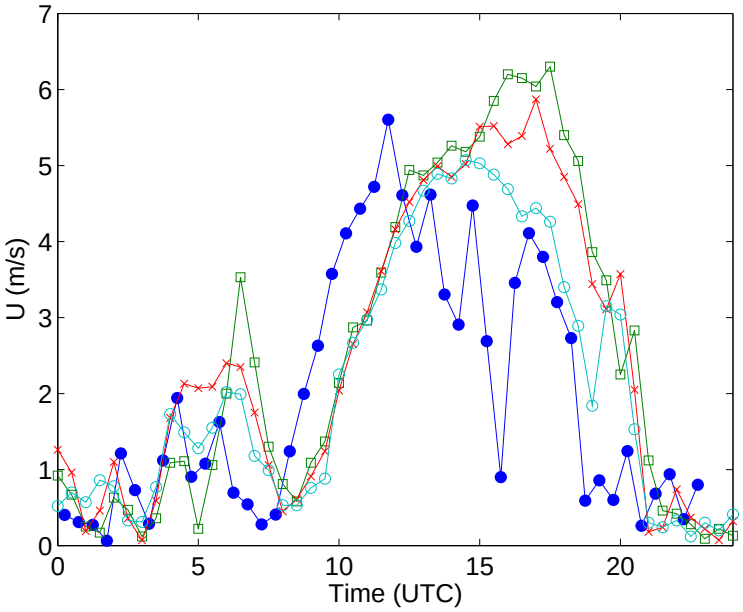

(a)

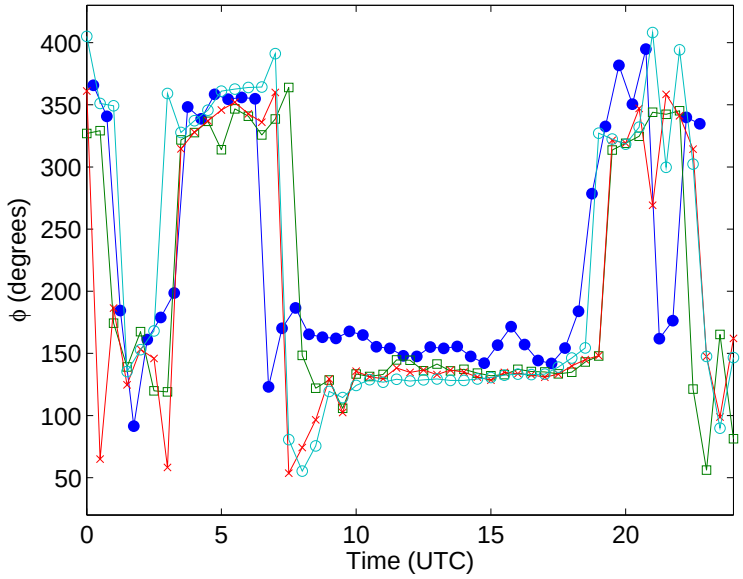

(b)

Figure 8.39: Surface time series comparisons at Bosco di Sotto (site A1) for (a) wind speed and (b) wind direction. —●— Observations; —○— MOISLU; —×— MOISLU-DWLSMAG; —□— MOISLU-DRM-ADM0-SMAG

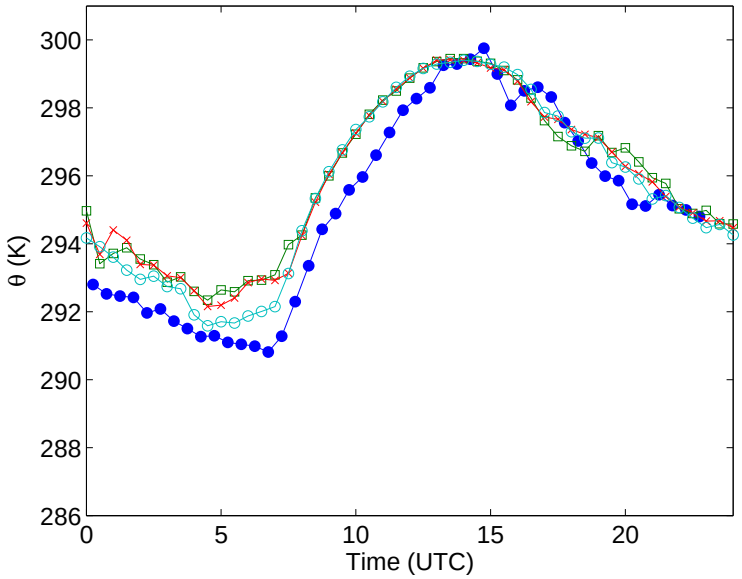

Figure 8.40: Surface potential temperature time series. —●— Observations; —○— MOISLU; —×— MOISLU-DWLSMAG; —□— MOISLU-DRM-ADM0-SMAG

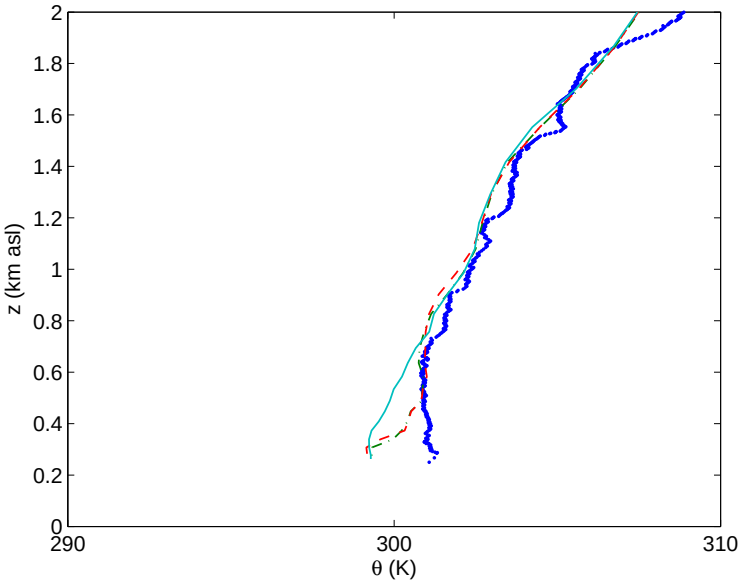

Figure 8.41: Potential temperature soundings at 1508 UTC. ····· Observations; ——— MOISLU; - - - - MOISLU-DWLSMAG; —·— MOISLU-DRM-ADM0-SMAG

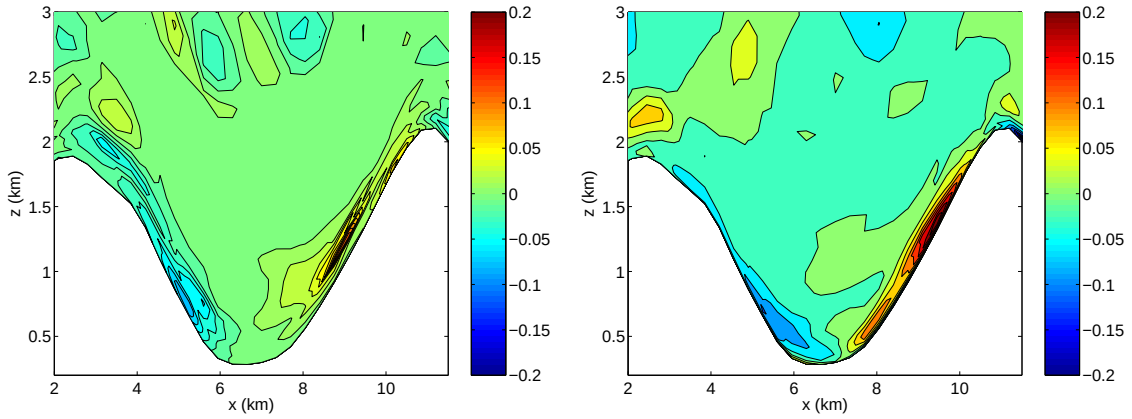

(a) (b)

Figure 8.42: Vertical cross-sections of (a) resolved uw and (b) SFS τ_{13} stress (m^2/s^2) perpendicular to valley axis at site A1 using DRM-ADM0-SMAG. Time averaged between 1300 and 1500 UTC at 300 s intervals.

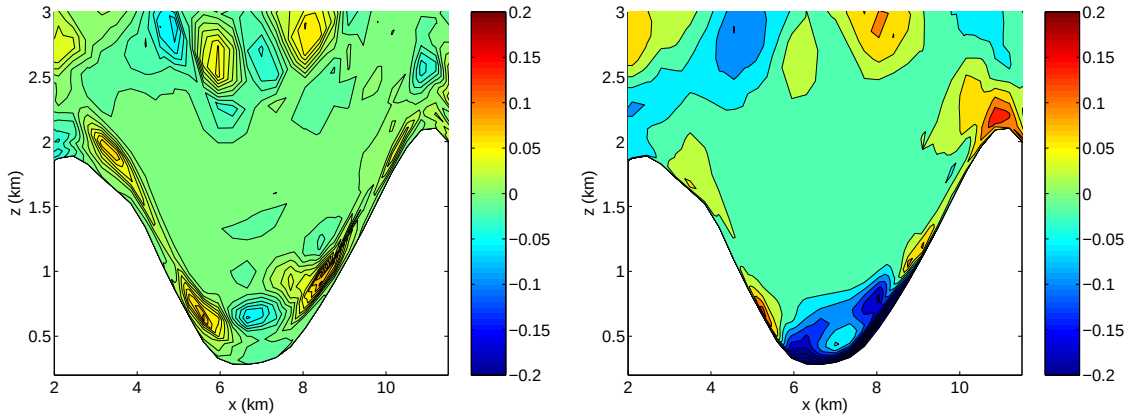

(a) (b)

Figure 8.43: Vertical cross-sections of (a) resolved vw and (b) SFS τ_{23} stress (m^2/s^2) perpendicular to valley axis at site A1 using DRM-ADM0-SMAG. Time averaged between 1300 and 1500 UTC at 300 s intervals.

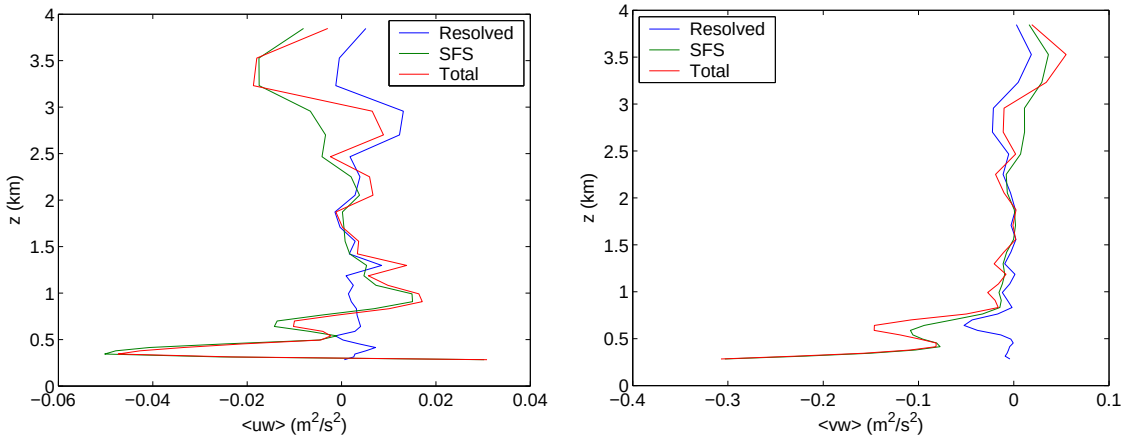

(a) (b)

Figure 8.44: Vertical profile of resolved, subfilter-scale, and total stress for (a) uw and (b) vw at the valley floor using DRM-ADM0-SMAG. Time averaged between 1300 and 1500 UTC at 300 s intervals.

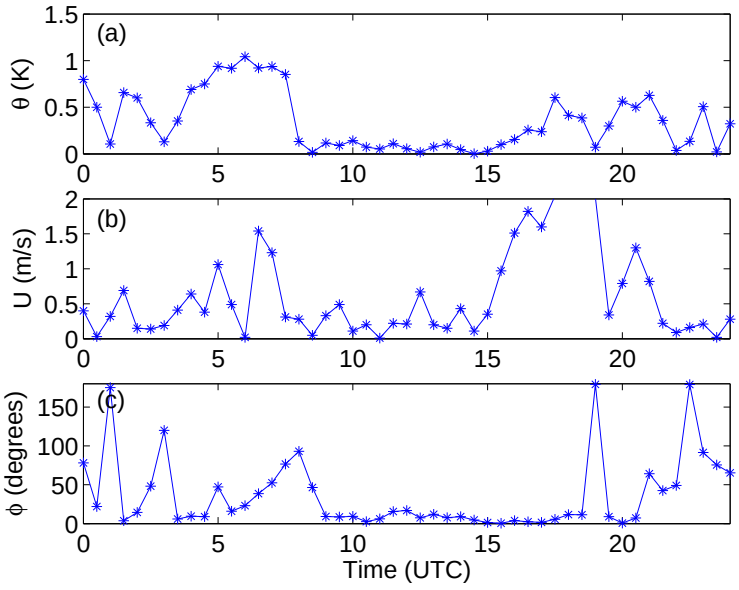

Figure 8.45: Absolute difference for surface station time series at site A1 for MOISLU and MOISLU-DRM-ADM0-SMAG simulations, for (a) potential temperature, (b) wind speed, and (c) wind direction.

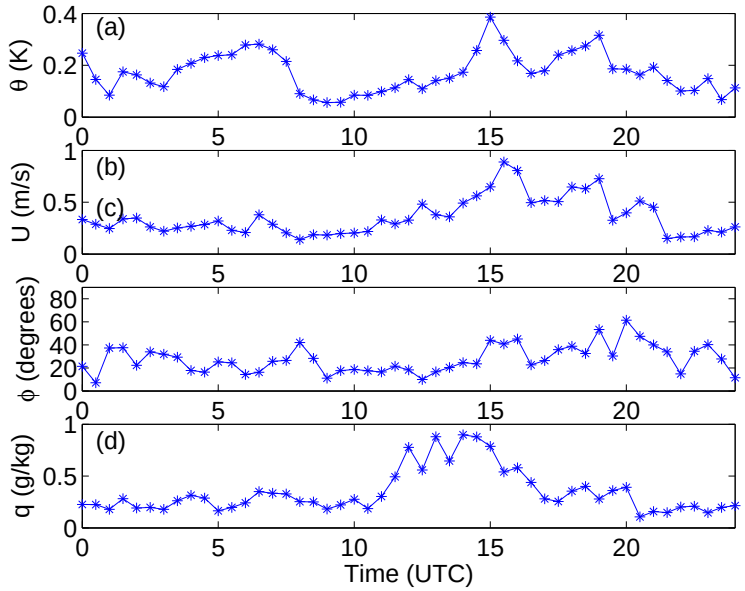

Figure 8.46: Root-mean-square difference for sounding profiles at site A1 for MOISLU and MOISLU-DRM-ADM0-SMAG simulations as a function of time, for (a) potential temperature, (b) wind speed, and (c) wind direction.

arise due to different turbulence models (or topographic shading and other parameterizations) do not have time to manifest themselves especially when along-valley winds are strong. Figure 8.47 shows the differences that occur in a one-hour simulation using identical initial and boundary conditions, but different turbulence models. It is clear that the effect of the turbulence closure is not negligible; however, it is difficult to quantitatively evaluate the performance of the models because of the lack of high-resolution observation data. Simulations over the entire day may be more strongly influenced by lateral boundary conditions and surface characteristics, but the finer details change as well. It is especially in the near-surface region of the flow, where turbulence models are important, that accurate predictions of mixing and transport are needed for air pollution.

8.7 Conclusions

We have shown that ARPS can accurately reproduce the valley winds and circulations that were observed under convective conditions during the MAP-Riviera project field

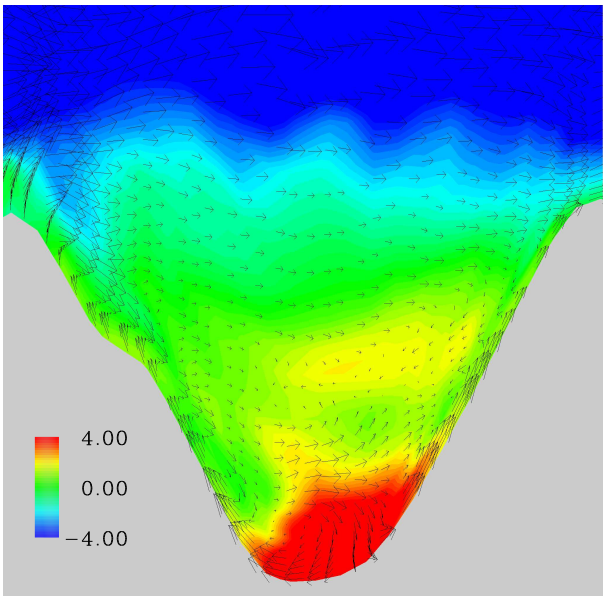

(a)

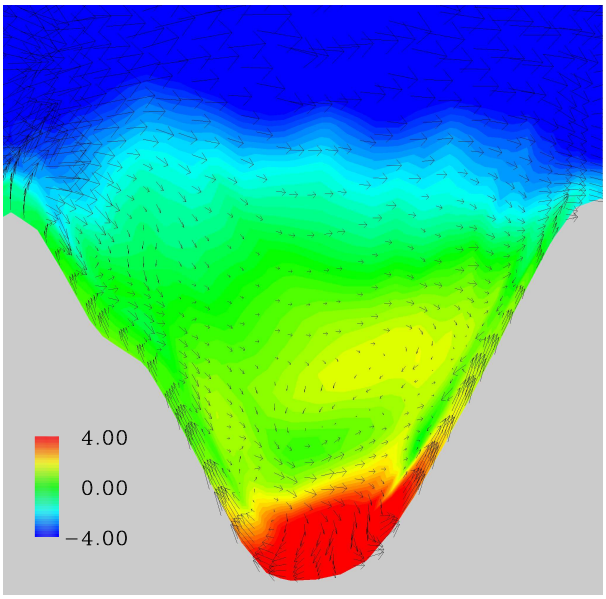

(b)

Figure 8.47: Cross-valley winds (vectors) and along-valley winds (m/s, shaded: blue (down-valley), red (up-valley)) at 1300 UTC from the 350 m grid for (a) TKE-1.5 and (b) DRM-ADM0-SMAG turbulence closures. Simulations are from 1200 to 1300 UTC using identical initial and boundary conditions.

campaign of 1999. This success required careful initialization with high-resolution land use and soil moisture data sets, among other considerations. In contrast, a straightforward grid nesting approach did not yield satisfactory results. The sensitivity of the results to changes in simulation settings was explored by comparisons to observed soundings and surface measurements on the Riviera Valley floor. It is found that even with strong local thermal forcing, the onset and magnitude of the up-valley winds are highly sensitive to surface fluxes in areas which are well outside the high-resolution domain. These processes directly influence the flow structure in the high-resolution domain via its lateral boundary conditions, but are inadequately resolved on the coarser grid of the previous nesting level. While the impact of topographic shading on the flow dynamics is small, the improvement in the radiation curves is significant. High-resolution landuse data also improve agreement with field measurements. The sensitivity to surface conditions, particularly soil moisture, points to a need for better surface characterization datasets for initialization.

The effect of different turbulence models in the Riviera Valley is unclear. Simulations without a turbulence model were poor. Results with the dynamic reconstruction approach (of Chapters 6 and 7), however, did not differ appreciably from the standard TKE-1.5 closure, perhaps because the turbulent stresses were only significant in the lowest 500 m near the surface. Strong forcing at the lateral boundaries may also limit the development of turbulent structures within the nested domain. The use of two-way grid nesting should be explored to determine the effects of interaction of higher-frequency motions (in time) across the boundaries. Higher grid resolution will allow the representation of finer-scale motions and may improve the ability of the SGS turbulence models to contribute appropriately under stable stratification.

Chapter 9

Summary and recommendations

9.1 Summary

Large-eddy simulations of the atmospheric boundary layer are strongly influenced by the selection of the lower boundary conditions and turbulence models near the surface. In this dissertation, a new turbulence closure approach has been developed and validated for a variety of turbulent flow applications. The method is based on scale partitioning which also accommodates the role of near-surface stresses for flow over rough surfaces. We have demonstrated that a systematic approach which takes into account the effect of numerical errors, such as finite-difference and aliasing (Chapter 4), is capable of providing significant improvements over traditional methods. This is the first time, to our knowledge, that reconstruction (scale-similarity) or dynamic turbulence models have been applied to full-scale simulations of the atmospheric boundary layer over either flat or complex terrain.

Our explicit filtering and reconstruction approach involves the application of an explicit filter to separate the resolved and subfilter scales in LES. The resolved subfilter scales can be reconstructed using a series expansion, such as the Taylor series (Chapter 3) or approximate deconvolution methods, while the subgrid-scale stresses must be modeled, for example with an eddy-viscosity model.

The first validation of this approach was for low Reynolds number channel flow (Chapter 5), where we found that increasing levels of reconstruction (for the RSFS component) improved the agreement with direct numerical simulation (DNS) results. The dynamic reconstruction model (DRM) combines reconstruction with a dynamic

eddy-viscosity model (Smagorinsky). A significant discovery was that the SFS stresses grow with increasing reconstruction with the DRM, largely from the contribution of the RSFS components. The agreement with stresses extracted from DNS data is excellent.

When applied to neutrally-stratified atmospheric boundary layer flows (Chapter 6), the explicit filtering and reconstruction approach requires augmentation from a near-wall stress layer. This enhanced stress layer represents the stresses induced by subgrid-scale surface roughness, poor resolution, and large grid aspect ratios near the wall. We use the DRM (with either the Taylor series or approximate deconvolution methods with the dynamic eddy-viscosity model of Wong & Lilly (1994)) together with the near-wall stress model of Brown *et al.* (2001). This hybrid approach corrects the near-wall behavior of the velocity profile in neutral boundary layer flow. Agreement with similarity theory is evidenced by the reproduction of the expected logarithmic profile near the wall. The level of reconstruction affects the partitioning of the RSFS and SGS stresses, with the RSFS (and total SFS) contributions increasing with increasing reconstruction level, as seen in the channel flow simulations in Chapter 5.

We next evaluated the performance of the DRM for flow over Askervein Hill in Scotland (Chapter 7). Field observations provided evidence of intermittent separation in the lee of the hill, which was not captured by simulations using standard closure models (e.g. TKE-1.5). The DRM results (with the near-wall stress model) did show the expected intermittent separation and hence improved agreement with time-averaged measurements of flow speed-up over the hill. The Askervein simulations also demonstrated that inclusion of terrain created difficulties for the dynamic eddy-viscosity model. Increasing levels of reconstruction could only be accommodated by removing the contribution of the dynamic model and replacing it with a static-coefficient Smagorinsky model in the lowest few levels near the wall. The reasons for the observed instabilities require future research on the behavior of stresses in the near-wall region.

The ultimate test for our turbulence modeling approach was performed in simulations of flow in the Riviera Valley in Switzerland (Chapter 8). Here, the steep terrain, heterogeneous surface conditions, and lateral boundary conditions pose severe challenges to any numerical simulation. We performed simulations over a 30-hour period

that coincided with observations during the MAP-Riviera project field campaign. The simulations required careful selection of appropriate surface datasets and boundary conditions. Results were particularly sensitive to soil moisture values. There was excellent agreement with observations at surface stations, soundings, and aircraft measurements. The use of the DRM (modified near the wall) in this valley flow was successful, but was overshadowed by differences in surface fluxes determined by the specification of surface characteristics. The lateral boundary conditions also largely determined the flow forcing; e.g. afternoon flow conditions in the 350 m nesting level were somewhat insensitive to small changes in the flow earlier in the day. The implementation of two-way interactive nesting and the use of larger grid domains could affect the development and impact of turbulent motions in the simulated Riviera Valley atmosphere.

9.2 Recommendations

Given the improved results for atmospheric boundary layer simulations using the explicit filtering and reconstruction approach, it is clear that all LES codes will benefit from the inclusion of scale-similar terms in the turbulence model. Implementation of the series expansion models is straightforward. The dynamic eddy-viscosity model of Wong & Lilly (1994) is also simple to implement, but does require modifications near the surface for flow over complex terrain. These adjustments are not yet clearly understood, and may perhaps be addressed by consideration of improved near-wall stress models. Instead of the dynamic model, which can lead to instabilities over terrain, a constant coefficient Smagorinsky model or the TKE-1.5 closure can easily be used. These models require tunable coefficients, which are undesirable for general flows. The improved correlations and reconstruction of the RSFS stresses will, however, still be beneficial, particularly in improving the alignment of stress tensors and allowing for energy backscatter in the flow.

The sensitivity to surface boundary conditions has also been clearly shown in all the simulations from the neutral boundary layer (flat terrain) to the complex Riviera Valley flow. Much research is needed to construct a more robust near-wall stress representation. Incorporation of tree and urban canopy information could, for example, be beneficial. Simulations of real flow conditions (e.g. the Riviera Valley

simulations, and general weather forecasting) also require detailed knowledge of the soil and vegetation properties at the surface. The lack of accurate soil moisture data at 1 km resolution, for example, was found to be the determining factor in the success of the Riviera flow simulations. Radiation models are also currently limited to one (vertical) dimension, but should include the influence of neighboring terrain on local radiative heat fluxes that are important in steep terrain.

Extensive field campaigns and remote sensing developments are needed to obtain the necessary input data for forecast models. The design of such field campaigns could be greatly improved by examining model results like those obtained here for the Riviera Valley. Grid nesting techniques at the lateral boundaries also need further exploration. The transmission of turbulent fluctuations from the coarse to the fine grid at the lateral boundaries (particularly for one-way grid nesting) is currently severely limited by the grid resolution and the frequency at which lateral boundary condition data are available. More frequent boundary condition updates and two-way nesting techniques should be investigated.

Appendix A

Taylor series expansion models

The forms of the models considered in the *a priori* tests are given below:

S: Smagorinsky

$$\tau_{ij} = -2(C_S\Delta)^2(\overline{S}_{ij}\overline{S}_{ij})^{1/2}\overline{S}_{ij}$$

B: Bardina scale-similarity

$$\tau_{ij} = \overline{\overline{u}_i\overline{u}_j} - \overline{\overline{u}}_i\overline{\overline{u}}_j$$

MC: Modified Clark

$$\tau_{ij} = \frac{\Delta^2}{12}\overline{\frac{\partial\overline{u}_i}{\partial x_m}\frac{\partial\overline{u}_j}{\partial x_m}}$$

T4: Series expansion, 4th order

$$\tau_{ij} = \overline{\overline{u}_i\overline{u}_j} - \overline{u}_i\overline{u}_j - \frac{\Delta^2}{24}\left(\overline{\overline{u}_i\nabla^2\overline{u}_j} + \overline{\overline{u}_j\nabla^2\overline{u}_i}\right)$$

MT4: Modified series expansion, 4th order

$$\tau_{ij} = \overline{\overline{u}_i\overline{u}_j} - \overline{\overline{u}}_i\overline{\overline{u}}_j - \frac{\Delta^2}{24}\left(\overline{\overline{u}_i\nabla^2\overline{u}_j} + \overline{\overline{u}_j\nabla^2\overline{u}_i}\right) + \frac{\Delta^2}{24}\left(\overline{\overline{u}}_i\nabla^2\overline{\overline{u}}_j + \overline{\overline{u}}_j\nabla^2\overline{\overline{u}}_i\right) \tag{A.1}$$

MT6: Modified series expansion, 6th order

$$\begin{aligned}
\tau_{ij} &= \overline{\overline{u}_i\overline{u}_j} - \overline{\overline{u}}_i\overline{\overline{u}}_j - \frac{\Delta^2}{24}\left(\overline{\overline{u}_i\nabla^2\overline{u}_j} + \overline{\overline{u}_j\nabla^2\overline{u}_i}\right) + \frac{\Delta^2}{24}\left(\overline{\overline{u}}_i\nabla^2\overline{\overline{u}}_j + \overline{\overline{u}}_j\nabla^2\overline{\overline{u}}_i\right) \\
&+ \frac{\Delta^4}{1152}\left(\overline{\overline{u}_i\frac{\partial^4\overline{u}_j}{\partial x^4}} + \overline{\overline{u}_i\frac{\partial^4\overline{u}_j}{\partial y^4}} + \overline{\overline{u}_i\frac{\partial^4\overline{u}_j}{\partial z^4}} + \overline{\overline{u}_j\frac{\partial^4\overline{u}_i}{\partial x^4}} + \overline{\overline{u}_j\frac{\partial^4\overline{u}_i}{\partial y^4}} + \overline{\overline{u}_j\frac{\partial^4\overline{u}_i}{\partial z^4}}\right) \\
&- \frac{\Delta^4}{1152}\left(\overline{\overline{u}}_i\frac{\partial^4\overline{\overline{u}}_j}{\partial x^4} + \overline{\overline{u}}_i\frac{\partial^4\overline{\overline{u}}_j}{\partial y^4} + \overline{\overline{u}}_i\frac{\partial^4\overline{\overline{u}}_j}{\partial z^4} + \overline{\overline{u}}_j\frac{\partial^4\overline{\overline{u}}_i}{\partial x^4} + \overline{\overline{u}}_j\frac{\partial^4\overline{\overline{u}}_i}{\partial y^4} + \overline{\overline{u}}_j\frac{\partial^4\overline{\overline{u}}_i}{\partial z^4}\right) \\
&+ \frac{5\Delta^4}{1728}\left(\overline{\overline{u}_i\frac{\partial^4\overline{u}_j}{\partial x^2\partial y^2}} + \overline{\overline{u}_i\frac{\partial^4\overline{u}_j}{\partial y^2\partial z^2}} + \overline{\overline{u}_i\frac{\partial^4\overline{u}_j}{\partial x^2\partial z^2}} + \overline{\overline{u}_j\frac{\partial^4\overline{u}_i}{\partial x^2\partial y^2}} + \overline{\overline{u}_j\frac{\partial^4\overline{u}_i}{\partial y^2\partial z^2}} + \overline{\overline{u}_j\frac{\partial^4\overline{u}_i}{\partial x^2\partial z^2}}\right) \\
&- \frac{5\Delta^4}{1728}\left(\overline{\overline{u}}_i\frac{\partial^4\overline{\overline{u}}_j}{\partial x^2\partial y^2} + \overline{\overline{u}}_i\frac{\partial^4\overline{\overline{u}}_j}{\partial y^2\partial z^2} + \overline{\overline{u}}_i\frac{\partial^4\overline{\overline{u}}_j}{\partial x^2\partial z^2} + \overline{\overline{u}}_j\frac{\partial^4\overline{\overline{u}}_i}{\partial x^2\partial y^2} + \overline{\overline{u}}_j\frac{\partial^4\overline{\overline{u}}_i}{\partial y^2\partial z^2} + \overline{\overline{u}}_j\frac{\partial^4\overline{\overline{u}}_i}{\partial x^2\partial z^2}\right) \\
&+ \frac{\Delta^4}{576}\left(\overline{\nabla^2\overline{u}_i\nabla^2\overline{u}_j} - \nabla^2\overline{\overline{u}}_i\nabla^2\overline{\overline{u}}_j\right)
\end{aligned}$$

where $\overline{S}_{ij}$ is the filtered velocity strain tensor, and C_S is the Smagorinsky constant, here taken to be 0.09 (Bardina *et al.*, 1983) (which does not affect correlations, but does affect ratios). The modified Clark model can be obtained from a rearrangement of the 4th-order series expansion model, as derived below, and is a variation of the model considered by Clark *et al.* (1979). Here filtering is applied to the product of the two derivatives, whereas in the original, each term is separately filtered.

The modified Clark model is derived by "unbarring" terms in the τ_{ik} expansion, *i.e.*, removing one level of filtering, using Eq. 3.10. Wherever terms of the form $\overline{u}_i - \frac{\Delta^2}{24}\nabla^2\overline{u}_i$ appear, they can be replaced (to 2nd-order accuracy) by the unfiltered variable u_i. This simplifies terms in the derivation of the evolution equation (3.12) for the modeled SFS stress. We now apply "unbarring" to the SFS stress model given in Eq. 3.13. First, rewriting the second-derivative terms using the product rule, we obtain

$$\begin{aligned}
\tau_{ik} &= \overline{\overline{u}_i\overline{u}_k} - \overline{u}_i\overline{u}_k - \frac{\Delta^2}{24}\overline{\overline{u}_i\nabla^2\overline{u}_k} - \frac{\Delta^2}{24}\overline{\overline{u}_k\nabla^2\overline{u}_i} + O(\Delta^4) \\
\tau_{ik} &= \overline{\overline{u}_i\overline{u}_k} - \overline{u}_i\overline{u}_k - \frac{\Delta^2}{24}\nabla^2\overline{\overline{u}_i\overline{u}_k} + \frac{\Delta^2}{12}\overline{\frac{\partial\overline{u}_k}{\partial x_j}\frac{\partial\overline{u}_i}{\partial x_j}} + O(\Delta^4) \; .
\end{aligned}$$

Now "unbarring" the first and third terms on the right-hand side, we obtain $\overline{u}_i\overline{u}_j$, which cancels the second term, and gives

$$\tau_{ik} = \frac{\Delta^2}{12}\overline{\frac{\partial\overline{u}_k}{\partial x_j}\frac{\partial\overline{u}_i}{\partial x_j}} + O(\Delta^4) \; , \tag{A.2}$$

which shows that the SFS stress is 2nd-order in the filter width. It can be shown that this form also satisfies the evolution equation for τ_{ik} to fourth order.

Appendix B

Subfilter-scale scalar transport modeling*

B.1 Introduction

Large-eddy simulation (LES) is an important tool for studying meso-scale atmospheric flow fields, where practical grid sizes are much larger than what is required to resolve all of the turbulent motions. The quality of the subfilter-scale (SFS) model used to represent the unresolved motions is thus very important for accurate calculations. Cederwall & Street (1999) showed that use of an improved SFS model revealed turbulent episodes known to occur in the stable boundary layer but not found in previous simulations.

The transport of pollutants is difficult to model but is of particular interest in the atmospheric boundary layer (ABL). Most simulations use an eddy-diffusivity model in which the SFS transport terms are aligned with the resolved-scale strain rate and are dissipative. Here, a series expansion model is described for the unclosed terms of the scalar transport equation, analogous to the model presented by Street (1999) and Katopodes *et al.* (2000*b*) (see Chapter 3) for the momentum equation. This model has no free parameters, is straightforward to derive, and correlates very well with direct numerical simulation (DNS) data in *a priori* tests. The model is of scale-similar form,

*This appendix is a reproduction (with minor modifications) of the paper "Subfilter-scale scalar transport for large-eddy simulation" by Fotini V. Katopodes (the principal author), Robert L. Street, and Joel H. Ferziger, published in the proceedings of the 14th Symposium on Boundary Layers and Turbulence, American Meteorological Society, August 2000, pages 472-475 (Katopodes *et al.*, 2000*a*).

and thus allows backscatter, or scalar flux from small to large scales. This is believed to be especially important when the large scales are not fully resolved in the ABL (Mason & Thomson, 1992).

To model the unclosed SFS terms in the scalar transport equation, we use successive inversion of a Taylor series expansion to express the unfiltered velocity and scalar concentration in terms of their filtered (resolved) counterparts. We then derive SFS models of arbitrary order of accuracy in the filter width. Furthermore, the SFS model satisfies the evolution equations for the SFS scalar transport to the specified order of accuracy.

This appendix presents the derivation of the new SFS model, followed by preliminary tests of the model using *a priori* tests with DNS data of sheared, stably-stratified homogeneous turbulence. We also describe the implementation of this model.

B.2 Closure models for scalar transport

The scalar transport equation is given by

$$\frac{\partial \theta}{\partial t} + u_j \frac{\partial \theta}{\partial x_j} = \kappa \frac{\partial^2 \theta}{\partial x_j \partial x_j} \tag{B.1}$$

where u_j denotes the velocity, θ is the scalar variable of interest (such as concentration or temperature), and κ is its diffusivity. Repeated indices indicate summation. Applying a spatial filter to this equation, we obtain

$$\frac{\partial \overline{\theta}}{\partial t} + \overline{u}_j \frac{\partial \overline{\theta}}{\partial x_j} = \kappa \frac{\partial^2 \overline{\theta}}{\partial x_j \partial x_j} - \frac{\partial Q_j}{\partial x_j} \tag{B.2}$$

where

$$Q_j = \overline{u_j \theta} - \overline{u}_j \overline{\theta} \tag{B.3}$$

is the subfilter-scale scalar flux which must be modeled. The anisotropic Gaussian filter is used here, where $\Delta_x, \Delta_y, \Delta_z$ are the filter widths in each direction. Other spatially compact filters, including asymmetric filters, give similar results, but with a change in the expansion coefficients, as described below (see Shah & Ferziger, 1995). The filtering operation is assumed to commute with the spatial derivatives, which

is true for spatially homogeneous filters. Some error is introduced if this is not so (Ghosal & Moin, 1995).

The traditional procedure uses scaling and physical arguments to model the unclosed terms in Eq. B.3. A gradient diffusion form is often assumed, where the SFS scalar flux is related to gradients of the resolved quantity by

$$Q_j = -\kappa_T \frac{\partial \overline{\theta}}{\partial x_j} \ , \tag{B.4}$$

where κ_T is the eddy diffusivity. In LES, a common treatment is to use the Smagorinsky model (1963), which assumes

$$\kappa_T = \frac{1}{\sigma_T}(C_S\Delta)^2(\overline{S}_{ij}\overline{S}_{ij})^{1/2}\overline{S}_{ij} \ , \tag{B.5}$$

where C_S is the Smagorinsky constant, σ_T the turbulent Schmidt number (usually chosen to be approximately 1), and $\overline{S}_{ij}$ the resolved scale strain rate tensor. In ABL simulations, prognostic equations are often used to determine κ_T based on the turbulent kinetic energy (TKE).

Further developments in SFS modeling for LES have led to dynamic and mixed models (see Piomelli, 1999). These improved models have not been widely applied in atmospheric simulations; Cederwall & Street (1999) used a dynamic mixed model to simulate a stable boundary layer with good results.

Here, we do not use an eddy-diffusivity model as above. Instead, we use a model of the scale-similarity form, and do not assume a form for the SFS flux, but seek to model the unresolved velocity and scalar fields directly. In the spirit of velocity estimation models recently introduced (Geurts, 1997; Domaradzki & Saiki, 1997; Stolz & Adams, 1999), we follow a mathematical approach to obtain an approximate expression for the the unresolved variables and use these to calculate the SFS scalar flux.

This model does not require calculation of extra prognostic equations and is free of adjustable coefficients. It can be shown (see Chapter 3) that the model presented here satisfies the evolution equations for the SFS scalar flux to fourth order in the filter width. Thus, the effects of buoyancy, Coriolis forcing, pressure, advection, and diffusion are naturally included in the model and do not need special treatment. Furthermore, the model can be specified to any desired order of accuracy.

The goal of a closure model is to express the unresolved quantities in terms of the known (computable) resolved quantities, *i.e.*, we seek to write $\theta = f(\overline{\theta})$. With that aim, we introduce a multi-dimensional Taylor expansion for the scalar field at any point,

$$\begin{aligned}\theta(x_j') &= \theta(x_j) + (x_m' - x_m)\frac{\partial\theta(x_j)}{\partial x_m} \\ &+ \frac{1}{2}(x_m' - x_m)(x_n' - x_n)\frac{\partial^2\theta(x_j)}{\partial x_m \partial x_n} + \cdots ,\end{aligned} \tag{B.6}$$

using index notation for compactness. A similar expression can be written for the velocity field.

We now apply the Gaussian filter, which eliminates all terms with odd powers of x, y, or z, due to the filter symmetry, so that

$$\begin{aligned}\overline{\theta}(x,y,z) &= \theta + \frac{\Delta_x^2}{24}\frac{\partial^2\theta}{\partial x^2} + \frac{\Delta_y^2}{24}\frac{\partial^2\theta}{\partial y^2} + \frac{\Delta_z^2}{24}\frac{\partial^2\theta}{\partial z^2} \\ &+ \frac{\Delta_x^4}{1152}\frac{\partial^4\theta}{\partial x^4} + \frac{\Delta_y^4}{1152}\frac{\partial^4\theta}{\partial y^4} + \frac{\Delta_z^4}{1152}\frac{\partial^4\theta}{\partial z^4} \\ &+ \frac{\Delta_x^2\Delta_y^2}{1728}\frac{\partial^4\theta}{\partial x^2\partial y^2} + \frac{\Delta_y^2\Delta_z^2}{1728}\frac{\partial^4\theta}{\partial y^2\partial z^2} \\ &+ \frac{\Delta_x^2\Delta_z^2}{1728}\frac{\partial^4\theta}{\partial x^2\partial z^2} + O(\Delta^6) .\end{aligned} \tag{B.7}$$

Rearranging and using this expression recursively, we obtain

$$\begin{aligned}\theta(x,y,z) &= \overline{\theta} - \frac{\Delta_x^2}{24}\frac{\partial^2\overline{\theta}}{\partial x^2} - \frac{\Delta_y^2}{24}\frac{\partial^2\overline{\theta}}{\partial y^2} - \frac{\Delta_z^2}{24}\frac{\partial^2\overline{\theta}}{\partial z^2} \\ &+ \frac{\Delta_x^4}{1152}\frac{\partial^4\overline{\theta}}{\partial x^4} + \frac{\Delta_y^4}{1152}\frac{\partial^4\overline{\theta}}{\partial y^4} + \frac{\Delta_z^4}{1152}\frac{\partial^4\overline{\theta}}{\partial z^4} \\ &+ \frac{5\Delta_x^2\Delta_y^2}{1728}\frac{\partial^4\overline{\theta}}{\partial x^2\partial y^2} + \frac{5\Delta_y^2\Delta_z^2}{1728}\frac{\partial^4\overline{\theta}}{\partial y^2\partial z^2} \\ &+ \frac{5\Delta_x^2\Delta_z^2}{1728}\frac{\partial^4\overline{\theta}}{\partial x^2\partial z^2} + O(\Delta^6) ,\end{aligned} \tag{B.8}$$

which expresses the full scalar at a point (x, y, z) in terms of the filtered scalar at that point. If the filter is isotropic, Eq. B.8 reduces to

$$\begin{aligned}\theta &= \overline{\theta} - \frac{\Delta^2}{24}\nabla^2\overline{\theta}_i + \frac{\Delta^4}{1152}\left(\frac{\partial^4\overline{\theta}}{\partial x^4} + \frac{\partial^4\overline{\theta}}{\partial y^4} + \frac{\partial^4\overline{\theta}}{\partial z^4}\right) \\ &+ \frac{5\Delta^4}{1728}\left(\frac{\partial^4\overline{\theta}}{\partial x^2\partial y^2} + \frac{\partial^4\overline{\theta}}{\partial y^2\partial z^2} + \frac{\partial^4\overline{\theta}}{\partial x^2\partial z^2}\right) + O(\Delta^6)\ . \end{aligned} \tag{B.9}$$

This simplified form of the expansion will be used in the remaining derivations, as the anisotropic form is more cumbersome algebraically. Terms of $O(\Delta^4)$ and higher will also be ignored subsequently. The anisotropic results to fourth order can be recovered by replacing $\frac{\Delta^2}{24}\nabla^2$ by

$$\frac{\Delta_x^2}{24}\frac{\partial^2}{\partial x^2} + \frac{\Delta_y^2}{24}\frac{\partial^2}{\partial y^2} + \frac{\Delta_z^2}{24}\frac{\partial^2}{\partial z^2}\ . \tag{B.10}$$

Now we can derive models for Q_j by substituting the series expansions for θ (Eq. B.9) and the analogous expression for velocity directly into Eq. B.3. When both the unclosed and explicit terms are expanded, and terms of fourth order and higher are neglected, we obtain

$$\begin{aligned}Q_j &= \overline{\overline{u}_i\overline{\theta}} - \overline{\overline{u}}_i\overline{\overline{\theta}} - \frac{\Delta^2}{24}\overline{\overline{u}_i\nabla^2\overline{\theta}} - \frac{\Delta^2}{24}\overline{\overline{\theta}\nabla^2\overline{u}_i} \\ &+ \frac{\Delta^2}{24}\overline{\overline{u}}_i\nabla^2\overline{\overline{\theta}} + \frac{\Delta^2}{24}\overline{\overline{\theta}}\nabla^2\overline{\overline{u}}_i + O(\Delta^6)\ . \end{aligned} \tag{B.11}$$

The first two terms are analogous to the Leonard terms in the SFS stress; the higher order derivative terms can be shown to be dissipative (Clark *et al.*, 1977).

B.3 *A priori* tests

A priori tests for several SFS models are performed using a direct numerical simulation (DNS) dataset for stably-stratified homogeneous shear flow computed by Shih *et al.* (2000). *A priori* tests indicate the degree of correlation between the modeled and exact subfilter-scale terms (see Clark *et al.*, 1977). These tests are useful indications of the expected performance of a SFS model in actual LES computations (*a posteriori* tests), even though in this case the DNS data is for low Reynolds number

flow. The DNS data are sampled on the scale of the LES grid and filtered using an anisotropic Gaussian filter to obtain the LES field, $\overline{u}_i$. Then the LES field can be used to generate higher order approximations using variations of Eq. B.11.

Tables B.1-B.2 show correlation coefficients (C) and ratios (R) for the subfilter-scale quantities: Q_i is the SFS flux, $\partial Q_j/\partial x_j$ is the divergence of the subfilter flux which appears in the transport equations, and $Q_j \partial\overline{\theta}/\partial x_j$ is the SFS scalar dissipation. The ratio is the exact DNS rms value divided by the modeled rms value, and should be close to one. For the scalar dissipation term, the ratio gives an indication of the magnitude of the scalar dissipation which is captured by the model. For comparison, the equivalent momentum terms are also listed.

Results are presented for the Smagorinsky (S), and 2nd- (E2), 4th- (E4), and 6th-order (E6) series expansion models (using Eq. B.11). The E2 model is of the scale-similar form considered by Bardina *et al.* (1983) for the SFS stress. LES to DNS grid ratios of $GR = 2, 4, 8$ are considered, where $\Delta_{LES} = GR\ \Delta_{DNS}$. (Only the $GR = 2, 8$ cases are shown here.) In each case the filter-grid ratio is $FGR = \Delta/\Delta_{LES} = 2$.

For the E6 model and $GR = 2$, the correlation for the SFS scalar dissipation is 0.999, with the ratio of rms exact to modeled values at 1.021, indicating that the SFS dissipation is captured to within 2%. On the other hand, the Smagorinsky model for this case exhibits a correlation of -0.010, and a ratio of 1.904, indicating that the representation of the SFS motions is extremely poor. In mesoscale simulations of the atmosphere, the grid size will be considerably larger than the DNS grid size, making it harder to construct the SFS motions accurately using knowledge of the resolved scales only. However, even for $GR = 8$, the E6 model gives a ratio for the SFS scalar dissipation of 1.273, with a correlation of 0.973, much higher than any other model tested.

To illustrate the performance of the series model in representing the unresolved field, Fig. B.1 shows contours of the scalar field with different levels of approximation for θ, as given by Eq. B.8. The raw DNS data, which is sampled on an LES grid defined by $GR = 8$, is best represented by the 6th-order model; contours shown for this case (Fig. B.1d) indicate that the smaller features of the DNS data (Fig. B.1a) are captured quite well, unlike the lower order models.

B.4 Implementation

The expression for Q_j given in Eq. B.11 can be directly substituted into the resolved flow equation (B.2), which can then be discretized and solved numerically. This series closure model eliminates the need for prognostic equations for quantities such as turbulent kinetic energy that are usually used for turbulence closure in atmospheric models. Furthermore, there are no parameters which need to be adjusted or calculated (*cf.* the standard TKE models or dynamic Smagorinsky or dynamic mixed closure models). The model should therefore not be computationally intensive.

No assumptions about the discretization were made in any of the derivations above. The effects of discretization require modifications to the turbulence closure approach, as described in Chapters 5 and 6. It is also important that the filter width be at least twice the size of the grid spacing. Otherwise, as shown in Chapter 4 and by Ghosal (1996), discretization error will be as large as the effect of the SFS model.

B.5 Conclusion

The series model is easy to implement and provides an estimate of the SFS flux to any order of accuracy desired. The *a priori* tests indicate that the series expansion model is considerably better than the eddy-diffusivity closure models traditionally used to represent SFS scalar transport. The model has no free parameters and does not require the solution of additional prognostic equations. The series model satisfies the evolution equations for the SFS flux to the appropriately predefined order of accuracy, meaning that it is influenced by buoyancy, Coriolis, pressure, advection, and diffusion effects. It is expected that an improved SFS closure model will lead to significantly more accurate simulations of the atmospheric boundary layer, yielding insight into turbulent motions which transport pollutants.

		τ_{12}	$\frac{\partial \tau_{1j}}{\partial x_j}$	$\tau_{ij}\frac{\partial u_i}{\partial x_j}$	Q_1	Q_2	Q_3	$\frac{\partial Q_j}{\partial x_j}$	$Q_j\frac{\partial \overline{p}}{\partial x_j}$
S	C	0.1610	0.4746	0.6962	−0.1678	−0.0098	0.0094	0.0019	−0.0097
	R	3.5042	2.8092	1.4780	3.6150	0.6964	1.1373	0.4328	1.9040
$E2$	C	0.9525	0.9194	0.9665	0.9697	0.9354	0.9451	0.9196	0.9876
	R	1.3367	1.9179	1.3666	1.4497	1.4200	1.4629	2.0252	1.4350
$E4$	C	0.9875	0.9763	0.9917	0.9921	0.9803	0.9851	0.9739	0.9973
	R	1.0702	1.2636	1.0724	1.1242	1.0933	1.1085	1.2968	1.1032
$E6$	C	0.9969	0.9937	0.9972	0.9980	0.9941	0.9959	0.9916	0.9994
	R	1.0097	1.0611	1.0062	1.0346	1.0160	1.0209	1.0750	1.0207

Table B.1: Gaussian Filter: Correlations, $GR = 2$, $FGR = 2$.

		τ_{12}	$\frac{\partial \tau_{1j}}{\partial x_j}$	$\tau_{ij}\frac{\partial u_i}{\partial x_j}$	Q_1	Q_2	Q_3	$\frac{\partial Q_j}{\partial x_j}$	$Q_j\frac{\partial \overline{p}}{\partial x_j}$
S	C	0.0925	0.3041	0.3920	−0.2494	0.0064	0.0842	0.0148	−0.0395
	R	4.9880	3.1754	2.0092	11.7193	1.8005	2.7365	1.3796	2.8186
$E2$	C	0.7759	0.7852	0.8181	0.8901	0.7516	0.7583	0.7857	0.9047
	R	2.8324	4.1177	3.1285	2.7467	2.8250	2.9520	4.5566	2.8349
$E4$	C	0.8769	0.8729	0.8939	0.9431	0.8553	0.8595	0.8684	0.9459
	R	1.5989	2.0326	1.7325	1.5968	1.6290	1.6734	2.2085	1.6354
$E6$	C	0.9407	0.9326	0.9422	0.9733	0.9231	0.9288	0.9284	0.9727
	R	1.2301	1.4111	1.3038	1.2506	1.2676	1.2895	1.5104	1.2727

Table B.2: Gaussian Filter: Correlations, $GR = 8$, $FGR = 2$.

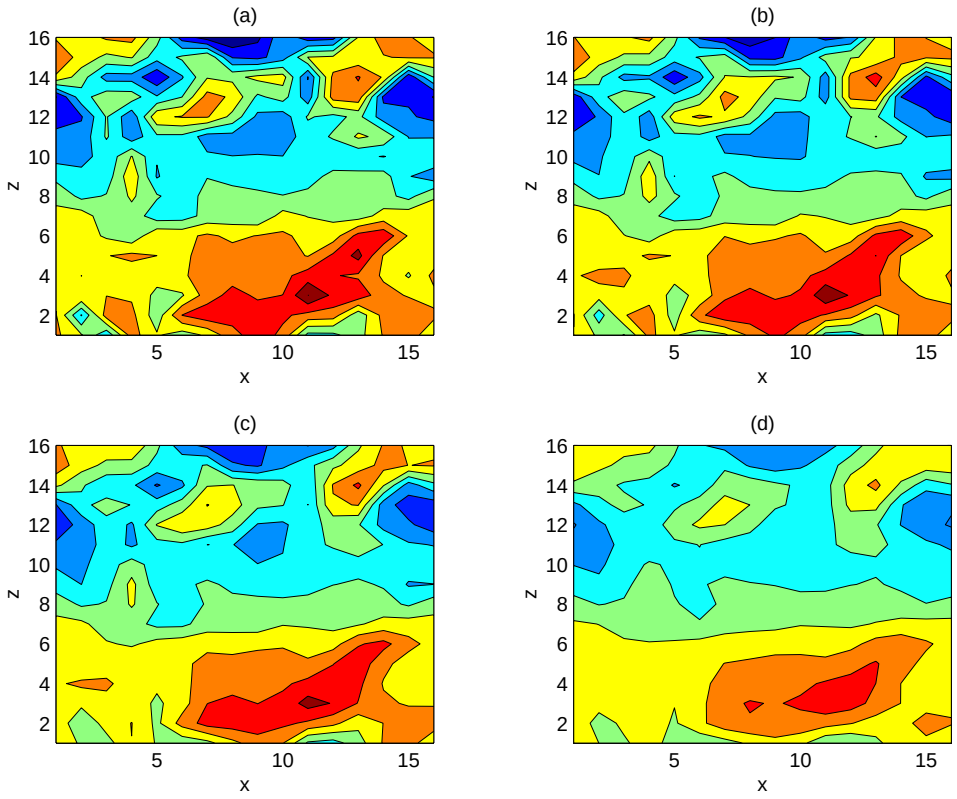

Figure B.1: Contour plots of LES estimates for θ on an x_1, x_3-plane, $GR = 8$. (a) Sampled DNS field; (b) 6th-order estimate; (c) 4th-order estimate; (d) 2nd-order estimate.

Appendix C

Advanced Regional Prediction System details

C.1 LES code selection

The essence of modeling turbulent flows lies in a synthesis of a robust numerical code, appropriate boundary conditions, an accurate SFS model, and a properly arranged grid. Several LES codes were considered for the atmospheric boundary layer simulations performed in this work, among those: the Stanford Environmental Fluid Mechanics Laboratory (EFML) code developed by Zang *et al.* (1994) (and subsequently modified by Calhoun (1998), Cui (1999), and Zedler (2002)), the RAMS code (Pielke *et al.*, 1992), NCAR's LES code (Moeng, 1984), and the ARPS code (Xue *et al.*, 1995). We note, however, that a study by Andren *et al.* (1994) concluded that differences in the numerics of the LES codes were less significant than SFS closure models. Andren *et al.* (1994) ran four LES codes (including the NCAR code considered here) with the same closure model and obtained fairly good convergence of the mean profiles. Generally, the differences due to SFS models were found to be more significant for the neutrally stratified flow than for previous tests of convective flow. Thus, while we prefer to have a code with good numerics, we need not be particularly concerned about enormous differences if different codes were used. The main reasons for choosing ARPS stem from our selected flow applications. The EFML code was intended for lower Reynolds number laboratory-scale flows and is not easily adapted

for the atmospheric boundary layer. The NCAR code is intended for idealized simulations and is not suited for complex terrain. RAMS can accommodate terrain and the appropriate initial and boundary conditions for a full-scale ABL simulation, but uses upwind advection schemes and requires a minimum eddy-viscosity value, both of which can cause excess dissipation. Also, the code is not documented as carefully as ARPS and therefore not as easy to modify.

C.2 ARPS numerical formulation

ARPS has been developed and tested at the Center for Analysis and Prediction of Storms at the University of Oklahoma over the last decade. This prediction system was designed for application to convective and cold-season storms, including real-time data assimilation and extensive post-processing features. A detailed description of this code is available in the ARPS User's Manual (Xue *et al.*, 1995) and in Xue *et al.* (2000, 2001). The numerical schemes are robust (see below) and the code can be run in parallel. These are attractive features for testing subfilter-scale models for simulations of the ABL.

The dynamic equations solved by ARPS are the three-dimensional, compressible* non-hydrostatic Navier-Stokes equations, over generalized terrain-following coordinates. The grid is orthogonal in the horizontal direction, but stretched in the vertical to follow the terrain, as in the so-called σ-z coordinate system. The model includes Coriolis forcing. Equations are solved for the three wind velocity components (u, v, w), pressure (p), potential temperature (θ), and turbulent kinetic energy (k), if used for the subfilter-scale model. Potential temperature is a conserved variable in adiabatic flows and is commonly used in atmospheric simulations; it is analogous to density,

*Though the atmosphere is compressible, compressibility effects are not generally very significant. Baines (1995) estimates that flows with vertical scales of less than 10 km are effectively incompressible. For vertical domains on the order of 10 km, the compressible flow equations should be used. The compressible Navier-Stokes equations are computationally more efficient than the incompressible equations which require solution of a Poisson equation for pressure. The compressible equations are thus often used for atmospheric flows with smaller vertical scales, even though the equations allow acoustic modes that reduce the time step required for stability. A mode-splitting algorithm for time advancement with the compressible equations, is an option that allows small time steps for the acoustic modes, and large time steps for other terms (Klemp & Wilhelmson, 1978), as used in ARPS.

and is defined as

$$\theta = T \left(\frac{p_0}{p} \right)^{0.286} \tag{C.1}$$

where T is absolute temperature, p is atmospheric pressure, and p_0 is a reference atmospheric pressure usually taken to be 100 kPa or the pressure at sea level. This scales the temperature with elevation in the atmosphere according to the adiabatic lapse rate, so that background hydrostatic variation is not considered when looking at temperature gradients.

A coordinate transformation is used to map the terrain-following coordinates to a regular grid in computational space. Several map projections can be used for larger scale simulations. The filtered momentum equations are derived in Appendix D and described in Chapter 6 of the ARPS User's Manual (Xue *et al.*, 1995). ARPS also solves prognostic equations for water vapor, cloud water, rainwater, cloud ice, snow, and graupel (hail). These quantities are affected by surface radiative forcing and convective fluxes which are parameterized in the code.

ARPS has options for 2nd- or 4th-order quadratically conservative differencing for momentum terms, as well as a corrected transport scheme and a positive-definite centered difference scheme for scalar transport advection terms. Second order central difference schemes are used for all other terms. The discretization uses a staggered Arakawa-C grid, uniform in the horizontal, and stretched in the vertical. Temporal discretization uses a mode-splitting technique to accommodate high-frequency acoustic waves. The large time steps use the leapfrog method, while first-order backward explicit time stepping is used for the small time steps, except for terms responsible for vertical acoustic propagation, which are treated implicitly (Klemp & Wilhelmson, 1978).

ARPS has options for a Rayleigh damping layer or radiation boundary conditions at the upper boundary. At the lateral boundaries, solid wall, periodic, zero-gradient, or radiation conditions can be used. Externally specified boundary conditions can also be applied. The top and bottom boundaries are treated as rigid or free-slip boundaries, and surface fluxes are parameterized to account for the influence of the bottom surface. ARPS parameterizes surface momentum, heat, and moisture fluxes at the surface using bulk aerodynamic drag laws and stability-dependent similarity forms (such as Monin-Obukhov). The soil model of Noilhan & Planton (1989) accounts for

radiative forcing at the surface. Surface data can be input using several pre-processing routines. Section 2.2 also provides details on the ARPS formulations.

Standard turbulence modeling options in ARPS currently include several eddy viscosity models: constant eddy viscosity, the Smagorinsky model, and constant eddy viscosity plus Smagorinsky, as well as a turbulent kinetic energy 1.5-order closure scheme (Deardorff, 1980). The SGS models can be used in anisotropic forms to allow for different horizontal and vertical filtering sizes. The models currently implemented often do not provide enough dissipation at the highest frequencies, so computational mixing terms (2nd- or 4th-order) are added for stability. Because acoustic modes in the atmosphere may become unstable, ARPS also includes divergence damping to diminish contributions from acoustic vibrations.

C.3 ARPS validation

ARPS has been extensively validated by the developers in a variety of test cases ranging from symmetry tests to full-scale storm-prediction. For example, the code was tested for symmetry with random initial perturbations. Simulations of viscous Beltrami flow, a Coriolis test case, and the Taylor-Green problem were performed to compare with the analytical solutions. Simulation of the May 20, 1977 Del City Supercell storm is provided as the standard test case for users of the code. Flows with inertial gravity waves were simulated to test the mode-splitting time integration technique. The interaction of terrain was included in several tests of linear and nonlinear mountain waves over an Agnesi hill. Benchmark tests have also been performed for the soil model on the Wangara and FIFE boundary layer profiles. Real-time forecasts were also performed in which the model was initialized with non-homogeneous initial and boundary conditions and used to predict storm evolution. ARPS successfully predicted a cluster of storms on a 3 km grid, a few hours in advance. Details of these tests are given in Chapter 13 of the ARPS User's Manual (Xue *et al.*, 1995) and Xue *et al.* (2003). ARPS has also been applied to many other mesoscale flows; see for example the work of Anquetin *et al.* (1998) and Rao *et al.* (1999).

Appendix D

Governing equations for ARPS

This appendix presents a derivation of the ARPS equations, taking special care with the explicit filtering and discretization operators so as to obtain the complete LES equations. The ARPS equations are given in Xue *et al.* (1995, 2000, 2001) but the definition of the exact SFS stress is unclear. As this dissertation focuses on the development and testing of SFS models, primarily with ARPS, it is important to define the SFS stresses carefully. The governing equations for ARPS are first written in a map projection system (x, y, z) and then transformed to curvilinear terrain-following coordinates (ξ, η, ζ) which allow stretching in the vertical direction. There are several ways to derive the ARPS equations. A stretching and rotation matrix can, for example, be applied to the Navier-Stokes equations in spherical coordinates (see e.g. Haltiner, 1971). Instead, we begin with the vector form of the Navier-Stokes equations, then transform directly to mapped coordinates. Much of this follows the discussion of Fiedler (1998) in his handout about the dynamical equations in ARPS. The last section of this appendix describes the approximations made when the governing equations are discretized.

D.1 Transformation to Lambert conformal coordinates

The vector form of the compressible Navier-Stokes equations with conservation of mass, neglecting the terms due to molecular viscosity is

$$\frac{\partial \mathbf{u}}{\partial t} + \mathbf{u} \cdot \nabla \mathbf{u} = -\frac{1}{\rho} \nabla p + 2\mathbf{\Omega} \times \mathbf{u} \tag{D.1}$$

$$\frac{\partial \rho}{\partial t} + \nabla \cdot (\rho \mathbf{u}) = 0 \, . \tag{D.2}$$

The viscous stress terms are generally neglected in atmospheric flows where the viscous layer comprises only the first few millimeters above the surface. We can now express this vector equation in our choice of coordinates. We choose the Lambert conformal mapping which is commonly used for mid-latitudes.

The transformation of the square of a linear segment ds^2 into orthogonal q-coordinates is useful for deriving the appropriate mapping factors. Following Kreyszig (1993, p. 490) we write

$$ds^2 = \sum_{i=1}^{3} dx_i^2 = dx_1^2 + dx_2^2 + dx_3^2 \tag{D.3}$$

where x_i are Cartesian coordinates. By the chain rule:

$$dx_i = \sum_{j=1}^{3} \frac{\partial x_i}{\partial q_j} dq_j \tag{D.4}$$

where q_i are the the new coordinates, which are a function of x_1, x_2, x_3. The squared length of the element ds can then be expressed

$$ds^2 = \sum_{i=1}^{3} dx_i dx_i = \sum_{i=1}^{3} \left(\sum_{j=1}^{3} \frac{\partial x_i}{\partial q_j} dq_j \sum_{k=1}^{3} \frac{\partial x_i}{\partial q_k} dq_k \right) \tag{D.5}$$

where we can define

$$h_1^2 = \sum_{i=1}^{3} \left(\frac{\partial x_i}{\partial q_1} \right)^2 \, , \quad h_2^2 = \sum_{i=1}^{3} \left(\frac{\partial x_i}{\partial q_2} \right)^2 \, , \quad h_3^2 = \sum_{i=1}^{3} \left(\frac{\partial x_i}{\partial q_3} \right)^2 \tag{D.6}$$

and after some simplification (invoking orthogonality of the q-coordinates), we obtain

$$ds^2 = h_1^2 dq_1^2 + h_2^2 dq_2^2 + h_3^2 dq_3^2 \ . \tag{D.7}$$

Similarly, the vector $d\mathbf{x}$ is written

$$d\mathbf{x} = dx_1\mathbf{i} + dx_2\mathbf{j} + dx_3\mathbf{k} \tag{D.8}$$

and for q-coordinates

$$d\mathbf{q} = h_1 dq_1 \mathbf{e}_1 + h_2 dq_2 \mathbf{e}_2 + h_3 dq_3 \mathbf{e}_3 \tag{D.9}$$

where $\mathbf{e}_i$ are the orthogonal unit vectors in the directions of q coordinate system.

To express the governing equations in Lambert coordinates we must determine the metric terms h_i. The Lambert coordinate system (x, y, z) can be related to spherical coordinates (λ, ψ, r) with:

$$\psi(x, y) = \psi(Q) \tag{D.10}$$

$$\lambda(x, y) = \frac{1}{n} \arctan(-y, x) + \lambda_0 \ , \tag{D.11}$$

$$r = z + a \ , \tag{D.12}$$

where $Q = \sqrt{x^2 + y^2}$ and

$$x_c = r \cos\lambda \sin\psi \tag{D.13}$$

$$y_c = r \sin\lambda \sin\psi \tag{D.14}$$

$$z_c = r \cos\psi \ . \tag{D.15}$$

Here r is the distance from the center of the earth, a is the radius of the earth, λ denotes longitude, ψ is the co-latitude, and (x_c, y_c, z_c) are the Cartesian coordinates. The Lambert coordinates are conformal and describe the projection of the surface of a sphere onto a cone, which is then cut and flattened into a plane. The $-y$ axis

follows the longitude λ_0.

We define the base vectors

$$\mathbf{e}_x = \mathbf{e}_\lambda \frac{\partial \lambda}{\partial x} + \mathbf{e}_\psi \frac{\partial \psi}{\partial x} \tag{D.16}$$

$$\mathbf{e}_y = \mathbf{e}_\lambda \frac{\partial \lambda}{\partial y} + \mathbf{e}_\psi \frac{\partial \psi}{\partial y} \tag{D.17}$$

$$\mathbf{e}_z = \mathbf{e}_r \ . \tag{D.18}$$

To satisfy orthogonality, we must have $\mathbf{e}_x \cdot \mathbf{e}_y = 0$. Using this together with Eqs. D.10-D.11, we can solve for ψ:

$$\psi = 2 \arctan\left(\left(\frac{Q}{b}\right)^{1/n}\right) \tag{D.19}$$

and inversely, $Q = b \tan^n\left(\frac{\psi}{2}\right)$. b and n are determined by the choice of the true latitude and longitude.

Using Eq. D.6 to get $h_x^2 = \mathbf{e}_x \cdot \mathbf{e}_x$, $h_y^2 = \mathbf{e}_y \cdot \mathbf{e}_y$, and $h_z^2 = \mathbf{e}_z \cdot \mathbf{e}_z$ we find

$$h_x = h_y = \frac{r \sin \psi}{nQ} \ , \quad \text{and} \quad h_z = 1 \ . \tag{D.20}$$

We define the map factor m to be the inverse of h_x, representing the ratio of the distance traveled in the Lambert coordinate system to the physical distance traveled on the earth's surface.

We can use

$$\mathbf{u} \cdot \nabla \mathbf{u} = \sum_i \sum_j \frac{u_i}{h_j} \left(\frac{\partial u_i}{\partial x_j} + \frac{u_i}{h_i} \frac{\partial h_i}{\partial x_j} - \frac{u_j}{h_i} \frac{\partial h_j}{\partial x_i} \right) \mathbf{e}_i \tag{D.21}$$

to obtain

$$\begin{aligned} \mathbf{u} \cdot \nabla \mathbf{u} &= \left(mu \frac{\partial u}{\partial x} + mv \frac{\partial u}{\partial y} + w \frac{\partial u}{\partial z} - uv \frac{\partial m}{\partial y} + v^2 \frac{\partial m}{\partial x} \right) \mathbf{e}_x \\ &+ \left(mu \frac{\partial v}{\partial x} + mv \frac{\partial v}{\partial y} + w \frac{\partial v}{\partial z} + u^2 \frac{\partial m}{\partial y} - uv \frac{\partial m}{\partial x} \right) \mathbf{e}_y \end{aligned}$$

$$+ \quad \left(mu\frac{\partial w}{\partial x} + mv\frac{\partial w}{\partial y} + w\frac{\partial w}{\partial z} \right) \mathbf{e}_z \tag{D.22}$$

where we have neglected vertical derivatives of the metric terms. For the pressure gradient, we can use

$$\nabla A = \frac{1}{h_1}\frac{\partial A}{\partial q_1}\mathbf{e}_1 + \frac{1}{h_2}\frac{\partial A}{\partial q_2}\mathbf{e}_2 + \frac{1}{h_3}\frac{\partial A}{\partial q_3}\mathbf{e}_3 \tag{D.23}$$

to obtain

$$\nabla p = m\frac{\partial p}{\partial x}\mathbf{e}_1 + m\frac{\partial p}{\partial y}\mathbf{e}_2 + \frac{\partial p}{\partial z}\mathbf{e}_3 \tag{D.24}$$

The Coriolis term can be written directly in Lambert coordinates by first projecting the rotation vector $\mathbf{\Omega}$ into the Lambert coordinate directions:

$$2\mathbf{\Omega} = 0\mathbf{e}_x + f^v\mathbf{e}_y + f\mathbf{e}_z \ , \tag{D.25}$$

where f^v is the vertical Coriolis parameter. Then the cross product gives

$$2\mathbf{\Omega} \times \mathbf{u} = (f^v w - fv)\mathbf{e}_x + fu\mathbf{e}_y - f^v u\mathbf{e}_z \tag{D.26}$$

Combining all these terms, we obtain the momentum equations in transformed Lambert coordinates:

$$\frac{\partial u}{\partial t} \quad + \quad mu\frac{\partial u}{\partial x} + mv\frac{\partial u}{\partial y} + w\frac{\partial u}{\partial z} - uv\frac{\partial m}{\partial y} + v^2\frac{\partial m}{\partial x} = -\frac{m}{\rho}\frac{\partial p}{\partial x} - (f^v w - fv) \tag{D.27}$$

$$\frac{\partial v}{\partial t} \quad + \quad mu\frac{\partial v}{\partial x} + mv\frac{\partial v}{\partial y} + w\frac{\partial v}{\partial z} + u^2\frac{\partial m}{\partial y} - uv\frac{\partial m}{\partial x} = -\frac{m}{\rho}\frac{\partial p}{\partial y} - fu \tag{D.28}$$

$$\frac{\partial w}{\partial t} \quad + \quad mu\frac{\partial w}{\partial x} + mv\frac{\partial w}{\partial y} + w\frac{\partial w}{\partial z} = -\frac{1}{\rho}\frac{\partial p}{\partial z} + g + f^v u \tag{D.29}$$

Finally, to transform Eq. D.2 we can use

$$\nabla \cdot \mathbf{A} = \frac{1}{h_1 h_2 h_3}\left(\frac{\partial h_2 h_3 A_1}{\partial q_1} + \frac{\partial h_1 h_3 A_2}{\partial q_2} + \frac{\partial h_1 h_2 A_3}{\partial q_3} \right) \tag{D.30}$$

to obtain

$$\frac{\partial \rho}{\partial t} + m^2 \frac{\partial}{\partial x}\left(\frac{\rho u}{m}\right) + m^2 \frac{\partial}{\partial y}\left(\frac{\rho v}{m}\right) + \frac{\partial}{\partial z}(\rho w) = 0 \; . \tag{D.31}$$

D.2 The filtered momentum equations

We must apply an explicit spatial filter to formally derive the large-eddy simulation equations. Before doing so, we put the momentum equations into divergence form. We can use Eq. D.31 to write D.27 as

$$\begin{aligned} \frac{\partial \rho u}{\partial t} \;+\; & m^2 \frac{\partial}{\partial x}\left(\frac{\rho u u}{m}\right) + m^2 \frac{\partial}{\partial y}\left(\frac{\rho u v}{m}\right) + \frac{\partial \rho u w}{\partial z} - \rho u v \frac{\partial m}{\partial y} + \rho v^2 \frac{\partial m}{\partial x} \\ = \; & -m \frac{\partial p}{\partial x} - \rho(f^v w - f v) \; . \end{aligned} \tag{D.32}$$

The v and w equations follow similarly and are not presented here. Now we apply a discretization operator $\widehat{\ }$ as well as a filter operator $\breve{\ }$. We define a density-weighted Favre combined filter with

$$\breve{\widehat{\rho}}\,\overline{\widetilde{\phi}} \equiv \breve{\widehat{\rho\phi}} \; . \tag{D.33}$$

The tilde ($\widetilde{\ }$) and overbar operators denote the density-weighted discretization and filtering operators, respectively (and are consistent with notation used elsewhere in this dissertation). We assume everywhere that filters commute with differentiation and that the map factor is constant over the filter width. For the u-equation, we obtain

$$\begin{aligned} \frac{\partial \breve{\widehat{\rho}}\,\overline{\widetilde{u}}}{\partial t} \;+\; & m^2 \frac{\partial}{\partial x}\left(\frac{\breve{\widehat{\rho}}\,\overline{\widetilde{u}\widetilde{u}}}{m}\right) + m^2 \frac{\partial}{\partial y}\left(\frac{\breve{\widehat{\rho}}\,\overline{\widetilde{u}\widetilde{v}}}{m}\right) + \frac{\partial \breve{\widehat{\rho}}\,\overline{\widetilde{u}\widetilde{w}}}{\partial z} - \breve{\widehat{\rho}}\,\overline{\widetilde{u}\widetilde{v}} \frac{\partial m}{\partial y} + \breve{\widehat{\rho}}\,\overline{\widetilde{v^2}} \frac{\partial m}{\partial x} \\ = \; & -m \frac{\partial \overline{\widetilde{p}}}{\partial x} - \breve{\widehat{\rho}}(f^v \overline{\widetilde{w}} - f \overline{\widetilde{v}}) \end{aligned} \tag{D.34}$$

We can rearrange by moving the unclosed filtered terms to the right-hand side to obtain the traditional LES equation structure:

$$\frac{\partial \breve{\widehat{\rho}}\,\overline{\widetilde{u}}}{\partial t} \;+\; m^2 \frac{\partial}{\partial x}\left(\frac{\breve{\widehat{\rho}}\,\overline{\widetilde{u}}\,\overline{\widetilde{u}}}{m}\right) + m^2 \frac{\partial}{\partial y}\left(\frac{\breve{\widehat{\rho}}\,\overline{\widetilde{u}}\,\overline{\widetilde{v}}}{m}\right) + \frac{\partial \breve{\widehat{\rho}}\,\overline{\widetilde{u}}\,\overline{\widetilde{w}}}{\partial z} - \breve{\widehat{\rho}}\,\overline{\widetilde{u}\widetilde{v}} \frac{\partial m}{\partial y} + \breve{\widehat{\rho}}\,\overline{\widetilde{v^2}} \frac{\partial m}{\partial x}$$

$$= -m\frac{\partial \overline{\tilde{p}}}{\partial x} - \breve{\tilde{\rho}}(f^v\overline{\tilde{w}} - f\overline{\tilde{v}}) - m^2\frac{\partial}{\partial x}\left(\frac{\breve{\tilde{\rho}}}{m}(\widetilde{\widetilde{uu}} - \overline{\tilde{u}}\,\overline{\tilde{u}})\right)$$

$$- m^2\frac{\partial}{\partial y}\left(\frac{\breve{\tilde{\rho}}}{m}(\widetilde{\widetilde{uv}} - \overline{\tilde{u}}\,\overline{\tilde{v}})\right) - \frac{\partial}{\partial z}\left(\breve{\tilde{\rho}}(\widetilde{\widetilde{uw}} - \overline{\tilde{u}}\,\overline{\tilde{w}})\right) \ . \tag{D.35}$$

We have not separated the unclosed filtered terms associated with the derivatives of the map factors. We can put Eq. D.35 back in convective form using the filtered conservation of mass equation

$$\frac{\partial \breve{\tilde{\rho}}}{\partial t} + m^2\frac{\partial}{\partial x}\left(\frac{\breve{\tilde{\rho}}\overline{\tilde{u}}}{m}\right) + m^2\frac{\partial}{\partial y}\left(\frac{\breve{\tilde{\rho}}\overline{\tilde{v}}}{m}\right) + \frac{\partial}{\partial z}(\breve{\tilde{\rho}}\overline{\tilde{w}}) = 0 \ , \tag{D.36}$$

to obtain

$$\frac{\partial \overline{\tilde{u}}}{\partial t} + m\overline{\tilde{u}}\frac{\partial \overline{\tilde{u}}}{\partial x} + m\overline{\tilde{v}}\frac{\partial \overline{\tilde{u}}}{\partial y} + \overline{\tilde{w}}\frac{\partial \overline{\tilde{u}}}{\partial z} - \overline{\widetilde{uv}}\frac{\partial m}{\partial y} + \overline{\widetilde{v^2}}\frac{\partial m}{\partial x}$$

$$= -\frac{m}{\breve{\tilde{\rho}}}\frac{\partial \overline{\tilde{p}}}{\partial x} - (f^v\overline{\tilde{w}} - f\overline{\tilde{v}}) - \frac{m^2}{\breve{\tilde{\rho}}}\frac{\partial}{\partial x}\frac{\breve{\tilde{\rho}}\tau_{11}}{m} - \frac{m^2}{\breve{\tilde{\rho}}}\frac{\partial}{\partial y}\frac{\breve{\tilde{\rho}}\tau_{12}}{m} - \frac{1}{\breve{\tilde{\rho}}}\frac{\partial \breve{\tilde{\rho}}\tau_{13}}{\partial z} \tag{D.37}$$

The turbulence terms on the right-hand side have been grouped together under the definition of the turbulent stress:

$$\tau_{ij} = \overline{\widetilde{u_i u_j}} - \overline{\tilde{u}}_i\overline{\tilde{u}}_j) \tag{D.38}$$

We can also separate the turbulent stresses into the resolved subfilter-scale (RSFS) and subgrid-scale (SGS) portions:

$$\tau_{ij} = \overline{\widetilde{u_i u_j}} - \overline{\tilde{u}}_i\overline{\tilde{u}}_j = (\overline{\widetilde{u_i u_j}} - \overline{\tilde{u}_i\tilde{u}_j}) + (\overline{\tilde{u}_i\tilde{u}_j} - \overline{\tilde{u}}_i\overline{\tilde{u}}_j) \ , \tag{D.39}$$

where the second group of terms can be explicitly calculated using a reconstruction procedure (see Chapters 5 and 6).

D.3 Terrain-following coordinate transformation

We now transform the equations to a vertical coordinate $\zeta(x, y, z)$ which is constant along the bottom topography. The transformation to terrain-following coordinates is relatively simple, because the stretching occurs only in the vertical direction. We define $\xi = x$ and $\eta = y$. The transformation rules are given by

$$\sqrt{G}\frac{\partial \phi}{\partial x} = \frac{\partial J_3 \phi}{\partial \xi} + \frac{\partial J_1 \phi}{\partial \zeta} \tag{D.40}$$

$$\sqrt{G}\frac{\partial \phi}{\partial y} = \frac{\partial J_3 \phi}{\partial \eta} + \frac{\partial J_2 \phi}{\partial \zeta} \tag{D.41}$$

$$\sqrt{G}\frac{\partial \phi}{\partial z} = \frac{\partial \phi}{\partial \zeta} \tag{D.42}$$

where the Jacobians of transformation are

$$J_1 = -\frac{\partial z}{\partial \xi}\,, \quad J_2 = -\frac{\partial z}{\partial \eta}\,, \quad J_3 = \frac{\partial z}{\partial \zeta}\,, \tag{D.43}$$

and $\sqrt{G}$ is the determinant of the Jacobian matrix and equal to J_3.

The transformed version of D.37 becomes

$$\begin{aligned}
\frac{\partial \overline{\tilde{u}}}{\partial t} &+ \frac{m\overline{\tilde{u}}}{\sqrt{G}}\left(\frac{\partial J_3 \overline{\tilde{u}}}{\partial \xi} + \frac{\partial J_1 \overline{\tilde{u}}}{\partial \zeta}\right) + \frac{m\overline{\tilde{v}}}{\sqrt{G}}\left(\frac{\partial J_3 \overline{\tilde{u}}}{\partial \eta} + \frac{\partial J_2 \overline{\tilde{u}}}{\partial \zeta}\right) + \frac{\overline{\tilde{w}}}{\sqrt{G}}\frac{\partial \overline{\tilde{u}}}{\partial \zeta} \\
&- \frac{\widetilde{\overline{u}\overline{v}}}{\sqrt{G}}\left(\frac{\partial J_3 m}{\partial \eta} + \frac{\partial J_2 m}{\partial \zeta}\right) + \frac{\widetilde{\overline{v^2}}}{\sqrt{G}}\left(\frac{\partial J_3 m}{\partial \xi} + \frac{\partial J_1 m}{\partial \zeta}\right) \\
&= -\frac{m}{\breve{\overline{\rho}}\sqrt{G}}\left(\frac{\partial J_3 \overline{\tilde{p}}}{\partial \xi} + \frac{\partial J_1 \overline{\tilde{p}}}{\partial \zeta}\right) - (f^v \overline{\tilde{w}} - f\overline{\tilde{v}}) \\
&- \frac{m^2}{\breve{\overline{\rho}}\sqrt{G}}\left(\frac{\partial}{\partial \xi}\left(\frac{J_3 \breve{\overline{\rho}}\tau_{11}}{m}\right) + \frac{\partial}{\partial \zeta}\left(\frac{J_1 \breve{\overline{\rho}}\tau_{11}}{m}\right)\right) \\
&- \frac{m^2}{\breve{\overline{\rho}}\sqrt{G}}\left(\frac{\partial}{\partial \eta}\left(\frac{J_3 \breve{\overline{\rho}}\tau_{12}}{m}\right) + \frac{\partial}{\partial \zeta}\left(\frac{J_2 \breve{\overline{\rho}}\tau_{12}}{m}\right)\right) - \frac{1}{\breve{\overline{\rho}}\sqrt{G}}\left(\frac{\partial \breve{\overline{\rho}}\tau_{13}}{\partial \zeta}\right)
\end{aligned} \tag{D.44}$$

and we note that the derivative of m in the ζ direction is zero. We can now define

the contravariant velocity

$$\overline{\widetilde{W}}^c = \frac{1}{J_3}(m(\overline{\tilde{u}}J_1 + \overline{\tilde{v}}J_2) + \overline{\tilde{w}}) \tag{D.45}$$

and rearrange the advective terms to obtain

$$\begin{aligned}
\frac{\partial \overline{\tilde{u}}}{\partial t} &+ \frac{m\overline{\tilde{u}}}{\sqrt{G}}\frac{\partial J_3 \overline{\tilde{u}}}{\partial \xi} + \frac{m\overline{\tilde{v}}}{\sqrt{G}}\frac{\partial J_3 \overline{\tilde{u}}}{\partial \eta} + \overline{\widetilde{W}}^c \frac{\partial \overline{\tilde{u}}}{\partial \zeta} \\
&+ \frac{m\overline{\tilde{u}}}{\sqrt{G}}\left(\overline{\tilde{u}}\frac{\partial J_1}{\partial \zeta} + \overline{\tilde{v}}\frac{\partial J_2}{\partial \zeta}\right) \\
&- \frac{\overline{\widetilde{uv}}}{\sqrt{G}}\left(\frac{\partial J_3 m}{\partial \eta} + \frac{\partial J_2 m}{\partial \zeta}\right) + \frac{\overline{\widetilde{v^2}}}{\sqrt{G}}\left(\frac{\partial J_3 m}{\partial \xi} + \frac{\partial J_1 m}{\partial \zeta}\right) \\
&= -\frac{m}{\breve{\overline{\rho}}\sqrt{G}}\left(\frac{\partial J_3 \overline{\tilde{p}}}{\partial \xi} + \frac{\partial J_1 \overline{\tilde{p}}}{\partial \zeta}\right) - (f^v \overline{\tilde{w}} - f\overline{\tilde{v}}) \\
&- \frac{m^2}{\breve{\overline{\rho}}\sqrt{G}}\left(\frac{\partial}{\partial \xi}\left(\frac{J_3 \breve{\overline{\rho}}\tau_{11}}{m}\right) + \frac{\partial}{\partial \zeta}\left(\frac{J_1 \breve{\overline{\rho}}\tau_{11}}{m}\right)\right) \\
&- \frac{m^2}{\breve{\overline{\rho}}\sqrt{G}}\left(\frac{\partial}{\partial \eta}\left(\frac{J_3 \breve{\overline{\rho}}\tau_{12}}{m}\right) + \frac{\partial}{\partial \zeta}\left(\frac{J_2 \breve{\overline{\rho}}\tau_{12}}{m}\right)\right) - \frac{1}{\breve{\overline{\rho}}\sqrt{G}}\left(\frac{\partial \breve{\overline{\rho}}\tau_{13}}{\partial \zeta}\right)
\end{aligned} \tag{D.46}$$

To simplify the left-hand side further, first, we multiply by $< \breve{\overline{\rho}} >$ (plane-averaged $\breve{\overline{\rho}}$) and $\sqrt{G}$ and define

$$\rho^* = < \breve{\overline{\rho}} > \sqrt{G}\,, \quad \overline{\tilde{u}}^* = \rho^* \overline{\tilde{u}}\,, \quad \overline{\tilde{v}}^* = \rho^* \overline{\tilde{v}}\,, \quad \text{and} \quad \overline{\widetilde{W}}^* = \rho^* \overline{\widetilde{W}}^c\,. \tag{D.47}$$

Then we use the chain rule on the first two advection terms and the terms containing derivatives of the map factor together with the fact that

$$\frac{\partial J_3}{\partial \xi} + \frac{\partial J_1}{\partial \zeta} = 0 \quad \frac{\partial J_3}{\partial \eta} + \frac{\partial J_2}{\partial \zeta} = 0\,, \quad \text{and} \quad \sqrt{G} = J_3 \tag{D.48}$$

to obtain

$$\frac{\partial \overline{\tilde{u}}^*}{\partial t} + m\overline{\tilde{u}}^*\frac{\partial \overline{\tilde{u}}}{\partial \xi} + m\overline{\tilde{v}}^*\frac{\partial \overline{\tilde{u}}}{\partial \eta} + \overline{\widetilde{W}}^*\frac{\partial \overline{\tilde{u}}}{\partial \zeta}$$

$$
\begin{aligned}
- \quad & \overline{\widetilde{uv}}<\breve{\overline{\rho}}>J_3\frac{\partial m}{\partial \eta} + \overline{\widetilde{v^2}}<\breve{\overline{\rho}}>J_3\frac{\partial m}{\partial \xi} \\
= \quad & -\frac{m<\breve{\overline{\rho}}>}{\breve{\overline{\rho}}}\left(\frac{\partial J_3\overline{\overline{p}}'}{\partial \xi} + \frac{\partial J_1\overline{\overline{p}}'}{\partial \zeta}\right) - (f^v\overline{\widetilde{w}}^* - f\overline{\widetilde{v}}^*) \\
- \quad & \frac{m^2<\breve{\overline{\rho}}>}{\breve{\overline{\rho}}}\left(\frac{\partial}{\partial \xi}\left(\frac{J_3\breve{\overline{\rho}}\tau_{11}}{m}\right) + \frac{\partial}{\partial \zeta}\left(\frac{J_1\breve{\overline{\rho}}\tau_{11}}{m}\right)\right) \\
- \quad & \frac{m^2<\breve{\overline{\rho}}>}{\breve{\overline{\rho}}}\left(\frac{\partial}{\partial \eta}\left(\frac{J_3\breve{\overline{\rho}}\tau_{12}}{m}\right) + \frac{\partial}{\partial \zeta}\left(\frac{J_2\breve{\overline{\rho}}\tau_{12}}{m}\right)\right) - \frac{<\breve{\overline{\rho}}>}{\breve{\overline{\rho}}}\left(\frac{\partial\breve{\overline{\rho}}\tau_{13}}{\partial \zeta}\right) \qquad \text{(D.49)}
\end{aligned}
$$

where $\overline{\overline{p}}$ has been replaced by $\overline{\overline{p}}' = \overline{\overline{p}} - <\overline{\overline{p}}>$ since horizontal derivatives of the plane-averaged pressure are by definition zero.

To simplify the right-hand side, we expand the SFS terms using the chain rule for division, e.g.,

$$
m^2\frac{\partial}{\partial \xi}\left(\frac{J_3\breve{\overline{\rho}}\tau_{11}}{m}\right) = m\frac{\partial}{\partial \xi}\left(J_3\breve{\overline{\rho}}\tau_{11}\right) - \breve{\overline{\rho}}J_3\tau_{11}\frac{\partial m}{\partial \xi}\,. \qquad \text{(D.50)}
$$

The derivatives of the map factor can be combined with those on the left-hand side of Eq. D.49.

The final form of the equation reads

$$
\begin{aligned}
\frac{\partial\overline{\widetilde{u}}^*}{\partial t} \quad & + \quad m\overline{\widetilde{u}}^*\frac{\partial\overline{\widetilde{u}}}{\partial \xi} + m\overline{\widetilde{v}}^*\frac{\partial\overline{\widetilde{u}}}{\partial \eta} + \overline{\widetilde{W}}^*\frac{\partial\overline{\widetilde{u}}}{\partial \zeta} \\
& = \quad -\frac{m<\breve{\overline{\rho}}>}{\breve{\overline{\rho}}}\left(\frac{\partial J_3\overline{\overline{p}}'}{\partial \xi} + \frac{\partial J_1\overline{\overline{p}}'}{\partial \zeta}\right) - (f^v\overline{\widetilde{w}}^* - f\overline{\widetilde{v}}^*) \\
& - \quad \frac{<\breve{\overline{\rho}}>}{\breve{\overline{\rho}}}\left[m\frac{\partial}{\partial \xi}\left(J_3\breve{\overline{\rho}}\tau_{11}\right) + m\frac{\partial}{\partial \eta}\left(J_3\breve{\overline{\rho}}\tau_{12}\right)\right. \\
& + \quad \left.\frac{\partial}{\partial \zeta}\left(\breve{\overline{\rho}}\tau_{13} + + mJ_1\breve{\overline{\rho}}\tau_{11} + mJ_2\breve{\overline{\rho}}\tau_{12}\right)\right] \\
& - \quad \overline{\widetilde{v}}^*\left(\overline{\widetilde{v}}\frac{\partial m}{\partial \xi} - \overline{\widetilde{u}}\frac{\partial m}{\partial \eta}\right) - \rho^*(\tau_{11} + \tau_{22})\frac{\partial m}{\partial \xi}\,. \qquad \text{(D.51)}
\end{aligned}
$$

D.4 Implementation in ARPS

A few approximations are made when Eq. D.51 (and the equivalents for v and w) is discretized for use in ARPS. First, the pressure gradient is absorbed into the Coriolis forcing term, as is standard in atmospheric codes which use the geostrophic pressure balance to relate the two. The ratio $< \breve{\tilde{\rho}} > / \breve{\tilde{\rho}}$ is therefore ignored. Second, this ratio is neglected in the calculation of the SFS stress derivatives. In the calculation of the scale-similarity terms, we use, e.g.

$$\breve{\tilde{\rho}} \tau_{11} = \breve{\tilde{\rho}} (\widetilde{\overline{u}\overline{u}} - \overline{\tilde{u}}\,\overline{\tilde{u}}) \approx < \breve{\tilde{\rho}} > (\widetilde{\overline{u^\star u^\star}} - \overline{\tilde{u}^\star}\,\overline{\tilde{u}^\star}) \tag{D.52}$$

where $\tilde{u}^\star$ indicates the reconstructed velocity (and is not the same as $\tilde{u}^*$). ARPS also simplifies to, e.g., $\tau_{11} = < \breve{\tilde{\rho}} > \nu_T S_{11}$, for the eddy viscosity terms, where ν_T is the eddy viscosity and S_{11} is the strain-rate component, which includes appropriate map factor and Jacobian terms. Finally, the last term in Eq. D.51 is neglected, as it is much smaller than the contribution from the other map factor derivative terms. The latter are often negligible in small domains where m does not vary much.

The application of the explicit filter is straightforward as it appears only in the computation of the SFS stress terms. The discrete variable we solve for is, e.g. $\overline{\tilde{u}}$. Thus the explicit filter is needed only when computing τ_{ij}, to prevent build-up of energy in the high-wavenumber portion of the spectrum. The only change to the code when filtering is treated explicitly is in the RSFS and SGS computations. The explicit filter (usually a tophat or Gaussian) is used to reconstruct the RSFS terms. An explicit test filter (usually twice the width of the explicit filter) is used in the SGS computation for dynamic eddy-viscosity models. This is described in further detail in Appendix E.

Appendix E

Dynamic reconstruction model details

This appendix describes the procedure for calculating dynamic eddy-viscosity coefficients. The derivation is given for the dynamic mixed model using the tensor-diffusivity model for the scale-similarity (RSFS) portion and Smagorinsky for the SGS portion. The modifications for using the Bardina and high-order reconstruction for the RSFS stress are also described. The Smagorinsky model described here was used for the SGS stress in Chapter 5. The dynamic procedure for the Wong-Lilly model used in Chapters 6-8 follows similarly.

E.1 Dynamic mixed model derivation

The static Smagorinsky model is known to be too dissipative (even in laminar flow), to have incorrect wall behavior, and to give low correlations with the true SFS stress. Eddy viscosity models do not allow backscatter from smaller to larger scales. Several of these deficiencies are addressed when the coefficient is calculated dynamically. The dynamic model must be implemented with care to correctly calculate the explicit and test-filtered terms.

The procedure for calculating the Smagorinsky coefficient dynamically depends on the Germano identity (Germano *et al.*, 1991) which relates motions at the "grid filter" and "test filter" levels. The test filtered equations are considered to be solved on a coarser grid. The grid filter is more accurately termed the "explicit filter" and

is usually related to the grid spacing.

In the dynamic equations, the exact SFS stress is given by

$$\tau_{ij} = \overline{u_i u_j} - \overline{\tilde{u}}_i \overline{\tilde{u}}_j \tag{E.1}$$

whereas in the test-filtered dynamic equations, the exact stress is

$$\mathcal{T}_{ij} = \widehat{\overline{u_i u_j}} - \widehat{\overline{\tilde{u}^c}}_i \widehat{\overline{\tilde{u}^c}}_j \ . \tag{E.2}$$

This is clear from governing equations. We begin from the unfiltered Navier-Stokes equations (as written in Eq. 5.1):

$$\frac{\partial u_i}{\partial x_i} = 0 \ , \qquad \frac{\partial u_i}{\partial t} + \frac{\partial u_i u_j}{\partial x_j} = -\frac{\partial p}{\partial x_i} + \frac{1}{Re_\tau} \frac{\partial u_i}{\partial x_j \partial x_j} \ . \tag{E.3}$$

Filtering and discretizing Eq. E.3, we obtain

$$\frac{\partial \overline{\tilde{u}}_i}{\partial t} + \frac{\partial \widetilde{\overline{\tilde{u}}_j \overline{\tilde{u}}_i}}{\partial x_j} = -\frac{\partial \overline{\tilde{p}}}{\partial x_i} + \frac{1}{Re_\tau} \frac{\partial^2 \overline{\tilde{u}}_i}{\partial x_j \partial x_j} - \frac{\partial}{\partial x_j} \left(\overline{u_i u_j} - \overline{\tilde{u}}_i \overline{\tilde{u}}_j \right) \tag{E.4}$$

We coarsen the grid (denoted by $\tilde{u}^c$) and apply the test filter (which is essentially the explicit filter on the coarser grid resolution):

$$\frac{\partial \widehat{\overline{\tilde{u}^c}}_i}{\partial t} + \frac{\partial \widetilde{\widehat{\overline{\tilde{u}^c}}_j \widehat{\overline{\tilde{u}^c}}_i}^{\,c}}{\partial x_j} = -\frac{\partial \widehat{\overline{\tilde{p}^c}}}{\partial x_i} + \frac{1}{Re_\tau} \frac{\partial^2 \widehat{\overline{\tilde{u}^c}}_i}{\partial x_j {x_j}^2} - \frac{\partial}{\partial x_j} \left(\widehat{\widetilde{\overline{u_i u_j}}}^{\,c} - \widehat{\overline{\tilde{u}}_i \overline{\tilde{u}}_j}^{\,c} \right) - \frac{\partial}{\partial x_j} \left(\widehat{\widetilde{\overline{\tilde{u}}_i \overline{\tilde{u}}_j}}^{\,c} - \widehat{\widetilde{\overline{\tilde{u}^c}_i \overline{\tilde{u}^c}_j}}^{\,c} \right) \tag{E.5}$$

noting that $\tilde{\tilde{u}}^c = \tilde{u}^c$ since the discretization operator is treated as a spectral cutoff filter.

If instead we apply the coarse grid discretization operator, the explicit filter, and the test filter in one step, we obtain

$$\frac{\partial \widehat{\overline{\tilde{u}^c}}_i}{\partial t} + \frac{\partial \widetilde{\widehat{\overline{\tilde{u}^c}}_j \widehat{\overline{\tilde{u}^c}}_i}^{\,c}}{\partial x_j} = -\frac{\partial \widehat{\overline{\tilde{p}^c}}}{\partial x_i} + \frac{1}{Re_\tau} \frac{\partial^2 \widehat{\overline{\tilde{u}^c}}_i}{\partial x_j {x_j}^2} - \frac{\partial}{\partial x_j} \left(\widehat{\widetilde{\overline{u_i u_j}}}^{\,c} - \widehat{\widetilde{\overline{\tilde{u}^c}_i \overline{\tilde{u}^c}_j}}^{\,c} \right) \tag{E.6}$$

To solve each equation separately, the last terms on the right-hand sides would be modeled. Since Eqs. E.5 and E.6 are equivalent, we can simply equate the SFS

terms:

$$\underbrace{\left(\widehat{\overline{u_i u_j}}^c - \widehat{\overline{\tilde{u}_i \tilde{u}_j}}^c\right)}_{\tilde{\tau}_{ij}^c} + \underbrace{\left(\widehat{\overline{\tilde{u}_i \tilde{u}_j}}^c - \widehat{\overline{\tilde{u}^c}_i \overline{\tilde{u}^c}_j}^c\right)}_{\tilde{L}_{ij}^c} = \underbrace{\left(\widehat{\overline{u_i u_j}}^c - \widetilde{\overline{\tilde{u}^c}_i \overline{\tilde{u}^c}_j}^c\right)}_{\widetilde{\mathcal{T}}_{ij}^c} . \tag{E.7}$$

$\tilde{L}_{ij}^c$ can be computed from the resolved velocities $\overline{\tilde{u}}_i$. The other two groups of terms must be modeled. We use the same type of mixed model for both:

$$\left(\widehat{\overline{m^c}}_{ij} - C\,\widehat{\overline{a^c}}_{ij}\right) + \tilde{L}_{ij}^c \approx \left(\widetilde{M}_{ij}^c - C\widetilde{A}_{ij}^c\right) \tag{E.8}$$

where

$$m_{ij} \approx \overline{\Delta}^2 \frac{\partial \overline{\tilde{u}}_i}{\partial x_k} \frac{\partial \overline{\tilde{u}}_j}{\partial x_k} \tag{E.9}$$

$$M_{ij} \approx \alpha^2 \overline{\Delta}^2 \frac{\partial \widehat{\overline{\tilde{u}^c}}_i}{\partial x_k} \frac{\partial \widehat{\overline{\tilde{u}^c}}_j}{\partial x_k} \tag{E.10}$$

$$a_{ij} \approx 2\overline{\Delta}^2 |\overline{\tilde{S}}| \overline{\tilde{S}}_{ij} \tag{E.11}$$

$$A_{ij} \approx 2\alpha^2 \overline{\Delta}^2 |\widehat{\overline{\tilde{S}^c}}| \widehat{\overline{\tilde{S}^c}}_{ij} \tag{E.12}$$

Terms m_{ij} and M_{ij} are the RSFS component of the closure model, here shown with the tensor-diffusivity model or Clark model (Winckelmans *et al.*, 2001).

The SGS model represented in the terms a_{ij} and A_{ij} is the Smagorinsky model,

$$\tau_{ij}^{SGS} = -2\tilde{\nu}_T \overline{\tilde{S}}_{ij} = -2(C\Delta)^2 |\overline{\tilde{S}}| \overline{\tilde{S}}_{ij}, \tag{E.13}$$

where ν_T is the eddy viscosity, Δ the filter width and S_{ij} the strain rate tensor. We now need to solve Eq. E.8 for the coefficient C, assuming that the same coefficient can be used at both levels of the equations (Germano *et al.*, 1991). The model parameter $C\Delta$ is calculated dynamically (Germano *et al.*, 1991) using the least squares approximation of Lilly (1992). We also assume that C is locally invariant and can be pulled out of the explicit filter and test filters.

First let

$$\tilde{r}_{ij}^c = \tilde{L}_{ij}^c + \widehat{\tilde{m}^c}_{ij} - \tilde{M}_{ij}^c \tag{E.14}$$

$$\tilde{q}^c_{ij} = \widehat{\tilde{a}^c}_{ij} - \tilde{A}^c_{ij} \tag{E.15}$$

so that

$$\tilde{r}^c_{ij} \approx C\tilde{q}^c_{ij} \; . \tag{E.16}$$

The error is defined as $E_{ij} = C\tilde{q}^c_{ij} - \tilde{r}^c_{ij}$. Using the method of least squares, we have

$$E = \langle E_{ij}E_{ij} \rangle = \left\langle C^2\tilde{q}^c_{ij}\tilde{q}^c_{ij} - 2C\tilde{q}^c_{ij}\tilde{r}^c_{ij} + \tilde{r}^c_{ij}\tilde{r}^c_{ij} \right\rangle \tag{E.17}$$

where E is the square of the error, and the brackets denote a local average in space. (Planar averaging is usually performed in geometries which allow it, but here we use the explicit filter to perform a local spatial average to be able to apply these models to complex geometries.) Equating dE/dC to zero and solving for the location where the squared error has a minimum, we obtain

$$C = \frac{\left\langle \tilde{q}^c_{ij}\tilde{r}^c_{ij} \right\rangle}{\left\langle \tilde{q}^c_{ij}\tilde{q}^c_{ij} \right\rangle} \tag{E.18}$$

E.2 Dynamic mixed model - Bardina

The dynamic model can also be written using the scale-similarity model of Bardina *et al.* (1983), by simply replacing m_{ij} with

$$m_{ij} = \overline{\overline{\tilde{u}_i}\overline{\tilde{u}_j}} - \overline{\tilde{u}_i}\,\overline{\tilde{u}_j} \; . \tag{E.19}$$

and likewise for M_{ij}. Note that care must be taken to correctly calculate the explicit filter and the test filter when computing the Bardina scale-similarity term.

E.3 Dynamic reconstruction model

The dynamic mixed model can also be formulated using the approximate deconvolution method (ADM) (Stolz *et al.*, 2001*a*) to reconstruct the RSFS portion of the SFS stress. The ADM uses the van Cittert iterative method (van Cittert, 1931) to

reconstruct the unfiltered velocity from the filtered velocity:

$$\tilde{u}_i = \overline{\tilde{u}}_i + (I - G) * \overline{\tilde{u}}_i + (I - G) * ((I - G) * \overline{\tilde{u}}_i) + \cdots \tag{E.20}$$

The coefficients for the van Cittert series are easily obtained from Pascal's triangle. For example, when $n = 5$, row $n + 1$ (where the first row contains only the number 1) contains 1 5 10 10 5 1. Adding neighboring pairs in a tree pattern and alternating signs gives the coefficients for this series:

$$u_i^\star = 6\overline{u} - 15\overline{\overline{u}}_i + 20\overline{\overline{\overline{u}}}_i - 15\overline{\overline{\overline{\overline{u}}}}_i + 6\overline{\overline{\overline{\overline{\overline{u}}}}}_i - \overline{\overline{\overline{\overline{\overline{\overline{u}}}}}}_i \tag{E.21}$$

Similarly, for $n = 10$ reconstruction we obtain

$$u_i^\star = 11\overline{u} - 55\overline{\overline{u}}_i + 165\overline{\overline{\overline{u}}}_i - 330\overline{\overline{\overline{\overline{u}}}}_i + 462\overline{\overline{\overline{\overline{\overline{u}}}}}_i - 462\overline{\overline{\overline{\overline{\overline{\overline{u}}}}}}_i + 330\overline{\overline{\overline{\overline{\overline{\overline{\overline{u}}}}}}}_i - 165\overline{\overline{\overline{\overline{\overline{\overline{\overline{\overline{u}}}}}}}}_i + 55\overline{\overline{\overline{\overline{\overline{\overline{\overline{\overline{\overline{u}}}}}}}}}_i - 11\overline{\overline{\overline{\overline{\overline{\overline{\overline{\overline{\overline{\overline{u}}}}}}}}}}}_i + \overline{\overline{\overline{\overline{\overline{\overline{\overline{\overline{\overline{\overline{\overline{u}}}}}}}}}}}}_i \tag{E.22}$$

Appendix F

Convective boundary layer simulations

The evolution of the convective boundary layer (CBL) has been studied using LES for the past 30 years (see e.g. Deardorff, 1970). Flows where surface heating is important are generally easier to simulate using LES because the eddy motions are larger and easier to resolve. However, much is still unknown about the evolution of the CBL in more realistic scenarios, for example with wind shear and entrainment at the top of the CBL. Conzemius & Fedorovich (2002) investigated the effect of wind shear by performing three idealized sets of simulations. We have performed similar simulations with ARPS as part of a comparison exercise organized by Conzemius and Fedorovich (University of Oklahoma) (Fedorovich *et al.*, 2004). Here we summarize the setup of the numerical simulations and present a description of the resulting flows. As our emphasis is on the performance of different turbulence models, we then focus on comparisons to similarity theory for the case with constant shear.

Three different flow conditions are used. In the shear-free case (NS), the geostrophic wind velocity is zero, and convection dominates completely. The second case considers geostrophic wind with shear (GS), such that the wind increases linearly from 0 at the surface to 20 m/s at the top of the domain. The last case uses a constant geostrophic (GC) wind of 20 m/s to drive the flow. The flow is thus driven by the constant geostrophic pressure gradient which would balance a geostrophic wind of (U_g, V_g); in all cases $V_g = 0$. The initial flow is given by the specified geostrophic winds, and then evolves due to drag at the surface and convective motions. The

background stratification is set to 0.003 K/m uniformly over the domain. The CBL grows due to a surface heat flux set constant at 0.1 K m/s. Perturbations (2 K) in the initial potential temperature field at the surface trigger instabilities in the flow so that it becomes fully turbulent.

The grid size is $256 \times 256 \times 103$ with grid spacings of 40 m in the horizontal. In ARPS this corresponds to a square domain, $\Delta x(nx - 3) = 10240$ m on a side. A stretched vertical grid is used, with 10 m spacing near the bottom, expanding to 30 m near the top of the domain; the average spacing is 20 m and the domain height is 2000 m. ARPS is run for approximately 12000 s, until the CBL depth reaches about 60% of the domain depth (1600 m). The latitude is 40° N. Fourth-order spatial differencing is used for the advection terms. Temporal discretization is performed using a mode-splitting technique to accommodate high-frequency acoustic waves; the large time steps (0.5 s) use the leapfrog method, while first-order forward-backward explicit time stepping is used for the small time steps (0.05 s), except for terms responsible for vertical acoustic propagation, which are treated implicitly.

ARPS parameterizes momentum fluxes at the surface by applying an instantaneous logarithmic drag law (used here with constant drag coefficients) at each grid point. The bottom roughness is set to 0.01 m and the drag coefficient is derived by applying the logarithmic velocity condition to the first grid cell above the wall (at height $\Delta z_{min}/2$). Rayleigh damping is used above 1400 m to minimize reflections from the rigid lid boundary at the top of the domain. At the lateral boundaries, periodic conditions are used for this idealized flat-terrain study.

This is a time-dependent flow, therefore no time averaging is performed. Statistics are output as horizontally-averaged profiles every 200 s. Convenient comparison measures for the GC case are the nondimensional velocity shear

$$\Phi_M = \frac{\kappa z}{u_*} \frac{dU}{dz} \tag{F.1}$$

and the nondimensional potential temperature gradient

$$\Phi_S = \frac{\kappa z}{\theta_*} \frac{d\theta}{dz} \tag{F.2}$$

where $\theta_* = -q_*/u_*$ and q_* is the heat flux at the ground. Similarity theory for the

convective boundary layer gives the theoretical values as

$$\Phi_M = (1 - 15z/L_{obu})^{-0.25} \tag{F.3}$$

$$\Phi_S = 0.74(1 - 9z/L_{obu})^{-0.5} \ , \tag{F.4}$$

where the Obukhov length is defined $L_{obu} = -u_*^3 < \overline{\theta} > /(\kappa g q_*)$. When the atmosphere is neutrally stratified, $L_{obu} \to \infty$ and $\Phi_M = 1$ (as seen in the neutral boundary layer simulations in Chapter 6) (Stull, 1988, p. 385).

These expressions for Φ_M and Φ_S can be integrated to obtain the profiles expected from similarity theory:

$$U = \frac{u_*}{\kappa}(\log(z/z_0) + \Psi_M) \tag{F.5}$$

$$\theta - \theta_0 = 0.74\frac{\theta_*}{\kappa}(\log(z/z_0) + \Psi_S) \tag{F.6}$$

where θ_0 is a reference temperature at the surface,

$$\Psi_M = -2\log((1+\chi)/2) - \log((1+\chi^2)/2) + 2\tan^{-1}(\chi) - \pi/2.0 \tag{F.7}$$

$$\Psi_S = -2\log((1+\xi)/2) \tag{F.8}$$

and

$$\chi = (1 - 15z/L_{obu})^{0.25} \tag{F.9}$$

$$\xi = (1 - 9z/L_{obu})^{0.5} \tag{F.10}$$

(see (Stull, 1988, p. 385) and (Garratt, 1992, p. 53-54)).

Figures F.1 and F.2 show the mean velocity U and potential temperature profiles at 10000 s obtained from GC simulations using four different turbulence models: the standard TKE-1.5 closure, the DWL, and the DRM-ADM0 and DRM-ADM5. The differences are apparent even in the mean profiles. The normalized profiles in Fig. F.2 show that the TKE-1.5 results are closer in magnitude to the similarity theory prediction, but the slopes of these profiles are also important. Figure F.3

shows the nondimensional velocity and potential temperature gradients compared to the expected value from similarity theory. Near the wall, the TKE model results overpredict Φ_M and underpredict Φ_S. Results using the DRM are better, especially near the wall where the slope of the profiles matches the theory more closely, though not as much for Φ_S. The DWL and DRM results exhibit small oscillations; the plots show vertically filtered data to remove $2\Delta x$ waves. Further research is needed to investigate the near-wall performance of the DRM in the CBL and the influence of the near-wall stress model.

Comparisons of resolved and subgrid heat fluxes are shown in Fig. F.4. Although these profiles are not time-averaged, it is easy to see that the results using reconstruction give increased SFS stresses, and consequently lower resolved stresses. This pattern was also observed in the neutral boundary layer simulations of Chapter 6 and in the small-scale channel flow simulations of Chapter 5.

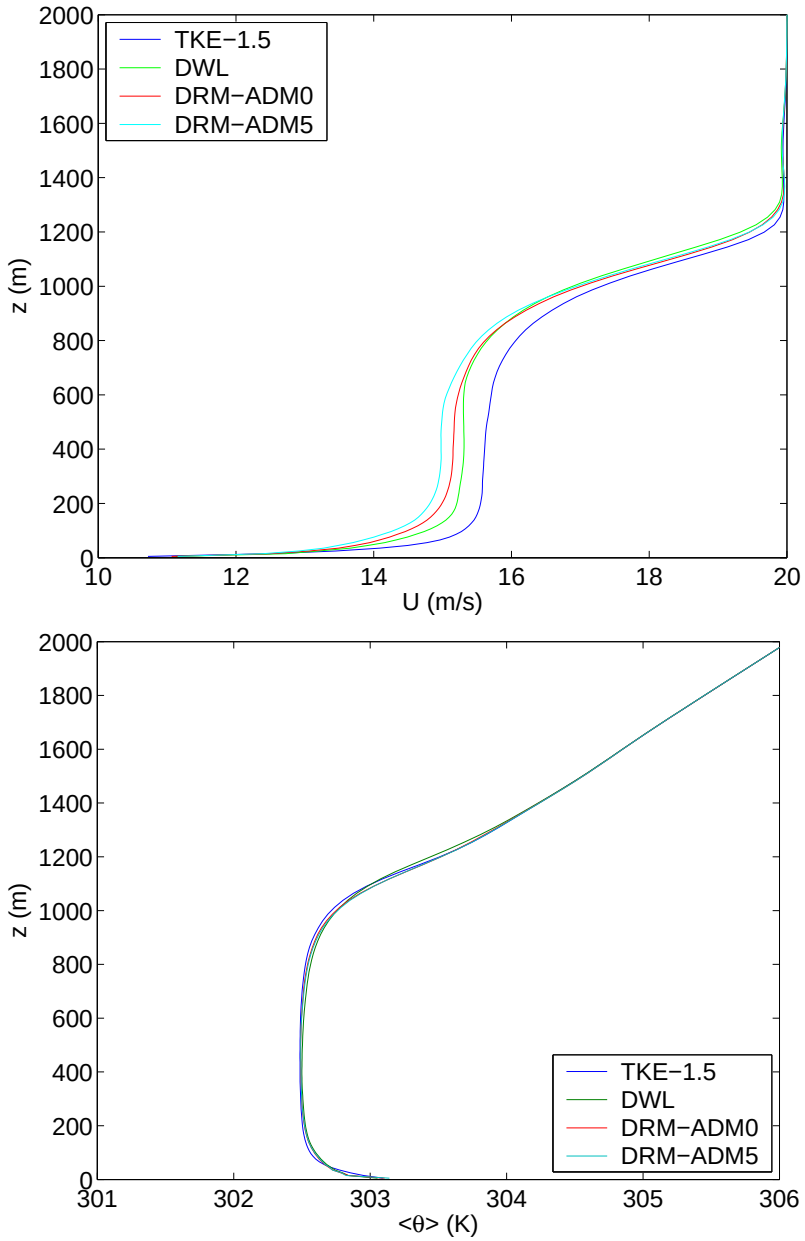

Figure F.1: Horizontally averaged velocity (top) and potential temperature (bottom) profiles at 10000 s.

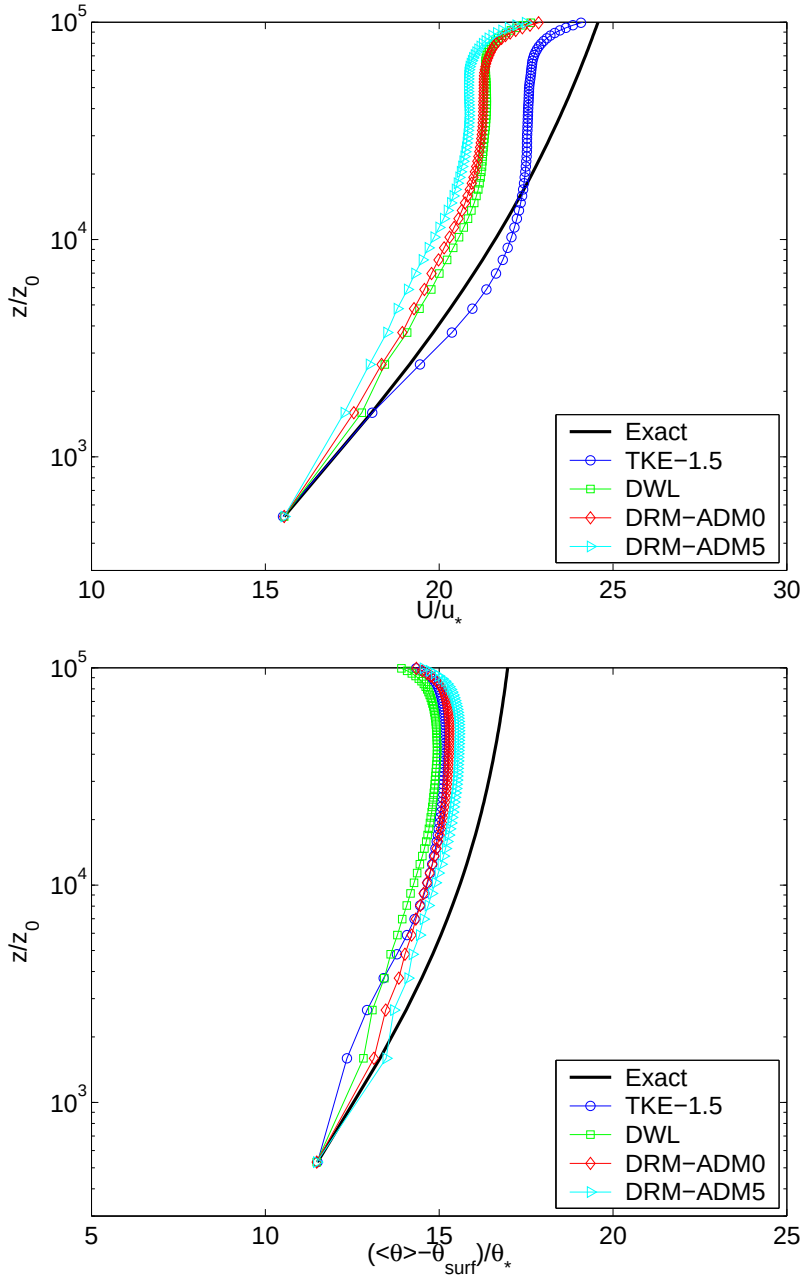

Figure F.2: Normalized profiles of U (top) and θ (bottom) at 10000 s.

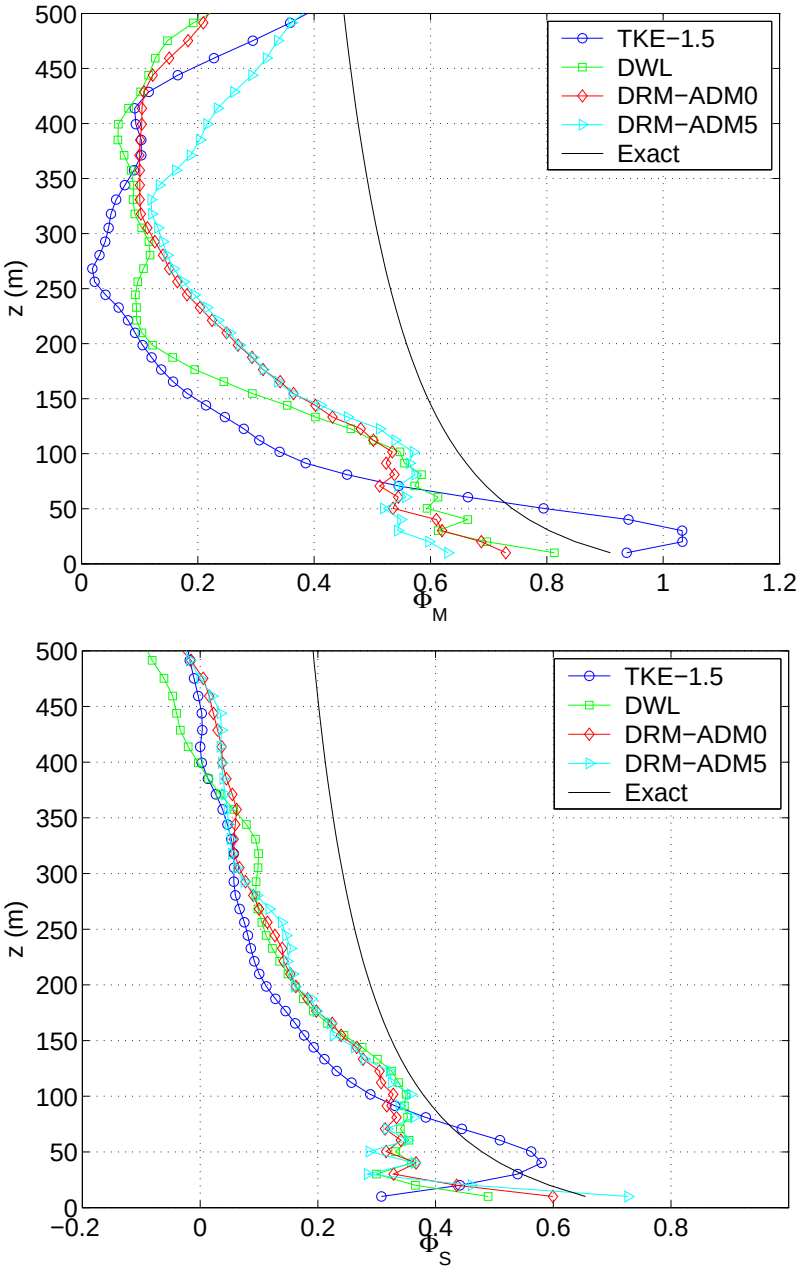

Figure F.3: Similarity functions Φ_M (top) and Φ_S (bottom) at 10000 s.

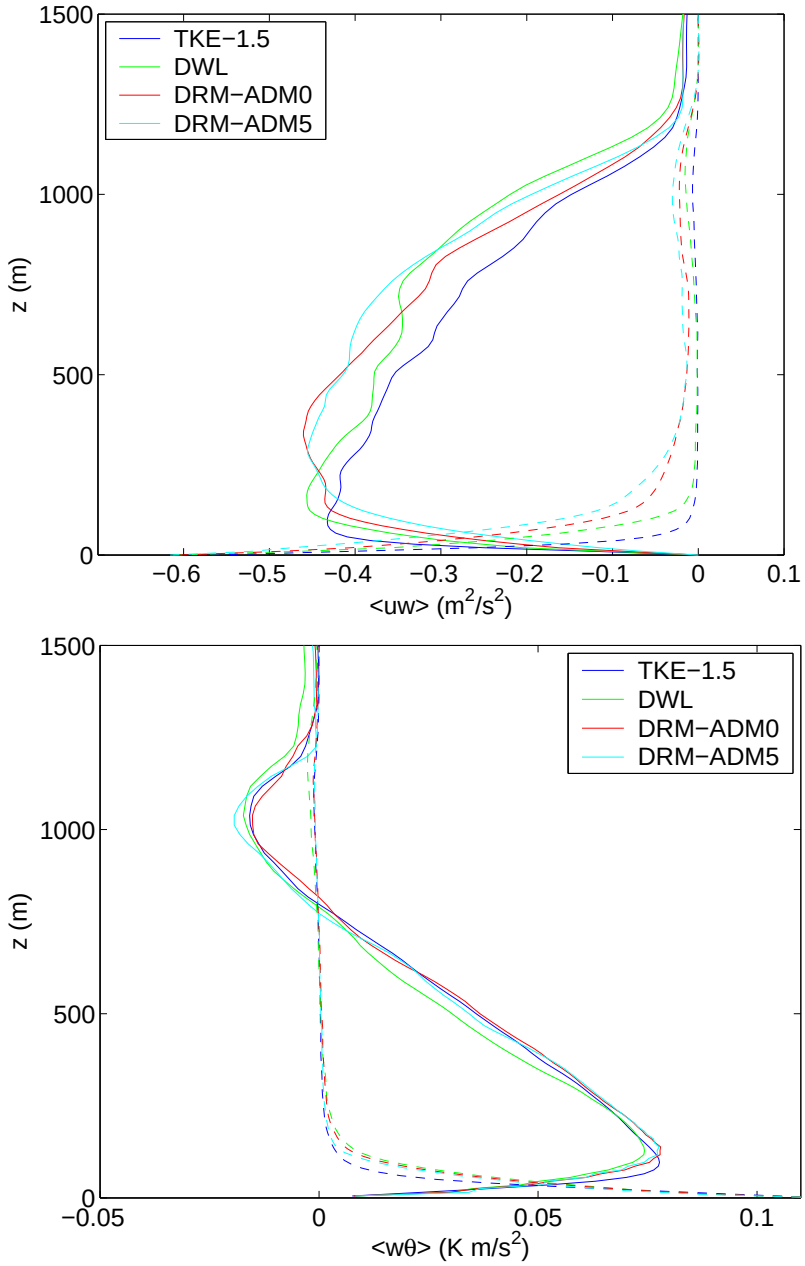

Figure F.4: Resolved (solid) and subgrid (dashed) uw stresses (top) and heat fluxes (bottom) $w\theta$ at 10000 s.

Appendix G

Computational cost

The CPU and memory requirements for the Riviera Valley simulations using ARPS are presented here. These calculations were performed as part of a proposal for computation time at NCAR's Scientific Computing Division. Based on a sample simulation, the total CPU time per timestep per grid point is calculated to be approximately 2×10^{-5} s. We then multiply by the total grid points for a new grid and the total number of timesteps for a 30 hour simulation period to obtain a total CPU time. Estimated values for a complete set of runs are shown in Table G.1.

A rough estimate of the memory used by ARPS is given by nx*ny*nz*284. Accordingly, for a 99x99x50 grid, we require about 140 MB of memory. For a fine grid of 160x160x160, this is about 140MB per processor if 8 processors are used. It is expected that this estimate will vary when different model components are used (e.g. radiation and moisture model components). A few examples are given below.

The ARPS code has been fine-tuned by the research team at the University of Oklahoma for maximum vectorization and parallelization. For example, all expensive power and exponential functions use lookup tables. In addition, we use the MASS library (Mathematical Acceleration Subsystem), available on `bluesky` to further speed up the code by about 3-5%.

The MPI version of the ARPS code has been tested on various machine architectures, and has good scalability. For example, on a single 250 MHz R12000 processor on an NCSA Origin 2000, ARPS performed at 110 megaflops for a 19x19x53 grid size. Using 256 processors on the Origin 2000, ARPS sustained rates of 22 gigaflops, giving a scalability rating of 73%. Simulations of flow over complex terrain similar to

Run	$\Delta t/\Delta\tau$(s)	Grid size	NP	Wall clock	Node res.	CPU hrs
riv9km	10/10	(103,103,53)	16	6 220 s	99 520 s	26.8
riv3km	2/4	(103,103,53)	16	26 325 s	421 200 s	116.0
riv1km	1/1	(99,99,63)	32	71 760 s	1 148 160 s	312.4
riv350m	1/0.2	(83,83,63)	16	59 010 s	944 160 s	259.3
*riv150m	1/0.1	(83,83,83)	32	38 872 s	1 243 900 s	345.5
*riv50m	0.5/0.05	(163,163,123)	64	222 170 s	14 219 000 s	3949.6

Table G.1: List of simulations and computational cost. * indicates estimated costs. Assume 8 processors/node. Node reserved time is wall-clock time multiplied by the number of processors (NP) and is roughly equivalent to CPU hours.

ours have also been performed with ARPS on the IBM Power 3 `seaborg` at NERSC. Using a grid of (243,243,80), the code achieved 11.8 Gflops for 64 processors or 185 Mflops/processor. The memory requirement was a total of 3.8 GB, or 61 MB per processor. These are significantly faster computations than previously achieved with ARPS, due in large part to the power of the IBM SP machine.

On `bluesky`, a 350 m resolution run for the Riviera valley with (83,83,63) grid points runs well on 16 processors. The performance of the `bluesky` simulations was measured using the IBM HPM utilities which gave about 11.5 Gflops or 359 Mflops/processor, and a memory use of 1.4 GB, or 44 MB/processor. Further data on the performance of ARPS are given at

`ftp://ftp.caps.ou.edu/pub/ARPS/ARPS.docs/ARPS4DOC.PDF/arpsch11.pdf`.

References

Adams, N. A. 1999 Advances in direct deconvolution modeling of subgrid-scales for flows with discontinuities. *Proceedings of the Summer Program, Center for Turbulence Research, NASA Ames – Stanford University* pp. 317 – 327.

Aldama, A. A. 1990 *Filtering techniques for turbulent flow simulation*. Berlin: Springer-Verlag.

Allen, T. & Brown, A. R. 2002 Large-eddy simulation of turbulent separated flow over rough hills. *Boundary-Layer Meteorology* **102** (2), 177 – 198.

Andren, A. 1995 The structure of stably stratified atmospheric boundary-layers - a large-eddy simulation study. *Quarterly Journal of the Royal Meteorological Society* **121** (525), 961 – 985.

Andren, A., Brown, A. R., Graf, J., Mason, P. J., Moeng, C.-H., Nieuwstadt, F. T. M. & Schumann, U. 1994 Large-eddy simulation of a neutrally stratified boundary layer: A comparison of four computer codes. *Q. J. R. Meteorol. Soc.* **120**, 1457–1484.

Anquetin, S., Guilbaud, C. & Chollet, J. P. 1998 The formation and destruction of inversion layers within a deep valley. *Journal of Applied Meteorology* **37** (12), 1547–60.

Baggett, J. S. 1998 On the feasibility of merging LES with RANS for the near-wall region of attached turbulent flows. *Annual Research Briefs, Center for Turbulence Research, NASA Ames – Stanford University* pp. 267–277.

Baggett, J. S., Jimenez, J. & Kravchenko, A. G. 1997 Resolution requirements in large-eddy simulations of shear flows. *Annual Research Briefs, Center for Turbulence Research, NASA Ames – Stanford University* pp. 51–66.

Baines, P. G. 1995 *Topographic effects in stratified flows*. Cambridge: Cambridge University Press.

Balaras, E., Benocci, C. & Piomelli, U. 1995 Finite-difference computations of high Reynolds number flows using the dynamic subgrid-scale model. *Theoretical and Computational Fluid Dynamics* **7** (3), 207–16.

Balsara, D. S. & Shu, C.-W. 2000 Monotonicity preserving weighted essentially non-oscillatory schemes with increasingly high order of accuracy. *Journal of Computational Physics* **160**, 405–452.

Banta, R. M. & Gannon, P. T. 1995 Influence of soil moisture on simulations of katabatic flow. *Theoretical and Applied Climatology* **52** (1/2), 85 – 94.

Bardina, J., Ferziger, J. H. & Reynolds, W. C. 1983 Improved turbulence models based on large eddy simulation of homogeneous, incompressible, turbulent flows. Technical Report TF-19. Department of Mechanical Engineering, Stanford University, Stanford, California.

Barr, S. & Orgill, M. M. 1989 Influence of external meteorology on nocturnal valley drainage winds. *Journal of Applied Meteorology* **28** (6), 497 – 517.

Benoit, R., Schär, C., Binder, P., Chamberland, S., Davies, H. C., Desgagne, M., Girard, C., Keil, C., Kouwen, N., Luthi, D., Maric, D., Muller, E., Pellerin, P., Schmidli, J., Schubiger, F., Schwierz, C., Sprenger, M., Walser, A., Willemse, S., Yu, W. & Zala, E. 2002 The real-time ultrafinescale forecast support during the Special Observing Period of the MAP. *Bulletin of the American Meteorological Society* **83** (1), 85 – 109.

Besio, S., Mazzino, A. & Ratto, C. F. 2003 Local log-law-of-the-wall in neutrally-stratified boundary-layer flows. *Boundary-Layer Meteorology* **107** (1), 115 – 42.

Blackadar, A. K. & Tennekes, H. 1968 Asymptotic similarity in neutral barotropic planetary boundary layers. *Journal of the Atmospheric Sciences* **25**, 1015–1020.

Blaisdell, G. A., Spyropoulos, E. T. & Qin, J. H. 1996 The effect of the formulation of nonlinear terms on aliasing errors in spectral methods. *Applied Numerical Mathematics* **21** (3), 207–219.

Blumberg, A. F., Galperin, B. & O'Connor, D. J. 1992 Modeling vertical structure of open-channel flows. *Journal of Hydraulic Engineering-ASCE* **118** (8), 1119 – 1134.

Bougeault, P., Binder, P., Buzzi, A., Dirks, R., Houze, R., Kuettner, J., Smith, R. B., Steinacker, R. & Volkert, H. 2001 The MAP special observing period. *Bulletin of the American Meteorological Society* **82** (3), 433 – 62.

Bradley, E. F. 1980 An experimental study of the profiles of wind speed, shearing stress and turbulence at the crest of a large hill. *Quarterly Journal of the Royal Meteorological Society* **106** (447), 101 – 23.

Brown, A. R., Hobson, J. M. & Wood, N. 2001 Large-eddy simulation of neutral turbulent flow over rough sinusoidal ridges. *Boundary-Layer Meteorology* **98** (3), 411–441.

Businger, J. A., Wyngaard, J. C., Izumi, Y. & Bradley, E. F. 1971 Flux-profile relationships in the atmospheric surface layer. *Journal of the Atmospheric Sciences* **28**, 181–189.

BUWAL 2002 Umleitung Gotthard 2001: Auswirkung der Verkehrsverlagerung auf die Luft- und Lärmbelastung in den Kantonen Graubünden, Tessin und Uri. Technical report. Bundesamt für Umwelt, Wald und Landschaft (BUWAL), und Kantonale Umweltschutzämter Graubünden, Tessin und Uri.

Byun, D. W. 1990 On the analytical solutions of flux-profile relationships for the atmospheric surface layer. *Journal of Applied Meteorology* **29**, 652–657.

Cabot, W. 1995 Large-eddy simulations with wall models. *Annual Research Briefs, Center for Turbulence Research, NASA Ames – Stanford University* pp. 41–50.

Cabot, W., Baggett, J. S. & Jimenez, J. 1999 On wakes and near-wall behavior in coarse large-eddy simulation of channel flow with wall models and second-order finite-difference methods. *Annual Research Briefs, Center for Turbulence Research, NASA Ames – Stanford University* pp. 343–354.

Cabot, W. & Moin, P. 2000 Approximate wall boundary conditions in the large-eddy simulation of high Reynolds number flow. *Flow, Turbulence and Combustion* **63** (1/4), 269 – 91.

Calhoun, R. J. 1998 Numerical investigations of turbulent flow over complex terrain. PhD dissertation, Stanford University.

Carati, D., Winckelmans, G. S. & Jeanmart, H. 2001 On the modelling of the subgrid-scale and filtered-scale stress tensors in large-eddy simulation. *Journal of Fluid Mechanics* **441**, 119–138.

Carlotti, P. 2002 Two-point properties of atmospheric turbulence very close to the ground: Comparison of a high resolution LES with theoretical models. *Boundary-Layer Meteorology* **104** (3), 381–410.

Castro, F. A., Palma, J. M. L. M. & Lopes, A. S. 2003 Simulation of the Askervein flow. Part 1: Reynolds averaged Navier-Stokes equations (k-epsilon turbulence model). *Boundary-Layer Meteorology* **107** (3), 501 – 530.

Cederwall, R. T. 2001 Large-eddy simulation of the evolving stable boundary layer over flat terrain. PhD dissertation, Stanford University.

Cederwall, R. T. & Street, R. L. 1999 Turbulence modification in the evolving stable boundary layer: a large-eddy simulation. *13th Symposium on Boundary Layers and Turbulence, American Meteorological Society* pp. 223–226.

Changnon, S. D. 2003 Measures of economic impacts of weather extremes - getting better but far from what is needed - a call for action. *Bulletin of the American Meteorological Society* **84** (9), 1231 – 1235.

Chow, F. K. & Moin, P. 2003 A further study of numerical errors in large-eddy simulations. *Journal of Computational Physics* **184** (2), 366 – 380.

Chow, F. K. & Street, R. L. 2002 Modeling unresolved motions in LES of field-scale flows. *15th Symposium on Boundary Layers and Turbulence, American Meteorological Society* pp. 432–435.

Chow, F. K. & Street, R. L. 2004*a* Evaluation of turbulence models for large-eddy simulations of flow over askervein hill. Paper 7.11. *16th Symposium on Boundary Layers and Turbulence, American Meteorological Society* .

Chow, F. K. & Street, R. L. 2004*b* Explicit filtering and reconstruction turbulence modeling for large-eddy simulations of field-scale flows. *Sixth International Conference on Hydro-Science and Engineering* .

Chow, F. K., Street, R. L., Xue, M. & Ferziger, J. H. 2004*a* Explicit filtering and reconstruction turbulence modeling for large-eddy simulation of neutral boundary layer flow. *Journal of the Atmospheric Sciences* **submitted**.

Chow, F. K., Weigel, A. P., Street, R. L., Rotach, M. W. & Xue, M. 2004*b* High-resolution large-eddy simulations of the Riviera Valley: methodology and sensitivity studies. Paper 6.2. *11th Conference on Mountain Meteorology, American Meteorological Society* .

van Cittert, P. 1931 Zum Einfluß der Spaltbreite auf die Intensitätsverteilung in Spektrallinien II. *Zeitschrift für Physik* **69**, 298–308.

Clark, R. A., Ferziger, J. H. & Reynolds, W. C. 1977 Evaluation of subgrid-scale turbulence models using a fully simulated turbulent flow. Technical Report TF-9. Department of Mechanical Engineering, Stanford University, Stanford, California.

Clark, R. A., Ferziger, J. H. & Reynolds, W. C. 1979 Evaluation of subgrid-scale models using an accurately simulated turbulent-flow. *Journal of Fluid Mechanics* **91**, 1–16.

Coleman, G. N. 1999 Similarity statistics from a direct numerical simulation of the neutrally stratified planetary boundary layer. *Journal of the Atmospheric Sciences* **56** (6), 891 – 900.

Colette, A., Chow, F. K. & Street, R. L. 2003 A numerical study of inversion-layer breakup and the effects of topographic shading in idealized valleys. *Journal of Applied Meteorology* **42** (9), 1255 – 1272.

Conzemius, R. & Fedorovich, E. 2002 Dynamics of convective entrainment in a heterogeneously stratified atmosphere with wind shear. *15th Symposium on Boundary Layers and Turbulence, American Meteorological Society* pp. 31–34.

Cui, A. 1999 On the parallel computation of turbulent rotating stratified flows. PhD dissertation, Stanford University.

Davies, J. T. 1972 *Turbulence phenomena; an introduction to the eddy transfer of momentum, mass, and heat, particularly at interfaces*. New York: Academic Press.

De Wekker, S. 2002 Structure and morphology of the convective boundary layer in mountainous terrain. PhD dissertation, University of British Columbia.

De Wekker, S., Steyn, D. G., Fast, J. D., Rotach, M. W. & Zhong, S. 2004 The performance of RAMS in representing the convective boundary layer structure in a very steep valley. *Environmental Fluid Mechanics* **in press**.

Deardorff, J. W. 1970 A numerical study of three-dimensional turbulent channel flow at large Reynolds numbers. *Journal of Fluid Mechanics* **41** (2), 453–480.

Deardorff, J. W. 1971 On the magnitude of the subgrid scale eddy coefficient. *Journal of Computational Physics* **7**, 120 – 33.

Deardorff, J. W. 1972 Parameterization of the planetary boundary layer for use in general circulation models. *Monthly Weather Review* **100**, 93–106.

Deardorff, J. W. 1980 Stratocumulus-capped mixed layers derived from a 3-dimensional model. *Boundary-Layer Meteorology* **18** (4), 495 – 527.

Ding, F., Arya, S. P. & Lin, Y.-L. 2001 Large-eddy simulations of the atmospheric boundary layer using a new subgrid-scale model. Part I: Slightly unstable and neutral cases. *Environmental Fluid Mechanics* **1**, 29–47.

Ding, L. 2000 Personal communication.

Ding, L. 2002 Simulation of stratified flow over three-dimensional topography. PhD dissertation, Stanford University.

Domaradzki, J. A. & Adams, N. A. 2002 Direct modelling of subgrid scales of turbulence in large eddy simulations - art. no. 024. *Journal of Turbulence* **3**.

Domaradzki, J. A. & Loh, K.-C. 1999 The subgrid-scale estimation model in the physical space representation. *Physics of Fluids* **11** (8), 2330–2342.

Domaradzki, J. A. & Saiki, E. M. 1997 A subgrid-scale model based on the estimation of unresolved scales of turbulence. *Physics of Fluids* **9** (7), 2148–2164.

Dubrulle, B., Laval, J. P., Sullivan, P. P. & Werne, J. 2002 A new dynamical subgrid model for the planetary surface layer. Part I: The model and a priori tests. *Journal of the Atmospheric Sciences* **59** (4), 861 – 876.

Dukowicz, J. K. & Dvinsky, A. S. 1992 Approximate factorization as a high-order splitting for the implicit incompressible-flow equations. *Journal of Computational Physics* **102** (2), 336–347.

Dutton, J. A. 2002 Opportunities and priorities in a new era for weather and climate services. *Bulletin of the American Meteorological Society* **83** (9), 1303 – 1311.

Esau, I. 2004 Simulation of Ekman boundary layers by large eddy model with dynamic mixed subfilter closure. *Environmental Fluid Mechanics* **4** (3), 273 – 303.

Fedorovich, E., Conzemius, R., Esau, I., Chow, F. K., Lewellen, D., Moeng, C.-H., Sullivan, P., Pino, D. & Vilà-Guerau de Arellano, J. 2004 Entrainment into sheared convective boundary layers as predicted by different large eddy simulation codes. Paper P4.7. *16th Symposium on Boundary Layers and Turbulence, American Meteorological Society* .

Ferziger, J. 2000 Personal communication.

Fiedler, B. 1998 Dynamical equations in the ARPS and COAMPS coordinate system. Research summary. University of Oklahoma.

Garratt, J. R. 1992 *The atmospheric boundary layer*. New York: Cambridge University Press.

Germano, M. 1996 A statistical formulation of the dynamic model. *Physics of Fluids* **8** (2), 565 – 70.

Germano, M., Piomelli, U., Moin, P. & Cabot, W. H. 1991 A dynamic subgrid-scale eddy viscosity model. *Physics of Fluids* **3** (7), 1760–1765.

Geurts, B. J. 1997 Inverse modeling for large-eddy simulation. *Physics of Fluids* **9** (12), 3585–3587.

Ghosal, S. 1996 An analysis of numerical errors in large-eddy simulations of turbulence. *Journal of Computational Physics* **125**, 187–206.

Ghosal, S., Lund, T. S., Moin, P. & Akselvoll, K. 1995 A dynamic localization model for large-eddy simulation of turbulent flows. *Journal of Fluid Mechanics* **286**, 229–255.

Ghosal, S. & Moin, P. 1995 The basic equations for the large eddy simulation of turbulent flows in complex geometry. *Journal of Computational Physics* **118**, 24–37.

Glendening, J. W. & Haack, T. 2001 Influence of advection differencing error upon large-eddy simulation accuracy. *Boundary-Layer Meteorology* **98** (1), 127–153.

Gohm, A., Zängl, G. & Mayr, G. J. 2004 South foehn in the Wipp Valley on 24 October 1999 (MAP IOP 10): Verification of high-resolution numerical simulations with observations. *Monthly Weather Review* **132** (1), 78 – 102.

Grell, G. A., Emeis, S., Stockwell, W. R., Schoenemeyer, T., Forkel, R., Michalakes, J., Knoche, R. & Seidl, W. 2000 Application of a multiscale, coupled MM5/chemistry model to the complex terrain of the VOTALP valley campaign. *Atmospheric Environment* **34** (9), 1435 – 1453.

Gronas, S. & Sandvik, A. D. 1999 Numerical simulations of local winds over steep orography in the storm over north Norway on October 12, 1996. *Journal of Geophysical Research* **104** (D8), 9107–20.

Gullbrand, J. 2000 An evaluation of a conservative fourth order DNS code in turbulent channel flow. *Annual Research Briefs, Center for Turbulence Research, NASA Ames – Stanford University* pp. 211–218.

Gullbrand, J. 2001 Explicit filtering and subgrid-scale models in turbulent channel flow. *Annual Research Briefs, Center for Turbulence Research, NASA Ames – Stanford University* pp. 31–43.

Gullbrand, J. & Chow, F. K. 2003 The effect of numerical errors and turbulence models in large-eddy simulations of channel flow, with and without explicit filtering. *Journal of Fluid Mechanics* **495**, 323 – 341.

Haltiner, G. J. 1971 *Numerical weather prediction*. New York: John Wiley and Sons, Inc.

Hanna, S. R. & Yang, R. X. 2001 Evaluations of mesoscale models' simulations of near-surface winds, temperature gradients, and mixing depths. *Journal of Applied Meteorology* **40** (6), 1095 – 104.

Hinze, J. O. 1975 *Turbulence*, 2nd edn. New York: McGraw-Hill.

Hughes, T. J. R., Mazzei, L., Oberai, A. A. & Wray, A. A. 2001*a* The multiscale formulation of large eddy simulation: Decay of homogeneous isotropic turbulence. *Physics of Fluids* **13** (2), 505–512.

Hughes, T. J. R., Oberai, A. A. & Mazzei, L. 2001*b* Large eddy simulation of turbulent channel flows by the variational multiscale method. *Physics of Fluids* **13** (6), 1784–1799.

Iizuka, S. & Kondo, H. 2003 Large eddy simulations of turbulent flow over complex terrain. *Proceedings of the 11th International Conference on Wind Engineering* pp. 2689–2696.

Iliescu, T. & Fischer, P. F. 2003 Large eddy simulation of turbulent channel flows by the rational large eddy simulation model. *Physics of Fluids* **15** (10), 3036 – 3047.

Jacobson, M. Z. 1998 *Fundamentals of Atmospheric Modeling*. Cambridge: Cambridge University Press.

Jacobson, M. Z. 2001 GATOR-GCMM - 2. A study of daytime and nighttime ozone layers aloft, ozone in national parks, and weather during the SARMAP field campaign. *Journal of Geophysical Research* **106** (D6), 5403 – 5420.

Jasper, K. 2001 Hydrological modelling of Alpine river catchments using output variables from atmospheric models. PhD dissertation, ETH No. 14385, Swiss Federal Institute of Technology, Zurich.

Jasper, K., Schulla, J., Gurtz, J. & Lang, H. 2004 The hydrological model system WaSiM-ETH. Part II: Model validation. *Hydrologic Science Journal, IAHS Press* **submitted**.

Jeanmart, H. & Winckelmans, G. S. 2002 Comparison of recent dynamic subgrid-scale models in the case of the turbulent channel flow. *Proceedings of the Summer Program, Center for Turbulence Research, NASA Ames – Stanford University* pp. 105–116.

Jordan, S. A. 1999 A large-eddy simulation methodology in generalized curvilinear coordinates. *Journal of Computational Physics* **148** (2), 322 – 340.

Juneja, A. & Brasseur, J. G. 1999 Characteristics of subgrid-resolved-scale dynamics in anistropic turbulence, with application to rough-wall boundary layers. *Physics of Fluids* **11** (10), 3054–3068.

Kaltenbach, H.-J. 1998 Towards a near-wall model for LES of a separated diffuser flow. *Annual Research Briefs, Center for Turbulence Research, NASA Ames – Stanford University* pp. 255–265.

Kaltenbach, H.-J. 2003 A priori testing of wall models for separated flows. *Physics of Fluids* **15** (10), 3048 – 3064.

Katopodes, F. V., Street, R. L. & Ferziger, J. H. 2000*a* Subfilter-scale scalar transport for large-eddy simulation. *14th Symposium on Boundary Layers and Turbulence, American Meteorological Society* pp. 472–475.

Katopodes, F. V., Street, R. L. & Ferziger, J. H. 2000*b* A theory for the subfilter-scale model in large-eddy simulation. Technical Report 2000-K1. Environmental Fluid Mechanics Laboratory, Stanford University.

Khanna, S. & Brasseur, J. G. 1998 Three-dimensional buoyancy- and shear-induced local structure of the atmospheric boundary layer. *Journal of the Atmospheric Sciences* **55** (5), 710–43.

Kim, H. G. & Patel, V. C. 2000 Test of turbulence models for wind flow over terrain with separation and recirculation. *Boundary-Layer Meteorology* **94** (1), 5 – 21.

Klemp, J. B. & Durran, D. R. 1983 An upper boundary condition permitting internal gravity wave radiation in numerical mesoscale models. *Monthly Weather Review* **111** (3), 430–44.

Klemp, J. B. & Wilhelmson, R. B. 1978 The simulation of three-dimensional convective storm dynamics. *Journal of the Atmospheric Sciences* **35**, 1070–1096.

Kosović, B. 1997 Subgrid-scale modelling for the large-eddy simulation of high-Reynolds-number boundary layers. *Journal of Fluid Mechanics* **336**, 151–182.

Kravchenko, A. G. & Moin, P. 1997 On the effect of numerical errors in large eddy simulations of turbulent flows. *Journal of Computational Physics* **131** (2), 310–322.

Kravchenko, A. G., Moin, P. & Moser, R. 1996 Zonal embedded grids for numerical simulations of wall-bounded turbulent flows. *Journal of Computational Physics* **127** (2), 412–423.

Kreyszig, E. 1993 *Advanced engineering mathematics*, 7th edn. New York: Wiley and Sons.

Lavery, T. F., Bass, A., Strimaitis, D. G., Venkatram, A., Greene, B. R., Drivas, P. J. & Egan, B. A. 1982 EPA complex terrain model development: First milestone report - 1981. EPA-600/3-82-036. Environmental Protection Agency.

Lele, S. K. 1992 Compact finite difference schemes with spectral-like resolution. *Journal of Computational Physics* **103**, 16–42.

Leonard, A. 1974 Energy cascade in large eddy simulations of turbulent fluid flows. *Advances in Geophysics* **18A**, 237–248.

Leonard, A. 1997 Large-eddy simulation of chaotic convection and beyond. *AIAA Paper 97-0204* pp. 1–8.

Lesieur, M. & Métais, O. 1996 New trends in large-eddy simulations of turbulence. *Annual Review of Fluid Mechanics* **28**, 45–82.

Lilly, D. K. 1962 On the numerical simulation of buoyant convection. *Tellus* **14** (2), 148–172.

Lilly, D. K. 1992 A proposed modification of the Germano subgrid-scale closure method. *Physics of Fluids* **4** (3), 633–635.

Liu, S., Meneveau, C. & Katz, J. 1994 On the properties of similarity subgrid-scale models as deduced from measurements in a turbulent jet. *Journal of Fluid Mechanics* **275**, 83–119.

Love, M. D. 1980 Subgrid modeling studies with Burgers-equation. *Journal of Fluid Mechanics* **100**, 87–110.

Lu, R. & Turco, R. P. 1995 Air pollutant transport in a coastal environment – II. three-dimensional simulations over Los Angeles basin. *Atmospheric Environment* **29** (13), 1499 – 1518.

Lund, T. S. 1997 On the use of discrete filters for large eddy simulation. *Annual Research Briefs, Center for Turbulence Research, NASA Ames – Stanford University* pp. 83–95.

Lund, T. S. & Kaltenbach, H.-J. 1995 Experiments with explicit filtering for LES using a finite-difference method. *Annual Research Briefs, Center for Turbulence Research, NASA Ames – Stanford University* pp. 91–105.

Mahrer, Y. 1984 An improved numerical approximation of the horizontal gradients in a terrain-following coordinate system. *Monthly Weather Review* **112** (5), 918 – 22.

Mason, P. J. & King, J. C. 1985 Measurements and predictions of flow and turbulence over an isolated hill of moderate slope. *Quarterly Journal of the Royal Meteorological Society* **111** (468), 617 – 40.

Mason, P. J. & Thomson, D. J. 1992 Stochastic backscatter in large-eddy simulations of boundary layers. *Journal of Fluid Mechanics* **242**, 51–78.

Matzinger, N., Andretta, M., Gorsel, E. V., Vogt, R., Ohmura, A. & Rotach, M. W. 2003 Surface radiation budget in an Alpine valley. *Quarterly Journal of the Royal Meteorological Society* **129** (588), 877 – 895.

McKee, T. B. & O'Neal, R. D. 1989 The role of valley geometry and energy budget in the formation of nocturnal valley winds. *Journal of Applied Meteorology* **28** (6), 445 – 56.

Meneveau, C. & Katz, J. 2000 Scale-invariance and turbulence models for large-eddy simulation. *Annual Review of Fluid Mechanics* **32**, 1 – 32.

Moeng, C.-H. 1984 A large-eddy-simulation model for the study of planetary boundary-layer turbulence. *Journal of the Atmospheric Sciences* **41** (13), 2052–2062.

Moin, P. 2001 *Fundamentals of engineering numerical analysis*. Cambridge University Press.

Morinishi, Y., Lund, T. S., Vasilyev, O. V. & Moin, P. 1998 Fully conservative higher order finite difference schemes for incompressible flow. *Journal of Computational Physics* **143**, 90–124.

Morinishi, Y. & Vasilyev, O. 1998 Subgrid scale modeling taking the numerical error into consideration. *Annual Research Briefs, Center for Turbulence Research, NASA Ames – Stanford University* pp. 237–253.

Moser, R. D., Kim, J. & Mansour, N. N. 1999 Direct numerical simulation of turbulent channel flow up to $Re_\tau = 590$. *Physics of Fluids* **11** (4), 943–945.

Najjar, F. M. & Tafti, D. K. 1996 Study of discrete test filters and finite difference approximations for the dynamic subgrid-scale stress model. *Physics of Fluids* **8** (4), 1076–1088.

Nakayama, A. & Sakio, K. 2002 Simulation of flows over wavy rough boundaries. *Annual Research Briefs, Center for Turbulence Research, NASA Ames – Stanford University* pp. 313–324.

Nicoud, F., Baggett, J. S., Moin, P. & Cabot, W. 2001 Large eddy simulation wall-modeling based on suboptimal control theory and linear stochastic estimation. *Physics of Fluids* **13** (10), 2968 – 84.

Noilhan, J. & Planton, S. 1989 A simple parameterization of land surface processes for meteorological models. *Monthly Weather Review* **117** (3), 536 – 49.

Nutter, P., Stensrud, D. & Xue, M. 2002 Effects of nesting frequency and lateral boundary perturbations on the dispersion of limited-area ensemble forecasts. Paper P11.3. *15th Conference on Numerical Weather Prediction and 19th Conference on Weather Analysis, American Meteorological Society* .

Ookouchi, Y., Segal, M., Kessler, R. C. & Pielke, R. A. 1984 Evaluation of soil moisture effects on the generation and modification of mesoscale circulations. *Monthly Weather Review* **112** (11), 2281 – 92.

Orlanski, I. 1975 Rational subdivision of scales for atmospheric processes. *Bulletin of the American Meteorological Society* **56** (5), 527–530.

Patton, E. G., Davis, K. J., Barth, M. C. & Sullivan, P. P. 2001 Decaying scalars emitted by a forest canopy: a numerical study. *Boundary-layer Meteorology* **100** (1), 91 – 129.

Perry, A. E., Henbest, S. & Chong, M. S. 1986 A theoretical and experimental-study of wall turbulence. *Journal of Fluid Mechanics* **165** (PR), 163 – 199.

Pielke, R. A. 1984 *Mesoscale meteorological modeling*. Orlando, FL: Academic Press.

Pielke, R. A., Cotton, W. R., Walko, R. L., Tremback, C. J., Lyons, W. A., Grasso, L. D., Nicholls, M. E., Moran, M. D., Wesley, D. A., Lee, T. J. & Copeland, J. H. 1992 A comprehensive meteorological modeling system – RAMS. *Meteorology and Atmospheric Physics* **49**, 69–91.

Piomelli, U. 1999 Large-eddy simulation: achievements and challenges. *Progress in Aerospace Science* **35** (4), 335–362.

Piomelli, U. & Balaras, E. 2002 Wall-layer models for large-eddy simulations. *Annual Review of Fluid Mechanics* **34**, 349 – 374.

Piomelli, U., Moin, P. & Ferziger, J. H. 1988 Model consistency in large eddy simulation of turbulent channel flows. *Physics of Fluids* **31** (7), 1884–91.

Pope, S. B. 2000 *Turbulent flows*. Cambridge, UK: Cambridge University Press.

Porté-Agel, F., Meneveau, C. & Parlange, M. B. 2000 A scale-dependent dynamic model for large-eddy simulation: application to a neutral atmospheric boundary layer. *Journal of Fluid Mechanics* **415**, 261–284.

Porté-Agel, F., Parlange, M. B., Meneveau, C. & Eichinger, W. E. 2001 A priori field study of the subgrid-scale heat fluxes and dissipation in the atmospheric surface layer. *Journal of the Atmospheric Sciences* **58** (18), 2673–2698.

Poulos, G. 1999 The interaction of katabatic winds and mountain waves. PhD dissertation, Colorado State University.

Press, W. H., Teukolsky, S. A., Vetterling, W. T. & Flannery, B. P. 1992 *Numerical Recipes in Fortran 77: The art of scientific computing. Vol. 1*. Cambridge, U.K.: Cambridge University Press.

Pruett, C. D. & Adams, N. A. 2000 *A priori* analyses of three subgrid-scale models for one-parameter families of filters. *Physics of Fluids* **12** (5), 1133–1142.

Raithby, G. D., Stubley, G. D. & Taylor, P. A. 1987 The Askervein Hill project: a finite control volume prediction of three-dimensional flows over the hill. *Boundary-Layer Meteorology* **39** (3), 247 – 67.

Rampanelli, G., Zardi, D. & Rotunno, R. 2004 Mechanisms of up-valley winds. *Journal of the Atmospheric Sciences* **submitted**.

Rao, P. A., Fuelberg, H. E. & Droegemeier, K. K. 1999 High-resolution modeling of the Cape Canaveral area land-water circulations and associated features. *Monthly Weather Review* **127** (8), 1808–1821.

Redelsperger, J. L., Mahe, F. & Carlotti, P. 2001 A simple and general subgrid model suitable both for surface layer and free-stream turbulence. *Boundary-Layer Meteorology* **101** (3), 375 – 408.

Revell, M. J., Purnell, D. & Lauren, M. K. 1996 Requirements for large-eddy simulation of surface wind gusts in a mountain valley. *Boundary-Layer Meteorology* **80** (4), 333–53.

Rotach, M. W., Calanca, P., Graziani, G., Gurtz, J., Steyn, D. G., Vogt, R., Andretta, M., Christen, A., Cieslik, S., Conolly, R., De Wekker, S., Galmarini, S., Kadygrov, E. N., Kadygrov, V., Miller, E., Neininger, B., Rucker, M., Van Gorsel, E., Weber, H., Weiss, A. & Zappa, M. 2004 Turbulence structure and exchange processes in an Alpine valley: The Riviera project. *Bulletin of the American Meteorological Society* **in press**.

Salmon, J. R., Teunissen, H. W., Mickle, R. E. & Taylor, P. A. 1988 The Kettles Hill project: field observations, wind-tunnel simulations and numerical model predictions for flow over a low hill. *Boundary-Layer Meteorology* **43** (4), 309 – 43.

Salvetti, M. V. & Banerjee, S. 1995 *A priori* tests of a new dynamic subgrid-scale model for finite-difference large-eddy simulations. *Physics of Fluids* **7** (11), 2831–2847.

Salvetti, M. V., Zang, Y., Street, R. & Banerjee, S. 1997 Large-eddy simulation of free-surface decaying turbulence with dynamic subgrid-scale models. *Physics of Fluids* **9** (8), 2405–2419.

Sarghini, F., Piomelli, U. & Balaras, E. 1999 Scale-similar models for large-eddy simulations. *Physics of Fluids* **11** (6), 1596–1607.

Schulla, J., Jasper, K., Gurtz, J. & Lang, H. 2004 The hydrological model system WaSiM-ETH. Part I: Theoretical basis. *Hydrologic Science Journal, IAHS Press* **submitted**.

Shah, K. B. 1997 Implementation of a new subgrid scale model in generalized coordinates. Research summary. Stanford University.

Shah, K. B. 1998 Large eddy simulations of flow past a cubic obstacle. PhD dissertation, Stanford University.

Shah, K. B. & Ferziger, J. H. 1995 A new non-eddy viscosity subgrid-scale model and its application to channel flow. *Annual Research Briefs, Center for Turbulence Research, NASA Ames – Stanford University* pp. 73–90.

Shaw, R. H. & Schumann, U. 1992 Large-eddy simulation of turbulent-flow above and within a forest. *Boundary-Layer Meteorology* **61** (1-2), 47 – 64.

Shih, L. H., Koseff, J. R., Ferziger, J. H. & Rehmann, C. R. 2000 Scaling and parameterization of stratified homogeneous turbulent shear flow. *Journal of Fluid Mechanics* **412**, 1–20.

Smagorinsky, J. 1963 General circulation experiments with the primitive equations. *Monthly Weather Review* **91**, 99–152.

Spalart, P. R., Moser, R. D. & Rogers, M. M. 1991 Spectral methods for the Navier-Stokes equations with one infinite and two periodic directions. *Journal of Computational Physics* **96** (2), 297–324.

Speziale, C. G. 1985 Galilean invariance of subgrid-scale stress models in the large-eddy simulation of turbulence. *Journal of Fluid Mechanics* **156**, 55–62.

Steinacker, R. 1984 Area-height distribution of a valley and its relation to the valley wind. *Contributions to Atmospheric Physics* **57** (1), 64 – 71.

Stolz, S. & Adams, N. A. 1999 An approximate deconvolution procedure for large-eddy simulation. *Physics of Fluids* **11** (7), 1699–1701.

Stolz, S., Adams, N. A. & Kleiser, L. 1999*a* Analysis of subgrid scales and subgrid scale modeling for shock-boundary-layer interaction. *First International Symposium on Turbulence and Shear Flow Phenomena* pp. 881–886.

Stolz, S., Adams, N. A. & Kleiser, L. 1999*b* The approximate deconvolution model applied to LES of turbulent channel flow. In *Direct and Large-Eddy Simulation III* (ed. Sandham, Voke & Kleiser). Kluwer.

Stolz, S., Adams, N. A. & Kleiser, L. 2001*a* An approximate deconvolution model for large-eddy simulation with application to incompressible wall-bounded flows. *Physics of Fluids* **13** (4), 997–1015.

Stolz, S., Adams, N. A. & Kleiser, L. 2001*b* The approximate deconvolution model for large-eddy simulations of compressible flows and its application to shock-turbulent-boundary-layer interaction. *Physics of Fluids* **13** (10), 2985–3001.

Street, R. L. 1999 Setting the stage: Large eddy simulation of laboratory scale flows. *Second International Symposium on Environmental Hydraulics* pp. 277–286.

Strimaitis, D. G., Venkatram, A., Greene, B. R., Hanna, S., Heisler, S., Lavery, T. F., Bass, A. & Egan, B. A. 1982 EPA complex terrain model development: Second milestone report - 1982. EPA-600/3-83-015. Environmental Protection Agency.

Stull, R. B. 1988 *An introduction to boundary layer meteorology*. Boston: Kluwer Academic Publishers.

Sullivan, P. P., Horst, T. W., Lenschow, D. H., Moeng, C. H. & Weil, J. C. 2003 Structure of subfilter-scale fluxes in the atmospheric surface layer with application to large-eddy simulation modelling. *Journal of Fluid Mechanics* **482**, 101 – 139.

Sullivan, P. P., McWilliams, J. C. & Moeng, C.-H. 1994 A subgrid-scale model for large-eddy simulation of planetary boundary-layer flows. *Boundary-Layer Meteorology* **71** (3), 247–76.

Takemi, T. & Rotunno, R. 2003 The effects of subgrid model mixing and numerical filtering in simulations of mesoscale cloud systems. *Monthly Weather Review* **131** (9), 2085 – 2101.

Taylor, P. A. & Teunissen, H. W. 1985 The Askervein Hill project: Report on the September/October 1983 main field experiment. Report MSRB-84-6. Atmospheric Environment Service, Downsview, Ontario.

Taylor, P. A. & Teunissen, H. W. 1987 The Askervein Hill project: overview and background data. *Boundary-Layer Meteorology* **39** (1/2), 15 – 39.

Tsubokura, M. 2001 Proper representation of the subgrid-scale eddy viscosity for the dynamic procedure in large eddy simulation using finite difference method. *Physics of Fluids* **13** (2), 500–504.

Vasilyev, O. V. 2000 High order finite difference schemes on non-uniform meshes with good conservation properties. *Journal of Computational Physics* **157** (2), 746–761.

Vasilyev, O. V., Lund, T. S. & Moin, P. 1998 A general class of commutative filters for LES in complex geometries. *Journal of Computational Physics* **146** (1), 82–104.

Volkert, H. 1990 An Alpine orography resolving major valleys and massifs. *Meteorology and Atmospheric Physics* **43** (1/4), 231 – 4.

Vreman, A. W. 2003 The filtering analog of the variational multiscale method in large-eddy simulation. *Physics of Fluids* **15** (8), L61 – L64.

Vreman, B., Geurts, B. & Kuerten, H. 1994 On the formulation of the dynamic mixed subgrid-scale model. *Physics of Fluids* **6** (12), 4057 – 4059.

Vreman, B., Geurts, B. & Kuerten, H. 1996 Large-eddy simulation of the temporal mixing layer using the Clark model. *Theoretical and Computational Fluid Dynamics* **8**, 309–324.

Walmsley, J. L. & Taylor, P. A. 1996 Boundary-layer flow over topography: impacts of the Askervein study. *Boundary-Layer Meteorology* **78** (3/4), 291 – 320.

Wang, M. & Moin, P. 2002 Dynamic wall modeling for large-eddy simulation of complex turbulent flows. *Physics of Fluids* **14** (7), 2043–2051.

Warner, T. T., Peterson, R. A. & Treadon, R. E. 1997 A tutorial on lateral boundary conditions as a basic and potentially serious limitation to regional numerical weather prediction. *Bulletin of the American Meteorological Society* **78** (11), 2599 – 617.

Weigel, A. P., Chow, F. K., Rotach, M. W. & Street, R. L. 2004*a* Assessment of large-eddy simulations of the atmospheric boundary layer in a steep and narrow Alpine valley. *Geophysical Research Abstracts* **6**, EGU04–A–03496.

Weigel, A. P., Chow, F. K., Rotach, M. W., Street, R. L. & Xue, M. 2004*b* High-resolution large-eddy simulations of the Riviera Valley: assessment of the flow structure and the heat and moisture budgets. Paper 6.4. *11th Conference on Mountain Meteorology, American Meteorological Society* .

Weigel, A. P. & Rotach, M. W. 2004 Flow structure and turbulence characteristics of the daytime atmosphere in a steep and narrow Alpine valley. *Quarterly Journal of the Royal Meteorological Society* **in press**.

Whiteman, C. D. 1982 Breakup of temperature inversions in deep mountain valleys. I. Observations. *Journal of Applied Meteorology* **21** (3), 270 – 89.

Whiteman, C. D. 2000 *Mountain meteorology: fundamentals and applications*. New York: Oxford University Press.

Winckelmans, G. S. & Jeanmart, H. 2001 Assessment of some models for LES without/with explicit filtering. In *Direct and Large-Eddy Simulation IV* (ed. Geurts, Friedrich & Métais), pp. 55–66. Kluwer.

Winckelmans, G. S., Jeanmart, H. & Carati, D. 2002 On the comparison of turbulence intensities from large-eddy simulation with those from experiment or direct numerical simulation. *Physics of Fluids* **14** (5), 1809–1811.

Winckelmans, G. S., Wray, A. A., Vasilyev, O. V. & Jeanmart, H. 2001 Explicit-filtering large-eddy simulation using the tensor-diffusivity model supplemented by a dynamic smagorinsky term. *Physics of Fluids* **13** (5), 1385–1403.

Wong, V. C. & Lilly, D. K. 1994 A comparison of two dynamic subgrid closure methods for turbulent thermal-convection. *Physics of Fluids* **6** (2), 1016 – 1023.

Wyngaard, J. C., Peltier, L. J. & Khanna, S. 1998 LES in the surface layer: Surface fluxes, scaling, and SGS modeling. *Journal of the Atmospheric Sciences* **55** (10), 1733–1754.

Xiu, A. J. & Pleim, J. E. 2001 Development of a land surface model. Part I: Application in a mesoscale meteorological model. *Journal of Applied Meteorology* **40** (2), 192 – 209.

Xu, Q., Xue, M. & Droegemeier, K. K. 1996 Numerical simulations of density currents in sheared environments within a vertically confined channel. *Journal of the Atmospheric Sciences* **53** (5), 770–786.

Xue, M., Droegemeier, K. K. & Wong, V. 2000 The Advanced Regional Prediction System (ARPS): A multi-scale nonhydrostatic atmospheric simulation and prediction model. Part I: Model dynamics and verification. *Meteorology and Atmospheric Physics* **75** (3-4), 161–193.

Xue, M., Droegemeier, K. K., Wong, V., Shapiro, A. & Brewster, K. 1995 *ARPS Version 4.0 User's Guide*. University of Oklahoma, Norman, OK: Center for Analysis and Prediction of Storms.

Xue, M., Droegemeier, K. K., Wong, V., Shapiro, A., Brewster, K., Carr, F., Weber, D., Liu, Y. & Wang, D. 2001 The Advanced Regional Prediction System (ARPS): A multi-scale nonhydrostatic atmospheric simulation and prediction tool. Part II: Model physics and applications. *Meteorology and Atmospheric Physics* **76** (3-4), 143–165.

Xue, M., Wang, D., Gao, J., Brewster, K. & Droegemeier, K. K. 2003 The Advanced Regional Prediction System (ARPS), storm-scale numerical weather

prediction and data assimilation. *Meteorology and Atmospheric Physics* **82** (1/4), 139 – 70.

Yamada, T. & Mellor, G. 1975 A simulation of the Wangara atmospheric boundary layer data. *Journal of the Atmospheric Sciences* **32** (12), 2309 – 29.

Yeo, W. K. & Bedford, K. W. 1988 Closure-free turbulence modeling based upon a conjunctive higher order averaging procedure. In *Computational methods in flow analysis* (ed. Niki & Kawahara), pp. 844–851. Okayama University of Science, Okayama.

Zang, T. 1991 On the rotation and skew-symmetric forms for incompressible flow simulations. *Applied Numerical Mathematics* **7**, 27–40.

Zang, Y. 1993 On the development of tools for the simulation of geophysical flows. PhD dissertation, Stanford University.

Zang, Y., Street, R. L. & Koseff, J. R. 1993 A dynamic mixed subgrid-scale model and its application to turbulent recirculating flows. *Physics of Fluids* **5** (12), 3186–3196.

Zang, Y., Street, R. L. & Koseff, J. R. 1994 A non-staggered grid, fractional step method for time dependent incompressible Navier-Stokes equations in curvilinear coordinates. *Journal of Computational Physics* **114** (1), 18–33.

Zängl, G., Chimani, B. & Haberli, C. 2004 Numerical simulations of the foehn in the Rhine Valley on 24 October 1999 (MAP IOP 10). *Monthly Weather Review* **132** (1), 368 – 389.

Zappa, M. & Gurtz, J. 2003 Simulation of soil moisture and evapotranspiration in a soil profile during the 1999 MAP-Riviera campaign. *Hydrology and Earth System Sciences* **7** (6), 903–919.

Zedler, E. 2002 Large eddy simulation of sediment transport in oscillatory flow over wavy terrain. PhD dissertation, Stanford University.

Zhong, S. Y. & Fast, J. 2003 An evaluation of the MM5, RAMS, and Meso-Eta models at subkilometer resolution using VTMX field campaign data in the Salt Lake Valley. *Monthly Weather Review* **131** (7), 1301 – 1322.

Zhou, Y., Brasseur, J. G. & Juneja, A. 2001 A resolvable subfilter-scale model specific to large-eddy simulation of under-resolved turbulence. *Physics of Fluids* **13** (9), 2602–2610.